CRANFIELD UNIVERSITY

MIKOLAJ LUKASZEWICZ

STEAM OXIDATION OF ADVANCED HIGH TEMPERATURE RESISTANT ALLOYS FOR ULTRA-SUPERCRITICAL APPLICATIONS

SCHOOL OF APPLIED SCIENCES

PhD

Academic Year: 2009 - 2012

Supervisor: Dr Nigel Simms and Prof John Nicholls
June 2012

CRANFIELD UNIVERSITY

SCHOOL OF APPLIED SCIENCES

PhD

Academic Year 2009 - 2012

MIKOLAJ LUKASZEWICZ

STEAM OXIDATION OF ADVANCED HIGH TEMPERATURE RESISTANT ALLOYS FOR ULTRA-SUPERCRITICAL APPLICATIONS

Supervisor: Dr Nigel Simms and Prof John Nicholls
June 2012

This thesis is submitted in partial fulfilment of the requirements for the degree of PhD

© Cranfield University 2012. All rights reserved. No part of this publication may be reproduced without the written permission of the copyright owner.

ABSTRACT

Steam oxidation of heat exchanger tubing is of growing interest as increasing the efficiencies of conventional pulverised fuel fired power plants requires higher steam temperatures and pressures. These new, more severe steam conditions result in faster steam oxidation reactions, which can significantly reduce the lifetime of boiler components. This thesis reports results from an investigation of the steam oxidation of the high temperature resistant alloys. It covers an analysis of the impact of temperature, steam flow rate, specimen shape and specimen surface finish on oxidation of resistant materials. Additionally, the mechanism of steam oxidation was invastigated with the oxygen 18 water. The results show that an increased steam flow rate not only causes faster oxidation rates but also a change in oxide scale morphology. In case of T23, it triggers formation of micro-layered inner oxide, whereas for T92 it promotes the formation of an outer haematite layer. For austenitic steels, the faster steam flow increases the formation of initially protective oxide scales, but also accelerates the growth of oxide nodules with prolonged exposure times. The analysis of the different surface finishes show that clearly the change of the surface finish from ground to polish and pickled (as received) accelerates the oxidation process for austenitic steels, the ground specimens show the slowest oxidation, whereas the pickled specimens oxidise much faster and form thicker scales. Finally, the study of oxidation mechanism show that steam oxidation is not only controlled by the inner diffusion of the oxygen ions but the diffusion of the hydroxides have a significant impact on oxides formation. The results of the study suggest that the hydroxide ions influence formation of the inner oxides.

ACKNOWLEDGEMENTS

I would like to express my gratitude to Dr Nigel Simms and Prof. John Nicholls for their guidance and moral support of my research. I also thank to Dr Tomasz Dudziak and Dr Tanvir Hussain.

My special thanks are offered to technical staff at Cranfield University; Dr Matthew Kershaw, Mr Peter West and Mr Andrew Dayer.

I would finally like to express my deepest gratitude to my whole family and friends for their moral support during my time in cranfield.

Last, but not least I wish to express my greates thanks to my girfriend Aleksandra for her undestanding, support and love, without them my time in Cranfield would be much less interesting and definitelly not so happy.

I would like to dedicate this thesis to my father Jan Lukaszewicz, who i will always love and try to make him proud of who I am.

TABLE OF CONTENTS

LIST OF FIGURES

LIST OF TABLES

LIST OF EQUATIONS

1 INTRODUCTION

1.1 Project background

Since the industrial revolution, world energy demands have grown rapidly [1, 2, 3, 4] with the main sources of electricity being conventional power pants of which ~ 40% are coal-fired units % [2, 3, 5]. There are a variety of coal-fired power plant designs, which have different operating conditions and thus have different energy generation efficiencies [6, 7, 8, 9]. Power plant efficiency is a strong function of the steam temperature and pressure, which is explained thermodynamically by the Carnot cycle (ideal cycle) [10]. Since the efficiency of the Carnot cycle is defined as $(T_{max}-T_{min})/T_{max}$, where T_{max} is a maximum temperature in the thermodynamic cycle and T_{min} is minimum temperature, the most practical way to increase efficiency is to increase the maximum steam temperature [10, 11, 12].

Currently, most of the coal-fired power plants operate with steam at temperatures between 540-565°C and pressures up to 24.3 MPa, which allows efficiencies of 38-40%. In newly designed units the efficiency of energy generation is above 40% due to higher steam conditions (600-620°C) [6, 13]. The most efficient power plants, which are currently being developed, are expected to have 44 - 46% efficiency with following steam conditions: 700-720°C and 36.5-38.5 MPa [13, 14].

To generate energy from the steam more efficiently, there is a need to identify high temperature resistant alloys, which are able to withstand more severe steam conditions [15, 16, 17]. The R&D goal for new high-temperature resistance materials for Ultra Supercritical (USC) applications is to develop alloys, which could be used in the temperature in range of 650-810°C [18]. The more detail goals are listed below with the steam temperature as follows [19]:

- European COST-522 – 650°C;
- European Thermie program – 700°C;
- The Japanese national program - 650°C;
- US Department of Energy's Vision 21 - 760°C; and

- European FP7 NEXTGENPOWER - 760°C.

Alloys for such applications must have good high temperature oxidation resistance [20, 21], good thermal conductivity [22] and at the same time good creep resistance [15]. Moreover, good weldability [22]; fabricability [21]; and ability to be coated [17] are considered as the important factors. The severity of the higher steam conditions (temperatures and pressures) increases the steamside and fireside oxidation kinetics (oxidation rates) that results in thicker scale formation, faster metal loss and more extensive scales spallation [23, 24]. In consequence, the heat transfer within the boiler would be changed and tubes would overheat locally (24). All these factors have an impact on the boiler lifetime, power plant operations and performance [25, 26, 27]. To mitigate those problems extensive research into high temperature steam oxidation is needed, with special consideration of temperature, time, alloy type, material composition and steam conditions (flow rates) [19, 24]. There has been some research conducted for the ferritic and austenitic steels in the temperature range 550-650°C, [23, 24, 28, 29, 30] and nickel-based alloys in the temperature between 700-800°C [23, 24]. However such tests do not consider the impact of following variables: specimen geometry, steam flow and surface pre-treatment.

1.2 Aim and Objectives

This PhD is an integrated part of the EPSRC SUPERGEN PLE project, which is focused on extending the lifetime of coal-fired power plants. This PhD was targeted at improving the understanding of high temperature steam oxidation and its prediction under more severe operating conditions. It aimed to deliver a detail analysis of steam oxidation that involved understanding the processes controlling it. From academic view point novel topic includes the impact of specimen geometry and steam flow rates. In addition the impact of different surface treatments of austenitic steels (T347HFG and Super 304H) were studied. The industrial aim was to deliver a model predicting the performance of particular alloy types under selected steam conditions, to assist evaluating the potential lifetimes of components formed from these alloys.

These academic and industrial aims have been combined to established common objectives:

1. Investigation of the impact of the specimen geometry, steam flow and temperature on steam oxidation in the temperature between 600 and 750°C
2. Analysis of steam oxidation kinetics and morphological changes of the tested alloys to determine:
    - Mass change development with time;
    - Thickness change development with time;
    - Metal loss development with time; and
    - Voids formation and their development with time.
3. Analysis of seven different alloys selected from three particular alloy groups used for boiler tubing:
    - Ferritic steels: T23 (2.25 wt% Cr) and T92 (9 wt% Cr);
    - Austenitic steels: T347HFG (18 wt% Cr), Super304H (18 wt% Cr) and HR3C (25 wt% Cr);
    - Nickel-based alloys: Inconel 740 (25 wt% Cr); and
    - 800H (25Cr-32.5Ni-46Fe) alloy to fulfil gap between iron-base and nickel-base alloys.
4. Evaluation of the impact of the different specimen surface finishes on the steam oxidation of austenitic steels (ground, polished, as received),
5. Identification of the mechanisms controlling the steam oxidation with use of the marker of oxygen 18,
6. Development of the heat transfer model of the steam tube; and
7. Identification of an empirical (statistical) model predicting the lifetime of materials used for the USC steam tubing.

2 LITERATURE REVIEW

2.1 Introduction to coal-fired power plant technology

2.1.1 Introduction

The fast world development is increasing energy demand [2], which is rising on average around two percent per annum [2, 31]. Electricity is an important form of the energy and is essential for the operation of many industries and therefore for economic development [2, 4]. The main source of the electricity generated is coal-fired power plants with 40% of the overall generation [2, 32, 33]. The increased energy demands in the 20th century have driven the development of large-scale power plants [8, 32, 33]. Other reasons for the development of such system were lower initial costs, higher reliability and efficiency of the power supply and lower energy losses. The design of modern combustion power plants means that all the processes are contained together in energy block; it involves interaction between the steam generators, steam turbine and auxiliary installations. The continuous development of such power plant designs led to the size of the energy blocks used today with maximum capacities around 1,100-1,300MW and the steam conditions of 600 - 620°C for both live and reheater steam and pressure between 250 – 300 bar [33]. Changes in the steam conditions were resulted in the progressively higher efficiencies of the coal-fired plant (Figure 2-1).

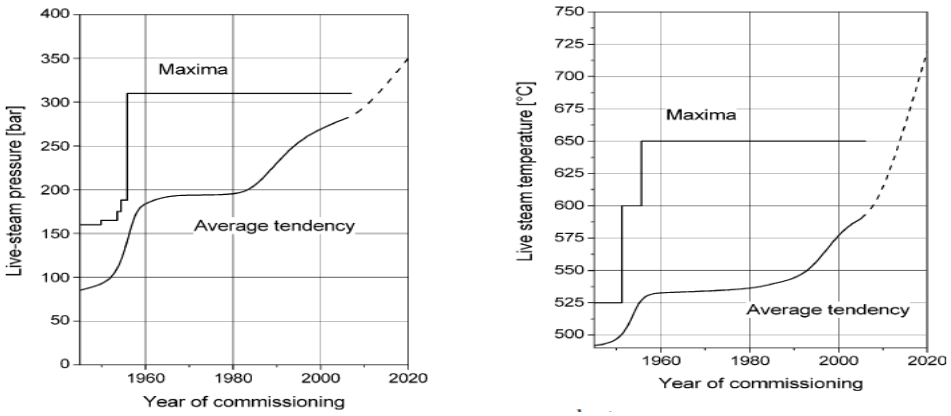

Figure 2-1 Changes in the live steam parameter in the coal-fired power plants [32]

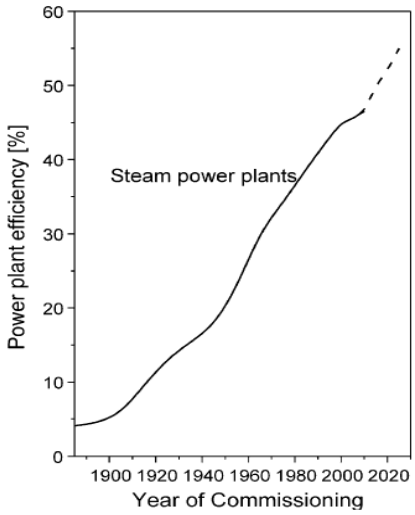

Figure 2-2 Change in the efficiency of the pulverised coal-fired power plant [32]

2.1.2 Pulverised coal-fired power plant design

Currently most of the coal-fired plants operate within sub-critical and supercritical steam a condition, which allows efficiencies of 38-39% and 40-41% respectively [32]. Figure 2-3 show the diagram of a typical pulverised coal-fired power plant design.

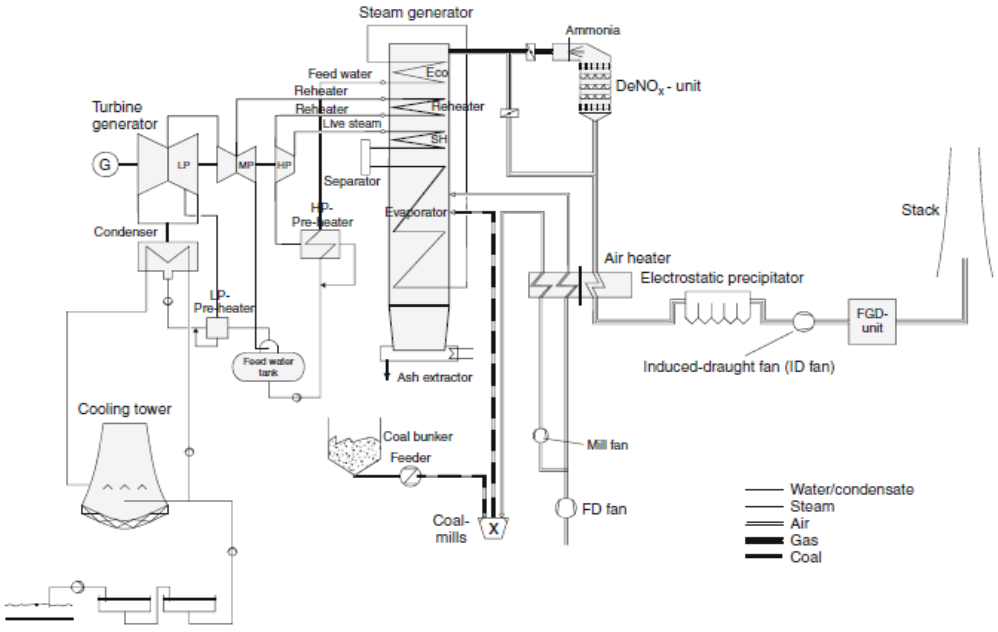

Figure 2-3 Schematic diagram of the pulverised coal-fired power plant [32]

In the typical pulverised fuel power plant (Figure 2-3), the coal pulverised in mills at a rate adjusted according to the requirements of the firing [32]. The furnace is fired up with use of the hot air (350-400°C). The pulverised coal is transported to the burners by pre-heated air, which is us as a primary air in the combustion process [8]. Complete combustion is achieved as a result of the injection of secondary air into the furnace. Inside the furnace coal burns producing radiation heat that is transported to the furnace walls; it gives flame temperatures around 1,400-1,600°C. In the combustion process the gas flow within the furnace increases ~ 10 times (volumetric value); however, travelling through the cooling path it decreases to the primary input volume. The furnace walls form the evaporating heating surface, which vaporise the feed water. At the end of the furnace the flue gas has cooled down to around 1,200-1,300°C. Flue gas cooling continues by the convective heating surfaces of the superheater (SH), reheater (RH) and feed water preheater (economiser) [8].

In the steam generator the energy of the hot, post-combustion gases is transferred to the steam and the enthalpy of the steam changes into the mechanical work in the turbines.

The steam from the turbines exhaust, condensates into water inside the condenser. The steam-water cycle is the most critical parameter in the overall power plant design [32]. The thermodynamics of this cycle is crucial in determining the configuration of steam generation, the steam turbine and finally the power plant efficiency [9, 32]. The condensate is transported by the pumps to the feed water tanks then through the low-pressure preheaters, which are heated by the steam coming from the low-pressure turbine [32]. Inside the tanks, the water is preheated and degassed by the steam. The high-pressure feed water pump sets up the operating pressure of the feed water inside the water-steam section of the boiler; additionally it transports the feed water to the boiler inlet via the high-pressure preheaters. Those preheater are heated up using the steam from the upper stages of the HP turbine. Inside the preheater the extraction steam cools down condenses and is drained back into the condensate or feed water flow before the preheater [32]. According to Spliethoff

[32] higher temperature of the feed water in the preheating stage is, the higher boiling temperature have to be. The final water preheating stage, before boiler is fed with steam, uses steam taken from the reheater or high-pressure turbine (it is dependent on the plant design).

Inside the boiler, the feed water is heated up in the economiser, which is the last convective heating surface in the path of the gas, and then is fed to the evaporator. Following this the steam is heated up in the superheater to the exit temperature (live steam temperature). However, the entry temperature of the steam coming to the turbine is slightly lower due to the heat losses in the connection of the high-pressure steam piping. After initial expansion in HP turbine, in most power plant designs the steam is heated back to a similar level to the live steam temperature in the reheater. Higher temperatures are possible inside the reheater due to the steam lower pressures. Finally, in the condenser the steam from the LP turbine exhaust condenses; the waste heat generated in the process is transported to the cooling water circuit. The water circuit is closed system, which in most of the cases is equipped with the cooling tower.

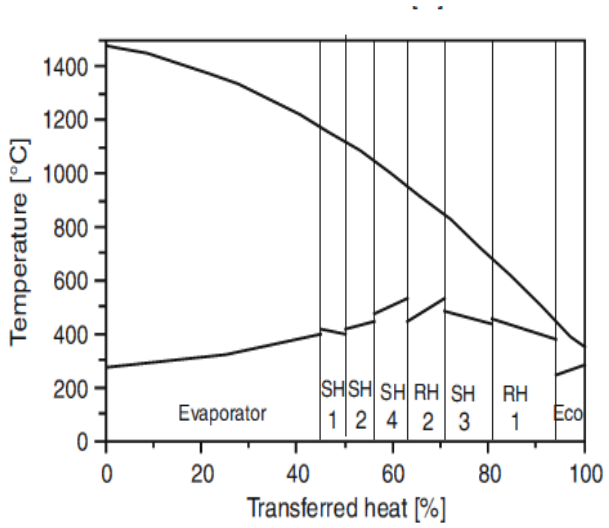

Figure 2-4 Heat transfer and flue gas temperature in the following section of the coal-fired boiler [32]

2.1.3 Importance of the super-heater and reheater

The roles of the super-heater and reheater in the power plant are essential for achieving high efficiency of the energy generation [8, 32, 34]. The SH and RH are used to heat up the steam to the turbine inlet temperatures of HP and IP turbines respectively. In general, the convective surfaces of the SH and RH consist of number of the parallel tubes in the cross-flow arrangement against the hot gas flow. The convection heat transfer applies heat to the whole tube circumference, thus the heat transfer banks are small [35]. The heat transfer in the SH/RH depends firstly on the flue gas velocity and secondly on the process temperature gradient (differences) during the process. In order to have high transfer the tubes in the banks have to be mounted as close as possible to each other. However, the distance is limited due to the pressure loss of the flue gas and ash deposition [36]. The heating surfaces used for SH and RH are designed as hanging or horizontal tube bundles. In mainland Europe the single-pass construction is common; in such just the horizontal heating surfaces are used. In comparison, for two-pass constructions there are two types of the surfaces: hanging used in cross-pass for superheating or reheating and horizontal. The distance between the tubes (tube pitch) changes with the flue gas temperature and dust concentration within it; in this regard with the decreasing temperature and ash levels within the flue gas stream the tube pitch narrows [32].

The superheater and reheater are designed for high temperatures; thus only low differences in the temperature between different tubes are allowed due to the uneven flow through the tubes or imbalanced heating of the material. SH and RH have to be designed and constructed in manner to guarantee an even flow and counteract the impacts of imbalanced heating.

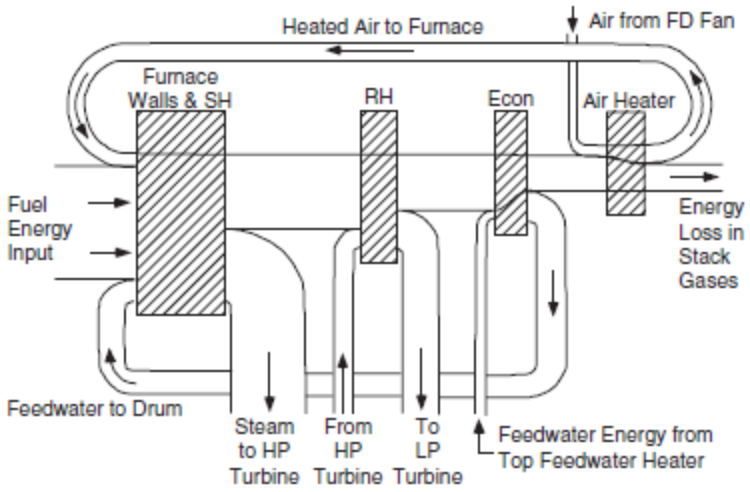

Figure 2-5 Steam generation energy flow [8]

2.1.4 Ultra supercritical (USC) power plant

Increasing electricity demands and fossil fuel prices are stimulating the electricity generation industry to build and commission more efficient power plants, which operate within the USC conditions [4]. Moreover, an increasing interest in USC technology is driven by environmental policy, energy market and government pressures. The interactions between those factors drive the technology innovation [37]. Figure 2-6 shows simplified model of technology innovation mechanism.

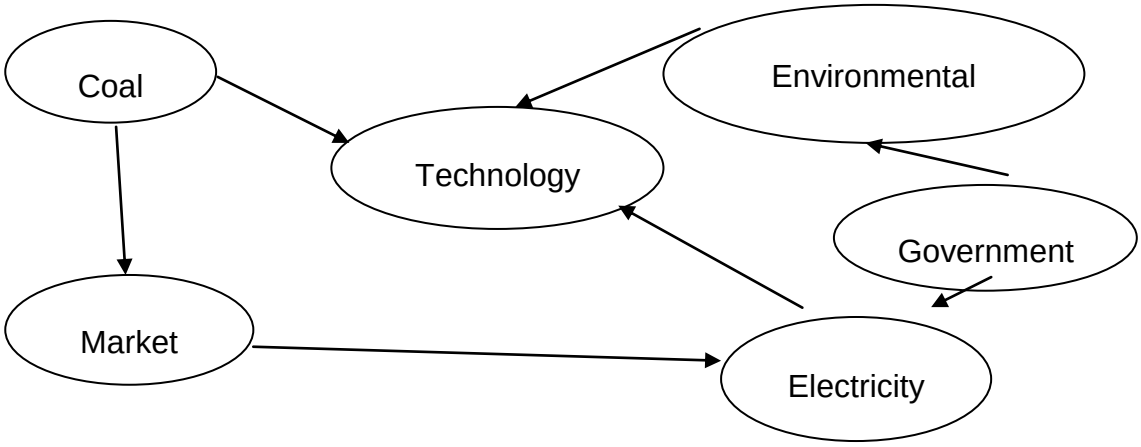

Figure 2-6 Simplified model of the Interactions between factors influencing the technology innovation [37]

Table 2-1 Change of the steam conditions and its impact on the power plant efficiency [37]

Unit type	SC	USC	USC	USC
Steam pressure [MPa]	24.1	31	31	34.5
Temperature [°C]	538/566	566/566/566	593/593/593	649/593/593
Efficiency [%]	40	42.8	43.1-43.3	43.7-44
Coal consumption [g/kWh]	300	287	284-285	279-291

There are a limited number of the operational USC power plants [37]. Foster Wheeler is one of the companies, which are currently designing USC units. This chapter describes the design of the 400MW circulating fluidized bed (CFB) USC unit [38]. The main parts of this boiler are fuel feed, sorbent feed, draft system, bottom as system, furnace hot loop, heat recovery area and start up burners. In such designed the hot flue gas from the boiler is directed to the heat recovery area (HRA) via the two, steam cooled ducts. The HRA consists of convection reheater and primary superheater, these are supported by steam-cooled tubing, and the economiser, which is positioned at the bottom of the HRA. The HRA is an important part of the steam/water circuitry [38].

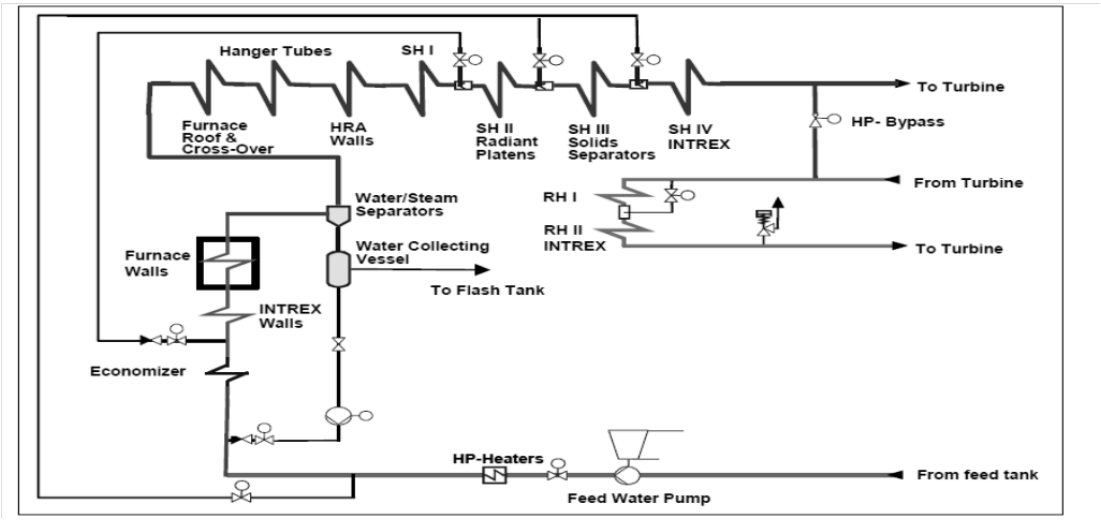

Figure 2-7 Diagram of steam/water circuitry of 400MW USC power plant [38]

This section focuses on the steam/water circuitry of the USC power plant; it aims to deliver basic information regarding the system and its constituent parts. Figure 2-7 presents the steam/water circuitry diagram of USC circulating fluidized bed power plant. Steam/water circuitry involves for major steps: preheat, evaporation, superheat and reheat.

The first part of the steam/water circuitry is preheat. In this, the preheated feed water enters the boiler via the economiser; from the economiser it is directed through a single transfer pipe into the walls of the fluidized bed to ensure a uniform water temperature. From this heat exchanger the heated water is transported to the common transfer line before it is distributed to the inlet headers of the furnace walls, such organisation of preheat ensures uniform fluid conditions. Surfacing of the economiser enclosure walls ensures the water entering the evaporation circuits is sub-cooled and single-phase.

In evaporator circuits the sub-cooled water is heated up inside the enclosure furnace walls and internal panels, before it reaches the top of the furnace the water is converted to superheated and dry steam. For steam to be superheated and dry the sufficient evaporation heat transfer surface has to be provided. Different qualities of fuel used can result in shift of the duty distribution between the hot loop and HRA, therefore an evaporator bypass is used. It allows accommodation of the range of fuel qualities due to fact that it can direct part of water to attemperator station upstream of the radian superheater (SH II), what ensures that steam leaving the evaporator circuitry is superheated. From the evaporator steam is transferred through pipes to the water/steam separators.

After separators, the steam is transported through the furnace roo and cross-over duct to heat recovery area (HRA). Then steam passes down through the HRA serpentine tube coil tubes, which transport water to the lower enclosure inlet header. From there the steam flows across the convection superheater (SH I), then steam is directed to panels of the radiant superheaters (SH II). The bottom of the SH II panels is covered with refractory, which protect

it against the erosion. Leaving the radiant superheater the steam is directed to compact solid separators (SH III) and finally the steam is transported to the four INTREX^{TM} superheaters positioned on the furnace sidewalls; in this stage, the final superheat is achieved. Subsequently, the superheated steam is transported to HP turbine and after expansion it is directed to reheater.

Steam is initially reheated in HRA in the upper and lower tube bundles of the first reheter (RH I). The reheater is designed in such matter that during full load operation part of the reheated steam is bypassed around the RH I to ensure the final reheat steam temperature. The fully reheated steam flows in parallel through four INTREX^{TM} heat exchangers. Reheated steam is transported to IP turbine.

To summarise, the superheater and re-heater are important parts of the boiler and their proper operation is essential for the high performance of the power generation process. To ensure the proper operation of SH/RH and their highest possible performance the steam inside the tubing has to be under high pressure and at high temperature, therefore such elements have to be manufactured from good high temperature resistant materials. These materials have to exhibit good steam oxidation resistance at high temperatures and so an understanding of their steam oxidation and its proper modelling, is essential for the selection of the optimum materials for SH/RH tubing materials in USC applications.

2.2 Introduction to heat transfer

Heat transfer is an important phenomenon used to study and to describe the mechanism of the energy transfer in form of heat [39, 40, 41]. It occurs between two or more objects as a result of a temperature gradient and proceeds from the body with higher temperature to the body with lower temperature until the temperature gradient is close to zero [42, 43]. There are three methods of heat transfer: conduction, convection and radiation [40, 43].

2.2.1 Conduction

Conduction is a type of heat transfer where energy is transfered through substance without the actual movements of the substance itself [41]. In this mode heat could be transfer through liquids, gasses as well as solids [42, 43]. In dense solids the conduction is the only method of heat transfer; it occurs as a result of the motion of free electrons, lattice waves, magnetic excitations, as well as the electromagnetic radiation; however for metals the free electron movement is the most important [39, 40] Heat transfer due to the movement of free electrons is only able to proceed only in good conductors, which have free electrons moving across the lattice in the way electricity is conducted. The conduction, is described and defined by the Fourier's Law of Heat Conduction; this states that the rate of heat transfer with respect to time is proportional to the negative temperature gradient and the area at right angles to the gradient across which heat flows. It could be expressed as follows [42, 43]:

$$\frac{q_x}{A} = -k\frac{dT}{dx} \qquad \textbf{(2-1)}$$

where q_x is a heat flow [W] in direction x, k is the thermal conductivity of material [W/m/K], whereas minus ensures the proper direction of decreasing temperature (it decreases with distance), A is area [m^2], dT/dx is the temperature gradient in direction x [K/m].

In engineering heat transfer, conduction often proceeds across materials with complex geometries [40] and with more than one layer. Therefore, a useful tool is an overall heat transfer coefficient, which combines the thermal conductivity of each material's layer and its specific thickness [39, 40, 43].

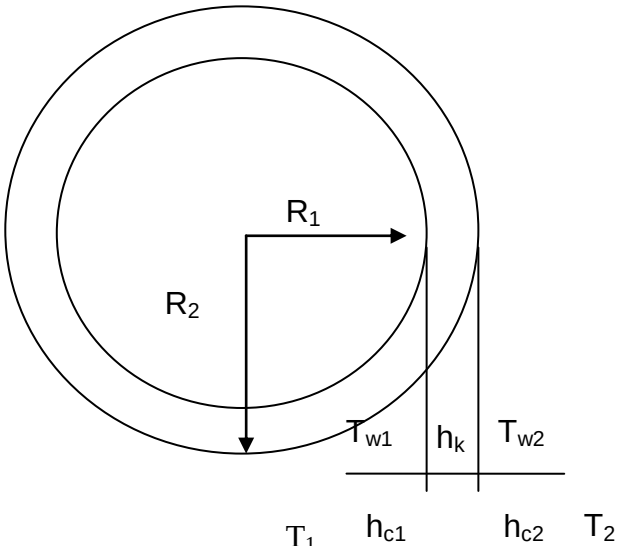

Figure 2-8 Heat transfer across cylinder wall

In case of the conduction in the cylinder, as in Figure 2-8 the heat transfer can be written as following [42]:

$$q_{conduction} = \frac{2\pi kL(T_{w1} - T_{w2})}{\ln(R_2/R_1)} \quad \textbf{(2-2)}$$

where $q_{conduction}$ is heat transfer [W], T is the temperature [K], R is radius [m] and k is conduction coefficient [W/m/K], L is length [m]

2.2.2 Convection

Convection is a mode of the heat transfer that proceeds due to the bulk movement of a fluid; thus fluid mechanics is a crucial subject to be understood for studying the convection phenomena [43]. There are two types of convection [40]:

- Forced when the flow of the fluid is caused by external driving force, which enhances the heat transfer
- Natural when a result of a thermally induced density gradient

Considering the heat transfer from the wall to fluid, the mechanism of heat transfer at the wall would be conduction due to that liquid velocity being zero, but it changes to convection with distance from wall surface [39, 40]. The rate of heat transfer varies with the angle between wall and temperature; the steeper

the angle the larger the temperature difference. Convection is proportional to the temperature difference and is written as the Newton's law of cooling [43]:

$$q_{convection} = h_c(T_w - T_\infty) \quad \textbf{(2-3)}$$

where h_C is the convection coefficient [W/m^2/K], T is temperature [K] (T_w is temperature of the wall T_∞ is temperature at infinitive distance perpendicular to the wall).

Derivation of the convection coefficient varies with types of convection and flow. In this particular study forced convection with turbulent flow is the subject of interest; therefore, the example of a pipe with an internal flow of gas (fully turbulent flow and forced convection) and external heat transfer along the surface between flue gas and tube wall (turbulent flow and force convection) is presented [40, 42, 43].

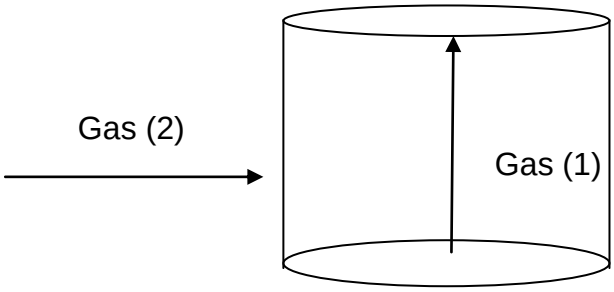

Figure 2-9 Graphical representation of studied case

For the fully developed turbulent flow inside the tube, the Nusselt number is expressed as [42]:

$$Nu_1 = 0.23(Re_1)^{0.8}(Pr_1)^{0.4} \quad \textbf{(2-4)}$$

where Re_1 and Pr_1 are the Reynolds and Prandt numbers inside the tube respectively. For the forced convection inside the tube, the Reynolds and Prandtl numbers are expressed as following [44]:

$$Re_1 = \frac{4\dot{m}_1}{\pi d \mu_1} \quad \textbf{(2-5)}$$

where m_1 is a mass flow rate of gas [kg/h], d is the inner diameter of the tube [m] and μ_1 is gas viscosity [kg/s/m]

$$Pr_1 = \frac{u_1 Cp_1}{k_1} \quad \textbf{(2-6)}$$

where Cp_1 and k_1 are the specific conductivity of the gas (1).
Finally, the convection coefficient for the gas inside the tube could be written as [44]:

$$h_1 = 0.023 \frac{k_1}{D} (Re)^{0.8} (Pr)^{0.4} \quad \textbf{(2-7)}$$

Considering the heat transfer across gas flowing on the outside of the tube and its surface the Nusselt number for the gas outside the tube is expressed as [42]:

$$Nu_2 = 0.46 (Re_2)^{0.6} (Pr_2)^{0.33} \quad \textbf{(2-8)}$$

where Prandtl and Reynolds numbers. Considering the gas outside the tube the Prandtl and Reynolds numbers are derived as follows:

$$Pr_2 = \frac{\mu_2 Cp_2}{k_2} \quad \textbf{(2-9)}$$

$$Re_2 = \frac{\rho_2 v L}{\mu_2} \quad \textbf{(2-10)}$$

where v is a velocity of the flowing gas [m/s]. Finally, the convection coefficient for the gas outside the tube is expressed as [42]:

$$h_1 = \frac{Nu_2 k_2}{D} \quad \textbf{(2-11)}$$

2.2.3 Radiation

Radiation is defined as the heat transfer resulting from electromagnetic radiation with a defined length of radiation waves [40]. Net heat transfer by radiation is a result of a temperature difference; however, it proceeds with or without a second body at another temperature [42, 43]. In order to define energy transfer by radiation, the surface or substance emitting radiation ideally

has to be introduced – it is known as a black body. The black body emits the energy at the rate proportional to the fourth power of its absolute temperature [39]:

$$q_{radiation} = \sigma A T^4 \quad \textbf{(2-12)}$$

where σ is the Stefan-Boltzmann constant [W/m^2/K^4]. However, the surfaces of the real materials do not emit energy by radiation ideally; therefore the idea of a grey body has been created, which is expressed by the introduction of a dimensionless emissivity factor (ε). Thus for a grey body equation (2-12) is written [39, 42, 43]:

$$q_{radiation} = \sigma \varepsilon A T^4 \quad \textbf{(2-13)}$$

It is crucial to recall that electromagnetic radiation travels in straight lines therefore, an additional factor (called the view factor) has been introduced [10, 39, 40]. It is a function of the geometry of the surface configuration, in general that factor is defined as the fraction of total energy that leaves one surface and arrives directly on the second surface (F≤1). Applying that factor to equation (2-13) the total heat transfer by radiation would be expressed [42]:

$$q_{radiation} = \sigma \varepsilon A_1 F_{1-2} ({T_1}^4 - T_2^4) \quad \textbf{(2-14)}$$

where $F_{1\text{-}2}$ is a view factor describing how surface 2 is viewed by surface 1.

2.2.4 Heat transfer across the tube

Heat transfer across the tube involves convection from the hot gas outside the tube (q_1), conduction across the tube itself (q_2) and finally convection to the gas inside the tube (q_3).

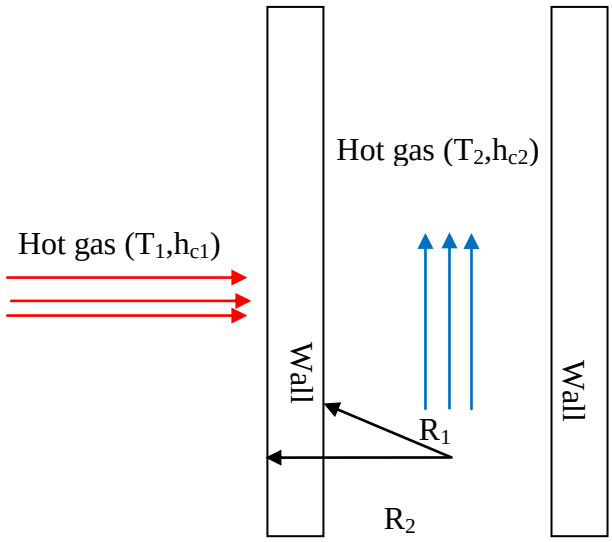

Figure 2-10 Heat transfer across the heat exchanger tube

Assuming that the heat transfer is constant ($\sum q = 0$) one equation describing the overall heat transfer can be derived:

$$q_1 = q_2 = q_3 \tag{2-15}$$

and finally could be expressed as:

$$q_1 + q_2 + q_3 = 0 \tag{2-16}$$

Considering the example of tube in which heat is transferred from the gas inside through the pipe to the gas outside thus the heat flow could be expressed as [42]:

$$q = \frac{2\pi L(T_{w1} - T_{w2})}{\frac{1}{h_{c1}R_1} + \frac{Ln(R_1/R_2)}{k} + \frac{1}{h_{c2}R_2}} \tag{2-17}$$

where h_{c1}, h_{c1} are convection coefficient for gas inside and outside of the tube [W/m/K], R_1, R_2 are inner and outer radius of the tube [m] and k is the conduction coefficient of the tube [W/m/K], L is the length of the tube [m].

For the power plant applications, the heat transfer across the heat exchangers includes also radiation from the hot gas side. In such case, the heat transfer outside the tube is a sum of heat transfer by convection and radiation, which can be written as following:

$$q_{total} = q_{radiation} + q_{convection} \quad \textbf{(2-18)}$$

$$q_{total} = \sigma \varepsilon A_1 F_{1-2}({T_1}^4 - T_2^4) + h_{c1} A_1 (T_1 - T_2) \quad \textbf{(2-19)}$$

Incorporation of the radiation into equation describing the heat transfer inside the heat exchanger tube results in change in the heat transfer (1 – 10 %).

2.2.5 Heat transfer in superheater/reheater tube

The heat transfer on both the steam and flue gas sides is believed by Pronobis and Wojnar [45] to have a marginal effect on boiler operating under supercritical conditions. However, the growing interest in the more efficient power plants requires change of the steam conditions which result in faster corrosion. At higher temperature the effect of the heat transfer is believed to be more significant as such it drives development of the accurate model which enables more accurate material lifetime predictions. The literature review has shown limited number of heat transfer models for superheater/reheter (SH/RH) tubing. The popular model, used for theoretical predictions of oxide scale growth in SH/RH was developed by Purbolaksono et al. [44], however this model does not include many variables which are important for the proper scale growth predictions that can result in underestimation of the scale growth. In model developed Purbolaksono et al. [44] have assumed:

- T22 forms single oxide scale of magnetite, whereas the scale formed and this kind of steal is double/triple layered with inner layer of mixed

iron and chromium oxides, outer scale of magnetite and outermost of haematite;

- No oxides forming on outside of the tube (no fireside corrosion);
- No metal loss during exposure; and
- No radiation heat transfer from the hot gas.

The second model of the heat transfer across the SH/RH tube, which has been found in literature, has been developed by Pronobis and Wojnar [45]. This model is believed to enable a quantitative description of steam-side and flue gas side oxidation as a function of the boiler operational conditions. It gives more accurate prediction of the oxide scale growth then model developed by Purbolaksono et al. [44] due to more realistic assumptions. The model assumes that:

- Material oxidises on both steam and fireside;
- Oxidation follows firstly the parabolic rate low, which change to linear after longer oxidation;
- Oxide scales formed on ferritic steels are triple-layered;
- Metal loss is half of the oxide scale thickness;
- Fireside corrosion is on average 26 time faster than steam side oxidation; and
- No radiation heat transfer from the hot gas.

To summarise, both models presented are believed to underestimate the heat transfer due to wrong assumption taken. Analysis of both of the models showed that for delivering more accurate model the detail analysis of the steam oxidation and fireside corrosion is required. The important factor for the proper heat transfer calculation is metal loss of the tube material, which has been neglected by Purbolaksono et al. [44] and assumed by Pronobis and Wojnar [45] to be half of the oxidation rate. Moreover, both models seem to neglect the radiation heat transfer from the hot gas, which can possibly cause some underestimations.

2.2.6 Introduction to heat exchangers

A heat exchanger is a device designed to exchange heat, with the energy often being transferred from one fluid to another [39, 40]. Due to the fact that the fluids used in engineering processes often contains large amounts of energy, there is a considerable interest in recovering part of it and recycling it back to the process, and so heat exchangers are desirable pieces of equipment [10]. There are number of different heat exchanger classifications based on either their construction or the relationship between the moving fluids [39, 40]. Considering the fluids movement relation to each other the following types of heat exchangers exist: a parallel flow (fluid streams moving in the same direction), counter-flow (fluid streams moving in opposite direction) and cross-flow (the paths of the fluids cross each other) [40]. In terms of design, there are double-pipe and shell-and-tube heat exchangers [44].

The double-pipe heat exchangers consist of on tube within another, the fluid flows through the inner tube, whereas second flows through the annulus [40]. Figure 2-11 show the double-pipe heat exchanger with counter-flow (Figure 2-11A) and parallel flow (Figure 2-11B) as well as the temperature-length relationship for the particular type of exchanger.

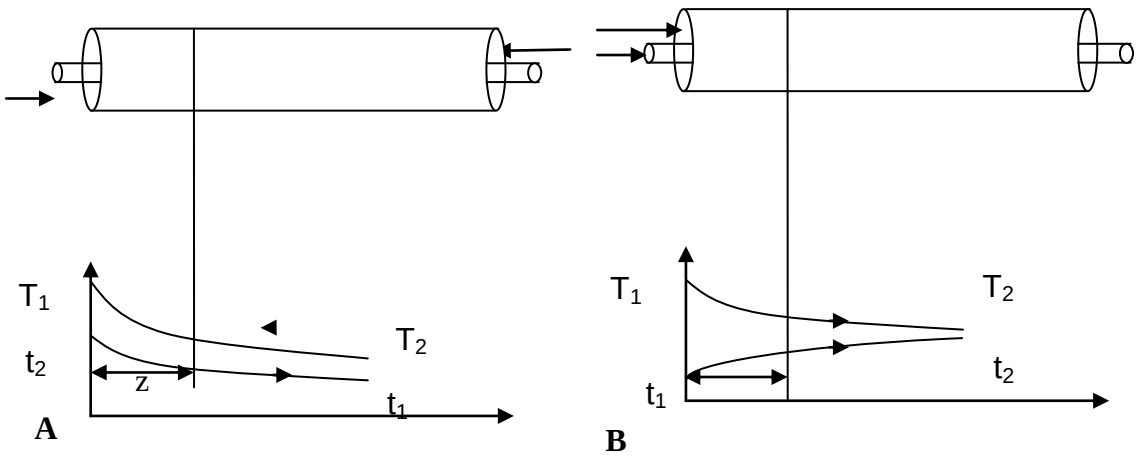

Figure 2-11 Temperature-length relationship for double-pipe exchanges [39]

In both cases presented (Figure 2-11) the fluid in annulus heats up whereas the pipe fluid cools down [39]. The temperature of the streaming fluids differ with

distance z; it is assumed that all heat lost by the warmer fluid is transferred to the cooler one. The transfer of the heat involves three resistances: film resistance from the inside tube, tube wall conduction and film resistance from the outside tube. The resulting overall heat transfer coefficient (U_o) could be written as [39]:

$$\frac{1}{U_o} = \frac{1}{h_i(A_i/A_o)} + \frac{D_o}{2k}\ln\left(\frac{D_o}{D_i}\right) + \frac{1}{h_o} \quad \textbf{(2-20)}$$

where D_o is outer diameter [m], D_i is inner diameter [m], A_o, A_i are area of the outer and inner surface of the tube [m^2] and h_i and h_o convection coefficients of inner and outer liquid respectively [W/m^2K] . If the tube is made from thin metal the tube-wall resistance can be neglected and therefore the overall heat transfer coefficient is expressed [39]:

$$\frac{1}{U_o} = \frac{D_o}{h_i D_i} + \frac{1}{h_o} \quad \textbf{(2-21)}$$

For both cases of the double-pipe exchangers considered the heat transfer is:

$$q = U_o A_o f(\Delta t) \quad \textbf{(2-22)}$$

where f(∆t) is a function of the temperature difference. In any of z distance (Figure 2-11) the temperature deference is T – t where T is temperature of the pipe fluid and t is temperature of annulus fluid [K]; this value varies with location along the exchanger. In order to determinate the heat transfer in the counter-flow exchanges there are following assumption to be made [39]:

- The overall heat transfer coefficient (U_o) does not change with the length of the heat exchanger;
- The situation considered is in steady flow;
- The fluid has constant properties, do not change with temperature or time;
- The system is assumed to be in one phase; and
- The heat losses are neglected.

Base on those assumptions the heat transfer for counter-flow and parallel-flow heat exchanger is described as [39, 42]:

$$q = U_o A_o LMTD \tag{2-23}$$

where LMTD is the log-mean temperature difference and for the counter-flow is expressed as follows [39, 40, 43]:

$$LMTD = \frac{(T_1 - t_2) - (T_2 - t_1)}{\ln\left[(T_1 - t_2)/(T_2 - t_1)\right]} \tag{2-24}$$

In contrast, for the parallel flow heat exchanger the LMTD is written as [39, 40, 43]:

$$LMTD = \frac{(T_1 - t_1) - (T_2 - t_2)}{\ln\left[(T_1 - t_1)/(T_2 - t_2)\right]} \tag{2-25}$$

Shell-and-tube heat exchangers are used when heat needs to be recovered from a high flow stream at high temperatures [39, 40]. A shell-and-tube exchanger is built from a large diameter pipe, inside which smaller tubes are placed. In such a design, two liquids are used: one flowing inside the tubes and second inside the shell.

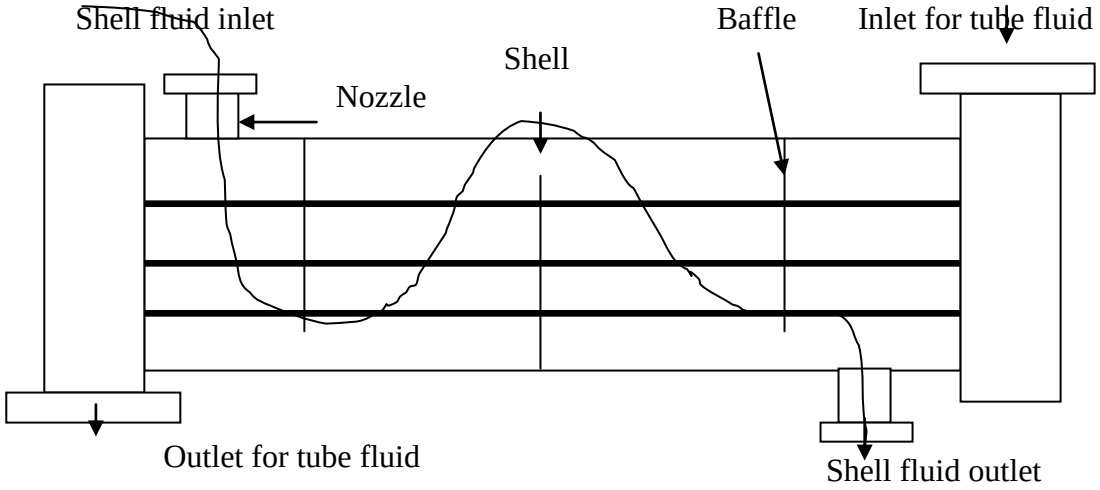

Figure 2-12 Shell-and-tube heat exchanger [39]

As for previous type of heat exchanger, in order to deriver the heat transfer some assumptions have to be made [39]:

- The shell fluid does not change temperature – it is the same at any location;
- A equal amount of heating occurs in each pass;
- The overall heat transfer coefficient is constant;
- The fluid flows are steady;
- No phase change occurs in either fluid; and
- The heat lost by the warm fluid is gained by the cool one.

In order to define the heat transfer two additional factors have been introduce: S which is defined as [40, 43]:

$$S = \frac{(t_2 - t_1)}{(T_1 - t_1)} \quad \textbf{(2-26)}$$

and restate R [40, 43]:

$$R = \frac{(T_1 - T_2)}{(t_2 - t_1)} = \frac{m_c \dot{C} p_c}{m_h C p_h} \quad \textbf{(2-27)}$$

For determination of the heat transfer for cross-flow shell-and-pipe heat exchangers, correction factor (F) is required. It can be calculated from the R and S values as follows [43]:

$$F_t = \frac{\sqrt{(R^2+1)}\ln\left[(1-S)/(1-RS)\right]}{(R-1)\ln\left[\frac{2-S\left(R+1-\sqrt{(R)^2+1}\right)}{2-S(R+1+\sqrt{R^2+1})}\right]} \quad \textbf{(2-28)}$$

Introducing the correction factor to eguation (2-23) the heat transfer for the cross-flow heat exchanger can be written as:

$$q = U_o A_o F_t LMTD \quad \textbf{(2-29)}$$

where U_o is overall heat transfer coefficient, A_o is external area of tubes [m^2], F_t is correction factor.

For the heat exchanger considered, the overall heat coefficient is derived as [42, 43]:

$$\frac{1}{U_o} = \frac{1}{h_i(ID_t - OD_t)} + \frac{1}{h_o} + \frac{1}{h_{io}} + \frac{1}{h_o} \quad \textbf{(2-30)}$$

where ID_t and OD_t are corrected inside and outside diameter of the tube [m]. Due to fact that surface of shell-and-tube heat exchanger are subject to fouling a fouling factor (R_d) also has to be included to obtain the correct value of the overall heat transfer coefficient [39, 40]:

$$\frac{1}{U} = \frac{1}{U_o} + R_d \quad \textbf{(2-31)}$$

The effectiveness of heat exchangers are important in comparing different design. It can be expressed as a relation between heat removed and the maximum heat, which could possibly be removed [40, 43]:

$$\varepsilon = \frac{actual\ heat\ removed}{maximum\ heat\ that\ might\ be\ removed} \quad \textbf{(2-32)}$$

The other widely used method is a comparison of the heat exchanger with the heat exchanger in cross-flow therefore, efficiency is defined as following [39, 43]:

$$\eta = \frac{temperature\ difference\ in\ the\ exchanger}{temperature\ difference\ for\ cross-flow} = F_t \quad \textbf{(2-33)}$$

2.3 Material science and engineering

2.3.1 Introduction

Material science is a discipline that involves investigating the relationships between materials structures and properties. Identification of such relationship is essential in order to design or select materials for the specific engineering processes. Material structures are often defined as an arrangement of material components and are often it is considered at two scales: microscopic when it involves the atomic scale and macroscopic if the structure can be viewed with the naked eye. Property is a more complex term and covers many phenomena. Callister [46] defines it as a materials trait in terms of the kind and magnitude of response to a specific alloy imposed cause. One classification system gives six groups of properties: mechanical, electrical, thermal, magnetic, optical and deteriorative [47]. Moreover, there are two aspects important for both material science and engineering: processing and performance. The relationships between these four aspects are essential to identified correctly the materials for the particular engineering process.

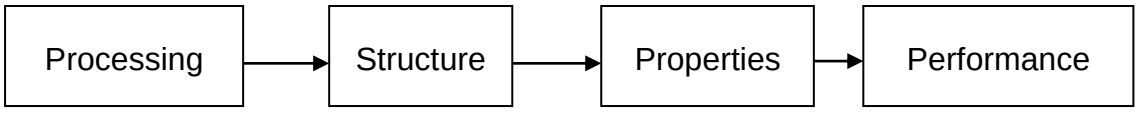

Figure 2-13 Interrelationship between four aspects of material science and engineering [46]

2.3.2 Mechanical properties of materials

Engineering materials are often subject to a specific force or load, therefore the properties describing their respond to the force are required [46]. Mechanical properties describe the behaviour or response of materials to a force or applied load [47]. Materials for a particular application have to exhibit desirable combination of mechanical properties; among them strength, hardness, ductility and stiffness are believed to be the most important [46, 48].

Strength, describes the ability of materials to withstand different forms of stresses: tension, compression or shear. There are two important factors, which are essential to define the material response to load/force engineering stress equation (2-34) and engineering strain equation (2-35).

$$\sigma = \frac{F}{A_o} \quad \textbf{(2-34)}$$

where F is load applied [N] and A_o is the initial cross-sectional area [m^2].

$$\varepsilon = \frac{l_i - l_o}{l_o} \quad \textbf{(2-35)}$$

where l_o is the length of the element before exposure, l_i is instantaneous length [m].

The mechanical characteristics of materials are defined by simple stress-strain tests. The comparison of stress and strain allows the evaluation of whether a material exhibits elastic or plastic deformation.

Hardness is defined as a material's resistance to a localised plastic deformation. It is assessed by tests in which an intender is forced into the surface of a material and an index number is assigned on the basis of the size/depth of the groove produced.

Ductility is a measure of the degree of plastic deformation that has been suffered by a material at fracture. Based on this criterion, materials are divided into; brittle, when there is a little or no plastic deformation at fracture; and, ductile, when plastic deformation is sustained.

Stiffness is defined as the resistance of a material to an elastic change of shape that. This means that after the stress is removed the material returns to its original shape [47].

2.3.3 Properties of materials at high temperatures

The properties of materials change with temperature [48] the relationship between temperature and properties is often linear (density, modulus, and electrical conductivity). However, there is a second group of properties for which defining the relationship is not easy or clear (rate of oxidation, yield strength) [47]. Two important temperatures for materials are the maximum and minimum service temperatures. The first, gives information about the highest temperature at which a material can be used safely without oxidation, chemical changes, excessive deflection or creep [49] The minimum service temperature is that below which a material starts to be brittle and therefore is unsafe to be used.

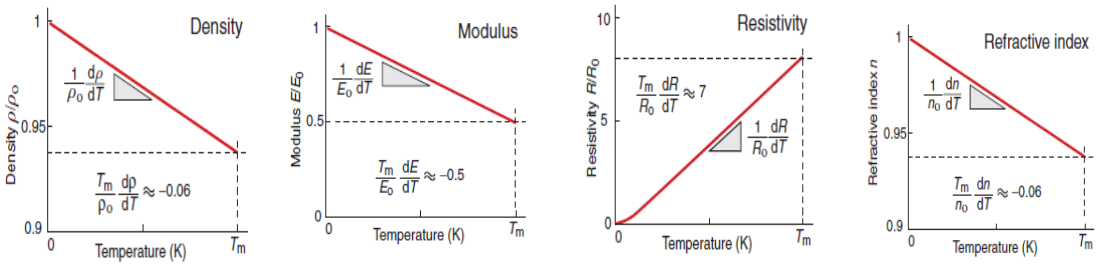

Figure 2-14 A Linear relationship between temperature and material properties [47]

Creep is an important property for materials [50], and creep resistance changes rapidly with temperature [48]. At low temperature, the deformation of materials is dominated by stress; the impact of time can be neglected. However, as the temperature increases, the loads that are not able to cause permanent deformation at low temperature can make a material creep – this also finishes in fracture (Figure 2-15A) [47, 48] At low temperature fracture is a time-independent process; however at higher it changes and the process clearly shows time dependence [47]. In order to currently design a component for good creep resistance, information concerning how the strain rate ($\dot{\varepsilon}$) or time to failure (t_f) depends on the exposure temperature (T) and stress applied (σ), are a necessity [47, 48, 50]. Therefore, many creep tests of the material have to be performed. For a creep test a specimen is loaded in tension or compression at

constant load, and place inside furnace, where it is kept at constant temperature whilst the extension of the specimen is measured with time [50]

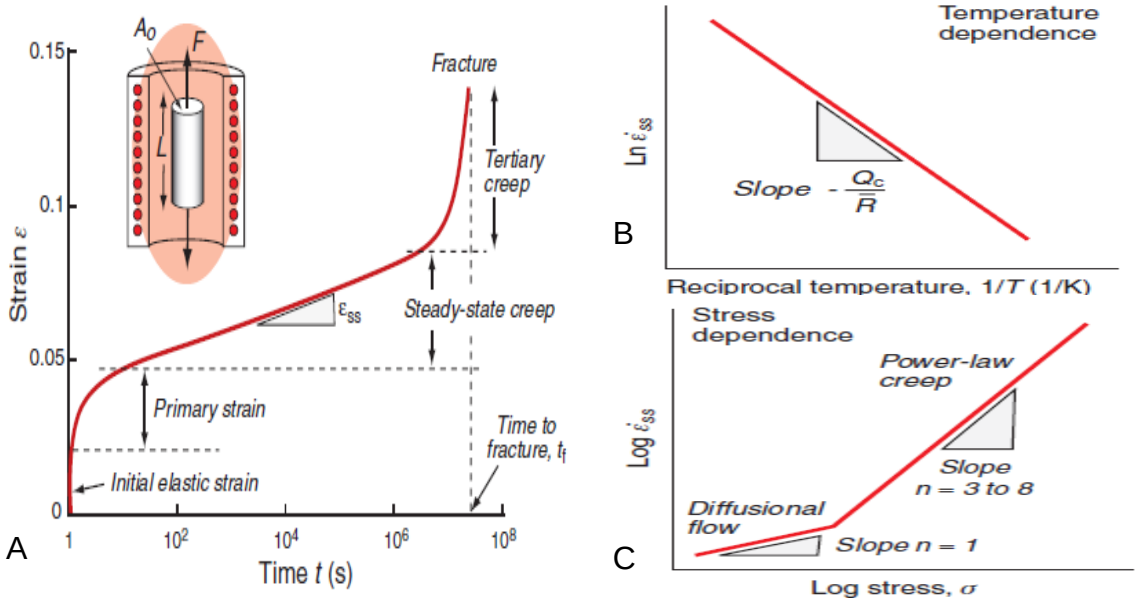

Figure 2-15 A - The creep curve, and B – temperature, C - stress dependences of the creep rate [47]

Figure 2-15A shows that the initial elastic and primary creep strains appears fast, thereafter a steady state creep zone occurs and after that the material goes into a tertiary creep zone and finally fracture [47, 50, 51] Theimportant factor to be defined is the time to failure (t_f) that is presented on a creep-rupture diagram. The use of such diagrams allows the identification of the lifetime for a particular material under certain stresses and temperatures. A second method is use of the Monkman-Grant law, which is defined as following [47, 50, 51]:

$$\dot{\varepsilon}_{ss} t_f = C \qquad \textbf{(2-36)}$$

where C is a Monkman-Grant constant and typically is in a range between 0.05-0.3, t_f is time to failure [s] and $\dot{\varepsilon}_{ss}$is steady state strain

The relation between steady state creep rate and temperature (Figure 2-15B) gives following dependence [51]:

$$\dot{\varepsilon}_{ss} = Cexp\left(-\frac{Q_c}{RT}\right) \quad \textbf{(2-37)}$$

where R is a gas constant [J/mol/K] and Q_c is activation energy for creep [J/mol], C is another material constant. Plotting the logarithmic value of the steady state creep rate against the stress applied Figure 2-15C) gives following relationship [46, 50]:

$$\dot{\varepsilon}_{ss} = B\sigma^n \quad \textbf{(2-38)}$$

where n is defined as a creep exponent, B as a material constant.

For this particular PhD, the creep resistance of tubing operating with an internal high pressure of steam and at high temperature is an important phenomenon. The design of the tubing allows a little creep, but a tube rupture would lead to violent release of hot, pressurised steam, which is dangerous and should be avoided [47, 50]. An example of a pressurised tube is considered, which carries hot steam with following parameters 650°C and 15MPa. Such a pipe experiences a hoop stress, which is defined as follows with the equation for thin wall approximation [47]:

$$\sigma = \frac{pR}{t} \quad \textbf{(2-39)}$$

where p is pressure [MPa], R is a tube radius [m] and t is the wall thickness [m]. equation (2-39) allows the calculation of the minimum thickness of the pipe for a particular operating condition. In order to calculate it the time to rupture data for the particular alloy under the conditions selected is required. The creep resistance is dependent; it decreases with increasing temperature [47, 48, 50, 51]. Therefore, information regarding the creep is necessary to select a material for a particular operating condition. Figure 2-16 presents one view of material selection in different a specific temperature ranges.

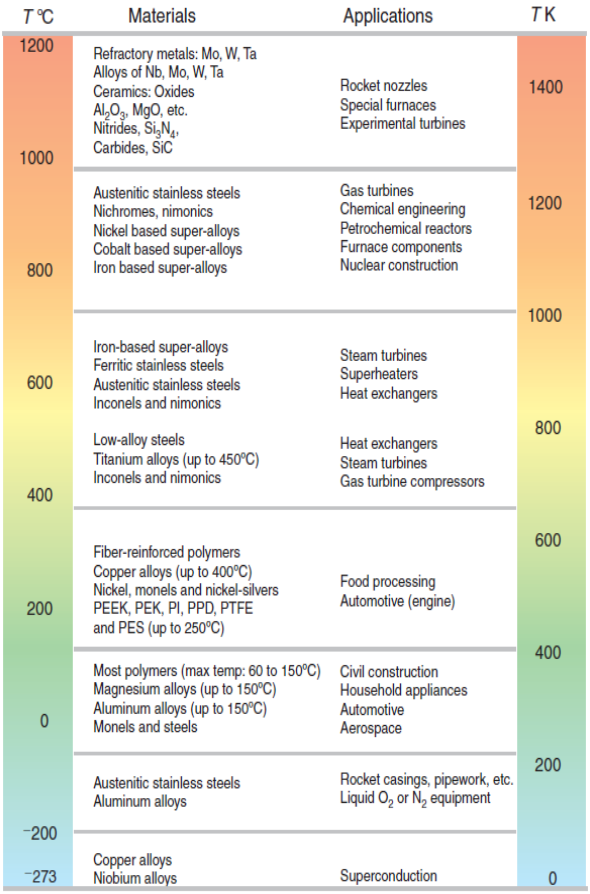

Figure 2-16 One view of materials selection for different temperature regimes [47]

2.3.4 Materials for ultra-supercritical application in coal-fired boilers

In general, Ultra-Supercritical (USC) steam conditions are defined as being above 24MPa and 593°C [18, 52, 53]. The materials, which could be used at such temperatures, are limited mainly due inadequate creep and oxidation/ corrosion resistance. Such limitations together with lobbing from the power plant industry, environmental groups and goverments towards more efficient power plant, is driving the development of new materials, which need to be successfully employed in the newly designed USC power plants [54]. The research goal for the new high temperature resistant alloys have good mechanical and physical properties at high temperatures (650-800°C) [18, 19]. The current literature shows that successful candidate materials must have the following properties: high steam oxidation resistance [20]; good temperature

capability in the range between 650 - 750°C [21]; high creep resistance [55]; high temperature strength [52]; good thermal conductivity [21]; good level of weld-ability [22]; fabric-ability [21]; and potential to be coated [17]. The development of the new more resistant alloys has driven design of various ferritic, austenitic and nickel-based alloys [17]. Such alloys are characterised by good thermal conductivity, high temperature steam oxidation and creep resistances, as well as significant cost differences – with their price growing in following order ferritic, austenitic and nickel-based alloys. Materials from these three groups are used to manufacture boiler components such as high-pressure piping and tubing as well as superheaters (SH) and reheaters (RH) [15]. Some elements operate at even higher temperatures that the steam conditions within them, and therefore the materials used for such components have to be able to withstand increased temperatures [11, 21]. SH and RH tubing are examples with the steam flowing within them being around 25-45°C cooler than the actual temperature of the tube surface [17].

Ferritic steels are currently widely used for the boilers-application as a result of their good creep resistance at current operating temperatures, as well as low coefficients of thermal expansion, high conductivity, fracture toughness and good weld-ability, as well as relatively low costs which are important from a business perspective [15, 17]. However, application of these steels to higher temperatures is limited by their lack of oxidation resistance at higher temperature and by creep resistance. According to Viswanathan and Bakker [17] the maximum temperature for ferritics is around 620°C (metal surface temperature). Current research aims to design more oxidation and creep resistant ferritc alloys with chromium levels of between 9-12% [19]. The application of advance ferritic steels has been in high-pressure piping and SH/RH tubing; however, for SH and RH the maximum operational temperature of steam within such tubing is limited to 565°C [17]. Current literature indicates that in coal-fired boilers 9Cr ferritics (among them T/P91) have been mostly used for SH/RH. However, this type of material does not have good enough creep and oxidation resistance at higher temperatures and so could not be used

for the final stages of the SH/RH in USC plants [56] To improve the creep and oxidation resistance of the 9Cr ferritic alloys part of the molybdenum has been substituted with tungsten to give a new alloy (T/P92); such substitution allows this material to be used at 620°C. Among more high temperature resistant 12Cr ferritic steels Viswanathan et al. [16] indicated HT91 can be used for piping and tubing in the power plants; however its application is limited and so new HCM12 and HCM12A have been developed, which can be applied at 620°C [15]. Holcomb et al. [52] have shown two other types of ferritic steels with good physical and mechanical properties, which are still in development phase - NF12 and SAVE12. These steels have very stable mechanical and physical properties at temperatures over 620°C. The SAVE12 alloy indicates acceptable oxidation rate even at 700°C, which could increase its application range for SH/RH tubing. Table 2-2 summarise the types of the ferritic steels used in power plant.

Table 2-2 Classification of ferritic steels

Group/ Cr level	Alloy
1-1.25	T11, NF1H
2Cr	T22, T23, HCM2S, TEMPALOY F2W
9Cr	T9, HCM9M, T91, T92, EM12, E911
12Cr	HT91, TEMPALOY F12W, HCM12A, NF12, SAVE12

Austenitic steels are believed to be more high temperature oxidation resistant; however their application is limited as a result of their lower creep resistance at higher temperatures [21]. These materials are used for SH/RH tubing above 620°C, the maximum operational temperatures are limited to between 675 and 700°C (at the material surface) [49]. Viswanathan et al. [16] indicate that in coal-fired boilers austenitic steels are used for the finishing sections of the SH/RH tubing, with the commonly used steels being: SS347HFG and SS304H. Hansson et al. [49] investigated oxidation of TP347HFG in great detail; the results of that a study show that T347HFG can be used for elements

operating at 700°C. Based on the results of a number of tests conducted Viswanathan et al. [16] and Wright and Pint [19] defined four main candidates for the USC application in power plant:

- SAVE25;
- NF709;
- HR3C; and
- Super304H.

Table 2-3 Classification of austenitic steels

Group/ Cr level	Alloy
18Cr-18Ni	ASME TP304H, Super 304H, ASME TP321H, TEMPALOY A-1, ASME TP316L, ASME TP347, ASME TP347HFG
15Cr-15Ni	17-14CuMo, Esshete 1250
20-25Cr	ASME TP310, HR3C, Alloy 800H, TEMPALOY A-3, NF709, SAVE25
High Cr-High Ni	CR30A, HR6W

Nickel-based alloys have the highest temperature resistance amongst the three groups identified for the USC applications. According to Viswanathan and Bakker [17] as a result of very good mechanical and physical properties nickel-based alloys have the highest potential maximum operational temperatures. These materials can be applied at temperatures above 675°C. Holcomb et al. [52] studied steam oxidation of commercially available Ni-based alloys (Alloy 617, Alloy 230 and Alloy 740) and concluded that even at 760°C these materials show slow oxidation rates and formation of protective oxides. This is in accordance with conclusions of Viswanathan et al. [15], whose tests confirmed the low oxidation rates of the nickel-based alloys under USC conditions. Applications of nickel-based alloys are however, significantly limited as a result of their high cost. Despite these high costs nickel-based alloys are believed to be crucial for development of the industrial size USC power plants [11]. Result of studies conducted on nickel-based alloys in high pressure testing rigs have shown that Inconel 617 and Inconel 740 are two of the most promising

candidates for the new steam boilers [16]. According to Viswanathan et al. [16], these two Inconels could be used for the SH/RH tubing in the temperature between 675-700°C. However, further development of the nickel-based materials should push their maximum temperatures to 760°C and above.

Table 2-4 Selection of Nickel-based alloys

Alloy
Inconel 617, Inconel 625
IN 708, IN 740, IN 780, Alloy 230, Alloy 617, Alloy 625
Inconel 617, Inconel 625
IN 708, IN 740, IN 780, Alloy 230, Alloy 617, Alloy 625

To summarise, the research topic of new, more steam oxidation resistant alloys for the steam boiler applications has been driven by development of the USC power plants [18]. Such materials must have good mechanical, physical and chemical properties. Due to the maximal operational temperatures, the materials for USC power plants may be divided into 3 groups: ferritic, austenitic and Ni-base alloys which could be applied up to following temperatures: 620°C with possible extension up to 700°C for the most advance, 675 - 700°C and 760°C respectively [11]. Among these, three groups Viswanthan et al. [15] indicated following to be typically used for the power plant applications:

- Ferritic steels: T22, T23, T91 and T92;
- Austenitic steels: TP347HFG, 316L and Super 304H; and
- Nickel-based: Inconel 740 and Alloy 625.

Table 2-5 shows the nominal composition of the typically used alloys for the power plant applications.

Table 2-5 Nominal composition of high temperature resistant materials used for power plant applications

Alloy	C	Ni	Cr	W	Co	Ti	Nb	Mn	Fe	Si	Cu
T23	0.06	-	2.25	1.5	-	-	0.04	0.45	bal	0.2	-
T22	0.05	-	2.25	-	-	-	-	0.45	bal	0.2	-
T91	0.12	0.4	9	-	-	-	-	0.6	bal	0.5	-
T92	0.13	0.4	9	1.9	-	-	0.09	0.6	bal	2	1
TP347HFG	0.1	10	18	-	-	-	0.8	1.6	bal	0.6	-
Super 304H	0.1	9	18	-	-	-	0.4	0.8	bal	0.2	3
316L	0.02	10.2	16.4	-	-	-	-	1.6	bal	0.5	-
HR3C	0.01	20	25	-	-	-	0.6	2	bal	0.75	-
Alloy 625	0.1	Bal	23	-	-	0.4	3.1	0.5	5.0	0.5	-
Inconel 740	0.03	bal	25	-	20	1.8	2	0.3	0.7	0.5	-

2.4 High temperature Oxidation

2.4.1 Introduction and basic concepts of the high temperature oxidation

During their operation materials are exposed to different destructive phenomenon, which significantly reduce their component lifetime and influence the selection of materials used for particular applications. Among the destructive processes influencing materials performance, oxidation is often of crucial importance due the fact that it takes place in most atmospheres and at all temperatures. It occurs in air and, oxygen, as well as gases with relatively low oxidising potentials as sulphur dioxide, carbon dioxide wet gas mixtures and pure steam. There are techniques to reduce the impact of oxidation on material performance but this process is still highly problematic. High temperature oxidation is described as a reaction between a material operating at high temperature and its surrounding atmosphere, which result in an oxide forming on the surface of the material [57, 58, 59]:

$$\mathrm{M_{(s)}} + \mathrm{O_{2(g)}} = \mathrm{MO_{2(S)}} \qquad \textbf{(2-40)}$$

Equation (2-40) shows basic oxidation of metal in oxygen resulting in formation of metal oxide on the surface [57] The basic model of high temperature oxidation divides the process into two basic stages: initial oxidation, which describes formation of the first, most stable oxides on the surface of the bare material, and thick layer oxidation [57, 58, 59, 60]. Study of the initial stage of the high temperature oxidation is of crucial importance; however, it is a difficult to predict the behaviour of the material during this period and to estimate the interaction between the gas/metal.

In general, the initial stage of oxidation involves adsorption of the oxygen and leads to the formation of an oxide; those scale a few nanometres thick. The initial period of oxidation starts with the adsorption of oxygen on the clean surface, which is followed by formation of a thin chemisorbed layer. The next step is development of additional oxide layers. This stage is controlled by island

growth and exchange [57, 61], which drives formation of the thicker oxides that spread along the surface. Finally, in order for the oxide growth to continue ions and electrons have to be transported across the layers formed; the kinetics of this process are depended on different possible transport mechanisms. In literature, the first two stages of initial oxidation are believed to follow linear rate dependencies the third stage exhibits a logarithmic kind of the rate dependency [57, 61].

After the initial oxidation stages, which for the high temperature processes are relatively short, thicker oxides start to grow, and for the reaction to occur either metal ions from the substrate or oxygen ions from the oxidising atmosphere have to be transported [46, 57. 58, 59, 60]. The migration of the ions involved is controlled by diffusion, which is enhanced by defects in the oxide(s) formed. The thicker oxides oxidation is described by Wagner's theory of oxidation that is often used in high temperature oxidation studies [57, 58]. For the theory to be applied following assumption have to be made [57, 60]:

1. Oxide scales are adherent and compact;
2. Migration of ions, electron and electron holes determines the process rate;
3. Thermodynamic equilibrium is established on both metal/oxide and oxide/gas interfaces;
4. Oxides are stoichiometric in nature (but small deviation from stoichiometry are possible); and
5. Oxygen solubility in the metal is neglected.

Because of the equilibrium at both interfaces (gas/oxide and scale/oxide) the activity gradients of metal and oxygen are established across the scale. In consequence, the metal and oxygen ions are able to counter - diffuse throughout the scales. Due to fact that ions are charged thus migration drives the formation of an electric field across the oxides (which moves from the metal to the atmosphere); thus the net migration of ions, electrons and electron holes has to be balanced in order to maintain the electro-neutrality condition.

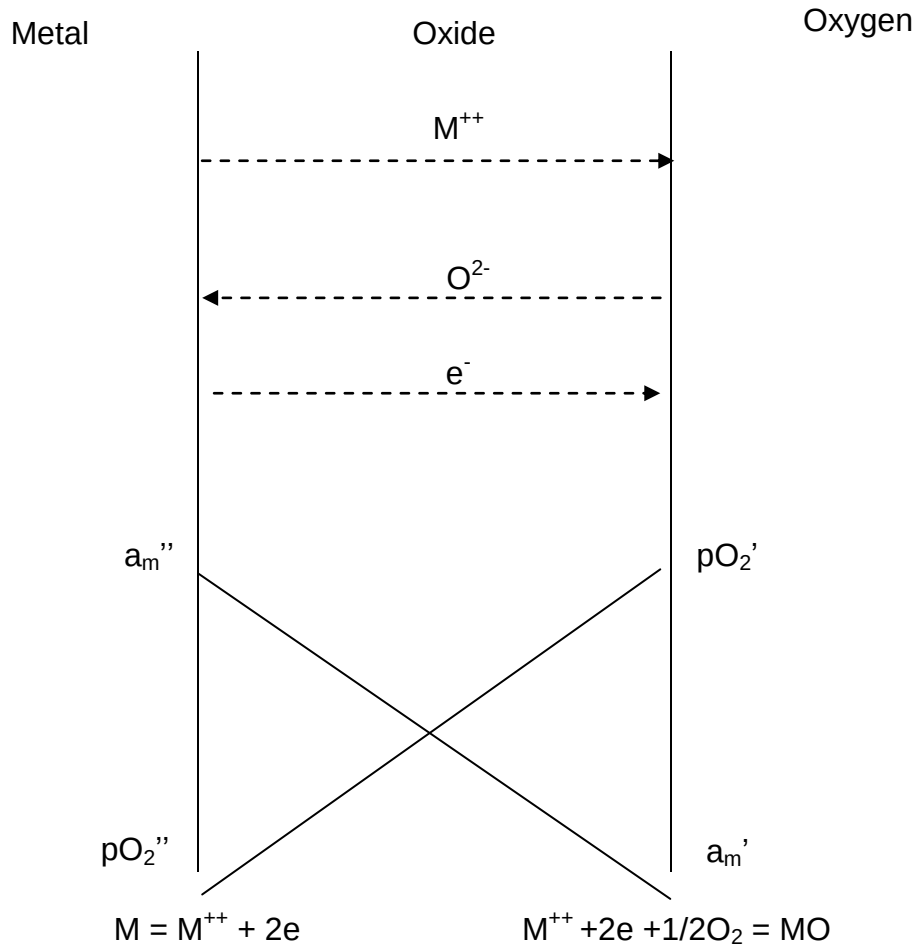

Figure 2-17 Schematic oxide scale formation following the wagner's theory of oxidation [57, 60]

Wagner's theory of oxidation is frequently quoted in the high temperature oxidation; however there are only a few oxides which strictly follow the Wagnerian model. This is a result of the basic assumptions; most of the oxides formed on metal are neither adherent nor compact in nature. Moreover, most oxides are not stoichiometric, and finally total equilibrium at each interface is rarely established.

2.4.2 Oxidation rates

Oxidation is controlled by diverse processes, which can change with time and exposure conditions. The literature review shows that high temperature oxidation can exhibit different rate law dependences:

- Linear for the initial phase of oxidation;
- Parabolic in the thicker oxides regime; and
- Logarithmic or inverse logarithmic in thin scales and at low temperatures.

Oxidation exhibits linear rate law dependence when the oxide scales are thin and the reactions on scale/gas interface are the rate-determining [60]. Under such conditions, the rate may be written as:

$$x = k_l t \quad \textbf{(2-41)}$$

where x is the oxide thickness [μm], k_l is linear rate constant [um/s], t is time [s]

In many cases oxidation of materials at high temperature is reported to exhibits a parabolic rate law dependence [57]. Since the oxides formed on the alloy surface are thicker, the diffusion of cations and anions throughout the scales become the rate determining processes. The cation and anions diffusion across the oxide scale shows parabolic rate dependence [62], therefore the oxidation process at this stage is believed to exhibit the parabolic rate dependence [59]. The oxidation rate is inversely proportional to the scale thickness and may be written as [57]:

$$x^2 = 2k_p t + c \quad \textbf{(2-42)}$$

where x is the oxide thickness [μm], k_p is parabolic rate constant [$\mu m^2/s$], C is constant [μm^2], t is time [s].

Oxidation follows the logarithmic rate law under specific conditions: firstly for thin oxide scales and secondly at low temperatures [60]. Under such conditions the reaction rate is rapid at the beginning at the process, however

after some period starts to decrease with time, following the direct or inverse logarithmic rate law.

$$x = klogt + A \quad \textbf{(2-43)}$$

$$\frac{1}{x} = B + k'logt \quad \textbf{(2-44)}$$

where x is the oxide thickness [μm], k', k are logarithmic rate constants, t is time [s], A, B constants.

2.4.3 Factors influencing the oxidation kinetics

Machlin [61] and Callister [46] indicate that the rate of the oxidation is significantly dependent on temperature, environment, oxygen partial pressure, composition, surface preparation and pre–treatment of the metal/alloy. Oxidation processes are characterised by different rates in different environments; Gaskell [63] show that changing of the environment from dry to water vapour containing gas significantly increases the oxidation rate. The alloy composition has also a significant impact on the oxidation resistance [64, 65] Sanchez et al. [66] believe that the most important elements, which improve the oxidation resistance of currently used alloys are chromium, silicon, tungsten and molybdenum.

In most cases, oxidation tends to increase with increasing temperature [57] according to a relationship described by the Arrhenius equation [17]:

$$k = k_o \exp(-\Delta Q/RT) \quad \textbf{(2-45)}$$

where ΔQ is the activation energy of the oxidation reaction [J/mol], R is the gas constant [J/mol/K] and T is the absolute temperature [K], k_o is constant [$\mu m^2/s$]. The Arrhenius relationship is explained as result of the increasing diffusion rate of ions in solids at elevated temperatures [60] and pressures [59]. In some environments (e.g. steam) the oxidation rates could decrease with increasing temperature or exhibits "bell-shape dependence" [67]; however this is

dependent on alloy type [67] and is a result of changes in mechanism with temperature.

2.4.4 Thermodynamic aspects of the high temperature oxidation

High temperature oxidation is often very complex in nature [59, 60]. For example, the material exposed to the oxidative atmosphere can be a multi-component alloy and the oxidising gas can contain more than one reactive component. Moreover, oxidation process may also be complicated by the presence of varies kinds of liquid or solid deposits, which significantly change surface reactions and therefore change the formation of the oxidation products [60]. For an understanding of the oxidation process, identification of the potential reactions between the material and oxidative gas and prediction of the possible reaction products, thermodynamic calculations are an essential tool [46, 58, 68].

In order to define if a proposed reaction is able to proceed the second law of thermodynamics is applied [57, 61, 63]; As the high temperature oxidation is a process during which conditions (temperature and pressures) are constant, the second law of thermodynamics can be written as the Gibbs free energy of a system (Gibbs – Helmholtz equation) [58]:

$$\Delta G' = \Delta H' - T\Delta S' \quad \textbf{(2-46)}$$

where ΔH' is the standard enthalpy of change [kJ/mol], ΔS' is the standard entropy of change for the considered system [kJ/mol/K]. Based on the second law of thermodynamics the reaction is spontaneous when the change in Gibbs free energy is negative; if $\Delta G'$ is positive the reaction is impossible; and, finally the system is in equilibrium when $\Delta G'$ equals zero [57, 60, 51]. For the simple chemical oxidation reaction between metal and oxygen ($M + O_2 = MO_2$) the total change in Gibbs free energy can be written as follows:

$$\Delta G' = \Delta G^{o} + RT\ln\left(\frac{a_{MO_2}}{p_{O_2} \cdot a_M}\right) \quad \textbf{(2-47)}$$

where ΔG^o is change in free energy in the standard state [kJ/mol], a_i is thermodynamic activity for the i^{th} species involved. Activity describes the deviation of the considered species from the standard state and for a gas is expressed as [60]

$$a_i = \frac{p_i}{p_i^o} \quad \textbf{(2-48)}$$

where p_i is the partial pressure of i^{th} gaseous species [bar] and p_i^o is the pressure corresponding to that gaseous species in standard state [bar]. In the equilibrium ($\Delta G' = 0$) the Gibbs energy of change can be written as:

$$\Delta G^o = -RT\ln\left(\frac{a_{MO_2}}{p_{O_2}.\, a_M}\right) \quad \textbf{(2-49)}$$

Moreover, assuming unity of the activity of the solid species (metal and oxide) equation (2-49) can be expressed as [57, 61]

$$\Delta G^o = -RT\ln\left(\frac{1}{p_{O_2}}\right) \quad \textbf{(2-50)}$$

and therefore the oxygen partial pressure in equilibrium is derived as follows [59, 60]:

$$p_{O_2} = e^{\frac{\Delta G^o}{RT}} \quad \textbf{(2-51)}$$

Formation of oxides is dependent on the partial pressure of oxygen; the oxide with lower partial pressure would form firstly due to its higher stability. In general, oxides can form on the surface of a metal if the oxygen partial pressure of the gas is greater than the oxygen partial pressure in equilibrium required at the temperature considered for the oxide to be formed [57, 59, 60]. Due to the complexity of high temperature oxidation most of the thermodynamic data has traditionally been acquired from graphical representation. There are four basic types of diagrams used to study the high temperature oxidation; with each of them defining a different parameter [60].

1. ‘Gibbs free energy versus composition’ diagrams or ‘activity versus composition’ diagrams are both used for describing the thermodynamics of a system;
2. ‘Standard Gibbs free energy of formation versus temperature’ diagrams (Ellingham diagrams), which are used to determinate of the products for a particular reaction under defined conditions;
3. Vapour-species diagrams used to plot the vapour pressures of a compound as a function of a convenient variable; and
4. Multi-dimensional isothermal stability diagrams, which map the stable phases in systems and can involve diverse metallic and non-metallic compounds.

For the identification of the conditions under which particular oxidation products develop, the Ellingham diagrams is an essential tool. Ellingham diagrams are a representation of the thermodynamic force required for a particular reaction to proceed plotted across a temperature range. The values of the Gibbs free energy of formation plotted in such diagrams are obtained from number of thermodynamic data sources [57]. From Ellingham diagrams, following data could be acquired: standard Gibbs free energy of formation for the temperature of interest and oxygen partial pressure in equilibrium. Those parameters give essential information for the further investigation of the oxidation phenomena.

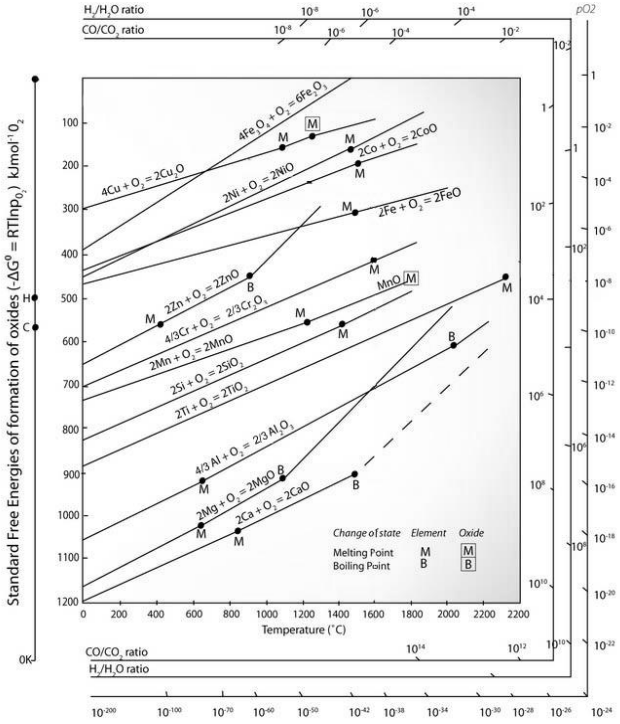

Figure 2-18 Ellingham diagram [69]

2.4.5 Transport mechanisms in high temperature oxidation of metal

Oxidation of a metal can cause the formation of an oxide on the metal surface which then acts a barrier between the two reactants. Therefore, in order for the reaction to continue one or more of the reactants have to penetrate the oxide layer [57, 59, 62] For oxidation to proceed, either the metal has to be transported through the oxide(s) to the oxide-gas interface or oxygen has to diffuse to the metal-oxide interface and their reaction continue at one or other of these interfaces [57, 59, 61]. This demonstrates the significance of the transport mechanism of the metal or oxygen across the oxide for the high temperature oxidation processes to continue.

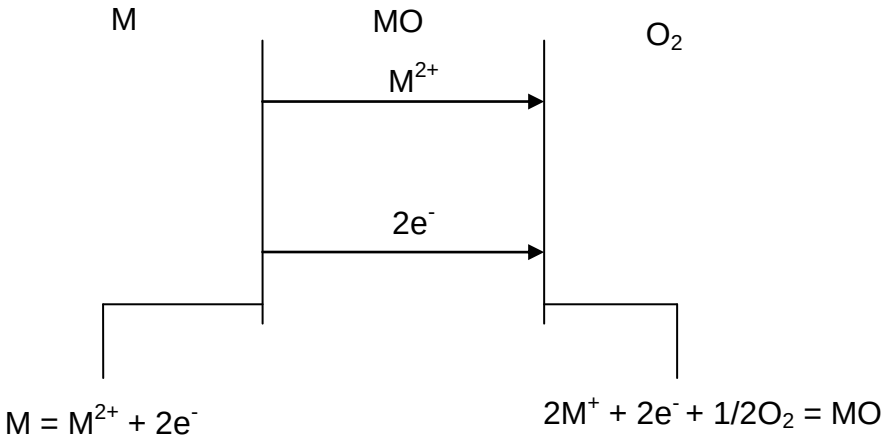

Figure 2-19 Transport process for the high temperature oxidation with mobile cations

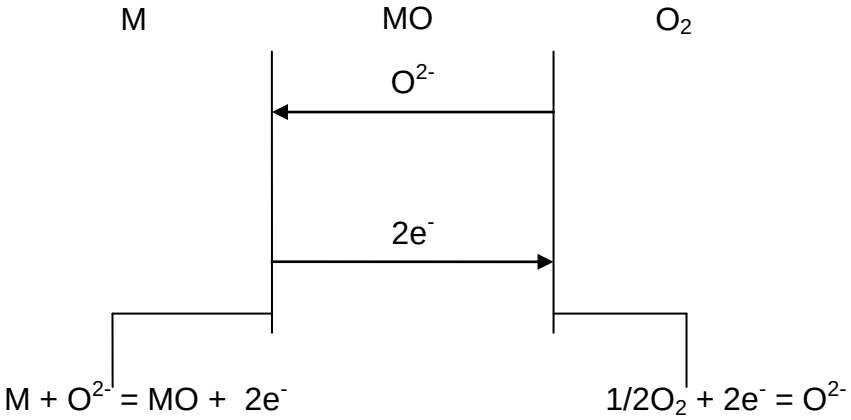

Figure 2-20 Transport process for the high temperature oxidation with mobile anions

Figure 2-19 and Figure 2-20 show diagrammatic representations of two alternative basic oxidation processes. These indicate that either metal ions or oxygen ions electrons have to move in order for reactions to continue after oxide formation at the metal surface [57, 60]. These two mechanisms presented link together the phase-boundary reactions, but they represent two different processes as controlling the scale growth. The first shows cation diffusion controlled scale growth, which leads to development of an oxide at the scale-gas interface (Figure 2-19), whereas anion migration drives formation of an oxide at the metal-scale interface (Figure 2-20).

Metal oxides are ionic in nature and so the transport mechanisms through the scales formed involves ions (and the transport of neutral metal or non-metals species can be neglected). There are several mechanisms explaining the ion transport in ionic solids with generally two groups being distinguished: one in stoichiometric crystals and a second in the non-stoichiometric crystals [60]. Metal oxides are believed to form compounds which belong to either of those two groups; therefore both cases have to be considered.

The highly stoichiometric compounds indicate two possible kinds of defects called Schottky and Frenkel defects [46, 57, 58].

In Schottky defects the mobility of the ions is believed to be result of existence of the ionic vacancies. To maintain electro-neutrality the concentration of vacancies the on cationic and anionic sub-lattices has to be the same. As a result of vacancies existing in both the sub-lattices, both ions are mobile [60].

In Frenkel defects only cations are mobile; this is a result of having a perfect anion lattice. Consequently, the cation lattice is imperfect and so for the whole crystal structure to be electro-neutral the cation lattice vacancies and concentration of interstitials have to be the same [61].

Non-stoichiometric compounds are describe as those which despite the fact that their metal to non-metal atom ration is not exactly given by the chemical formula are still electrically neutral. Non-stoichimetric compounds are classified as semiconductors and can indicate either negative or positive behaviour [61]. The negative semiconductors are those in which the charge is transfer by negative carriers and so it caused an excess of metal or a deficit of non-metal. The positive semiconductors are described as those in which charge is transfer by the positive carries and in consequence, the deficit of metal or excess of non-metal within can raise.

2.4.6 Adsorption

Adsorption is the first stage of a reaction between two heterogeneous reactants [60]. There are two types of the adsorption: physical and chemical [57]. Physisorption is a process whereby gases are weakly bonded to a solid surface; therefore the bonds are able to be broken, and the reaction is reversible. The gases are bound to the surface with weak Van der Waal forces [61, 70]. Physisorption does not required any activation energy and its rate is proportional to the flux of the gas molecules which hit the surface. This rate is not influence by crystallographic orientation or surface treatment; moreover, this phenomena has a low impact on the surface potential [60]. In contrast, chemisorption drives the formation of strong chemical bounds between gases and a surface; in consequence the reaction cannot be reversed [61, 70] Chemisorption proceeds slowly, has higher activation energy, moreover chemisorption needs a higher temperature than physical adsorption. Chemical adsorption is dependent on the crystallographic structure and surface type. Comparison of the oxides formed in chemical and physical processes show that the oxide formed during the chemisorption is significantly thicker than the formed by physisorption, and thus the surface potential decreases [57, 60].

2.4.7 Diffusion in solids

In solids the atoms are in constant motion around their lattice sites. Such atoms occasionally gain sufficient energy to enable them to move (jump) to the other sites – this movement is called diffusion [12, 46, 60, 61, 62]. In solids, diffusion is an important phenomenon which is crucial in many solid-state reactions, such as oxide growth.

Crystalline solids have a regular array of lattice sites; the atoms move from one lattice site to other by jumping [57]. In solids, there are a number of different atomic displacement mechanisms, which are dependent on the atom and type of the crystal structure [60, 61, 62]. Solids can have perfect and imperfect crystals, but in each of these causes different mechanisms of diffusion

occur. In perfect crystals, the exchange and ring mechanisms are possible [60, 61]:

1. Exchange mechanism, which demands high energy in order for neighbouring atoms to exchange their positions;
2. Ring mechanism engages four neighbouring atoms; it assumes that thermal vibrations are sufficient to cause atoms to jump by one position around the ring.

In imperfect crystals, there are three diffusion mechanisms to be identified [57, 60]:

1. Interstitialcy mechanism, in which an interstitial atoms moves to a regular lattice site and therefore force the atom at the regular site to move to an interstitial location;
2. Interstitial atom movements mechanism; it involves only interstitial atoms which move from one interstitial position to another; and
3. Vacancy mechanism; the most important mechanism in solids and can bet is described as the move of an atom from its regular site to the nearest vacant site.

In the literature diffusion in the perfect crystals is called volume diffusion. This mode of transport is significantly slower than along the surfaces, grain boundaries, dislocations or cracks [61, 62]. Diffusion along those four structures is referred to as short circuit, and its faster rate is believed to be a result of less densely packed structure than the bulk lattice, which makes therefore the jump (movements) of atoms easier and faster.

Diffusion of atoms is described as self-diffusion, the best way of study the self-diffusion is to use radioactive atoms, which at the beginning of the process are evenly distributed in the central region of a metal [61, 62]. With time those radioactive atoms diffuse to the adjoining regions [57, 60]. There are two laws describing the diffusion: the first does not include time as a variable (Fick's first law); and the second in which the concentration gradient changes with time (Fick'c second law).

Fick's first law states that the diffusion rate is directly promotional to the concentration gradient $\frac{dc}{dx}$, and it is written as follows [60, 71]:

$$J = -D\frac{\partial c}{\partial x} \quad \textbf{(2-52)}$$

where D is the diffusion coefficient [m^2/s].

Fick's second law describes diffusion with consideration of both distance and time, it is derived from the first law considering that the diffusion rate of the selected species in a given volume element is the difference between two fluxes, and therefore it could be written as [60]:

$$J - J' = -\frac{d}{dx}\left(-D\frac{\partial c}{\partial x}\right)dx \quad \textbf{(2-53)}$$

where J – J' is the accumulated flux per second [$mol/m^2/s$]. Considering that this is proportional to the rate of the concentration change in time ($\frac{dc}{dt}$), equation (2-53) could be expressed as [60]:

$$\frac{dc}{dt} = \frac{\partial}{\partial x}\left(\frac{\partial c}{\partial x}\right) = D\frac{\partial^2 c}{\partial x^2} \quad \textbf{(2-54)}$$

Diffusion in solids changes with many factors [71] that is associated with value of the diffusion coefficient (D). The diffusion coefficient is not constant, it is a function of many variables, among them temperature, concentration, impurities and crystal structure are the most important [57, 58, 61, 62]. The derivation of a specific diffusion coefficient it is not a simple process, it is often essential to consider the individual specific affects of one or more of the highlighted variables. Moreover, the overall diffusion is also affected by the short circuit diffusion along the grain boundaries, dislocations and metal surface [57, 60].

Temperature is the most critical factor influencing transport mechanisms. Its effect is associated with two phenomena: firstly an increase in the jump

frequency; and, secondly an increase in the equilibrium concentration of the vacancies N_V [62]:

$$N_V = \exp(-\Delta G/RT) = \exp(\Delta S_f/R)\exp(\Delta H_f/RT) \quad \textbf{(2-55)}$$

The value of diffusion coefficient is not constant; its temperature dependence is written as [46]:

$$D = D_O exp(-Q_d/RT) \quad \textbf{(2-56)}$$

where D_0 is a temperature independent pre-exponential diffusion coefficient [m^2/s], Q_d – the activation energy for diffusion [J/mol], R – the gas constant [J/mol/K] and T – absolute temperature [K].

The impact of short circuit diffusion on an overall diffusion coefficient is mainly associated with a different arrangement of the atoms at grains boundaries, near surface and adjacent to a dislocation (gaps, voids and cracks) [60, 61]. These factors clearly enhance the rate of the diffusion via the vacancy mechanism because of the larger numbers of vacancies and their greater mobility at the locations. Therefore, the activation energy for grain boundary diffusion is significantly smaller than for lattice diffusion [61].

2.5 Steam oxidation

2.5.1 Introduction and basic concepts

Steam oxidation is an important phenomenon for power plant operations because of its crucial influence on the performance of the material used for coal – fired boilers tubing [23, 24. 28, 29]. Development of more efficient power plants requires an increase in the operational conditions (temperatures and pressures) in order to convert the energy from the hot flue gas streams into electricity more efficiently. The rates of oxide growth on steam-exposed surfaces are of growing interest due to their implication for the power plant operations such as tube failures, overheating and oxide exfoliation [24, 28, 72].

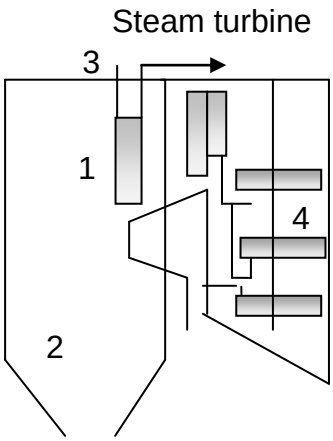

2. SH/RH • Creep • Fireside corrosion • Steam oxidation	1. Header • Creep • Steam oxidation • Type IV crack • Thermal Fatigue
3. Watrerwall • Corrosion Fatigue • Sulfidation • Hydrogen attack • Cracking	4. Economiser • Pitting • Erosion • Thermal Fatigue

Figure 2-21 List of the main material issues in coal-fired boiler [73]

Mitigation of these problems is essential to ensure the proper operation of the coal-fired boilers, therefore research is needed into high temperature steam oxidation to understand the impact of alloy type, composition and microstructure, as well as the evolution of oxide structures [23, 24]. Additionally the implications of temperature, time and operational conditions on the oxidation processes have to be studied. High temperature oxidation in steam is based on the same principles, presented in the high temperature oxidation chapter; the main difference is that the only source of oxygen for the process is the

dissociation of steam [28]. During the steam dissociation there are products other than oxygen forming, which could also have an impact on the oxidation, such as oxy-hydroxides (OH^-) and hydrogen (H^+) ions. In general, the metal oxidation in steam is initially fast as the first oxides grow on the clean metal surface; this stage is relatively short and exhibits a linear rate dependence [24]. After the first oxide layers are formed, the oxidation proceeds due to diffusion of ions across the scale formed thus the rate becomes parabolic [23]. Furthermore, the thermodynamically stable oxides grow on the material, with the most stable next to the surface. Among the oxides forming the scales haematite (Fe_2O_3), magnetite (Fe_3O_4) and Wuestite (FeO) are stable in steam; however, their formation is dependent on the exposure conditions. In general, however those oxides grow too fast to be considered as protective [23, 24, 28]. To increase the protectiveness of the materials at high temperatures (>620°C) alloy selection design has to promote the formation of three more protective oxides - chromia, alumina and silica [29]. However, the commercially used iron – based alloys, are designed to have sufficient levels of Cr to form less protective Cr, Fe spinels ($FeFe_{2-x}Cr_xO_4$); such structures are able to reduce non protective scale growth, and therefore improve the alloys 'steam oxidation resistance.

Oxidation in steam is a faster phenomenon than in air, oxygen or gas mixtures, as result of hydrogen evolution and chromia volatilisation [23, 74]. Evolution of hydrogen and its dissolution in the scales formed, increases oxides growth rates due to the impact of hydrogen on the bulk diffusion across the oxides layers [23, 24, 49].

2.5.2 Thermodynamics of steam oxidation process

In considering the potential oxidation processes in steam thermodynamics is an essential tool to examine the types of oxides that could form. For such a examination, the oxygen partial pressure in equilibrium is a crucial parameter to be defined. Under 100% steam conditions, the only source of the oxygen is dissociation of steam via reaction [23, 24]:

$$H_2O\ (g) \leftrightarrow\ H_2(g) +\ 1/2O_2\ (g) \quad \textbf{(2-57)}$$

The oxygen partial pressure for equation (2-57) is given by [24]:

$$k_1 =\ pO_2^{0.5}\ \frac{pH_2}{pH_2O} \quad \textbf{(2-58)}$$

k_1 is the equilibrium constant for the steam dissociation, which could be derived from the free energy of formation (G_1) and is expressed as:

$$log_{10}k_1 =\ -\frac{\Delta G_1^o}{2.303RT} \quad \textbf{(2-59)}$$

Dissociation is assumed to occur either at the metal-steam or metal-oxide interface and be at equilibrium. For the basic calculation, it is assumed that the partial dissociation of one mole of steam gives x moles of hydrogen and $\frac{x}{2}$ mole of oxygen thus the partial pressures of oxygen, hydrogen and steam could be written as [24]:

$$pO_2 =\ \frac{x}{2+x}P \quad \textbf{(2-60)}$$

$$pH_2 = \frac{2x}{2-x}P \quad \textbf{(2-61)}$$

$$pH_2O = \frac{2(1-x)}{2-x}P \quad \textbf{(2-62)}$$

Based on the data presented above, equation (2-58) can be written as follows [24]:

$${k_1}^2 = \left(\frac{x^3}{[(2+x)(1-x)^2]}\right)P \quad \textbf{(2-63)}$$

When x <<1 equation (2-63) can be approximated to [24]:

$${k_1}^2 = = \frac{x^3}{2}P \quad \textbf{(2-64)}$$

From equation (2-63) ‘x’ could be derived and its substitution into equation (2-64) allows the oxygen partial pressure in equilibrium to be expressed as [24]:

$$pO_2 = \left(\frac{k_1}{2}\right)^{\frac{2}{3}} P^{\frac{2}{3}} \quad \textbf{(2-65)}$$

Equation (2-65) allows calculating the oxygen partial pressure in system, which is resulted from steam dissociation under considered conditions. Calculated oxygen partial pressures allow the identification of the oxides species able to form. Such values could be acquired from Ellingham diagrams or the diagrams based on calculations such as shown in Figure 2-22 [23, 24]:

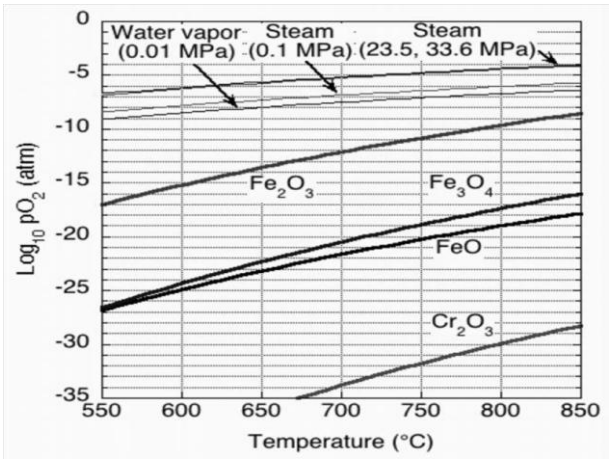

Figure 2-22 Effective oxygen partial pressures in steam [24]

As was highlighted in introduction, the formation of volatile chromium species is an important process, influencing the oxidation rate [23, 74]:

$$\frac{1}{2}Cr_2O_3(s) + H_2O + \frac{3}{4}O_2 = CrO_2(OH)_2(g) \quad \textbf{(2-66)}$$

Assuming that the oxygen is supplied just from the steam dissociation and chromia activity equals zero, the oxygen partial pressure in equilibrium could be expressed as [23]:

$$pCrO_2(OH)_2 = k_{10}\, pO_2^{\frac{3}{4}}\, pH_2O \quad \textbf{(2-67)}$$

where k_{10} is an equilibrium constant for chromia volatilisation. By using equation (2-67) the possibility of the chromia volatilisation can be assessed. This allows the identification of the conditions required for this volatile chromium oxy-hydroxide species to form. In the literature [24, 75, 76], the volatilisation of chromia is reported to be slow at low temperature and therefore, is often neglected, however according to Holcomb [77, 78] it can cause significant metal loss of the material exposed even below 700°C.

2.5.3 Steam oxidation of ferritic steels

Steam oxidation of ferritic steels varies with alloy type (mostly chromium content), time and exposure conditions [67, 74, 79]. Thus ferritics have been divided into low chromium steels (0 - 2.25Cr), and ferritic-martenistic steels (9 12% Cr). Moreover, there is a third group of ferritic steels with chromium contents above 12 % [18, 26]; however such steels are not widely used for the coal-fired boiler tubing. The literature shows that the oxidation of ferritic steels initially has a linear rate dependence, which changes into parabolic after first, thicker oxides layer has been formed [80]. While the transformation between oxidation rates is well known, the precise time of such transformation is believed to be complicated [15]. This is in agreement with findings of Ennis and Quadakkers [53], who believe that the transformation point between the rates is associated with fact that the initial period of oxidation under different exposure condition may last from a few seconds to hundreds of hours.

Wright and Pint [19] have found and described a general mode of oxidation for low chromium steels (up to 2¼ % Cr): the steam oxidation process follows the parabolic rate law up to 580°C, but above that temperature the rate changes to linear. This phenomenon was explained by the morphological changes in the scales formed during longer exposures. Moreover, tests conducted by Khanna et al. [81] have shown a parabolic rate dependence for steam oxidation process of 9 % Cr ferritic steels in the temperature range 500 – 800°C. This is also in agreement with Viswanathan et al. [15], who concluded that for 9 - 12 % Cr steels steam oxidation exhibits a parabolic dependence up

to 800°C in laboratory studies. However, Sarver and Tanzosh [29], have shown that above 700°C the oxidation rate transforms to linear for steels with chromium content below 15%, this is consistent with the power plant experience, which indicates 700°C as temperature, above which a linear rate dependence starts to prevail [15].

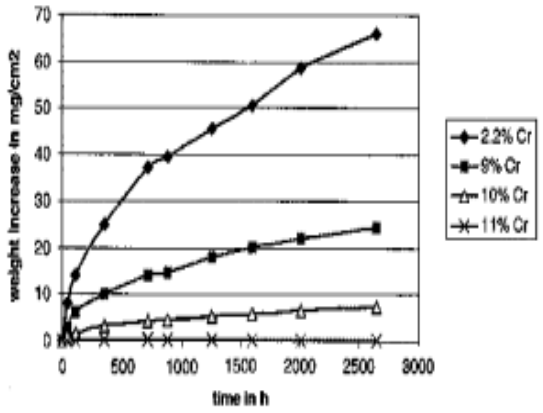

Figure 2-23 Weight changes rate for example ferritic steels in steam environment at 600^{O}C [56]

The oxidation behaviour of ferritic steels is significantly influenced by their chromium content [66], which is associated with the formation of highly protective chromia or semi-protective (Fe, Cr) spinels. However, there is no clear evidence for the minimum Cr content which is sufficient for development of the protective chromium oxides. Shibli and Starr [80] indicated that level of 10 - 11 % chromium is sufficient to chromia (Cr_2O_3) to form in the temperature between 600 - 650°C. In contrast, Sanchez et al. [66] have shown that such a level is around 11 – 12 % for steels exposed to steam at temperatures above 600°C.

Oxidation rates in steam exhibit strong temperature dependencies, which can be described by the Arrhenius relationship. An Arrhenius relationship can be used to calculate the activation energies of oxidation processes to give information about the rate controlling process [15]. Wright and Pint [19] have studied the activation energies for the oxidation of a diverse range of ferritic steels at elevated temperatures. The main conclusion of Wright and Pint [19] is

that the activation energy, for both classes of steels, does not show one clear mechanism which controls the oxidation process. The activation energy values are consistent with the top values corresponding to Fe diffusion in Wustite and low values to iron diffusion in magnetite. Activation energies derived from the service and tests for example ferritic steels in a steam environment are presented in Table 2-6.

Table 2-6 The parameters of oxidation kinetics in steam [23]

Alloy type	Temperature range [°C]	Pressure range [bar]	Oxidation Parameters	
			Arrhenius constant [μm^2/hours]	Activation energy [kJ/mole]
Service data				
T22	482-621	146	6.22×10^{20}	-326
2.25Cr-1Mo	500-700	-	1.51×10^{14}	-223
T91	550-700	-	2.51×10^{11}	-199
9Cr	495-700	-	3.97×10^{11}	-197
Laboratory data				
2.25Cr-10Mo	550-700		2.05×10^{20}	-368
T91	650-700	17	2.3×10^{8}	-142
T92	650-700	17	24	-19

Ferritic steels oxidised in steam in laboratory tests develop different scales which are dependent on the exposure conditions as well as alloy type. Typically the low chromium (2.25 % Cr) exposed to steam are expected to develop triple layered scales. Those scales consists of (Fe, Cr) spinel, magnetite and haematite; however in laboratory test only double-layered scales have been found. These scales consist of the inner (Fe, Cr spinel) and outer magnetite [19, 24, 26, 27]. The composition of the spinels formed, change with the chromium content of base material. Although the haematite is expected to form there is no continuous layer forming in the laboratory tests. In power plant after longer exposure the haematite is forming on the surface, often there are discontinuous patches of Fe_3O_4 growing at the outer surface [24].

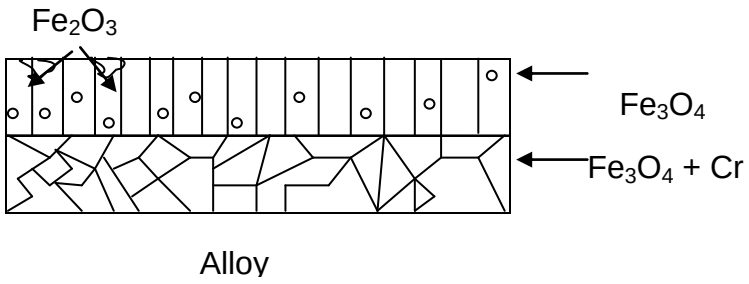

Figure 2-24 Typical cross-section of the scale formed on the feritic steels

Figure 2-24 shows the cross-section of a typical oxide scale formed on ferritic steels after service in power plant. The inner layer has an equiaxed grain structure with finer porosity, whereas the outer layer has columnar grains with pores at the grain boundaries [24]. The thickness ratio between these layers is believed to be independent of time for a selected alloy; however, it changes with alloy type and chromium content. In literature, the ratio between the inner and outer layer for the ferritics is often reported to be 1:1 [82]. Additionally, after longer exposures at elevated temperature (560°C) the low chromium steels can form micro-layered inner structures with repeating layers of magnetite and Fe-Cr spinel [23]. In laboratory exposures its formation is believed to be a result of the scales reaching the temperature for FeO formation, which after long exposures change (decompose) to magnetite [24]. In power plants, the formation of micro-layered inner oxides is reported to be a result of heat flux, which is not present in laboratory tests [79]. During steam oxidation exposures voids nucleate within the scales, which have significant impact on the ions diffusing across the oxide and therefore on the oxidation processes themselves [24]. In addition, there can be crack formation at the interfaces between the inner and outer oxide layers, which after long exposure could lead to scales exfoliation.

Figure 2-25 and Figure 2-26 show the scales formed on 1 and 2.25 Cr exposed at 625°C and 550°C respectively. In cases of 1 % Cr steels exposed at 625°C (Figure 2-25) the oxide scale is triple-layered with layer of wustite and chromia close to alloy surface and two layers of magnetite. The inner layer is not porous, whereas the outer magnetite shows significant porosity [67].

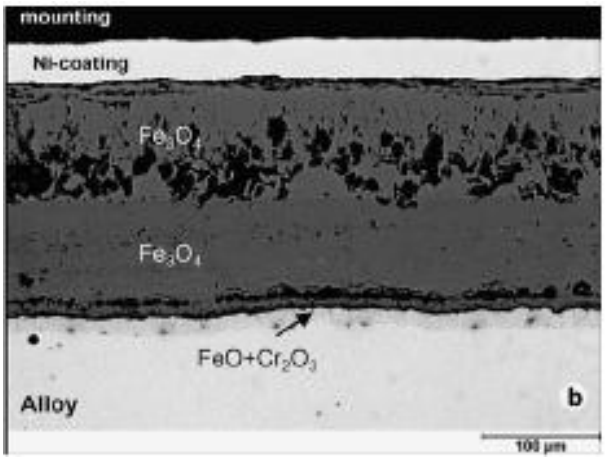

Figure 2-25 Scale morphology of 1Cr % steel at 625℃ after 1000h [67]

In comparison T22 exposed at 550°C has an inner layer of the (Fe, Cr) spinel and an outer layer of magnetite (Figure 2-26), such an oxides structure is in agreement with findings of Komai et al. [27] and also reported by Wright and Dooley [24], and EPRI [23].

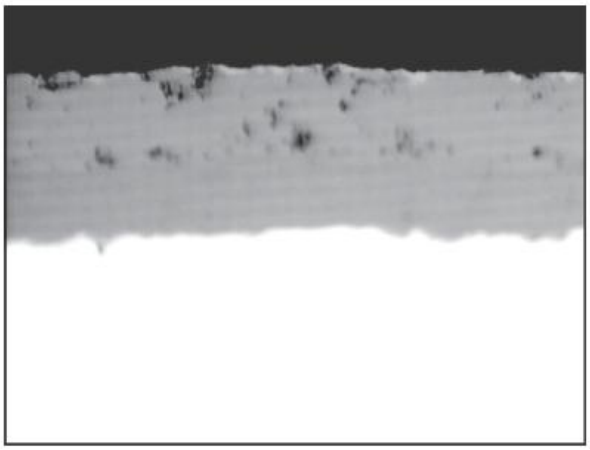

Figure 2-26 The scale formed on the T22 ferritic steel at 550°C [72]

Figure 2-27 and Figure 2-28 show the scales formed on 9 Cr steels exposed to steam at 650°C and 800°C respectively. At both temperatures, double-layered scales have developed with inner spinel and outer magnetite, but the thickness of those layers change with exposure temperature. The clear difference between the two temperatures is void formation and scale adherence. At 650°C the scale is not adherent to the surface and there is gap

formation at the interface between inner and outer layer [22], however this could be induced during the preparation of the specimen cross-section.

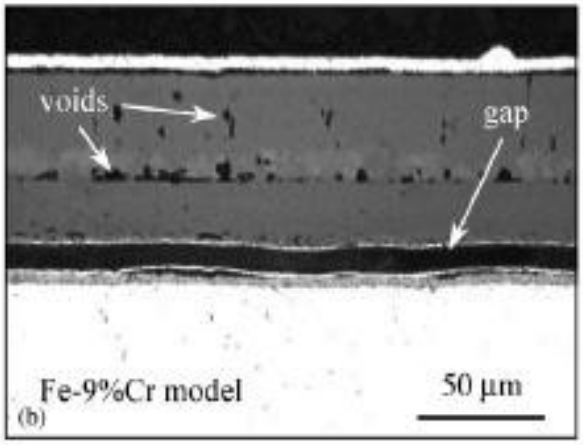

Figure 2-27 Morphology of 9Cr % alloy after exposure in steam at 650°C for 1000h [18]

At 800°C the scale is more adherent and there is no void formation within either of the two layers distinguished; moreover the scale is significantly thicker. Comparison of the scales formed on low and higher chromium steels showed that the largest differences are in terms of scales thickness, void formation and scale adherence [23. 26, 27].

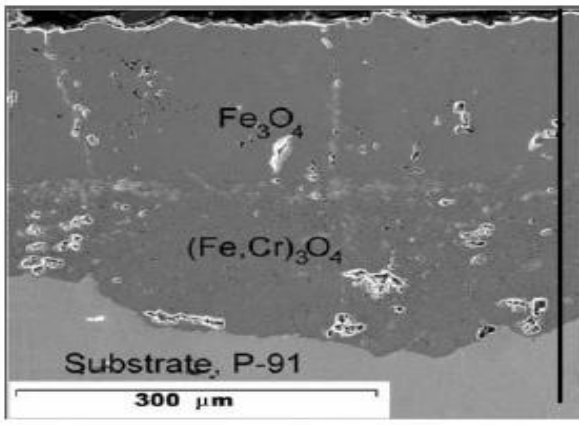

Figure 2-28 Scale morphology of P91 after 1000h exposure at 800°C [66]

Literature review showed that the formation of the oxides on ferritic steels grows simultaneously at both oxide/gas and metal/oxide interfaces, therefore the interface between inner and outer layer is believed to correspond to the original

metal surface [83] The mechanism of steam oxidation of ferritic steels is not completely clear and understood [24]. It has not jet been defined, which of the ions that could be formed during steam dissociation has the greatest impact on the oxidation process. The steam dissociation produces oxygen, hydrogen in gas as well as hydroxyl ions on the material [84]. Wright and Dooley [24] suggests that gaseous steam or hydroxyl ions can be involved in the process, however there is a significant uncertainty how the steam-derived species transport in scale and the form which they taking (ion, atom or molecules). To help identify the prevailing species the ionic size can be considered; H^+ is the smallest, whereas oxygen and hydroxyl ions have similar sizes [19]. Tomlison and Cory [85] have proposed that the oxidation mechanism involves outward diffusion of iron and electrons across the scales, and inward diffusion of steam molecules along fines pores; in addition to proton diffusion in both directions. There is also a theory proposing that the oxidation involves inward diffusion of hydroxyl ions with oxidation at the metal/oxide interface and hydrogen released during oxidation diffusing through the metal [24].

Wright and Dooley [24] proposed that in order for the uniformed scales with clearly distinctive layer to form, there have to be an equated number of ions species arriving at each interface. The iron ions, responsible for growth of the columnar outer layer, react at the gas/scale interface with oxidising species (mainly oxygen [15], however, there is a possibility that molecular steam is also involved at this stage); those ions arrive at the interface via lattice diffusion across the magnetite layer. In comparison, the inner spinel layer is assumed to grow at the alloy/oxide interface, for considered Fe-Cr alloy there is a competition between formation of magnetite and chromia, which according to thermodynamics calculation would form as internal oxides precipitates of Cr_2O_3 or inner iron, chromium spinel. Moreover, the oxidant is believed to be present in form of either oxygen ions, hydroxyl ions or the steam molecules. The ions arrive at this interface via short circuit diffusion along the grain boundaries, while the H_2O molecules are transported through pores. The important mechanism, which allows coupling between the ions involved in the scale

growth, is dissociation of Fe_3O_4 at the magnetite/spinel interface, which makes iron ions and oxygen ions available to diffuse to the reacting at the interfaces which enables oxidation to proceed.

Figure 2-29 presents mechanism for initial double-layered scales growth on ferritic steels exposed to 100% steam conditions, before any transition to multilayered scales. It presents the processes involve as being outward diffusion of chromium and iron ions and inward diffusion of oxygen, hydroxyl ions. The first stage of the steam oxidation is the most problematic to be defined, in literature five processes are suggested Figure 2-29A [24]:

- Formation of magnetite at the steam/oxide interface;
- Formation of magnetite at the inner/outer layer interface, which is controlled by reaction of iron diffusing outwardly with hydroxyl ions;
- Growth of internal chromia particles and inner magnetite due to reactions involving hydroxyl ions diffusing inwardly (short circuit diffusion) at the alloy/oxide interface;
- Development of discrete, internal particles of Cr_2O_3 and inner Fe_3O_4 layer as result of the reaction at the alloy/oxide interface between metal ions and molecular steam diffusing through the oxide; and
- Formation of Fe_3O_4 at steam/oxide interface and the internal chromia at alloy/oxide interface from the Fe and O ions produced via dissociation of magnetite.

The scales continue to grow with time, mostly as a result of diffusion of various ions across the scale layers and atoms from the alloys. The internal particles of chromia are incorporated into the magnetite and the (Fe, Cr) spinel forms. The chromium concentration within the inner layer increases with time, thus the diffusion of iron ions is expected to be impeded (Figure 2-29B). The further dissociation of the outer magnetite provides a sufficient level of oxygen for the oxidation to continue; however, it promotes the development of voids. When the level of chromium at the alloy/oxide interface is sufficient, a layer of chromia may form at his interface, which further reduces the oxidation rate and due to its

impact slowing down iron diffusion, it promotes the formation of haematite [23] (Figure 2-29C).

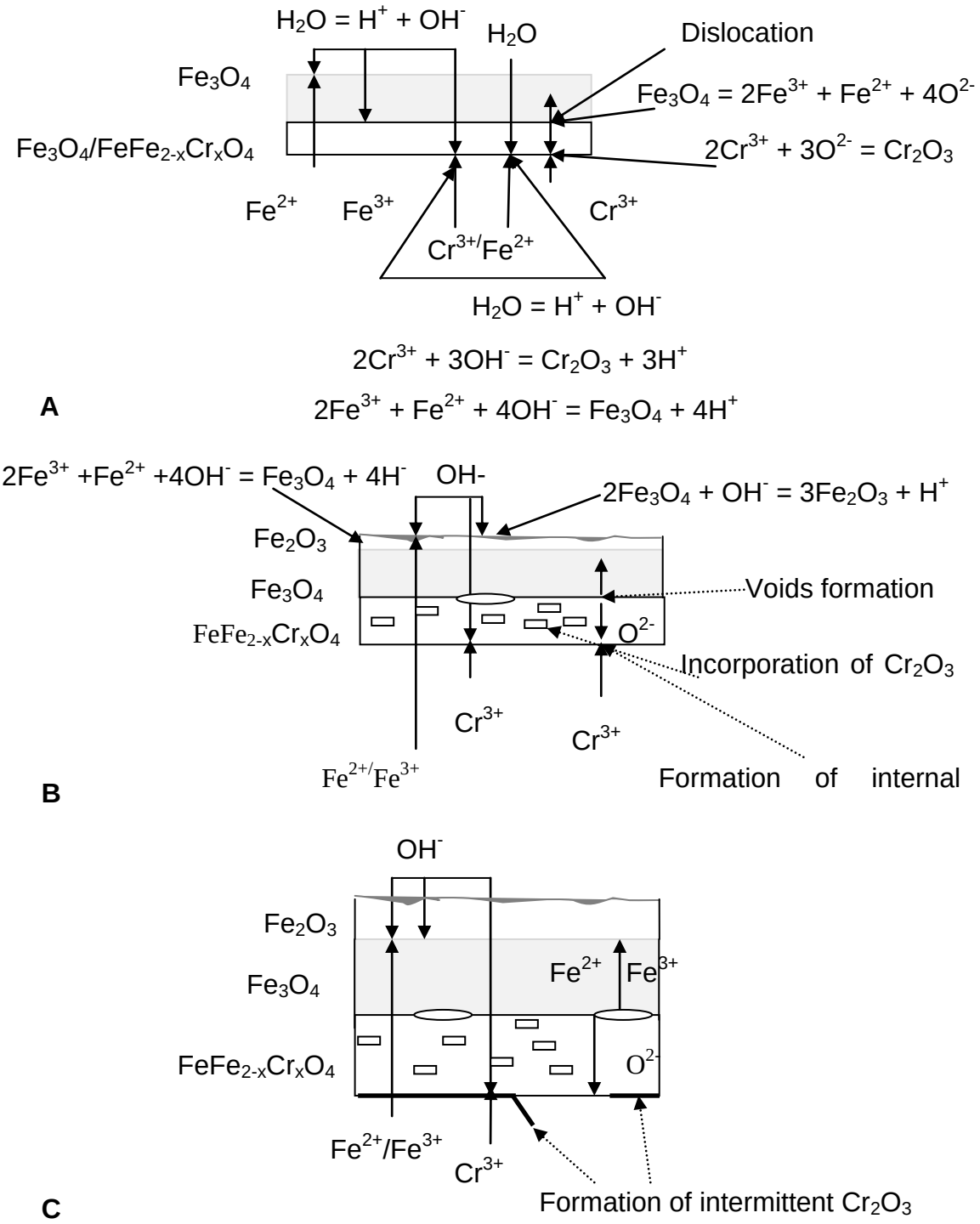

Figure 2-29 Schematic representation of the scale growth mechanism for the ferritic (≤9% CR)steels in steam [23]

2.5.4 Steam oxidation of austenitic steels

Wright and Pint [19] studied the oxidation behaviour of austenitic steels and compared it with various types of ferritic steels. They have found that austenitic steels show much better oxidation resistance than ferritics; their oxidation rates are slower due to formation of more protective chromium rich scales [23]. The oxidation of austenitic steels exhibits a parabolic rate law dependence; however after long exposures time it tends to change to linear as was observed for the ferritic steels. Moreover, Viswanathan et al. [15] indicate that fine grains and increasing Cr content decrease the oxidation rate, in contrast, the oxidation rates increase rapidly with temperature. Viswanathan et al. [15] have shown that the austenitic steels with the chromium levels above 25% have very good oxidation resistance due to their ability to form good, external, uniform Cr_2O_3, which has a low oxidation rate. Sarver and Tanzosh [29] also believe that the alloy grain types and sizes significantly influence the oxidation resistance. The impact of alloy grain structure were analysed in detail by Hansson and Montgomery [49] for TP347HFG and compared with coarse-grained TP347H. The results, of the study also show that T347H with finer grains exhibits s better oxidation resistance than the coarse-grained variety.

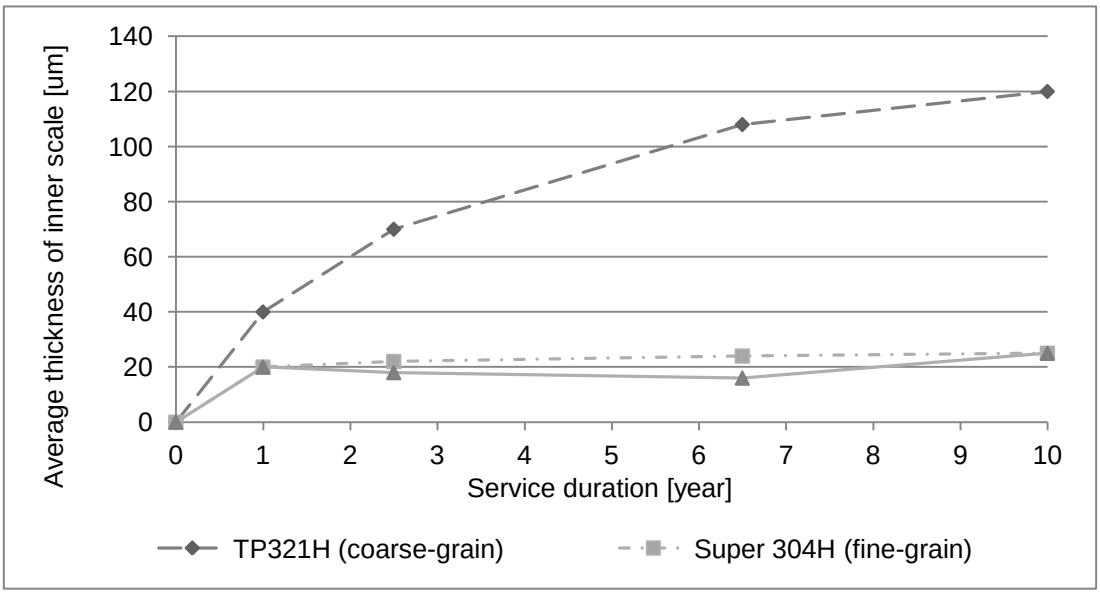

Figure 2-30 Change of the average thickness of the inner scale after service exposure as superheater tubes in a practical 571°C boiler [86]

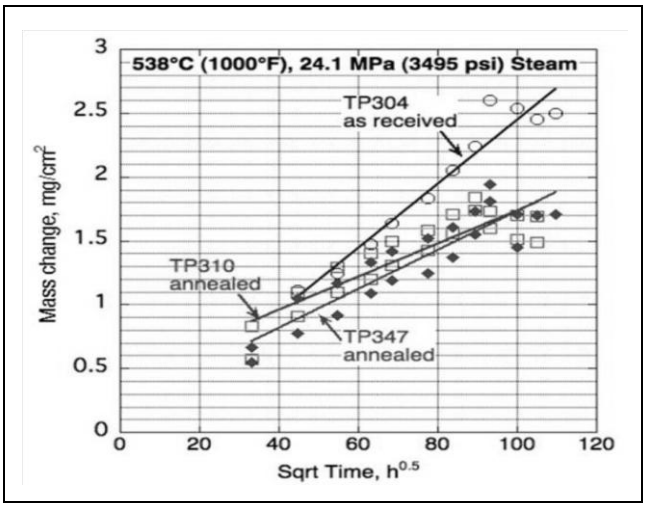

Figure 2-31 Oxidation kinetics of the 300 series austenitic steels at 538°C [24]

Figure 2-30 and Figure 2-31 show that the oxidation of austenitic alloys change with alloy composition and the grain structure. The activation energies for the oxidation processes of austenitic steels are presented in Table 2-7 for both service and laboratory exposures.

Table 2-7 The parameters of oxidation kinetics in steam (FG- Fine-Grained, CG-Coarse-Grained) [23,24]

Alloy type	Temperature range [°C]	Pressure range [bar]	Oxidation Parameters	
			Arrhenius constant [μm^2/hours]	Activation energy [kJ/mole]
Service data				
TP304H (FG)	571	1-350	$1.58x10^{11}$	-199
TP347H (CG)	650-700	1-350	$3.09x10^{7}$	-132
TP347 (FG)	525-675	1-196	$7.94x10^{7}$	-164
Laboratory data				
TP321H/347H	575-650	1	$2.16x10^{4}$	-38
Fe-25Cr-15Ni	500-900	1	$1.34x10^{9}$	-234
Fe-18Cr-15Ni	<650	1	$1.29x10^{16}$	-279

Steam oxidation of austenitic steels can be divided into two groups: first with the chromium and nickel levels below 20%, and with large grains (coarse-

grained); and, second with Cr concentration above 22% and >20%Ni and with smaller grains (fined grained) [49].

Alloys from the first group form double/triple-layered scales (Figure 2-32), which predominantly consist of an outer zone of Fe_3O_4 and an inner zone of Fe-Cr spinel and chromia layer next to the alloy surface [87]. The layers thicken with time, with the inner layer becoming non-uniform and the outer layer becomes more porous. The scales formed on TP347H change significantly with the exposure conditions [49, 88, 89]; Sumida et al. [90] reported that at temperatures of 575 - 650°C (and 1 bar steam) the outer layer is pure magnetite whereas the main constituent of the inner zone is $FeCr_2O_3$. Montgomery et al. [91] have also shown that at 540°C and at 91bar steam TP347H has a double-layered structure as identified by Sumida et al. [90] However, there is a significant exfoliation of the outer magnetite layer. In contrast, TP347HFG exposed at 670°C for 11khrs has formed an additional layer of haematite on the top of the magnetite layer; moreover, there is formation of external chromia at the alloy/oxide interface.

Alloys, from the second group, show double-layered oxide structures, which are much thinner (Figure 2-33). The initial scales are continuous with main constituents identified as high chromium Fe-Cr spinel ($FeCr_2O_4$), and Cr_2O_3. Such scales effectively suppress the non-protective oxide growth [15, 88]. After longer exposures, the Cr_2O_3 thickens and there are local breakdowns of the scales, and so surface nodules are able to form. Those nodules are double-layered with mixed (Fe, Cr) oxides as an inner layer and magnetite as the outer layer respectively; their further growth can be suppressed as a result of the rapid developed of a chromia layer [24].

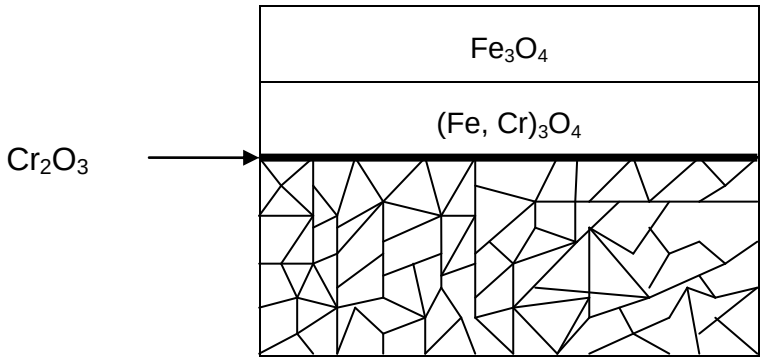

Figure 2-32 Scale formed on the fine-grained version austenitic steel [15, 88. 92]

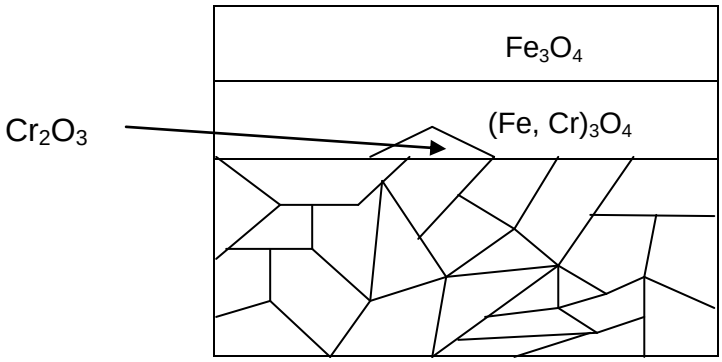

Figure 2-33 Scale formed on the coarse-grained version of austenitic steel [88, 92]

Wright and Dooley [24] collated data on mechanism of oxides growth during steam the oxidation of austenitic steels, and based on them following conclusions have been derived. Initially the oxide scale formed is an uniform layer of M_3O_4-type of oxides, where M is Fe Cr and Ni. These protective scales breakdown and thus nodules are able to form. Nodular growth is controlled by both inward and outward diffusion. Within a nodule, two layers can be distinguished: the first, growing outwardly, is pure Fe_3O_4; whereas the second is $FeFe_{2-x}Cr_xO_4$ spinel, which grows inwardly. The inner layer within the nodule grows by penetration of the spinel along the grain boundaries and so the level of chromium within those grains decreases as a result of chromium outward diffusion. Finally, the chromium-depleted grains oxidises to pure magnetite [88, 89]. In consequence the inner layer becomes a mixed of Fe_3O_4 and (Fe, Cr) spinel next to the alloy. The oxidation of austenitic steels is enhanced due to hydrogen dissolution [87, 93]; its presence in the alloy lattice results in internal

oxidation of chromium and formation of less protective scales. Moreover, the process is influenced by volatilisation of chromium oxides, the protective oxides are destroyed and the volatile $CrO_2(OH)_2$ forms [87, 93].

Figure 2-34 shows mechanism of the oxides development for T347HFG alloys, proposed by Jianmin et al. [88], it suggests four stages of the oxidation. Firstly, a thin layer of protective (Cr, Fe, Ni)$_3O_4$ spinel develops, its formation having been identified during 1000 hours exposure. The oxidation process continues and part of the oxidation front approaches the grain boundaries, where chromium rich Fe-Cr oxide grows. In parallel, the external spinel thickens. At this stage, nickel starts to contribute due to development of Fe-Ni oxide within the outer oxide.

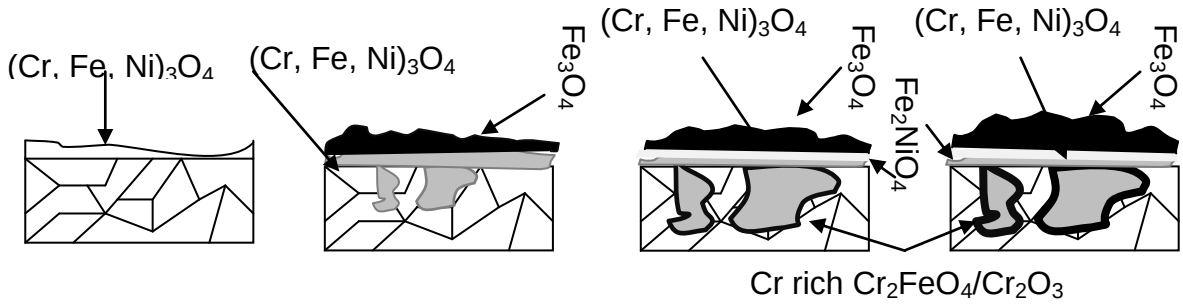

Figure 2-34 Development of oxide scale on austenitic alloys [88]

The third step is the healing of the grain boundaries due to the formation of chromium rich oxides; development of such oxides reduces the oxidation of that region. Formation of the chromium rich spinel or chromia layer results in reduction of the oxidation rate. In the forth step (after longer exposures) there is not enough chromium supplied to grain boundaries, therefore the protective layer starts to breakdown, which results in formation of the primary oxides and thus the oxidation rate increases.

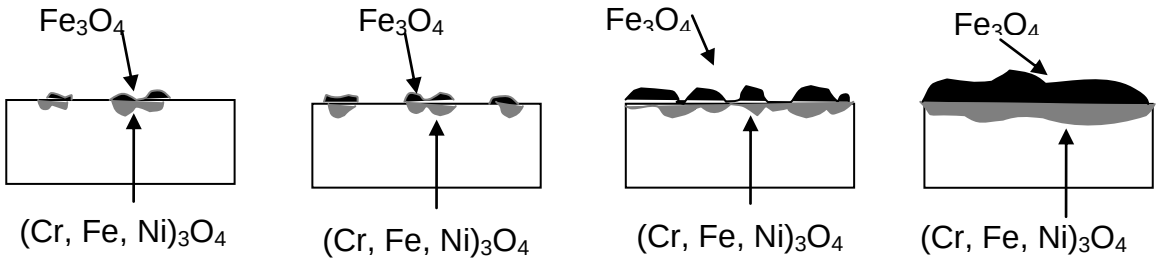

Figure 2-35 An inhomogeneous oxide growth on austenitic steels [82]

Figure 2-35 shows another view of the inhomogeneous growth of the oxides on the surface of 18Cr austenitic steels. It indicates localised growth of the corrosion products on the alloy surface, which grow as a result of the inward and outward diffusion of ions. The locations and thickness of the nodules increase with time so that during the exposure these oxides scales expand and finally cover the whole surface. After long exposure austenitic steels starts to develop voids within the outer layer, which are mainly concentrated at the inner/outer interface [23]. Those voids result in slow down of the outward iron diffusion and therefore part of magnetite can oxidise to haematite [92]. The amount of the haematite on the surface is a function of the porosity within the outer layer [23].

2.5.5 Steam oxidation of nickel-based alloys

Nickel–based alloys are the most steam oxidation resistant among the materials being considered as the candidates for the USC boiler tubing. However, their application is significantly limited due to their high costs. Most of the existing power plants operate under subcritical (170 bar and 540/540°C (SH/RH)) or supercritical (250 bar and 615/630°C) conditions and so such materials are not required. Steam oxidation of nickel-based alloys has been the subject of limited study [15]; and most of the information in the literature is presented as a mass change data as result of the very thin layers that developed on these alloy surfaces. Study of the oxidation kinetics of various types of nickel-based alloys has shown very little oxidation; eg Inconel 617 exhibits very slow oxidation rate at 480-538°C in 105 bar steam [15]. At higher

temperature (800°C) there was a breakdown of the scales formed and thus the oxidation rate significantly increased [24] Pearl et al. [94] report that the oxidation of Inconel 625 follows a parabolic oxidation rate law at temperatures between 566 – 621°C and at 67 bar steam pressure. However, the literature has a limited data showing parabolic rate dependence of nickel-based alloys, at high temperature and in high pressure steam [15, 24] Table 2-8 summarises values of the activation energies derived for nickel-based alloys available in literature [24]:

Table 2-8 The parameters of oxidation kinetics in steam [24]

Alloy type	Temperature range [°C]	Pressure range [bar]	Oxidation Parameters	
			Arrhenius constant [μm^2/hours]	Activation energy [kJ/mole]
Range of USC steam candidates PMCr	600-800	17-241	9.24×10^{-5}	-193
	650-800	17	1.27×10^{-6}	-160
	600-800	17	6.1×10^{-4}	-213

The oxide scales developed on nickel-based alloys vary with exposure conditions and alloy composition; however, in general they are very thin and protective. Below 700°C nickel-based alloys, with chromium level above 16 % show very slow oxidation and form protective scales [23, 28]. The scales developed under such conditions are very thin, mostly uniform, and protective with $MnCr_2O_4$ spinel or Cr_3O_4 as the main constituents [24]. Nickel-based alloys show some internal penetration but this varies with the alloy type and so is believed to be associated with the alloying additions. Internal penetration is reported by Wright and Dooley [24] to vary with exposure conditions and alloy type. It changes from discrete precipitates, directly underneath the external scales with some penetration along the grain boundaries to a large precipitation of internal oxides with frequent penetrations along grain boundaries [24].

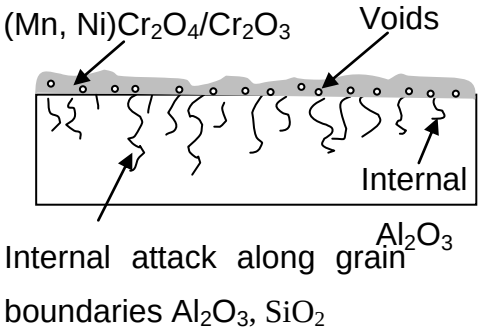

Figure 2-36 Schematic representation of the scale formed on nickel-based alloys in steam environment [23]

At 800°C Inconel 617 are reported to exhibit a breakdown of highly protective oxidation Figure 2-37, and as a consequences the double-layered nodules form, with the outer layer of NiO and a inner layer of the intern Cr_2O_3 precipitates. The breakdown in protective oxide is a result of the chromium concentration being too low next to the surface, (lower than the critical value of the external scale formation [57, 60]). The current literature shows that important factors for nickel-based alloy performance in steam environment are the depth of the internal penetration and difference in the diffusion rates of chromium within the alloys [24].

Figure 2-37 Scaled developed on Inconel 617 after 4000 hour exposure at 800°C in 17 bar steam [23]

2.5.6 Scale spallation

The scale formed on the ferritic steels mostly consist of two layers; inner layer of Fe, Cr spine oxides and the outer layer which main constituent is magnetite with haematite as the outermost layer. Viswanathan and Bakker [17]. indicated that inner and outer layer formed on alloys are uniform in thickness. The exfoliation mechanism has also been reported to change with increasing chromium content, therefore three mode of exfoliation were identified [23].

For the low chromium steels up to 9% Cr the oxide scale consist of two layers, magnetite (outer) and Fe, Cr spinel oxides (inner), the oxide scale thickens with time. It results in formation of new double oxide layer above original scale. Such mechanism drives to formation of multilayered scale, which tends to spall due to cracking and layers separation [15]. Flakes of the scale exfoliated from ferritic steel are reported by Saunders et al [74] to be larger than for austenitic steels due to their multilayered scale. The separation of the scale may not occur at the interface between the initial scale and the multilayered one [30] and two mechanisms are proposed to be in control of such exfoliation model. The First is different coefficient of thermal expansion for diverse layer and second cracking due to different stress distribution within the scale which may result in separation on metal/oxide and magnetite/haematite interfaces [96].

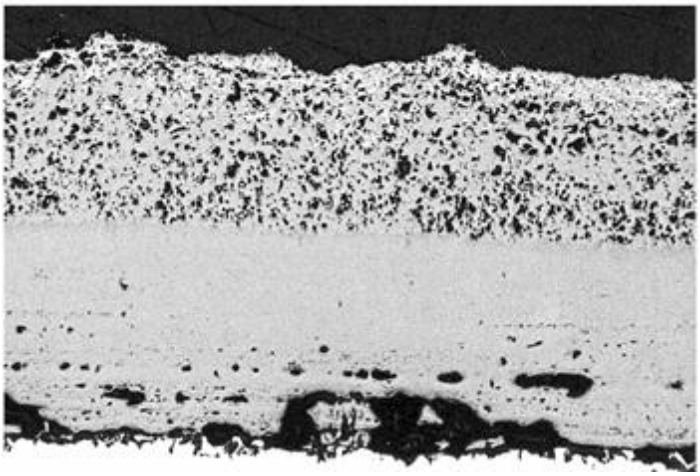

Figure 2.38 Scale of T22 alloy after exposure in steam at 550°C for 212 kh [23]

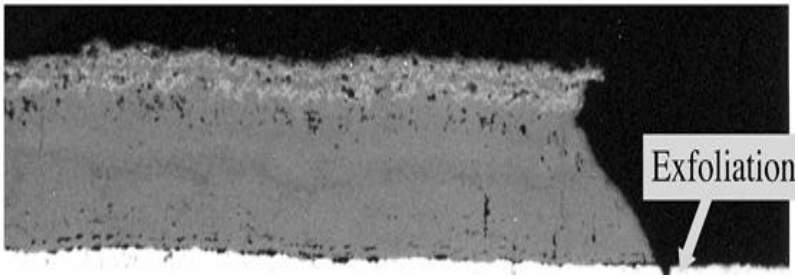

Figure 2.39 Spallation of T22 alloy after exposure in steam at 435°C for 189 kh [23]

The ferritic alloys with higher Cr content follow different exfoliation process; the main example of that group of steels is T91. As was discussed in previous section the scale developed on T91 is double layered. According to test conducted by EPRI [23] and Saunders and McCartney [74] the exfoliation on T91 appears over wide, the reaming scale is uniform in thickness. The spallation occurred between inner and outer layer. The same mechanism of spallation was proposed by [97] for P91 alloy. In both cases the spallation of outer layer is a result of voids and cracks nucleation at the interface between Fe, Cr spinel and outermost magnetite [97].

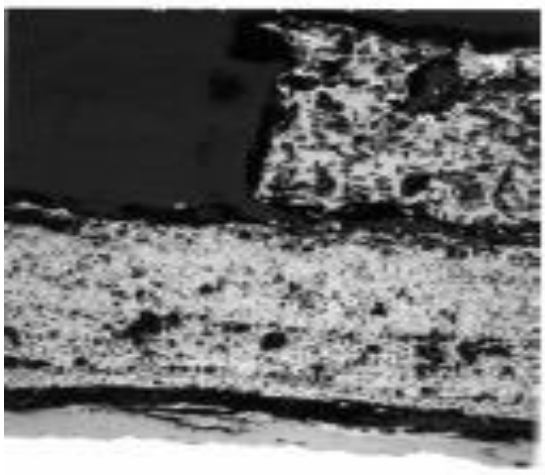

Figure 2.40 Exfoliation of outer layer from T91 alloy [23]

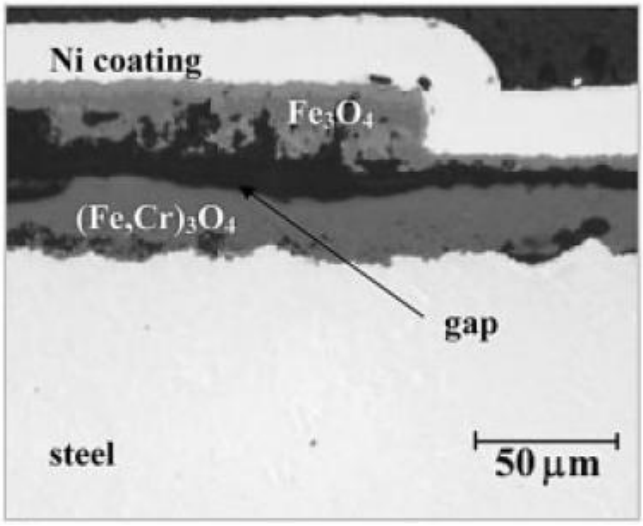

Figure 2.41 Gap formation between inner layer and magnetite on the P91 alloy [97]

Saunders and McCartney [74] propose that exfoliation on T91 is based on following mechanism. On the interface between inner and outer scale voids start to nucleate, which is believed to be a result of different diffusivities between its main constituent – iron and oxygen. Due to formation of voids the diffusivity of iron is reduced, therefore precipitates of magnetite in the outer layer oxidise to haematite [26]. The formation of haematite leads to different stress distribution within the scale during cooling down process EPRI believed that transformation of 10 % magnetite to haematite is sufficient to cause scale spalliation. Ennis and Quaddakers [53] indicate that scale spallation for diverse types of ferrtic steels occur due to voids formation within the magnetite layer. They have also proposed that such mechanism is significantly dependent on alloy composition, temperature and exposure time.

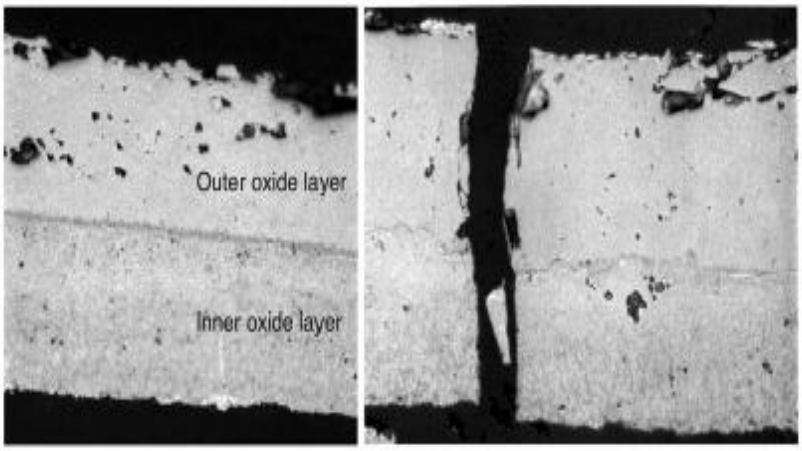

Figure 2.42 Exfoliation of oxide scale from T91 alloy [23]

The third mode of exfoliation was proposed for ferritic steels with chromium level about 12 %. EPRI [23] analyses the exfoliation process of X20CrMoV121 alloy (12Cr), the scale formed on such steels exhibits two layers, outer layer with high hematite levels and inner with Cr - rich spinel. The mode proposed by EPRI [23] indicate that exfoliation is a result of tensile stress which is develop during the cooling-down, the spallation involves mostly the outer layer.

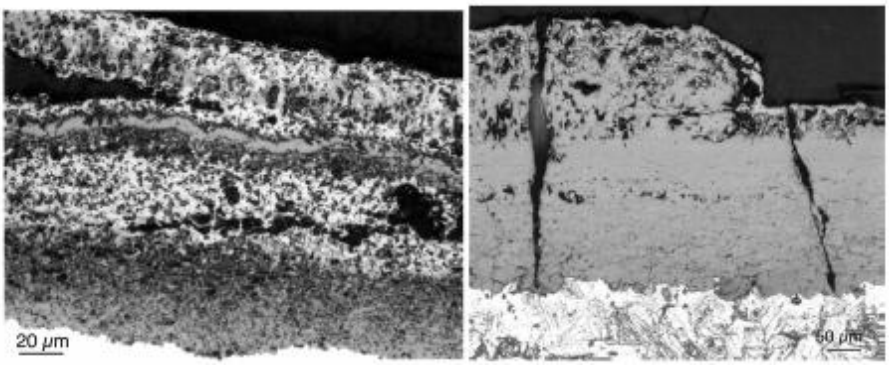

Figure 2.43 Scale exfoliation of X20CrMoV121 ferritic steel

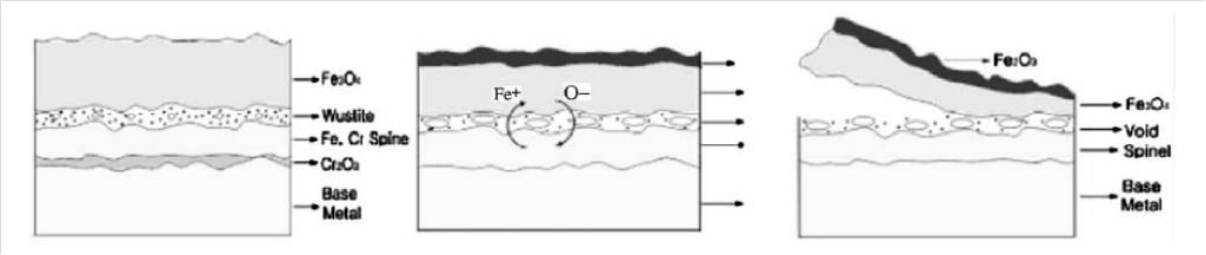

Figure 2.44 Mechanism of scale exfoliation for T91 alloy [25]

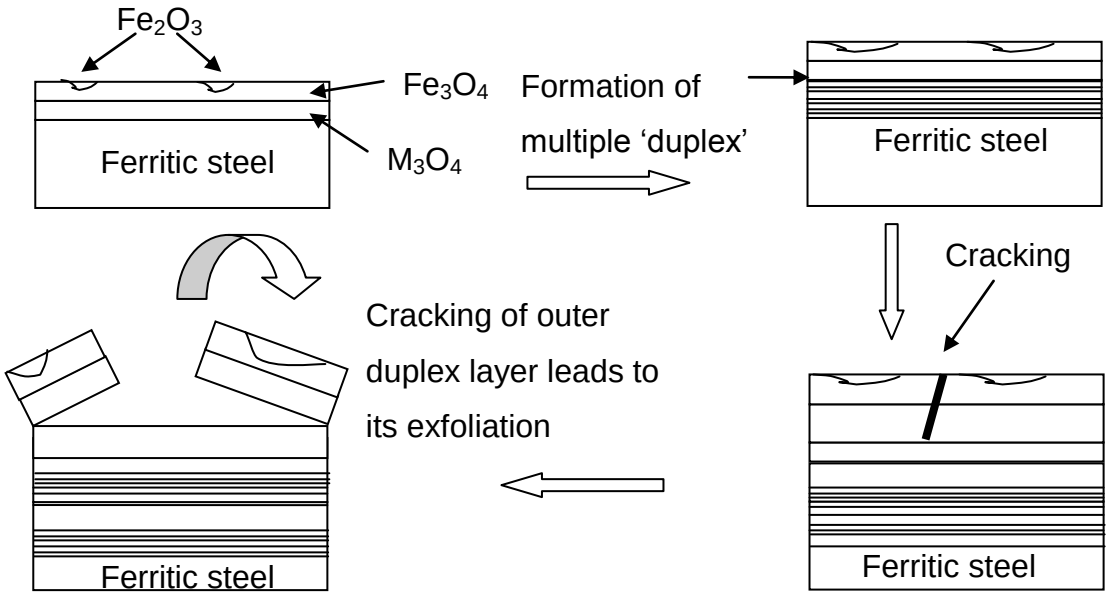

Figure 2-45 Schematic representation of the usual sequence of events in the scale spallation from low chromium ferritic steels [23]

Scales formed on the commonly used austenitic steels from 300 series stainless steels is double – layered, as in case of the 12 Cr ferritic steels. However, the formation time of the scale is significantly longer than for ferritic steels due to better protectiveness of Cr-Fe spinel. The scale developed on the 300 SS has two distinguished layers – inner with Fe, Ni, and Cr spinel oxides, and outer with magnetite as main constituent in some case especially for longer exposure time some precipitates of haematite can be identified as the outermost layer [30]

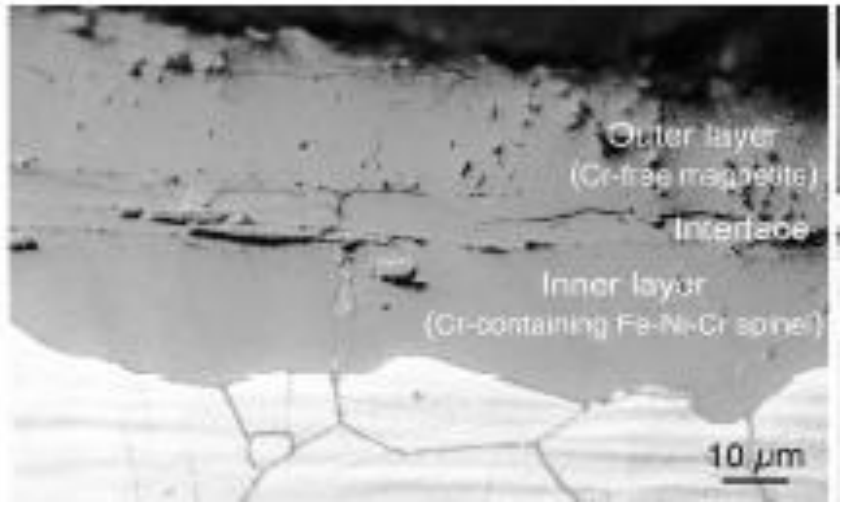

Figure 2.46 Scale formed on 304 austenitic steel in steam EPRI [23]

The inner layer is not regular in thickness as a result of different formation rates of protective oxides; due to this the interface between inner scale and alloy is convolute [87]. In comparison the outer layer is columnar – grain but it shows not – uniformity in thickness. The thickness irregularity of oxide layers has a positive impact on scale adherence. The appearance of haematite within the outer layer depends on following factors; rates of ionic diffusion through the scale and voids formation on the inner/outer interface. EPRI [23] report proposes that scale formation of 300 SS is associated with proportion between haematite and magnetite within the outer layer. The increasing concentration of haematite leads to development of the compressive stress during cooling-down [30]. This is result of differences in CTE between these two iron oxides. The austenitic steels with chromium content above 20 % in the long time exposure seams to develop scale with three different layers. The inner layer exhibits non – uniformity in thickness and consists of Cr-rich, Fe – Cr oxides. The scale has also two outer layers with magnetite and haematite as main constituents repetitively [87]. At the interface between outer and outermost layer number of voids may be seen, further nucleation of voids within this interface leads to scale exfoliation [30].

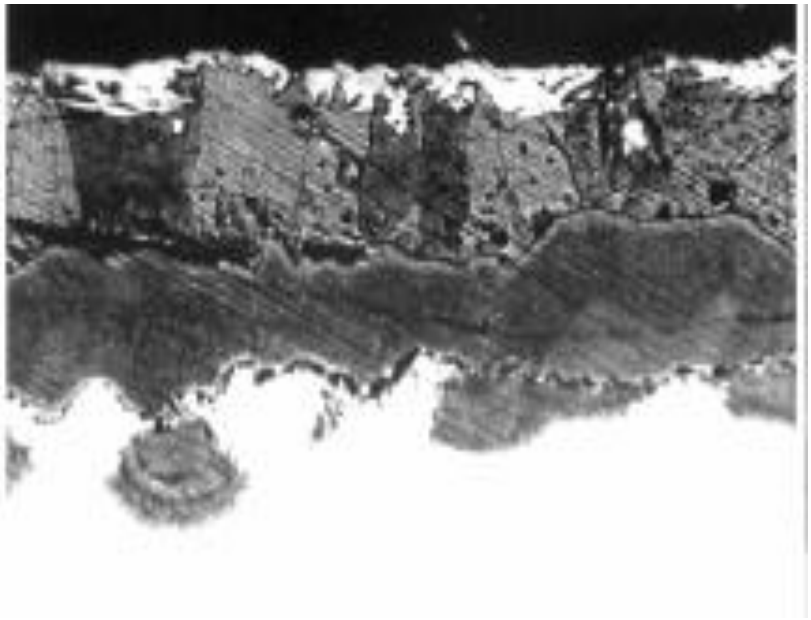

Figure 2.47 Development of the haematite within the outer scale of 304 Stainless steel EPRI [23]

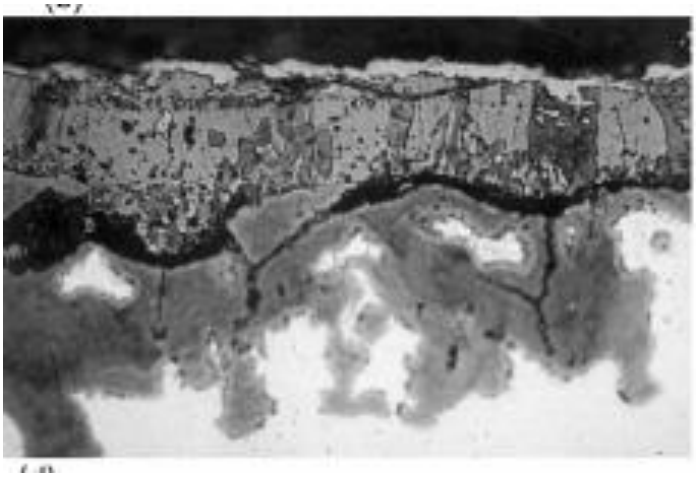

Figure 2.48 Separation of outer layer along magnetite layer EPRI [23]

Different mode of exfoliation was observed for alloys with higher chromium content - TP347H FG alloy [49]. It is important to remind that scale formed on the TP347H FG alloy is uniform and exhibits two layers [49]. After long time exposure the scale formed on TP347H FG became multilayered and the tracks of haematite appear. As it was mentioned before the concentration of hematite within the outermost layer is function of voids, cracks along the Fe, Cr spinel/magnetite interface EPRI [23].

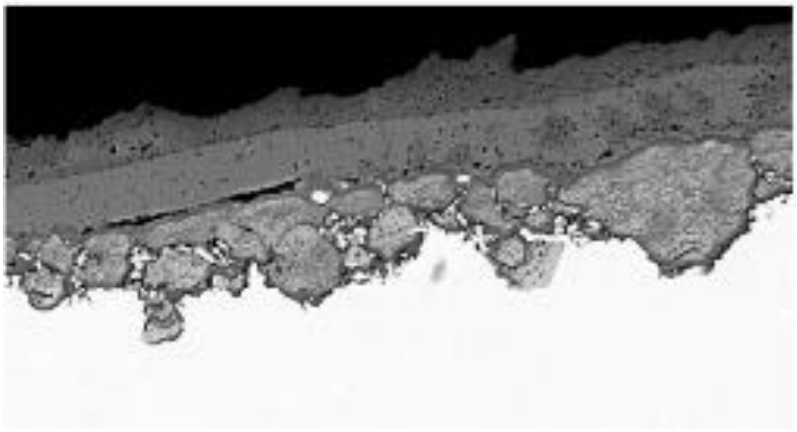

Figure 2.49 Multilayered scale developed on TP 347H FG [23]

The scale exfoliation appears at the interface between inner layer and outer layer, flakes of exfoliated scale consist of magnetite and haematite as presented in figure below Viswanathan et al [15].

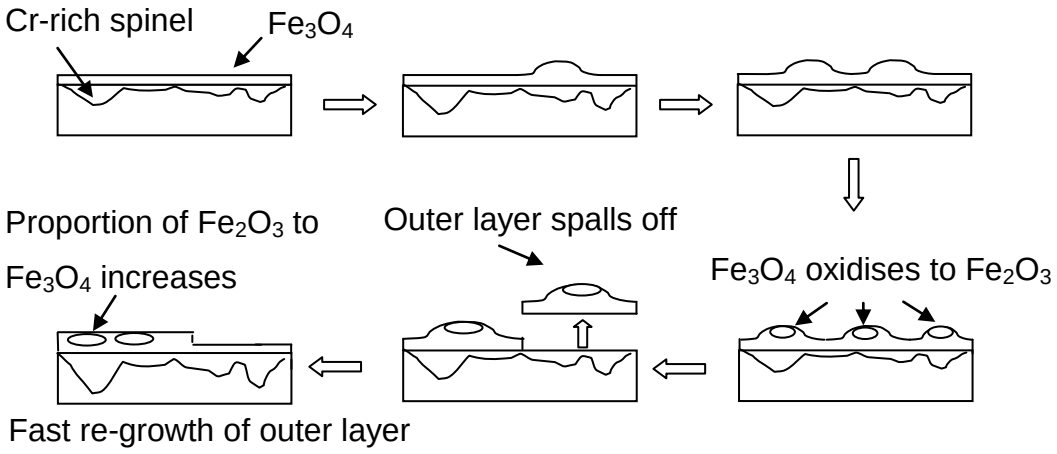

Figure 2-50 Schematic representation of the usual sequence of events in the scale spallation from austenitic steels [23]

2.5.7 Summary

The steam oxidation behaviour of materials used for heat exchangers in coal-fired boilers varies with alloy composition, exposure conditions (temperatures and pressures). In general, the lifetime increases with the chromium levels and smaller grain structures. Among the alloys considered, the nickel-based alloys are the most steam oxidation resistant.

3 EXPERIMENT PROCEDURES

3.1 Introduction and tests matrix

The literature review has shown that steam oxidation is an important phenomenon, which significantly limits lifetime of the coal-fired boiler tubing. Even though the growth of the oxides on material exposed to high temperature and pressure steam is an expected and unavoidable, the consequence of the oxide thickening and their failure are of growing concern in conventional power generation. In particular, reduction of heat transfer can lead to tube overheating, spallation of theses oxides can result in tube blockages. Mitigation of those consequences requires mechanistic understanding of oxide rate growth, evolution of the specific structures and finally influence of the factors such as time, steam conditions (temperature, pressure) and material composition. Currently, the power plant industry operates within the subcritical (540-565°C) and supercritical (600–620°C) conditions, however there is a growing interest in moving towards ultra supercritical conditions (700-760°C). Higher steam conditions will result in much faster oxidation, therefore the materials with higher chromium content or Ni-based alloys are required. Development of the modern, more efficient power plant requires maximising the use of the ferritic-martensitic steels to reduce use of the austenitic alloys in the hottest section of boiler, with maximum operating temperature of 620 and 670°C respectively. For higher temperatures, the Nickel-based alloys are required, with Alloy 617 and Inconel 740 as the most promising candidate. However, there is limited practical experience of their long-term behaviour is steam due to fact that those materials are not yet used in commercial boilers.

Literature research showed that laboratory studies in steam oxidation have covered wide range ferritic and austenitic steels. Steam oxidation of Ni-based alloys is still not well understood as there is limited information about their long-term as well as short-term steam oxidation behaviour. The literature covers many factors influencing the steam oxidation such as temperature, alloy type and composition on steam oxidation, as well as impact of the various

steam mixtures such as argon and steam or steam and oxygen. However, the data available is considering the material behaviour in the temperature range between 550-700°C. Literature research has indicated that there are a group of factors, that have not been extensively studied in the past or have never been considered as important to understand steam oxidation process. These factors are: steam flow rate, specimen shape, specimen surface finish. Moreover, there is uncertainty as to which of the species forming during steam dissociation are responsible for scale growth. To cover the gap identified in literature a test programme was designed to investigate following factors:

- Temperature effect in range between 600 and 750°C (for all materials tested);
- Alloy type and composition;
- Steam flow rate;
- Orientation against steam flow;
- Impact of material surface finish on oxidation of austenitic steels; and
- The steam oxidation mechanism of ferritic and austenitic steels by tracking an O^{18} isotope within the scales forming on the materials exposed

The steam oxidation test programme is divided into two groups of tests, the detailed breakdown of which is shown in Table 3-1. In the first group of tests (1-4) the impact of temperature in the temperature range between 600-750°C with low steam flow rate (4 mm/s) was studied. The second group of five tests analysed the impact of the steam flow rate on steam oxidation. In this group, materials were exposed to two different steam flow rates: middle (16 mm/s) and high (40 mm/s) at 650°C and 700°C. In addition, the specimens were exposed to high steam flow rate at 600°C.

Table 3-1 Test condition matrix

Test	Temperature [°C]				Steam flow rate [mm/s]		
	600	650	700	750	4	16	40
1		x			x		
2				x	x		
3	x				x		
4			x		x		
5			x			x	
6		x					x
7		x				x	
8			x				x
9	x						x

Each of the nine tests was 1000 hour exposure with four 250 hours cycles. During the first six tests, 37 samples were exposed to the 100% steam environment. Each of those samples were placed inside furnace in the alumina crucibles. In the last three tests, the number of specimens exposed differed. In the seventh test 27 specimens were exposed including ferritic, austenitic and nickel-based alloys, the specimens were weighed in 250 hour periods; however the destructive analyses were performed after 250 and 1000 hours. In the eighth and ninth tests 18 specimens were exposed and the post-exposure investigations of the specimens were carried out as for the seventh test. The eighth and ninth tests involved an investigation of impact of the specimen surface finish on steam oxidation of austenitic steels. Finally, in eighth test the specimens were exposed to steam doped with O^{18} to study the mechanisms involved in the general oxidation process (outward/inward diffusion). In total during the PhD project, 285 samples were exposed to pure steam and characterised, within a total sample exposure time of 9000 hours.

3.2 Material selection

Considering the material for the coal-fired boiler tubing there are three groups of materials for such applications: ferritic, austenitic and nickel-based alloys. For the steam oxidation tests the following materials from each of these three groups were selected (compositions shown in Table 3-2):

- T23, T92 alloys;
- TP347HFG, Super 304H, HR3C alloys;
- Inconel 740; and
- 800H alloy

Table 3-2 Nominal alloy composition [weight %]

Alloy	C	Ni	Cr	W	Co	Ti	Nb	Mn	Fe	Si	Cu
T23	0.06	-	2.25	1.5	-	-	0.04	0.45	bal	0.2	-
T92	0.13	0.4	9	1.87	-	-	0.09	0.6	bal	2	1
TP347HFG	0.1	10	18	-	-	-	0.8	1.6	bal	0.6	-
Super 304H	0.1	9	18	-	-	-	0.4	0.8	bal	0.2	3
800H	0.08	32.5	21	-	-	0.5	-	0.8	46	0.5	0.4
HR3C	0.01	20	25	-	-	-	0.6	2	bal	0.75	-
In740	0.03	bal	25	-	20	1.8	2	0.3	0.7	0.5	-

From the materials supplied, four different shape specimens were machined: full ring, curved-shape (1/8 full ring), rectangular and “bridge-shaped” specimens (Figure 3-1A-D). For tests 1 – 9 the surface of each specimen was ground to a 600 UK grit surface finish. For eighth and ninth tests four additional curved-shaped specimens where machined from austenitic T347HFG and Super 304H, two of those specimens were polished (the flat surface of the bridge-shaped specimen has been manually polished) and two left as received (pickled) from manufacturer. Ferritic and austenitic steels were tested in 3 different geometries (Figure 3-1A, B, C) whereas for Inconel 740 and 800H alloy just rectangular shape specimens were investigated (Figure 3-1D).

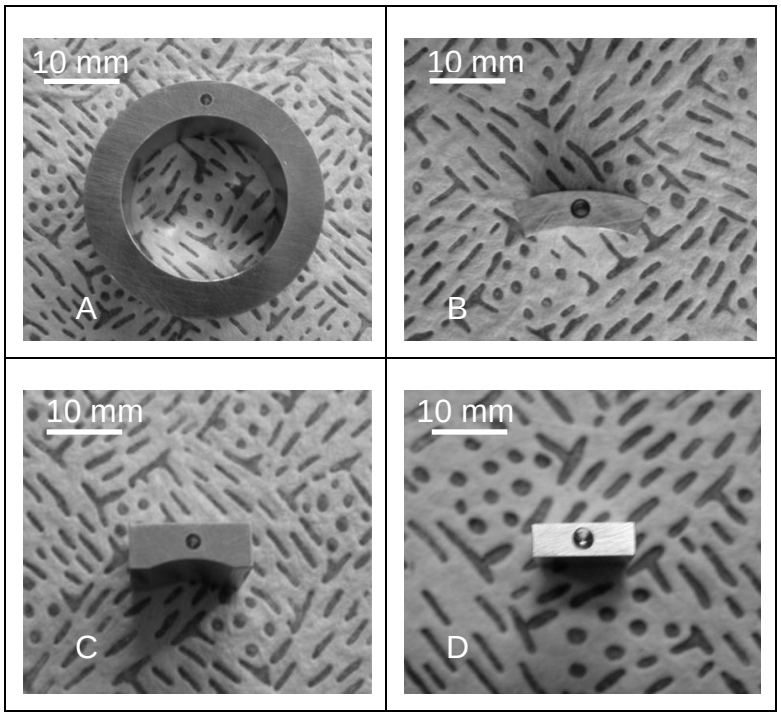

Figure 3-1 Specimen geometry tested

Table 3-3 Specimen geometry and alloy type

Alloy/geometry	Bridge-shape	Curved-shape	Full ring	Rectangular
T23	x	x	x	
T92	x	x	x	
TP347HFG	x	x	x	
Super 304H	x	x	x	
HR3C	x	x	x	
Incaloy 740				x
800H				x

3.3 Steam furnace and environment

The materials selected were tested in 100% steam at 0.1 MPa pressure (atmospheric pressure) in the temperature range between 600°C and 750°C. The specimens were exposed in horizontal furnaces lined with alumina tubes. For each of the tests performed the specimens have been arranged in the same manner. The specimens were placed on two levels (Figure 3-2); such an

arrangement was intended to allow determination of whether small temperature changes have an impact on steam oxidation. Ring specimens (of T23, T92, T304H and HR3C) were placed on the first level. On the second level, bridge and curved specimens were placed inside crucibles. In the first row the ferritic T23 specimens were put, following by more advanced materials with increasing chromium content. In the last row the specimens of Inconel 740 and 800H were placed. The last specimen on the second level was ring specimen machined form T347HFG (Figure 3-2).

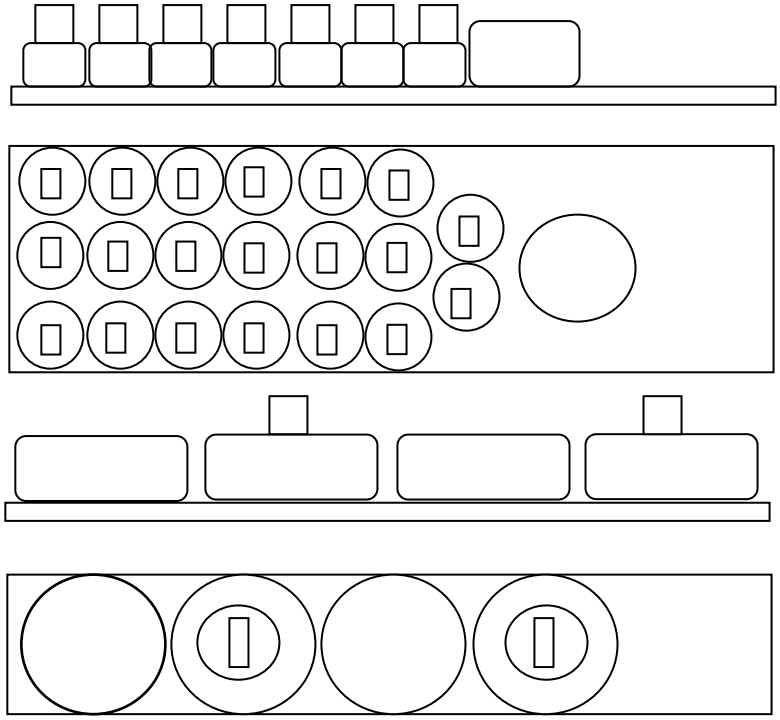

Figure 3-2 Specimens and crucible arrangement within the reaction chamber

Steam was generated inside the reaction chamber by the evaporation of water pumped from a water reservoir into the furnace with peristaltic pump. The steam passed over the samples and flowed into a condenser, where it cooled down and returned to reservoir as water. This is a closed system and so water losses are negligible. In order to ensure a low oxygen level within the water, the reservoir was purged with the oxygen free nitrogen (OFN) during the test with flow rate of 20 cc/min. Before each test the whole system was thoroughly

purged with OFN to remove the oxygen from the system, such procedure is also used before opening the system after each 250 hours exposure to remove the steam from the system. The OFN was supplied with 150 – 200 cc/min. The heating up procedure for each test was as follows: after placing the specimens in the furnace the system is sealed and thoroughly purged with OFN for four hours to remove oxygen from the system, while the atmosphere inside is heated up to 100°C. The time of such purge was calculated assuming that to remove the oxygen from the furnace, the furnace has to be purged with volume of OFN corresponding to 10 times the volume of the furnace chamber. When oxygen from the furnace was removed, the OFN purged was stopped and the peristaltic pump was turned on, and the system started to be fed with water, whilst the system was heated up to the temperature selected for the particular test.

Before each test was conducted, the furnace was profiled at the temperature of interest in order to identify the hot zone (in which temperature change was +/-10°C of the target). The temperature profile was obtain in the following manner: firstly the temperature was checked in 10 cm steps – along the furnace; then in 5 cm steps up to a temperature ~ 100°C lower than temperature of interest for a particular test; then the measurements were taken in 1 cm steps. Temperature profiling was carried out in three different location: first in the middle of the alumina tube; second next to the top wall of the tube, and third next to the bottom wall of the tube. Such organisation of the temperature profiling allowed identification the temperature differences between the specimens exposed at the same level and between those exposed at different levels.

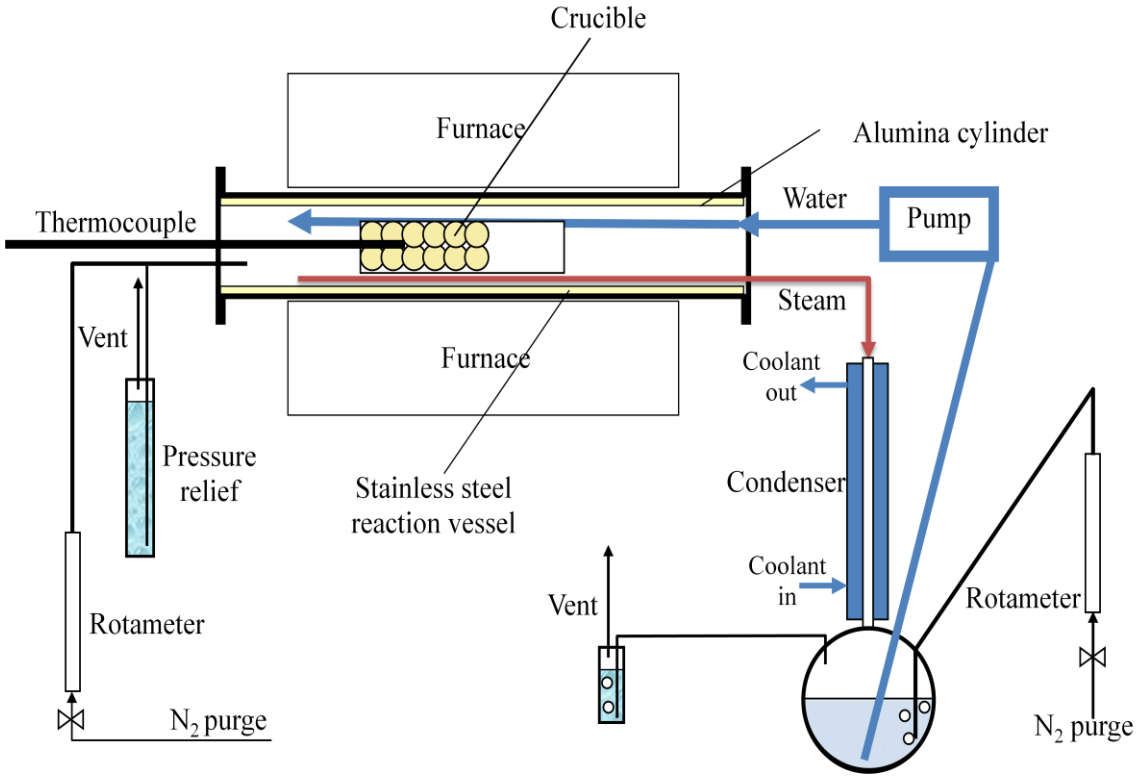

Figure 3-3 Schematic diagram of the steam oxidation system facility

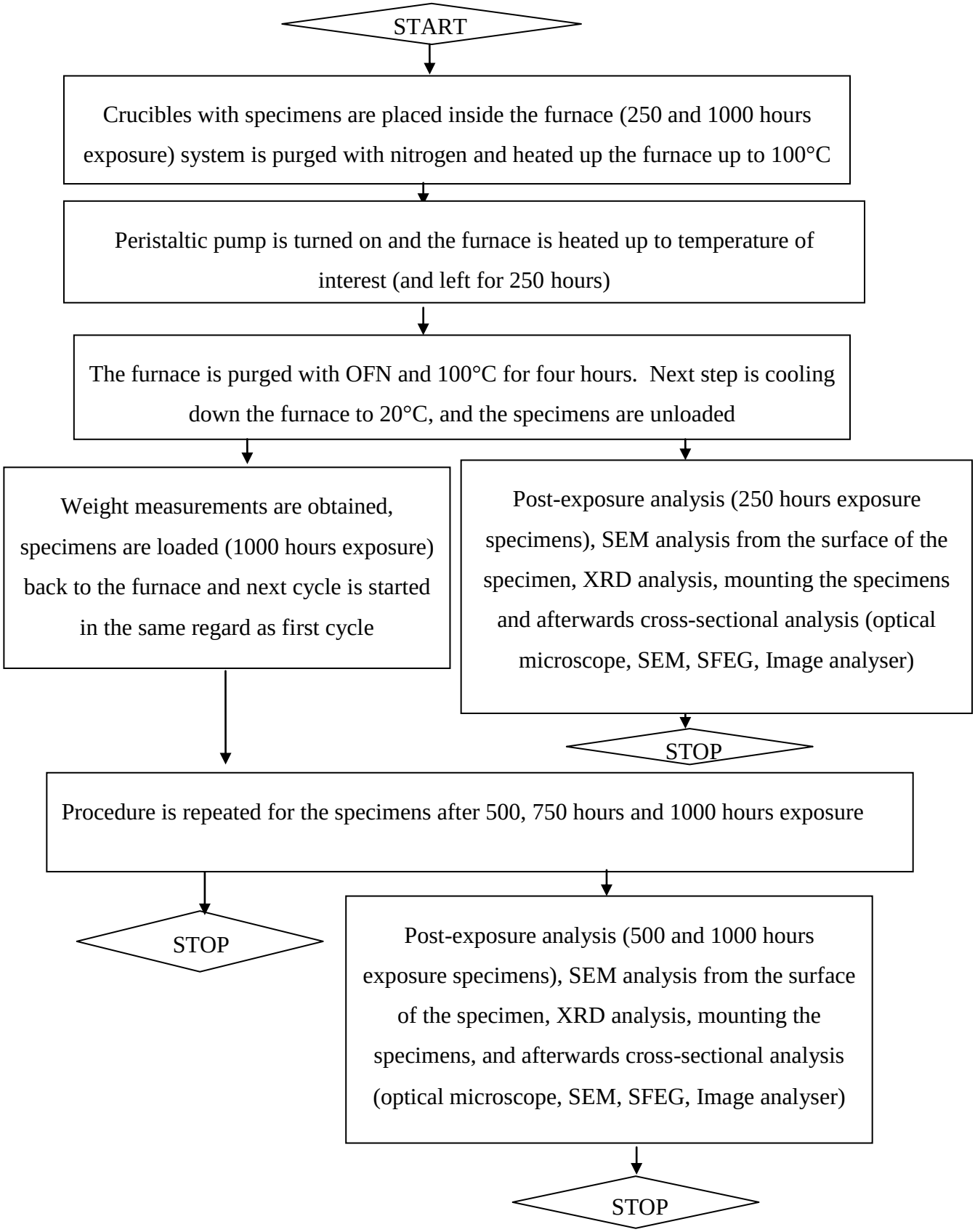

Figure 3-4 An algorithm of the steam oxidation tests

3.4 Pre-exposure procedures

3.4.1 Cleaning procedure

In order to ensure that specimen surfaces were free from contamination a cleaning procedure was adopted. This procedure was used before specimen measurement. The cleaning procedure adopted was performed as follows:

1. Initial cleaning with volasil;
2. Cleaning specimens in ultrasonic bath with volasil for 10 minutes at 30°C;
3. Flushing specimens with clean volasil;
4. Flushing specimens with isopropanol (IPA);
5. Cleaning specimens in ultrasonic bath with IPA for 10 min at 30°C;
6. Flushing specimens with IPA;
7. Drying specimens in air;

After cleaning the specimens were placed in separate bags and the unique reference number for each specimen was given.

3.4.2 Samples measurement

The next step is specimen measurement. Before the exposures, the specimens were measured with digital micrometers:

- Mitutoyo series 395 Digimatic Tube Micrometer with a resolution of 0.001 mm for bridge-, curved- and ring shape specimens; and
- Mitutoyo series Digimatic Outside Micrometer 293 with a resolution of 0.001 mm.

For each of the places selected on the specimens for measurements, three readings were taken; additionally for the curved-shape specimens an angle was measured in order to account for the chord length. Figure 3-5 (A-G) shows the measurement points for each of the specimen geometries studied. Obtaining three measurements at each of the points indicated allows the calculation of errors and variations in dimensions. The data acquired was transferred to Excel in order to calculate the area and volume of each specimen.

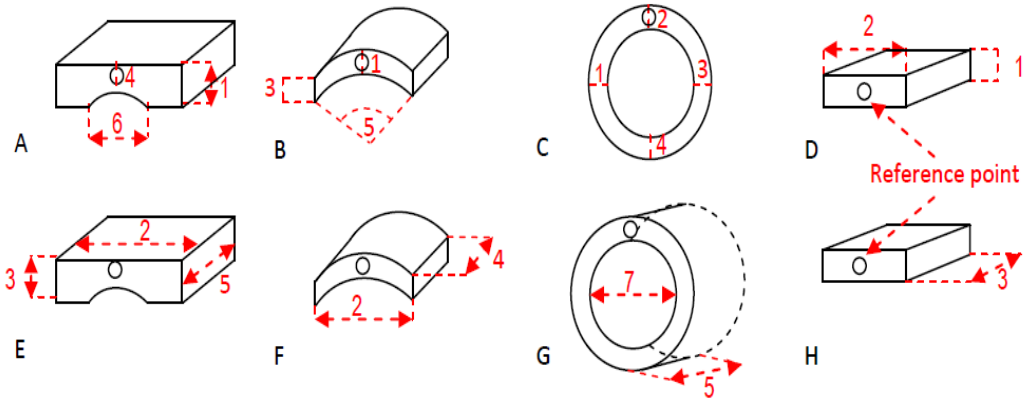

Figure 3-5 Arrangement of the Specific points on the specimens for the dimensional measurmentss on particular specimen geometry: bridge-shaped (A, E), burve-shaped (B, F), ring (C, G), rectangular coupons (D, H)

Before each test the specimens were removed from the bags, and their initial weight obtained with a digital microbalance (SATORIUS CP225D) with a resolution of ± 0.01 mg for masses < 80 g. The balance was calibrated frequently using its internal calibration function and periodically with test weights. For each specimen 3 measurement are taken and data obtained for are stored in Excel; for each test performed there is a separate excel file, where dimensional and weight data for each specimen in a particular test is stored. The same procedure is performed for crucibles and crucible, sample sets.

3.5 Post-exposure procedures – Oxidation kinetics

3.5.1 Mass change measurements

After exposure the specimens were weighed with a microbalance (SATORIUS CP225D) with a resolution of ± 0.01 mg for masses < 80 g in order to characterise the oxidation kinetics by comparing data before and after steam oxidation. For each specimen exposed three mass measurement were taken, the same procedure was applied for each crucible and crucible/sample set. The information obtained was transferred to Excel, and by comparing the weight before and after exposure the mass change for a particular specimens was

calculated. In order, to calculate the mass change as mg/cm^2 the following equation is used:

$$\Delta m = ((m_{(n+1)} - m_{(n)})1000)/A \quad \textbf{(3-1)}$$

where Δm is a mass change [mg/cm^2], m_n is a specimen mass after particular test cycle [g], 'A' is the initial area of the specimen [cm^2].

3.5.2 Rate constant and activation energy calculations

The data obtained were then used to identify oxidation rate dependence. In order to do so the specimen mass change data after each 250 hour exposure was grouped into tables and the logarithm of the mass change and exposure times were calculated. The last step is to identify a slope of the line defined by the points obtained this assumes

$$\Delta m^n = k_p t \quad \textbf{(3-2)}$$

Table 3-4 An example the table for n factor calculations

$Log_{10}(t)$	0	2,39	2,69	2,87	3	1/n factor
$Log_{10}\Delta M$	0	1,48	1,54	1,63	1,76	1.79

The next step was calculation of the oxidation rate constant. In particular study the following procedure is applied. Initially the rate constant (k) is calculated by identifying the slope of the line, which is defined by the points corresponding to squared value of the mass change and time in seconds.

Table 3-5 An example of the table for initial Parabolic rate constant calculations

Time [s]	900000	1800000	2700000	3600000	k [mg^2/cm^4/s]
$(\Delta m)^2$ [mg^2/cm^4]	927,99	1249,34	1827,29	3373,03	8,79E-04

The second step of the analysis involves using the Solver from the Microsoft Excel statistical package. For this calculation the following equation is used:

$$\Delta m^2 = k_p t + C \quad \textbf{(3-3)}$$

where k_p is a parabolic rate constant [$mg^2/cm^4/s$], t is time [s]

For further calculations following data were required:

1. Original mass change;
2. Initial value of the parabolic rate const [k_p];
3. Integration rate constant (C) which initially is assumed to be zero; and
4. Calculated mass change with use of the equation (5-1)

These data were grouped in Excel in order to calculate the difference with the mass change obtained during test after each 250 hour exposure and the theoretical calculation. Next step was calculation of the sum of the difference between calculated and test data. Finally, Solver was used to minimise the sum of difference between calculated and obtained mass change by changing the order of reaction (n), parabolic rate constant (k_p) and integration constant (C).

Table 3-6 An example of table for the parabolic rate constant (k_p) calculations

Time	Δm [mg/cm^2]	k_p [$mg^2/cm^4/s$]	n-factor	C	Cal(Δm) [mg/cm^2]	Cal(Δm) -Δm [mg/cm^2]
0	0	0,00088	2	0	0	0
900000	30,46296				28,13016	-2,3328
1800000	35,19517				39,78205	4,586879
2700000	39,66329				48,72286	9,059576
3600000	43,07777				56,26031	13,18254
					SUM	

The rate constants calculated were used for calculation of the activation energy for steam oxidation of the particular alloy in the temperature range 600-750°C with use of the Arrhenius equation. For determination of the activation energy over the temperature range 600-750°C the slope of the line defined by point corresponding to the natural logarithm of parabolic rate constant and 1000/T, where T corresponds to the particular temperature [K]. Identification of

the equation describing this line allows calculation of the activation energy with use of the following formula:

$$Q = Ra \tag{3-4}$$

where Q is activation energy [kJ/mol], R is gas constant [J/mol/K] and a is a slope of the line (y = ax + b).

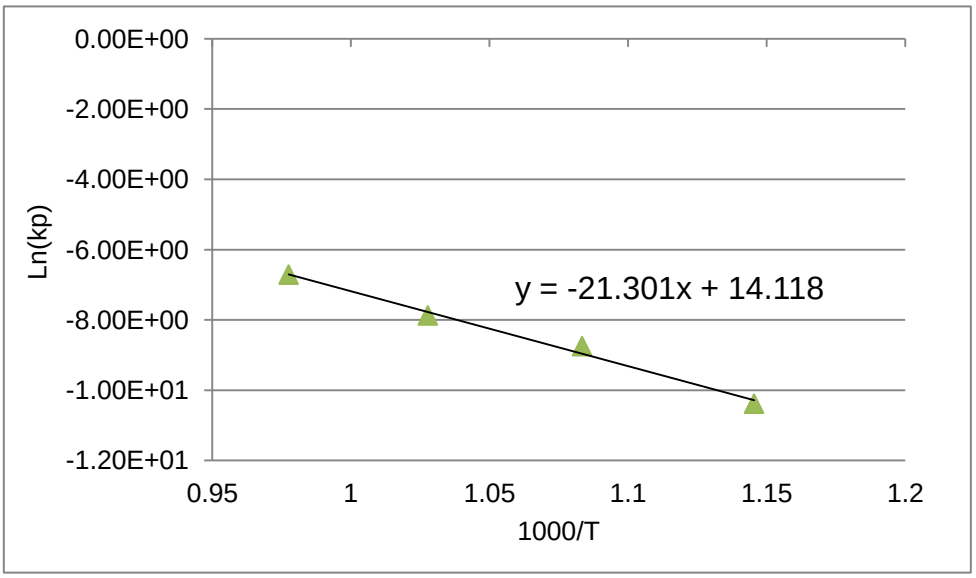

Figure 3-6 An example of the activation energy calculation

3.5.3 Post-exposure procedures – scale morphology investigations

To study the scales morphologies before and after steam oxidation exposures various types of microscopy techniques were used:

- Optical microscopy and Image Analysis;
- Confocal microscopy;
- Scanning electron microscopy (SEM) with Energy Dispersive X-rays (EDX);
- Focus Ion Beam (FIB) and Secondary Ion Mass Spectroscopy (SIMS); and
- X-ray Diffraction (XRD)

3.5.4 Post-exposure Specimen Preparation

In order to obtain the microscopic analysis on the exposed specimens, the samples have to be mounted. The specimens were mounted vertically in two specially designed mounting jigs (Figure 3-7 and Figure 3-8).

One mounting jig was designed to mount the bridge, curved and rectangular shape specimens, its schematic picture is presented in Figure 3-7. This mounting jig includes a metal base with two holes on the bottom, in which two reference pins are placed. The specimen was placed inside the metal base next to the reference pins. To secure parallel position of the samples against the pins the specimen was kept in place with a scalpel blade (as seen in Figure 3-7). In the next step the jig was filled up with the epoxy resin (Buehler Expoxicure Epoxy, mix ratio: 5 parts of resin and 1 part of hardener) in combination with Potters ballotini (silica glass powder in size range 0.04 – 0.07 mm) and carrying out a vacuum de-gasing.

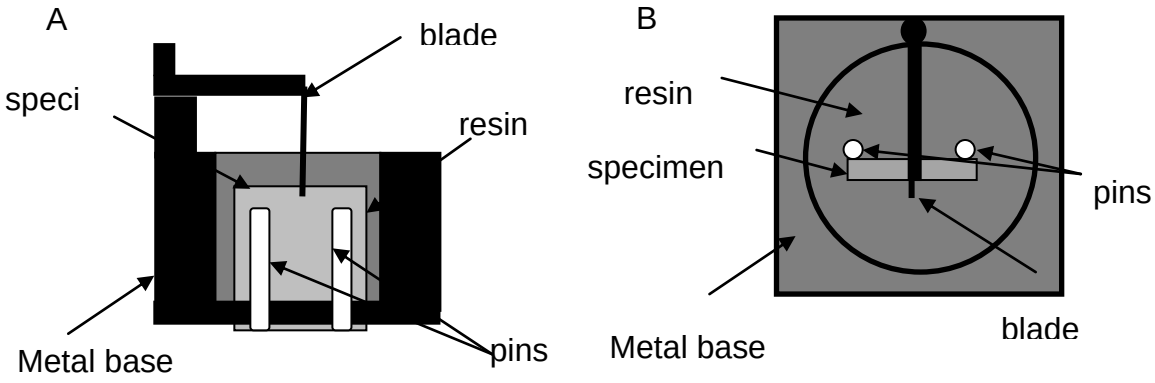

Figure 3-7 Specimens mounting jig used in the study

For the ring specimens a different mounting method was applied. The exposed ring specimens were mounted in a special mounting press, which is shown in Figure 3-8. The specimens were placed in the sections 1-3 (Figure 3-8B). After placing, the specimen in one of the 1-3 sections, metal rings were put around the specimens, and the mount filled up with the epoxy resin + Potters ballotini mix, following which the specimens were pressed to the metal base in order to ensure proper positioning of the specimens. After mounting, the cross-sections

of the specimens were prepared as follow: the mounted bridge-, curved- and rectangular-shape of specimens were cut with a precision cutting saw (ISOMet 5000). The curved-shaped specimens were cut across the reference point aiming to miss specimen centre by 1-1,5 mm; this allows proper identification of the metal loss, whereas in case of rectangular and bridge-shape specimens the cutting point does not have an impact on the accuracy of the metal loss calculations. Cross-sections were ground with a semi-automatic polishing machine (Mataserv Motopol 12), the grinding papers used were 120, 240, 600, 1200, 2400 UK grit followed by polishing: first with diamond paste (MetPrep LTD 6 µm Diamond compound) and second with a polishing silica base suspension (Buchler Masterpolish 0.05 µm). After mounting the ring specimens were ground and polished using the same method.

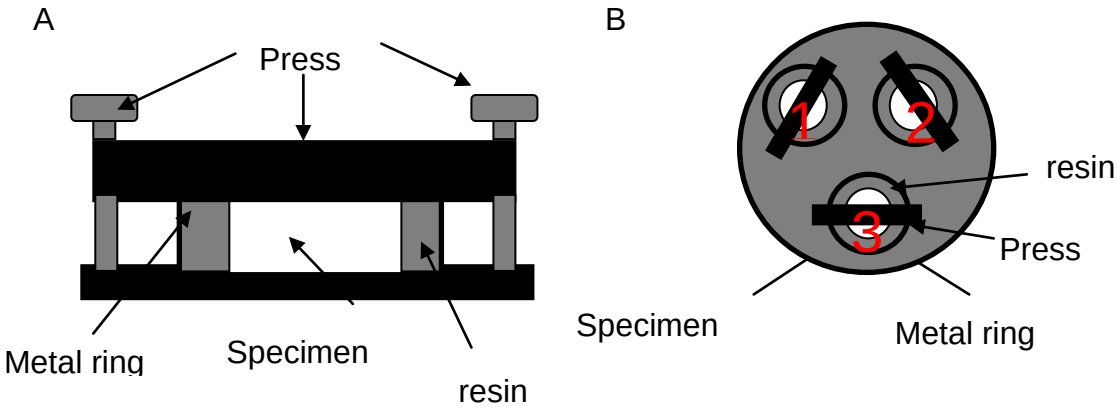

Figure 3-8 Ring specimen mounting jig used in the study

3.5.5 Optical microscopy

Optical microscopy was employed to analysed thick oxide scales formed on ferritic steels. For such analysis the cross-section of the specimens exposed were prepared and analysed with reflected light optical microscope (Nikon Optiphot). Use of the optical microscope allowed the identification of the oxide layers formed on the specimens during exposure. For each specimen thirty pictures were taken along the specimen surface. The pictures obtained were analysed using commercially available image analysis software (ImageJ) to study the level of voids within the oxide scales developed. For such analysis

each picture was opened in the software and saved as white and black image, a white region corresponds to voids whereas black to oxide. ImageJ has a function which allows calculating a percentage area of the white and black regions; this function was used to identify the total voids area within the scales formed. Information obtained in this method was plotted against exposure conditions (temperature and steam flow rate) and time.

3.5.6 Image analysis

To identify the metal loss of the materials exposed, the specimen cross-sections were measured using a reflected light reflected light optical microscope with calibrated motorised x, y stage and a commercially available image analysing software (Axiovision). The software controlled the stage as well as the camera and allowed the identification of a number of points around the specimen, where pictures were taken. The image analysis procedure adopted is performed as follows:

1. Microscope, stage and the image analysis software were switched on;
2. The cross-section of the specimens was mounted in the centre of the motorised stage (parallel to the horizontal edges of the stage;
3. The standard settings of microscope were applied (20 time magnification);
4. The microscope was focused on the specimen;
5. With the image analysis software four point on the specimen were selected (top, bottom, left and right);
6. The points selected were used by the software to calculate 60 points on the specimen, which were written as coordinate (x; y);
7. The software took the pictures at the 60 point selected, around each point 9 pictures were taken in 3x3 matrix;
8. The 3x3 group of pictures obtained were stitched together with the software; and
9. On each stitched picture two points at the interface between metal and oxide scale were manually selected, with each point being automatically recorded as coordinates (x, y) by the software.

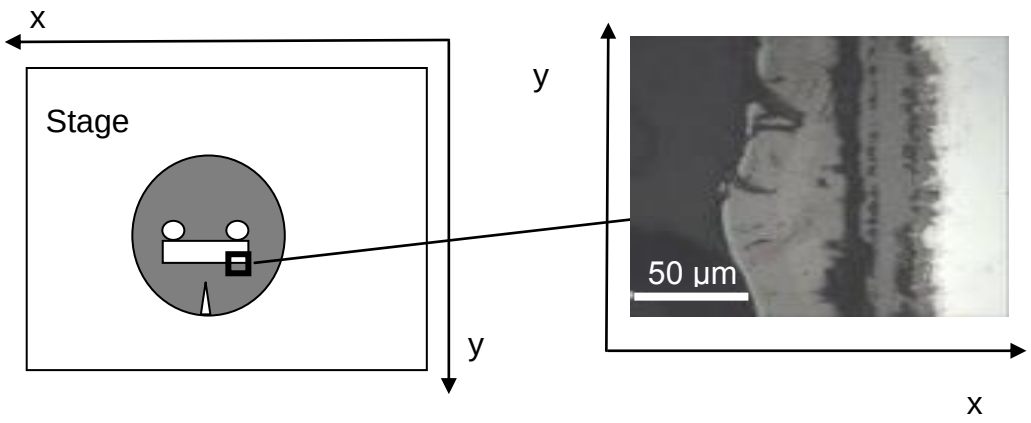

Figure 3-9 Ilustration of the image analysis procedure

For the identification of the metal loss, the data was transferred to specially designed Excel file. This file consists of three spread sheets. The data obtained in image analysis were transferred to the first spread sheet. These data were the x, y coordinates from each picture, and then these were used to construct diagram corresponding to the metal remaining after exposure. In the second spread sheet the pre-exposure and post-exposures dimensions were stored and compared, which allowed calculation of the change in metal thickness at the points around the specimen. The thickness change data was then transferred to third spread sheet, where the statistical analysis of the data is performed as following:

1. The metal change data were transferred;
2. For each point a data index was given;
3. Metal thickness change data were sorted from largest to smallest;
4. For each point the cumulative standard normal probability was calculated
5. The processed data were then plotted as a change in metal vs. Cumulative normal probability; this type of plot shows the probability (e.g. 4 %) of a certain degree of damage being observed (example shown in Figure 3-10).

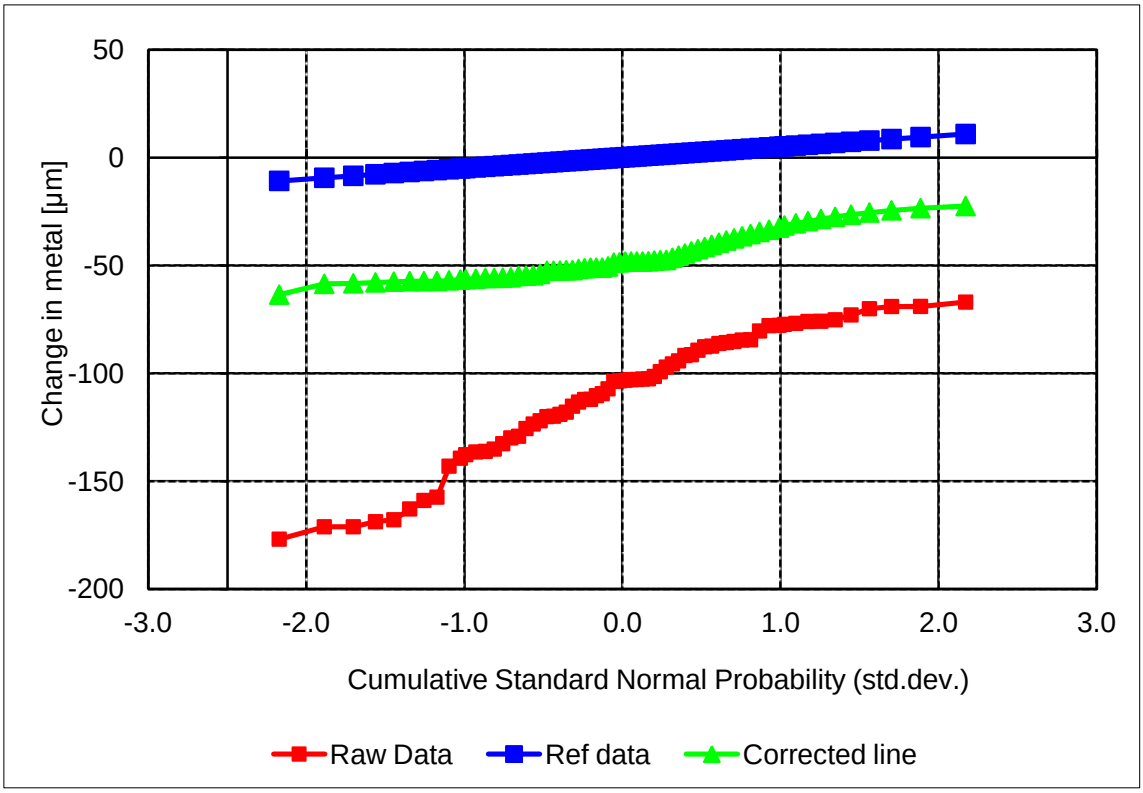

Figure 3-10 An example of metal loss data

To ensure that the metal loss results were accurate, unexposed reference specimens were prepared and investigated in the same manner as the exposed samples. On these reference samples, the metal loss analysis was performed to identify the difference between the micrometer and image analysis readings. The small differences allowed calibration differences between the two measurement techniques to be eliminated.

3.5.7 Confocal microscopy

For the roughness analysis the confocal laser scanning microscope was used (Olympus Lext OLS series) with commercially available software (Lext OLS). The specimens were analysed at 5, 10 and 20 times magnification. For this analysis the microscope was used in two modes: 3D to obtain a 3D picture of the specimen surface and 2D picture for a roughness analysis. For both analyses the fast method of scanning was used with fine resolution (4 µm). For the visual analysis the 3D pictures of the material surface were used (example

is shown in Figure 3-11), whereas the 2D picture was used for the roughness study (Figure 3-12). Analysis of the roughness involves following steps:

1. Manual selection of the profile line across the specimen surface (Figure 3-12) which length is dependent on the magnification used;
2. Selection of the function which allows identification of the change in the specimen roughness along the profile line selected;
3. Software calculate the roughness along the profile line selected (it includes peaks in both directions);
4. Data acquired is presented as a report, from which roughness data is extracted manually and copied to the Excel spread sheet; and
5. Graph representing the changes in roughness along the line selected (Figure 3-13).

For the different surface finishes diagrams were constructed, in which the roughness of the different surface finishes was compared.

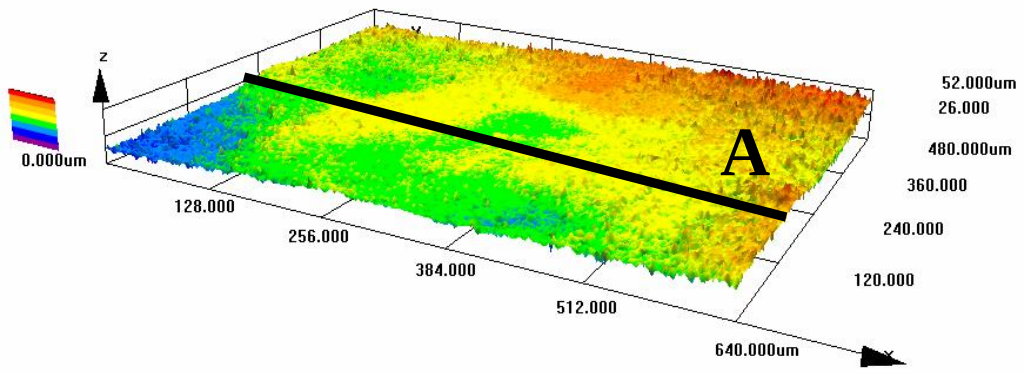

Figure 3-11 An example of 3D picture of the material surface taken at 20 times magnification

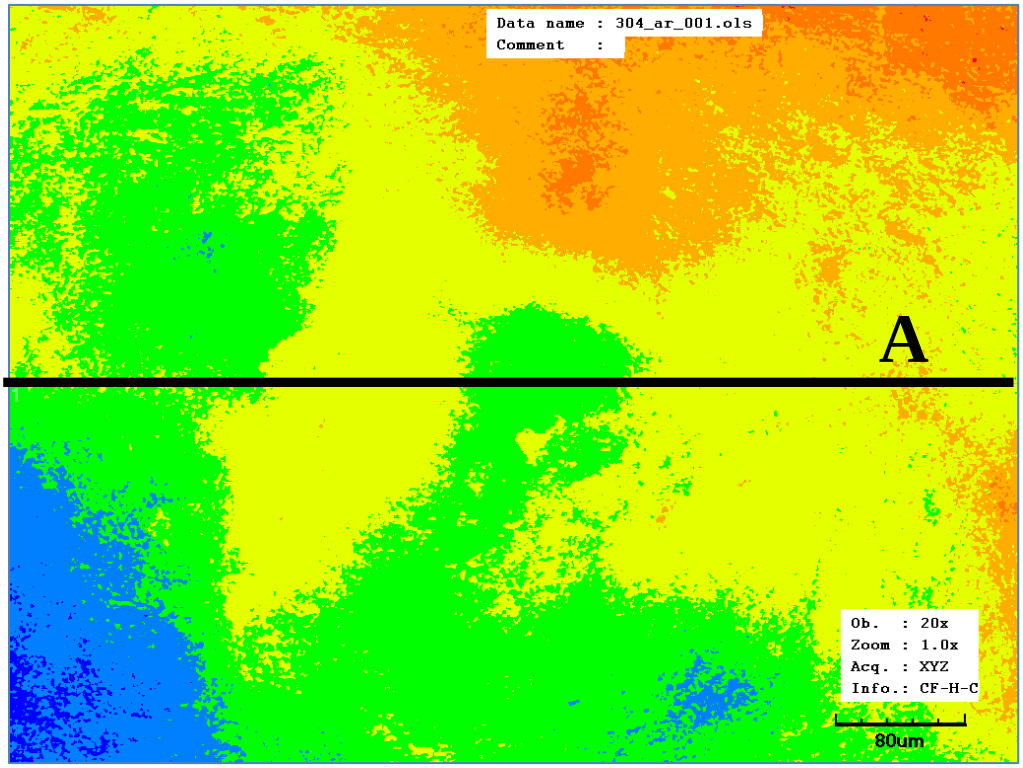

Figure 3-12 An example of 2D picture of the material surface taken at 20 times magnification

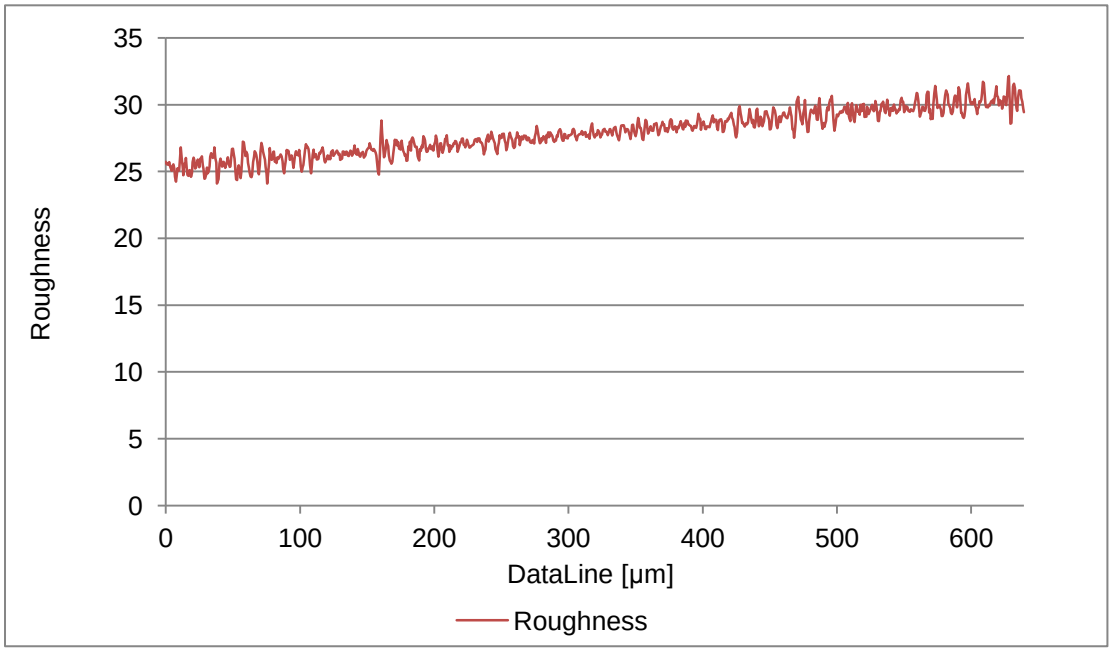

Figure 3-13 An example of the analysis of the roughness of the material surface along the profile line A (Figure 3-12)

3.5.8 Scanning Electron Microscopy

A Scanning Electron Microscopy was used to analyse the oxides scales formed on the materials tested. For that analysis an Environmental Scanning Electron Microscope (ESEM) with Energy Dispersive X-rays (EDX) (Philips XL series) was used. The microscope was controlled with INCA software, which enabled pictures to be taken in specific areas of interest and EDX analysis and elemental mapping to be performed. For all analyses conducted an electron beam with energy of 20 keV was used, the working distance was 10 mm and the scan rate was 1.68 second.

For the surface analysis the specimens were studied in high vacuum mode using a Secondary Electron Detector. Specimens were investigated at various magnifications between 125 and 2000 times. For all analyses, process times of 5 were used with spot sizes of 5-6, which keept the dead time in the 30 - 35 % range. On each specimen two surfaces were studied:

- Surface facing the direct steam flow; and
- Surface exposed to indirect steam flow.

On each specimen EDX analysis was performed to identify the elements forming the oxide scales.

The cross-section of specimens had to be studied in a low vacuum mode and a Backscattered Electron Detector was used. The cross-sections were studied in two different ways, for which different spot size and process time were required:

- Element analysis with EDX – spot size 5-6;
- Mapping – spot size 6-7;

For proper element identification the microscope had to be calibrated with cobalt; after calibration the microscope was ready to use. In this particular study the EDX was used to build the EDX profiles across the oxide scale formed, which enabled the identification of the element concentration across the different layers of the scales. Additionally, it was also used to identify the

compositions of interesting features forming on the specimens exposed. Such information was used as input for X-ray diffraction (XRD) analyses.

Mapping of the oxide scale did not require detector calibration. To obtained maps of the oxide scale, the proper function was selected in INCA and process time was changed to 3. Then the fast mapping function was selected from the functions available in the software. This function enabled qualitative identification of the particular element; the selection of the elements for analysis is dependent on the composition of the material studied (Figure 3-13 and Figure 3-14)

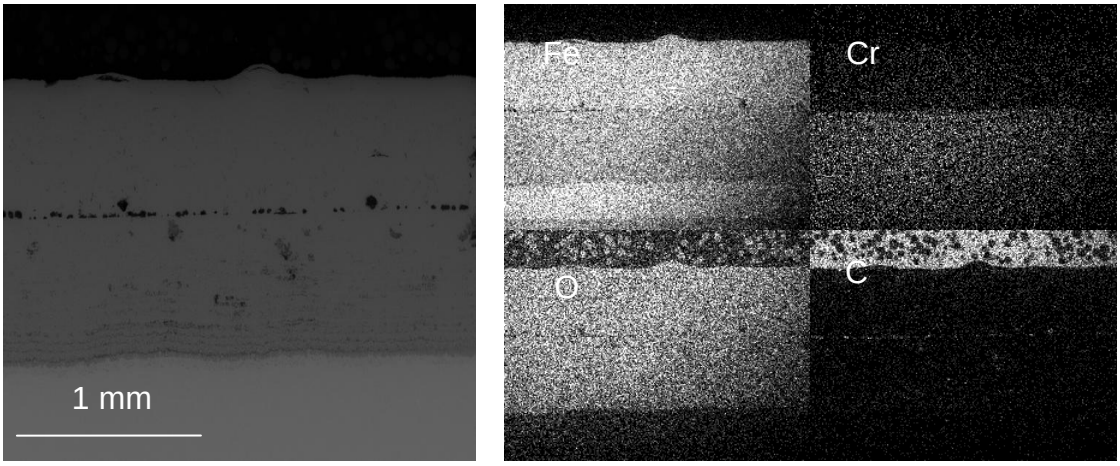

Figure 3-14 An example of mapping

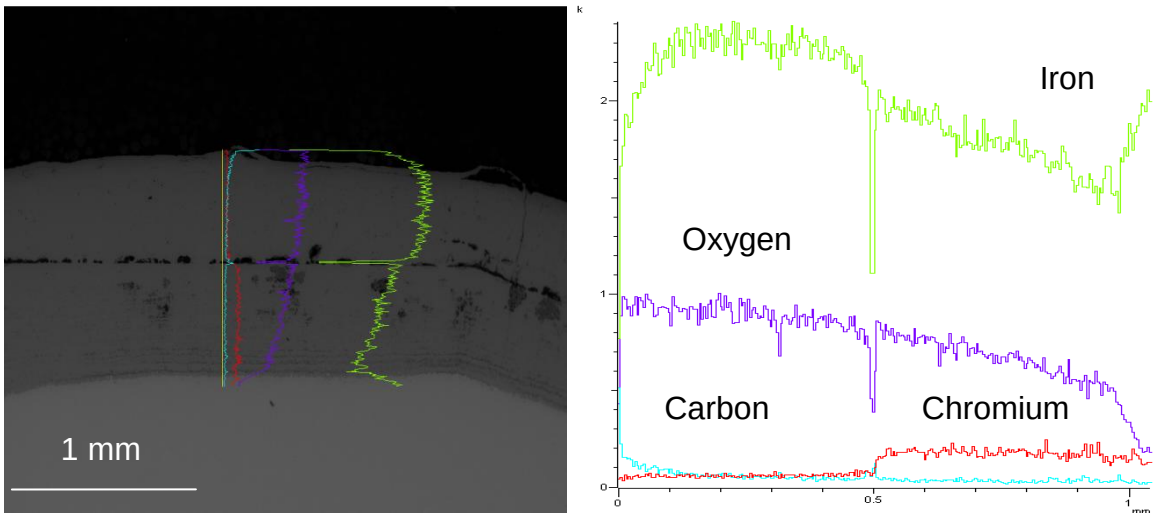

Figure 3-15 An example of line scan (mapping along the line)

3.5.9 Focus Ion Beam and Secondary Ion Mass Spectrometry

A Focused Ion Beam with Secondary Ion Mass Spectrometry (FIB-SIMS) was used to analyse the specimens exposed to steam generated from O^{18} doped water (O^{18} -10.1 at%, O^{17} – 0.1 at%, O^{16} – 89.8 at%). For such analyses the specimens were exposed to steam generated form O^{18} doped water for last 100 hours of the test at 700°C with 40 mm/s steam flow. For the analysis the (FIB-SIMS) was used in high vacuum mode ($5x10^{-6}$ mbar) with beam current in a range between 30 – 7000 pA and 30kV voltage. The specimens were investigated at various magnifications from 2.5 to 20 thousand times. SIMS analysis was performed for each specimen in areas of 25 μm^2. For proper characterisation the oxide scales were cut with the ion beam and then SIMS analysis was performed. Results of an initial characterisation enabled the selection of elements compounds with different masses for further analysis. For the tests performed those masses were: 16, 17, 18 which were believed to correspond to O^{16}, OH^{17}, O^{18}. An example of the FIB cut is presented in Figure 3-16. The crater in the oxide scale is 20 µm deep, during the cut the specimen was hit with the focused ion beam and the secondary ions escaping from the heated surface were directed to SIMS detector, where the analysis of the masses was performed. An example of such analysis is presented in Figure 3-17 (analysis performed on the crater A presented in Figure 3-16).

To investigate the relative change in number of counts for each ion detected following formula was used:

$$\mathrm{Ion_A}[\%] = \left(\frac{\text{Counts for } \mathrm{Ion_A}}{\sum \text{Counts for all Ions detected}}\right)(100) \qquad \textbf{(3-5)}$$

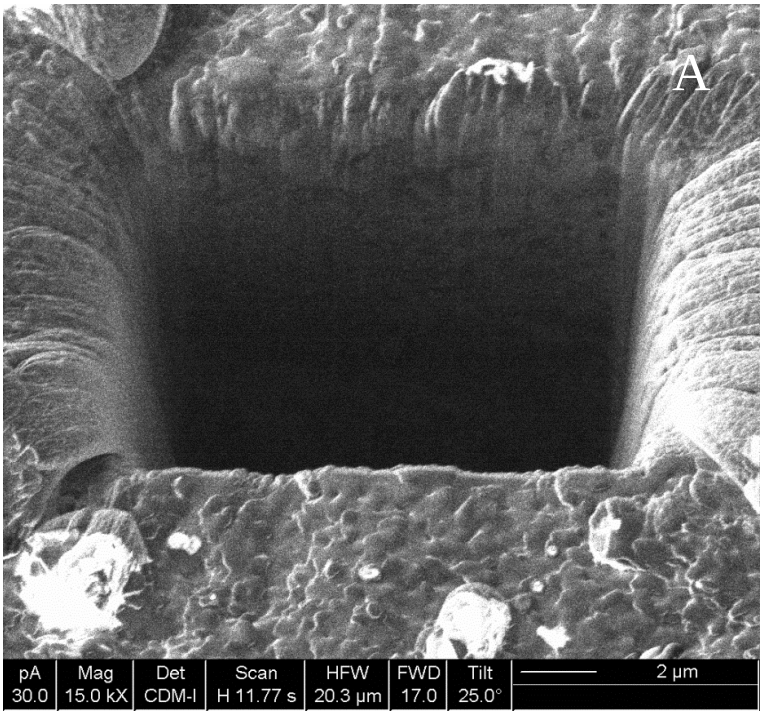

Figure 3-16 An example of the picture obtained with FIB

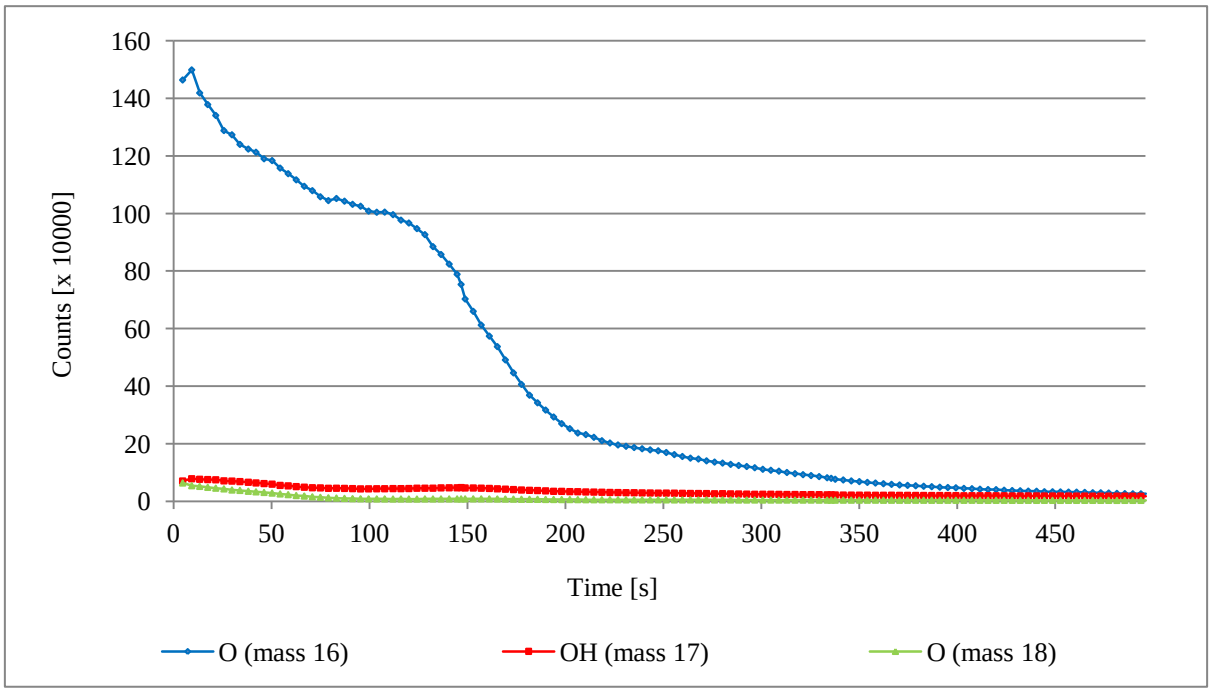

Figure 3-17 An example of SIMS analysis results for crater A (Figure 3-16)

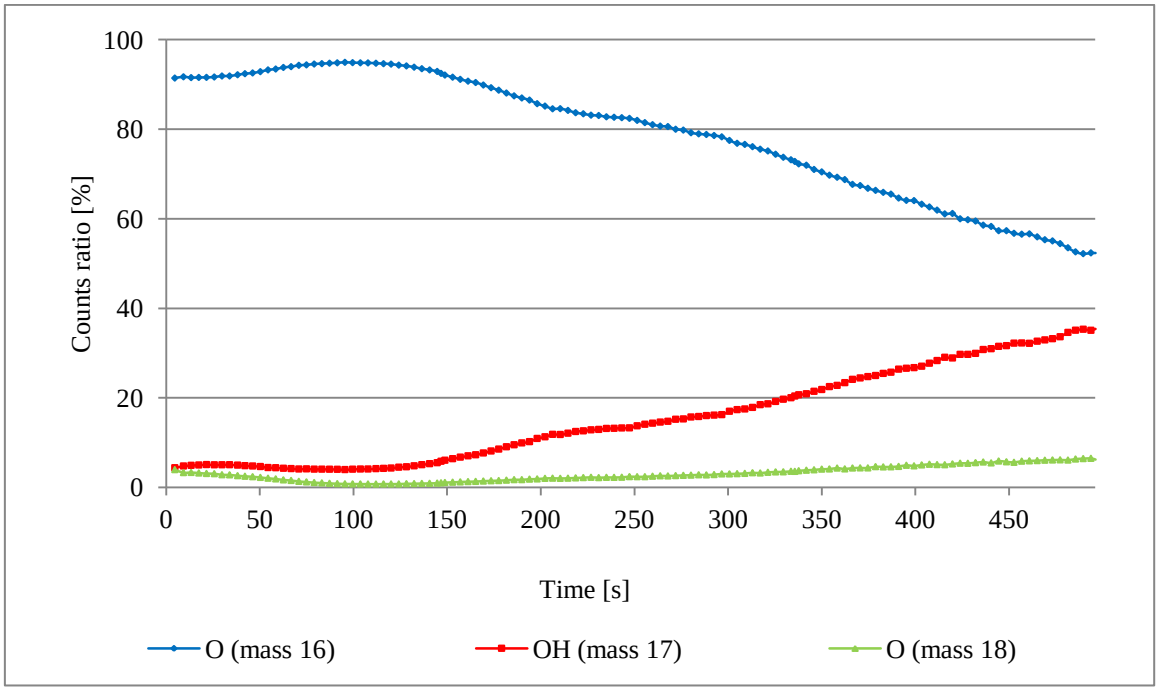

Figure 3-18 An example of SIMS analysis results for crater A (Figure 3-16).)

3.5.10 X-ray Diffraction

X-ray diffraction (XRD) was used to identify the types of oxide formed on the materials exposed. For specimen analyses a Siemens D5005 X-ray diffractometer was used to generated information about crystal structure of the oxides formed. XRD analysis was controlled by the XRD scanning software. The specimens were scanned at angles of incidence between 5 and 90°C with the step size of 0.05. For their analysis the results were transferred to a XRD evaluation program, which enabled the identification of the oxide types formed on the surfaces of the specimens. For a proper identification of the oxides the information from SEM analysis were used to select the elements that were found with EDX. After selection of the elements expected to be found within the oxides the XRD evaluation program suggested a number of different oxides types whose crystallographic structure corresponded to the peaks found. An example of a result obtained by XRD is presented in Figure 3-19.

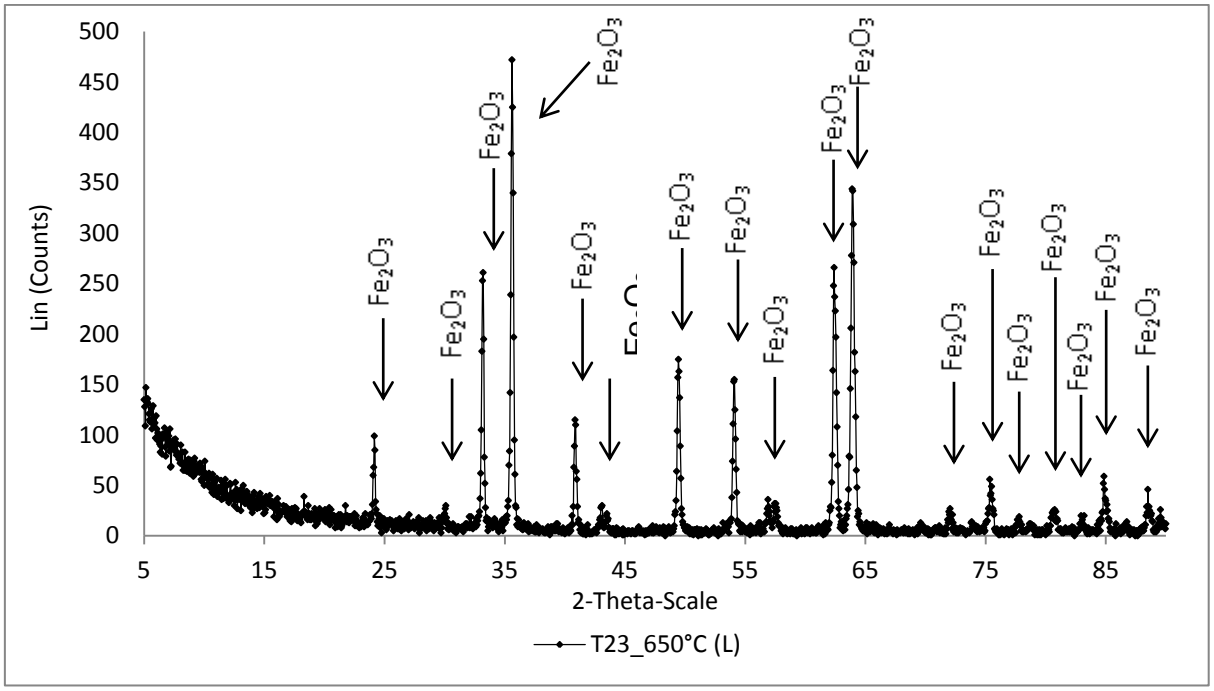

Figure 3-19 An example of XRD results for a specimen exposed to steam

4 RESULTS

This results section shows the data obtained during the post-exposure investigations. For better transparency and presentation of results, the chapter has been broken into three sub-sections, which discuss following topics: oxidation kinetics; morphology and chemistry of oxidation; and finally metal loss.

4.1 Oxidation kinetics

Investigation of the high temperature resistant alloys in steam has shown that the oxidation differs significantly with alloy type, which is mainly associated with the chromium content and in the case of the more advanced materials (austenitic and nickel-based) also with the interplay between other alloying additions such as Ni, Mn, Nb, Cu, Si. As was presented in the experimental design chapter, there were number of factors studied. To clearly present the results generated this chapter has been divided into subsections presenting data from the three groups the high temperature resistant alloys with emphasis put on: temperature, steam flow rate, specimen geometry, material composition and their impacts on the steam oxidation. The following section presents the oxidation kinetics in terms of mass change (net mass change) additioanlly the scale spalation is presented. Oxidation kinetisc as a metal loss and thickness change data are presented in the Appendix A.1.

4.1.1 Ferritic steels

During the tests two ferritic steels T23 (2.25Cr) and T92 (9Cr) have been exposed to 100 % steam at 1 bar pressure (absolute) and in temperature range 600-750°C. Additionally, at 600, 650 and 700°C the impact of steam flow rate was studied. Such selection of the materials and conditions was targeted at determination of the impact of alloy chromium levels on steam oxidation kinetics. Figure 4-1 - Figure 4-3 show a comparison of the average mass change, thickness change and median metal loss data for T23 and T92 after 1000 hours exposures. The bars represent changes in the mass change, scale thickness, and metal loss with temperature, steam flow rates and chromium content. Moreover, comparison between bars allows the identification of the relationship between chromium content and temperatures, steam flow and the combined effect of temperature and steam

flow rate. The results demonstrate that Cr has an important impact on steam oxidation behaviour. However its significance changes with exposure conditions: at low temperature (600°C) the difference in oxidation behaviours between T23 and T92 are smaller, then above 600°C, the impact of chromium content increases with temperature and steam flow rate. A higher concentration of chromium (9Cr) clearly influences the oxidation, it not just slows down the process at particular temperature but reduces the differences in the material performance with change in the exposure conditions.

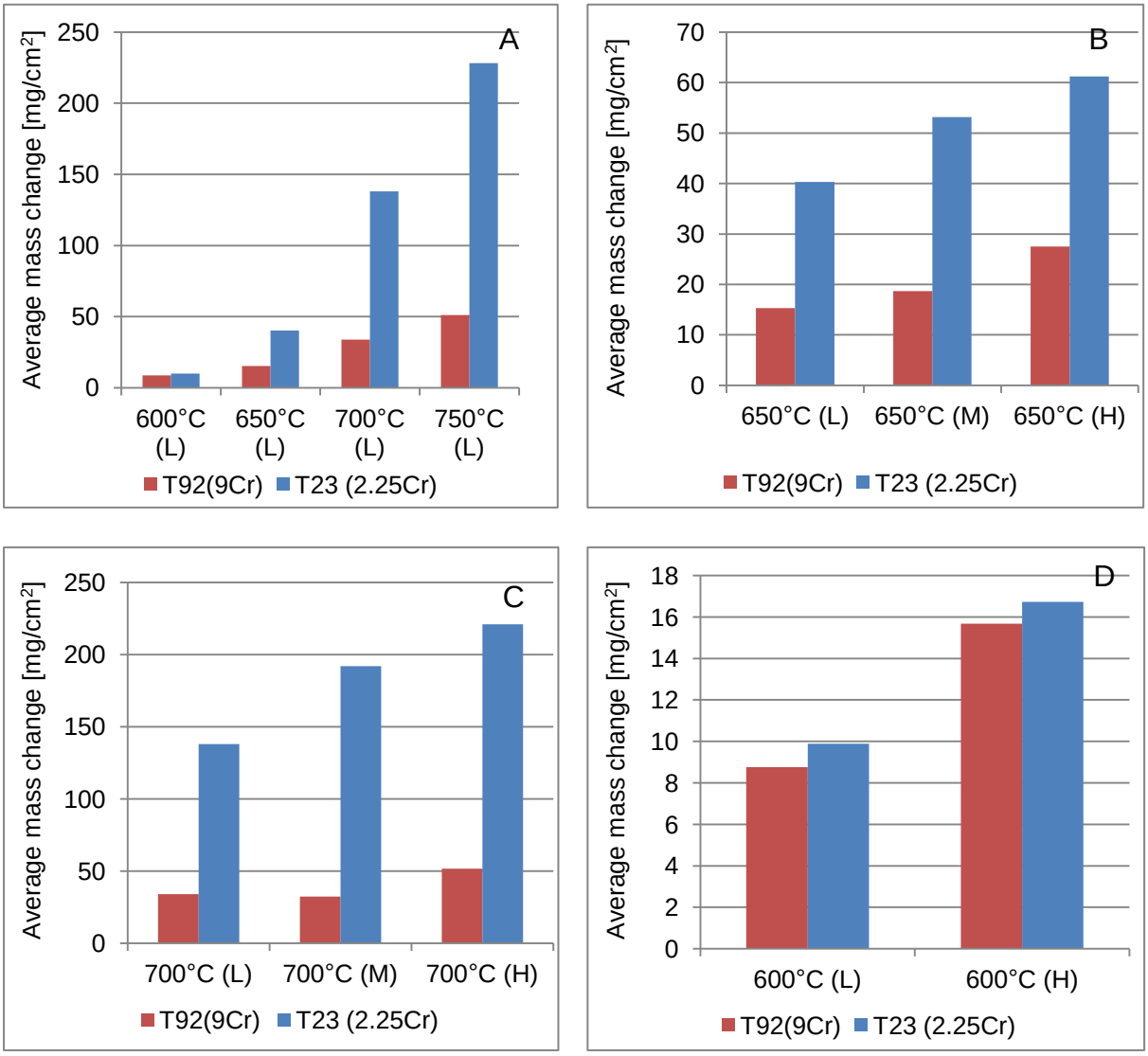

Figure 4-1 Differences in the average mass change between T23 and T92 ferritic steels after 1000 hours exposures - (A) Temperature and (B, C, D) Steam Flow Rate Effects

Figure 4-1 shows the impact of chromium and steam flow rate on steam oxidation at different temperatures. At 600°C regardless of the steam flow rate the mass change between the two ferritics tested does not indicate large differences with chromium level. Figure 4-1B, C show the relationship between the Cr content and steam flow at 650 and 700°C respectively. Comparison of the data leads to the conclusion that steam flow rate has a larger effect on material performance at higher than at lower temperatures.

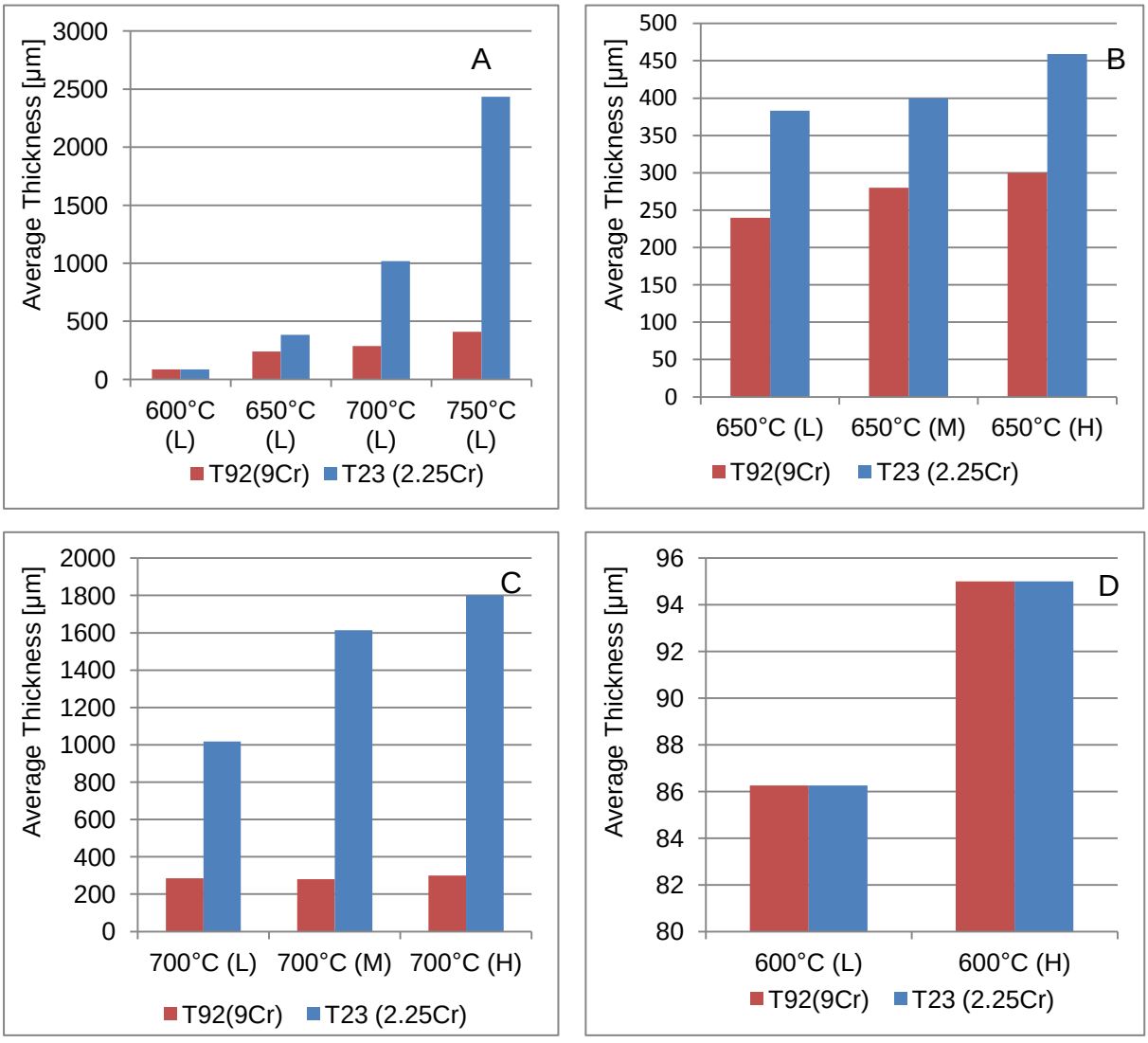

Figure 4-2 Differences in the average thickness between T23 and T92 ferritic steels after 1000 hours exposures - (A) temperature and (B, C, D) steam flow rate effects

Analysis of the scales thicknesses under the conditions studied indicated clear differences with temperature. These differences increase with temperatures. At 600°C there is no significant changes with steam flow rate. However, at 650°C the

difference in performance between T23 and T92 increases with steam flow rate. The thicknesses of the scales formed on T23 increases with flow, whereas for T92 the differences are less significant, however this could be a result of oxide scale spallation. In spite of the scale exfoliation Figure 4-2(B) clearly demonstrates that chromium levels have impact on the oxidation of both the ferritic alloys. The same situation has been identified at 700°C (Figure 4-2C).

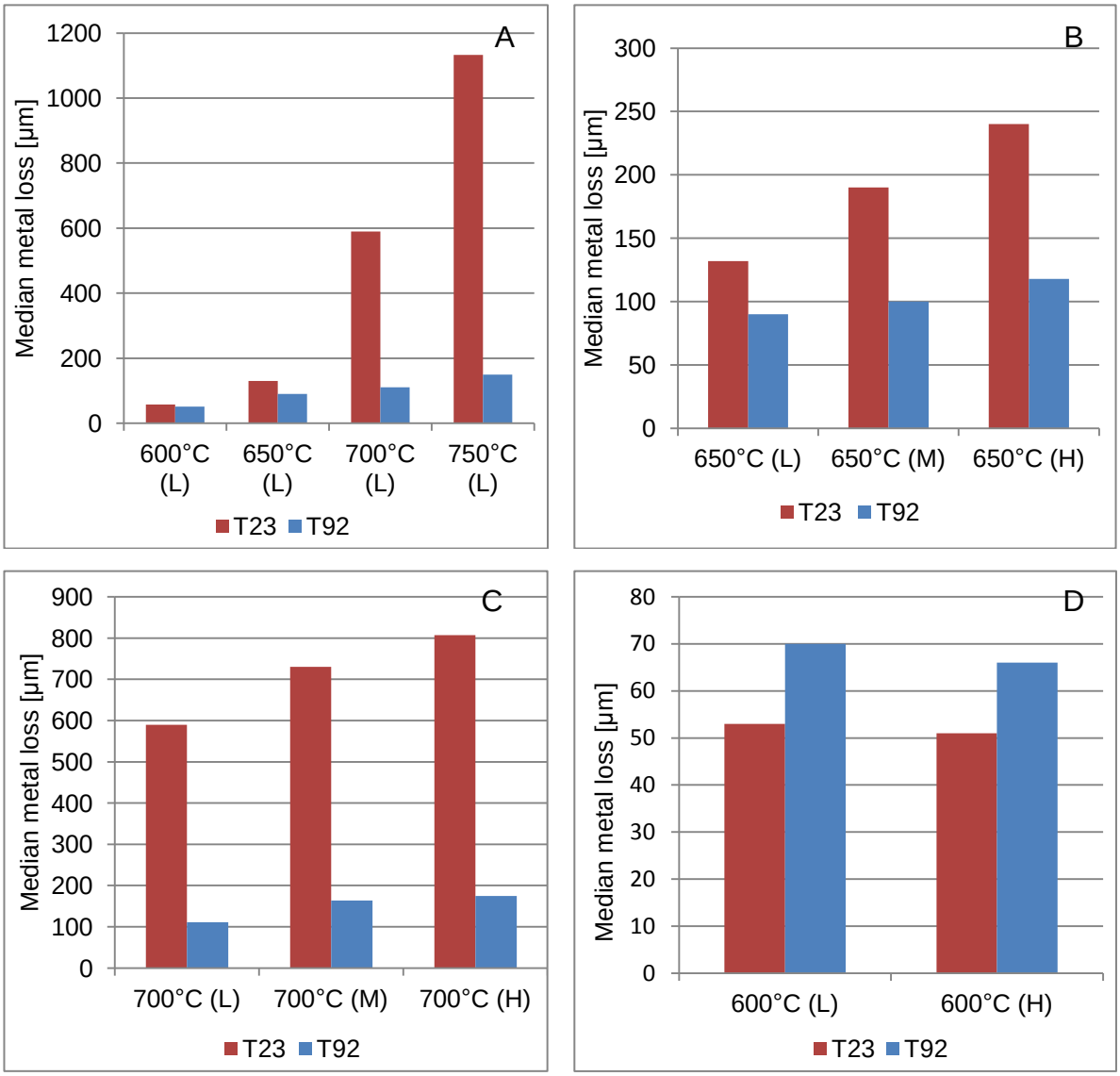

Figure 4-3 Differences in the average metal loss between T23 and T92 ferritic steels after 1000 hours exposures – (A) temperature and (B, C, D) steam flow Rates effects

The trends identified for both mass change and scale thickness data have also been confirmed by metal loss data (Figure 4-3). To summarise, Figure 4-1 - Figure 4-3 show that the mass change, scale thickness and metal loss are significantly

dependent on the temperature and steam flow rate. The temperature and flow dependence however is more pronounced for T23 than T92.

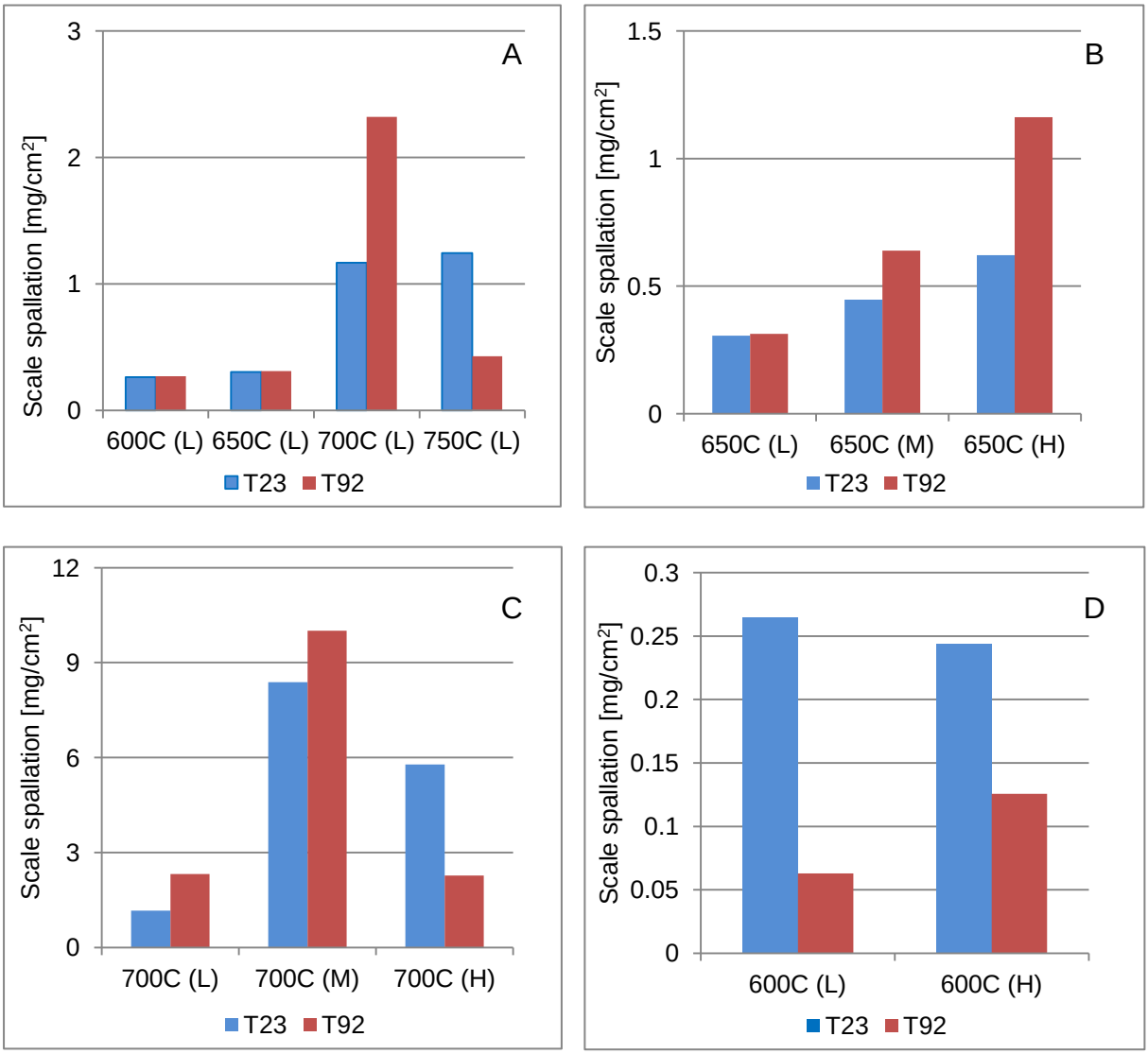

Figure 4-4 Comparison of the mass of the scales exfoliated from T23 and T92 ferritic steels after 1000 hours exposures – (A) temperature and (B, C, D) steam flow rates effects

Figure 4-4A-D shows the avarage total spallation for the ferritic steels at the conditions tested. Clearly the spallation changes with the temperature, the lowest spallation rate can be found at 600°C (L), there is no change in the mass of the exfoliated oxides for both alloys. At 700°C (L) the mass of the spalled oxides is higher for T92 then T23 which is consitent with the scale morphology. At the highest temperature, however the exfoliation for T23 is more severe, the scale on T92

seems to be more adherent. Figure 4-4B-D shows the change in the avarge spallation with the steam flow rate. It can be seen than T23 is less resistant to spallation then T92 at 600°C. However, at 650 and 700°C T92 shows more spallation after 1000 hour exposure. Comparison of the avarage mass change after 1000 hour exposure and the spallation of the scale formed on T23 and T92 shows that althought the scale exfoliation can be found its effect is not so significant. Following that conclusion the decision has been made that for the detail analysis of the ferritic steels mass change the effect of the spallation is going to be neglected.

4.1.1.1 T23 (2.25 Cr)

The steam oxidation mass change kinetics for T23, as presented Figure 4-5 - Figure 4-13, varies with the exposure conditions. Each line in the figures corresponds to the behaviour of one specimen exposed. Analysis of these curves indicates that at 600 – 700°C with low steam flow rate the oxidation of T23 follows a parabolic/sub-parabolic dependence, whereas at 750°C (L) and at medium and high steam flow rates the behaviour is closer to linear. The mass gain of T23 specimens varies with time; the mass change curves are steeper up to 250 hours then less steep as the mass change slows down. The only exception is at 750°C (L) when the slope of the line characterising both 0-250 and 250-1000 hour period does not vary significantly. There are no clear changes in the initial period duration with exposure conditions; however, the primary mass growth differs – the initial gain becomes steeper with temperature, and is also influenced by the steam flow rate. Similar trends have been identified for the second period of exposure (250 -1000 hour).

The change in the curve - shaped is also influenced by the specimen geometry; but the significance of this varies with temperature. Analysis of the mass change data shows that for T23 it differs with specimen shape. Among the shapes investigated, the ring specimens show the slowest mass growth, whereas the bridge shaped specimens exhibit the fastest mass gain (except at 600°C (L) when the curve - shaped samples have oxidised faster). The difference in the mass gain between the sample shapes is not constant; it fluctuates with time as well as the exposure condition. At higher temperatures with faster steam flow rate conditions (M, H) the

discrepancies between results obtained are less scattered than when samples exposed to low steam flow rates.

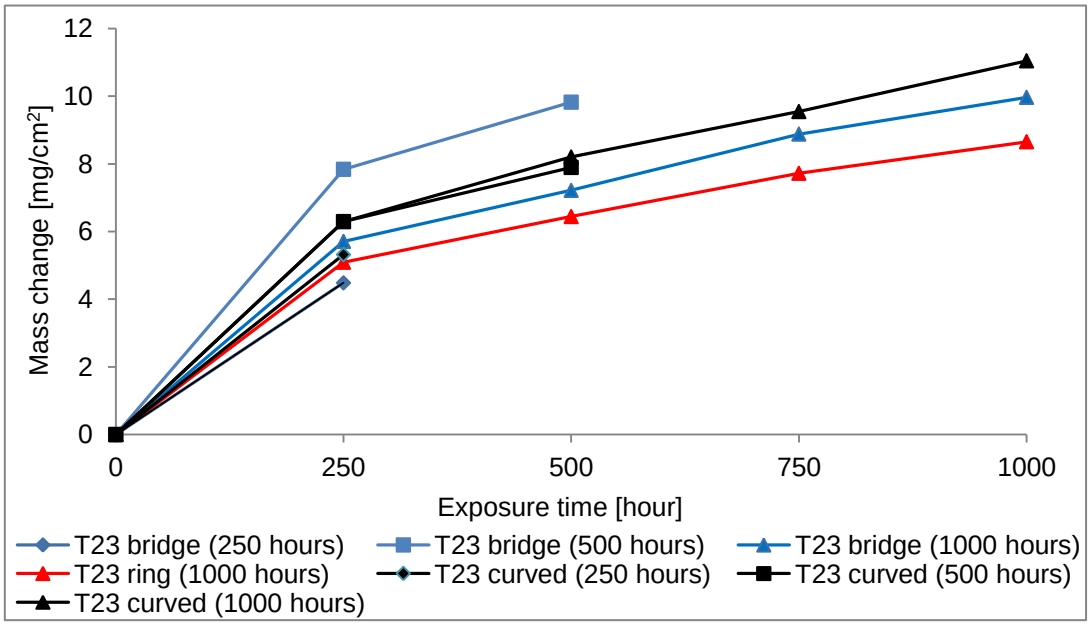

Figure 4-5 Net mass change of T23 with time and specimen geometry at 600°C with 4 mm/s steam flow rate (L)

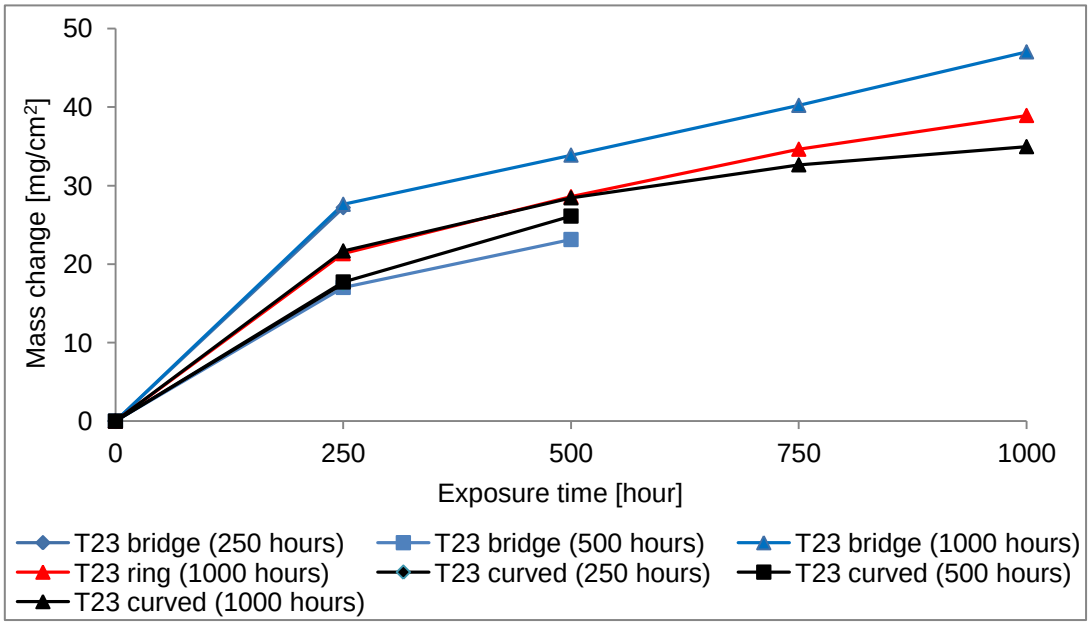

Figure 4-6 Net mass change of T23 with time and specimen geometry at 650°C with 4 mm/s steam flow rate (L)

Analysis of the graphs of Net mass change data for steam oxidation in the temperature between 600 – 700°C at low steam flow rates, showed a good

correlation between the lines corresponding to mass change of T23 after 250, 500, 1000 hour. This proved that the all specimens had been exposed to the same conditions regardless of their location within the furnace.

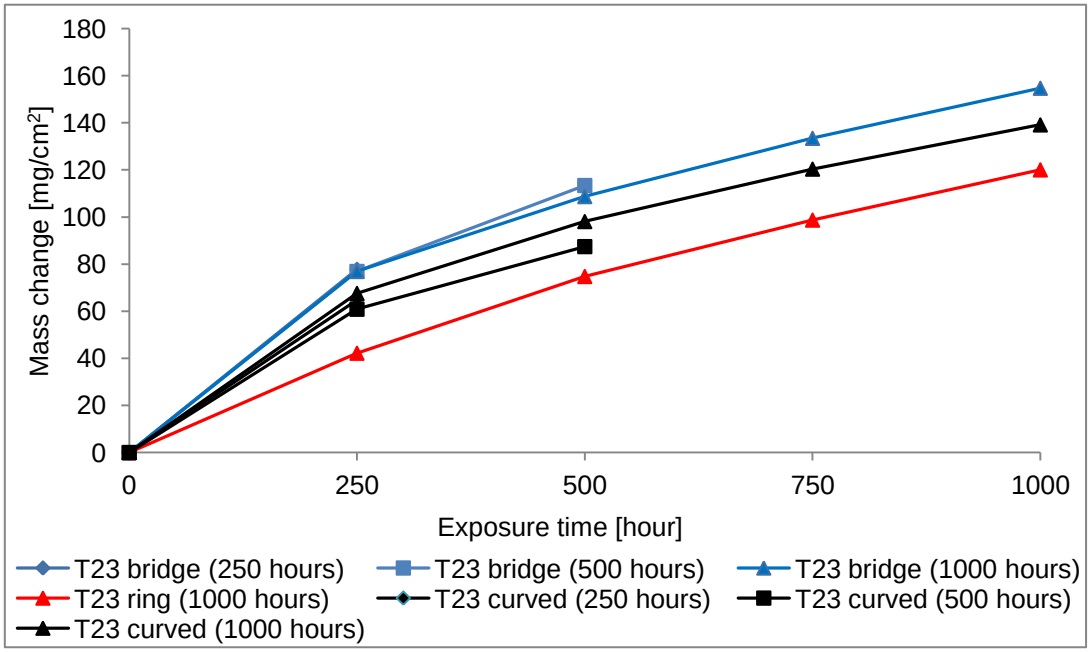

Figure 4-7 Net mass change of T23 with time and specimen geometry at 700°C with 4 mm/s steam flow rate (L)

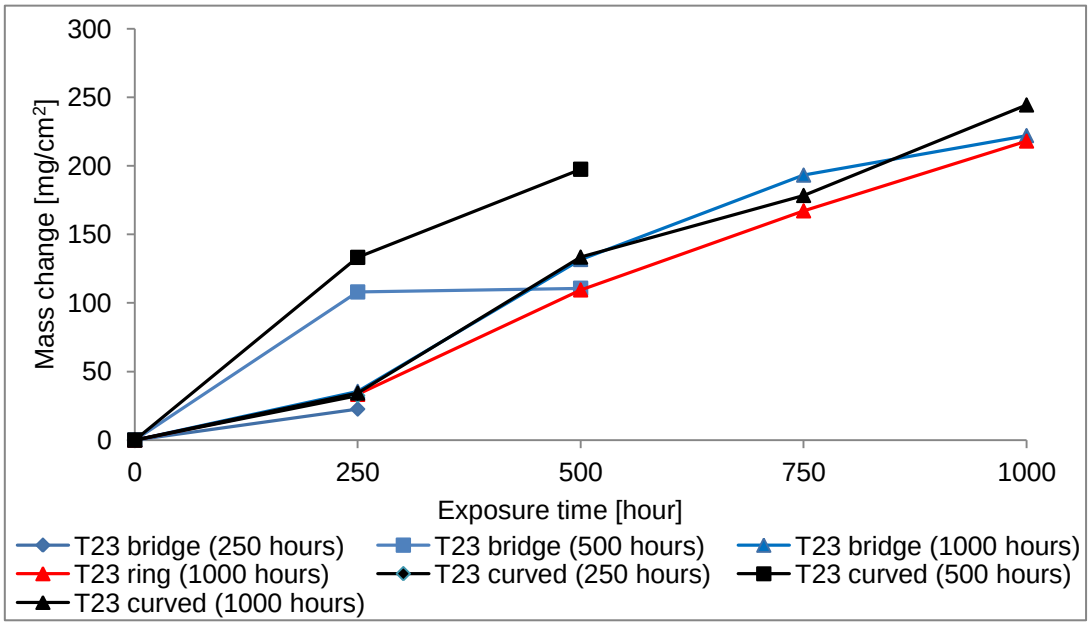

Figure 4-8 Net mass change of T23 with time and specimen geometry at 750°C with 4 mm/s steam flow rate (L)

At 750°C (L) there are clear differences between the lines corresponding to mass changes of T23 after 250, 500, 1000 hours, which could be a result of some minor changes in the exposure conditions.

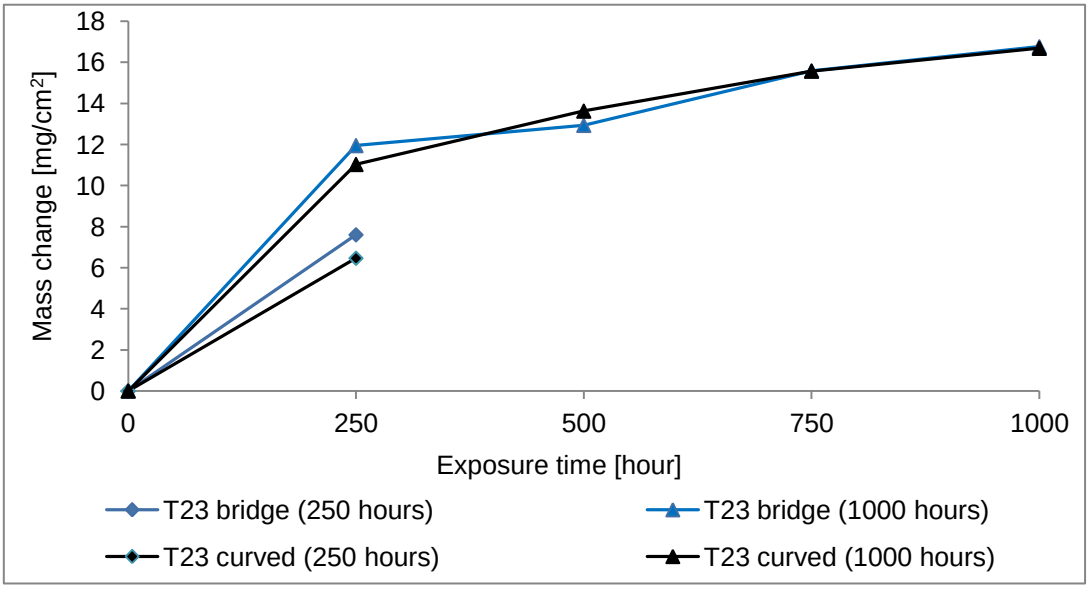

Figure 4-9 Net mass change of T23 with time and specimen geometry at 600°C with 40 mm/s steam flow rate (H)

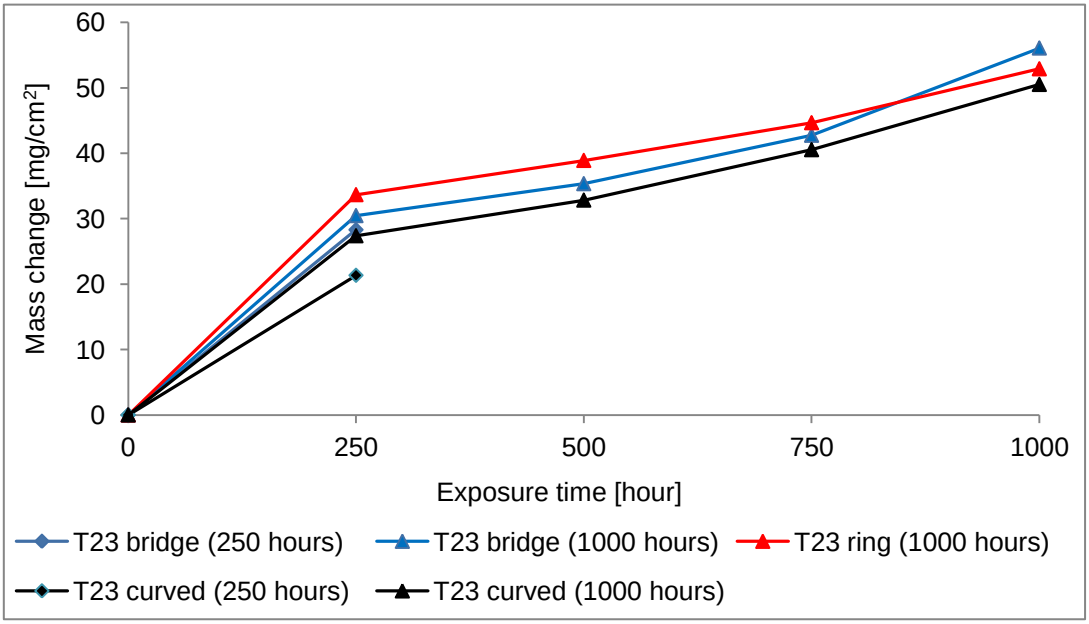

Figure 4-10 Net mass change of T23 with time and specimen geometry at 650°C with 16 mm/s steam flow rate (M)

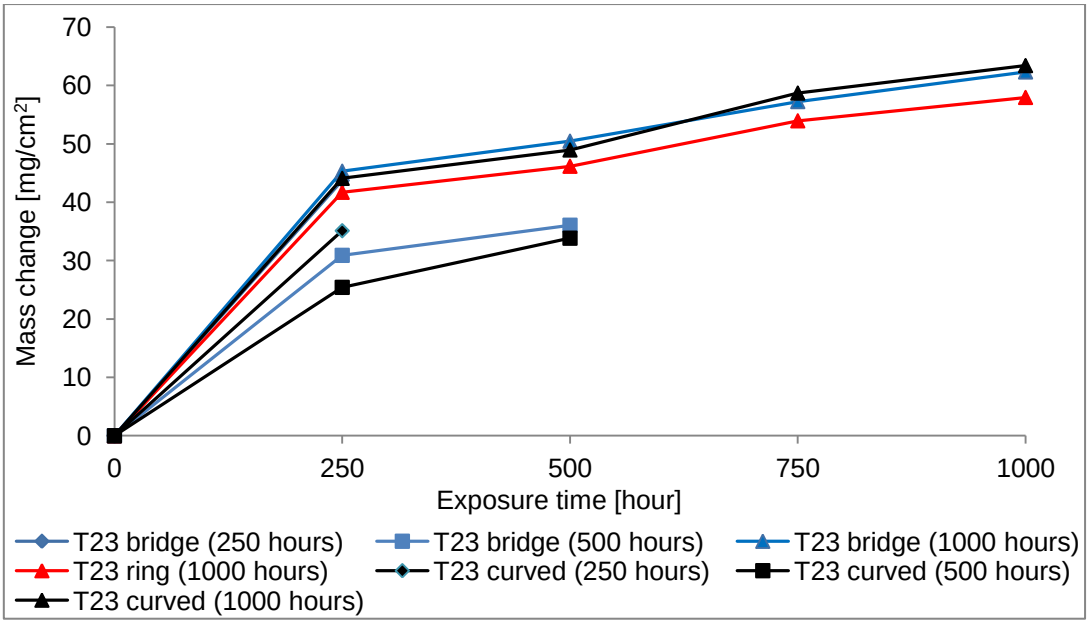

Figure 4-11 Net mass change of T23 with time and specimen geometry at 650°C with 40 mm/s steam flow rate (H)

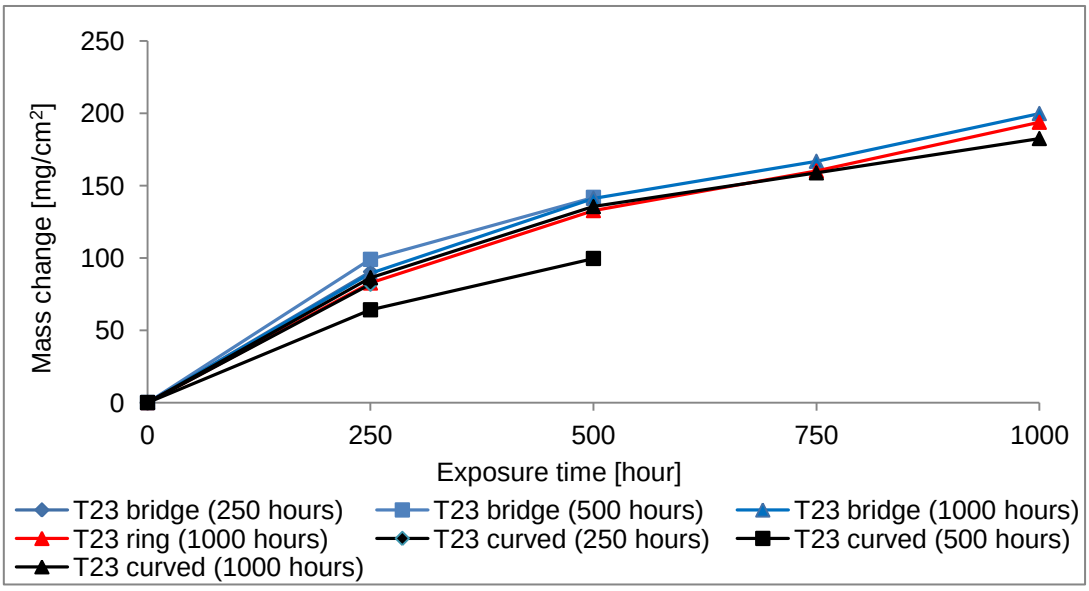

Figure 4-12 Net mass change of T23 with time and specimen geometry at 700°C with 16 mm/s steam flow rate (M)

Figure 4-9 - Figure 4-13 indicate that at higher steam flow rates the differences in the mass change between the specimen shapes are less significant.

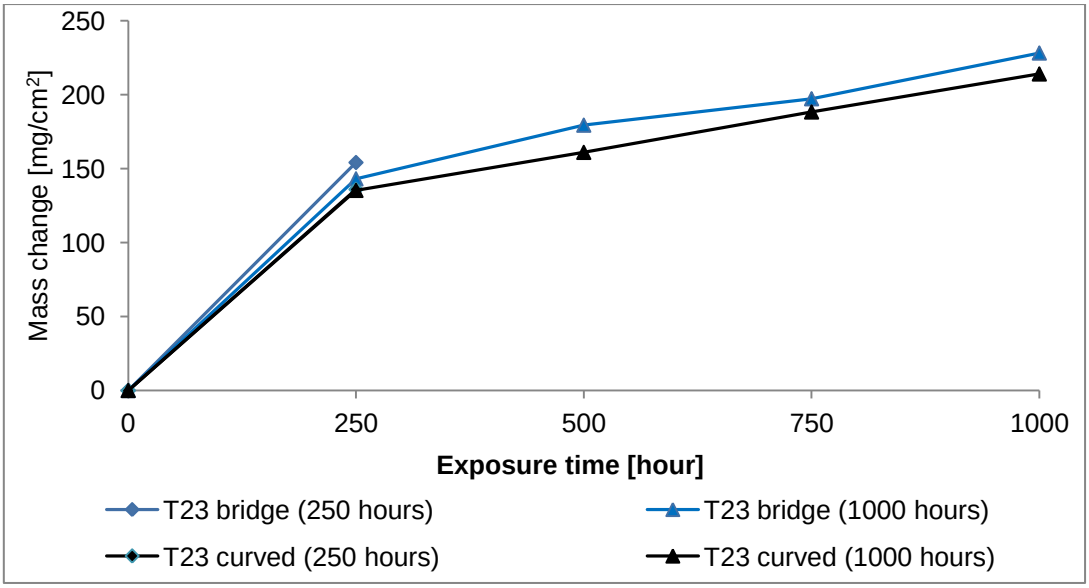

Figure 4-13 Net mass change of T23 with time and specimens geometry at 700°C with 40 mm/s steam flow rate (H)

Analysis of the data in Figure 4-5 - Figure 4-13 showed that at high temperature (>700°C) the oxidation kinetics in the first 500 hours is more influenced by the change in steam flow rates than temperature; however, after longer exposures temperature is believed to be the predominant factor. At lower temperatures, the mass change oxidation kinetics are more influenced by the temperature than increased steam flow rates.

4.1.1.2 T92 (9Cr)

The steam oxidation mass change kinetics of T92 is dependent on the exposure conditions as presented in Figure 4-14 - Figure 4-22. Analysis of these mass change curves shows that the oxidation of T92 follows the parabolic rate dependence, over the whole temperature range and steam flow rates tested. Examination of the mass change curves for T92 showed two regions; the first part with a higher slope and the second part with a shallower slope. The transition between those two stages fluctuates with temperature. Curves of the mass change of T92 shows similar slopes to T23 at 600°C (L), but above this temperature they differ. As was identified before, the slopes also differ with the specimen geometry. The mass change curves are steeper for bridge - shaped than for other samples;

however after longer exposures the discrepancies between the mass change values obtained are more randomised with geometry.

Analysis of the effect of specimen shape for T92 showed that its impact fluctuates with temperature; the most significant differences were identified at 650°C and 700°C, with three steam flow rates considered. At 600°C and 750°C the mass change curves show less scatter with samples shape. Among specimens tested, the ring shapes exhibit the slowest mass change, with the exception of exposure at 650°C with low steam flow rate (L). However, there is no shape which clearly shows the fastest steam oxidation at all temperatures tested – it changes with conditions.

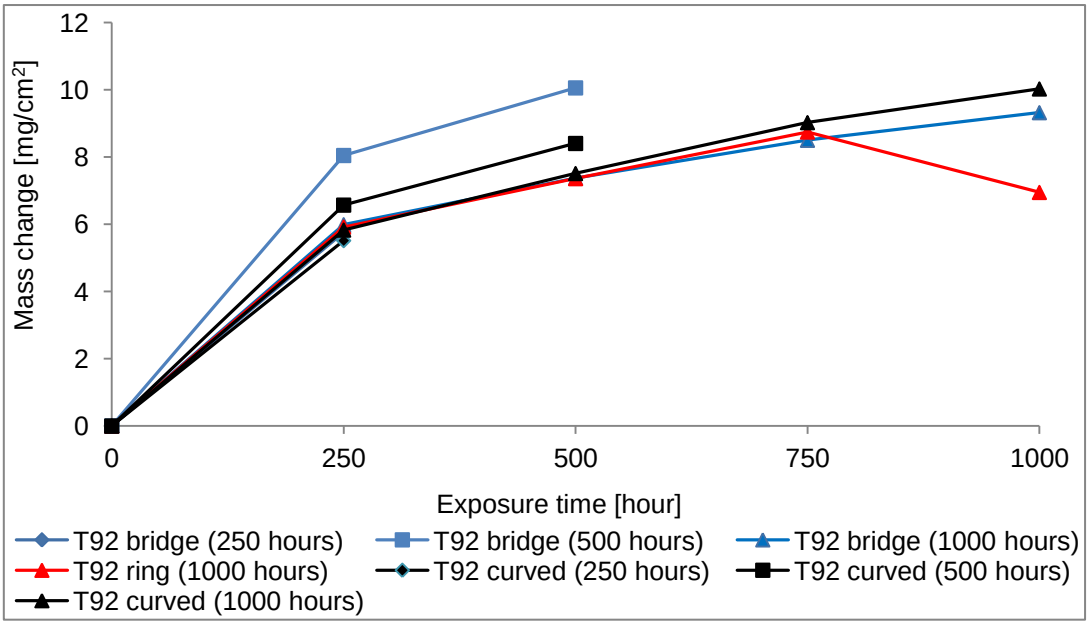

Figure 4-14 Net mass change of T92 with time and specimen geometry at 600°C with 4 mm/s steam flow rate (L)

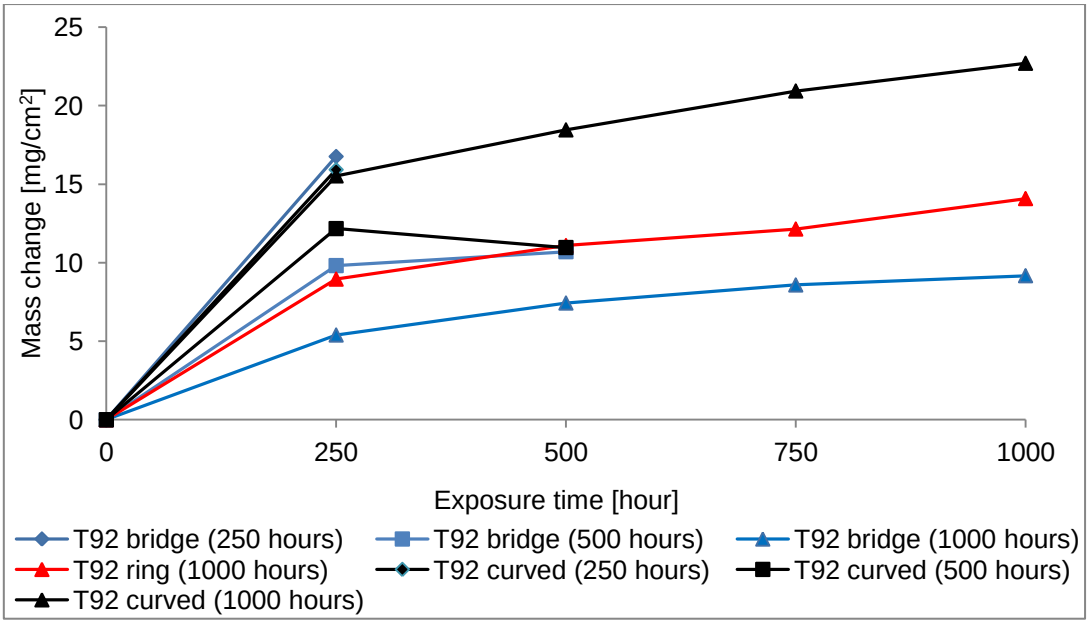

Figure 4-15 Net mass change of T92 with time and specimen geometry at 650°C with 4 mm/s steam flow rate (L)

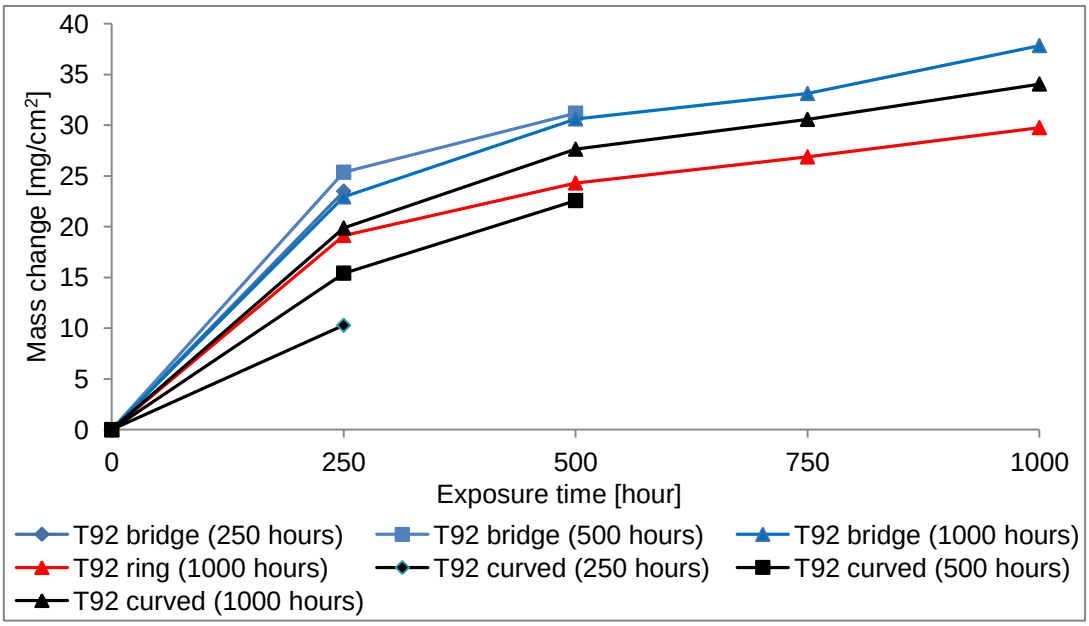

Figure 4-16 Net mass change of T92 with time and specimen geometry at 700°C with 4 mm/s steam flow rate (L)

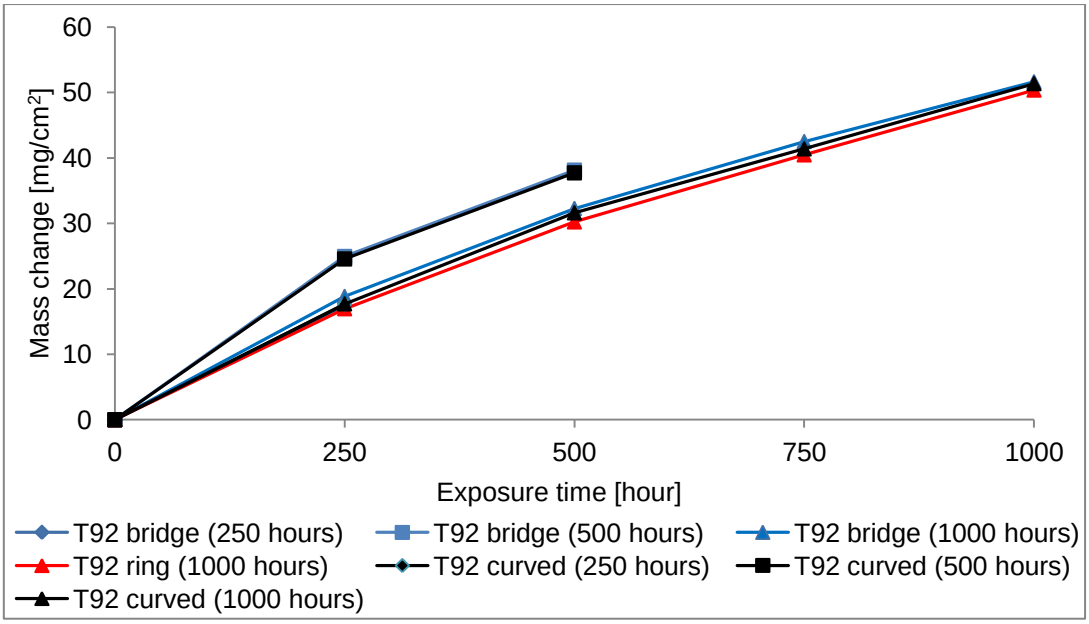

Figure 4-17 Net mass change of T92 with time and specimen geometry at 750^{O}C with 4 mm/s steam flow rate (L)

Examination of the net mass change data shows that at low steam rate the curve specimens have the largest mass changes at 600 and 750°C, whereas the middle temperatures (650 and 700°C) the bridge samples oxidise faster.

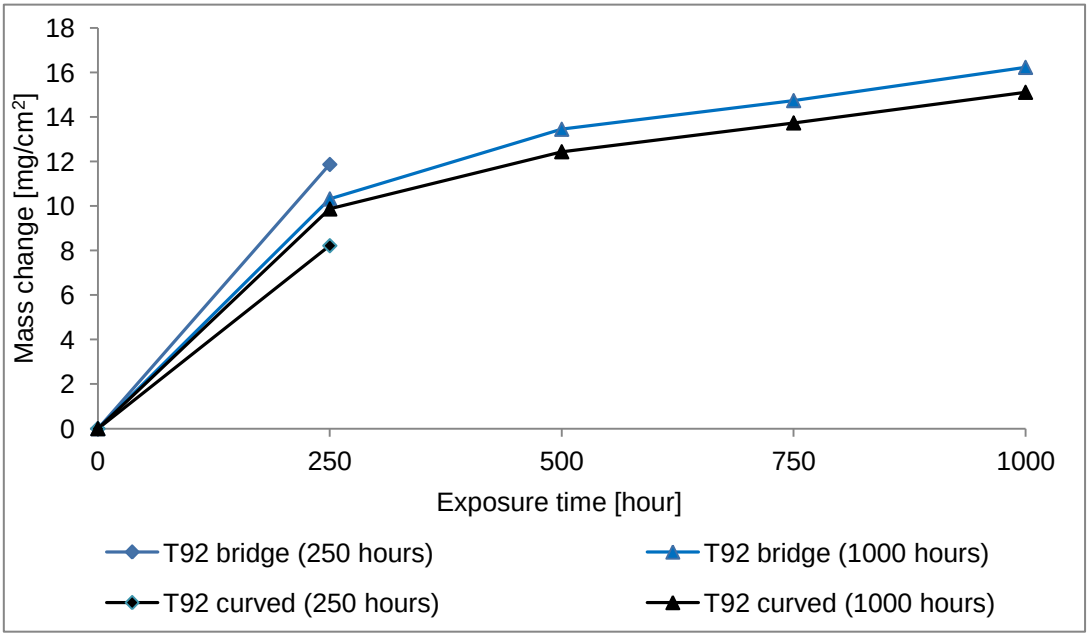

Figure 4-18 Net mass change of T92 with time and specimen geometry at 600°C with 40 mm/s steam flow rate (H)

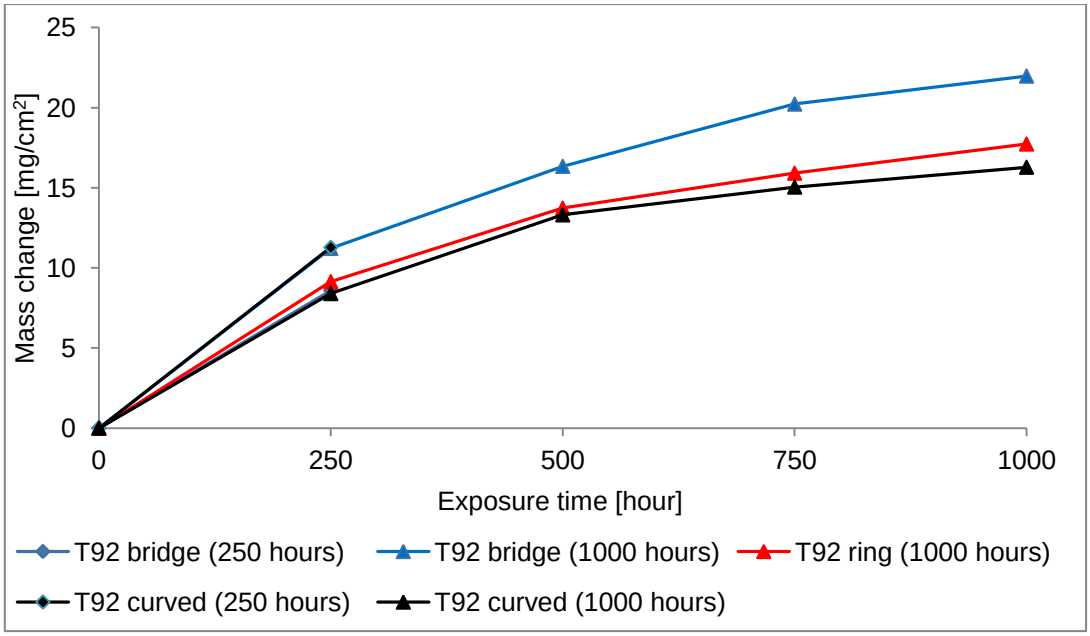

Figure 4-19 Net mass change of T92 with time and specimen geometry at 650°C with 16 mm/s steam flow rate (M)

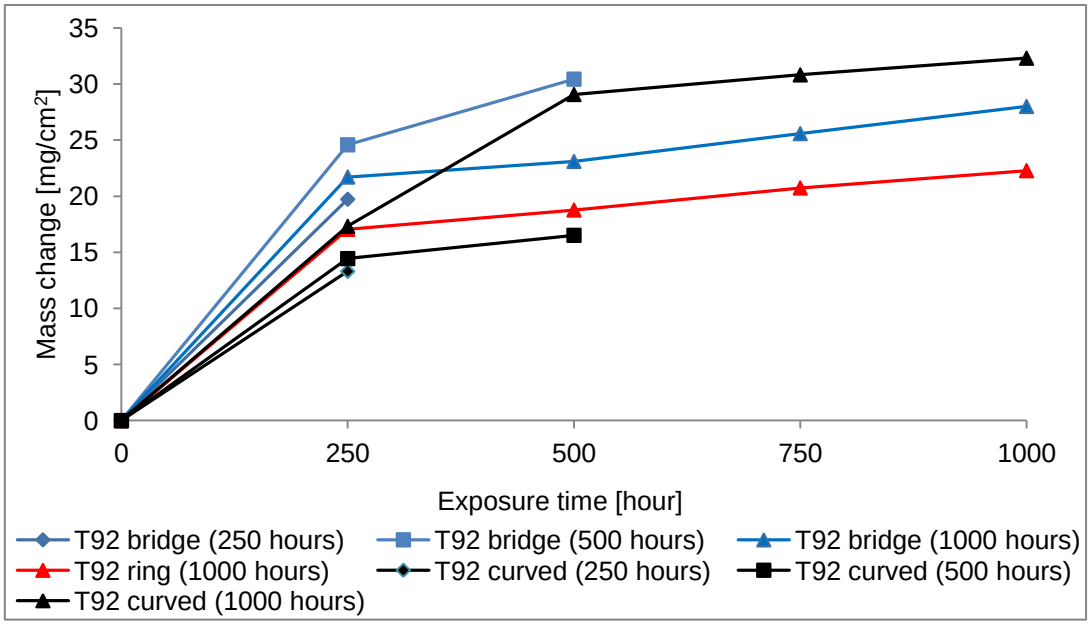

Figure 4-20 Net mass change of T92 with time and specimen geometry at 650°C with 40 mm/s steam flow rate (H)

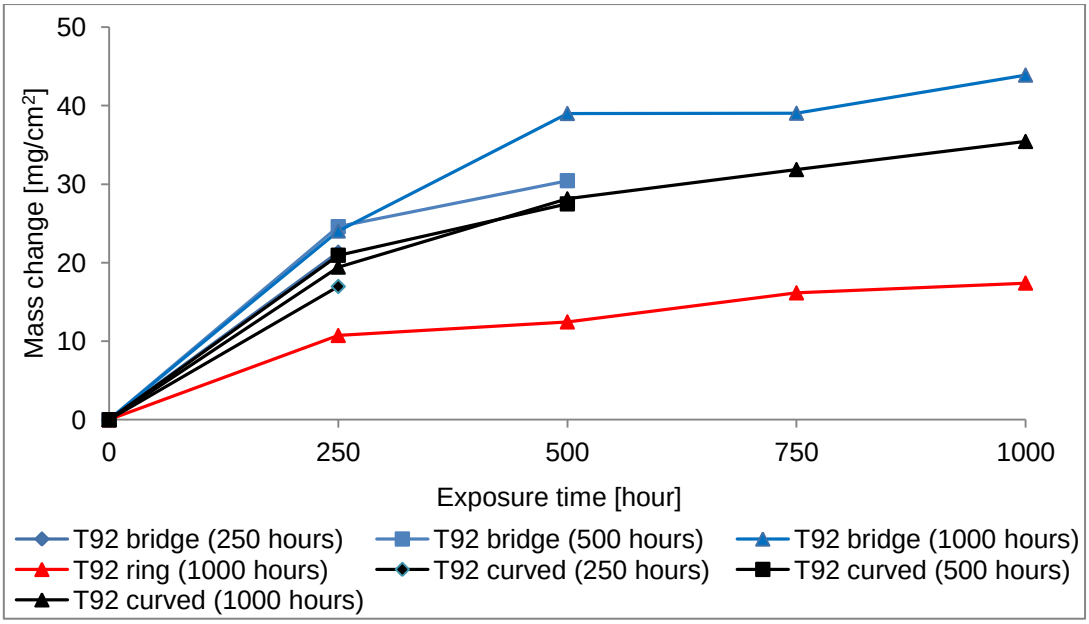

Figure 4-21 Net mass change of T92 with time and specimen geometry at 700°C with 16 mm/s steam flow rate (M)

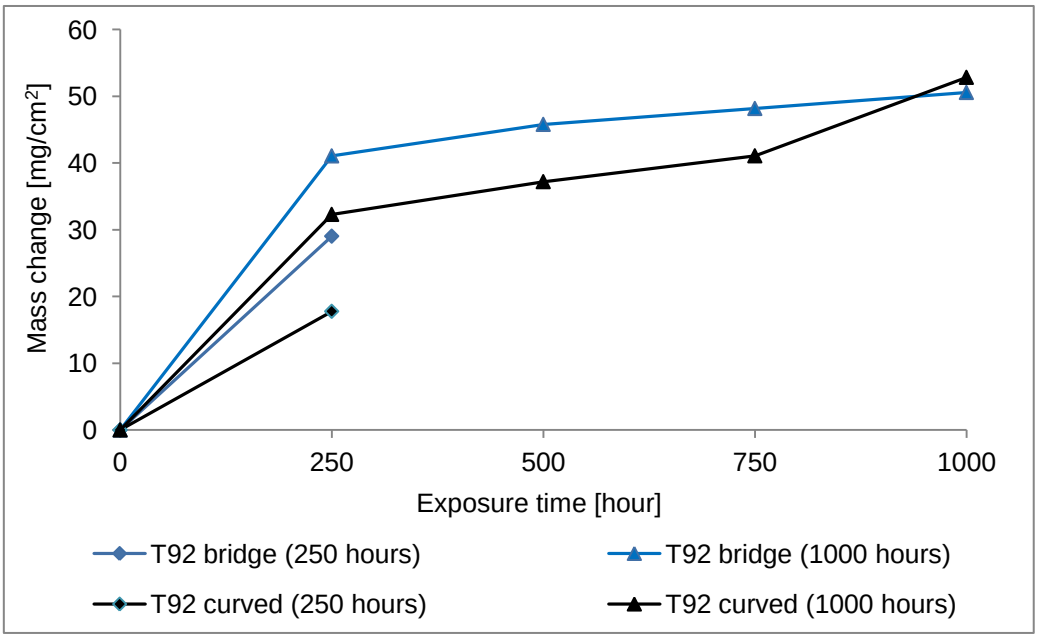

Figure 4-22 Net mass change of T92 with time and specimen geometry at 700°C with 40 mm/s steam flow rate (H)

Analysis of Figure 4-18 - Figure 4-22, representing T92 exposures at different steam flow rates, showed that the enhanced steam flow rates influence the mass change; however, the significance of this effect is lower than for T23. Moreover, the faster steam flow rates clearly enhance the differences in mass change of T92 with

specimen geometries. At higher steam flow rates, the bridge - shaped specimens oxidise faster than curve ones.

4.1.1.3 Summary

There are clear differences in the mass change oxidation kinetics of the ferritic steels tested; the performance of the both materials in steam is dependent on temperatures, steam flow rate, chromium level and additionally the specimen geometry. The specimen shape is believed to have an impact on the process; however, it is less significant than the first three factors mentioned. The significance of specimen geometry varies with exposure conditions and alloy type, with the largest impact being identified at 650°C and 700°C. Comparison of the impact of shape on oxidation between T23 and T92 showed that steam flow rate influences its significance. For T23 the faster steam flow reduces the effect of the geometry, whereas for T92 the differences became larger especially at 650°C.

4.1.2 Austenitic And Nickel-Based alloys

The various types of austenitic alloys and Inconel 740 specimens were exposed to pure steam environment in the temperature between 600 and 750°C and the three steam flow rate considered (L, M, H). Figure 4-23A-D show the average mass change, after 1000 hours exposure at different temperatures and steam flow rates. The bars correspond to mass gain of particular alloy after 1000 hour exposure at the temperature of interest. The comparison of the average mass change after 1000 hour exposure of austenitic and nickel-based alloys selected has shown that the chromium levels have an impact on the material performance. Moreover; the interplay of the alloying additions has also a positive impact. Generally, in the temperature between 600 – 750°C (L) the materials exposed oxidise relatively slow at low steam flow rate regardless of the chromium content. This changes at higher steam flow rates (M, H), when the higher chromium levels lower specimen mass changes and therefore increase the steam oxidation resistance.

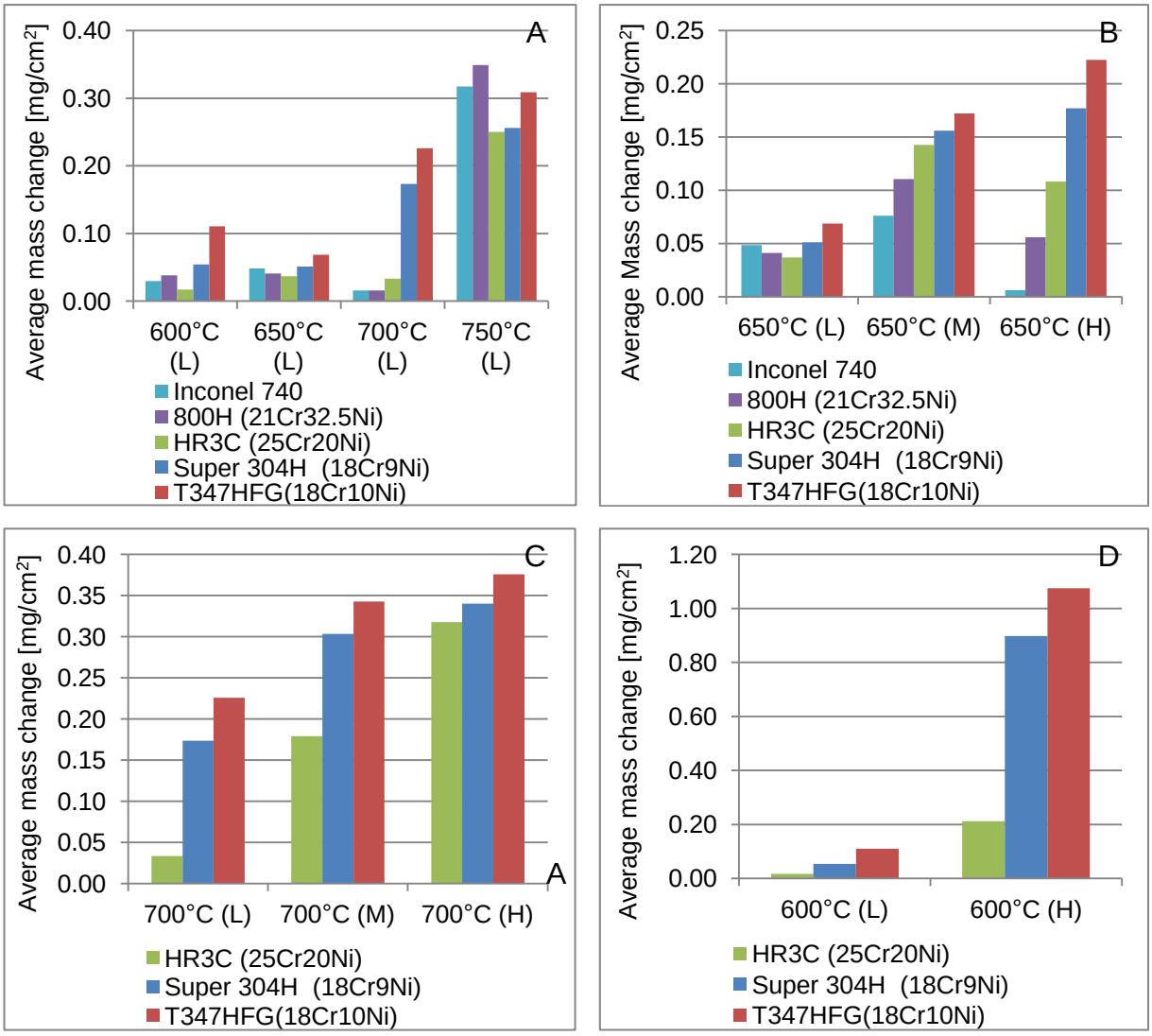

Figure 4-23 Differences in the average mass change between the austenitic and nickel-based alloys after 1000 hours (A) temperature and (B, C, D) steam flow rate effects

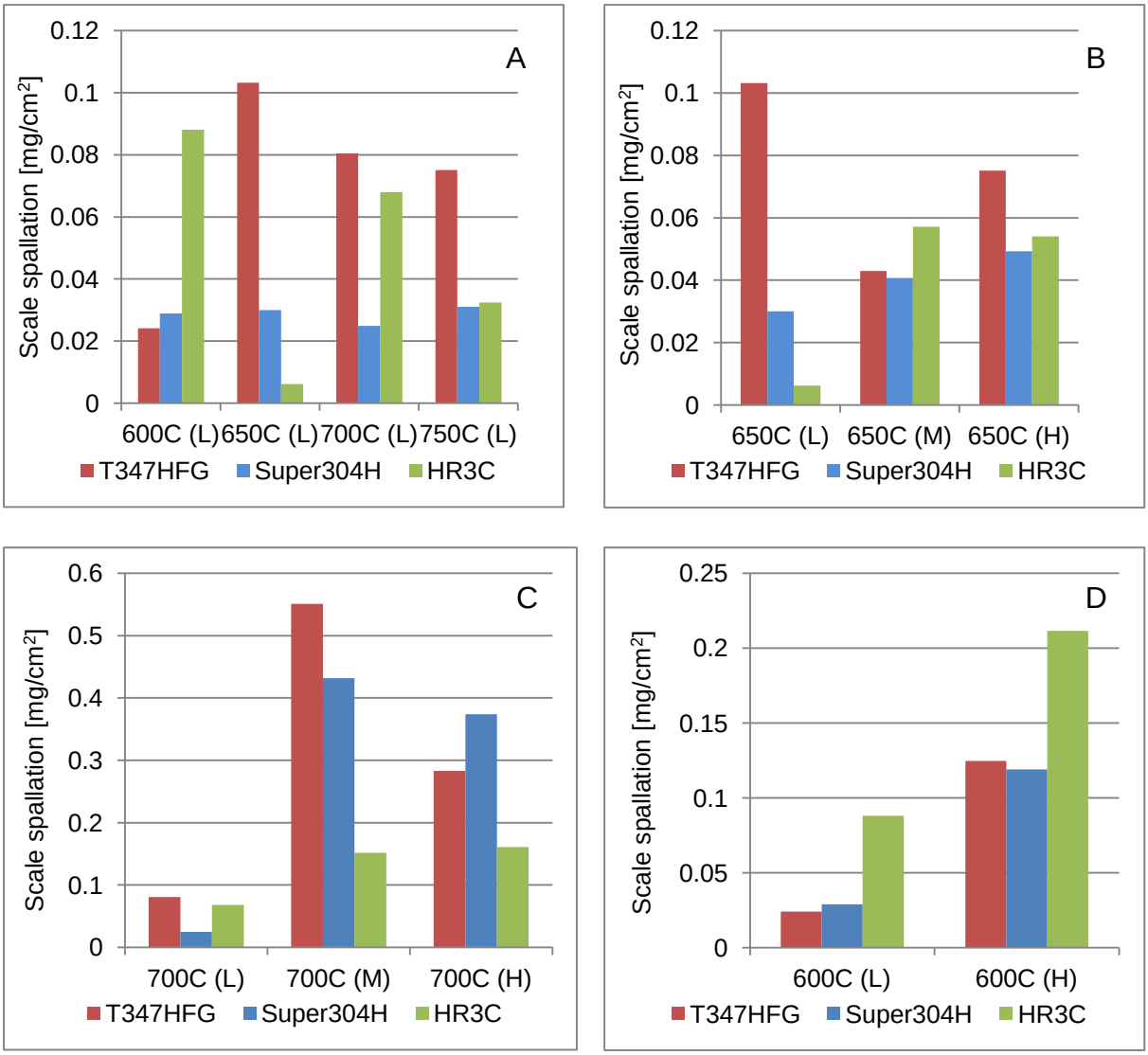

Figure 4-24 Comparison of the mass of the scales exfoliated from austenitic steels after 1000 hours exposures – (A) temperature and (B, C, D) steam flow rates effects

Figure 4-24A-D shows the avarage mass of the exfoliated scale for the austenitic steels, clearly the scale exoliation changes with test conditions as well as with the alloy type, hovever there is a concern about use of that data. Although, there are a change in the mass of the crucible with exposure time, there is a possibility that the crucible mass change for the austnitic steels is influenced by exfoliation of the ferritic steels (or the specimens close to each other). Based on that assumption the decision has been made to exlude the analysis of the mass of the oxides spalled from the detail analysis of oxidation kinetics.

4.1.2.1 T347HFG

Steam oxidation tests on T347HFG showed that the oxidation mass change kinetics depends on the exposure parameters, as demonstrated in Figure 4-25 - Figure 4-33. In comparison with the ferritics steels T347HFG shows much lower mass gains, moreover some samples exhibit a negative mass gain with time, which is associated with the spallation of the scales formed. Mass change curves are composed of a first faster period of oxidation, the duration of which changes from 250 up to 500 hours, depending on the exposure conditions. In general, however the slowdown of the mass gain is less significant than for ferritic steels, which is believed to be a result of their higher chromium content. Analysis of mass change curves indicate that under the conditions tested the oxidation of T347HFG does not always increase with temperature. For example at 600°C (L) the mass change is larger than at 650°C (L), but above it the oxidation rate increases with temperature; in addition the steam flow rate also accelerates the oxidation process.

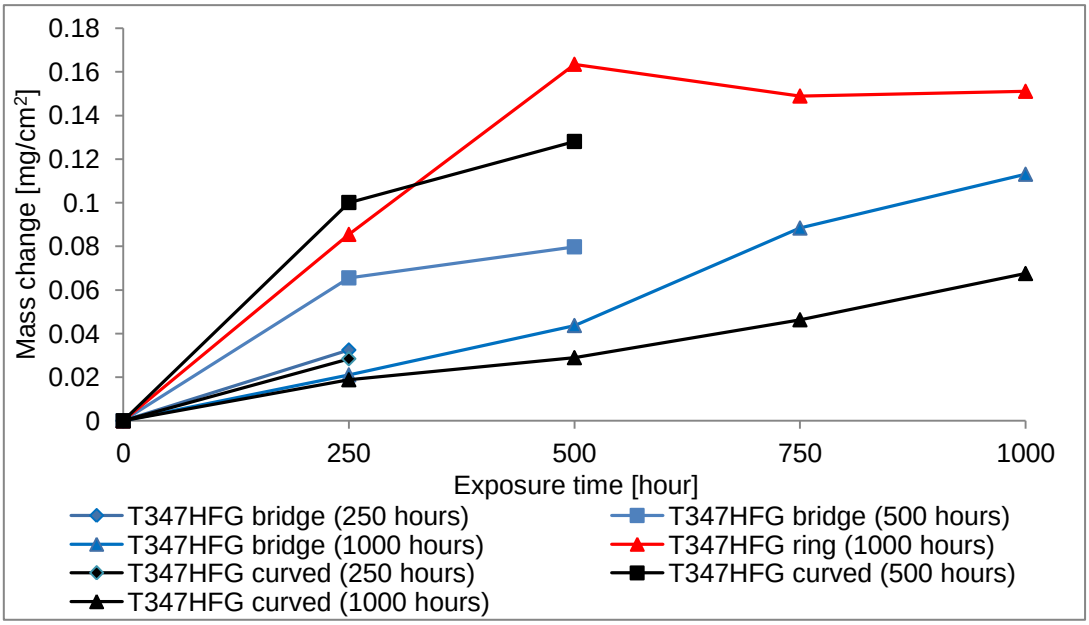

Figure 4-25 Net mass change of T347HFG with time and specimen geometry at 600°C with 4 mm/s steam flow rate (L)

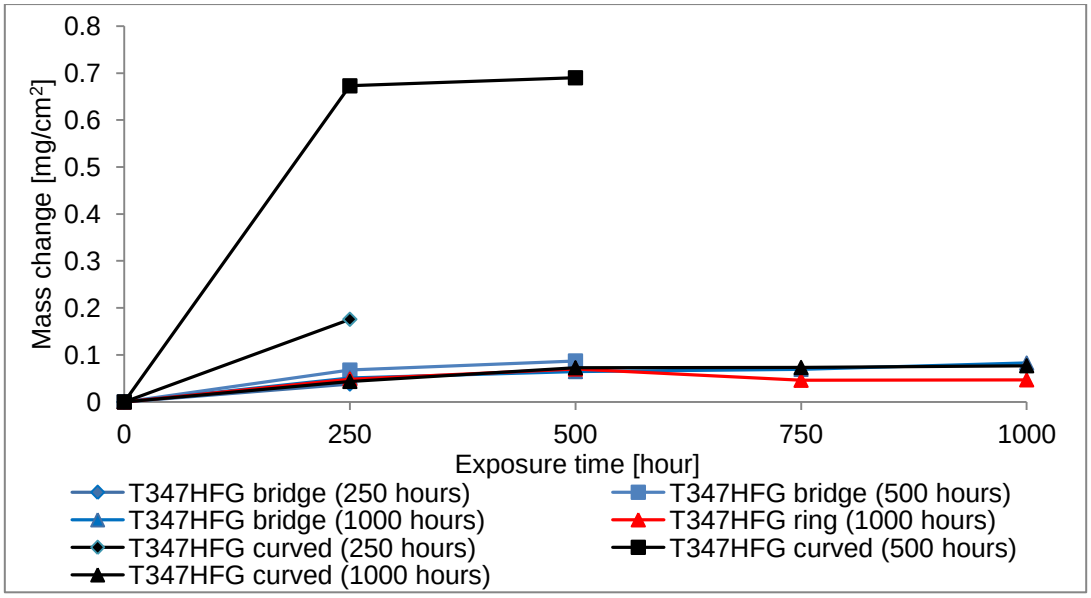

Figure 4-26 Net mass change of T347HFG with time and specimen geometry at 650°C with 4 mm/s steam flow rate (L)

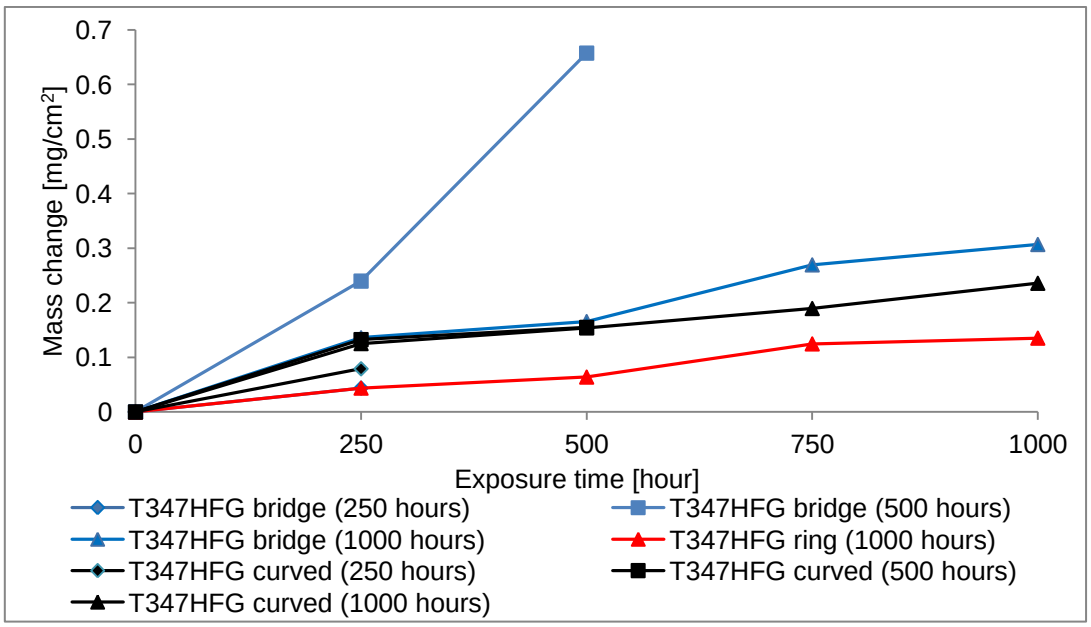

Figure 4-27 Net mass change of T347HFG with time and specimen geometry at 700°C with 4 mm/s steam flow rate (L)

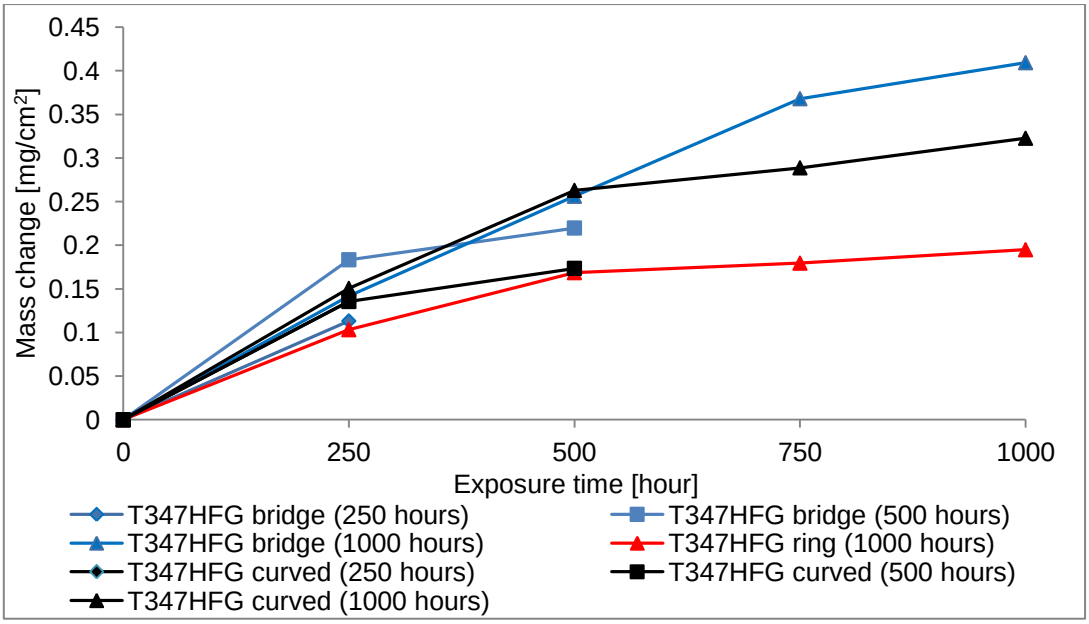

Figure 4-28 Net mass change of T347HFG with time and specimen geometry at 750°C with 4 mm/s steam flow rate (L)

Analysis of the behaviour of T347HFG specimens indicated that the impact of specimen shape varies with temperature. The largest differences were found at 600 and 750°C (L), whereas in the middle temperature range (650 and 700°C) the impact of geometry is less pronounced.

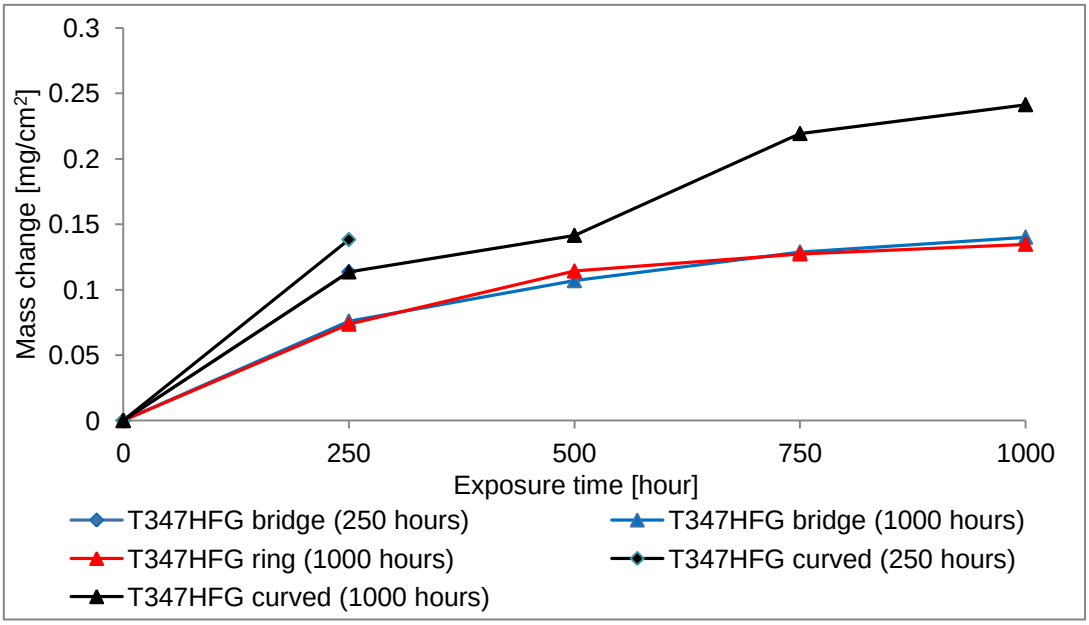

Figure 4-29 Net mass change of T347HFG with time and specimen geometry at 650°C with 16 mm/s steam flow rate (M)

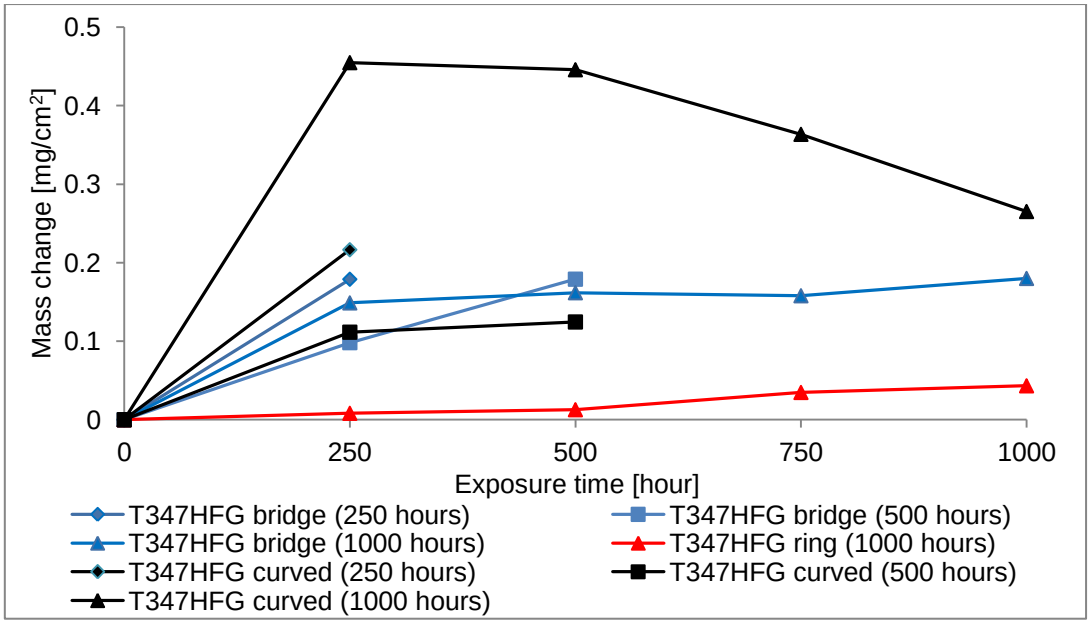

Figure 4-30 Net mass change of T347HFG with time and specimen geometry at 650°C with 40 mm/s steam flow rate (H)

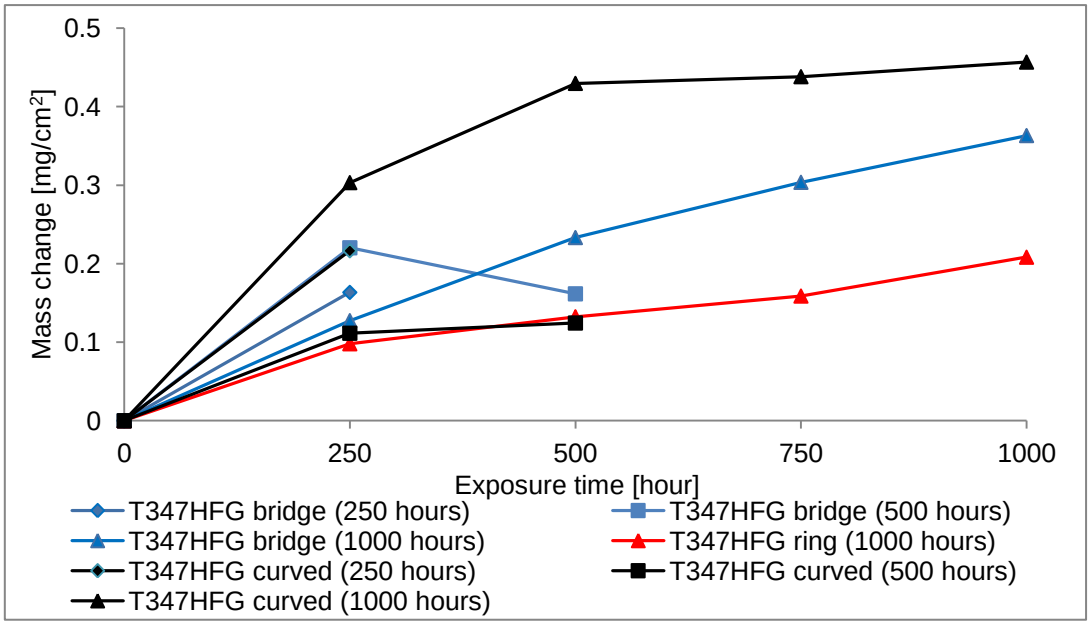

Figure 4-31 Net mass change of T347HFG with time and specimen geometry at 700°C with 16 mm/s steam flow rate (M)

Analysis of the steam flow rate impact indicates not only acceleration of the mass change with the flow rate but also an influence on the differences of the mass change with shape, which is the most pronounced at 700°C.

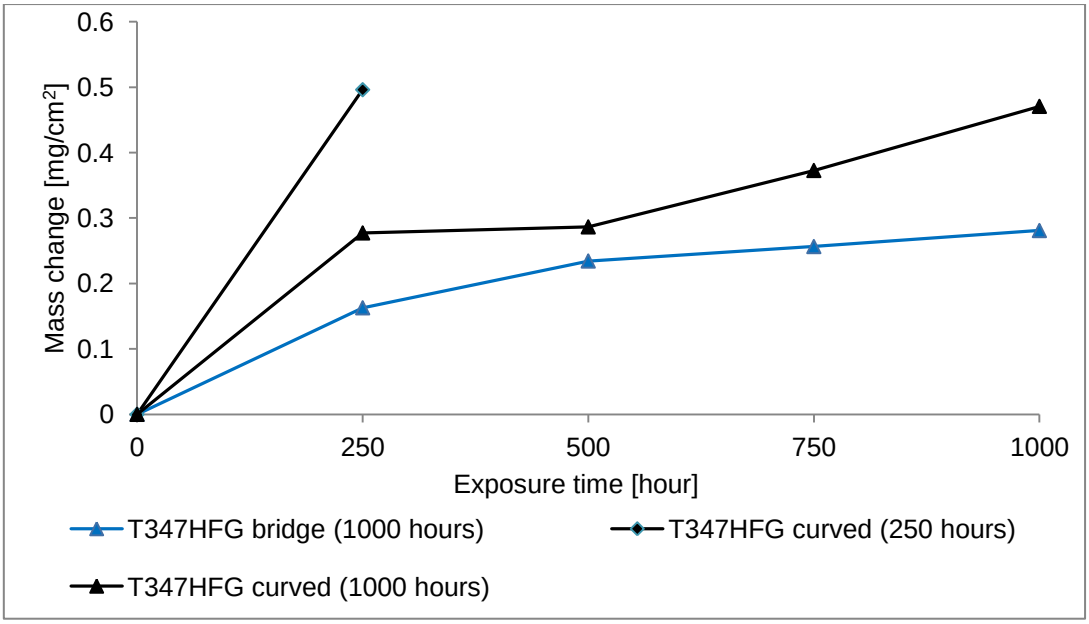

Figure 4-32 Net mass change of T347HFG with time and specimen geometry at 700°C with 40 mm/s steam flow rate (H)

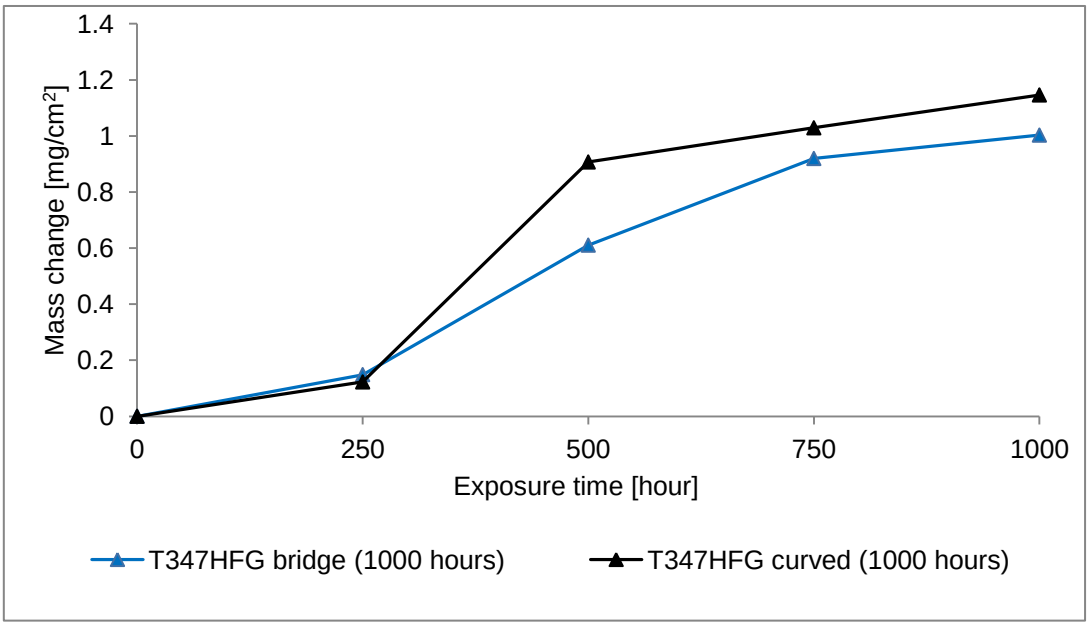

Figure 4-33 Net mass change of T347HFG with time and specimen geometry at 600°C with 40 mm/s steam flow rate (H)

Considering the effect of shape and its importance on the oxidation kinetics of T347HFG, there is an impact of geometry, however due to the relatively low mass change of the exposed specimens, there is an uncertainty as to whether the discrepancies are a result of the shape change itself or the error of the mass

balance. Assuming that the errors are the same for all the measurement taken, the ring specimens show the smallest mass gain. However, identification of the specimens with the fastest oxidation rate is not possible due to fluctuations in the results for the bridge and curve - shaped specimens.

4.1.2.2 Super 304H

Analysis of the oxidation behaviour of Super 304H, presented in Figure 4-34 - Figure 4-42, shows that its performances in steam changes with the exposure conditions, with the differences in the mass changes are being more significant than for T347HFG. The mass change curves show the initial higher slope period is longer than for T347HFG. At all steam flow rate exposures, the first phase of the oxidation is relatively long (up to 500 hours). The mass gain of Super 304H increases with temperature; between 600 - 650°C (L) its performance is significantly better than at higher temperatures. Comparison of data for T347HFG and Super 304H shows that in spite of the fact that both these alloys have the same chromium content (18%) Super 304H oxidises slower; however, the differences in the mass gain became smaller with change of the steam flow rates.

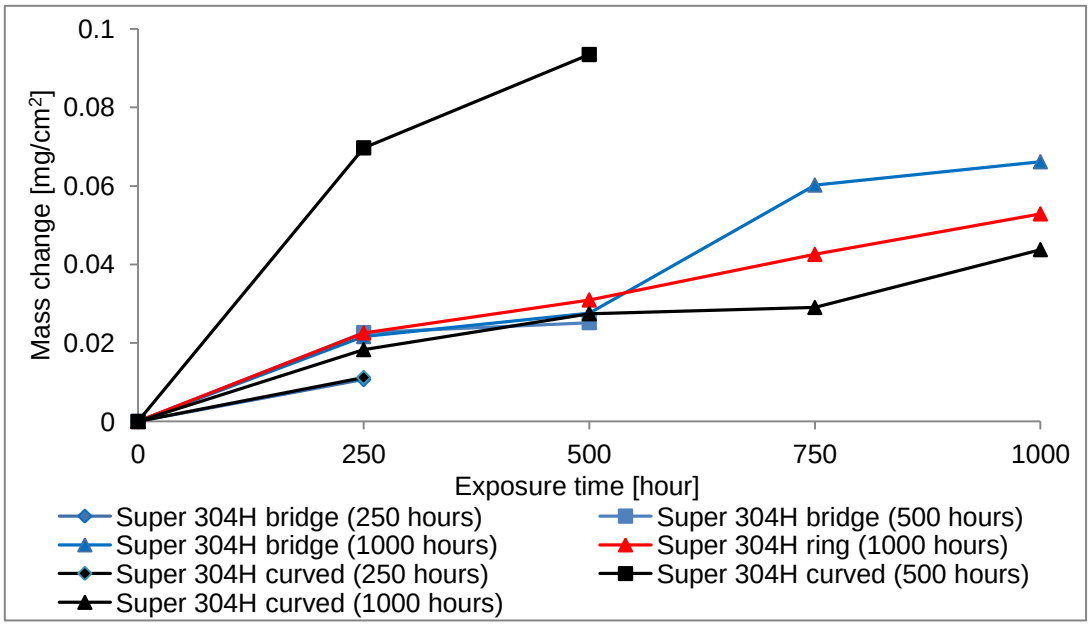

Figure 4-34 Net mass change of Super 304H with time and specimen geometry at 600°C with 4 mm/s steam flow rate (L)

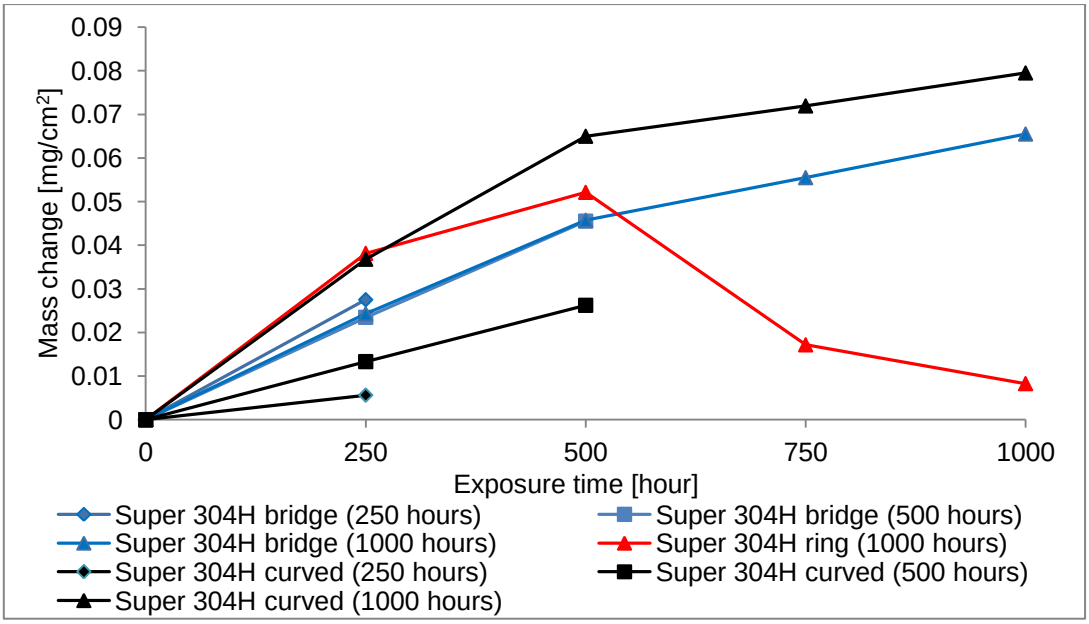

Figure 4-35 Net mass change of Super 304H with time and specimen geometry at 650°C with 4 mm/s steam flow rate (L)

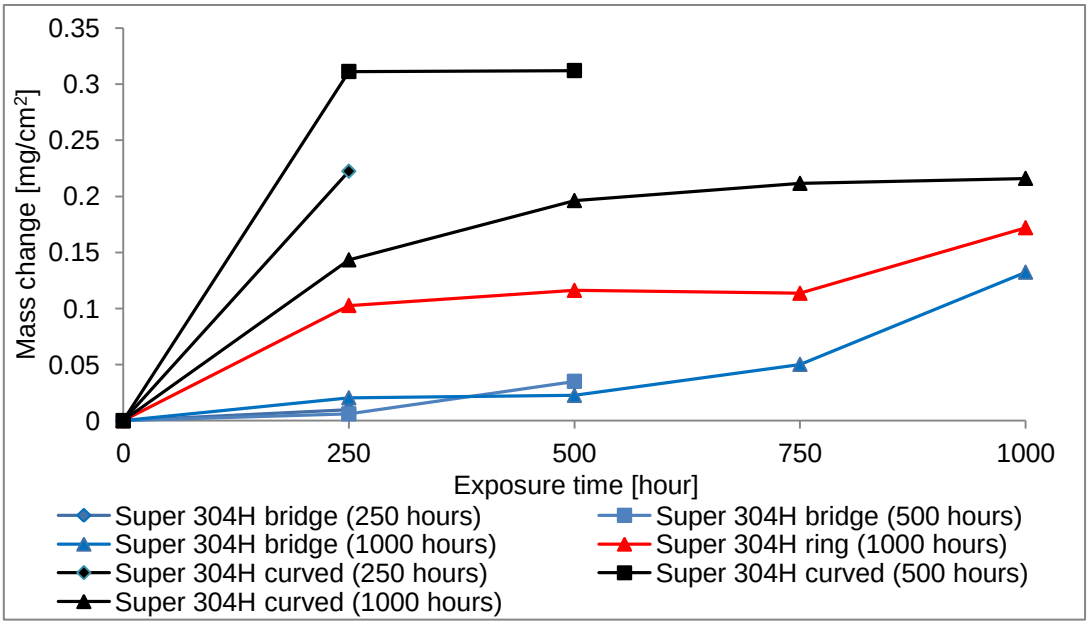

Figure 4-36 Net mass change of Super 304H with time and specimen geometry at 700°C with 4 mm/s steam flow rate (L)

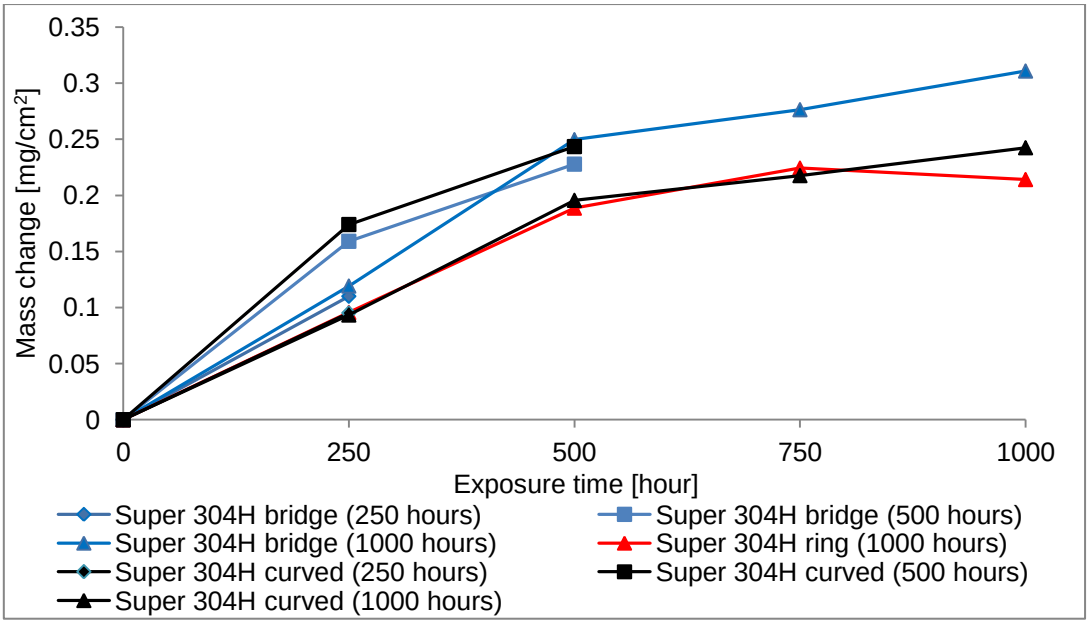

Figure 4-37 Net mass change of Super 304H with time and specimen geometry at 750°C with 4 mm/s steam flow rate (L)

Figure 4-34 - Figure 4-37 showed that under low steam flow rate conditions the oxidation of Super 304H varies with the specimen geometries. However it is not possible to identify one, clear trend or one shape, which exhibits the fastest mass change over the whole temperature range selected. An important finding is that ring specimens show a relatively stable trend - at all temperatures the mass change is the middle value, whereas for other shapes the mass change varies with temperature; at 600 and 700°C the bridge - shaped indicates the fastest mass change, whereas at 650 and 750°C curve specimens oxidise faster.

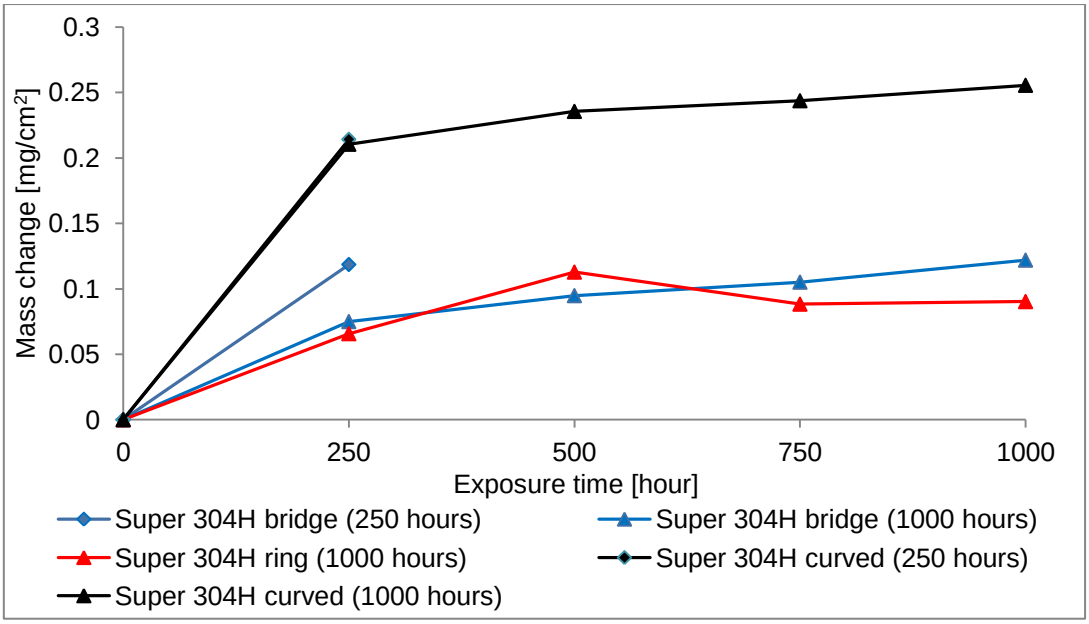

Figure 4-38 Net mass change of Super 304H with time and specimen geometry at 650°C with 16 mm/s steam flow rate (M)

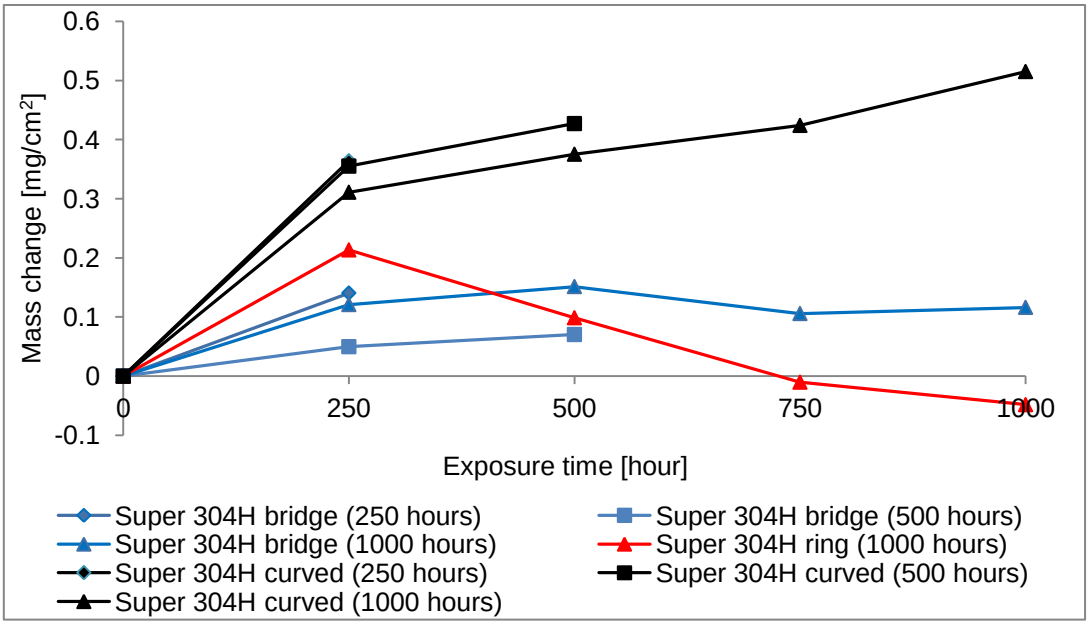

Figure 4-39 Net mass change of Super 304H with time and specimen geometry at 650°C with 40 mm/s steam flow rate (H)

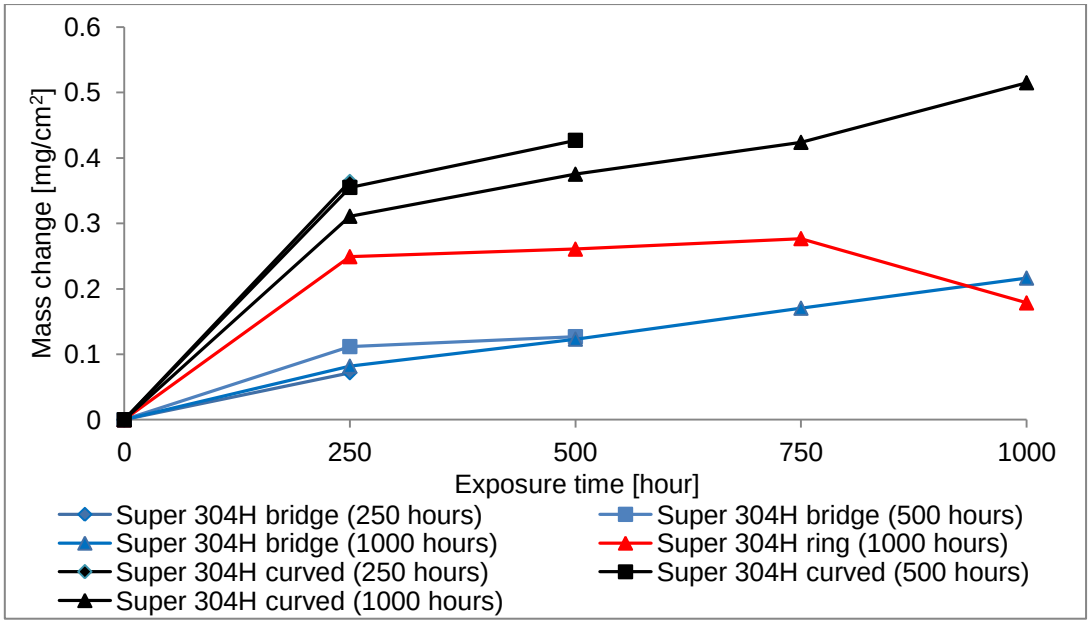

Figure 4-40 Net mass change of Super 304H with time and specimen geometry at 700°C with 16 mm/s steam flow rate (M)

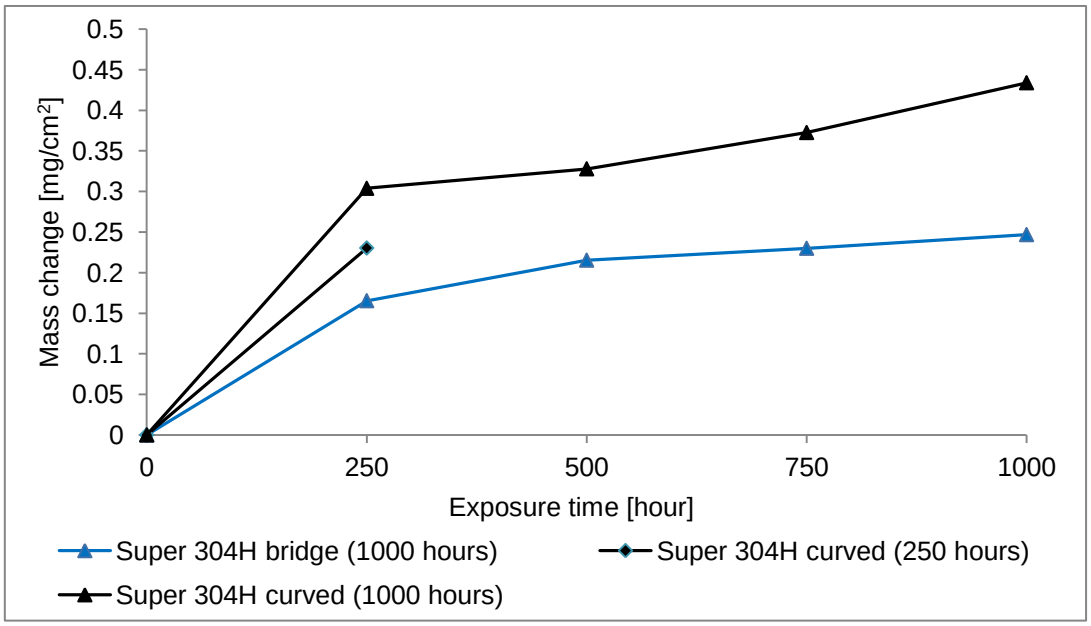

Figure 4-41 Net mass change of Super 304H with time and specimen geometry at 700°C with 40 mm/s steam flow rate (H)

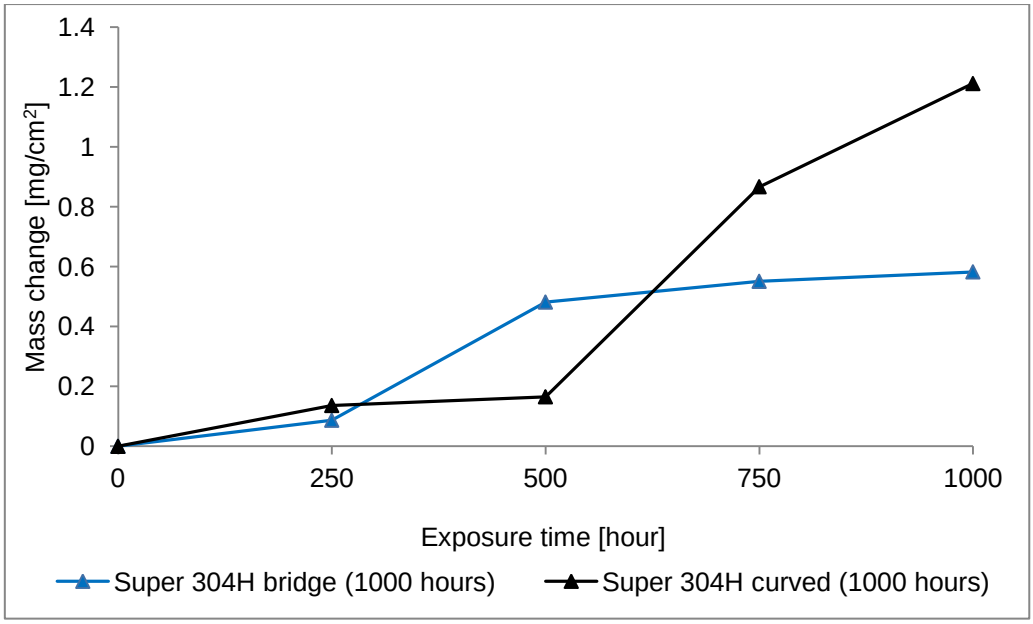

Figure 4-42 Net mass change of Super 304H with time and specimen geometry at 600°C with 40 mm/s steam flow rate (H)

Analysis of the impact of the steam flow rate indicates that with faster steam flow rates the effect of the specimen geometry is more pronounced and the curve samples show faster mass changes. Ring specimens exposed to faster steam velocity show more severe spallation of the scales formed, which explains the negative mass change.

4.1.2.3 HR3C

Steam oxidation of HR3C is considerably slower than for both 18Cr steels. In the temperature range 600 – 700°C (L) the performance of the alloy does not change significantly with temperature; the steam flow seems to have a larger impact in accelerating of the oxidation. At 750°C (L) there is a clear enhance went of the oxidation rate and there is no negative mass change. At the temperatures investigated the oxidation mass changes indicate growth with time; however, there is not a single clear trend showing the transition from fast linear mass change (high slope curve) to sub-parabolic behaviour (less steep curve), it is condition dependent.

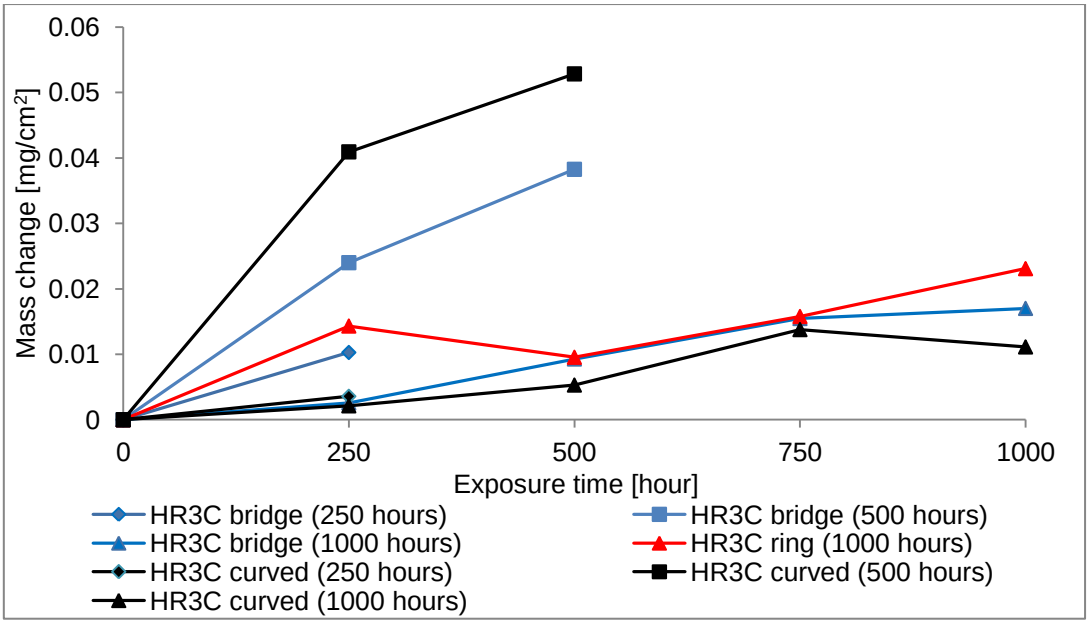

Figure 4-43 Net mass change of HR3C with time and specimen geometry at 600°C with 4 mm/s steam flow rate (L)

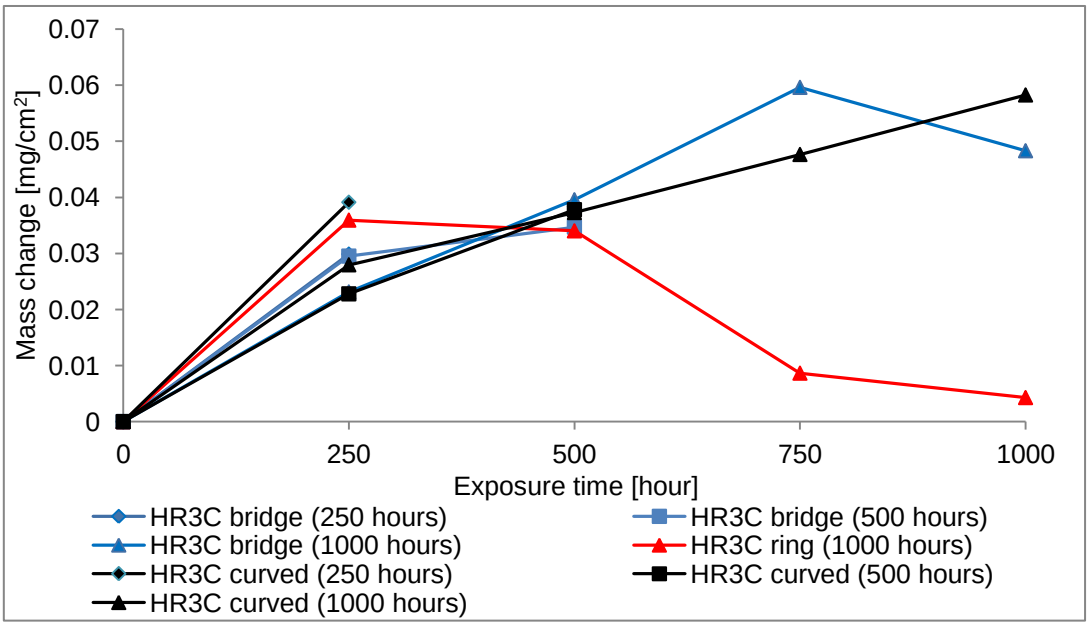

Figure 4-44 Net mass change of HR3C with time and specimen geometry at 650°C with 4 mm/s steam flow rate (L)

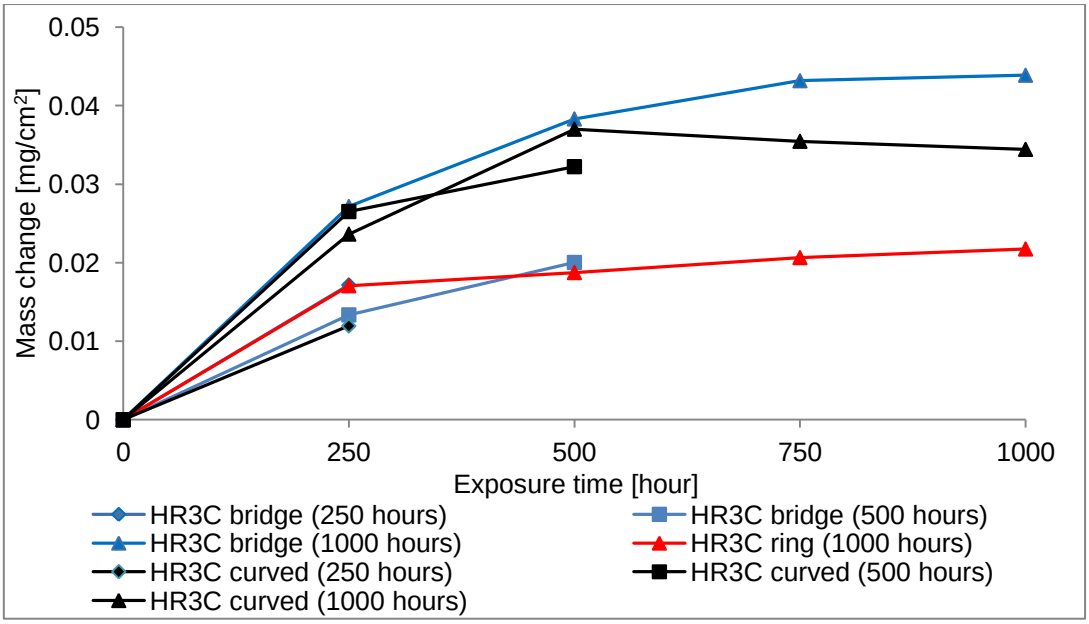

Figure 4-45 Net mass change of HR3C with time and specimen geometry at 700°C with 4 mm/s steam flow rate (L)

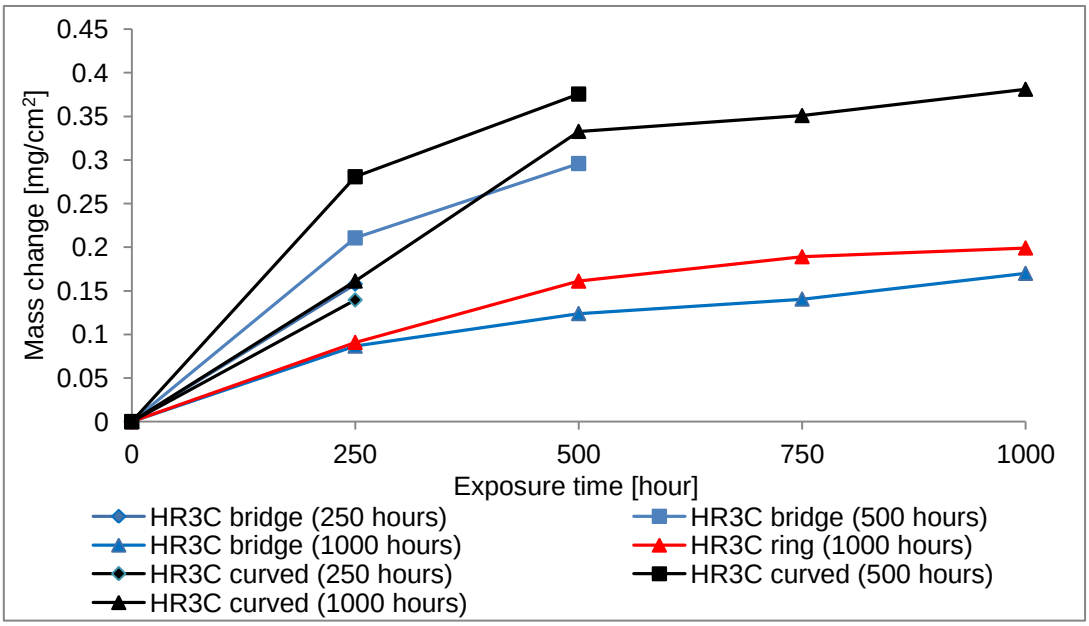

Figure 4-46 Net mass change of HR3C with time and specimen geometry at 750°C with 4 mm/s steam flow rate (L)

Analysis of the oxidation of HR3C at the low steam flow rate shows that at 600 and 650°C there is a negative mass change, which is most likely a result of scale spallation. At higher temperatures (>650°C) HR3C shows positive mass change. The specimen geometry influence the oxidation behaviour of this alloy tested, but there is

no single shape which exhibits the fastest oxidation over the whole temperature range.

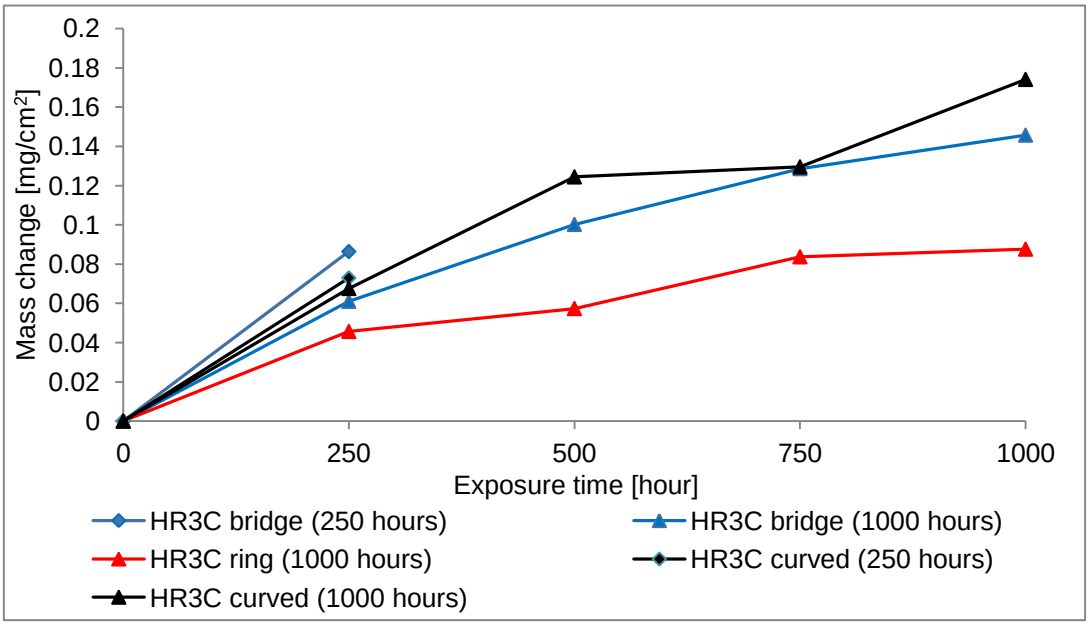

Figure 4-47 Net mass change of HR3C with time and specimen geometry at 650°C with 16 mm/s steam flow rate (M)

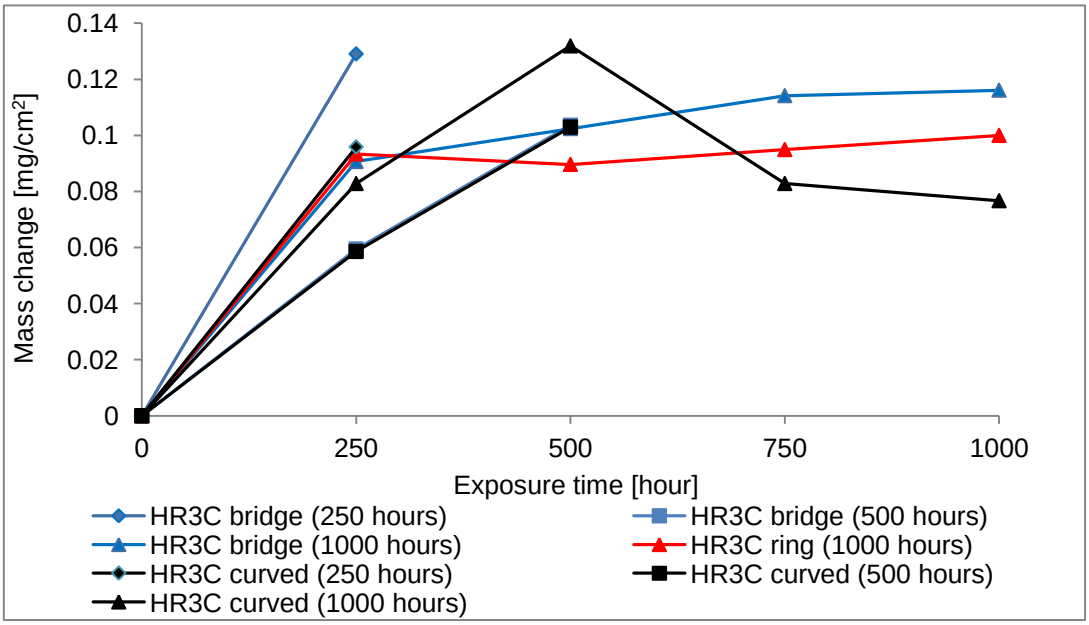

Figure 4-48 Net mass change of HR3C with time and specimen geometry at 650°C with 40 mm/s steam flow rate (H)

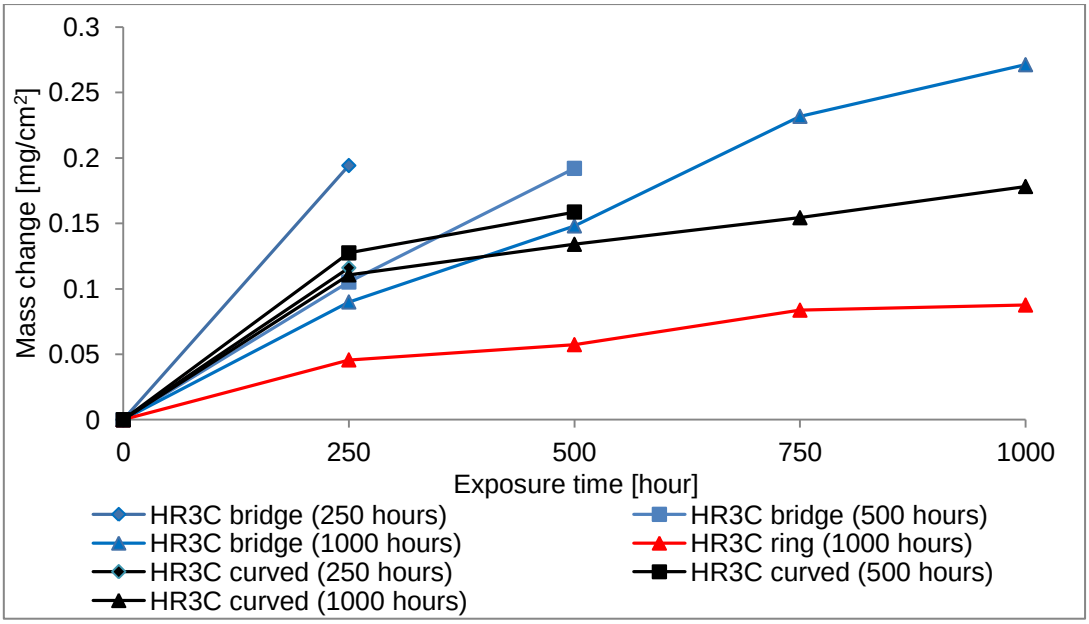

Figure 4-49 Net mass change of HR3C with time and specimen geometry at 700°C with 16 mm/s steam flow rate (M)

Considering the higher steam flow rates (M, H), the main finding is a more pronounced effect of the specimen shape, which varies with the temperature. At lower temperatures, the curve - shaped samples seem to show the fastest mass change, whereas at 700°C the bridge shape specimens oxidise faster.

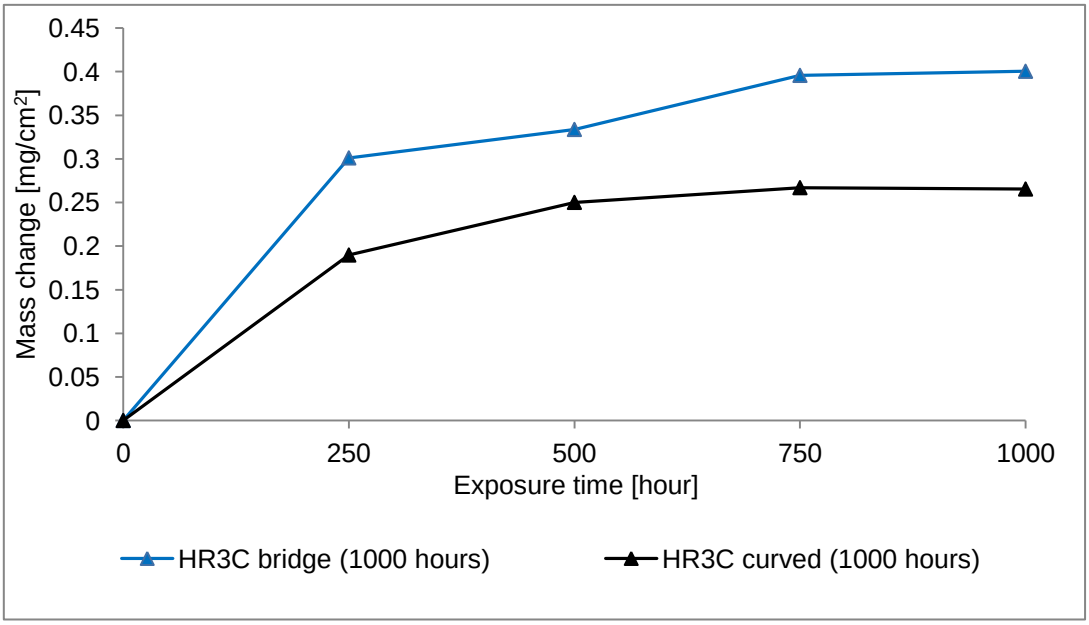

Figure 4-50 Net mass change of HR3C with time and specimen geometry at 700°C with 40 mm/s steam flow rate (H)

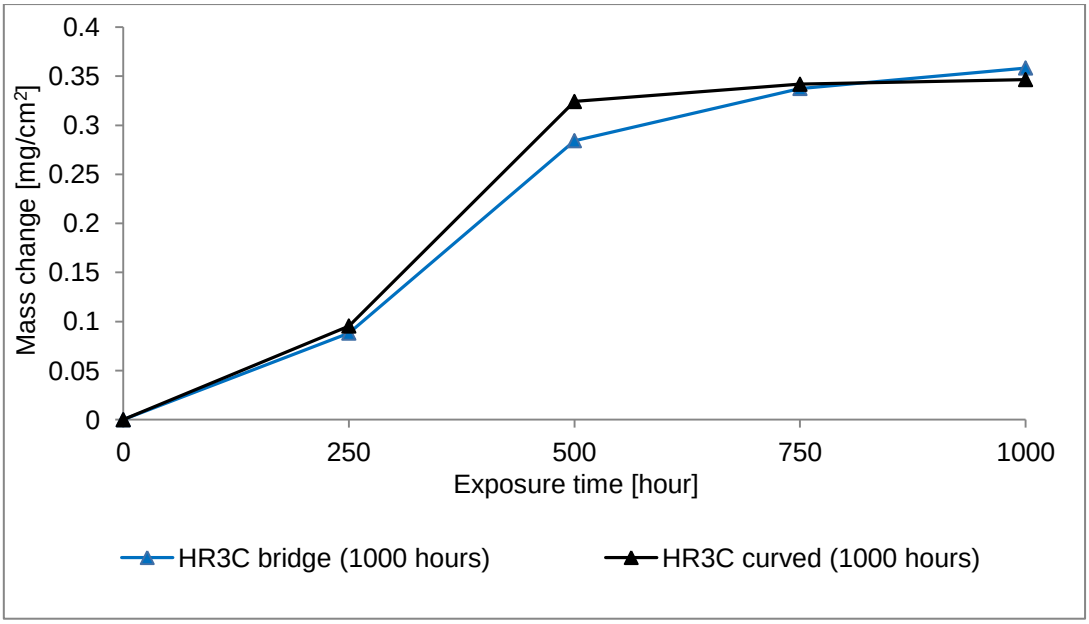

Figure 4-51 Net mass change of HR3C with time and specimen geometry at 600°C with 40 mm/s steam flow rate (H)

To summarise, the good oxidation behaviour of HR3C does not allow the identification of a shape, which always shows the fastest mass change, unlike for the ferritic steels. This could be initially explained as a result the scale spallation as in temperature range exposure times investigated the oxide formed on HR3C is in buckling regime.

4.1.2.4 800H

The oxidation behaviour of 800H, as presented in Figure 4-52, changes with the exposure conditions. However, there is not a single trend – the oxidation rate does not increase with temperature, as was identified for the rest of the austenitic alloys. The slowest oxidation kinetics were identified at 700°C (L). The mass change curves show that steam flow rate has a significant impact on the materials oxidation resistance, effect of which seems to be larger than the temperature effect at 600 and 700°C. The fastest mass growth of the alloy tested was identified at 750°C (L); there is a clear mass gain after first 250 hours exposure, which does not slow down for the whole test duration.

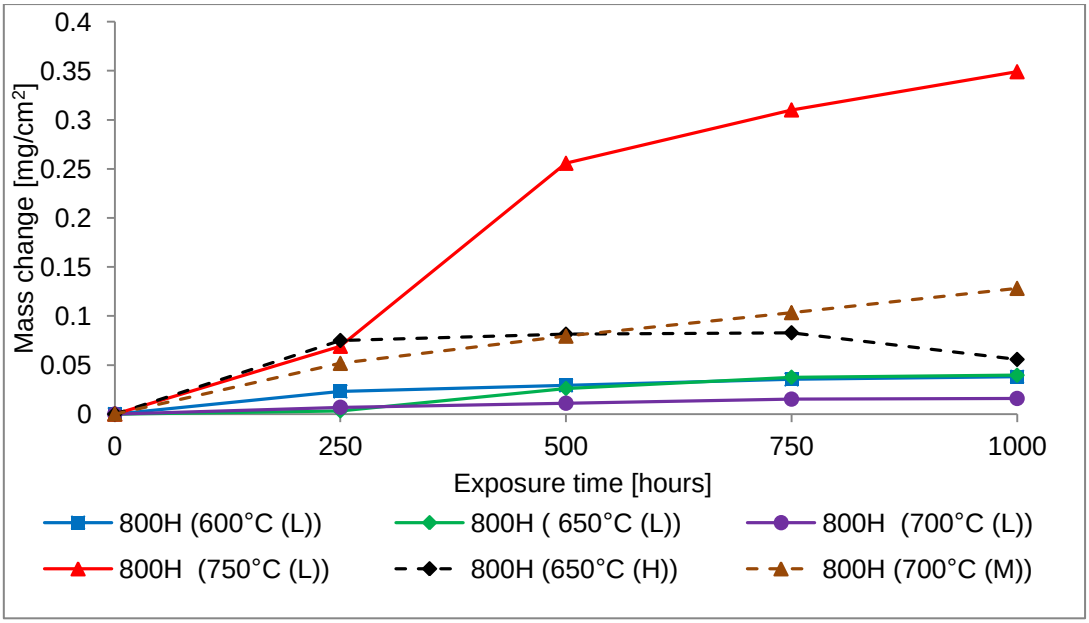

Figure 4-52 Net mass change of 800H with time and exposures conditions

4.1.2.5 Inconel 740

The oxidation behaviour of Inconel 740 shows similar trend to that identified for 800H; however, there are some differences with the main one being a smaller impact of the increased steam flow conditions (M, L) on the mass gain. Under the conditions tested, apart from 750°C (L) the mass change does not differ so clearly with temperature as it was identified before. However, some changes in behaviour are identified; at 750°C (L) there is the largest mass gain, which increases with time for the whole test duration.

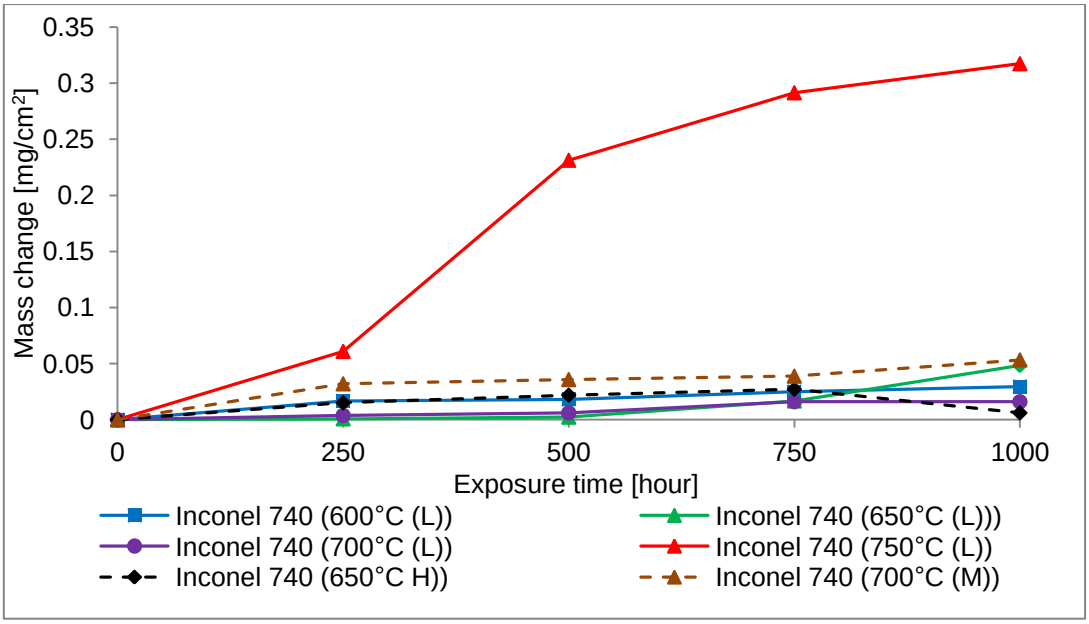

Figure 4-53 Net mass change of Inconel 740 with time and exposures conditions

4.1.2.6 Summary

The oxidation kinetics of the austenitic and nickel-based alloys changes with temperature and chromium content. There is a direct relationship between the change in the oxidation behaviour with temperature and chromium content – the alloys with higher chromium levels show fewer morphological changes and slower mass change at temperature investigated. The only exception is at 750°C (L) where the alloys, regardless of their chromium content, show the fastest mass gain and the most significant acceleration of the oxidation process. The specimen shape seems to have an impact on the oxidation of the austenitic steels; however it less significant than that identified for ferritics. Additionally, there is not a single shape characterised with the faster mass gain as it was identified for T23 and T92. Analysis of the data acquired for the austenitic and Inconel 740 has shown deviation from parabolic rate law dependence, therefore further analysis involving the identification of the activation energies for the steam oxidation process should be performed, for both linear and parabolic rate laws.

4.1.2.7 Impact of the surface preparation on austenitic steels

Figure 4-54 - Figure 4-57 illustrate the changes of the mass changes of the austenitic steels with different surface finishes exposed at 600 and 700°C to the highest steam flow rate (40 mm/s). Clearly, at both temperatures the as received specimens (pickled surface) showed the largest mass change, which is the most pronounced for T347HFG. At 600 and 700°C (H) the T347HFG as received samples, showed fast initial oxidation as the first, thick oxides form and then a second period in which oxidation slows down significantly.

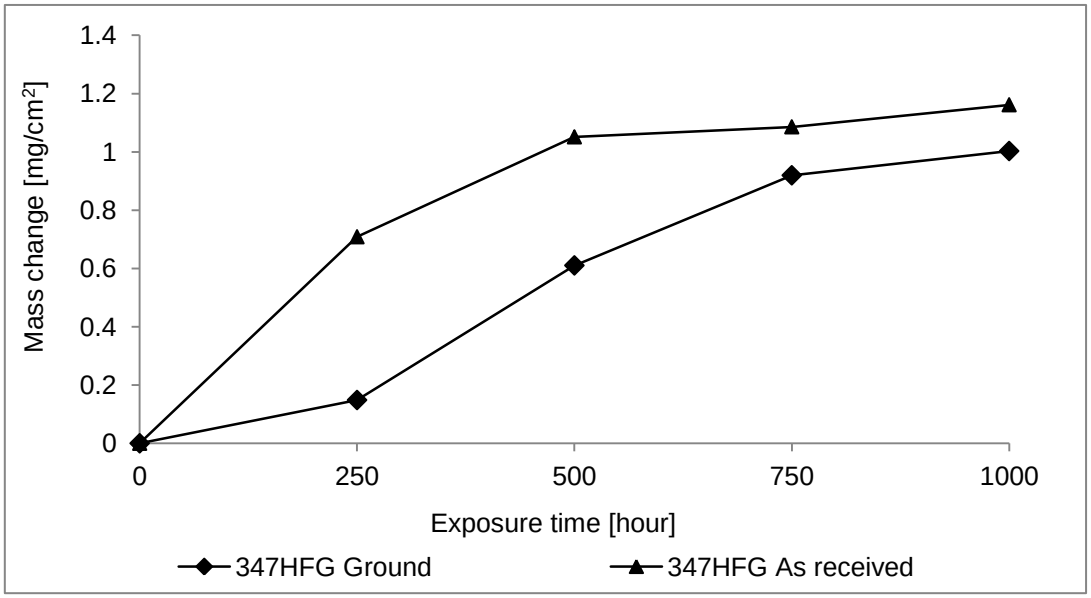

Figure 4-54 Net mass change of the mass gain of T347HFG at 700°C (H) with specimen surface finish

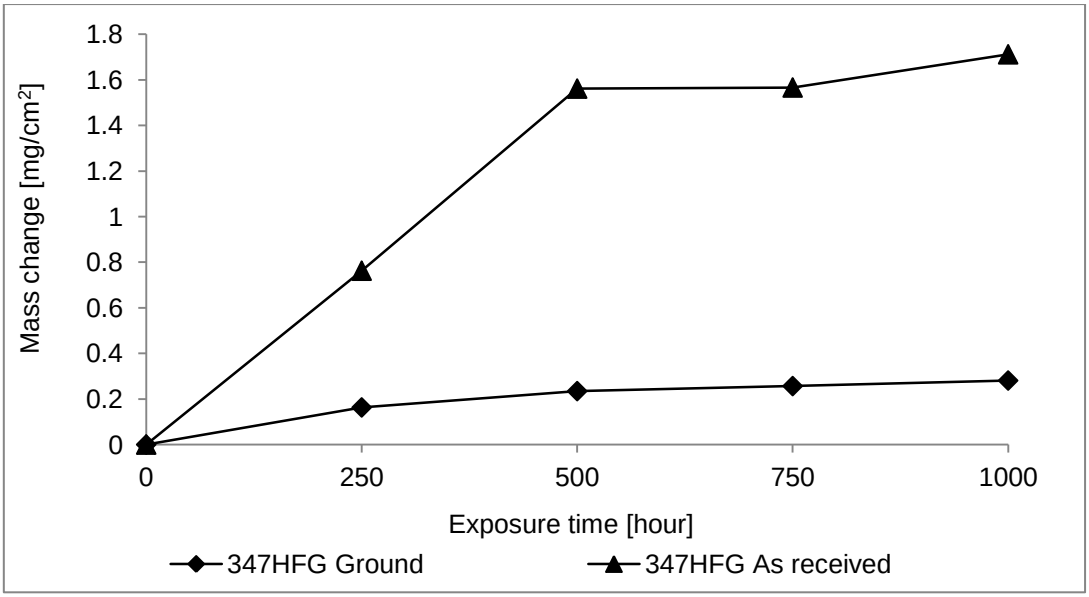

Figure 4-55 Net mass change of T347HFG at 700°C (H) with specimen surface finish

The ground specimens show slower mass change, the difference between mass gain between ground and as received specimens changes with exposure conditions. It is more pronounced at higher temperatures.

Steam oxidation of Super 304H at 600°C (H) does not vary significantly in the initial period as it was identified for T347HFG, however it changes with time up to 1000 hour exposure when the difference between the mass change of the specimen with different surface finished are the most pronounced. At higher temperature as-received specimen (pickled), oxidises faster than rest of the specimens exposed, the difference in the mass change increases with time up to 500 hours, which is believed to be an initial period when first oxides are forming and second period with less significant mass change.

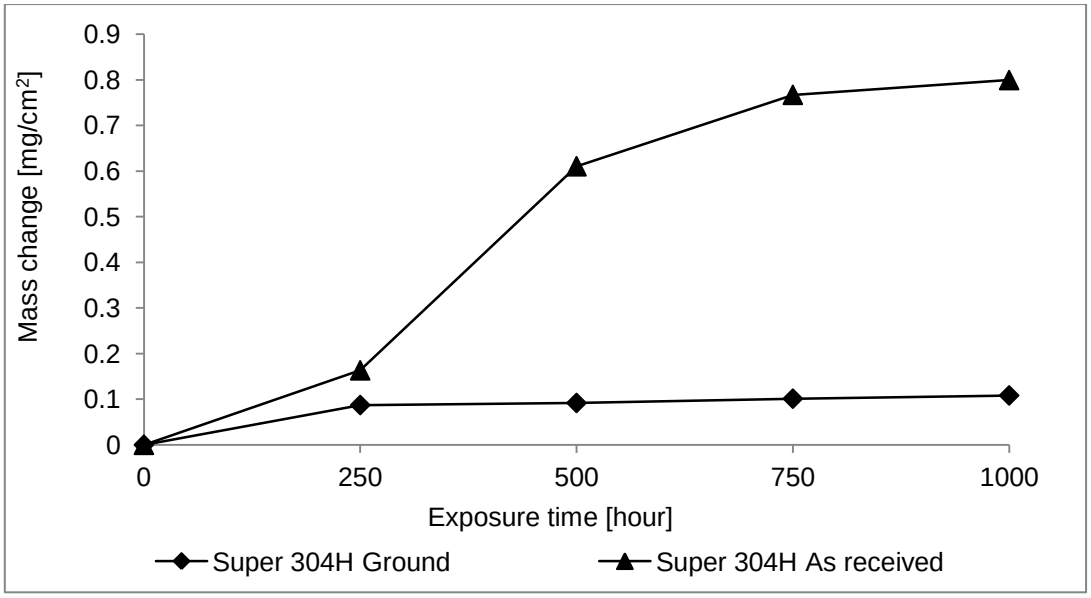

Figure 4-56 Change of the mass gain of Super 304H at 600°C (H) with specimen surface finish

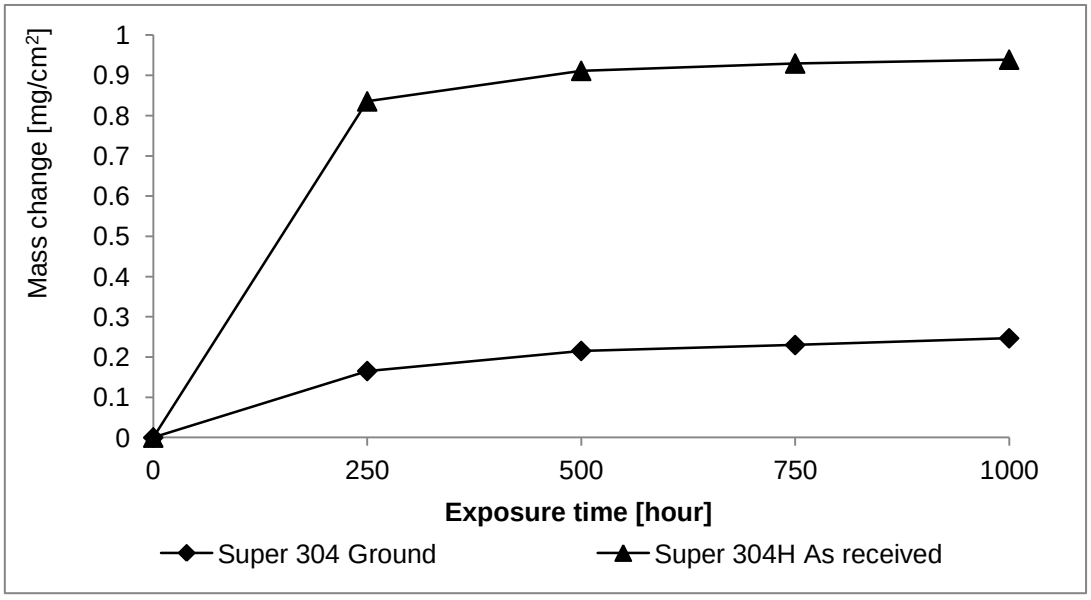

Figure 4-57 Change of the mass gain of Super 304H at 700°C (H) with specimen surface finish

To summarise, there is a clear impact of the specimen surface finish on steam oxidation of the austenitic steels. For the three surface finishes investigated, the ground specimens show the slowest mass gain whereas the as-received specimens showed the largest mass gain at both temperatures. Because for the polished specimens just one surface is actually polished the mass change of this specimens

could be misleading. Therefore, the impact of the polishing on the steam oxidation of austenitic steels has not been described here. The full analysis of the impact of the different surface finish on steam oxidation could be found in the morphology chapter.

4.2 Morphology of oxides

Steam oxidation of high temperature resistant alloys drives the formation of diverse oxides, which change with the exposure conditions (temperature, steam flow rate), time, orientation against the steam flow and the alloy type. In addition, the specimen geometry has an impact on the scale thicknesses (for ferritic steels) and formation of protective continuous oxides (for austenitic steels). This chapter describes the morphological changes on two levels: first investigation of the oxide surfaces and second analyses of cross-sections.

4.2.1 Analysis of the oxide surfaces

4.2.1.1 Ferritic steels

In general, the T23 and T92 form thick oxide scales even at the lowest temperatures in this study however, type of the scale, its thicknesses varies with conditions, time and chromium levels. The oxides nucleated on these two materials during their exposures are not protective and consist of distinctive layers; detail analyses of them is presented in the subsections below.

4.2.1.1.1 T23 (2.25Cr)

Due to its low chromium level T23, forms less protective scales, which significantly reduce its steam oxidation resistance and therefore limits its application at high temperature. T23 shows the gradual growth of oxides on the surface with time, as presented in Figure 4-58 - Figure 4-66 . For the surface analysis, the bridge shape specimens were selected it was found that there were no significant changes in the oxide surfaces with the specimen shape. Micrographs obtained with the SEM in secondary electron detector mode showed that the surfaces were covered with clear grains of the iron oxides which sizes increase with time, temperature and the steam flow rate. XRD analyses (Figure 4-67 - Figure 4-74) showed that in temperature range 600°C – 700°C (L), as well as under faster steam flow conditions, the oxide on the surface is mostly haematite, whereas at 750°C (L) the main constituent is magnetite. The sizes of the oxide grains growing were also found to be influenced by sample orientation against the steam flow; grains on the surface facing the direct steam flow are larger and more compact however, some cracks had formed. Analysis of the micrographs of the scales developed indicate that at 750°C

(L) there were clear changes of the oxide surface. The XRD analyses acquired showed that the surfaces were covered mostly with magnetite. Grains of haematite are significantly smaller and more condense than magnetite.

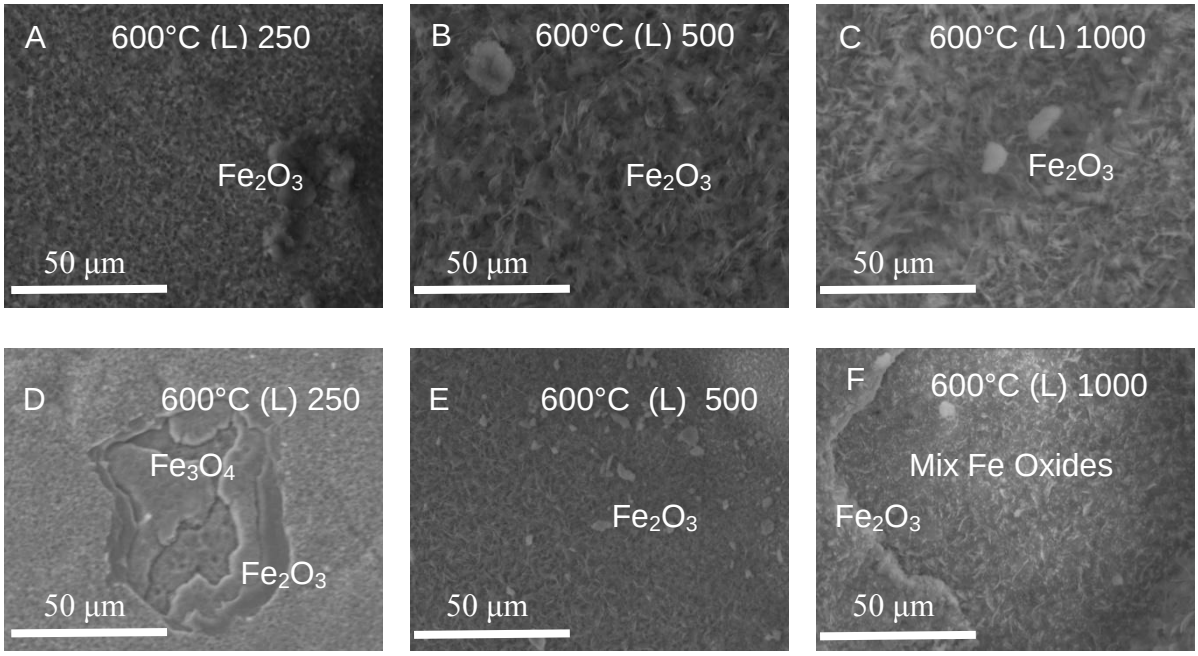

Figure 4-58 Micrographs showing morphologies of T23 surfaces facing direct (A-C) and indirect (D-F) steam flow at 600°C (L) after 250, 500 and 1000 hour exposure

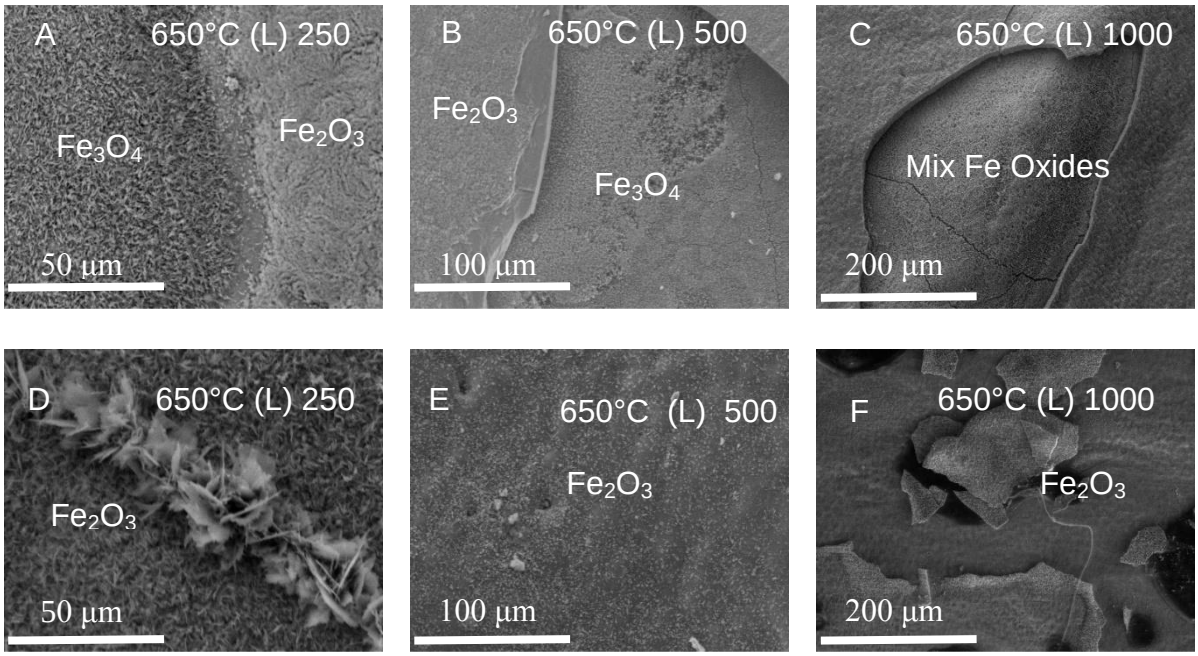

Figure 4-59 Micrographs showing morphologies of T23 surfaces facing direct (A-C) and indirect (D-F) steam flow at 650°C (L) after 250, 500 and 1000 hour exposure

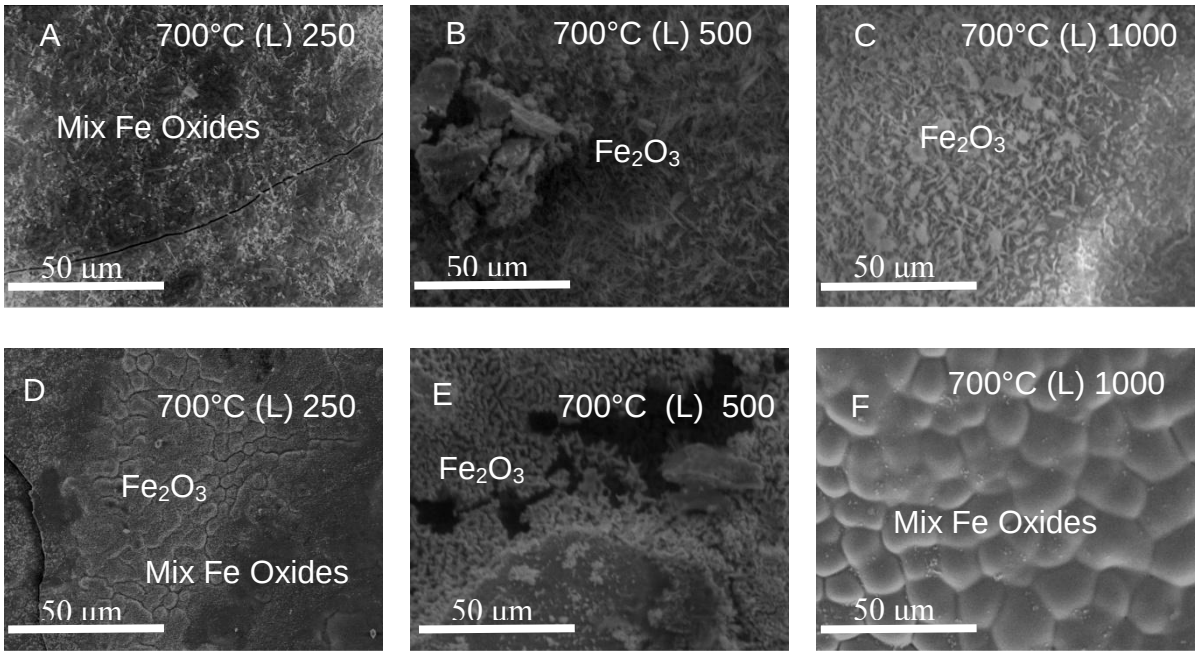

Figure 4-60 Micrographs showing morphologies of T23 surfaces facing direct (A-C) and indirect (D-F) steam flow at 700°C (L) after 250, 500 and 1000 hour exposure

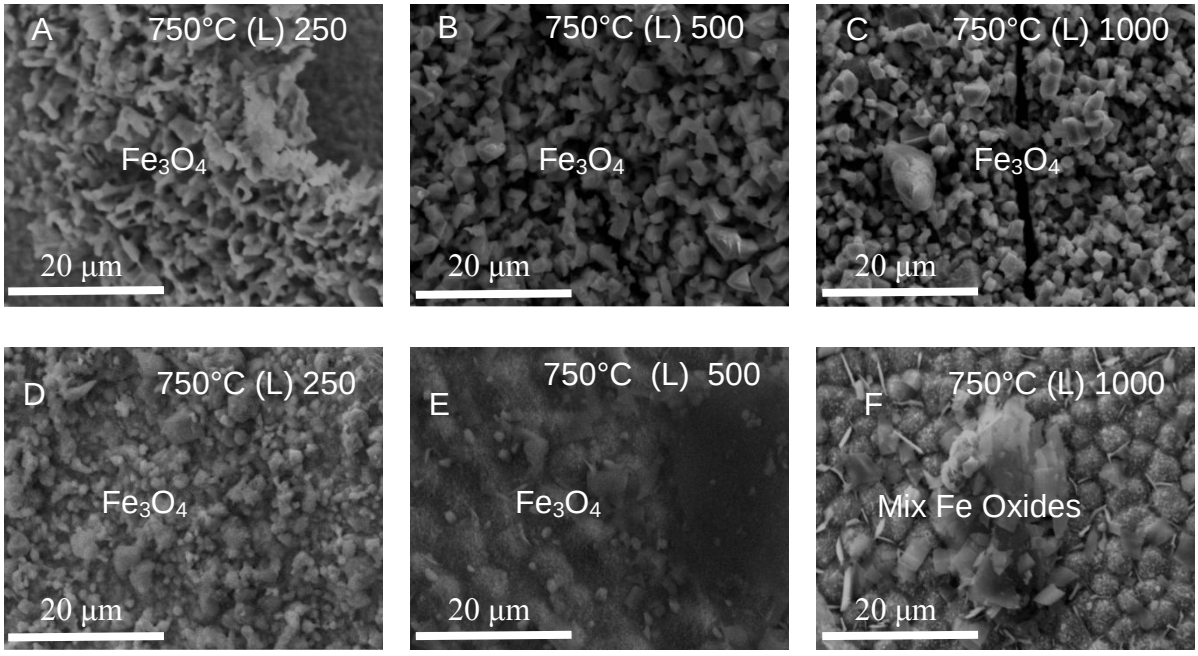

Figure 4-61 Micrographs showing morphologies of T23 surfaces facing direct (A-C) and indirect (D-F) steam flow at 750°C with (L) after 250, 500 and 1000 hour exposure

Analysis of the micrographs (Figure 4-62 - Figure 4-66) presenting the surface of T23 with different steam flow rate show that there is an impact of the steam flow rate on the development of the oxides.

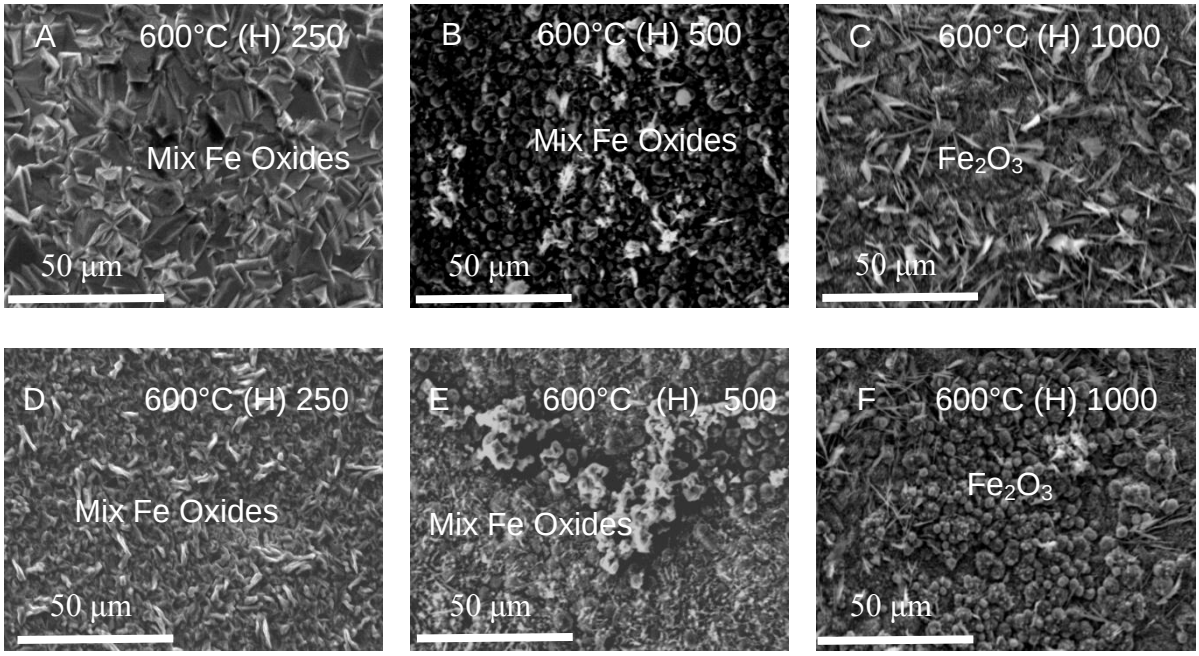

Figure 4-62 Micrographs showing morphologies of T23 surfaces facing direct (A-C) and indirect (D-F) steam flow at 600°C (H) after 250, 500 and 1000 hour exposure

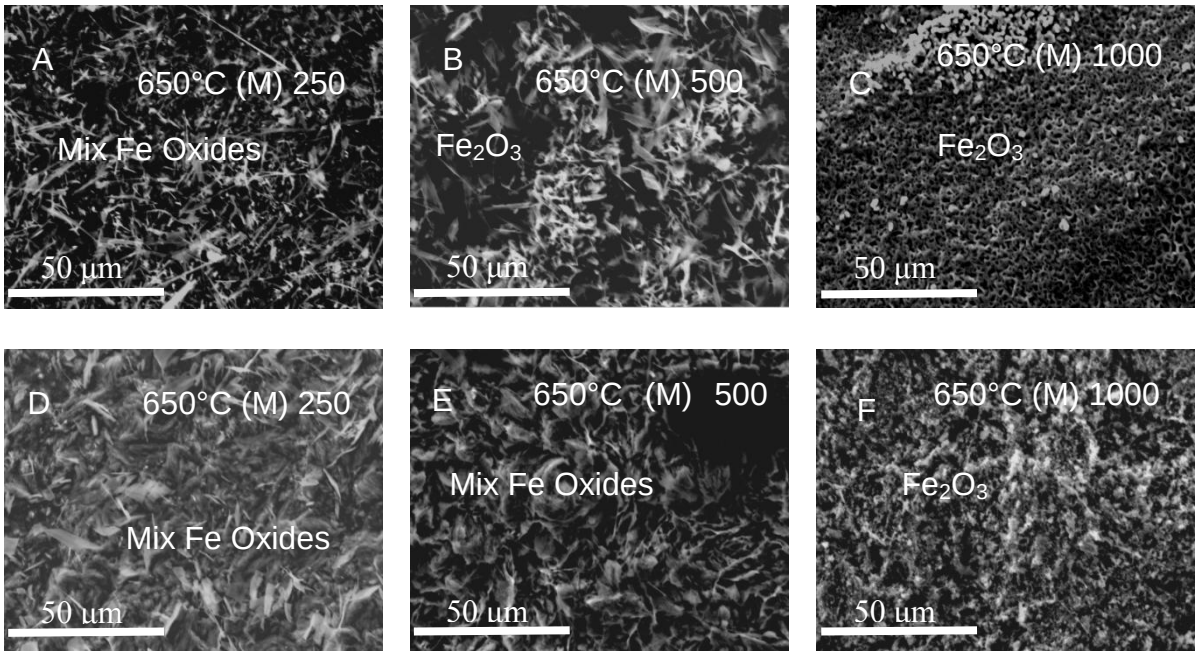

Figure 4-63 Micrographs showing morphologies of T23 surfaces facing direct (A-C) and indirect (D-F) steam flow at 650°C (M) after 250, 500 and 1000 hour exposure

The oxides grains on the specimens exposed to higher steam flow rates are larger as well as more packed. A comparison of the oxides formed on the different sides of the specimens indicate that direct steam flow results in more grains with larger sizes. Similar trends have been identified for exposures at slower steam flow rates; however, the specimen's orientation is less significant.

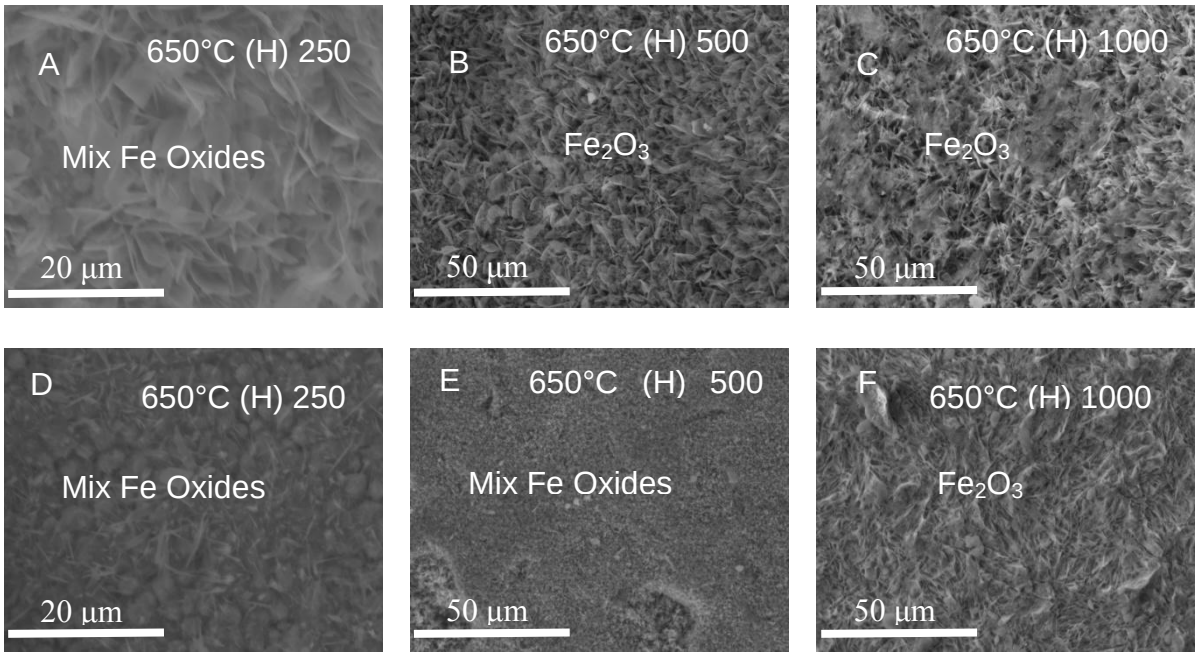

Figure 4-64 Micrographs showing morphologies of T23 surfaces facing direct (A-C) and indirect (D-F) steam flow at 650°C (H) after 250, 500 and 1000 hour exposure

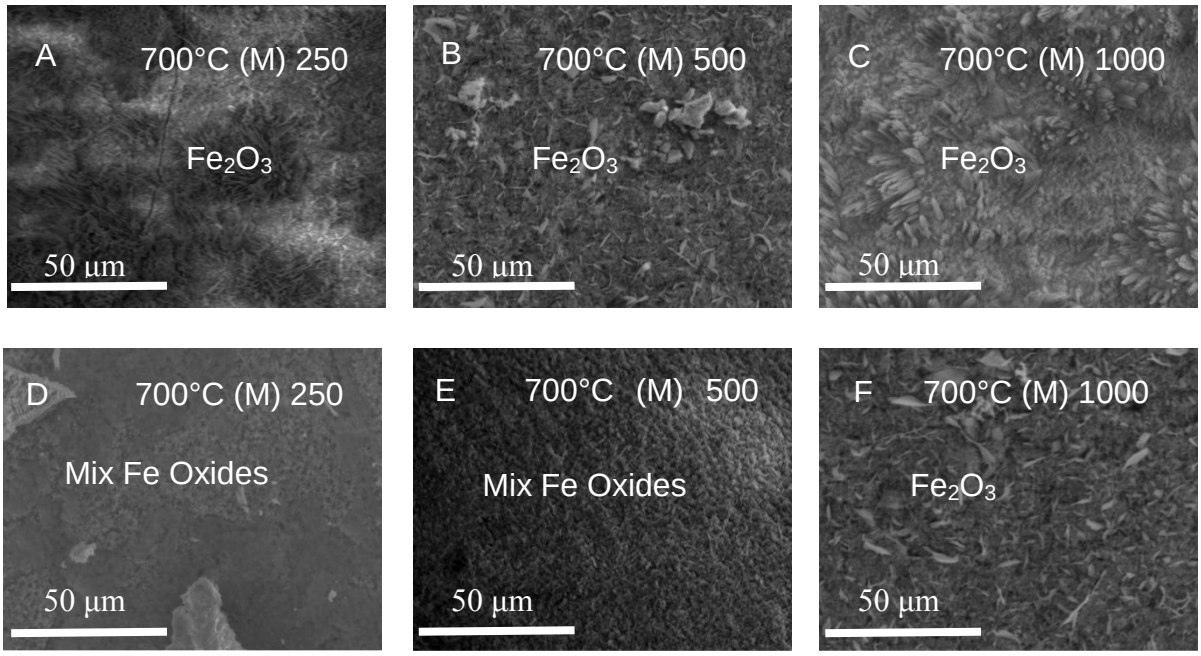

Figure 4-65 Micrographs showing morphologies of T23 surfaces facing direct (A-C) and indirect (D-F) steam flow at 700°C (M) after 250, 500 and 1000 hour exposure

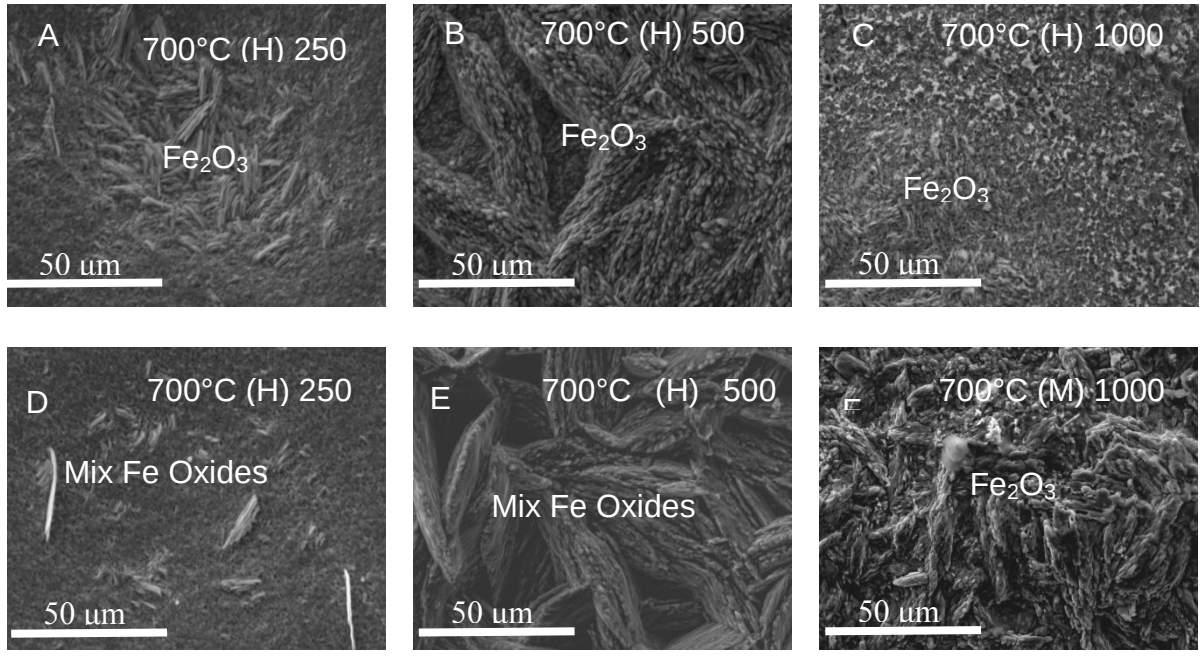

Figure 4-66 Micrographs showing morphologies of T23 surfaces facing direct (A-C) and indirect (D-F) steam flow at 700°C (H) after 250, 500 and 1000 hour exposure

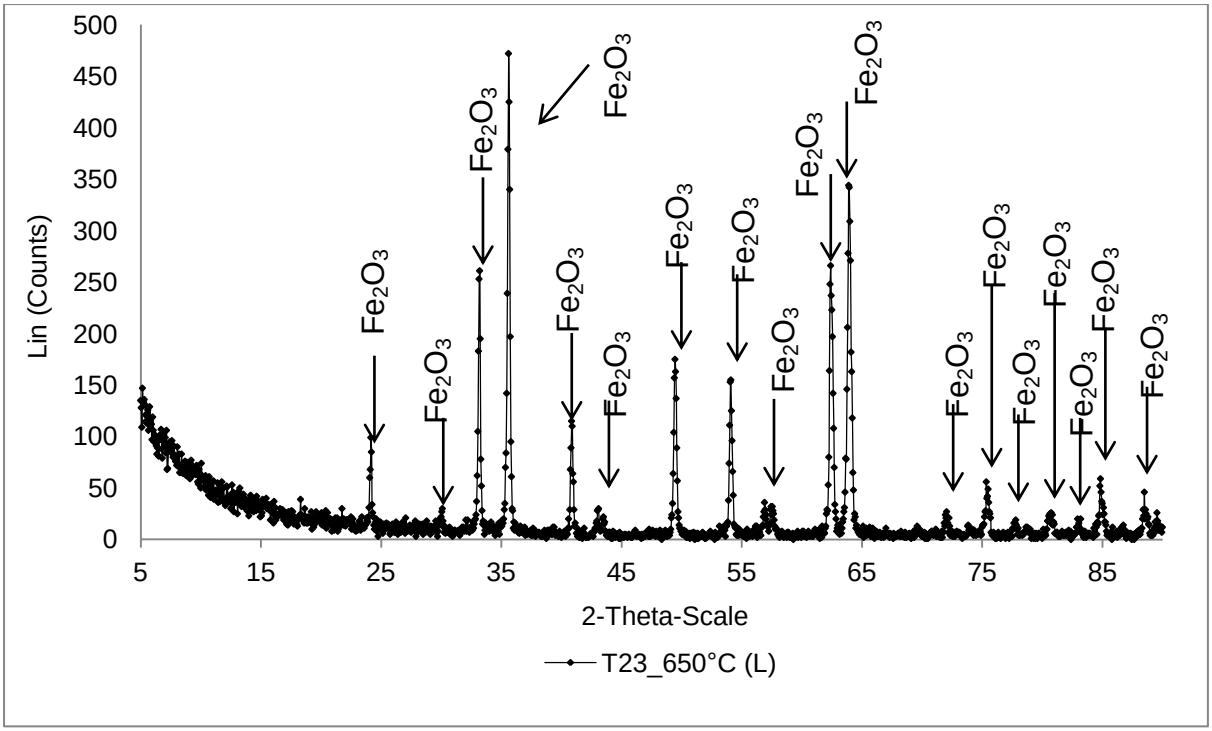

Figure 4-67 XRD of the oxide scale formed on T23 at 650°C with low steam flow rate

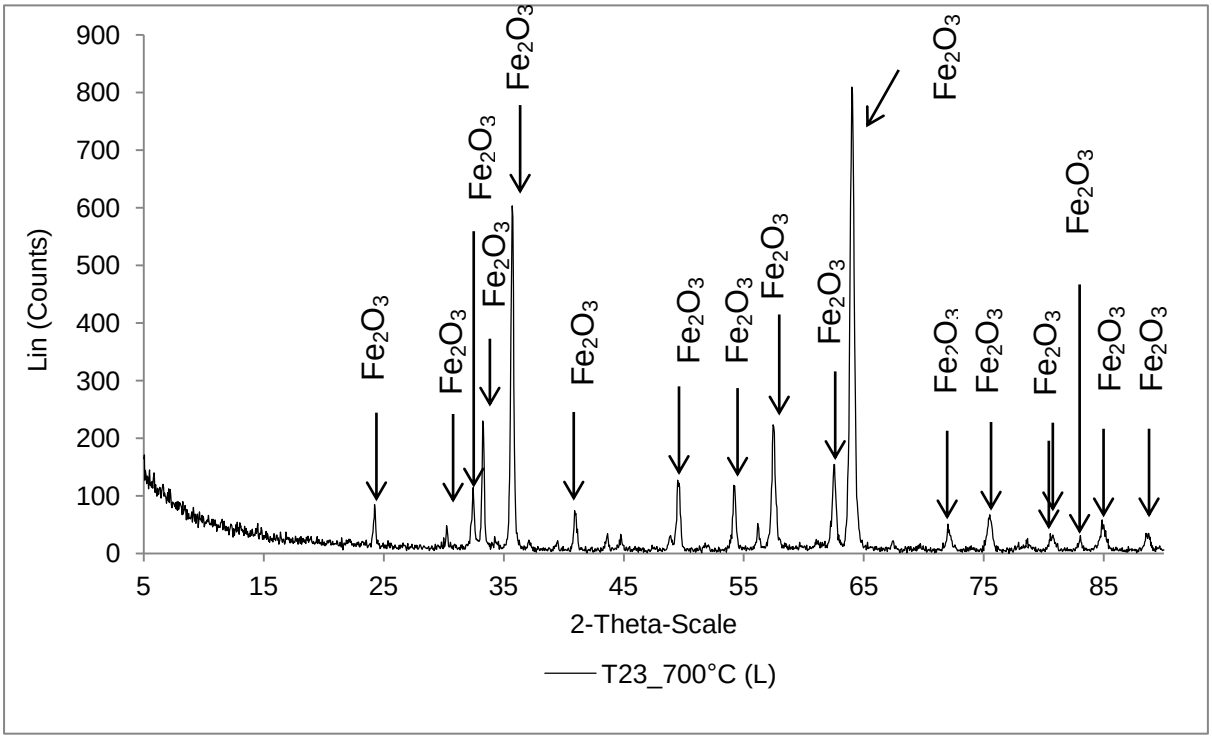

Figure 4-68 XRD of the oxide scale formed on T23 at 700°C with low steam flow rate

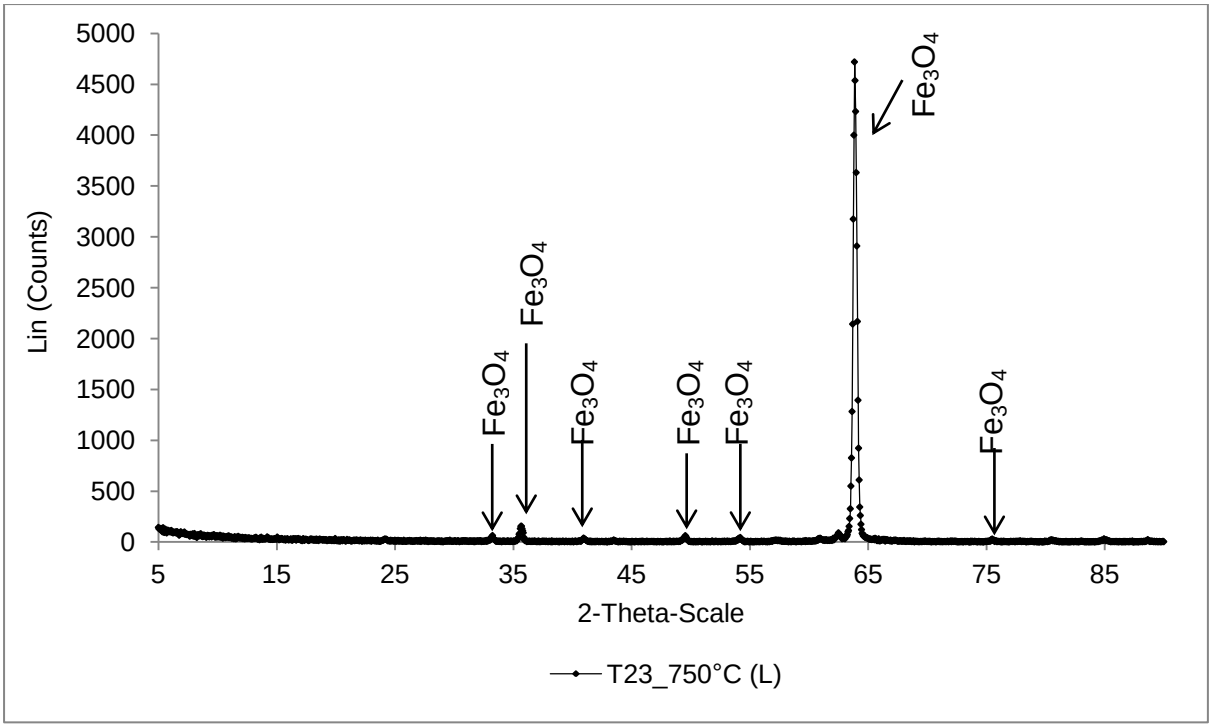

Figure 4-69 XRD of the oxide scale formed on T23 at 750°C with low steam flow rate

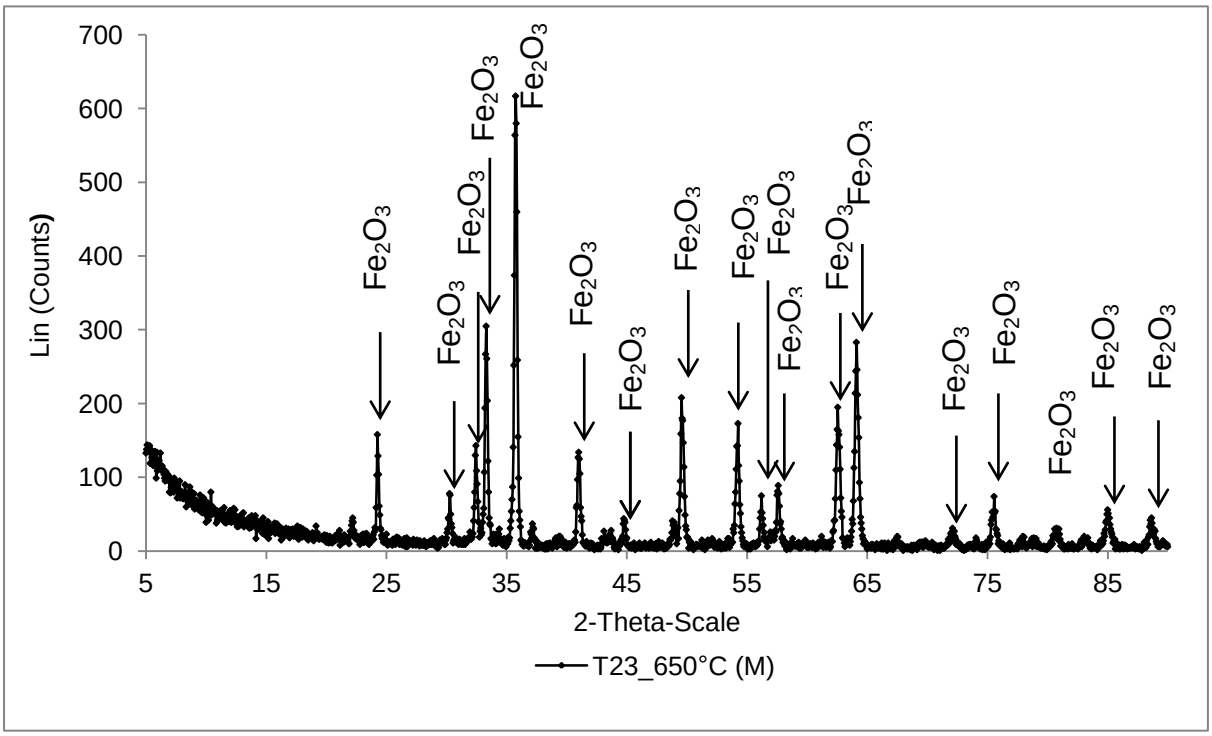

Figure 4-70 XRD of the oxide scale formed on T23 at 650°C with medium steam flow rate

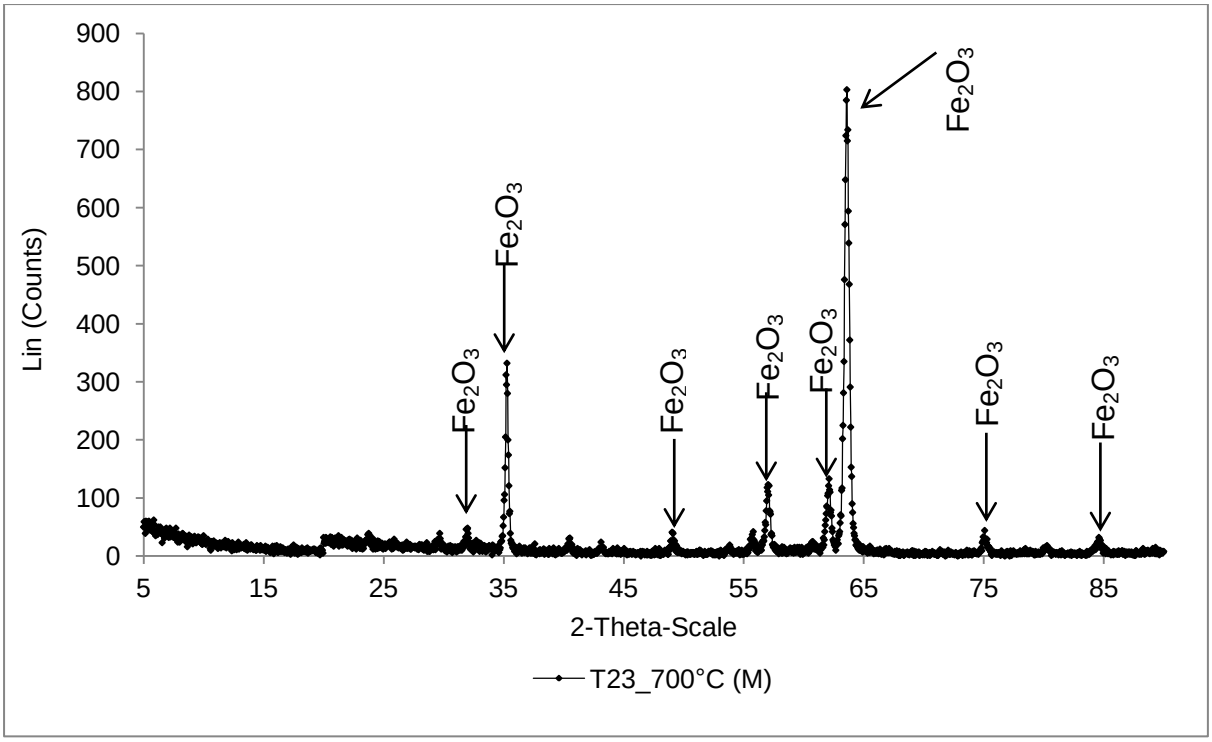

Figure 4-71 XRD of the oxide scale formed on T23 at 700°C with medium steam flow rate

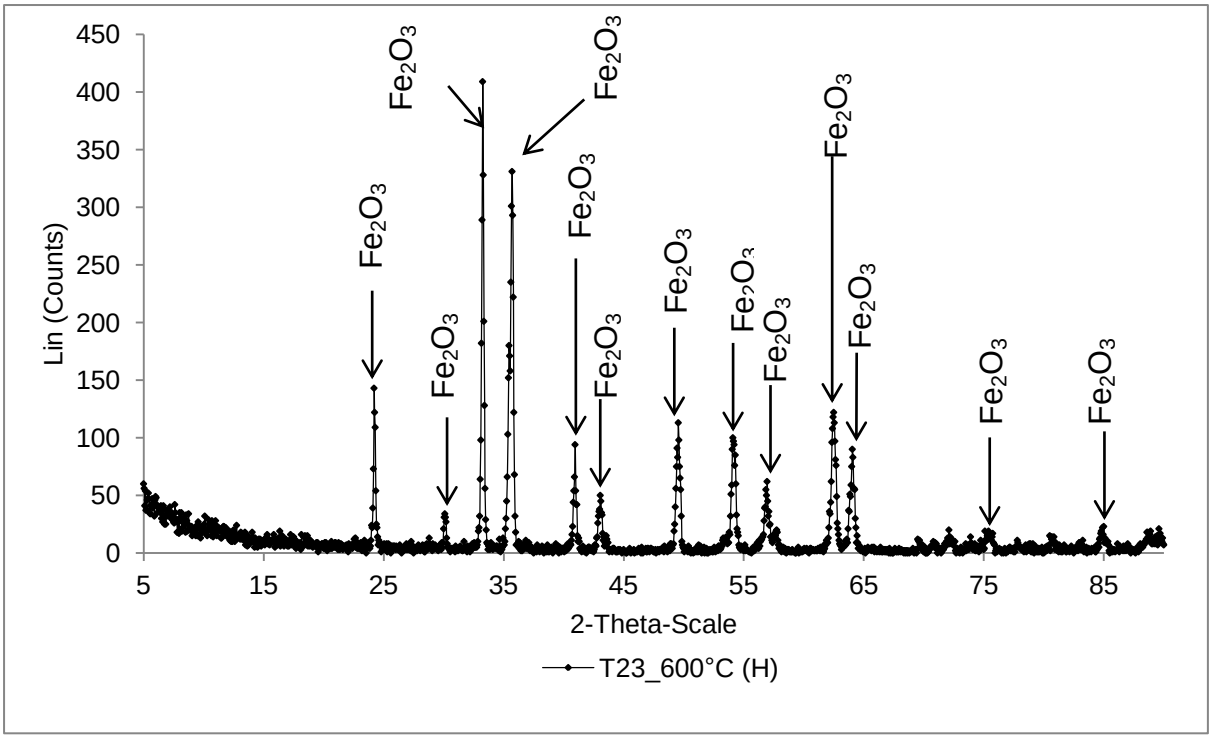

Figure 4-72 XRD of the oxide scale formed on T23 at 600°C with high steam flow rate

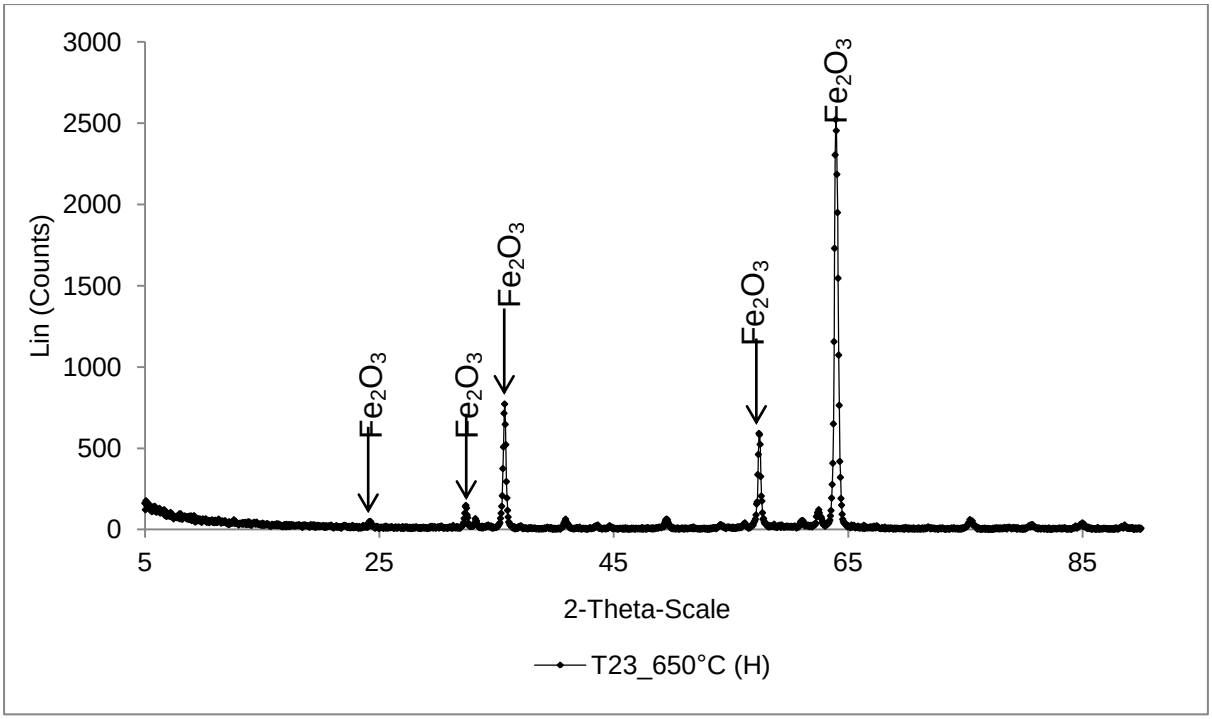

Figure 4-73 XRD of the oxide scale formed on T23 at 650°C with high steam flow rate

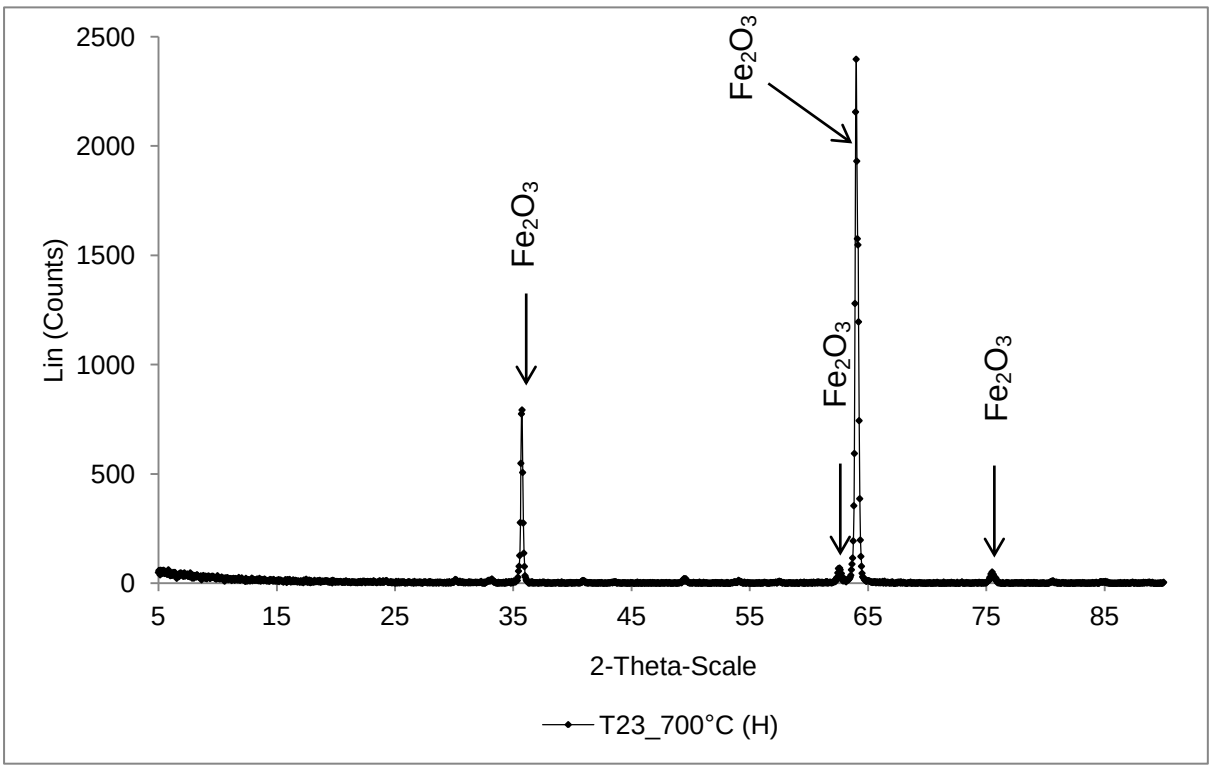

Figure 4-74 XRD of the oxide scale formed on T23 at 700°C with high steam flow rate

4.2.1.1.2 T92 (9Cr)

Steam oxidation of T92 drives the formation of the various oxides on the surface (Figure 4-75 - Figure 4-83), the types of which change with exposure conditions. XRD and EDX analyses showed that main oxide on the surfaces at low steam flow rates was magnetite but there are also some islands of haematite, which have been identified visually and during EDX analyses. Under faster steam flow rates the surfaces are covered with haematite, the amount of which changes with the steam flow rate (M, H). Comparison of micrographs of the oxides on the surfaces of T92 and T23 indicated that there are significant differences, firstly the oxides phases, secondly the oxides on the surfaces of T92 are more cracked and exhibit spallation even after short exposures.

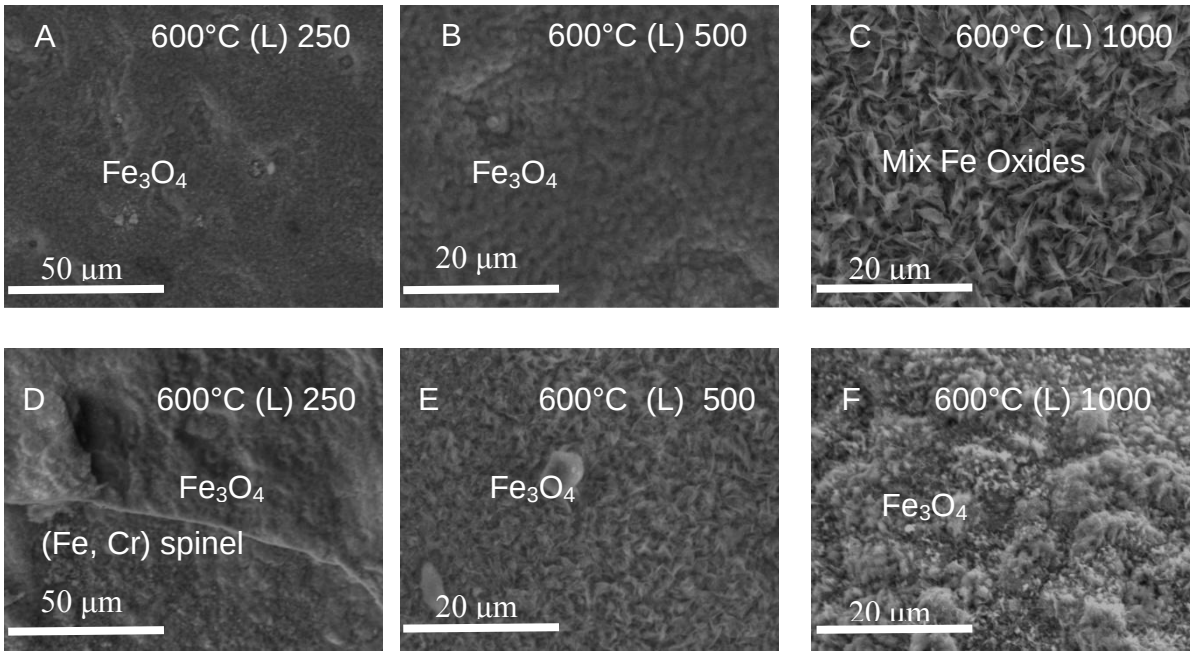

Figure 4-75 Micrographs showing morphologies of T92 surfaces facing direct (A-C) and indirect (D-F) steam flow at 600°C (L) after 250, 500 and 1000 hour exposure

As for T23 the grains of the oxides on T92 grow with exposure temperature, steam flow rate and time; at low temperature up to 700°C (L) the surfaces do not show clear grains in the first 500 hours. The steam flow rate has a clear impact on the grain sizes. Under higher steam flow rate conditions (M, H) there is clear grow of the large, distinctive grains of the oxides. XRD and EDX analysis showed that under such conditions the oxides on the surface are a mix of magnetite and haematite.

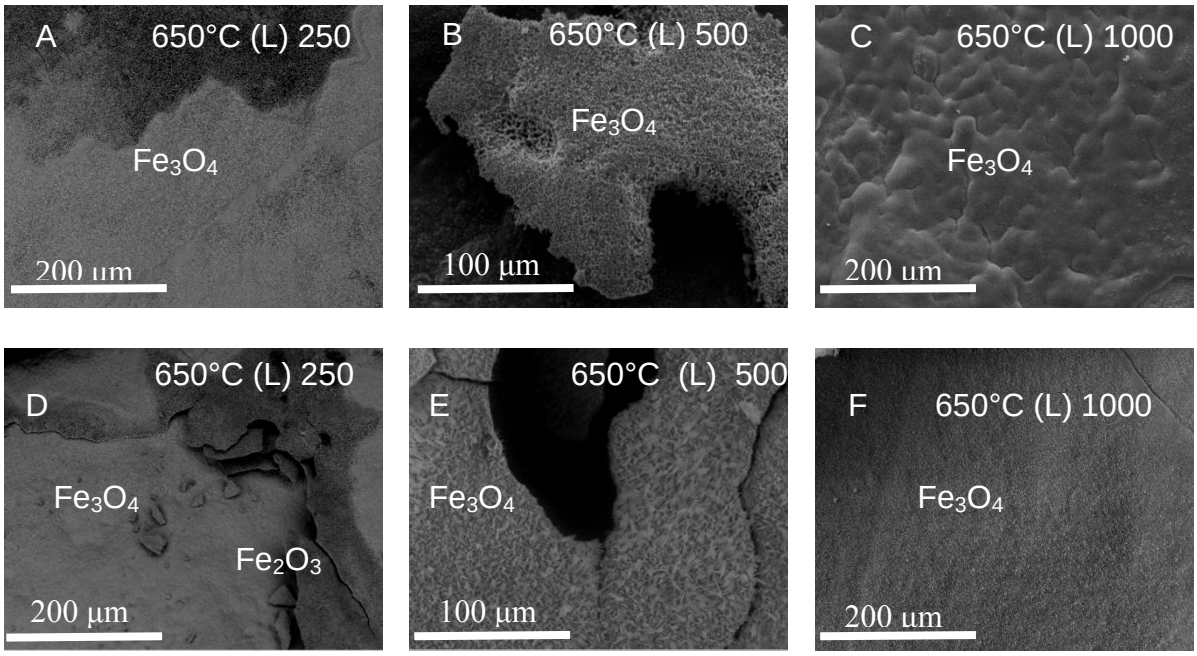

Figure 4-76 Micrographs showing morphologies of T92 surfaces facing direct (A-C) and indirect (D-F) steam flow at 650°C (L) after 250, 500 and 1000 hour exposure

The orientation against the direct steam flow has an impact on the size of the oxides growing, the sizes vary with the steam flow rate. There is no a significant impact of direct steam on the spallation of the scales formed.

Interesting finding is the fact that under the conditions tested there is a significant change of the oxides properties at 750°C (L), 700°C (M) and 600 – 700°C with high steam rate flow. The scales formed under these conditions seem to maintain adherence, exfoliate less, and form haematite.

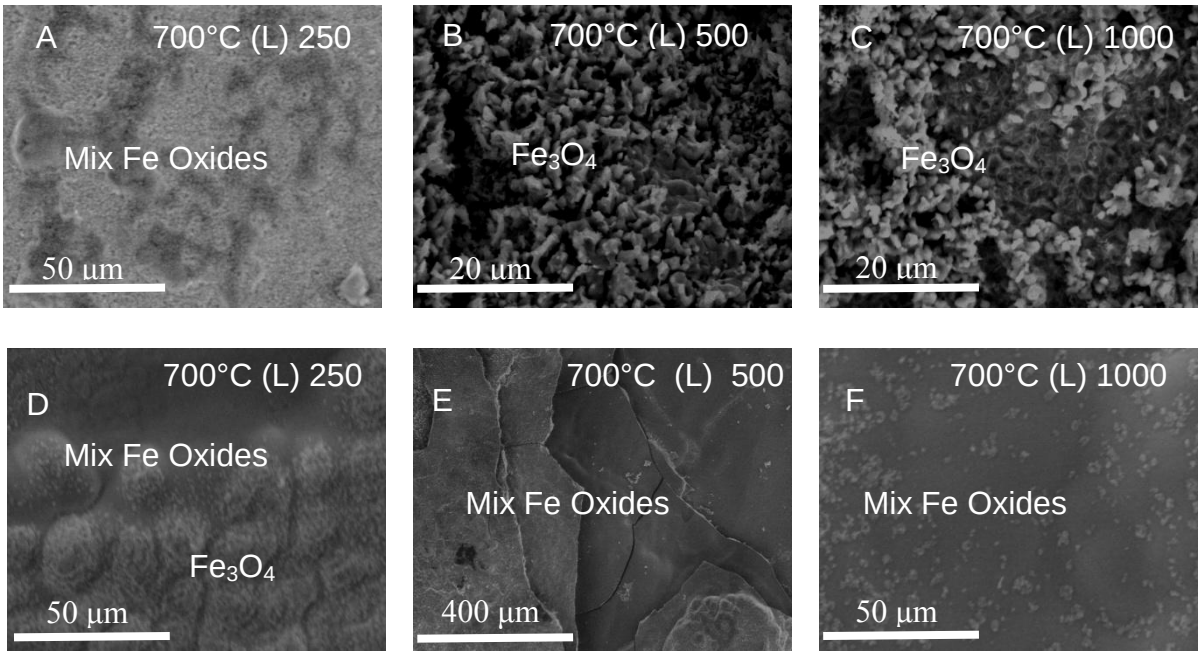

Figure 4-77 Micrographs showing morphologies of T92 surfaces facing direct (A-C) and indirect (D-F) steam flow at 700°C (L) after 250, 500 and 1000 hour exposure

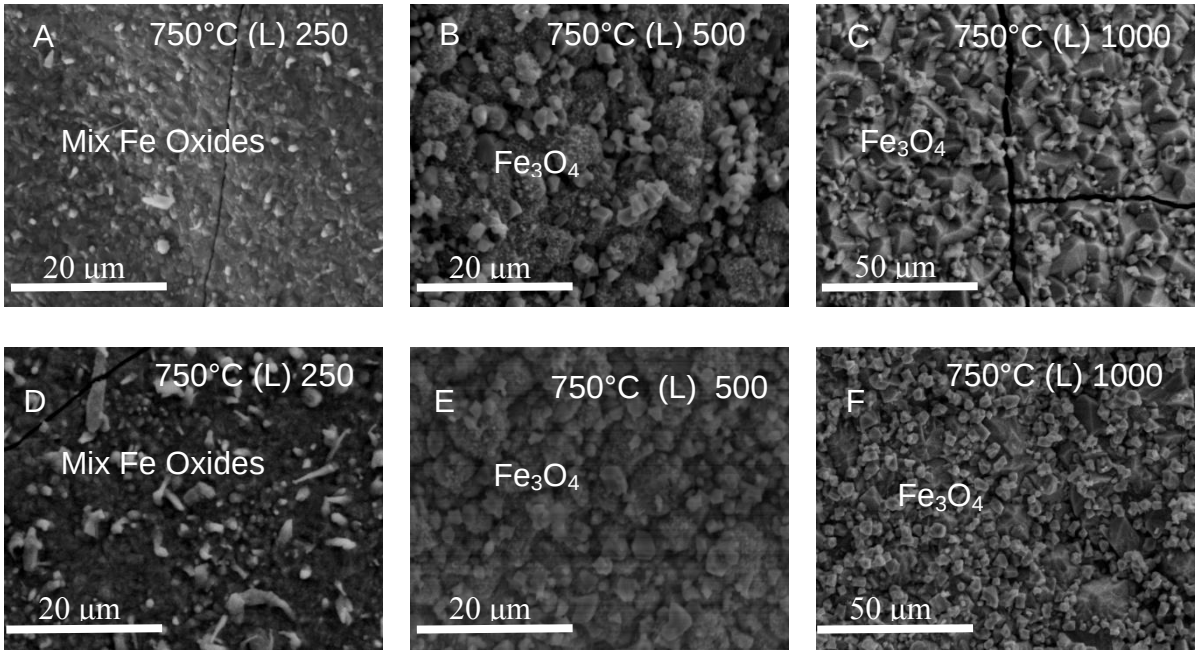

Figure 4-78 Micrographs showing morphologies of T92 surfaces facing direct (A-C) and indirect (D-F) steam flow at 750°C (L) after 250, 500 and 1000 hour exposure

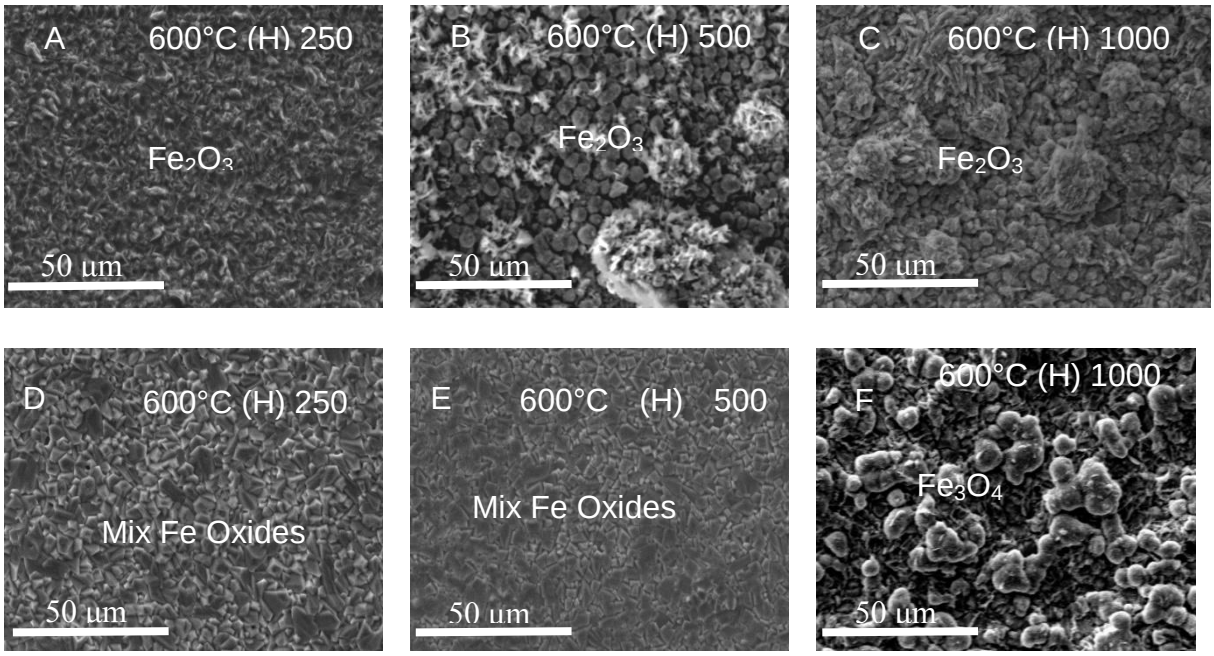

Figure 4-79 Micrographs showing morphologies of T92 surfaces facing direct (A-C) and indirect (D-F) steam flow at 600°C (H) after 250, 500 and 1000 hour exposure

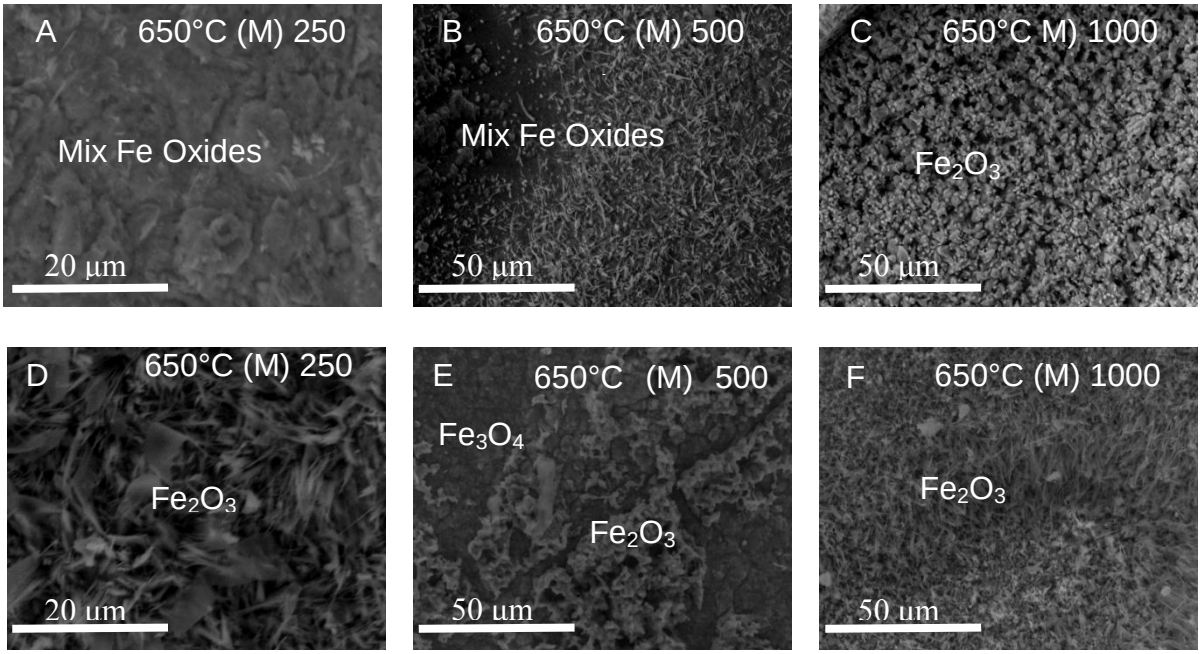

Figure 4-80 Micrographs showing morphologies of T92 surfaces facing direct (A-C) and indirect (D-F) steam flow at 650°C (M) after 250, 500 and 1000 hour exposure

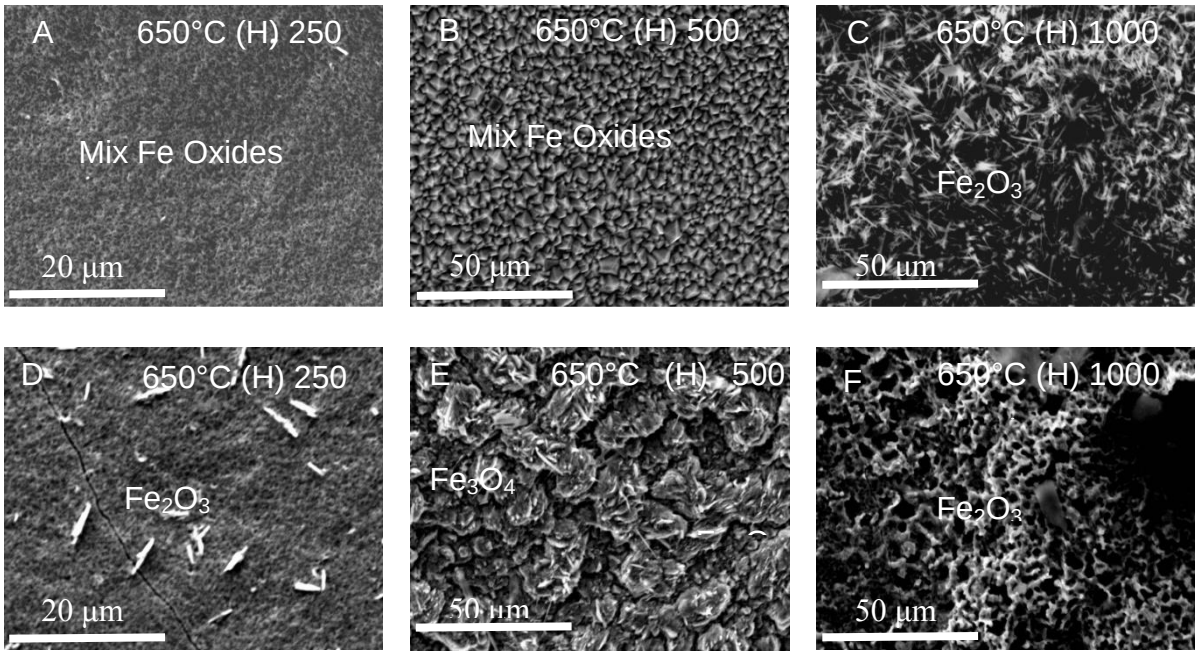

Figure 4-81 Micrographs showing morphologies of T92 surfaces facing direct (A-C) and indirect (D-F) steam flow at 650°C (H) after 250, 500 and 1000 hour exposure

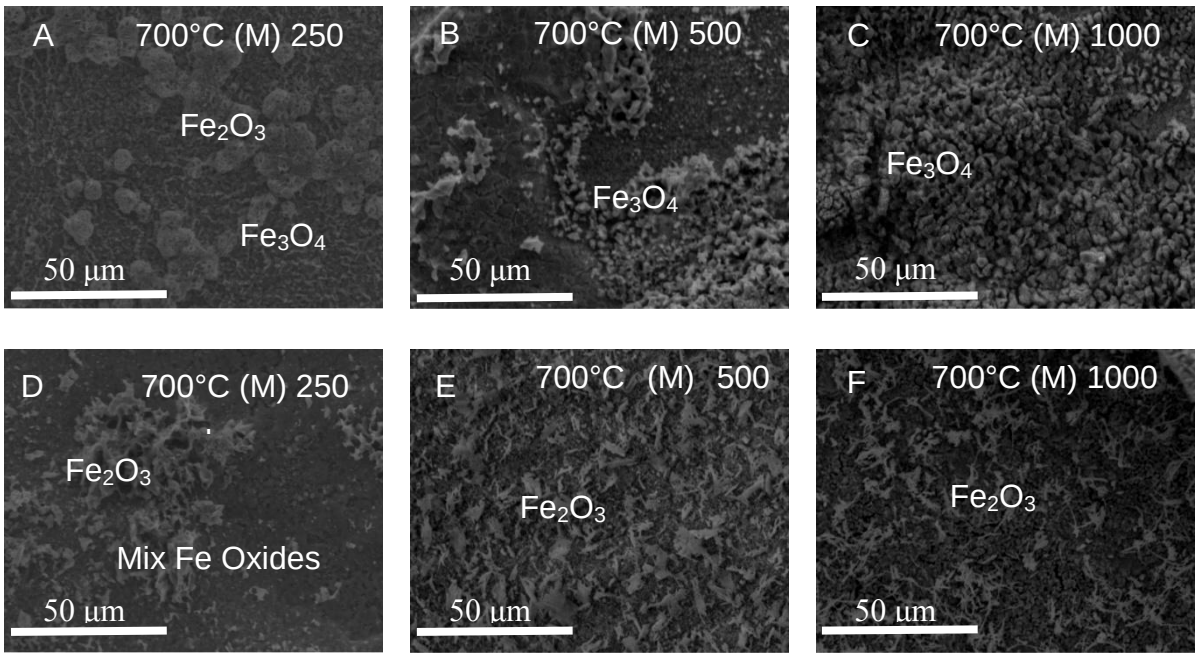

Figure 4-82 Micrographs showing morphologies of T92 surfaces facing direct (A-C) and indirect (D-F) steam flow at 700°C (M) after 250, 500 and 1000 hour exposure

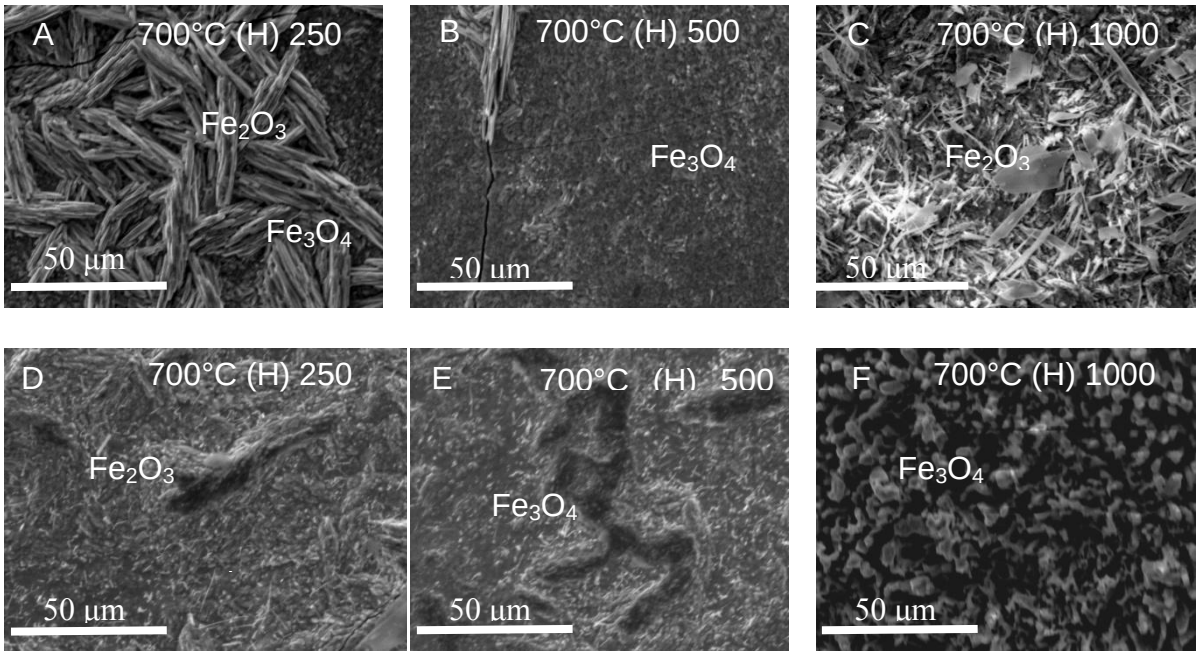

Figure 4-83 Micrographs showing morphologies of T92 surfaces facing direct (A-C) and indirect (D-F) steam flow at 700°C (H) after 250, 500 and 1000 hour exposure

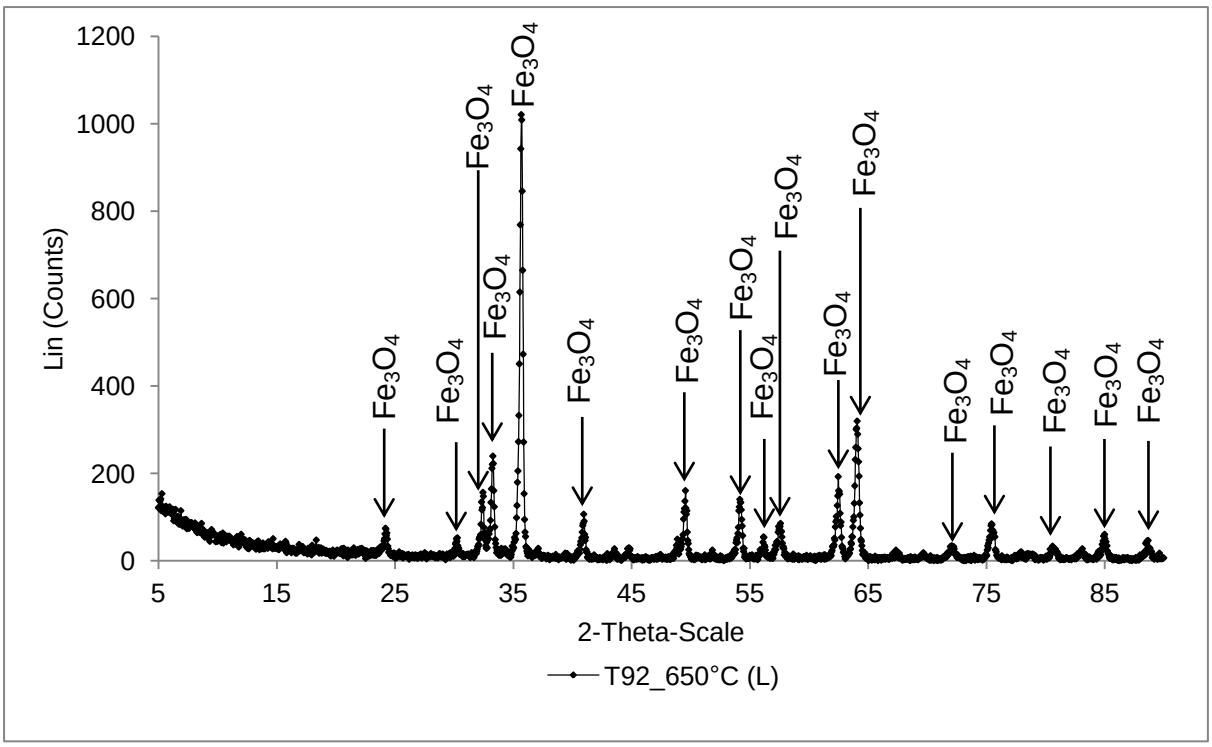

Figure 4-84 XRD of the oxide scale formed on T92 at 650°C with low steam flow rate

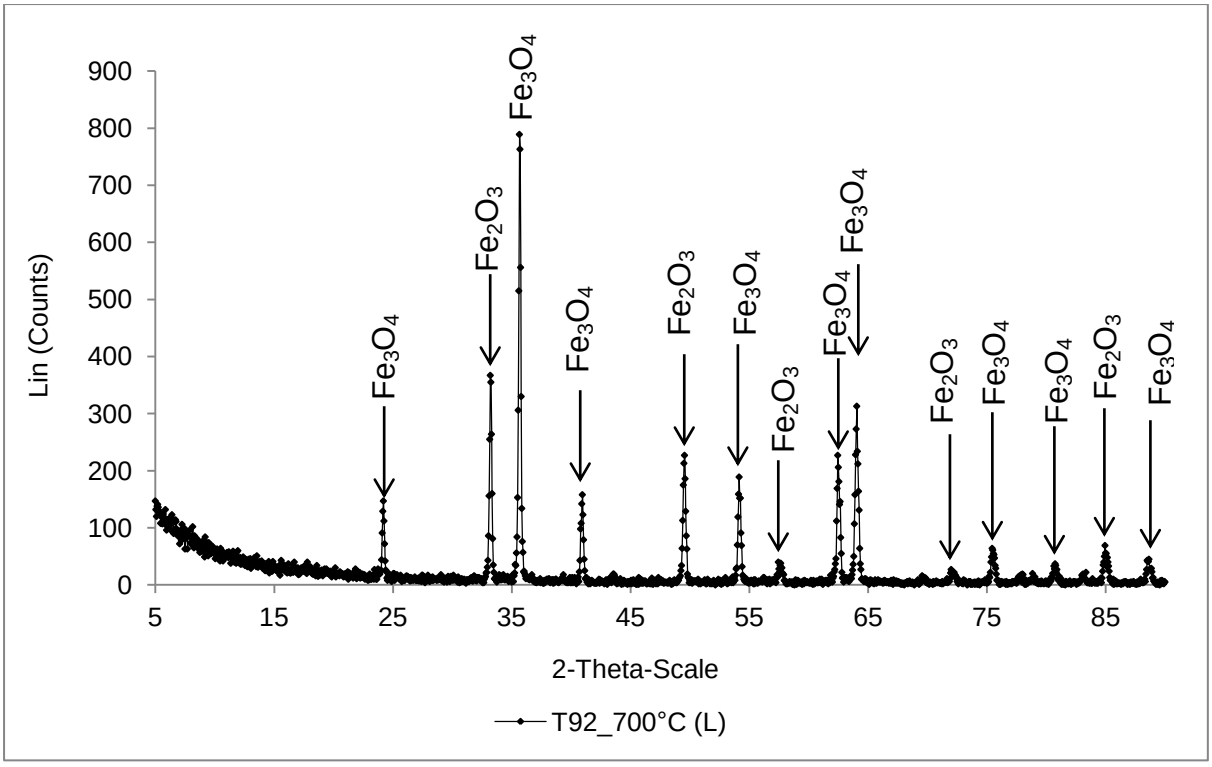

Figure 4-85 XRD of the oxide scale formed on T92 at 650°C with low steam flow rate

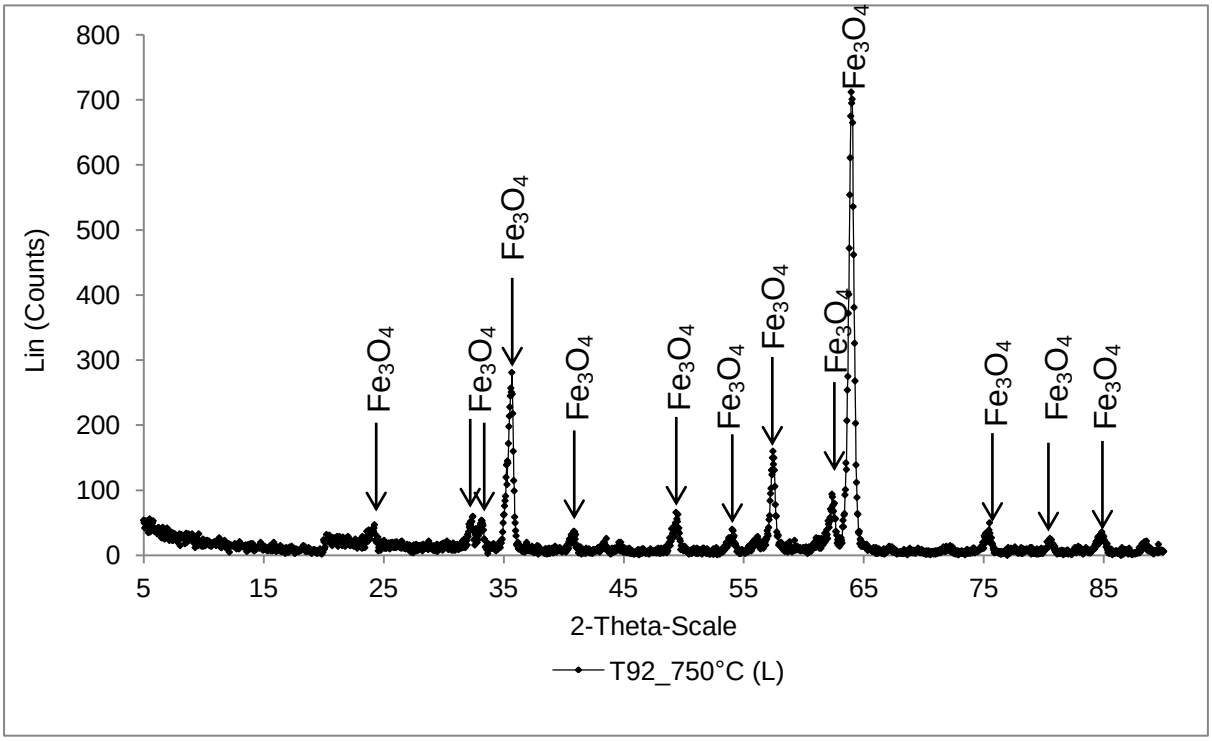

Figure 4-86 XRD of the oxide scale formed on T92 at 750°C with low steam flow rate

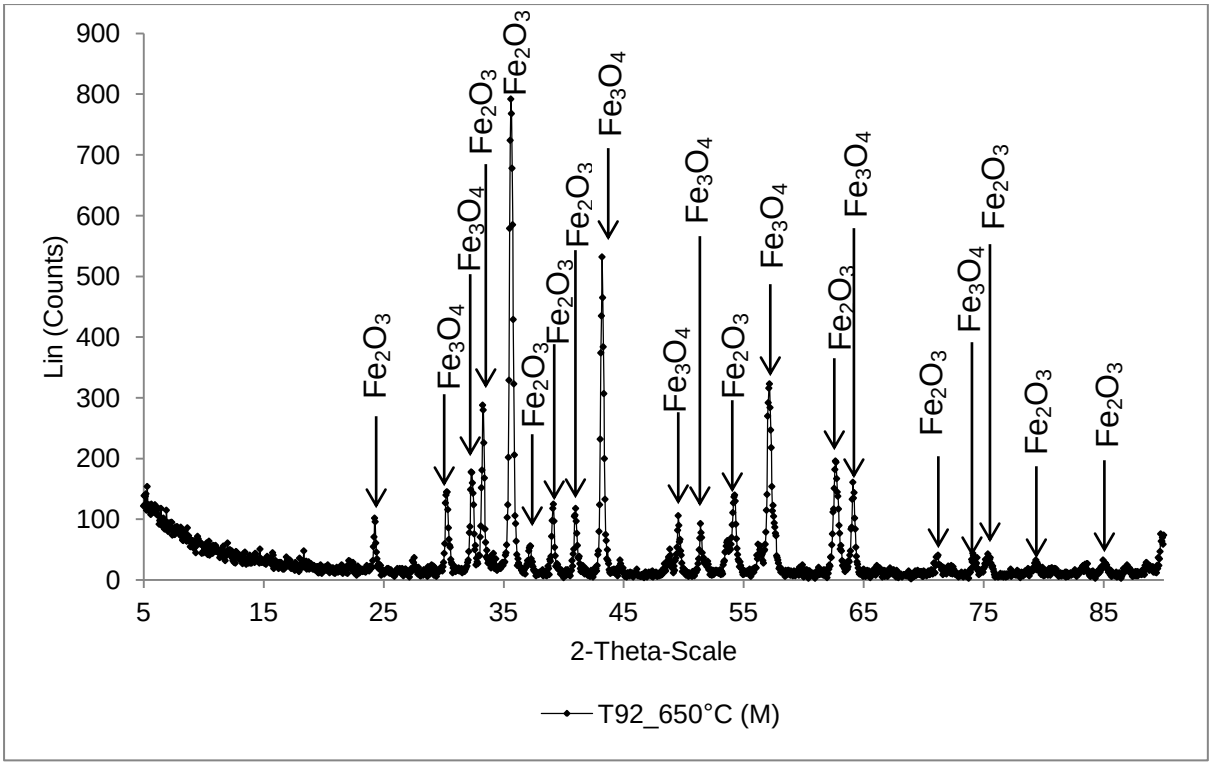

Figure 4-87 XRD of the oxide scale formed on T92 at 650°C with medium steam flow rate

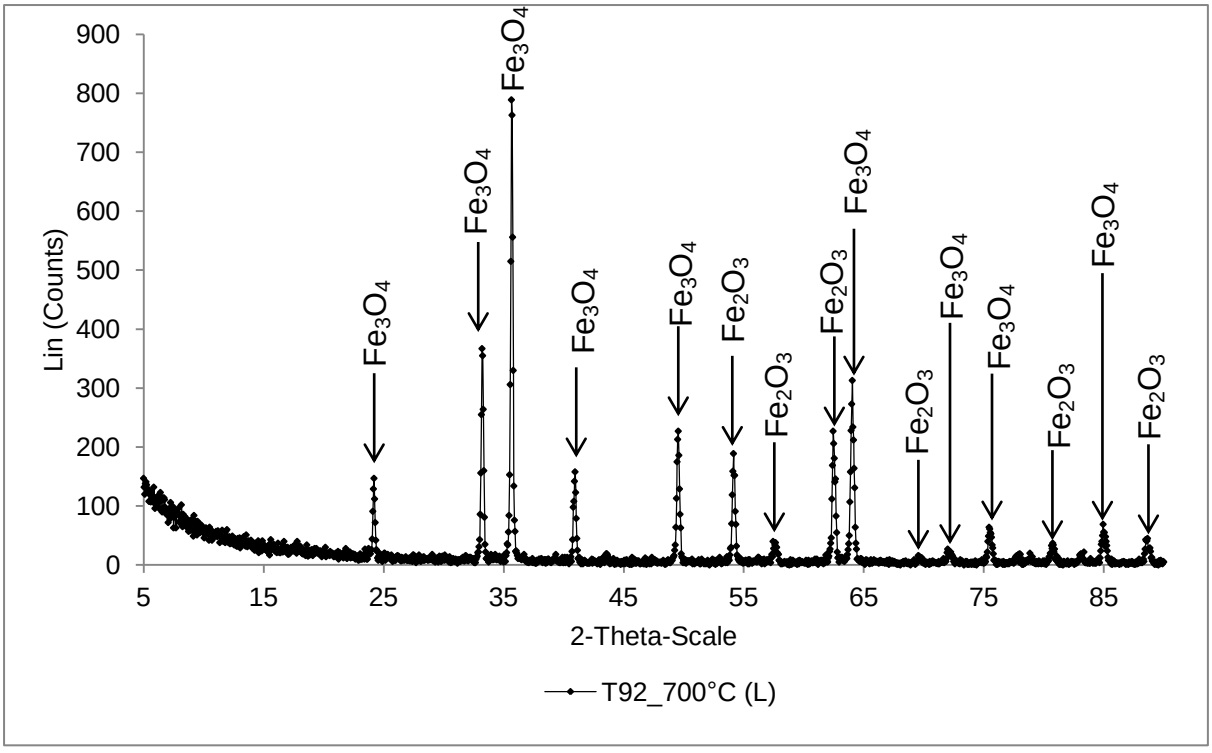

Figure 4-88 XRD of the oxide scale formed on T92 at 700°C with medium steam flow rate

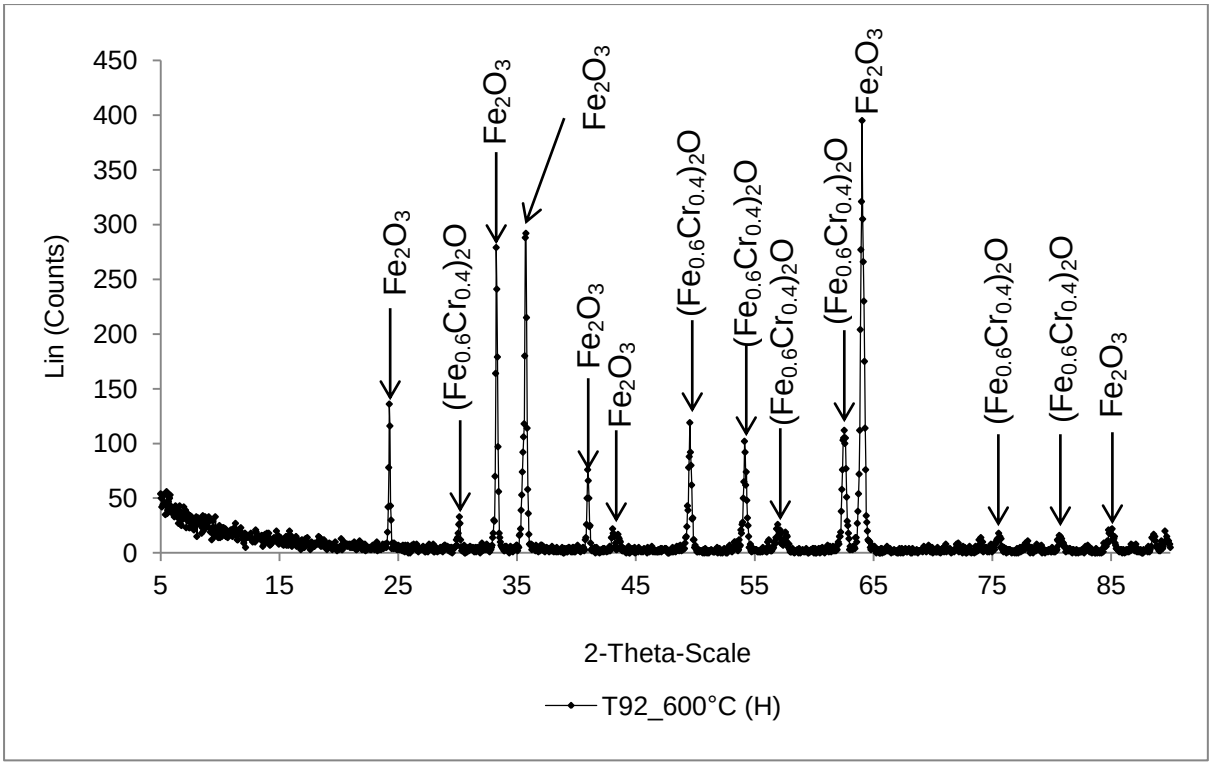

Figure 4-89 XRD of the oxide scale formed on T92 at 600°C with fast steam flow rate

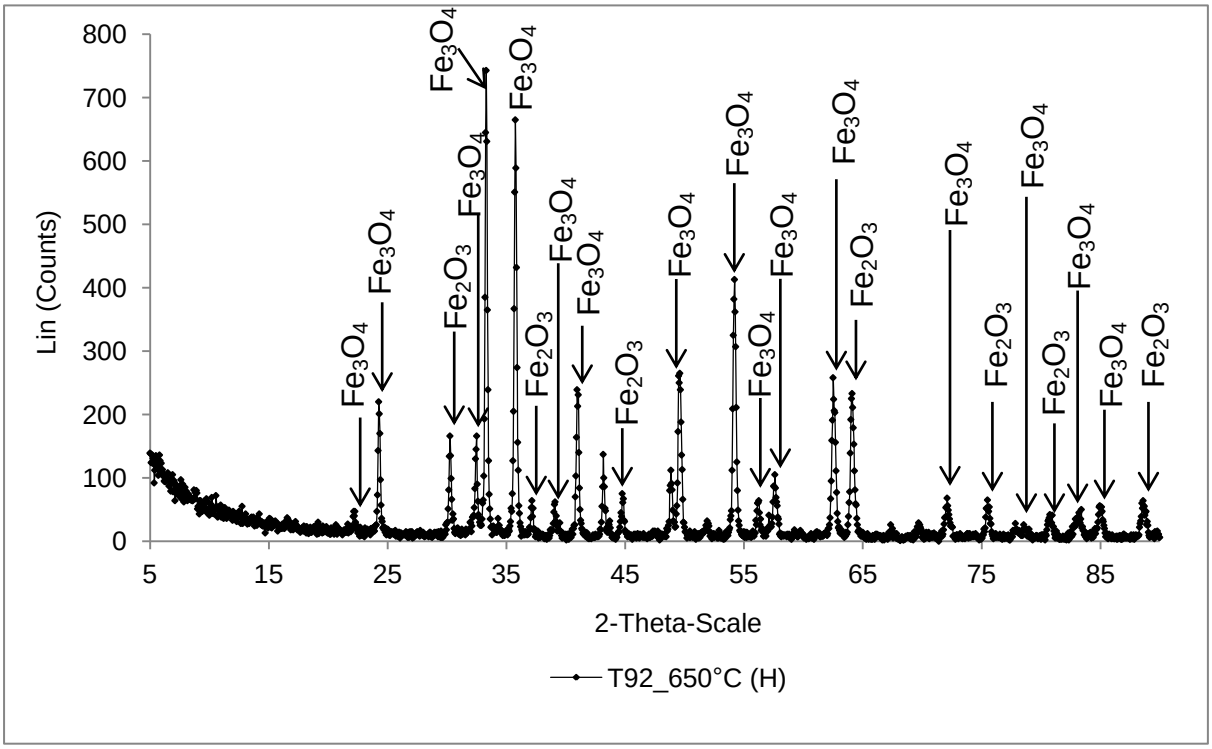

Figure 4-90 XRD of the oxide scale formed on T92 at 650°C with fast steam flow rate

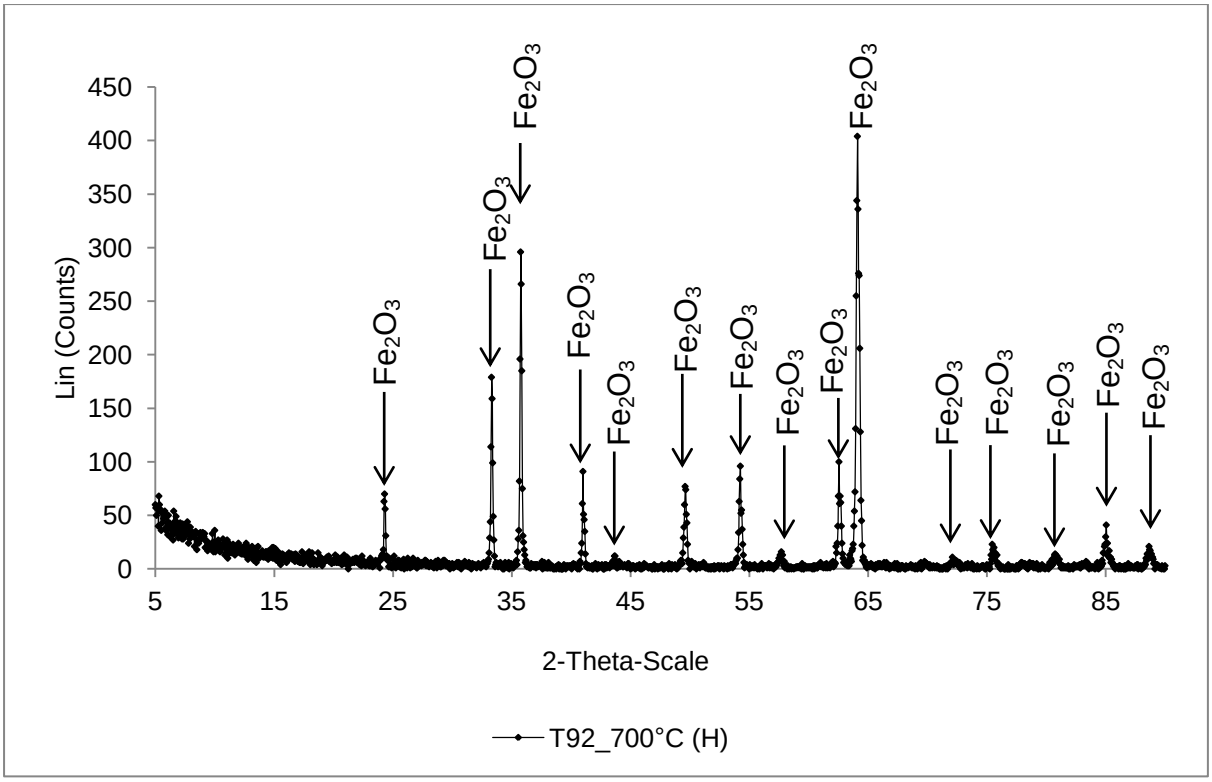

Figure 4-91 XRD of the oxide scale formed on T92 at 700°C with fast steam flow rate

4.2.1.2 Austenitic and nickel-based alloys

As a result of the slow morphological changes on the surfaces of the scales developed, the surface study of austenitic and nickel-based alloys is limited to investigation of the surfaces after 1000 hour exposures. On the surfaces of the materials selected, only thin oxides have nucleated. In regions where there have been local breakdowns of the protective scales nodular growth of oxides have been identified. The sizes as well as concentration of nodules are believed to be depended on the exposure time and temperature as well as alloy type and the orientation relative to the steam flow.

4.2.1.2.1 T347HFG (18Cr)

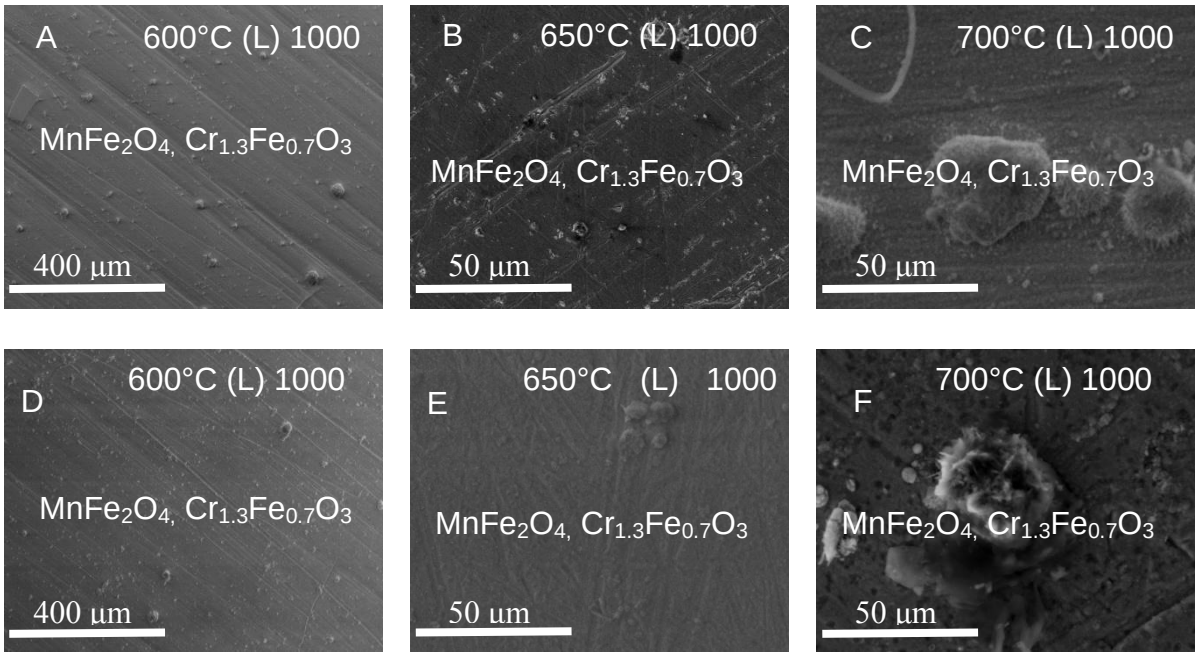

Figure 4-92 Micrographs showing morphologies of T347HFG surfaces facing direct (A-C) and indirect (D-F) steam flow at 600°C (L), 650°C (L) and 700°C (L) after 250, 500 and 1000 hour exposure

T347HFG oxidises slowly, even at higher temperatures it shows slow nodular growth, the nodules mostly nucleate on the surfaces facing direct steam flow. XRD and EDX analyses of the surfaces showed that they are covered with protective scales, identified as Jacobsite ($MnFe_2O_4$) and chromium, iron oxide ($Cr_{1.3}Fe_{0.7}O_3$). As for the ferritic steels, exposures to increased steam flow rates increases the oxidation process of T347HFG, and more nodules are identified on the surfaces

(Figure 4-93 and Figure 4-94). Under the fastest steam flow rate the oxide scales are thicker, with clear grain growth in time. XRD analyses indicated that the scales formed, under medium steam flow rates conditions, consisted of chromium iron oxide $Cr_2(FeO_2)_6$ at 650°C (M), jacobte and $Cr_2(FeO_2)$ at 700°C (M) (Figure 4-87 - Figure 4-88). In comparison T347HFG exposed to fast steam flow forms considerably thicker oxides with haematite and chromium iron oxide $Cr_2(FeO_2)_6$ at all temperatures tested (600, 650, 700°C) (Figure 4-98 - Figure 4-100).

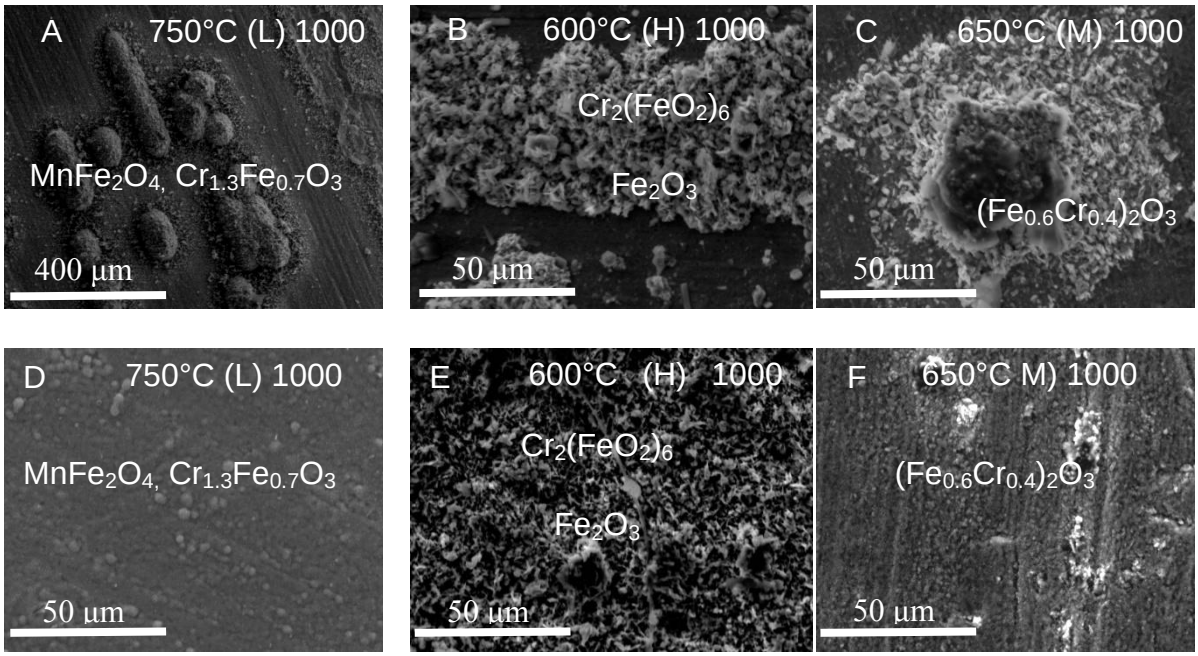

Figure 4-93 Micrographs showing morphologies of T347HFG surfaces facing direct (A-C) and indirect (D-F) steam flow at 750°C (L), 600°C (H) and 650°C (M) after 1000 hour exposure

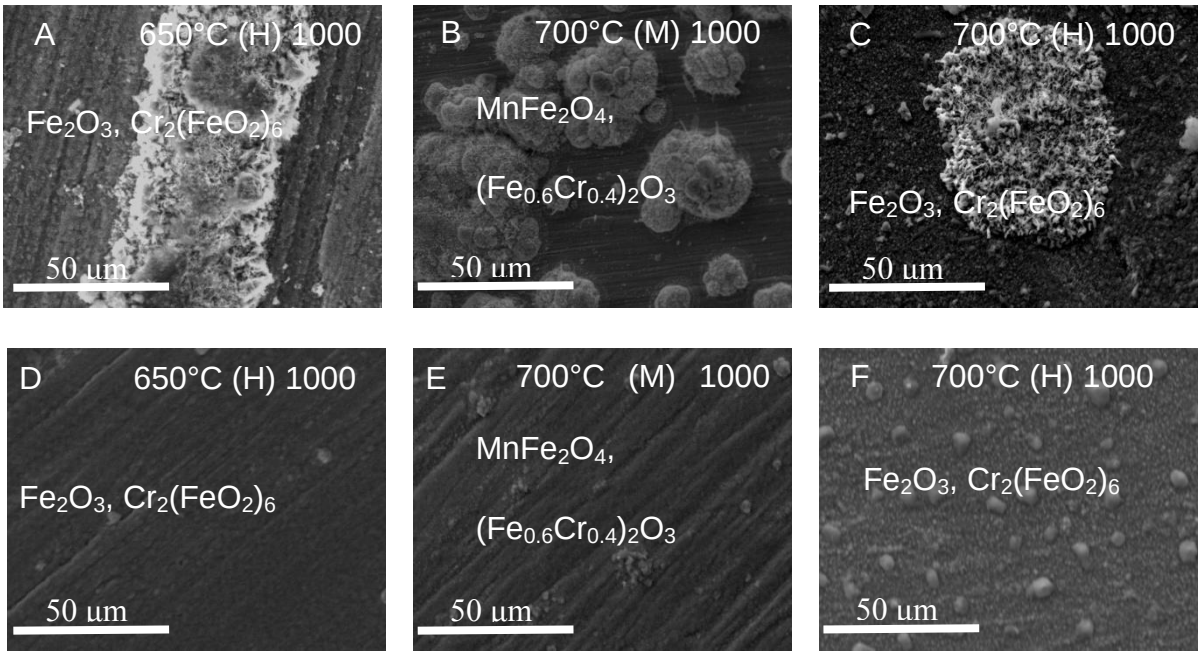

Figure 4-94 Micrographs showing morphologies of T347HFG surfaces facing direct (A-C) and indirect (D-F) steam flow at 650°C (H), 700°C (M) and 700°C (H) after 1000 hour exposure

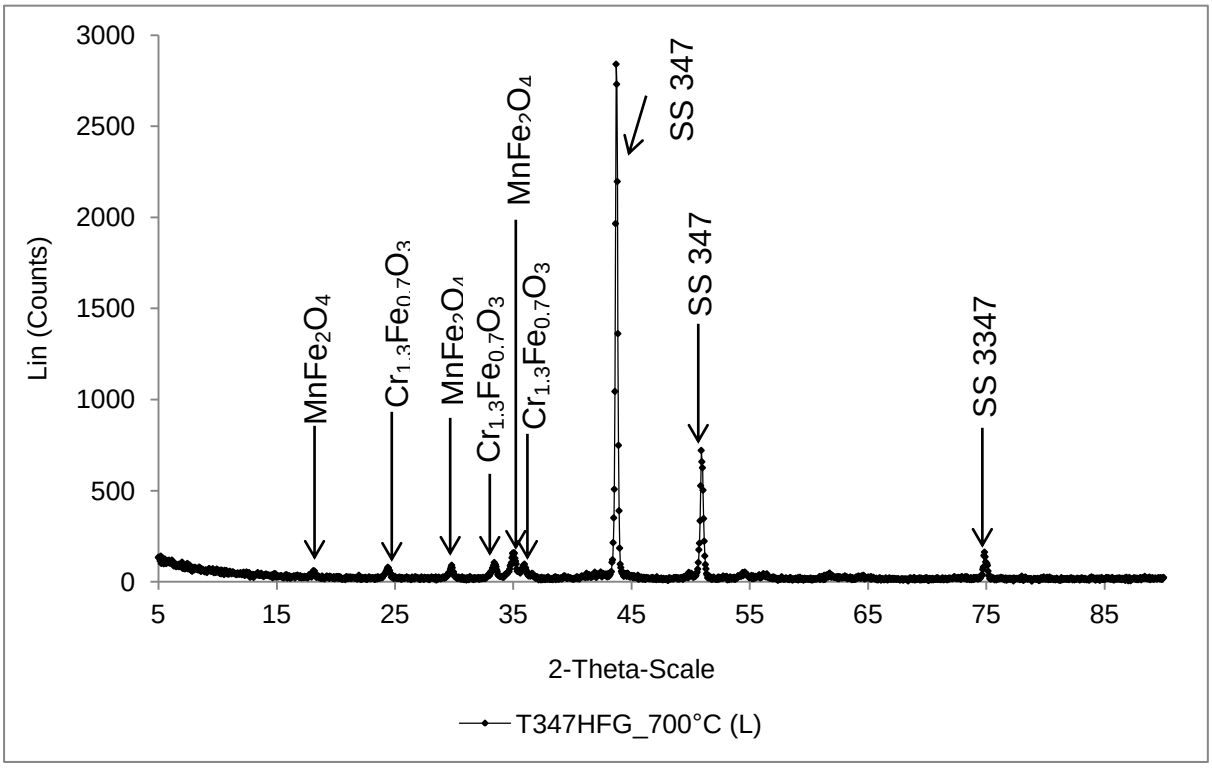

Figure 4-95 XRD of the oxide scale formed on T347HFG at 700°C with slow steam flow rate

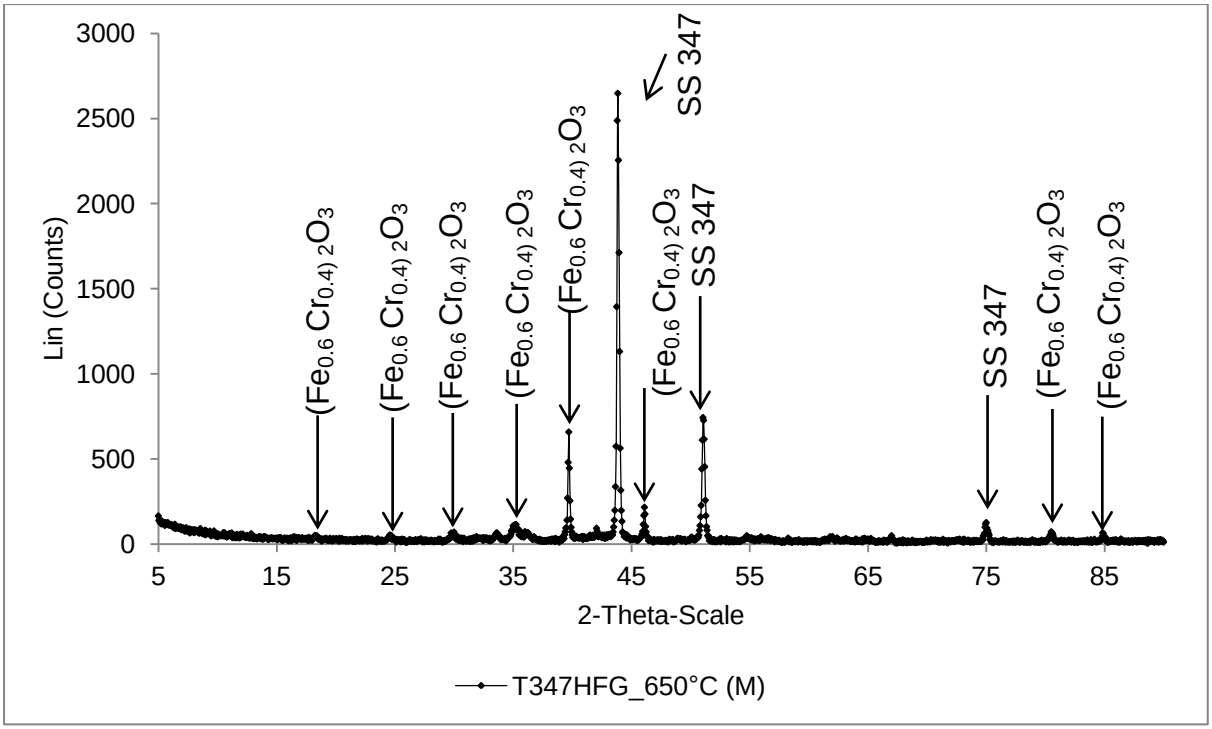

Figure 4-96 XRD of the oxide scale formed on T347HFG at 650°C with medium steam flow rate

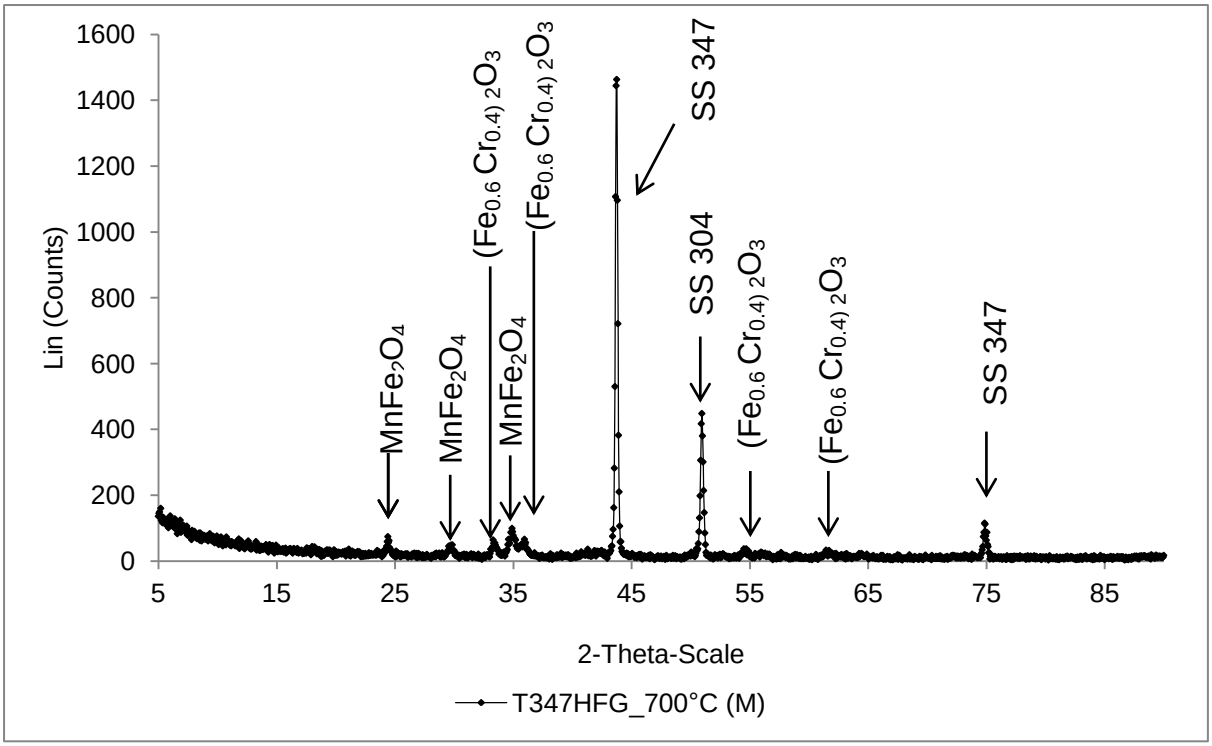

Figure 4-97 XRD of the oxide scale formed on T347HFG at 700°C with medium steam flow rate

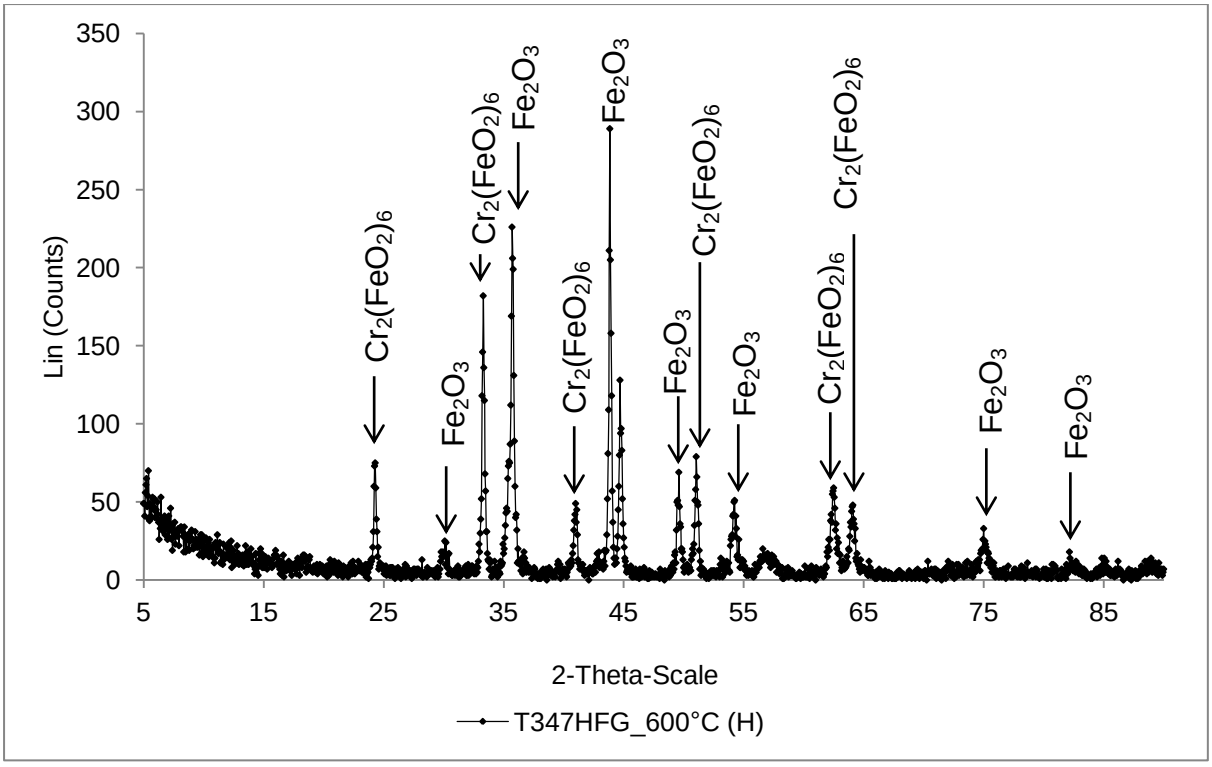

Figure 4-98 XRD of the oxide scale formed on T347HFG at 600°C with fast steam flow rate

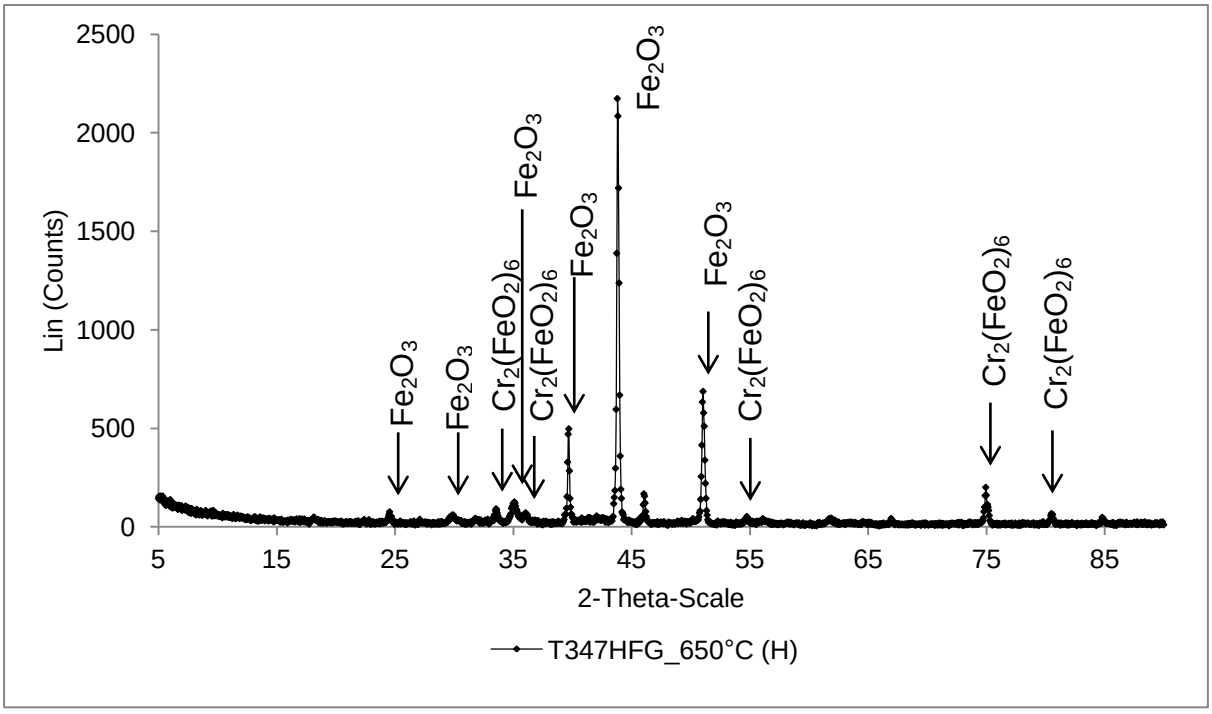

Figure 4-99 XRD of the oxide scale formed on T347HFG at 650°C with fast steam flow rate

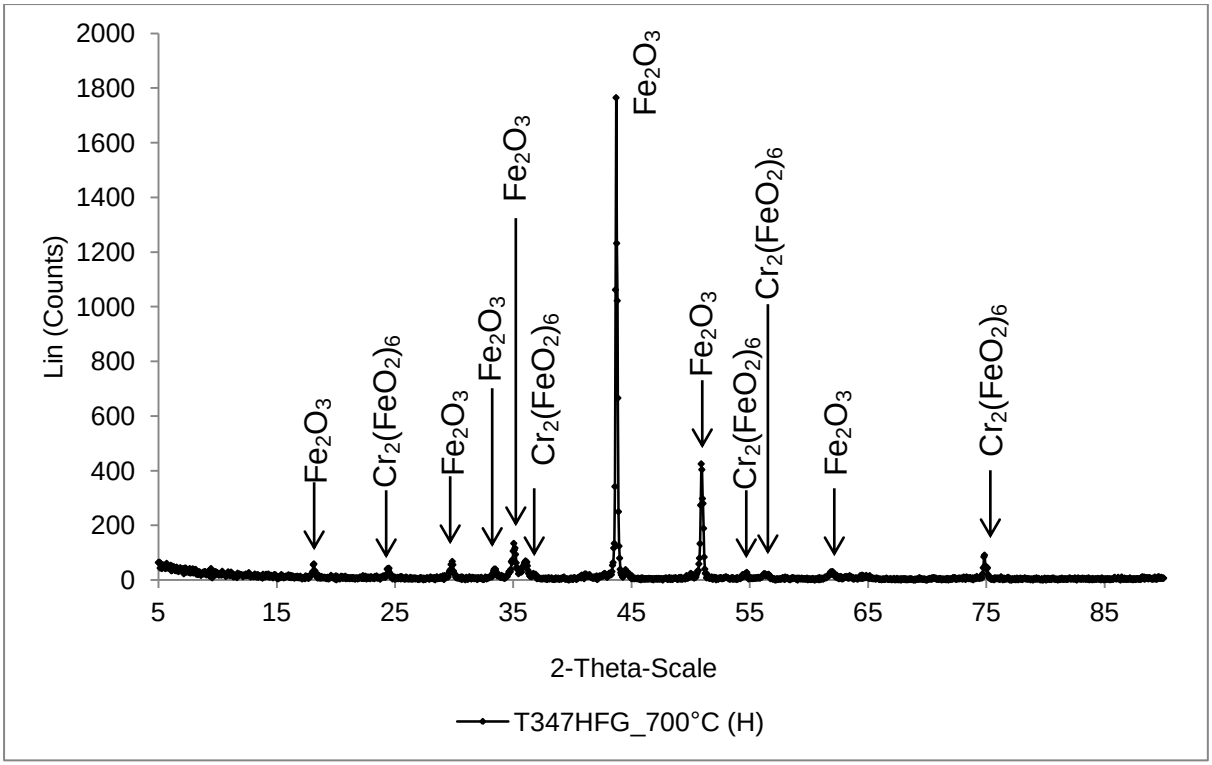

Figure 4-100 XRD of the oxide scale formed on T347HFG at 700°C with fast steam flow rate

4.2.1.2.2 Super 304H (18Cr)

In spite of the fact that Super 304H and T347HFG are both 18 % austenitic steels the oxidation of Super 304H is slower and produces thinner scales. There are fewer nodules formed, even at 750°C (L). Under higher steam flow rate conditions more nodules start to develop on the surface. The scales developed on Super 304H have been identified with the XRD as Jacobsite ($MnFe_2O_4$). Steam flow rates have also an impact on the scales developed however; it is less significant than for T347HFG. Comparison of data for both 18Cr alloys shows that oxide growth on T347HFG is more temperature dependent than Super 304H; however the steam flow rate clearly influences the growth of the nodules on Super 304H. XRD analyses showed that at medium steam flow rates regardless of exposure temperature, the scale developed is a mix of $MnFe_2O_4$ and iron chromium oxide $(Fe_{0.6}Cr_{0.4})_2O_3$. Finally, exposure to the fastest steam flow rate drives the development of the thickest oxides, which have been identified as mixed haematite and iron chromium oxide $(Fe_{0.6}Cr_{0.4})_2O_3$.

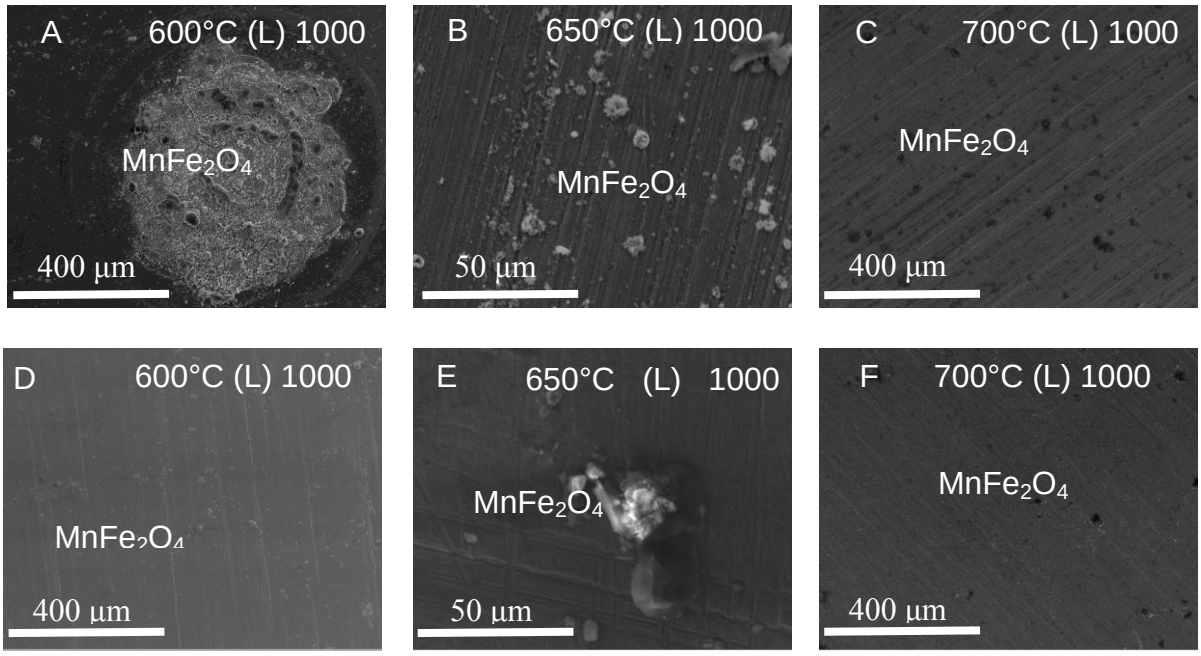

Figure 4-101 Micrographs showing morphologies of Super 304H surfaces facing direct (A-C) and indirect (D-F) steam flow at 600°C (L), 650°C (L) and 700°C (L) after 1000 hour exposure

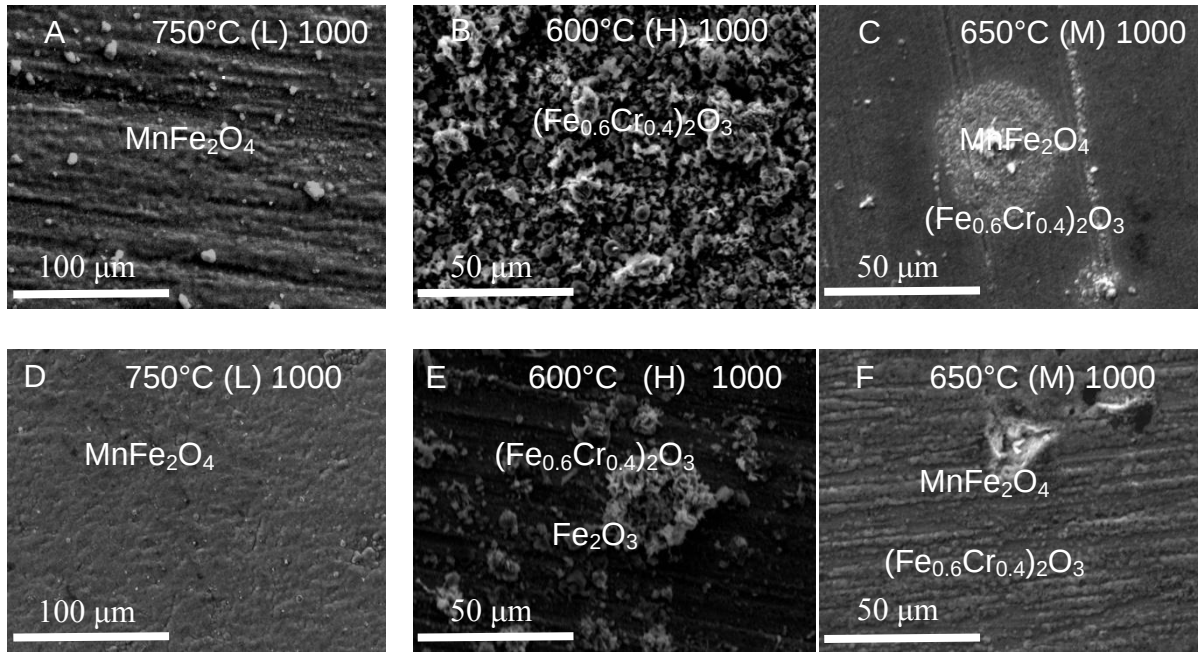

Figure 4-102 Micrographs showing morphologies of Super 304H surfaces facing direct (A-C) and indirect (D-F) steam flow at 750°C (L), 600°C (H) and 650°C (M) after 1000 hour exposure

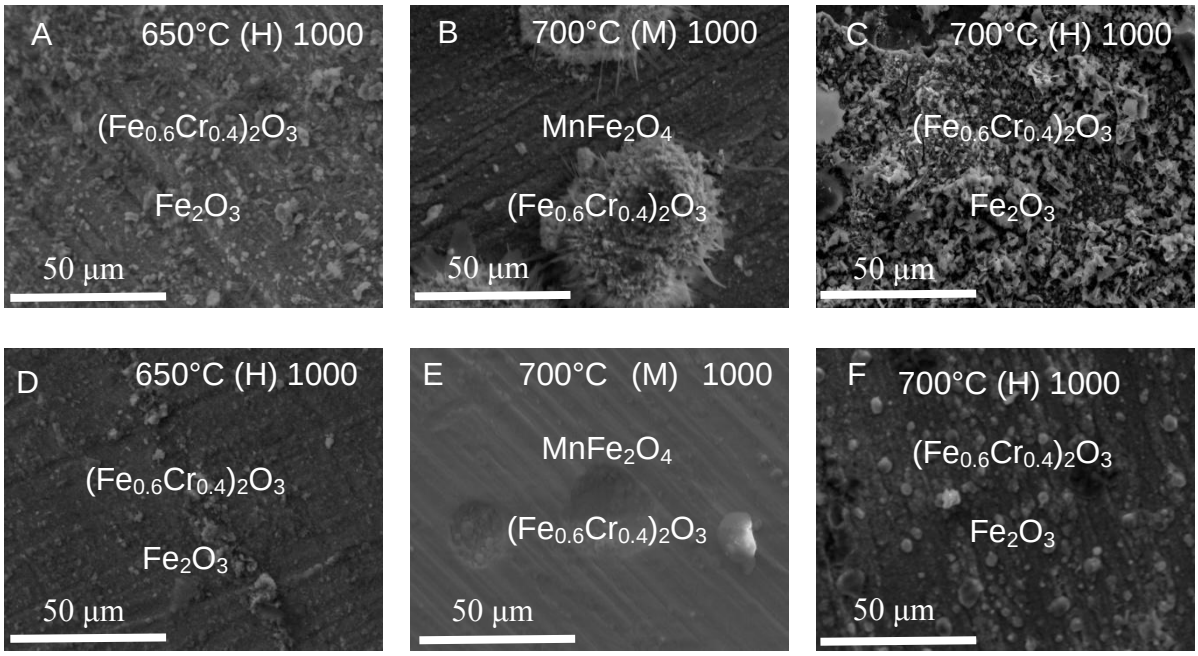

Figure 4-103 Micrographs showing morphologies of Super 304H surfaces facing direct (A-C) and indirect (D-F) steam flow at 650°C (H), 700°C (M) and 700°C (H) after 1000 hour exposure

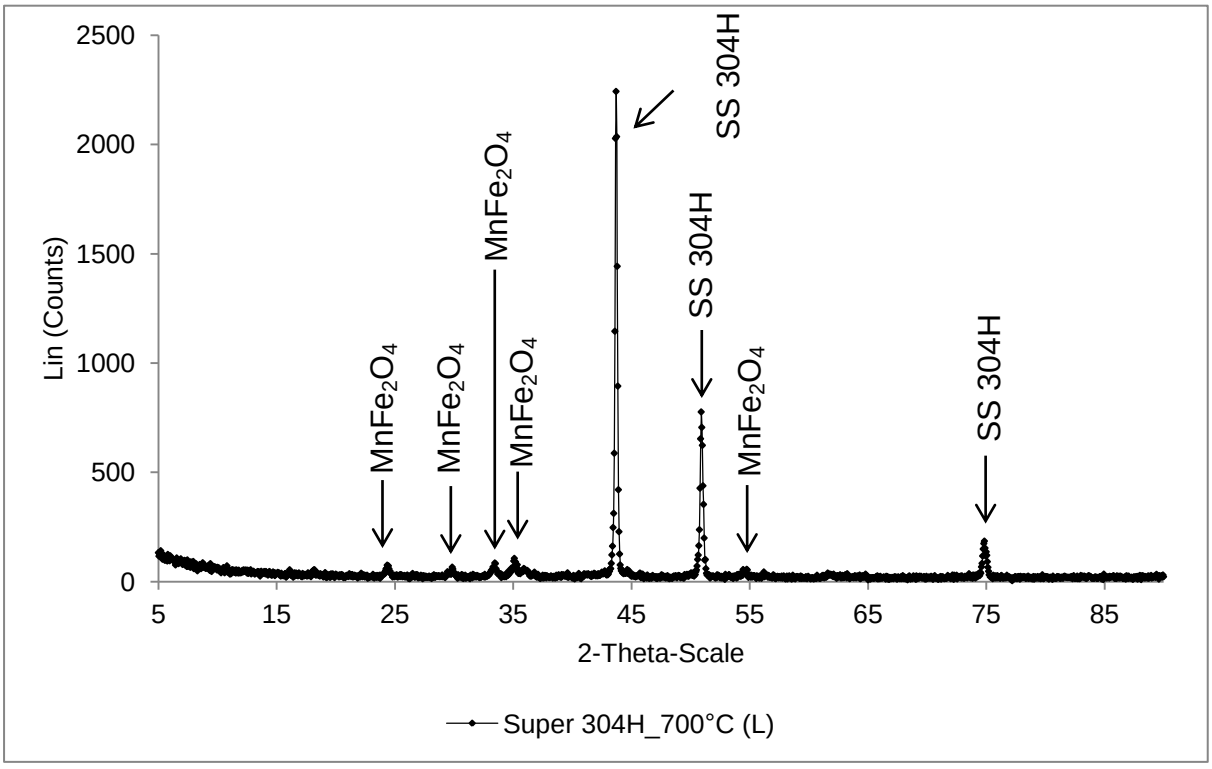

Figure 4-104 XRD of the oxide scale formed on Super 304H at 700°C with low steam flow rate

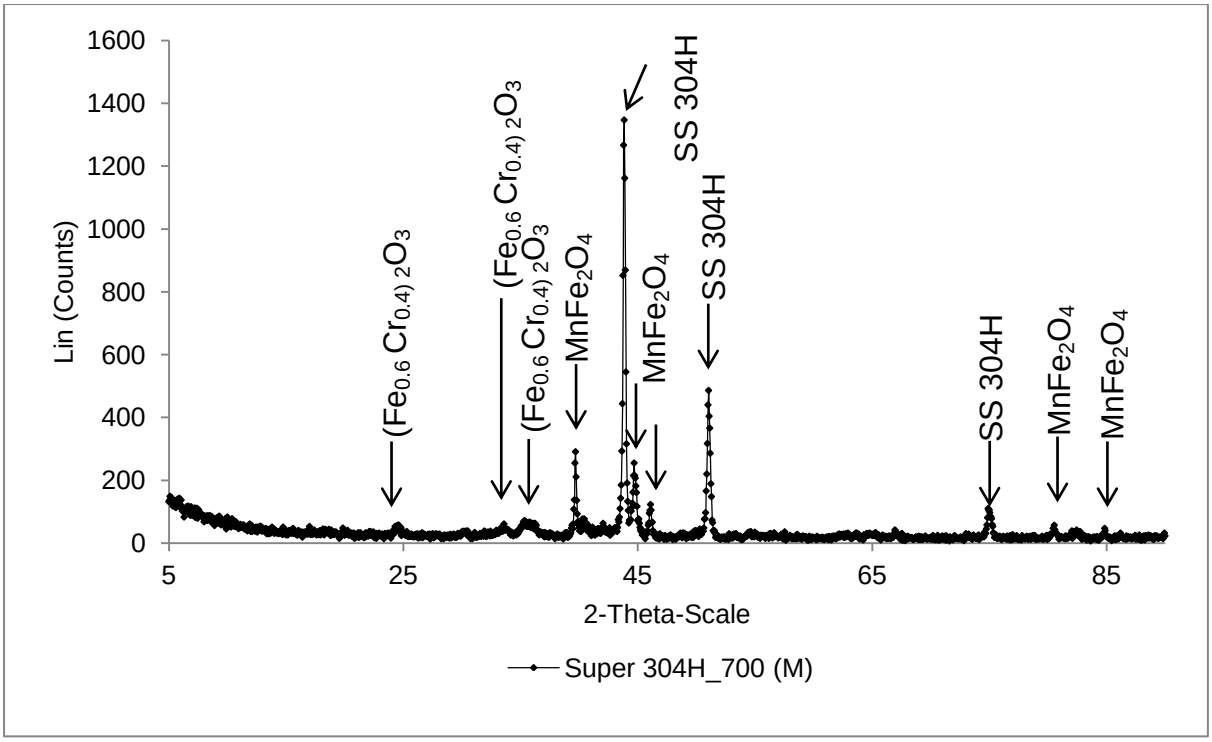

Figure 4-105 XRD of the oxide scale formed on Super 304H at 700°C with medium steam flow rate

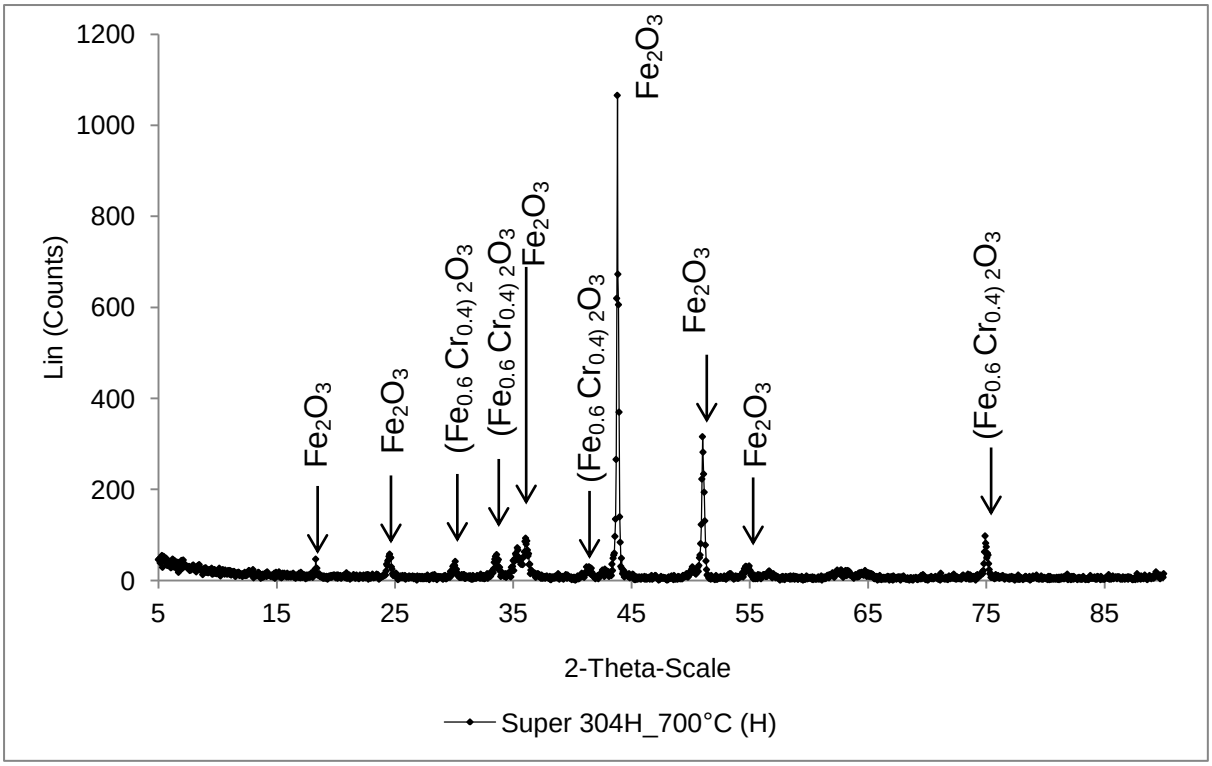

Figure 4-106 XRD of the oxide scale formed on Super 304H at 700°C with high steam flow rate

4.2.1.2.3 HR3C (25Cr)

HR3C does not show a little changes in the scales formed in the temperature range 600 -700°C (L) and 700°C (M), it develops thin protective scales, and there is fewer nodules formation than for both 18Cr steels, moreover the nodules formed tend to be found inside the marks left after polishing. The protective scales formed have been identified with XRD as a mixture of iron, chromium oxide ($(Fe_{0.6}Cr_{0.4})_2O_3$) and nickel, chromium oxide ($NiCrO_3$). At 750°C (L) and at 650°C (H) the scales develop more nodules, which have been found in many location not only in the grinding marks as it was at lower temperatures. The impact of the steam flow rate and orientations are clear for this alloy. With higher steam flow rates the scales became significantly thicker, and the XRD analyses showed that under the medium and fastest steam flow rates the scales developed have only one constituent identified as $(Fe_{0.6}Cr_{0.4})_2O_3$.

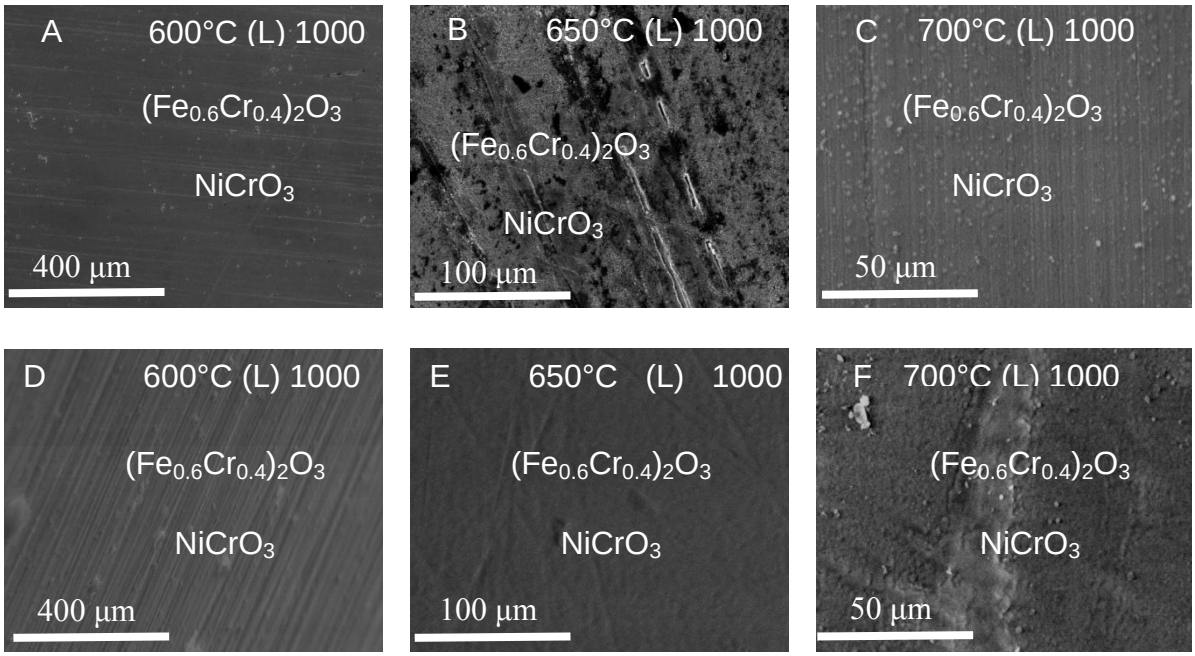

Figure 4-107 Micrographs showing morphologies of HR3C surfaces facing direct (A-C) and indirect (D-F) steam flow at 600°C (L), 650°C (L) and 700°C (L) after 1000 hour exposure

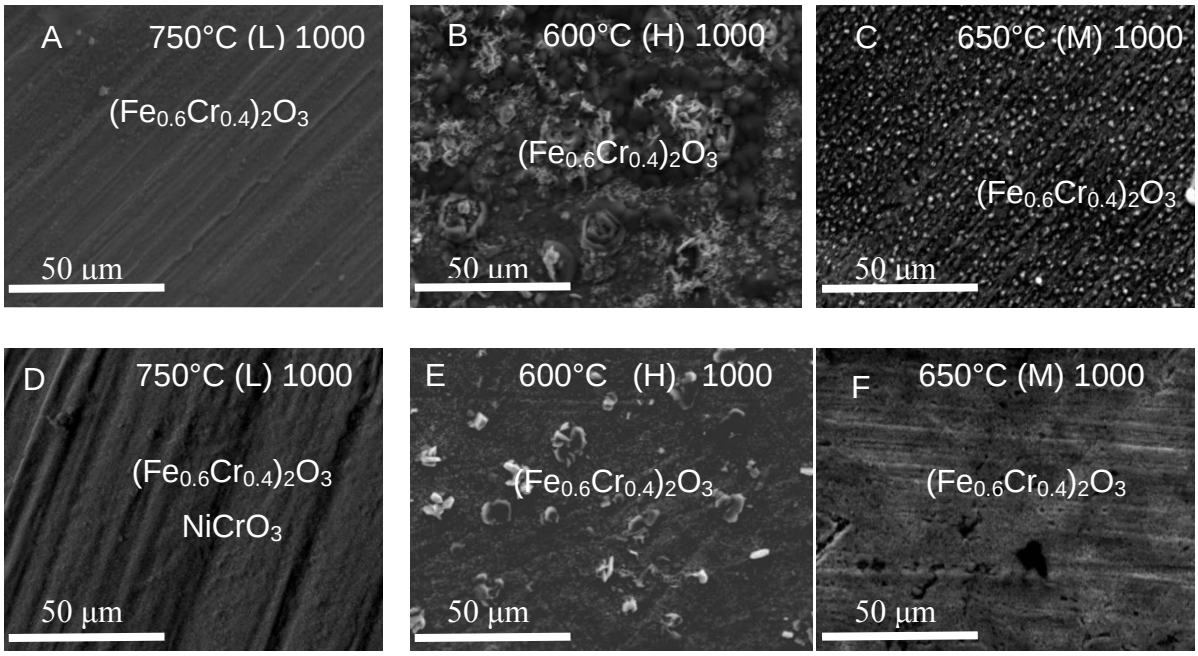

Figure 4-108 Micrographs showing morphologies of HR3C surfaces facing direct (A-C) and indirect (D-F) steam flow at 750°C (L), 600°C (H) and 650°C (M) after 1000 hour exposure

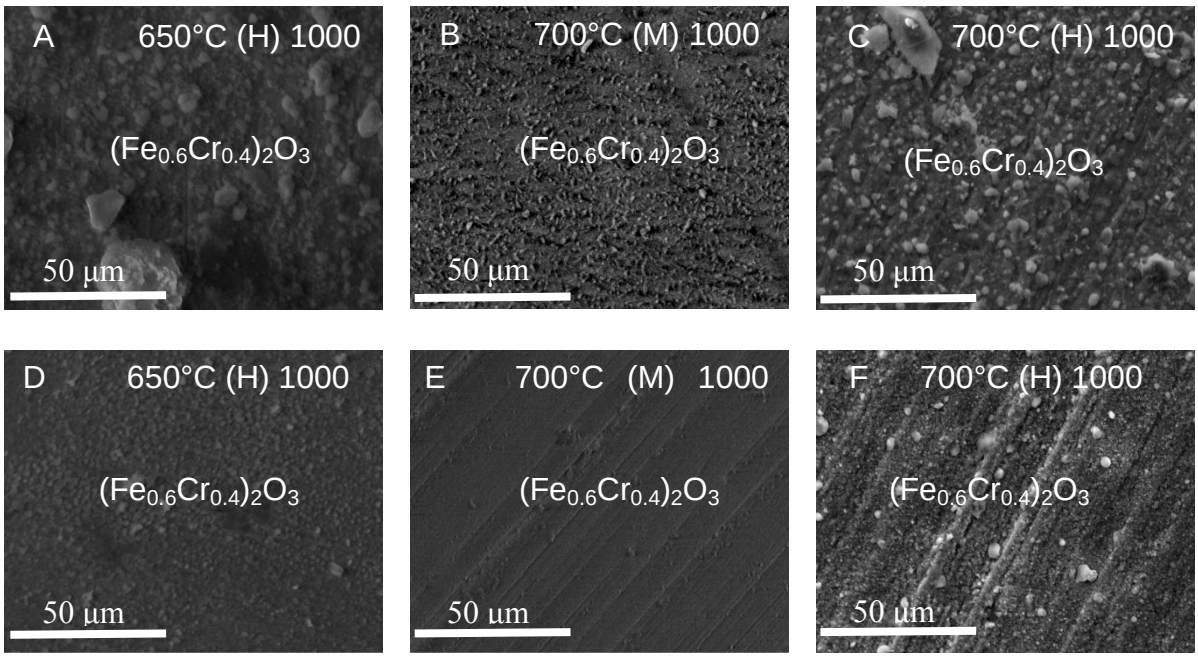

Figure 4-109 Micrographs showing morphologies of HR3C surfaces facing direct (A-C) and indirect (D-F) steam flow at 650°C (M), 700°C (M) and 700°C (H) after 1000 hour exposure

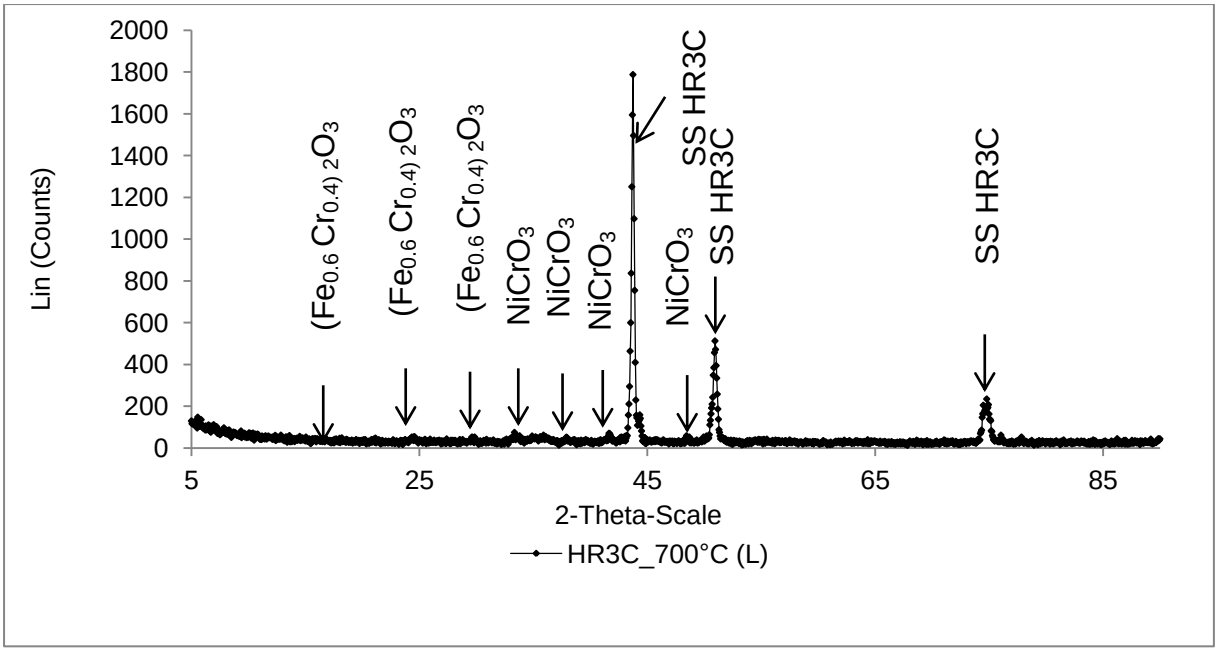

Figure 4-110 XRD of the oxide scale formed on HR3C at 700°C with low steam flow rate

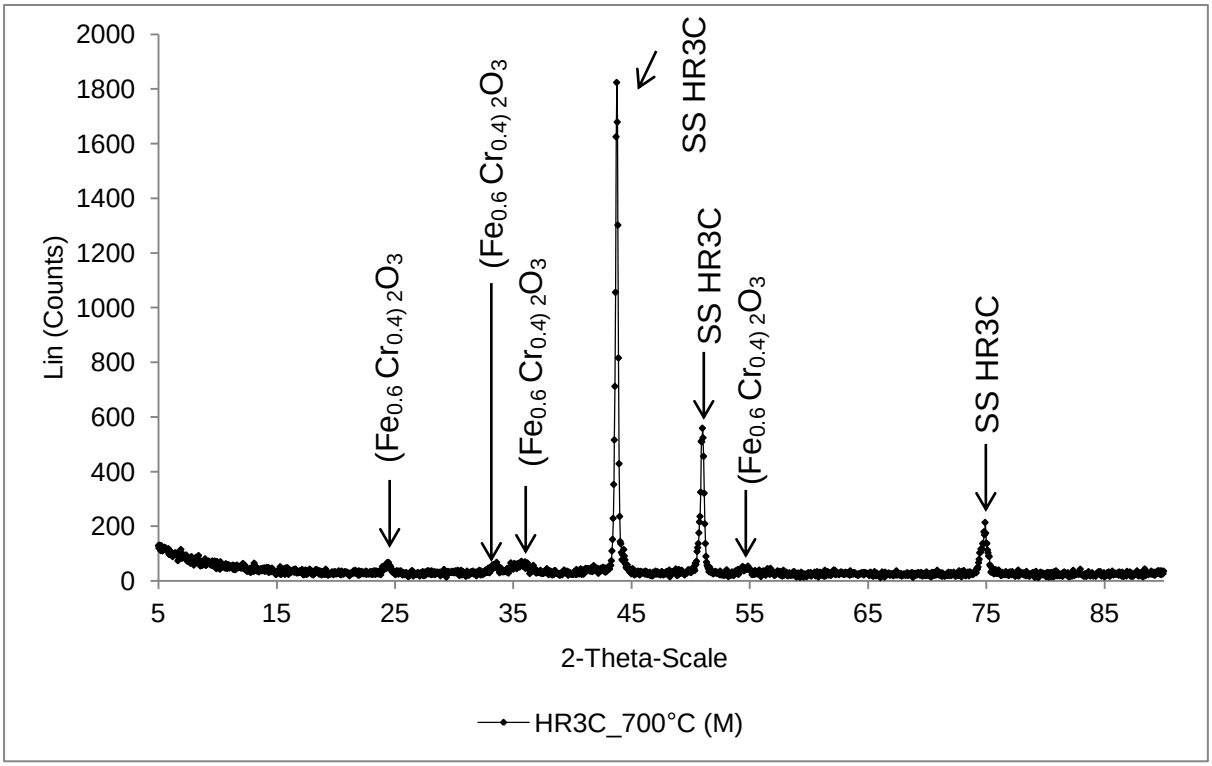

Figure 4-111 XRD of the oxide scale formed on HR3C at 700°C with medium steam flow rate

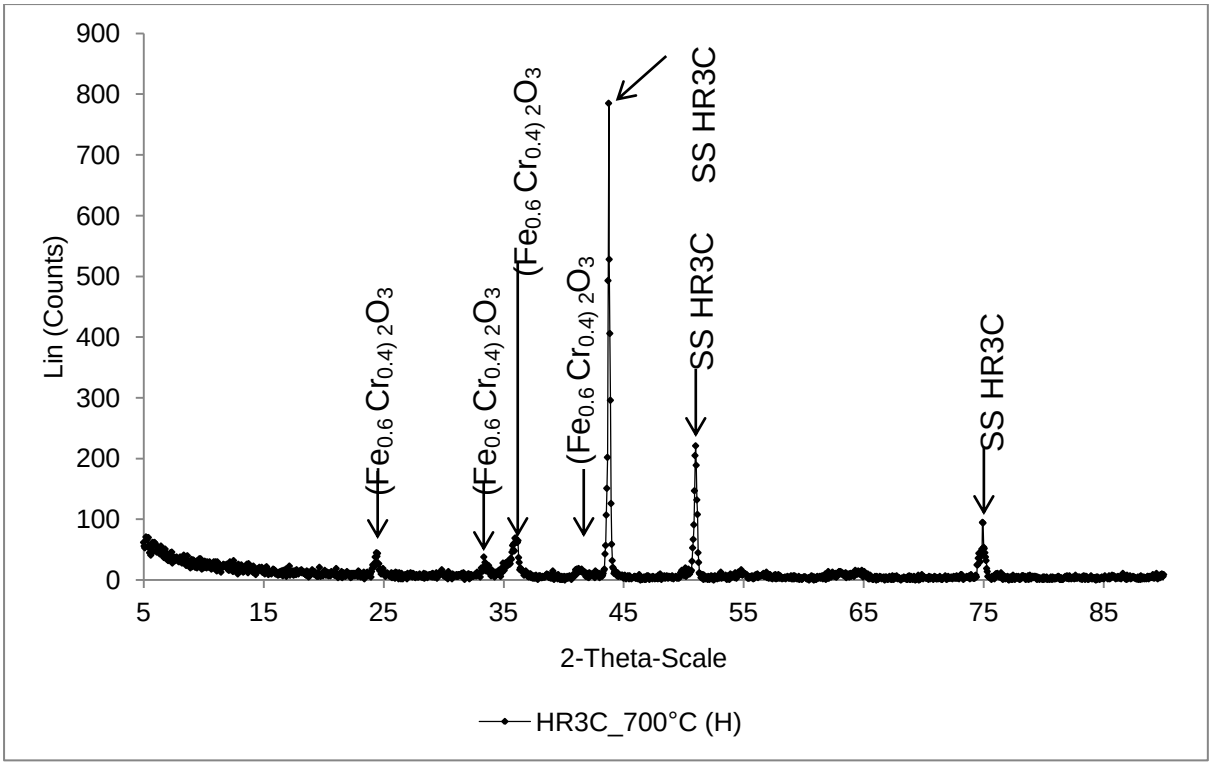

Figure 4-112 XRD of the oxide scale formed on HR3C at 700°C with high steam flow rate

4.2.1.2.4 800H (21Cr) and Inconel 740 (25Cr)

800H and Inconel 740 show similar behaviours in steam; in case of both alloys the oxidation is slow even under the highest steam flow rate conditions. 800H did not show any nodular scale growth; it seems to develop protective and adherent scales, which suppress non-protective oxide growth. The scales have been identified as a mixture of iron, chromium oxide $(Fe_{0.6}Cr_{0.4})_2O_3$ and nickel, chromium oxide ($NiCrO_3$). Inconel 740 is the most resistant of the materials tested; it developed the thinnest scales and these provided the most protection. The thin scales have been identified with XRD as nickel, chromium ($NiCr_2O_4$). The composition of the oxides formed on both alloys does not change with exposure conditions. Even at the fastest steam flow rates the Inconel 740 composition did not trigger any minor changes in oxides composition.

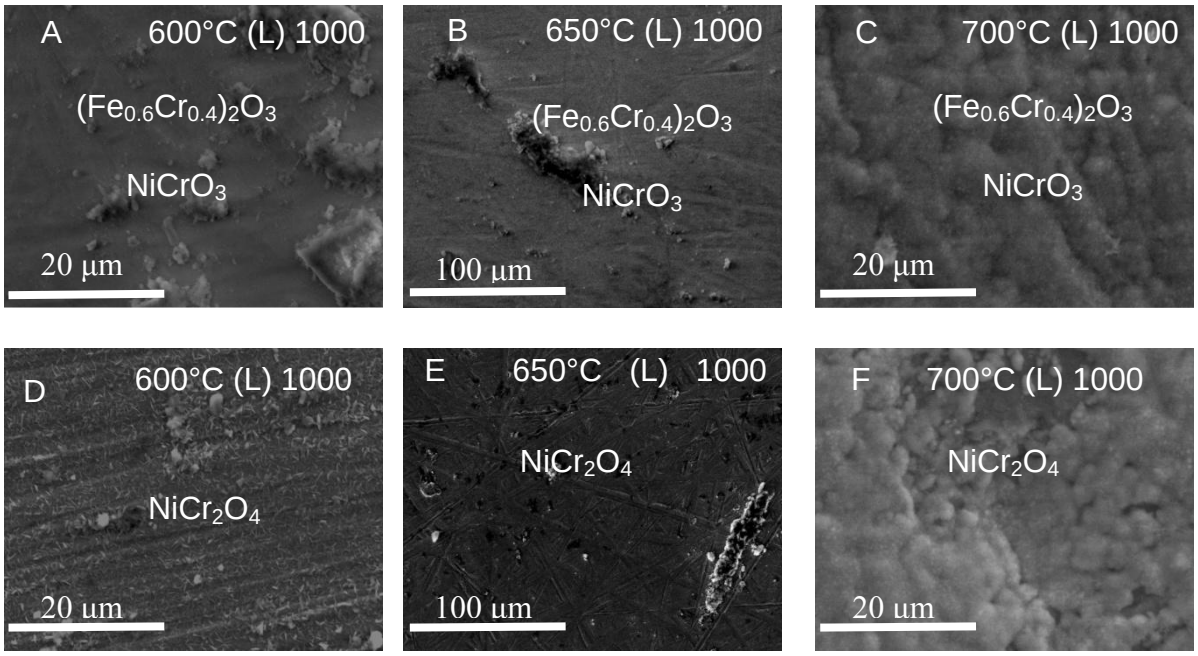

Figure 4-113 Micrographs showing morphologies of 800H (A-C) and Inconel 740 (D-F) surfaces facing the direct steam flow at 600°C (L), 650°C (L) and 700°C (L) after 1000 hour exposure

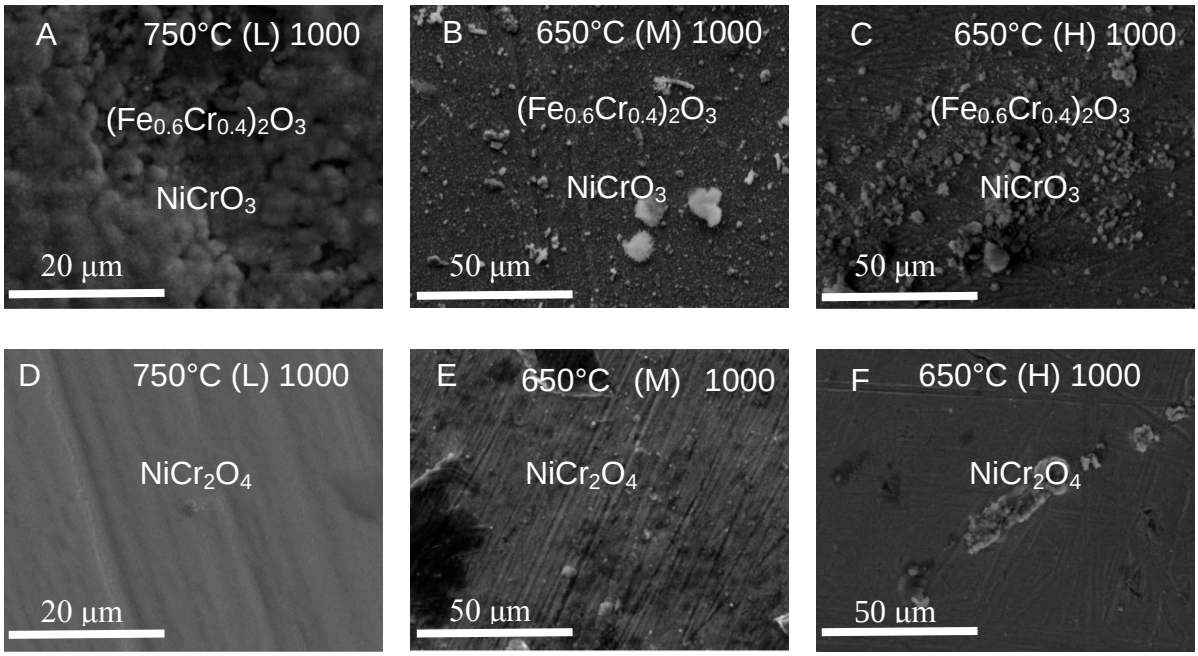

Figure 4-114 Micrographs showing morphologies of 800H (A-C) and Inconel 740 (D-F) surfaces facing the direct steam flow at 750°C (L), 650°C (M) and 650°C (H) after 1000 hour exposure

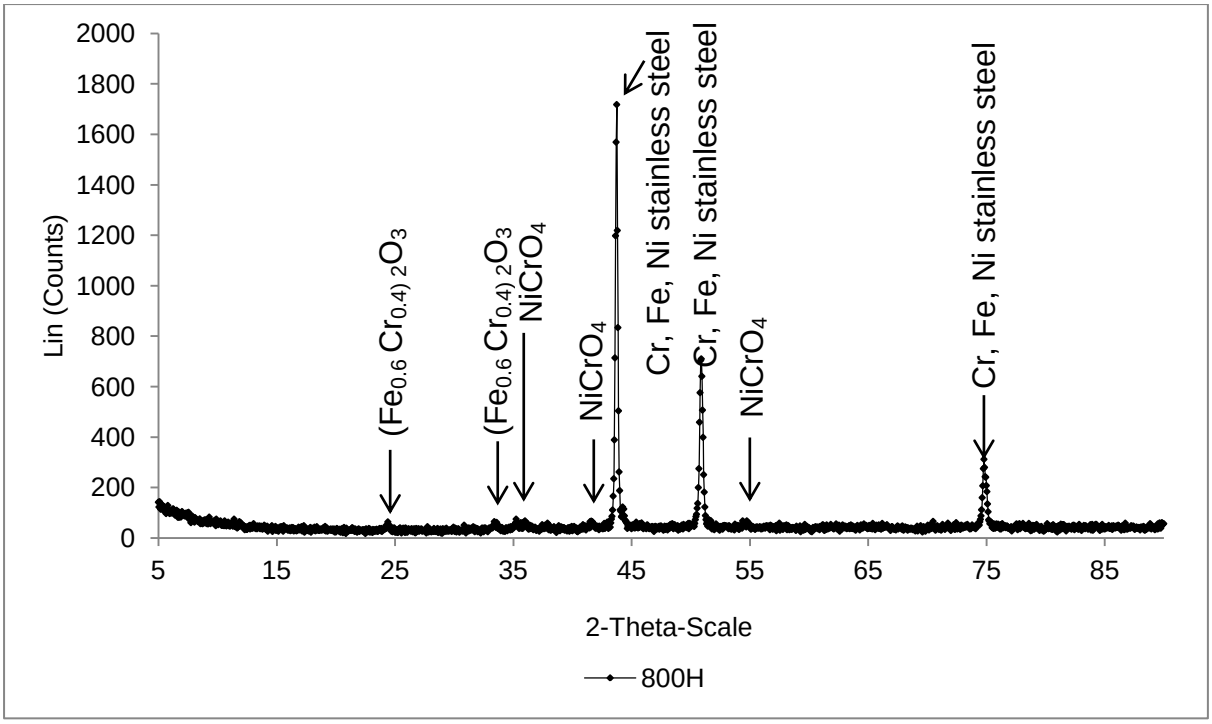

Figure 4-115 XRD of the oxide scale formed on 800H at 700°C with slow steam flow rate

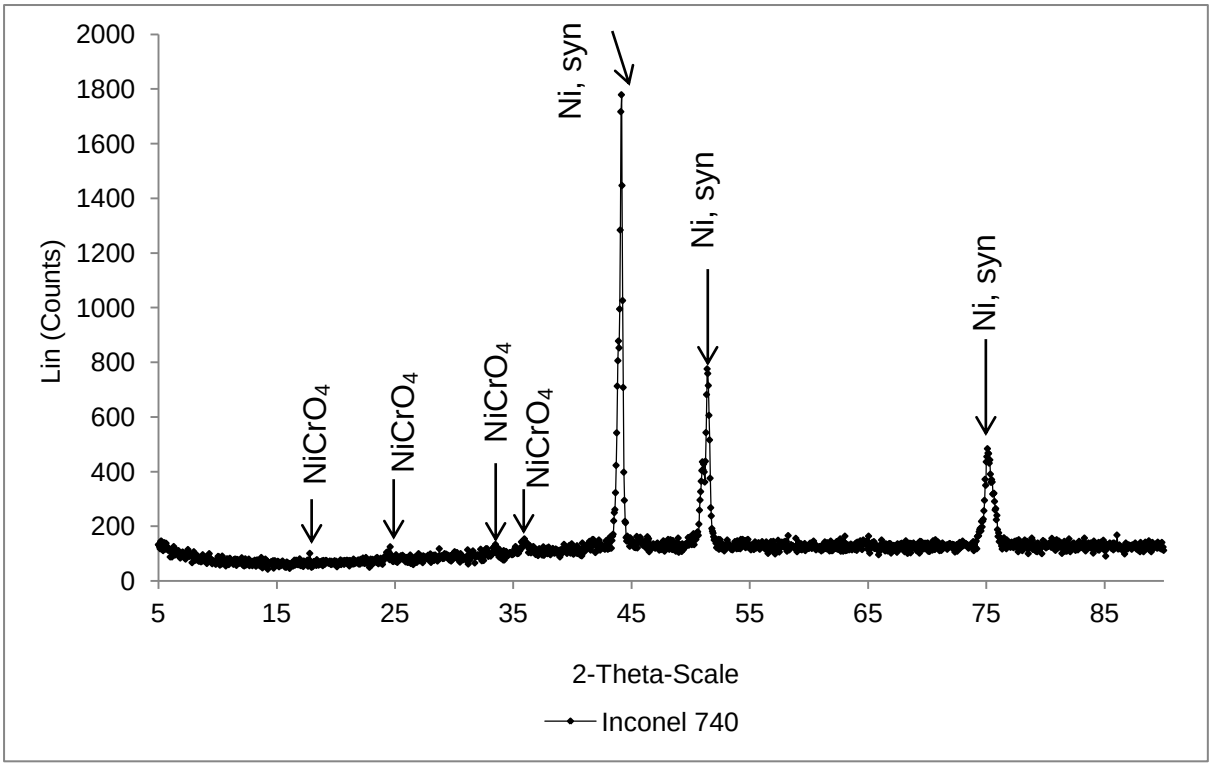

Figure 4-116 XRD of the oxide scale formed on Inconel 740 at 700°C with slow steam flow rate

4.2.2 Cross-sections through oxide scales

The following sections describe the morphology of the scales formed on the alloys tested. In order to understand the behaviours of the materials in the steam environments a number of factors influencing the process have been investigated such as: temperature, time, steam flow, orientation relative to steam flow and alloy chromium concentration.

4.2.2.1 Ferritic steels

The morphology of in cross-sections through the scales formed on the ferritic alloys vary with the chromium levels; however as was identified from the kinetics data there are less significant changes at lower temperatures. The thicknesses of the oxides change with the parameters mentioned above, detail results from this study of the specimens' cross-sections are presented below.

4.2.2.1.1 T23 (2.25 Cr)

T23 showed the fastest oxidation under the steam oxidation conditions studied , which leads to formation of the thickest scales (Figure 4-120 - Figure 4-123). Analysis of the pictures of the scales obtained with an SEM indicated that there was a transformation of the scales structure with exposure conditions (temperature and steam flow rate). At low temperatures (600 – 650°C (L)), and the first 250 hours of an inner Cr, Fe spinel, outer magnetite and outer most layer of haematite as the main constituent (Figure 4-117).

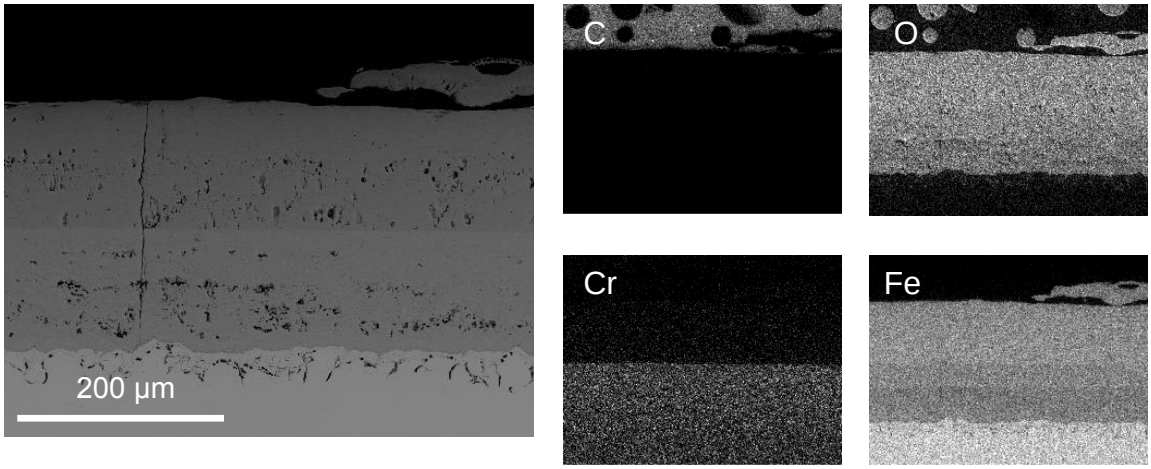

Figure 4-117 BSE SEM + EDX maps of oxide scale formed on T23 at 650°C with low steam flow after 1000 hour exposure

The ratio between thicknesses of the inner spinel and combined outer layers is 1:1 up to 650°C, however this changes at higher temperatures where the inner layer becomes thicker. At 750°C (L) and 700 °C (L) after 500 hour exposures as well as under higher steam flow rate conditions (M, H), the inner layer becomes micro-layered; with magnetite and Cr, Fe spinel as the main constituents of the micro-layers (Figure 4-118). Moreover, at 750°C (L) there is no outermost layer of haematite at the surface.

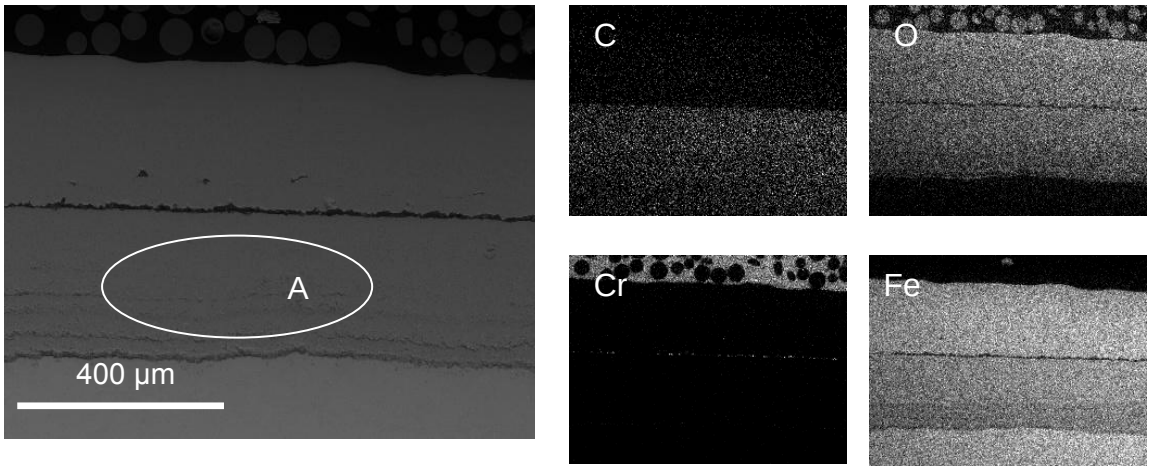

Figure 4-118 BSE SEM + EDX maps of oxide scale formed on T23 at 700°C with low steam flow after 1000 hour exposure

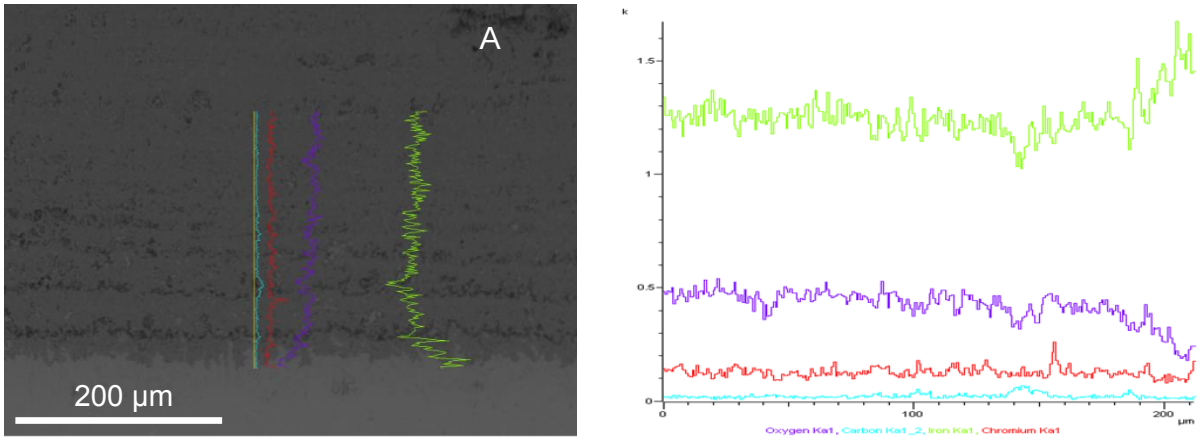

Figure 4-119 BSE SEM EDX line scan of the microlayered-layer inner scale formed on T23 (Figure 4-118 Area A)

Figure 4-119 indicated that dark region in the microlayered-layered is richer in chromium whereas the brighter parts are iron-richer. This confirms that the

microlayered-inner layer consists of magnetite and magnetite + chromium layers in parallel to each other.

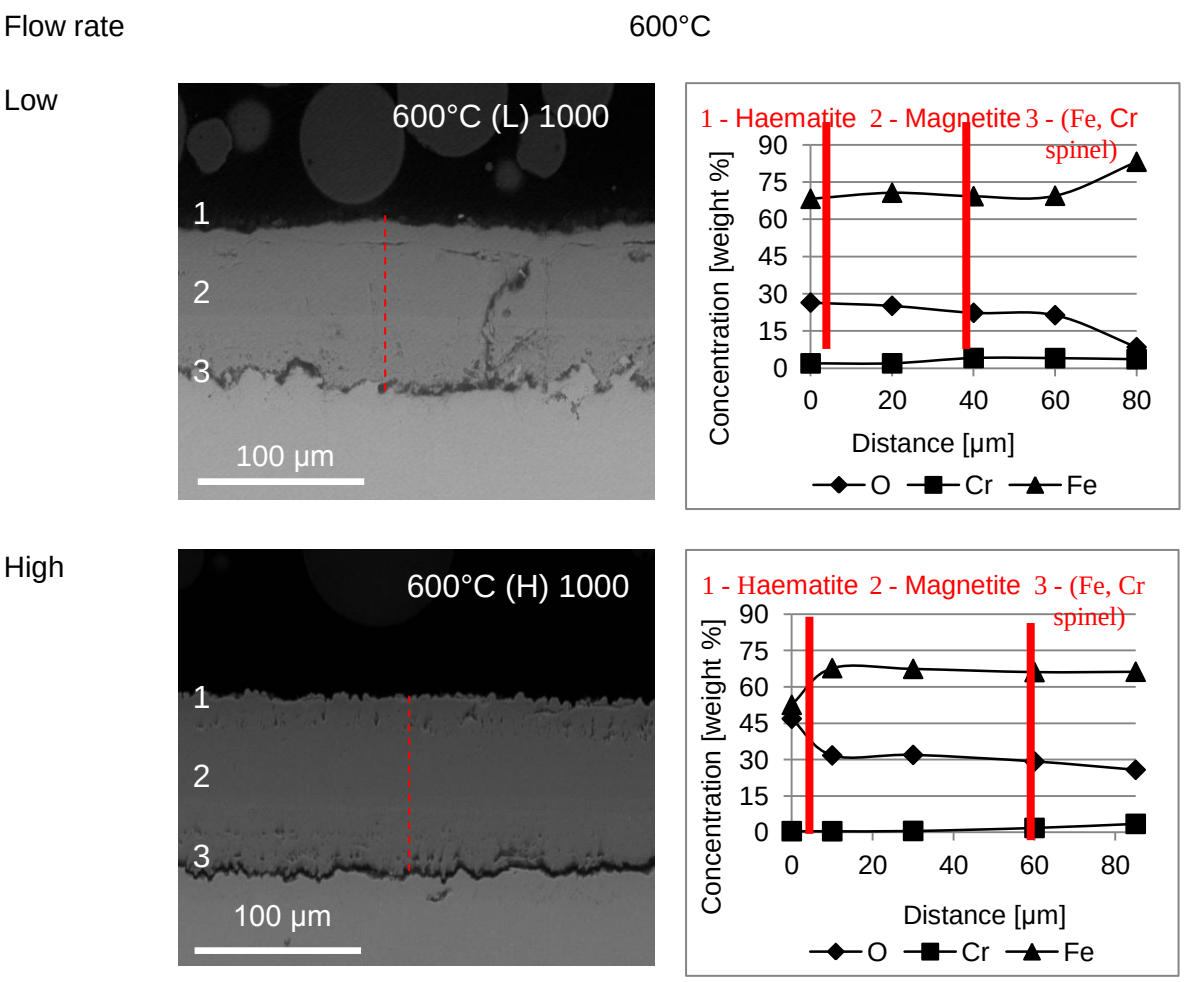

Figure 4-120 BSE SEM pictures + EDX spot scans of the scale formed on bridge – shaped T23 after 1000 hours exposure at 600°C with different steam flow rates

Flow rate

650°C

Low

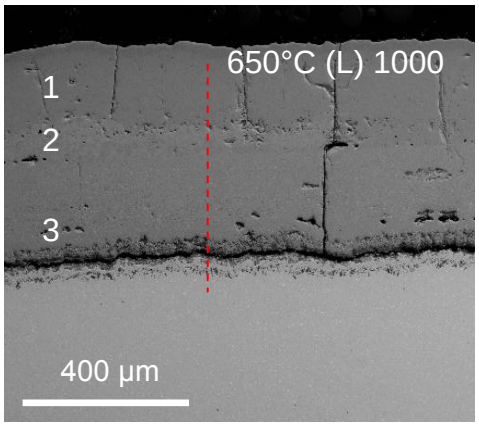

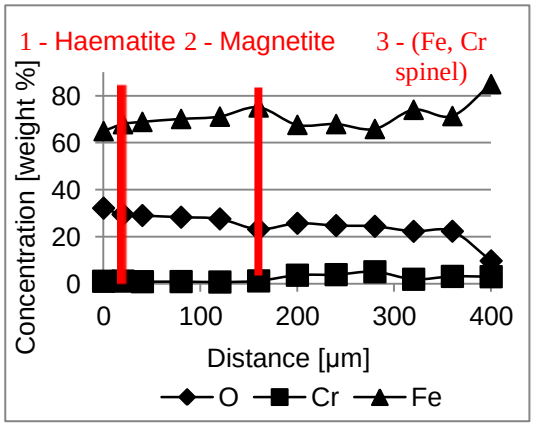

Middle

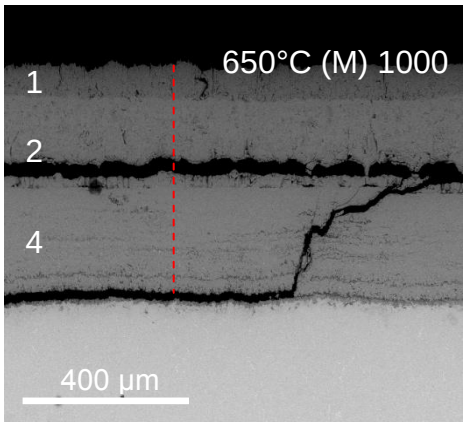

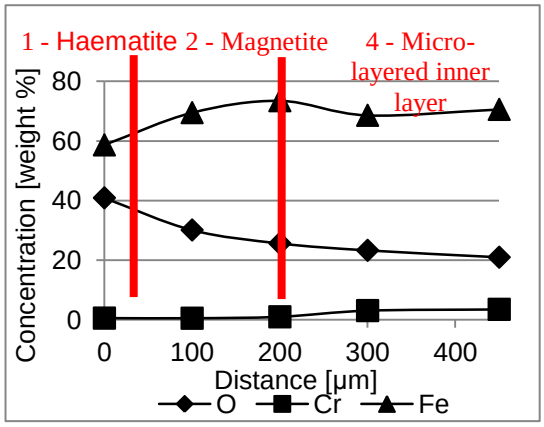

High

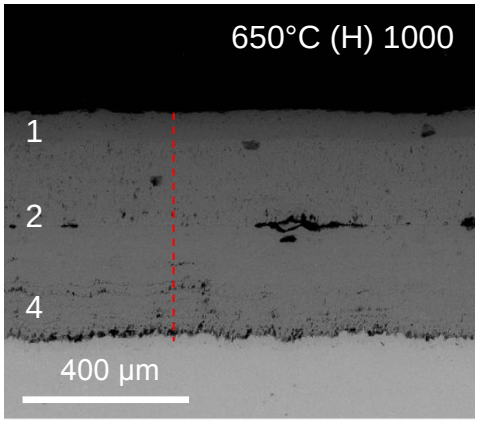

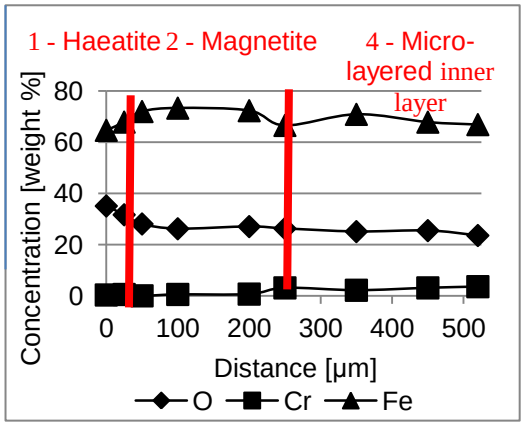

Figure 4-121 BSE SEM pictures + EDX spot scans of the scale formed on bridge – shaped T23 after 1000 hours exposure at 650°C with different steam flow rates

Flow rate 700°C

Low

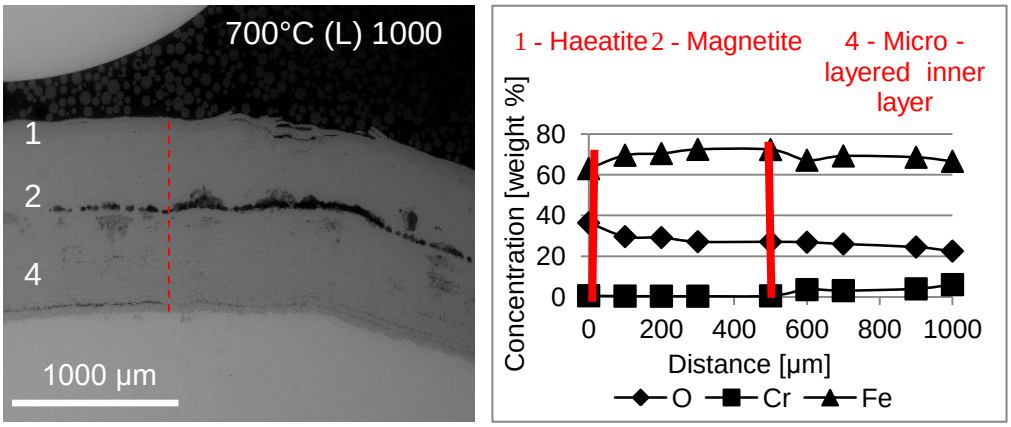

Middle

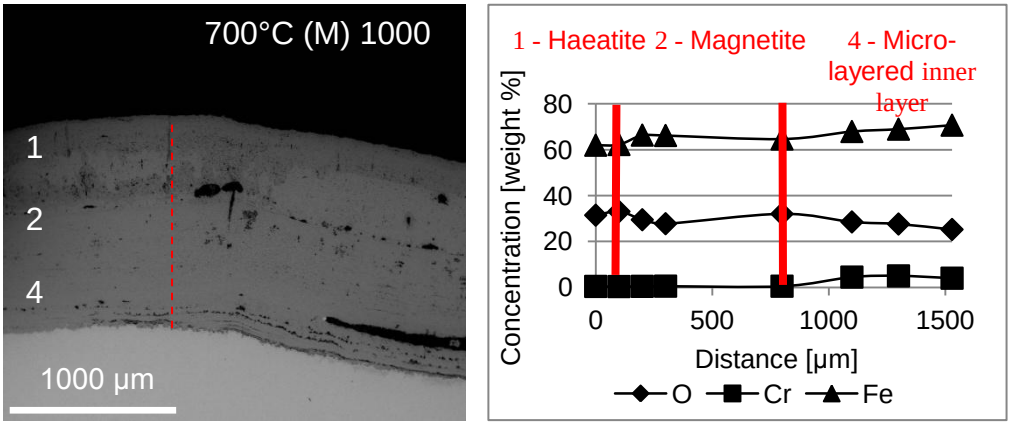

High

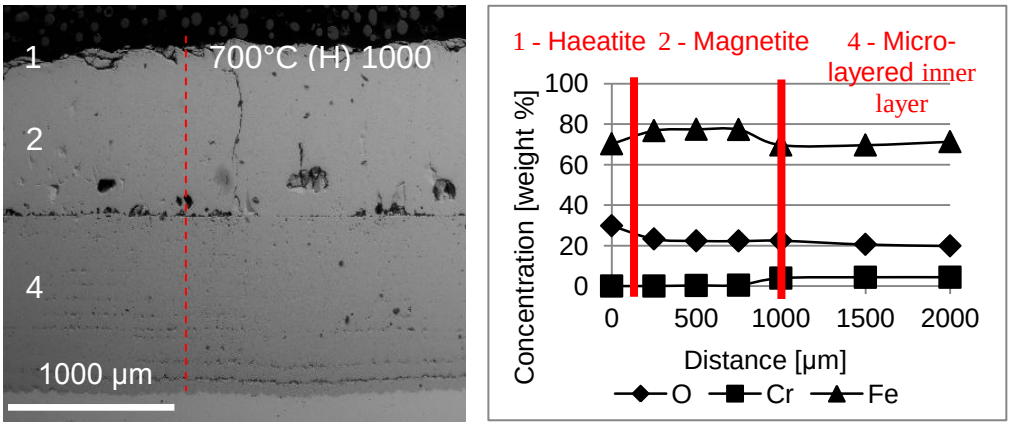

Figure 4-122 BSE SEM pictures + EDX spot scans of the scale formed on bridge – shaped after 1000 hours exposure at 700°C with different steam flow rates

Flow rate 750°C

Low

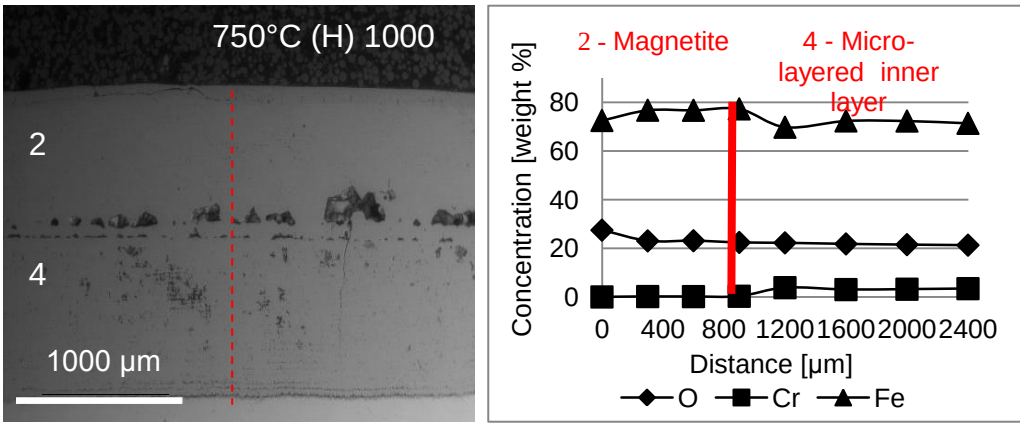

Figure 4-123 BSE SEM picture + EDX spot scans of the scale formed on bridge – shape T23 after 1000 hours exposure at 750°C with low steam flow rate

The oxide scales also vary with the steam conditions, there is a significant change at 650°C (H) when the micro-layered inner scales formed in addition to haematite at the outer surfaces (most of the specimens are covered with the red oxide). The increased steam flow rates (M, H) led to the formation of the thicker oxides (Figure 4-120 - Figure 4-122), under some exposure conditions the impact of the steam flow rate seems to be slightly more significant than temperature (750°C (L) and 700°C (M)). Moreover, steam velocity influences formation of haematite and the micro-layered inner scales.

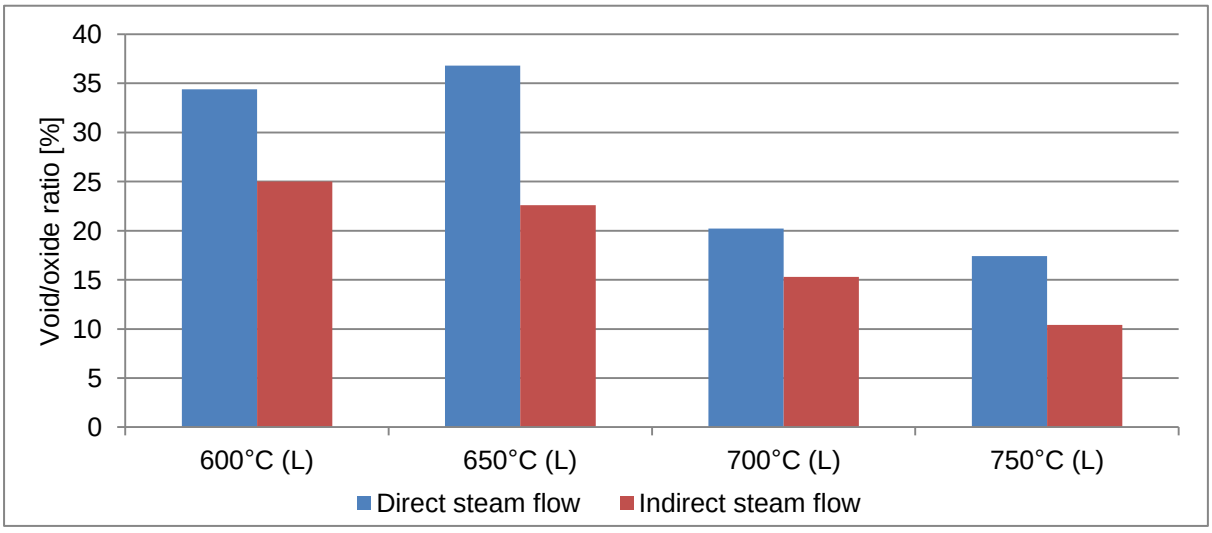

Figure 4-124 Voids/oxide for T23 bridge - shaped specimens after 1000 hours exposure - temperature effect

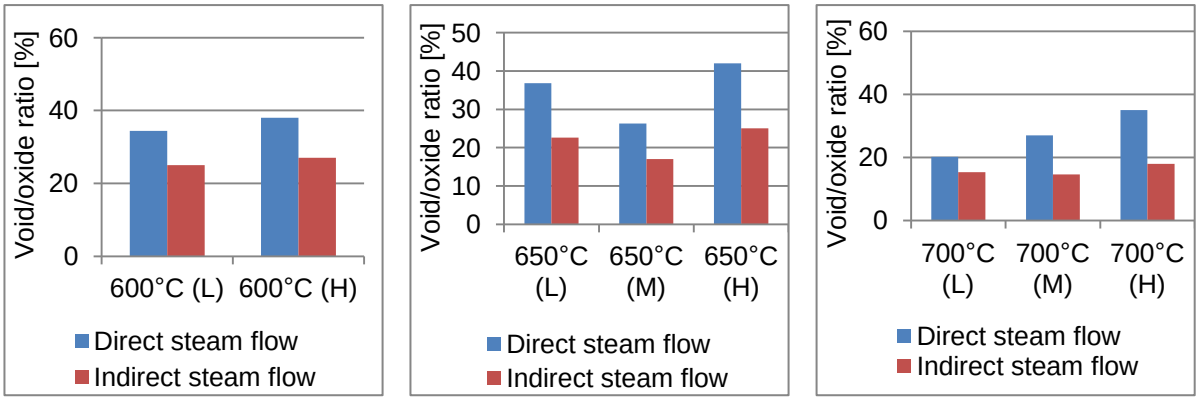

Figure 4-125 Voids/oxide for T23 bridge - shaped specimens after 1000 hours exposure – steam flow rate effect

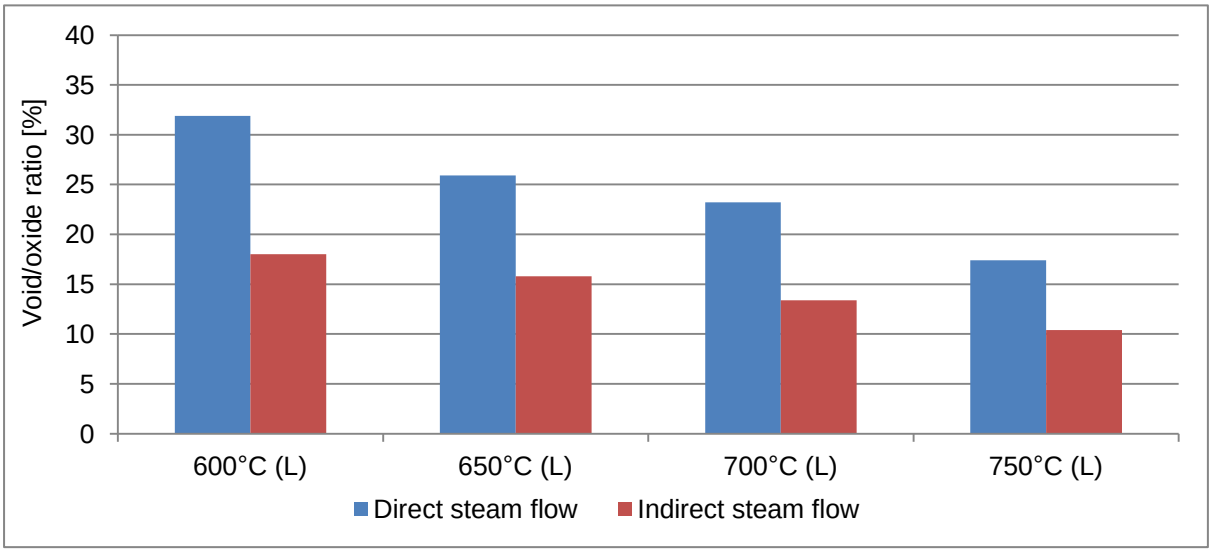

Figure 4-126 Voids/oxide for T23 curve - shaped specimens after 1000 hours exposure in the temperature between 600-750°C – temperature effect

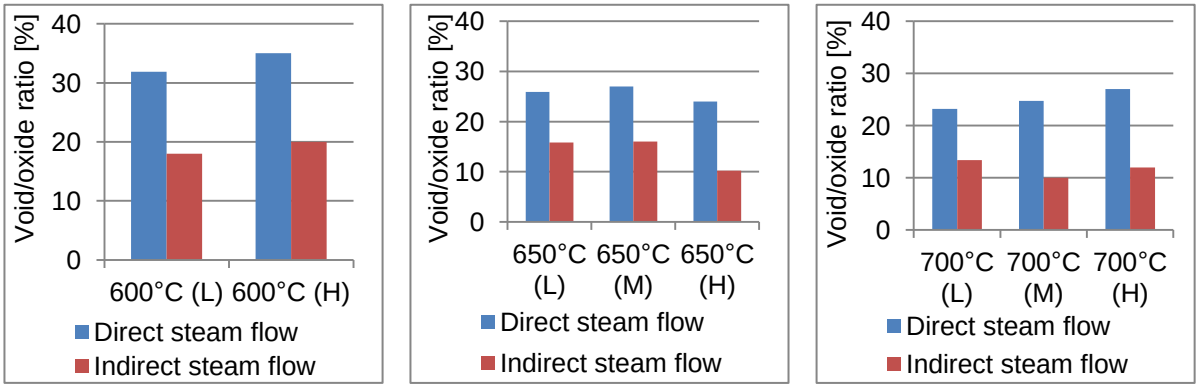

Figure 4-127 Voids/oxide for T23 curve - shaped specimens after 1000 hours exposure – steam flow rate effect

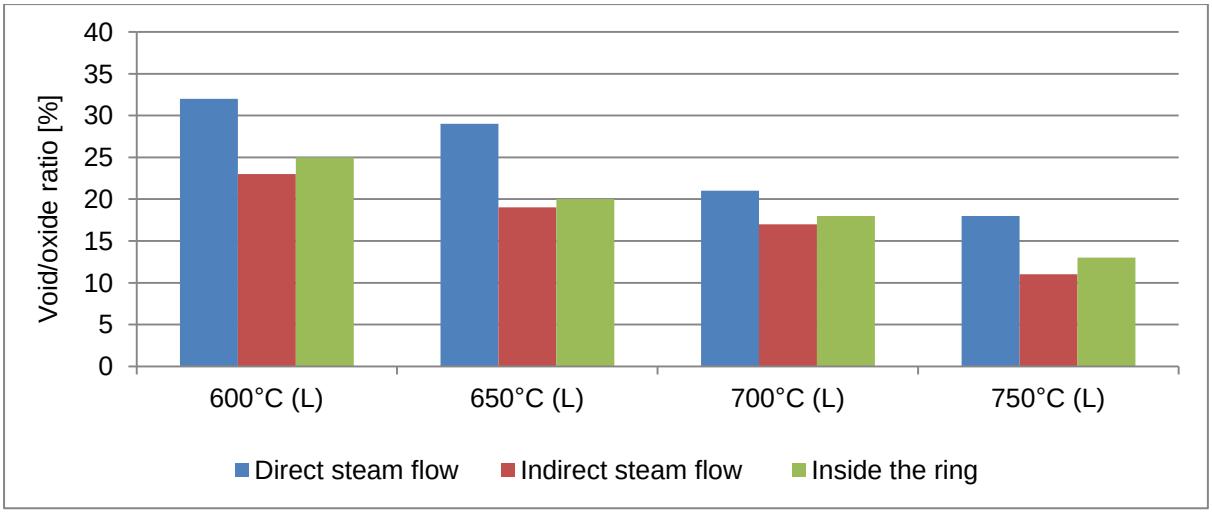

Figure 4-128 Voids/oxide for T23 ring - shaped specimens after 1000 hours exposure in the temperature between 600-750°C – temperature effect

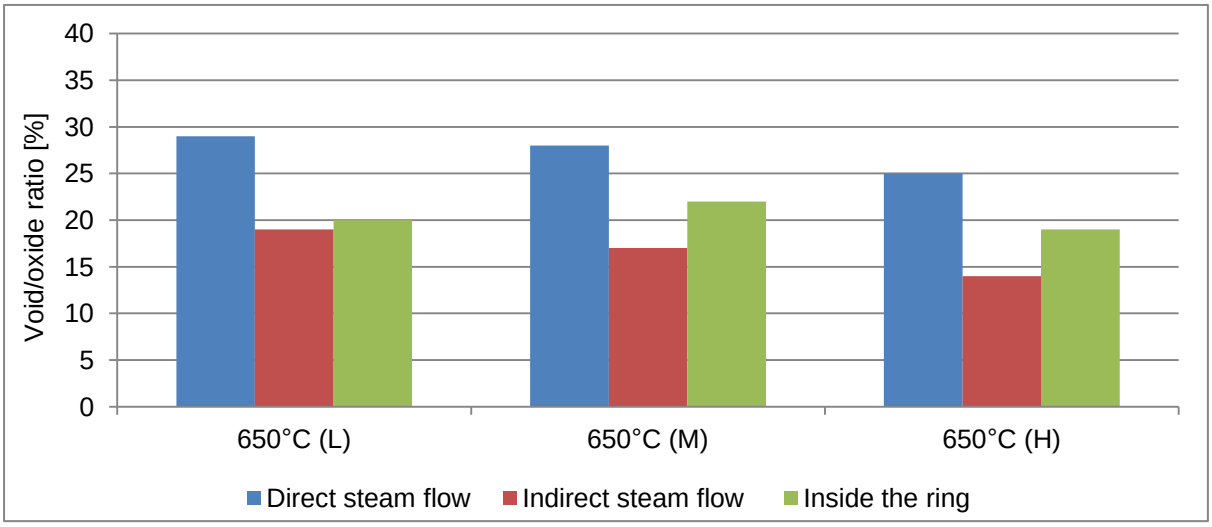

Figure 4-129 Voids/oxide for T23 ring - shaped specimens after 1000 hours exposure - steam flow rate effect

The orientation of the specimen relative to the steam flow is believed to have an impact on thicknesses of the scales formed (Figure 4-130 - Figure 4-133) as well as the voids formation (Figure 4-124 - Figure 4-129). Analysis of the SEM and optical microscope pictures, obtained with, of the scales formed on different shaped specimens (curve and ring) and under different conditions (temperatures and steam flow rates) showed that scales facing the direct flow are thicker. Moreover, the parts of the specimens facing the direct steam flow rate show higher voidage levels (Figure 4-124 - Figure 4-129).

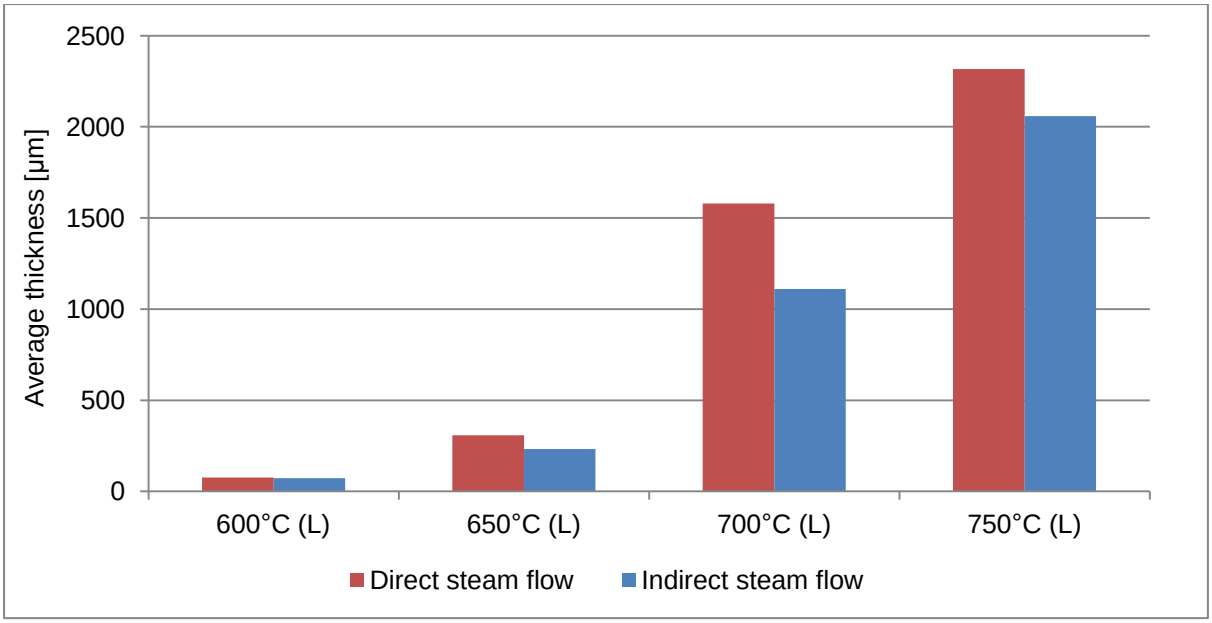

Figure 4-130 Changes in scale thickness on T23 curve – shaped specimens with orientation against steam flow - temperature effect

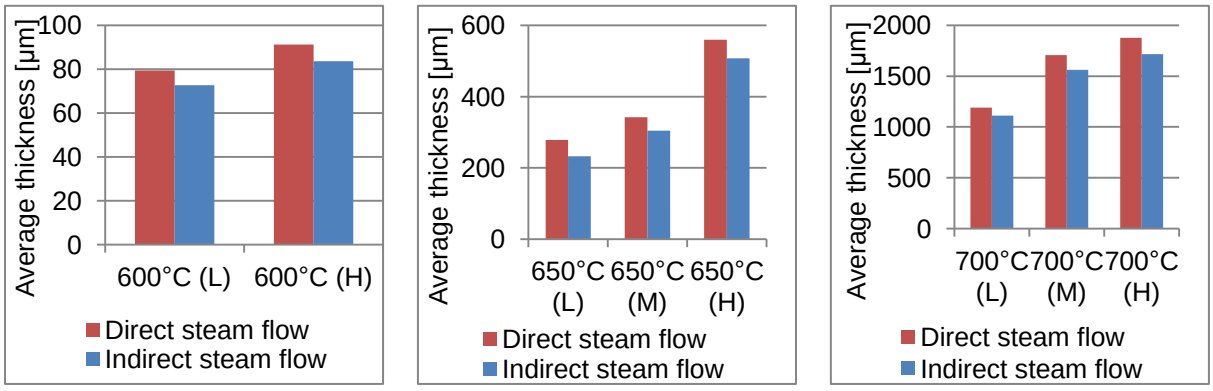

Figure 4-131 Changes in scale thickness on T23 curve – shaped specimens with orientation relative to steam flow

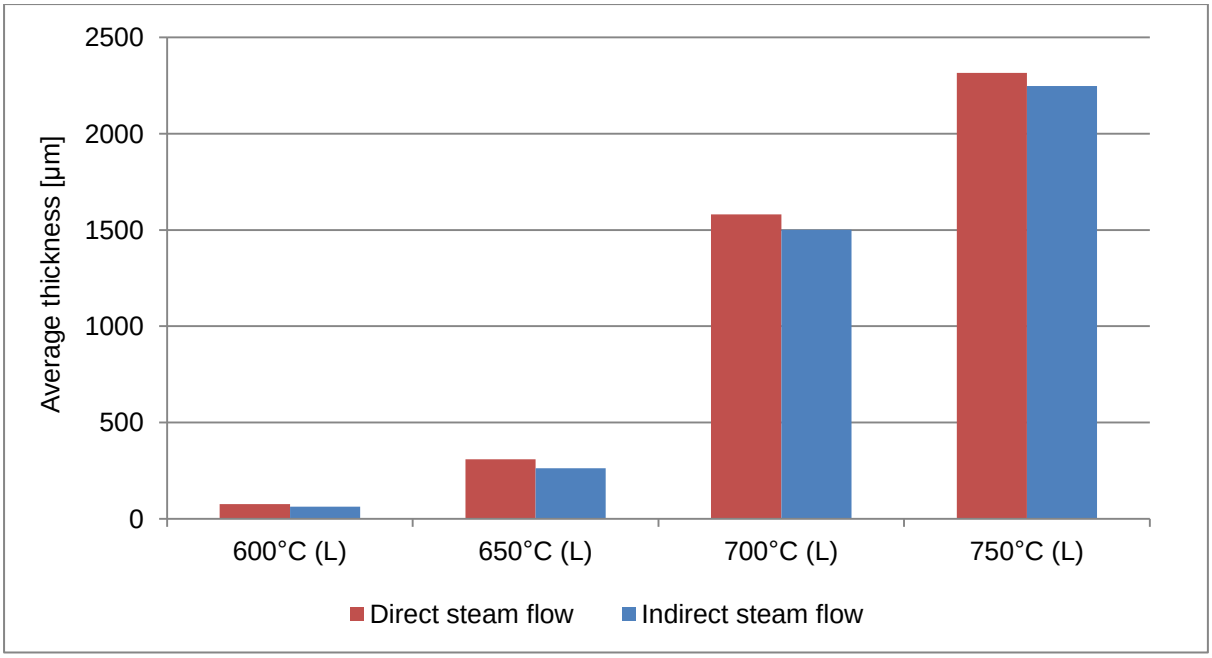

Figure 4-132 Changes in scale thickness on T23 ring – shaped specimens with orientation against steam flow - temperature effect

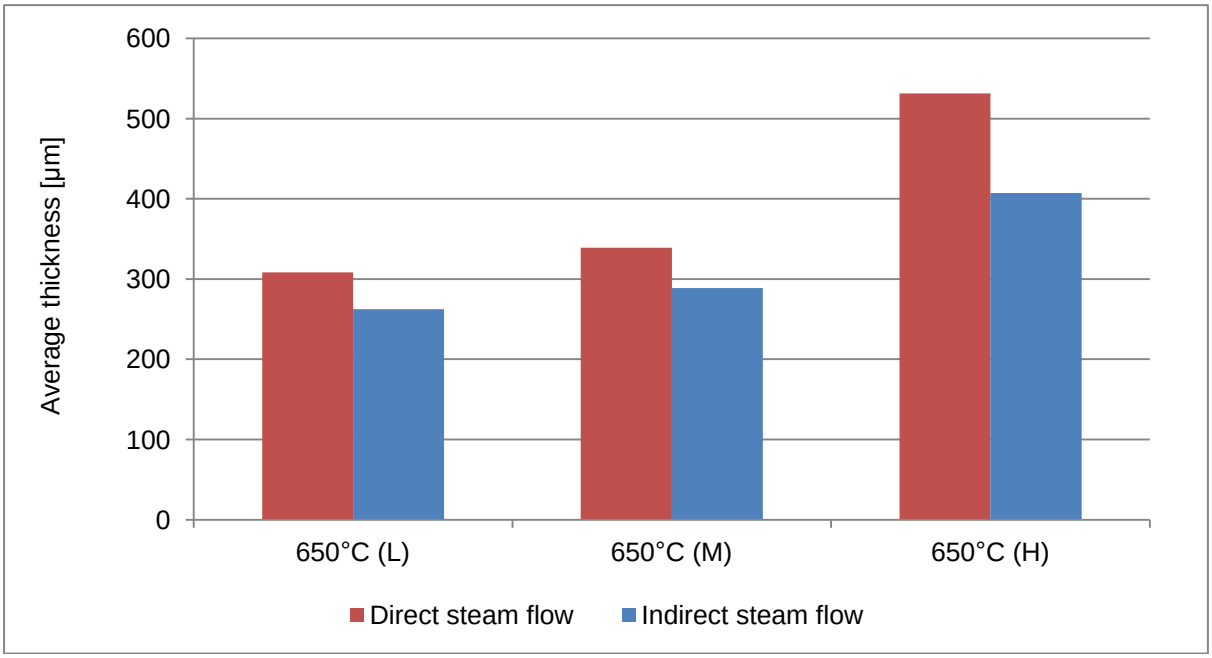

Figure 4-133 Changes in scale thickness on T23 ring – shaped specimens with orientation against steam flow - steam flow rate effect

4.2.2.1.2 T92 (9 Cr)

T92 is significantly more resistant to steam oxidation than T23 above 600°C, which is associated with larger chromium content. Under the conditions tested, the specimens developed double-layered scales: inner iron/chromium spinel and outer magnetite. An example of mapping of the typical scale found on T92 exposed to steam is presented Figure 4-134. It shows two distinctive regions; an inner scale with chromium rich oxide and outer with iron oxides.

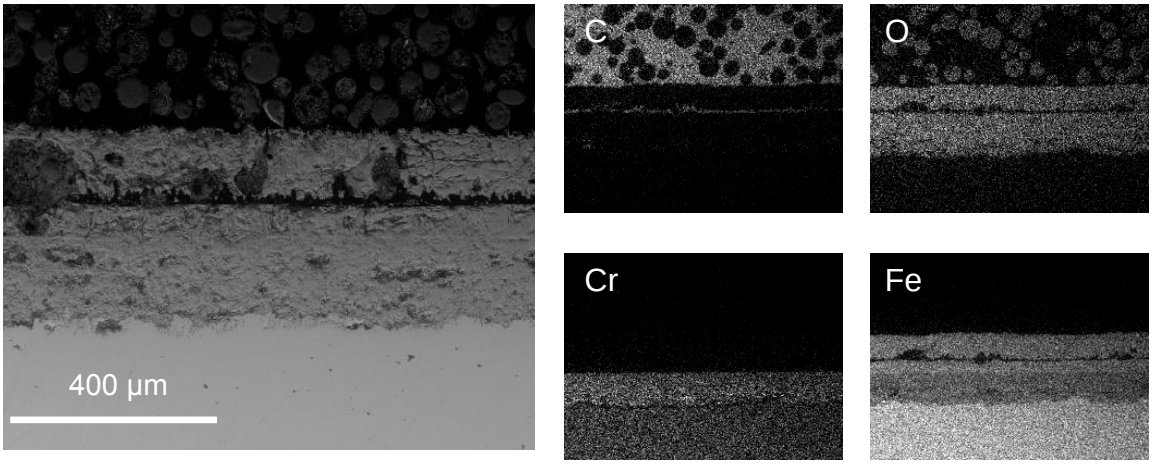

Figure 4-134 BSE SEM + EDX maps of oxide scale formed on T23 at 650°C with low steam flow after 1000 hour exposure

Exposures of T92 at 600 - 750°C resulted in thinner scale formation than were identified for T23, however at lower temperatures the scales formed tend to exfoliate. Analysis of the results showed that the scales exfoliated above or at the interface between the inner and outer layers. The specimens shape influences the levels of spallation; it is more significant for bridge and curve - shaped specimens than for full rings (A.2).

Flow rate 600°C

Low

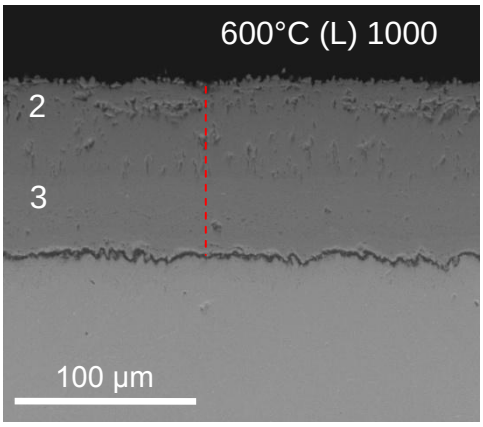

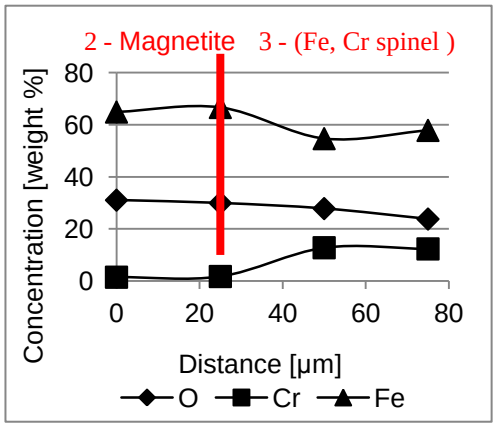

High

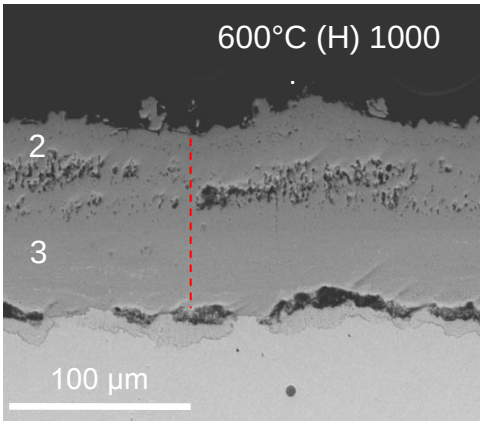

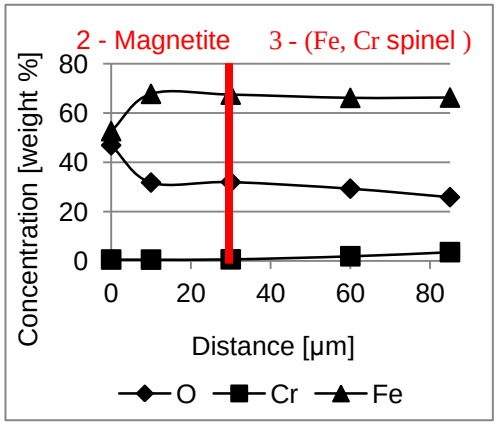

Figure 4-135 BSE SEM pictures + EDX spot scans of the scale formed on T92 after 1000 hours exposure at 600°C with different steam flow rates

Flow rate 650°C

Low

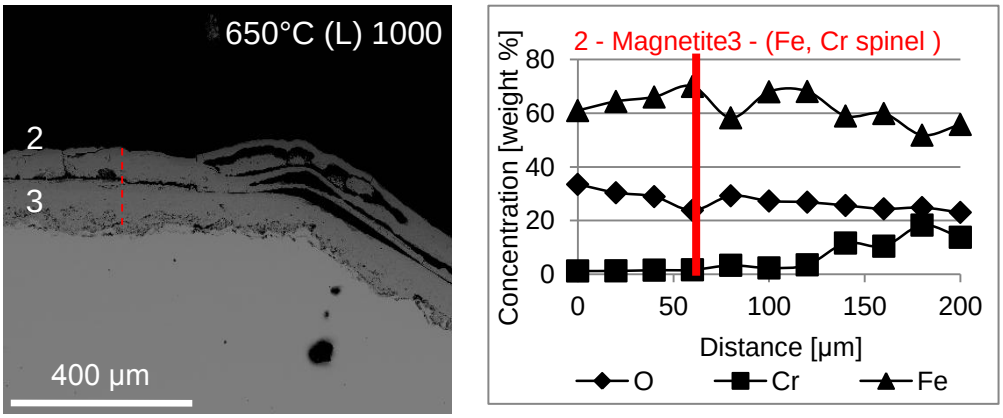

Middle

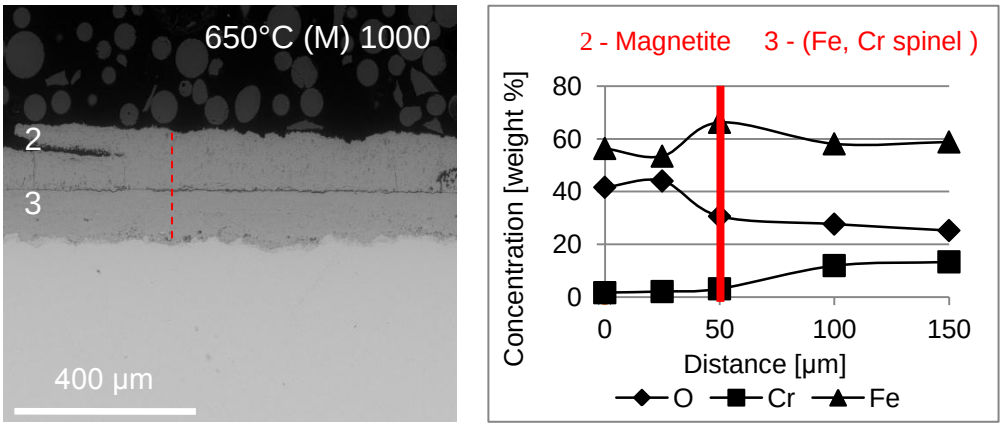

High

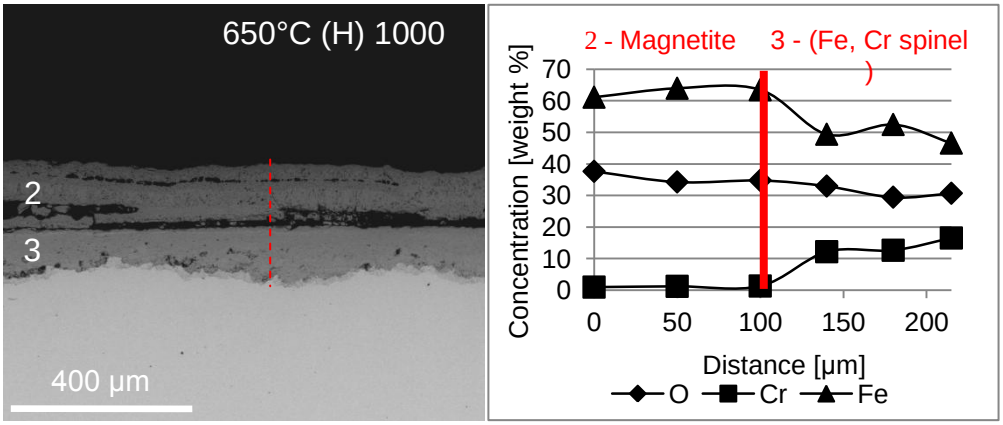

Figure 4-136 BSE SEM pictures + EDX spot scans of the scale formed on T92 after 1000 hours exposure at 650°C with different steam flow rates

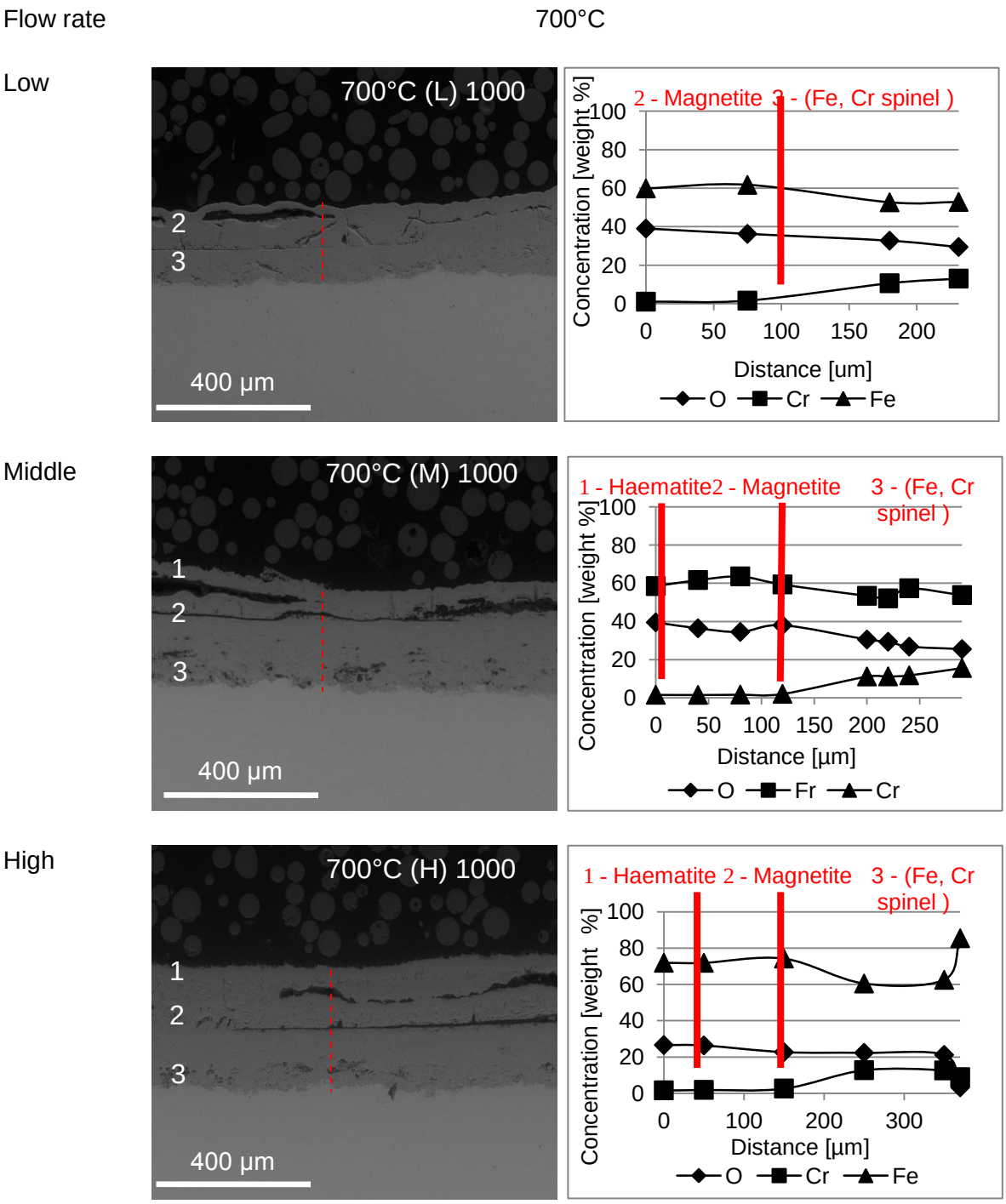

Figure 4-137 BSE SEM pictures + EDX spot scans of the scale formed on T92 after 1000 hours exposure at 700°C with different steam flow rates

Flow rate 750°C

Low

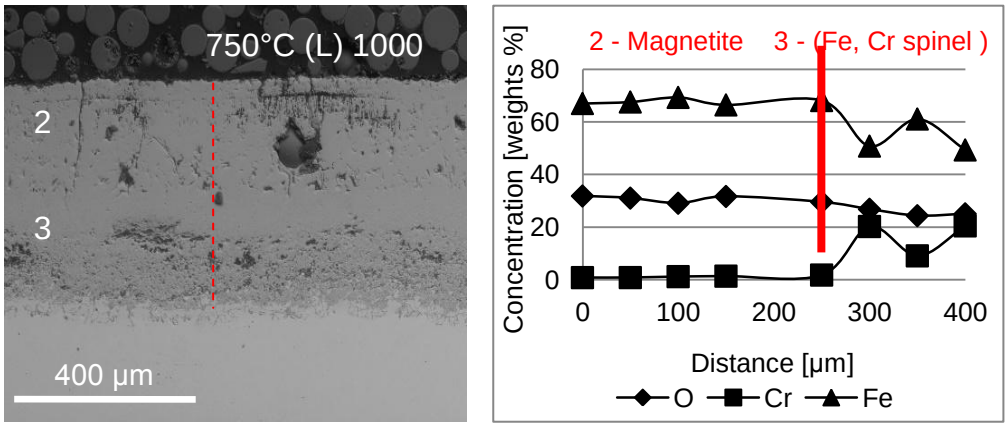

Figure 4-138 BSE SEM picture + EDX spot scan of the scale formed on T92 after 1000 hours exposure at 750°C

Figure 4-135 - Figure 4-138 indicated that there was no change in the scales structure with temperature in contrast to T23. However, the steam flows have an impact on the haematite formation. Specimens exposed to the middle steam flow rate showed the formation of Fe_2O_3 patches on the surface of magnetite, whereas under the highest steam flow rate whole surfaces facing the direct steam flow are covered with it. Due to at least partial scale spallation there is not a possibility of identifying the impact of steam flow rate and specimen orientation relative to the steam flow on scales thicknesses. However, there is a clear impact on scale spallation and void formation within the oxides still adherent to the surface. Analysis of the SEM pictures showed that at the interfaces between inner and outer layers the voids formed could coalesce into gaps and that could lead to the scale spallation.

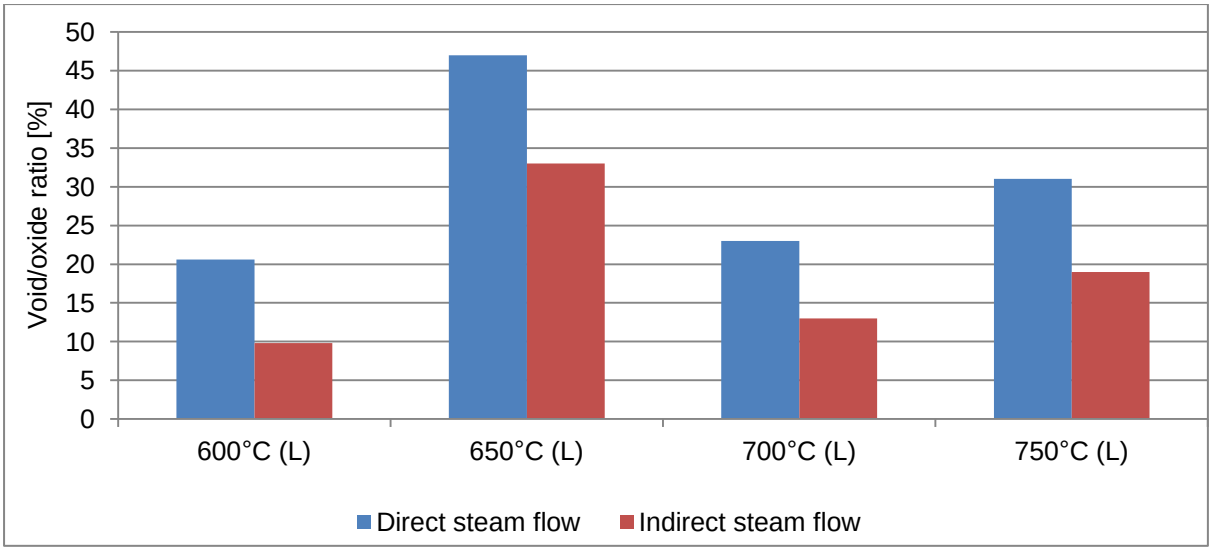

Figure 4-139 Voids/oxide for T92 bridge - shaped specimens after 1000 hours exposure under conditions tested – temperature effect

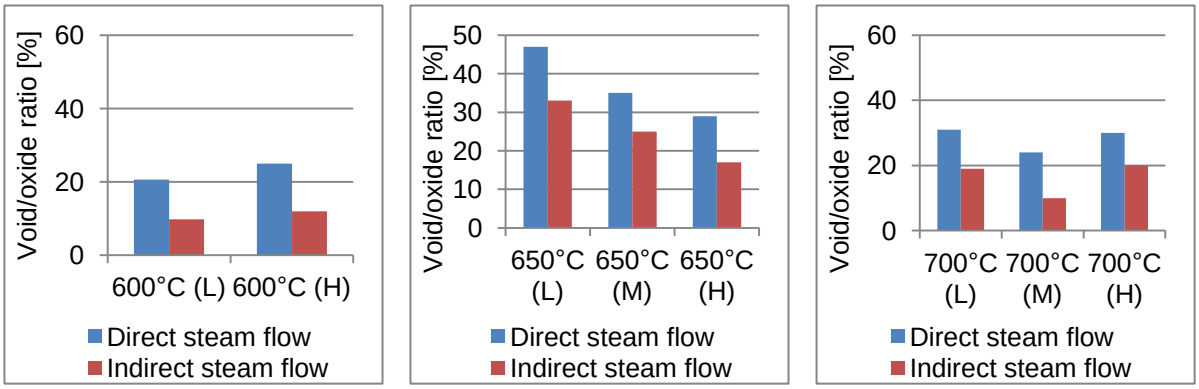

Figure 4-140 Voids/oxide for T92 bridge - shaped specimens after 1000 hours exposure under conditions tested – steam flow rate effect

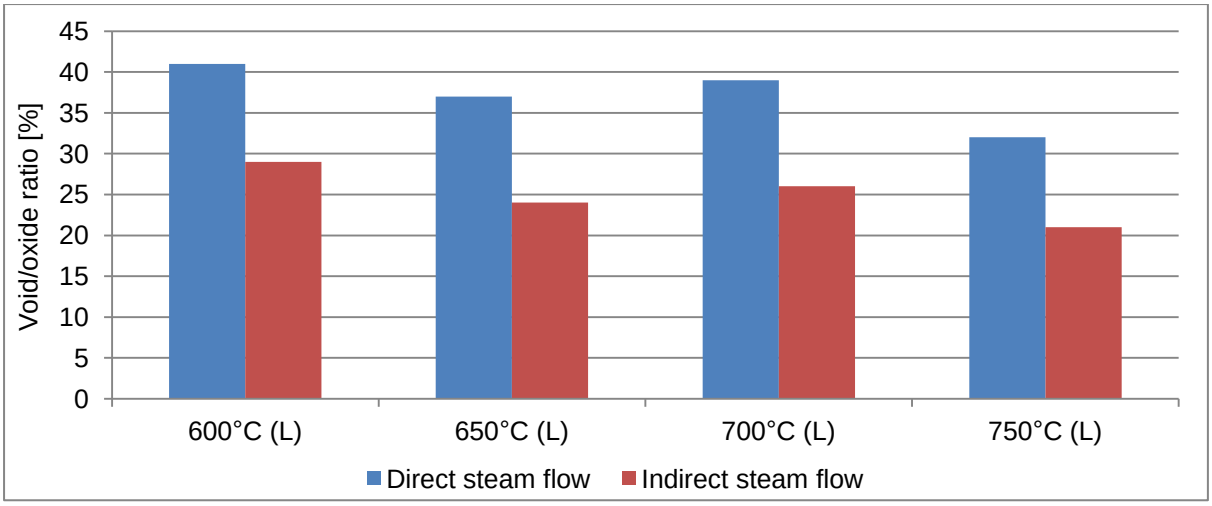

Figure 4-141 Voids/oxide for T92 curve - shaped specimens after 1000 hours exposure under conditions tested – temperature effect

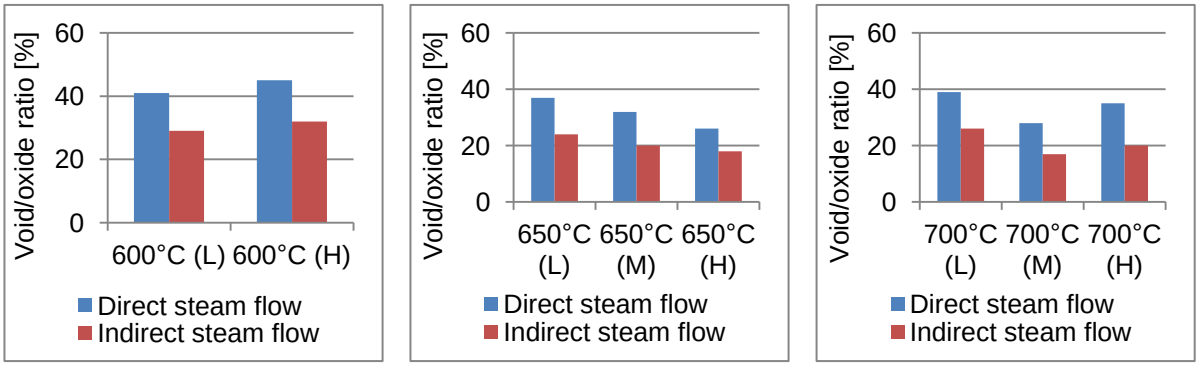

Figure 4-142 Voids/oxide for T92 curve - shaped specimens after 1000 hours exposure under conditions tested – steam flow rate effect

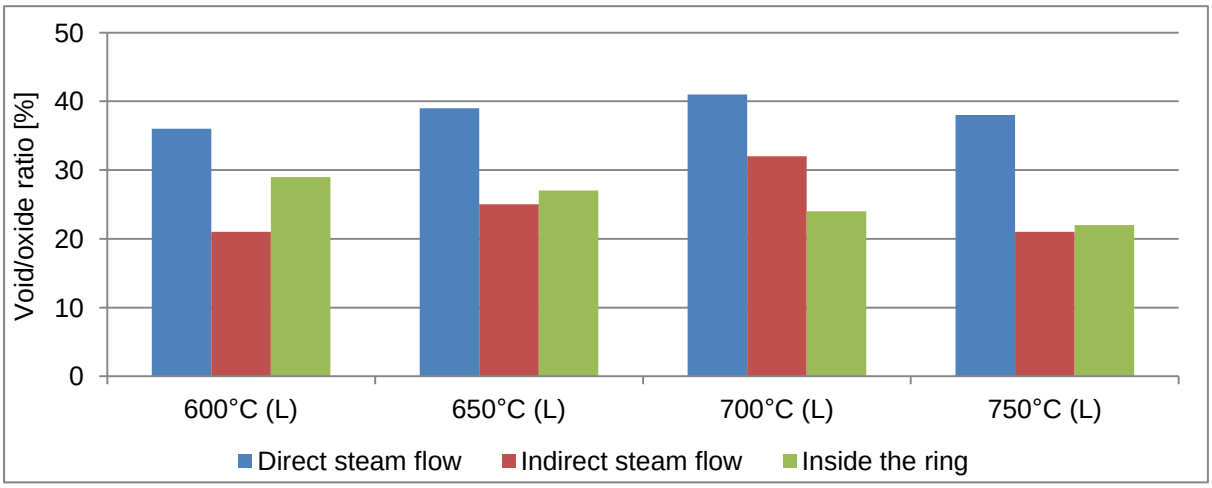

Figure 4-143 Voids/oxide for T92 ring - shaped specimens after 1000 hours exposure under conditions tested – temperature effect

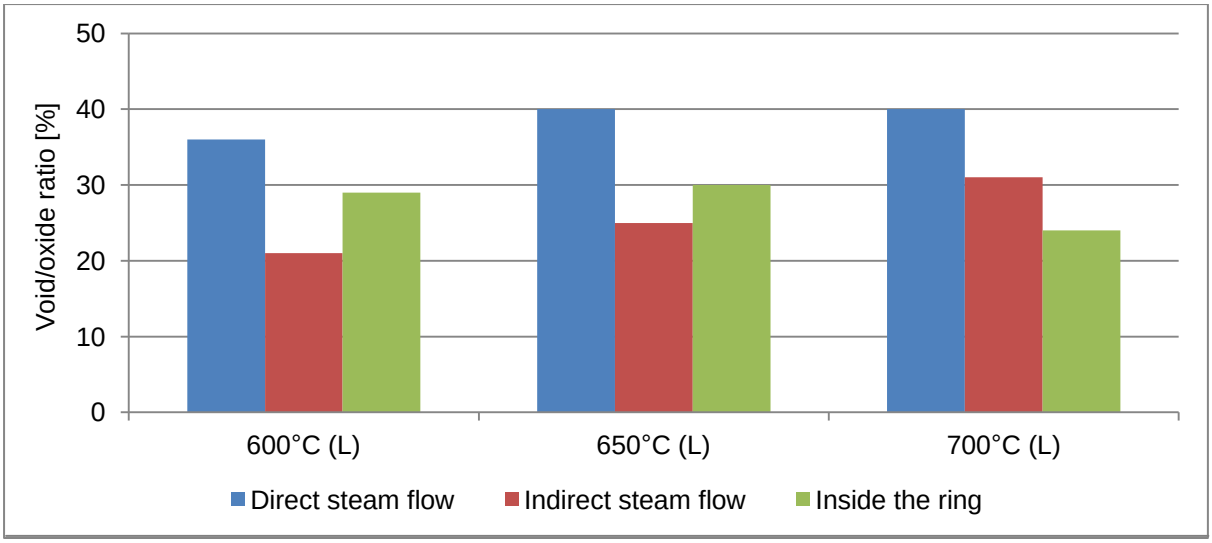

Figure 4-144 Voids/oxide for T92 ring - shaped specimens after 1000 hours exposure under conditions tested – steam flow rate effect

4.2.2.2 Austenitic and nickel-based alloys

This introduction section shows the general finding for the morphology of the cross-section of the austenitic and nickel-based alloys tested. The results describe in this paragraph are for the ground specimens, the results for different surface treatment can be find in section 4.2.2.3. The morphological changes observed on cross-sections through the oxides on austenitic and nickel-based alloys were slow and associated with the formation of thin oxide scales. The properties of these scales change with the chromium content and exposure conditions; however, under these conditions selected the changes are relatively slow in comparison with the ferritics alloys. The austenitic materials exposed can be divided into two groups: with chromium level at ~ 18% (T347HFG and Super 304H) and above 18 % (HR3C and 800H). These groups show different morphological changes, the ~ 18Cr alloys form thicker scales, and also show nodular oxide growth. The number, size of nodules varies firstly with alloy type secondly with exposure conditions. 800H and HR3C are the most resistant austenitic materials studied; their surface oxide grow very slow even at high temperatures and fast steam flow rates. Finally, Inconel 740 does not show significant changes in the scales formed with temperature, steam flow rates or times studied.

4.2.2.2.1 T347HFG

T347HFG exposed to steam in the temperature 600 – 750°C forms thin, protective scales, their thicknesses change with exposure time and temperature and steam flow rate. In general, two kinds of the scales have been identified. Firstly in temperature 600 – 650°C with low steam flow the scales are discontinuous and non-adherent and nodular growths were identified. Secondly at 700 – 750°C and under faster (M, H) steam flow rates the oxides growth involves nodular growth of the scales in the regions where the protective oxides have broken down. The sizes of nodules change with orientation against the steam flow.

The specimens shapes have an impact on the adherence of the scales properties for both bridge and curve – shaped specimens the oxides are non-adherent and are discontinuous. In comparison, the ring samples on the other hand tend to form continues and adherent scales, which improve the performance of the specimen. Nonetheless where protective continuous scales were found to developed, the nodules also formed. Most nodules were identified on the surfaces facing the direct steam flow, there were no nodules found inside the ring specimens.

Analyses of BSE SEM pictures and EDX profiles of through oxides formed on the bridge - shaped specimens under different steam flow rate conditions showed that the change of the steam flow rates improved the formation of continuous, adherent and protective scales.

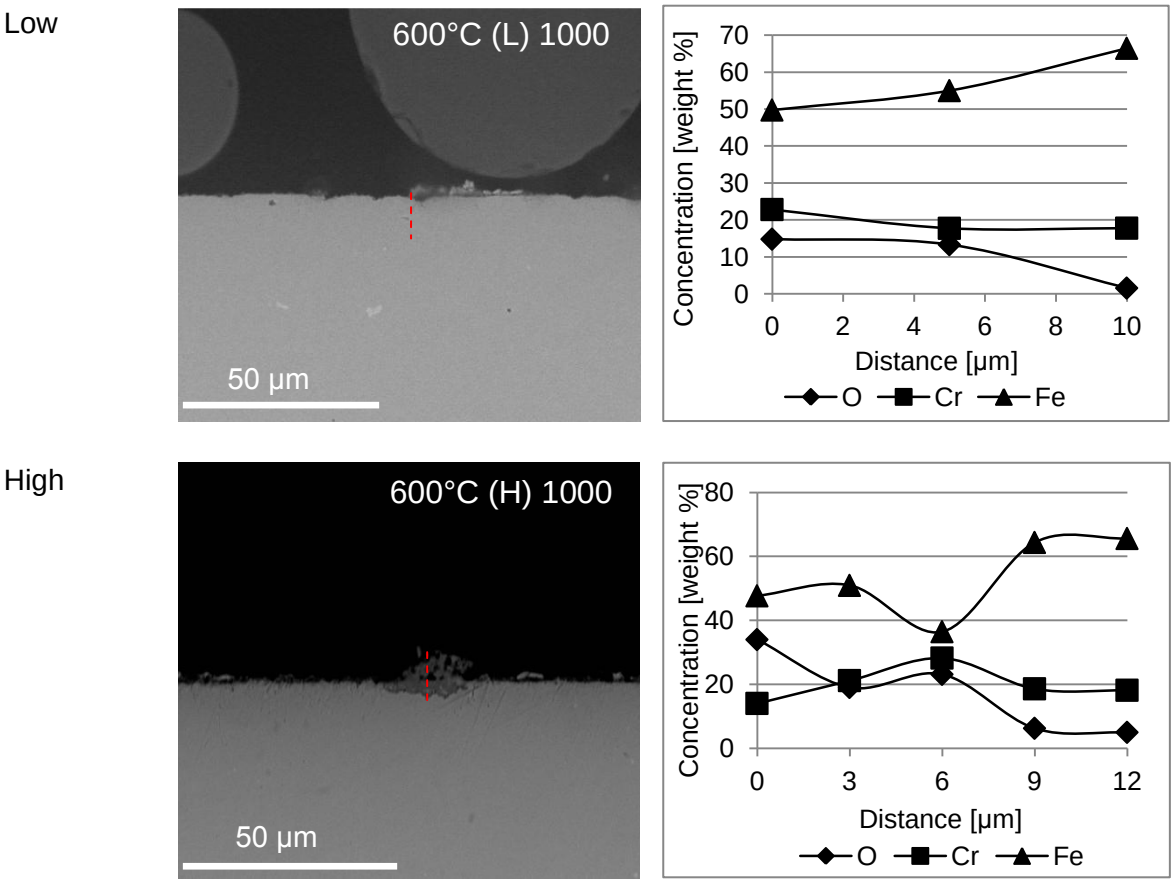

Figure 4-145 BSE SEM pictures + EDX spot scans of the scale formed on bridge – shaped T347HFG after 1000 hours exposure at 600°C with different steam flow rates

At 600°C, regardless of the steam flow, T347HFG showed slow changes in the scale structure, the main difference between exposure at 4 and 40 mm/s steam flow was the formation of nodules. The nodules were identified in the regions facing the steam. EDX analysis of the nodules showed two main constituents, which are iron and chromium oxides. Further exposure at this condition would be expected to cause further similar damage to the alloy and finally the whole surface would be covered with iron chromium oxides.

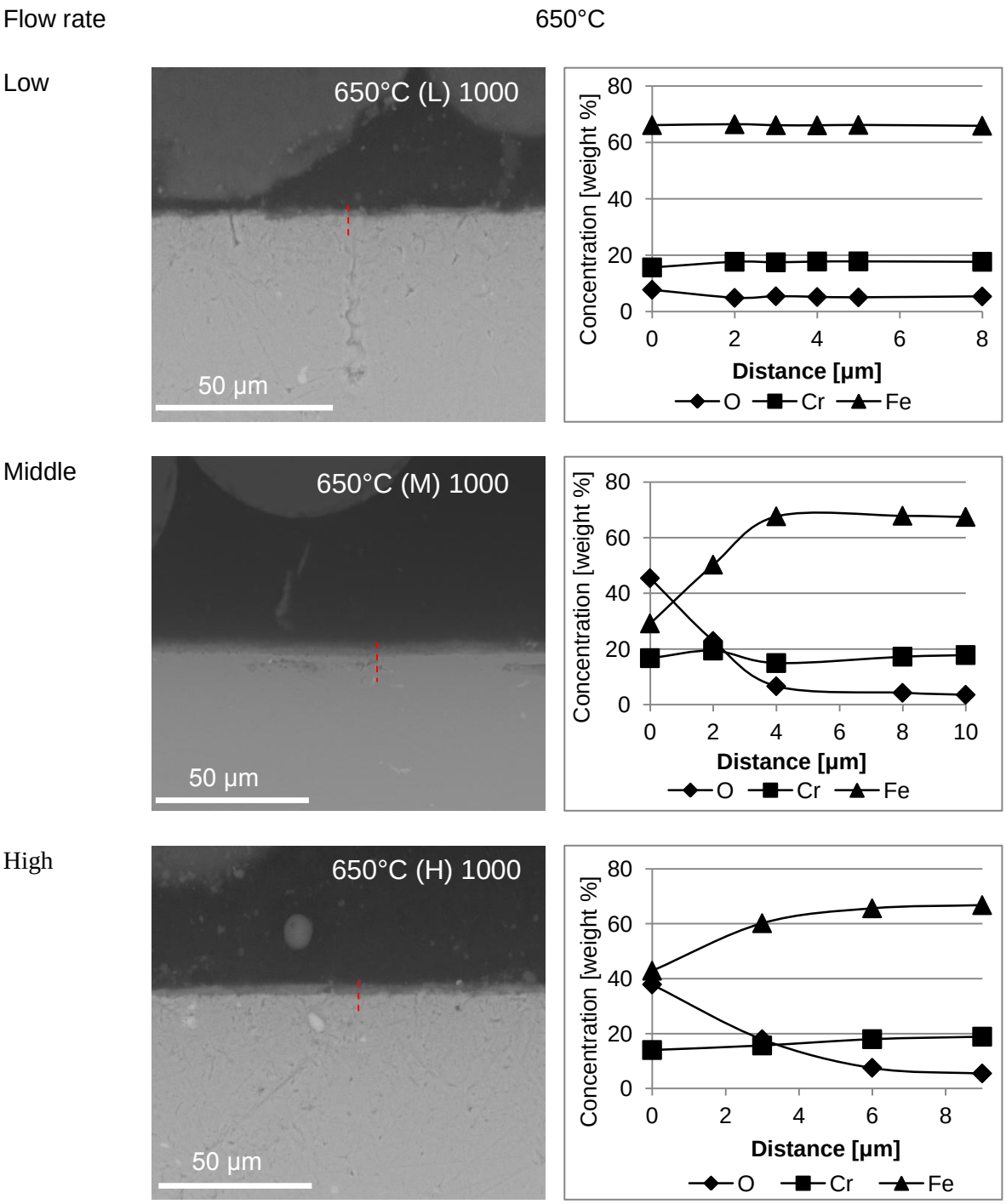

Figure 4-146 BSE SEM pictures + EDX spot scans of the scale formed on bridge – shaped T347HFG after 1000 hours exposure at 650°C with different steam flow rates

Figure 4-146 shows that an increase in the steam flow rate accelerates the formation of the oxides on the surface. The main constituents of the layers formed are identified as iron and chromium oxides. This oxide is expected to be protective and

suppress non-protective oxide growth; however at faster steam flow rate it can break down and nodules will develop.

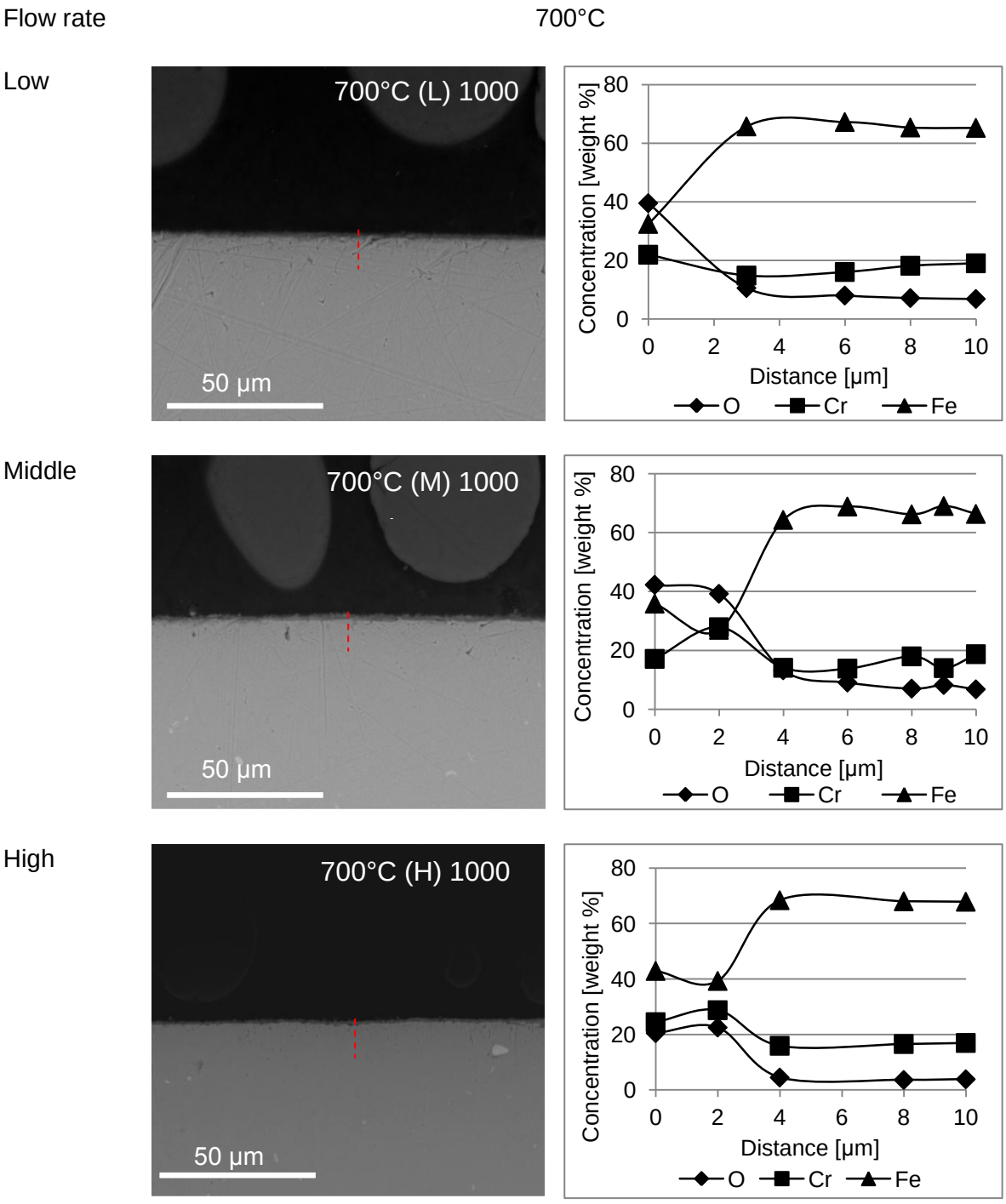

Figure 4-147 BSE SEM pictures + EDX spot scans of the scale formed on bridge – shape T347HFG after 1000 hours exposure at 700°C with different steam flow rates

At 700°C regardless of the steam flow rate, there is a formation of thin, mixed iron and chromium scale. Faster steam flow rates result in formation of a thicker scale;

however these are still just a couple of micron thick. Such scales exhibit good oxidation resistance.

Flow rate	750°C
Low	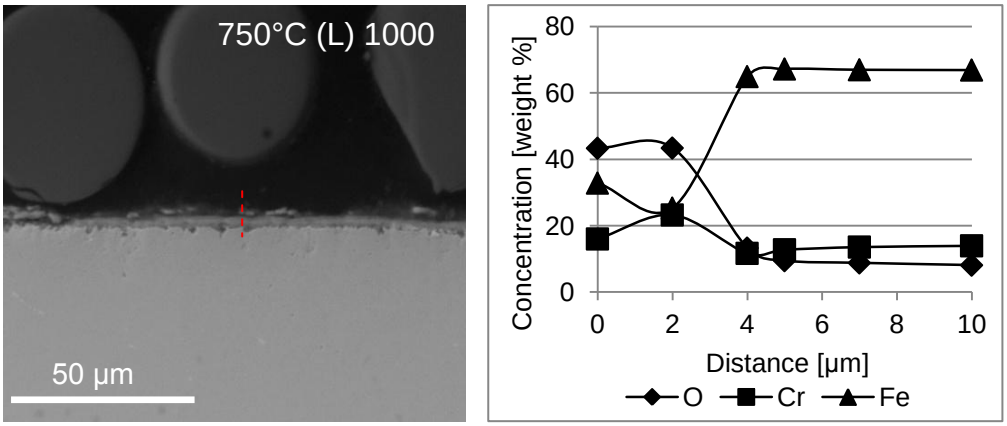

Figure 4-148 BSE SEM picture + EDX spot scan of the scale formed on bridge – shaped T347HFG after 1000 hours exposure at 750°C with low steam flow rate

The nodules formed on the T347HFG are double layered with inner layers of (Fe, Cr) spinel and outer layers of magnetite. Example of the nodule formed on T347HFG is presented in Figure 4-149.

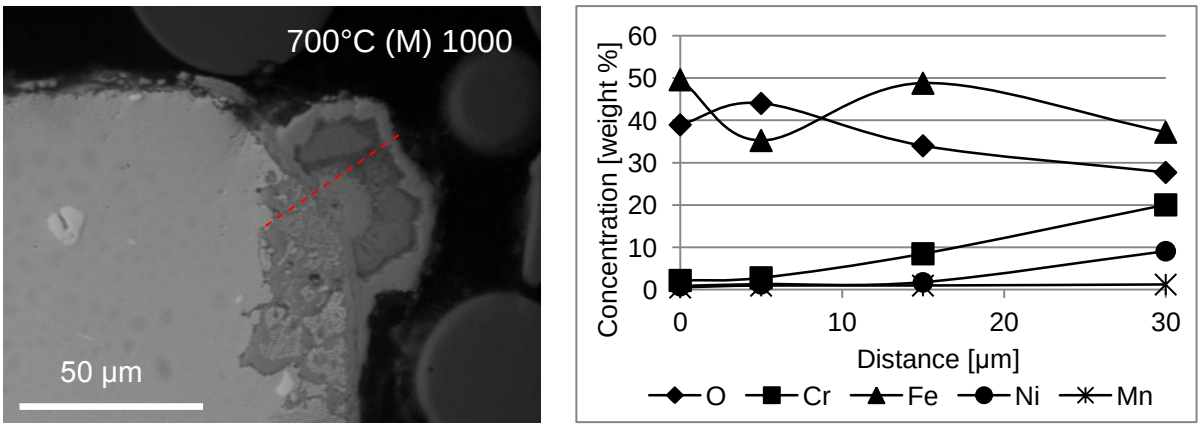

Figure 4-149 BSE SEM picture + EDX spot scan of nodule formed on bridge – shaped T347HFG after 1000 hours exposure at 700°C with middle steam flow rate

4.2.2.2.2 Super 304H

Super 304H shows different oxidation behaviour compared to T347HFG. There oxide scales formed on Super 304H changes with temperature. In the temperature range 600 – 700°C the scales formed are discontinuous and non-adherent. In comparison, at 750°C and under faster steam flow conditions the scales become more adherent and continuous with the thicknesses of around 4 µm. In some locations the scales seem to break down and the nodules start to develop. There is a clear increase of the size and number of the nodules developed with temperature and steam flow rate. Analyses of the SEM pictures and EDX profiles of the bridge specimens exposed at different steam flow rates indicated that the steam flow rate influences the diffusion of the ions to the surface, which accelerates formation of the protective oxides.

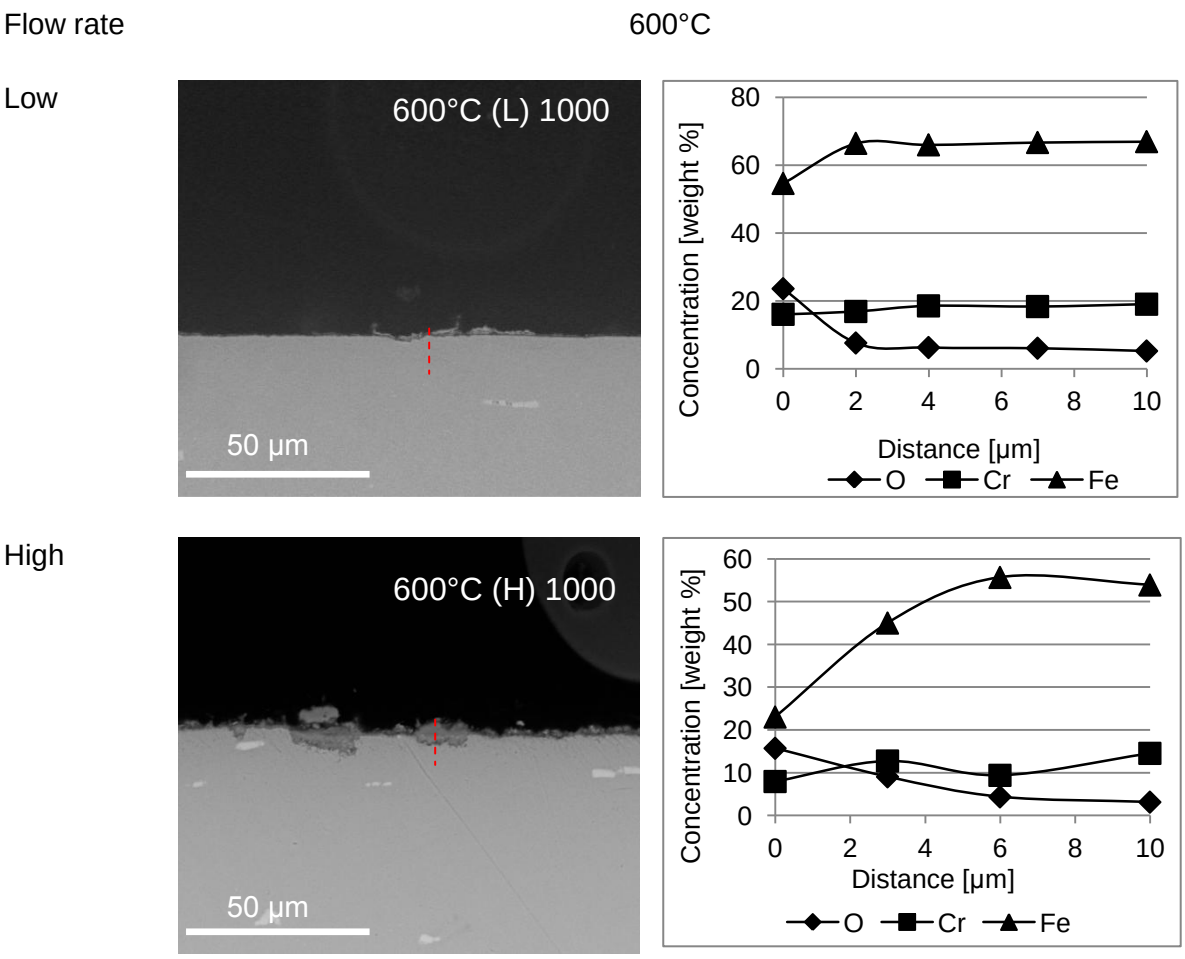

Figure 4-150 BSE SEM pictures + EDX spot scans of the scale formed on bridge – shaped Super 304H after 1000 hours exposure at 600°C with different steam flow rates

As it was indentified for T347HFG increased steam flow rate clearly increases the rate of growth of the oxide scales as well as the development of nodular growth in the regions where the protective scales have exfoliated.

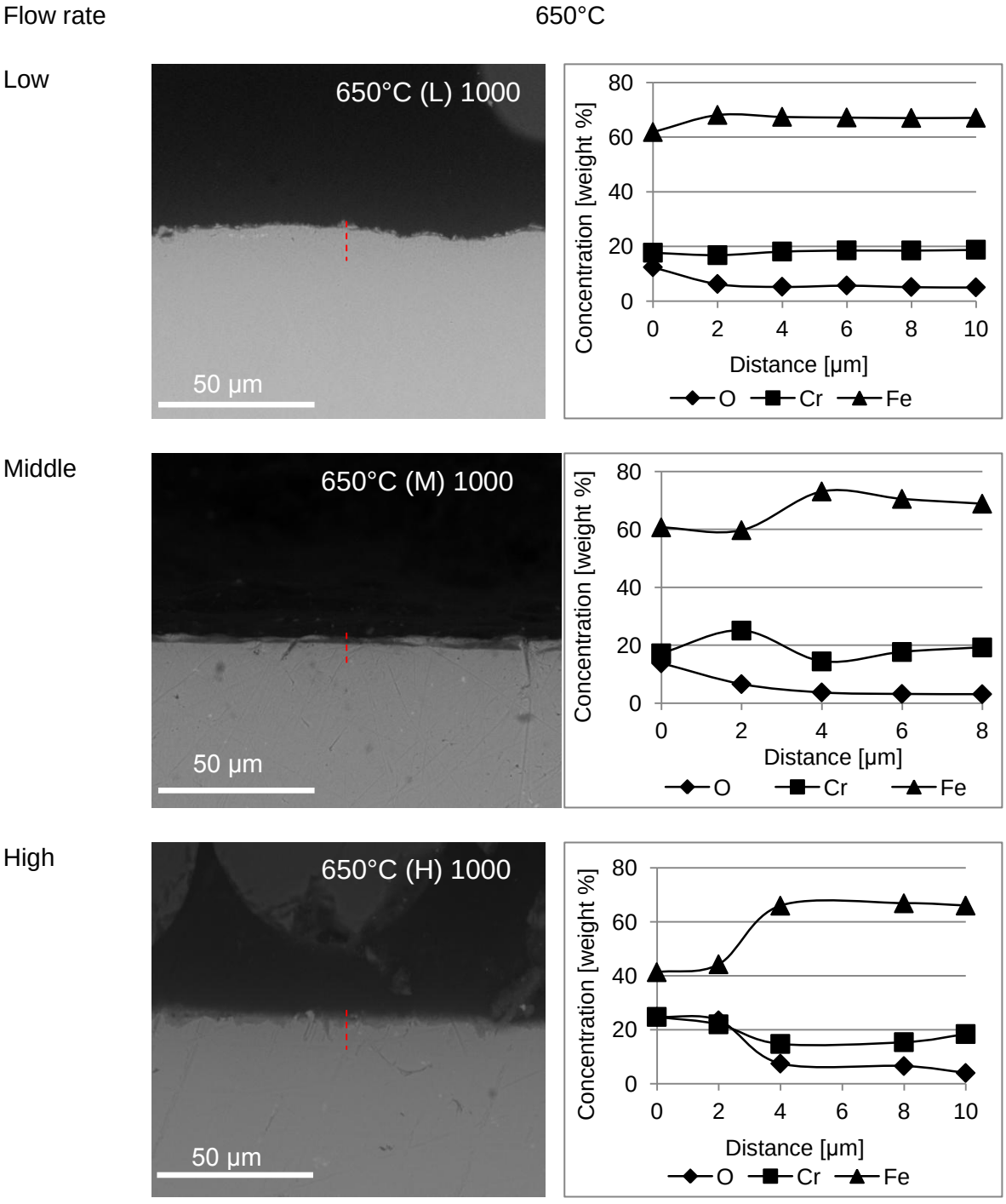

Figure 4-151 BSE SEM pictures of the scales + EDX spot scans of formed on bridge – shaped Super 304H after 1000 hours exposure at 650°C with different steam flow rates

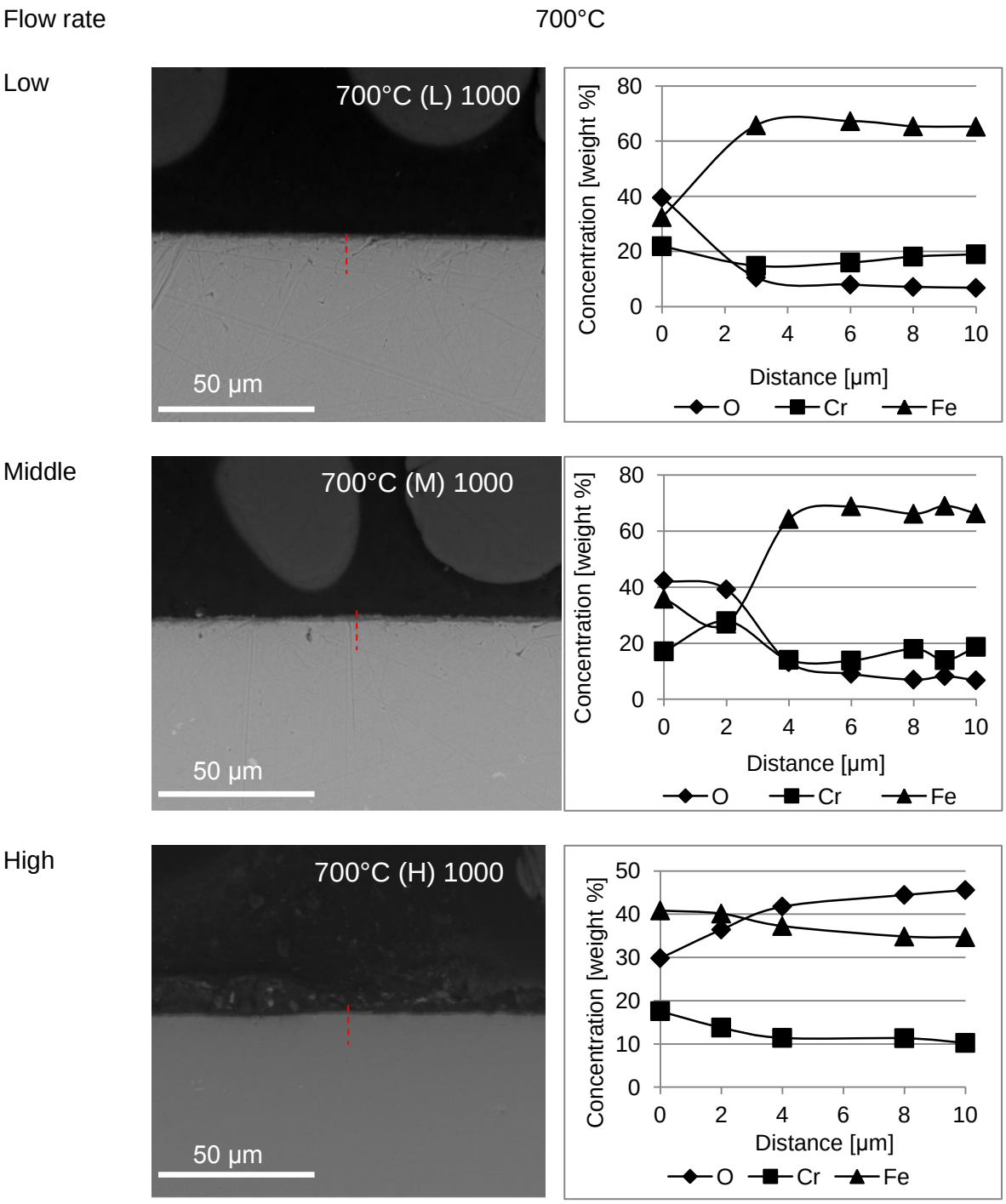

Figure 4-152 BSE SEM pictures + EDX spot scans of the scale formed on bridge – shaped Super 304H after 1000 hours exposure at 700°C with different steam flow rates

Comparison of the SEM pictures and EDX profiles obtained at 650°C and 700°C with different steam flow rates for both T347HFG and Super 304H (Figure 4-146, Figure 4-147 and Figure 4-151, Figure 4-152) showed that in case of Super 304H impact of the temperature on the acceleration of oxidation process is more significant than steam flow rate. In case of T347HFG the impact of the steam flow rate seems to be more pronounced.

Flow rate	750°C
Low	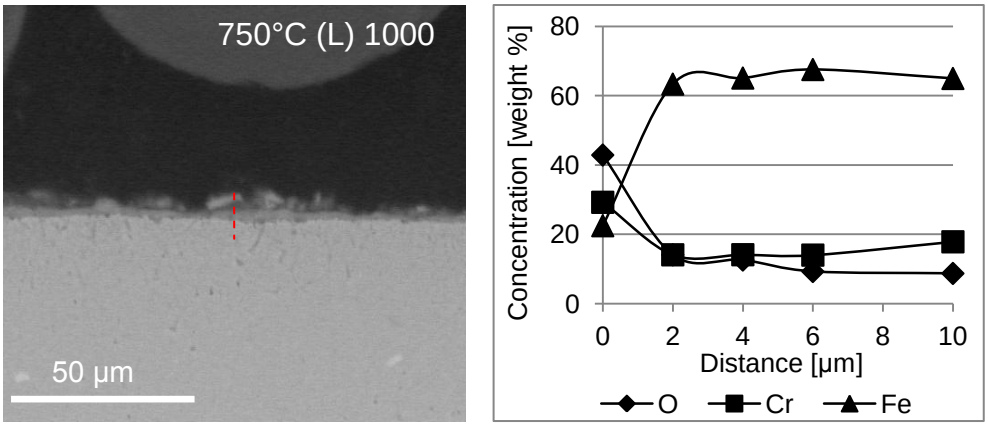

Figure 4-153 BSE SEM picture + EDX spot scan of the scale formed on bridge – shaped Super 304H after 1000 hours exposure at 750°C with low steam flow rate

4.2.2.2.3 HR3C

HR3C has the highest chromium content among the austenitic alloys tested (25Cr), and it has a relatively good steam oxidation behaviour. In the temperature range 600 – 700°C the scales developed, regardless of the specimen shape are discontinuous and non-adherent, but no nodules were identified. At 750°C for all of the specimens tested continuous, adherent and protective scales were found, with thicknesses around 4 µm. In addition, the protective scales were identified for the higher steam flow rate (M, H). The growth of nodule appers to have been suppressed due to formation of protective oxides on the surfaces of material exposed; the nodules formed at 750°C with low steam flow and at 600, 650 and 700°C with faster steam flow rates.

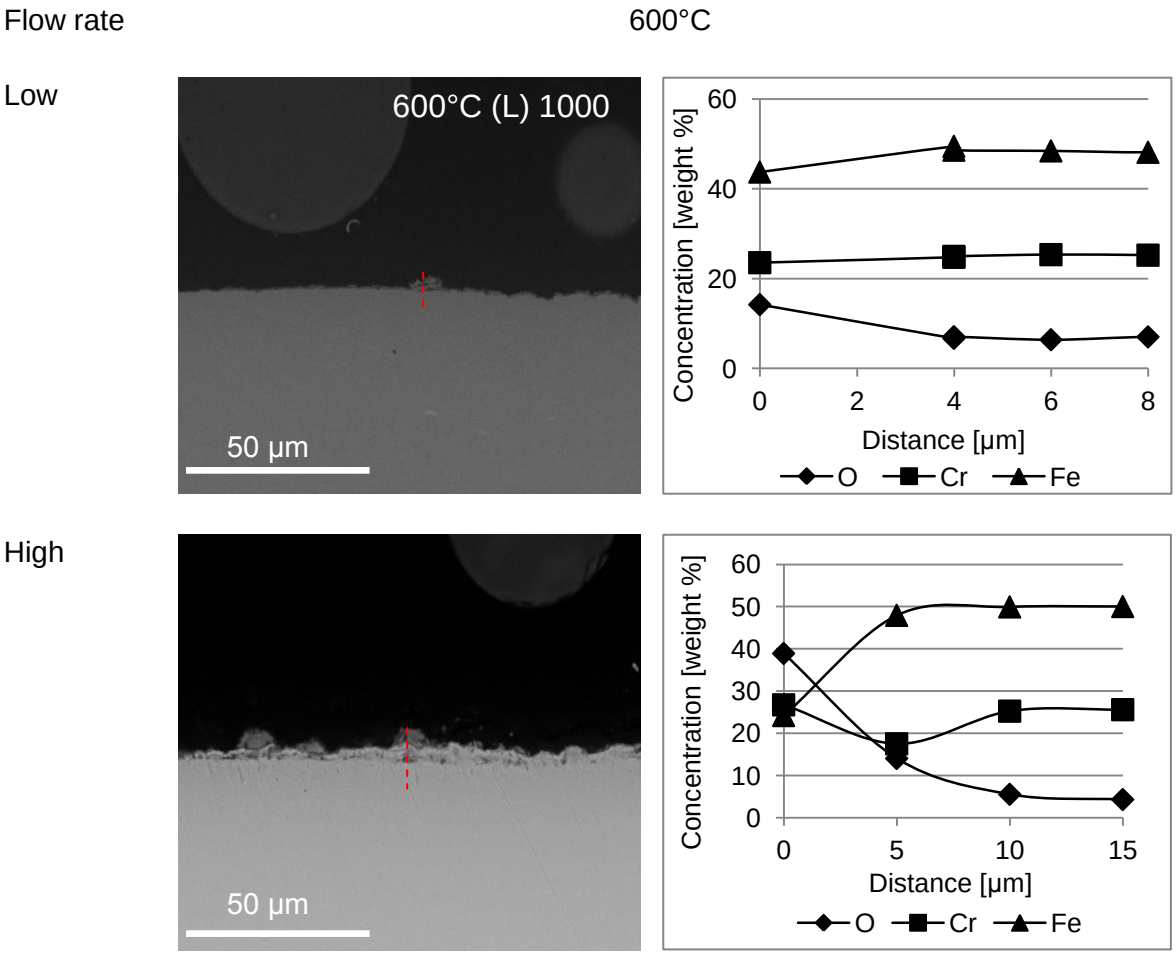

Figure 4-154 BSE SEM pictures + EDX spot scans of the scale formed on bridge – shaped Super HR3C after 1000 hours exposure at 600°C with different steam flow rates

Analysis indicated that faster steam flow rates promoted the formation of protective oxides on the surfaces of HR3C; identified as mixed iron, chromium oxides. which are expected to inhibit non-protective nodular oxide growths.

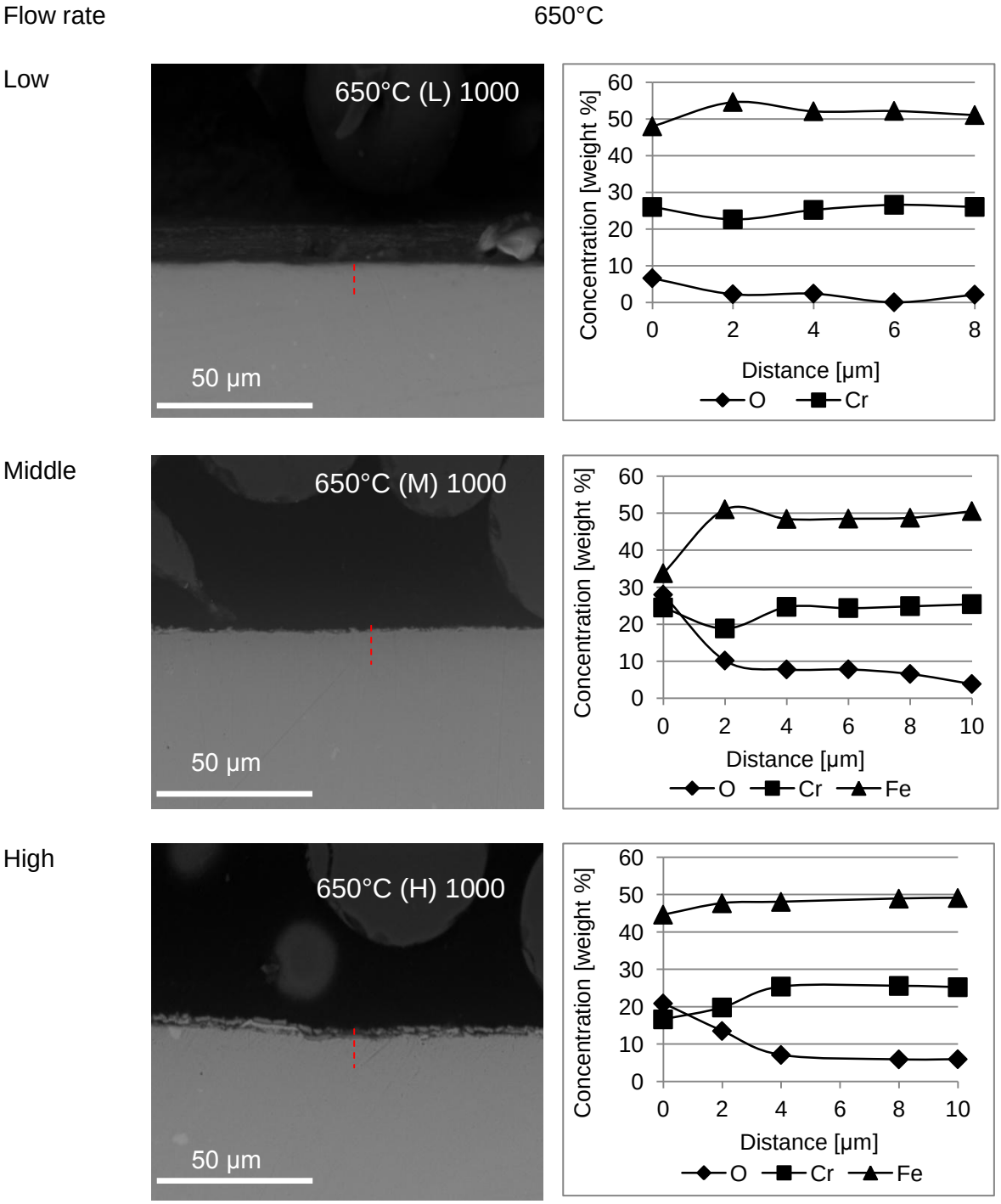

Figure 4-155 BSE SEM pictures + EDX spot scans of the scales formed on bridge – shaped HR3C after 1000 hours exposure at 650°C with different steam flow rate

At 650°C the increase in the steam flow rates triggers the formation of the protective oxides, which slow down the oxidation and suppress formation of the thick iron oxides.

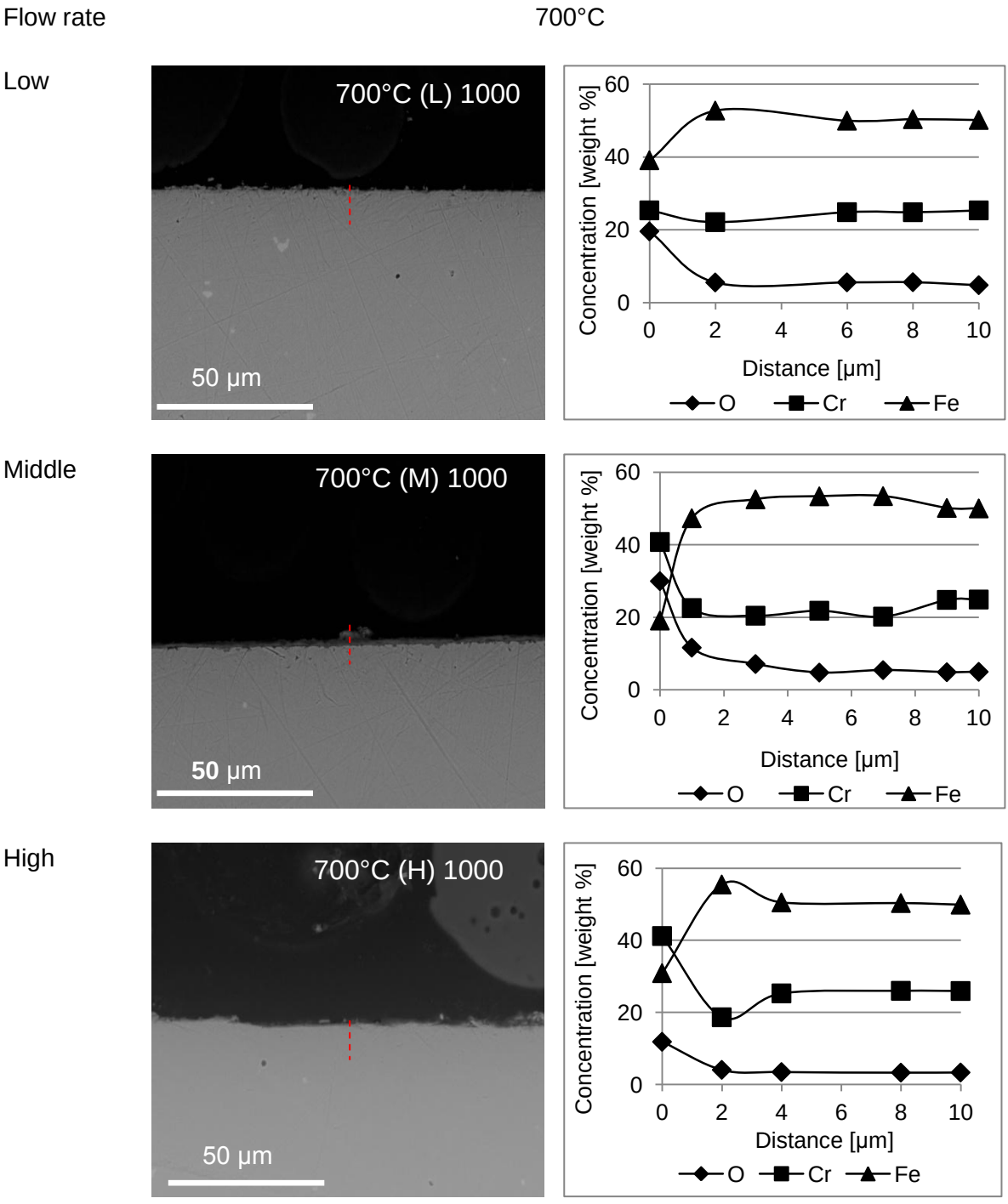

Figure 4-156 BSE SEM pictures + EDX spot scans of the scale formed on bridge – shaped HR3C after 1000 hours exposure at 700°C with different steam flow rate

Comparison of the specimens exposed at 600 and 650°C shows that the oxidation is slow, even the faster steam flow rates do not trigger the scales breakdown and nodule formation (Figure 4-154 - Figure 4-155).

In general, analysis of the data for HR3C shows that the steam flow rates promotes a formation of the protective oxides on the surface. HR3C exposed to 750°C showed clear growth of the protective oxides with high levels of iron and chromium. Those oxides are around 4 – 6 µm thick and cover most of the specimen surface. In the region facing the direct steam flow the specimens shows oxidation along crack to a depth of around 50 µm.

Flow rate		750°C

Low

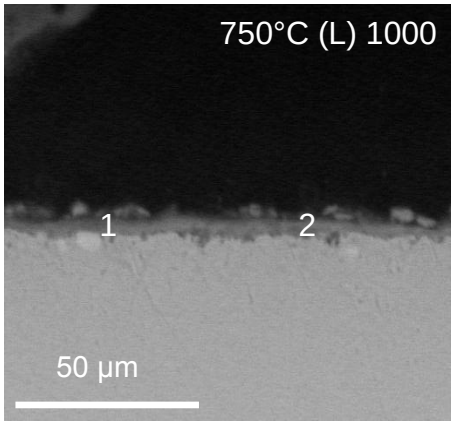

Spectrum	O	Cr	Fe	Ni
1	32	29.3	22.3	7.9
2	21	23.0	26.5	13.4

Low

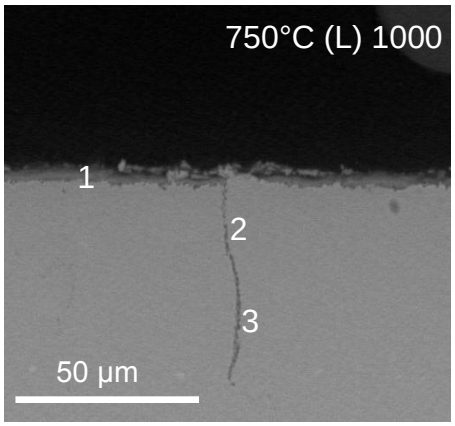

Spectrum	O	Cr	Fe	Ni
1	20	44.1	19.4	6.8
2	11	30.0	39.2	14.5
3	12	30.1	38.1	14.0

Figure 4-157 BSE SEM pictures + EDX point analysis of the scale formed on bridge – shaped HR3C after 1000 hours exposure at 750°C with low steam flow rate

4.2.2.2.4 800H and Inconel 740

800H and Inconel 740 are the most resistant alloys among the material selected; both show very slow morphological changes in the scales developed for both alloys.

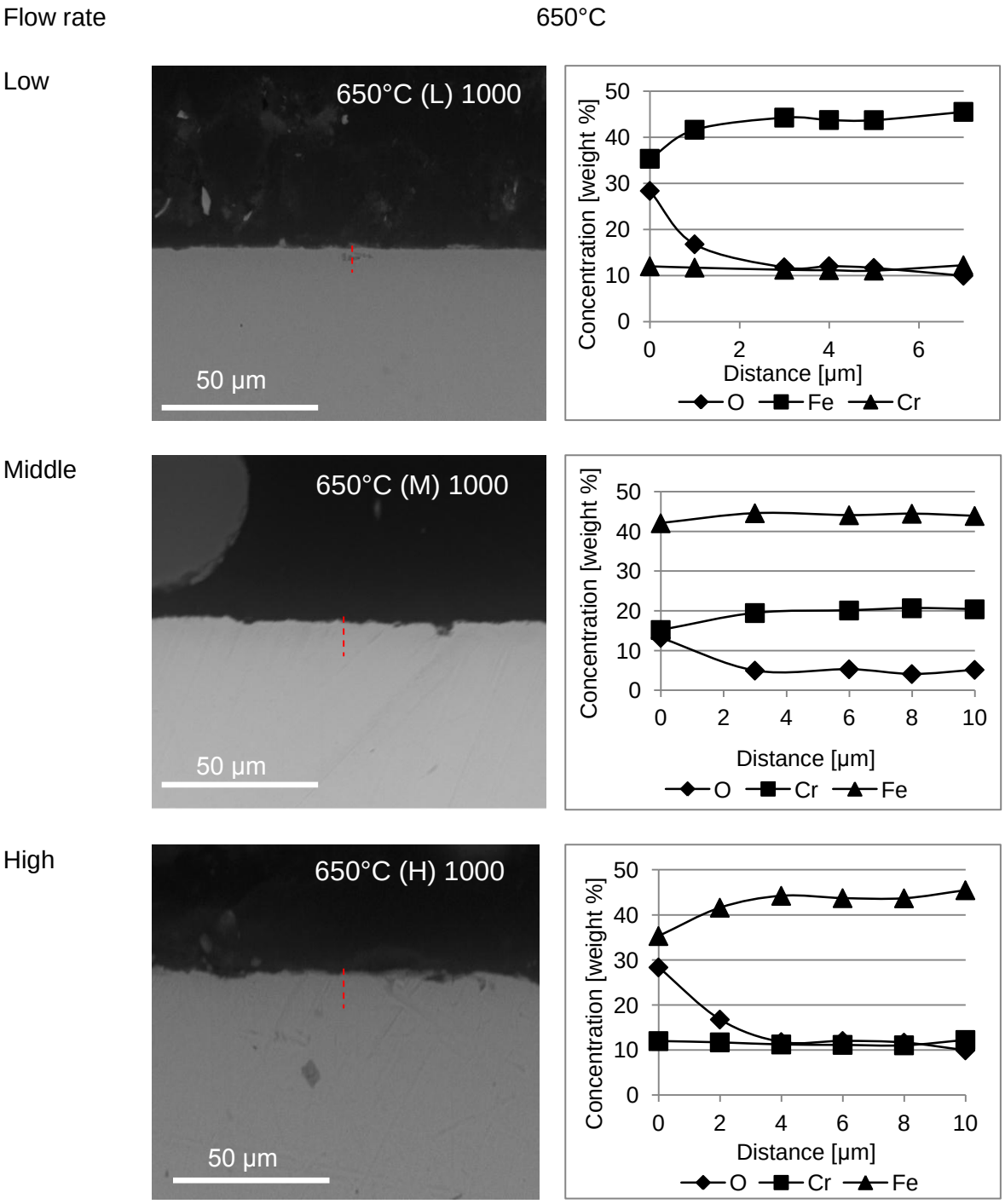

Figure 4-158 BSE SEM pictures + EDX spot scans of the scale formed on 800H after 1000 hours exposure at 650°C with different steam flow rates

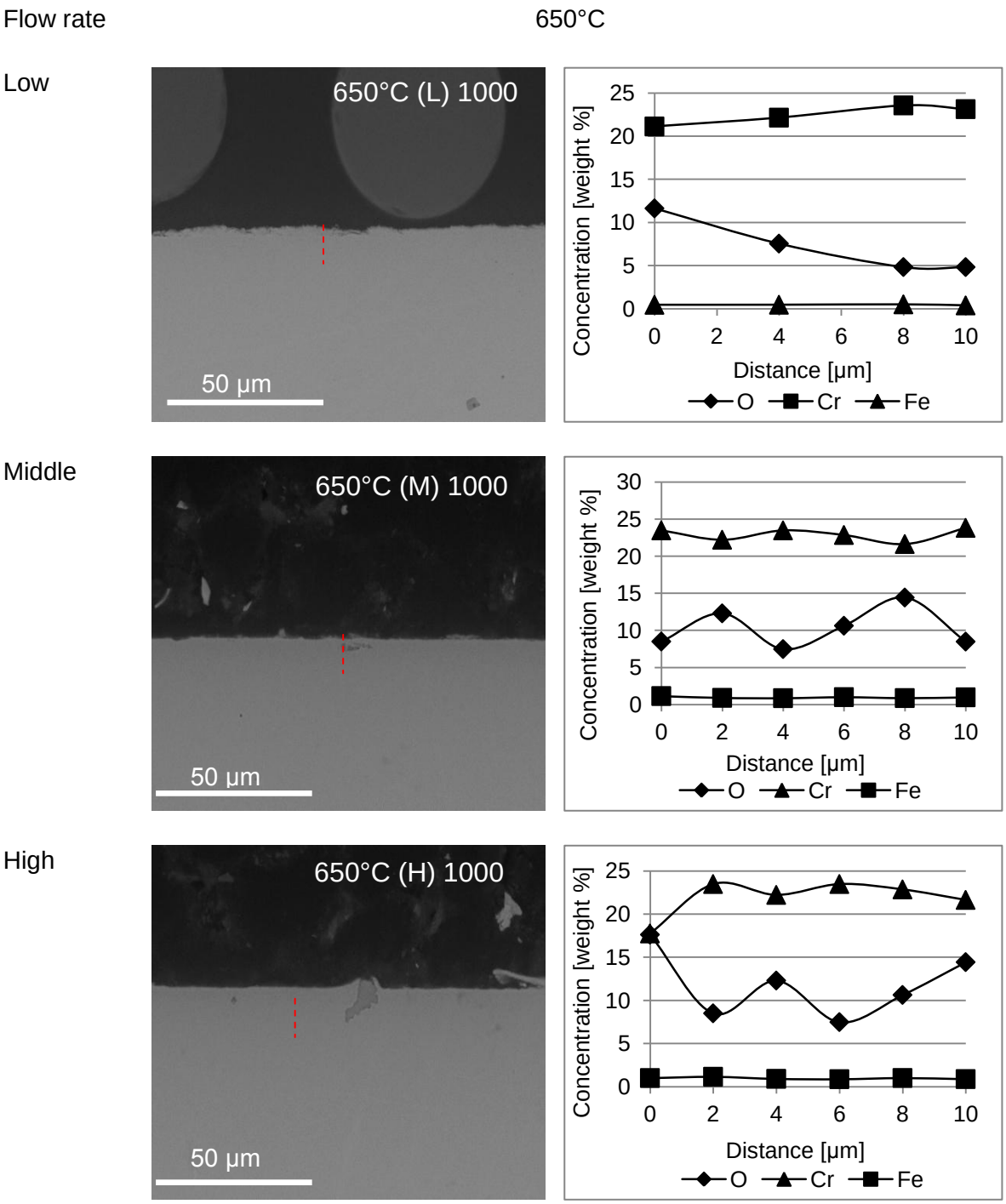

Figure 4-159 BSE SEM pictures + EDX spot scans of the scale formed on Inconel after 1000 hours exposure at 650°C with different steam flow rates

The visual analysis of the specimens show change in the surfaces colour, which corresponds to the couple hounded nanometre thick scales, formed. The BSE SEM pictures of the scales at low temperatures does show some thin oxides,

however it is also possible that the scales formed during the oxidation have partially exfoliated.

At 700°C both materials started to develop protective oxides, moreover in the regions facing the steam flow these protective scales have started to break down and in case of both alloy just one nodule have been found on the surface facing the direct steam flow.

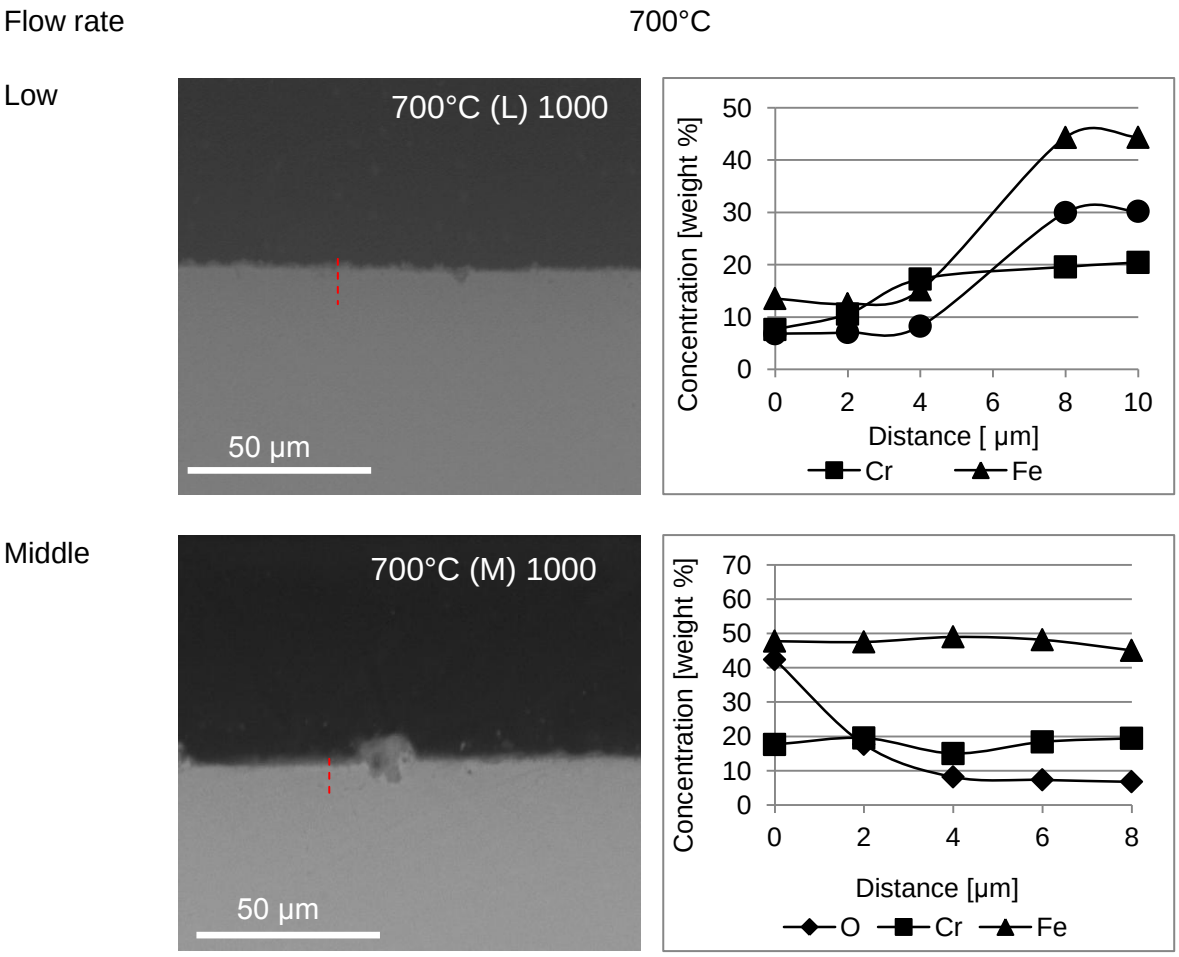

Figure 4-160 BSE SEM pictures + EDX spot scans of the scale formed on 800H after 1000 hours exposure at 700°C with different steam flow rates

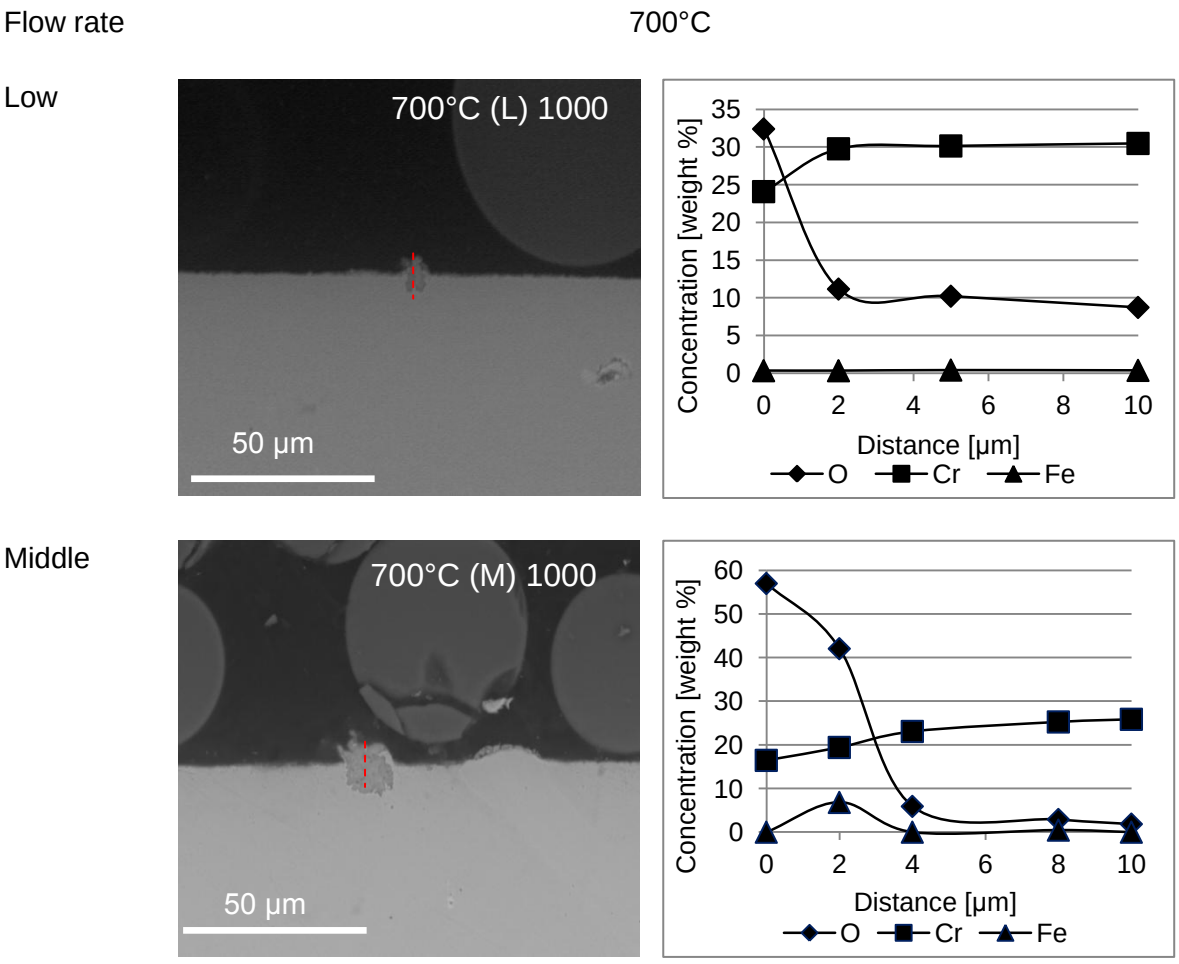

Figure 4-161 BSE SEM pictures + EDX spot scans of the scale formed on Inconel 740 after 1000 hours exposure at 700°C with different steam flow rates

At 750°C both alloys developed thicker protective scales, which covered the part of the specimen facing the direct steam flow; but there was also nodule formation. The nodules identified at 750°C were larger than those formed at 700°C.

Flow rate 750°C

Low

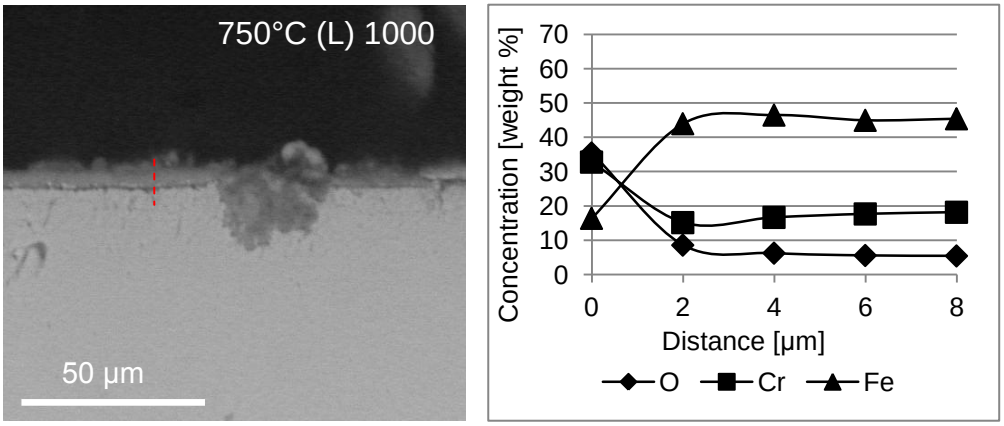

Figure 4-162 BSE SEM picture + EDX spot scan of the scale formed on 800H after 1000 hours exposure at 750°C with low steam flow rate

Flow rate 750°C

Low

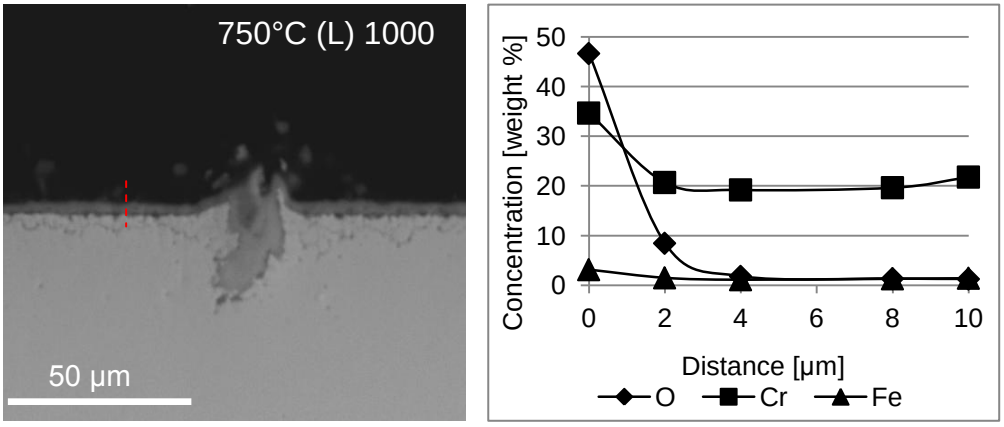

Figure 4-163 BSE SEM picture + EDX spot scan of the scale formed on Inconel 740 after 1000 hours exposure at 750°C with low steam flow rate

The nodules are covered with re-growing protective oxides, which suppress their further growth up to the moment when material is not able to supply enough chromium to surface in order to maintain the protective scales. In case of the Inconel 740 there is some internal oxidation below the protective oxides, this was not identified for the 800H. Under faster steam flow rates conditions the formation of nodules increases. Analyses of the scales formed on Inconel 740 and 800H showed that under faster steam conditions oxides are still discontinues and non-adherent to the surface, which could be result of the scale spallation upon cooling.

4.2.2.3 Effect of the specimen surface finish

The effect of surface finish was investigated on examples of two austenitic steels (T347HFG and Super 304H). For that purpose, three different surface finish methods were applied. The specimens exposed to steam were either ground, polished or pickled (as received). The main differences between the surface finishes were roughness and depth of the deformation below the surface (in the grains below material surface). For identification of roughness a confocal laser scanning microscopy technique was used to generate 3D images of the specimen surfaces. The surfaces of T347HFG (Figure 4-164 - Figure 4-166) and Super 304H (Figure 4-168 - Figure 4-170) with different surface finishes are presented as 3D height images. The different colours correspond to the surface height, which changes along the surface. The specimen surfaces are not even, there changes in height in 3D image which are believed to correspond to fluctuations of the material surface. Moreover, the surfaces of the specimens tested are curve, which can caused significant errors in the roughness test readings, therefore a graphical method of result presentation was selected. This method allows a comparison of the results for different surface finishes, without generating a one, defined number.

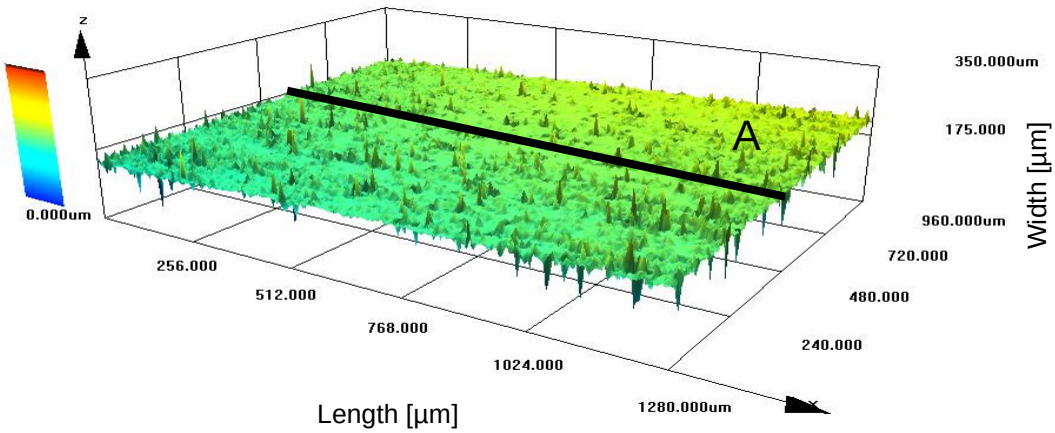

Figure 4-164 3D image of the as received surface of a T347HFG specimen

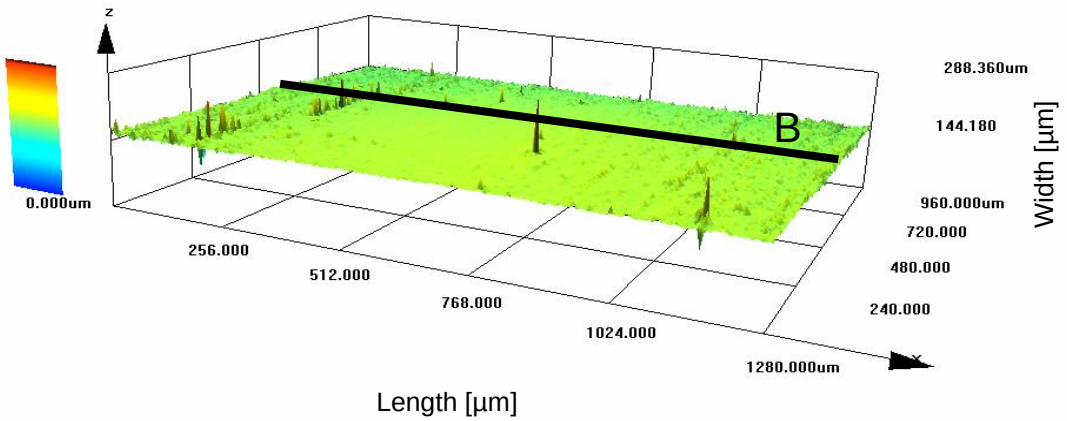

Figure 4-165 3D image of the ground surface of a T347HFG specimen

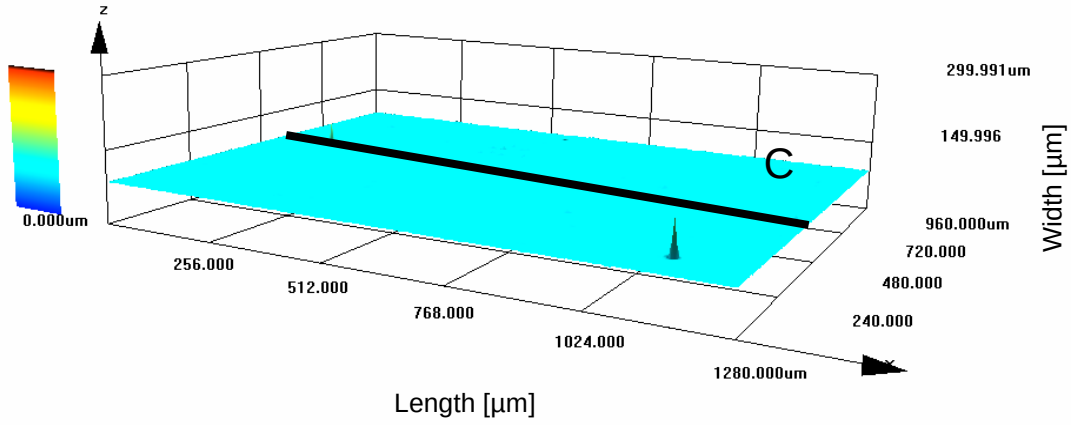

Figure 4-166 3D image of the polished surface of a T347HFG specimen

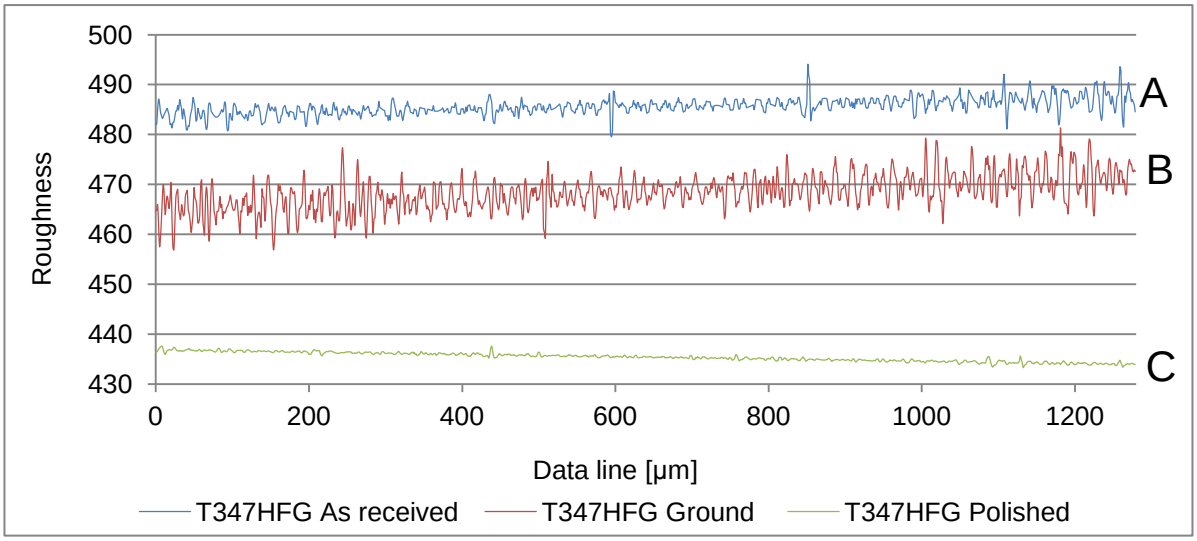

Figure 4-167 Comparison of the surface profiles for different surface finishes of T347HFG (A - As received, B - Ground, C - polished surface)

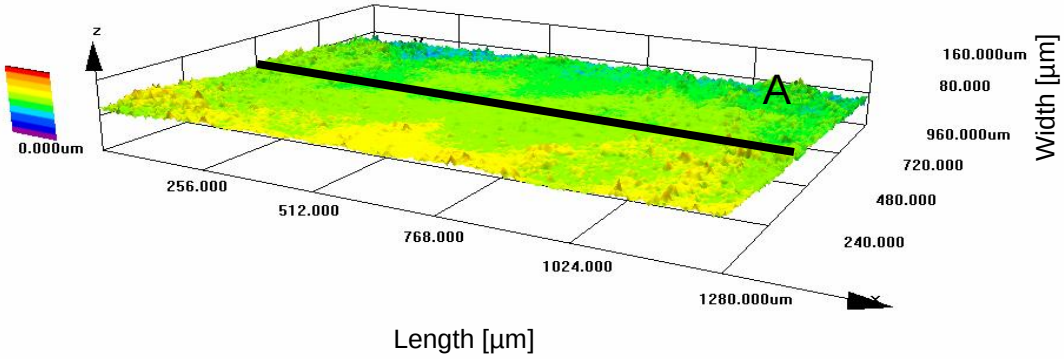

Figure 4-168 3D image of the as received surface of Super 304 H specimen

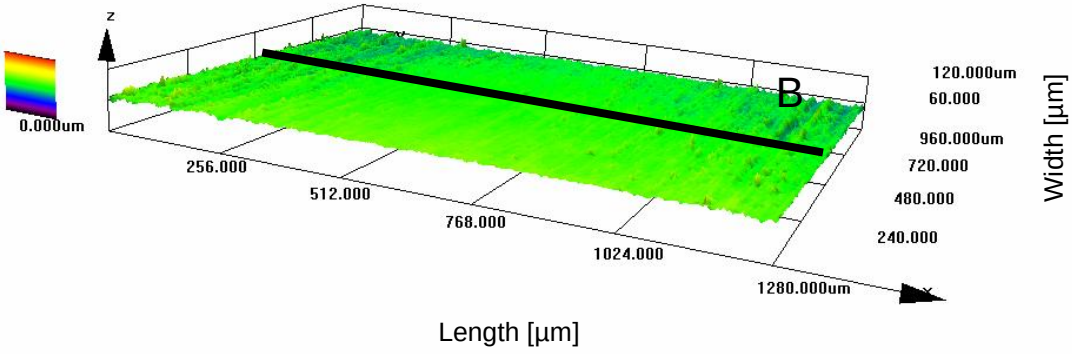

Figure 4-169 3D image of the ground surface of Super 304 H specimen

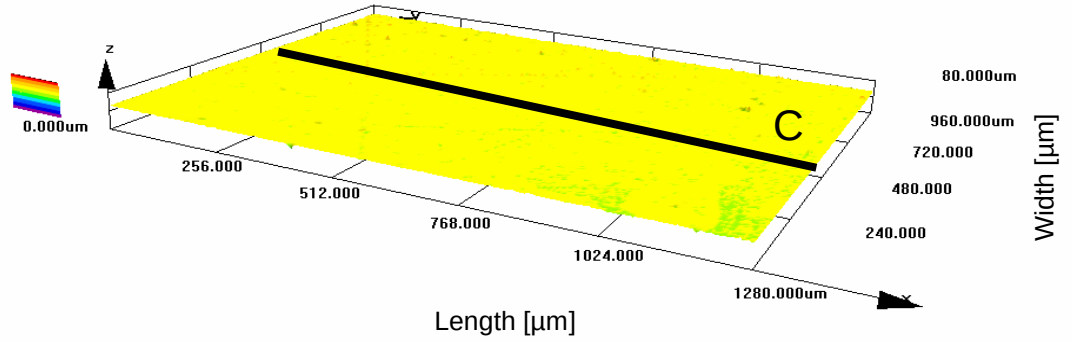

Figure 4-170 3D image of the polished surface of Super 304H specimens

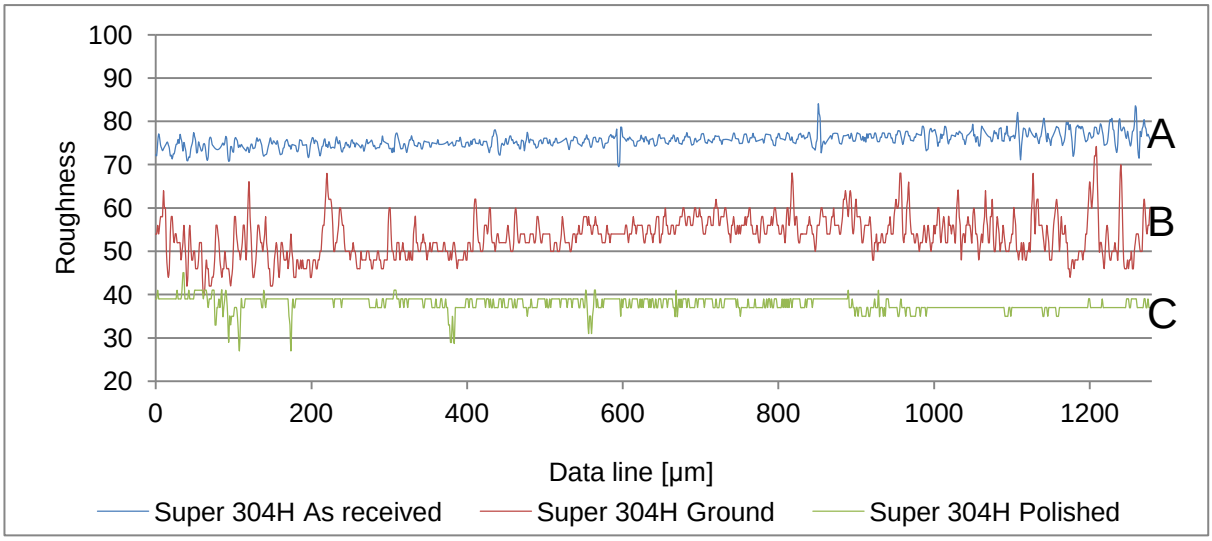

Figure 4-171 Comparison of the surface profiles for different surface finishes of Super 304H (A - As received, B - Ground, C - polished surface)

Figure 4-167 and Figure 4-171 show that the change of the surface finish for austenitic steels influences roughness. The highest roughness levels were from 'as received' specimens. The profile lines for as received specimens (A) in Figure 4-167 and Figure 4-171 indicated that roughness fluctuates along the scanning line, however the differences between values are low The largest differences in surface profile have been identified for ground specimens (scan lines B); the roughnesses for these specimens fluctuates significantly, which is dependent on location of the scanning point. At this point it is necessary to remember that on the surface of the ground specimens a number of the grinding marks could be found which are represented on the profile as the high peaks. Finally, the polished specimens are characterised by relatively, constant surface profile, which is a result of the scratch-free surface (Figure 4-167 and Figure 4-171 scan lines C).

The investigations of the surface finishes were carried out at two temperatures (600 and 700°C) with high steam flow rate (40 mm/s).

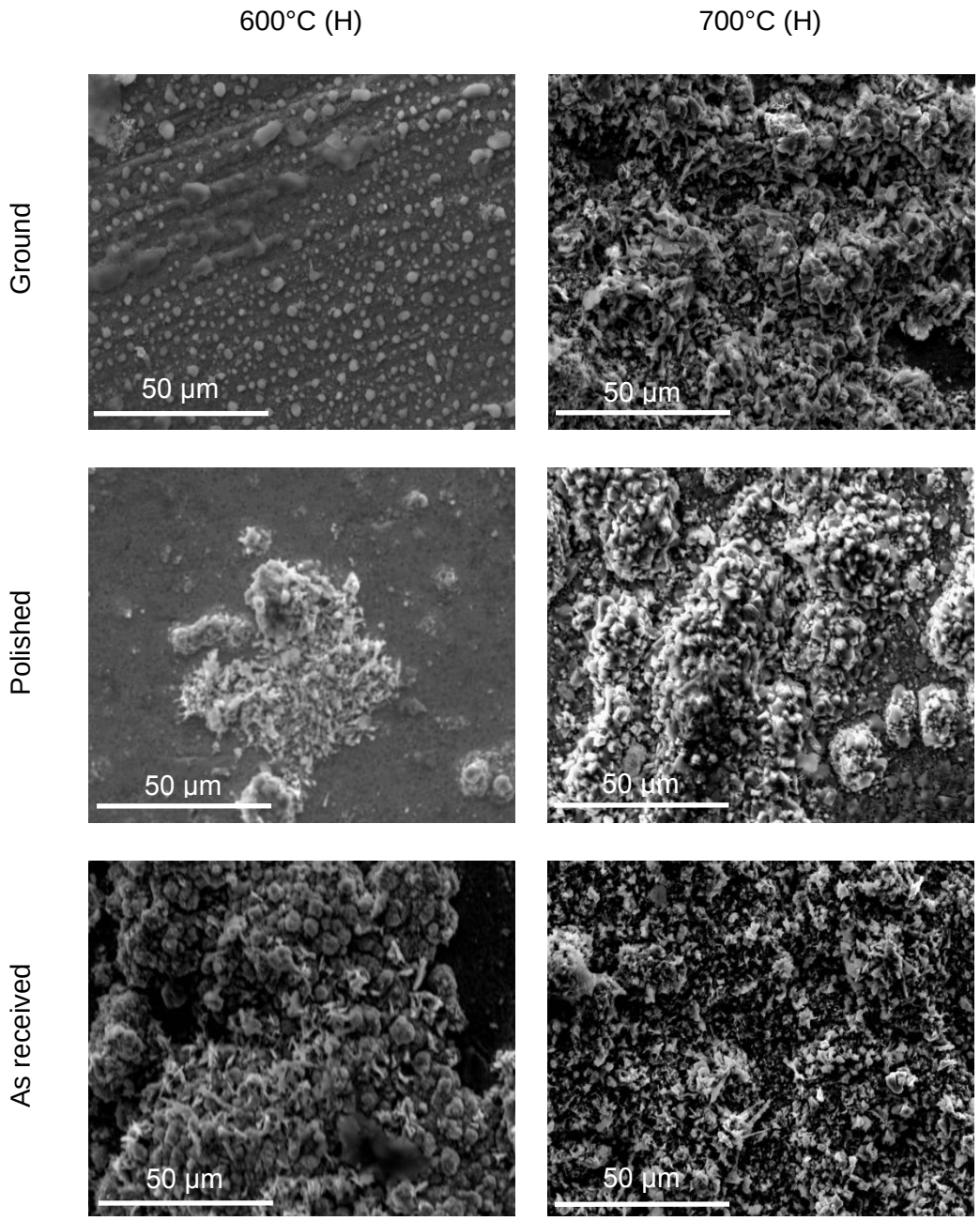

Figure 4-172 Effect of the surface treatment on the oxides formed on the specimen surface of T347HFG at 600 and 700°C with high steam flow (40 mm/s)

Figure 4-172 shows the surface pictures of T347HFG, obtained with scanning microscope in secondary electron detector mode. Clearly the sizes of growing oxides vary with the surface finish. This is more pronounced at lower temperature, where the as-received specimen is covered with oxides grains. Those grains have been identified with EDX as mixed chromium and iron oxides. At 700°C (H) oxidation is much faster and results in the formation of thicker oxides, those oxides covered most

of the specimens surface regardless of the surface finish. Comparison of pictures corresponding to the particular surface finish show that on the as- received specimens clearly the oxides are growing and cover large part of the specimen surface.

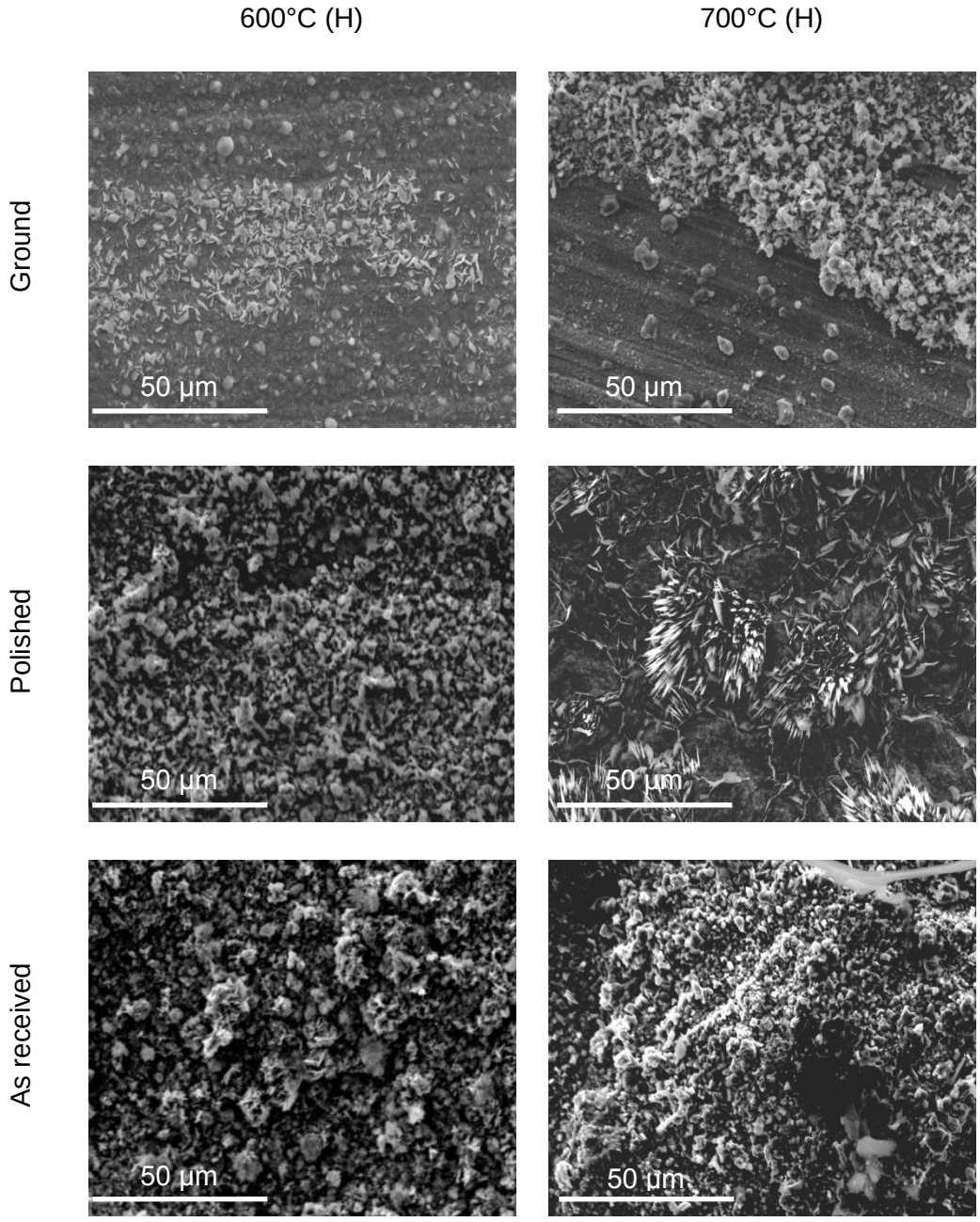

Figure 4-173 Effect of the surface treatment on the oxides formed on the specimen surface of Super 304H at 600 and 700°C with high steam flow (40 mm/s)

Exposures of Super 304 confirmed findings of the previous tests, that this material is more resistant to steam oxidation than T347HFG. At 600°C (H), as well

as at 700°C (H) the ground specimens oxide slower than T347HFG and, there are nodules identified on the surface at both temperatures. The size and distribution of the nodules vary with exposure conditions; they are more evenly distributed at 700°C (H). The polished specimens exhibit similar behaviour to T347HFG, the growing oxides have been found at both temperatures, at higher temperature the oxide are spike-like, whereas at lower temperatures the oxides are less sharp. This may suggest that the oxides varies with the exposure temperature. Finally, the surface of the 'as-received' samples indicates the most significant oxide growth, the oxides grains are the largest at both temperatures, and moreover the surface of the specimens is fully covered with the oxide scales.

Figure 4-174 show the cross-sections through the T347HFG exposed at 600°C (H);clearly there are significant differences between the oxides formed on the specimens with different surface finishes. The ground specimens have very thin layer of protective oxides, which are mixed of chromium and iron oxides. The same types of oxides have been found for polished specimens, however they are thicker and nodules have started to form on the surface due to the local break down of the protective layer. Finally, as expected from surface analysis, the 'as-received' specimen developed the thickest scales with iron and chromium oxides as main constituents. Such oxides are continuous and cover whole specimen.

600°C (H)

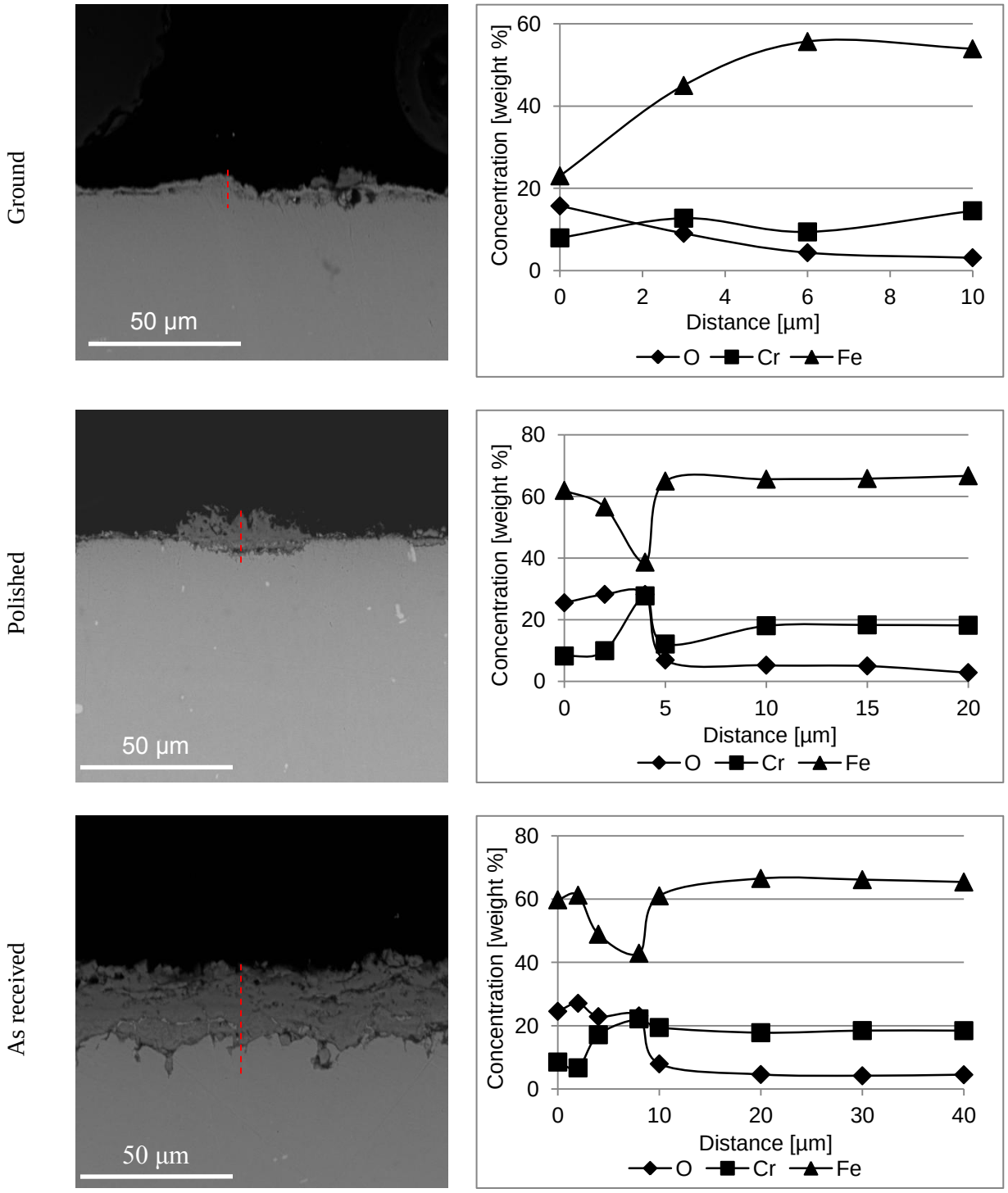

Figure 4-174 BSE SEM + EDX spot scans of the scales formed on T347HFG with different surface treatments at 600°C with fast steam flow rate

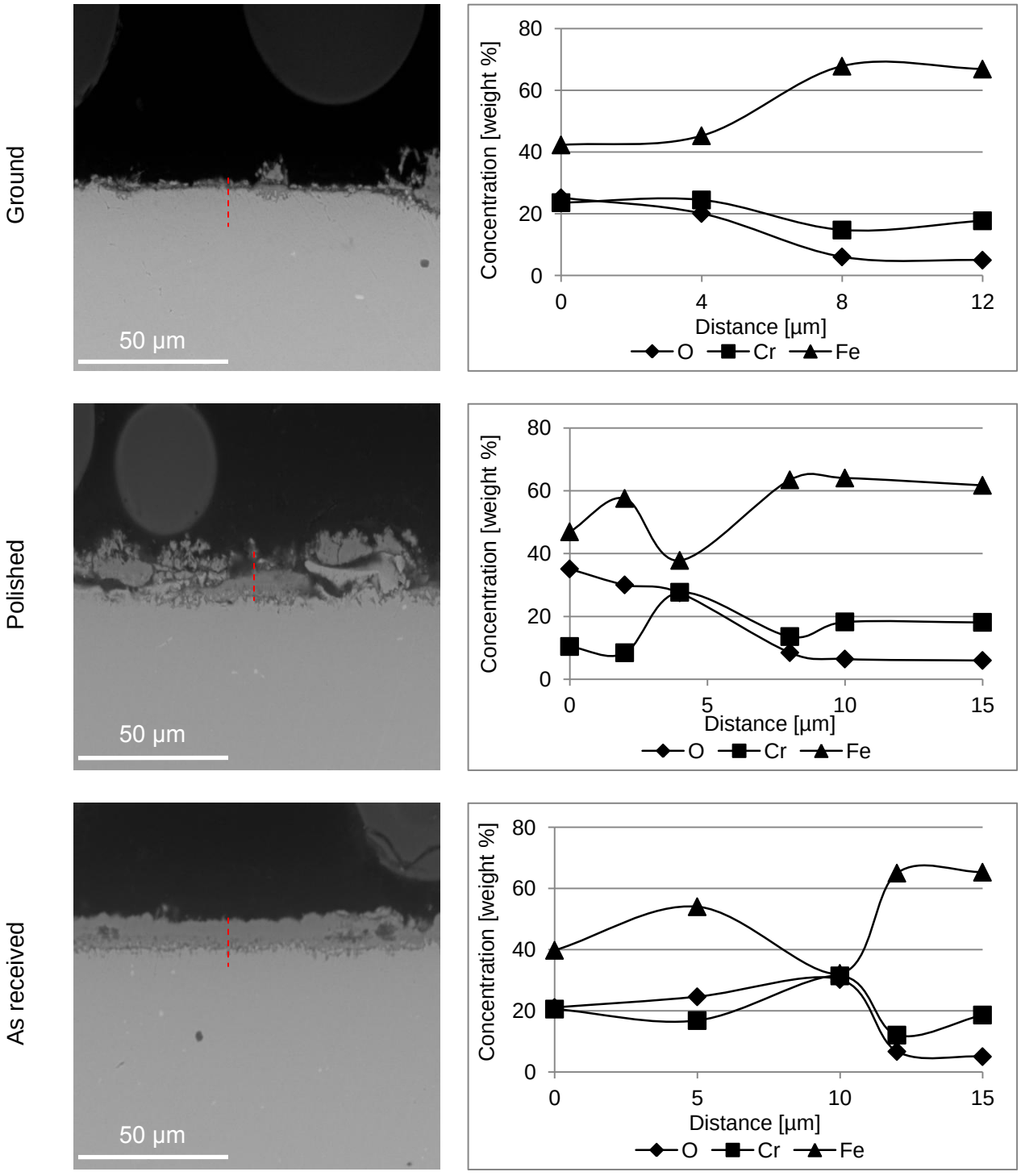

Figure 4-175 BSE SEM pictures + EDX spot scans of the scales formed on Super 304H with different surface treatments at 600°C with fast steam flow rate

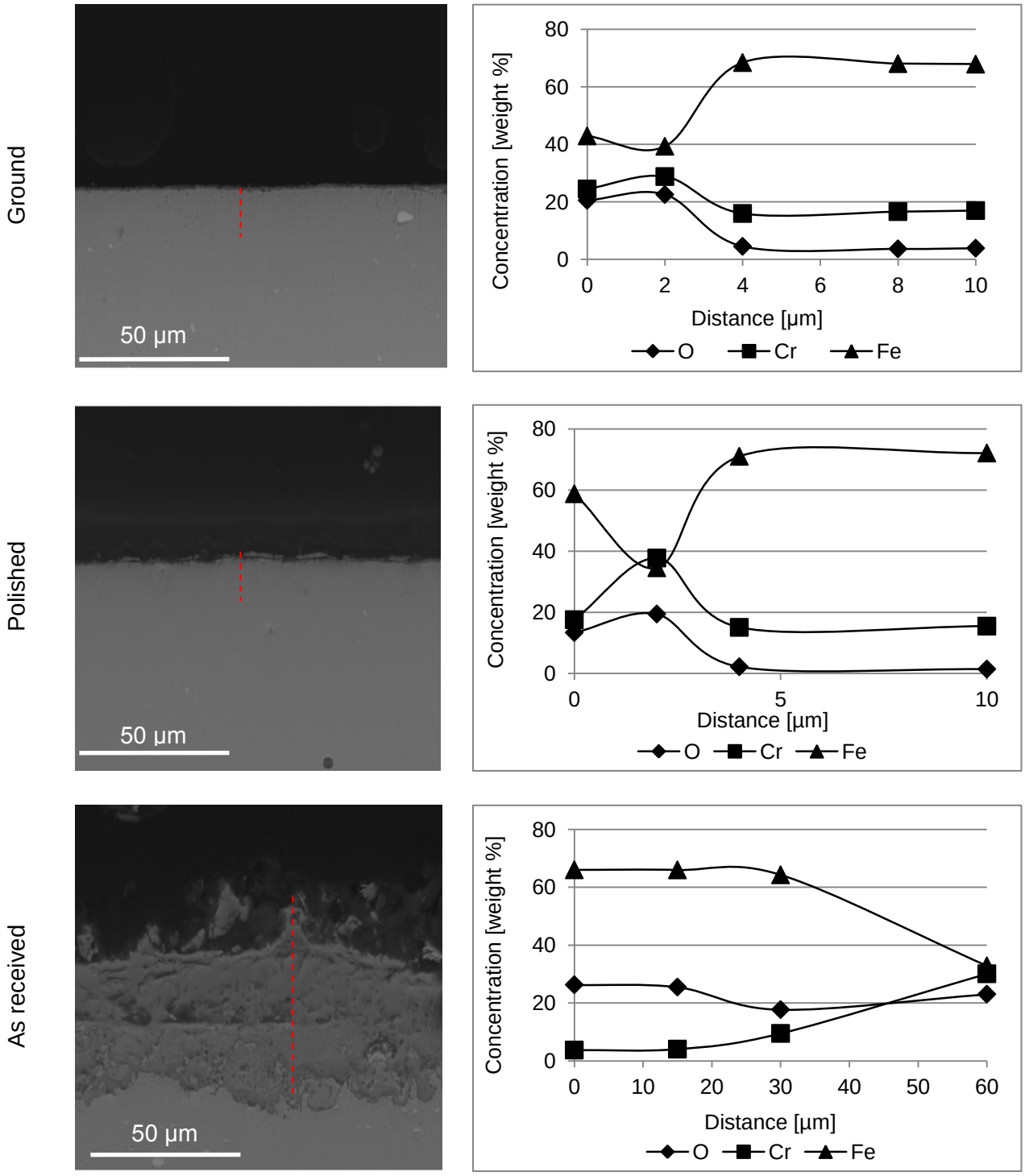

Figure 4-176 BSE SEM pictures + EDX line scans of the scales formed on T347HFG with different surface treatments at 700°C with fast steam flow rate

Oxidation of Super 304H also varies with surface finish, however in comparison with T347HFG oxides are thinner and do not always cover the whole surface, which could be result of the scale spallation. Ground specimens show the thinnest scales, which were identified as mixed iron and chromium oxides. Analysis of the two other surface finishes indicate that the concentrations of iron and chromium on their surfaces are lower than for T347HFG. This could be explained as a result of the better protectiveness of the inner part of the oxides, which slows down diffusion and therefore the scales formed are thinner. On polished specimen there is nodular scale growth; these nodules will eventually coalesce after longer exposures and form a continuous layer. The ,as-received, sample oxidises much faster than the others tested, resulting in the formation of thick, continues scales that cover most of the surface.

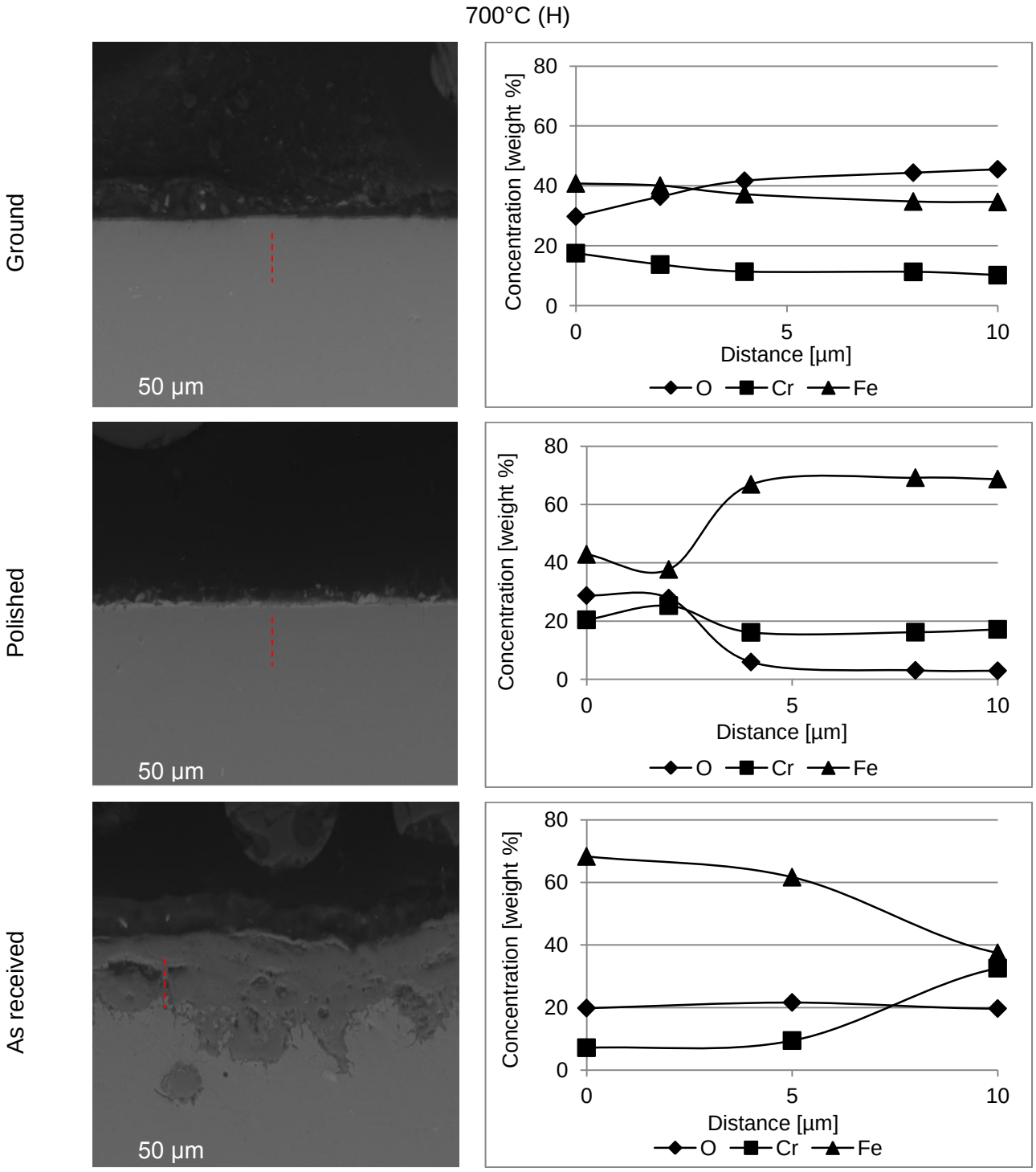

Figure 4-177 BSE SEM pictures + EDX line scans of the scales formed on Super 304H with different surface treatments at 700°C with fast steam flow rate

Figure 4-178 shows changes in the depth of the deformation/damage zone with different specimen surface finishes. To invastigate it the specimens were etched with 10% oxalic acid electrolytic etchent and the direct current of 6V was applied for 20 seconds. Clearly the ground specimens show the deepest sub-surface deformation,

whereas the polished specimens and 'as-received' specimens show less sub-surface damage. The grains dislocations for the ground specimens are up to 30 µm deep, whereas for polished and as received they are < 10 µm and 15 -20 µm, respectively.

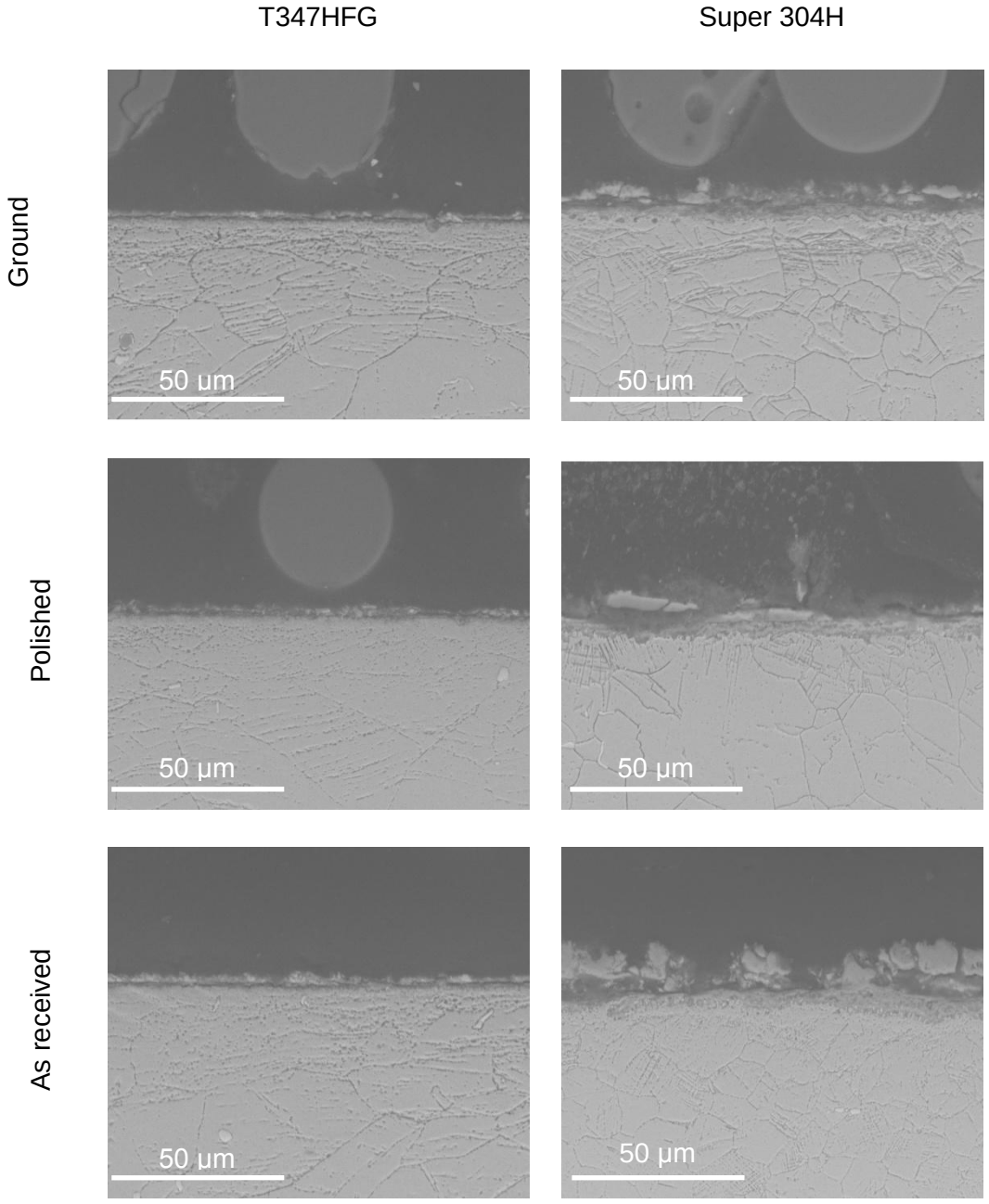

Figure 4-178 An impact of the specimen surface finish on the depth of the deformation/damage zone in specimen sub-surface

Table 4-1 Average area of deformation/damage zone in the specimen sub-surface

Surface finish/alloy type	Average concentration of deformation within the single grain [%]	
	T347HFG	Super 304H
Ground	15	10
Polished	4	3
As received (pickled)	2-3	2-3

Table 4-1 shows the average concentration of the damage in the gains in specimen sub-surface, it was calculated for 10 randomly selected grains found on ground, polished and 'as-received' specimens of T347HFG and Super 304H after etching. It indicates that the area (concentration) of damages in the grains in the specimen sub-surface is significantly larger for ground specimens than for the others. In the 'damaged' grains the diffusion is much faster than in the deformation-free grains, this is believed to influence the formation of the protective oxides on the surface of ground specimens.

4.2.3 Investigation of steam oxidation mechanisms

Steam oxidation is a well-known subject; however there still is a debate about which of the analysis elements and the ions forming during steam dissociation are responsible for the oxide scale growth. This chapter summarises the result of the research conducted to study the diffusion mechanism of oxygen during the formation of the oxide scales on ferritic and austenitic steels. For such analysis the specimens were exposed in last 100 hours of their test to steam generated from O^{18} doped water. These scales were studied with Secondary Ion Mass Spectrometry (SIMS) to track the O^{18} ions. Due to very thick scales formed on T23 the SIMS analysis has been performed in regions where the outer scales have partially exfoliated. This allowed the analyses to be performed on the outer oxide layer (A) and inner oxide layer (B) (Figure 4-179).

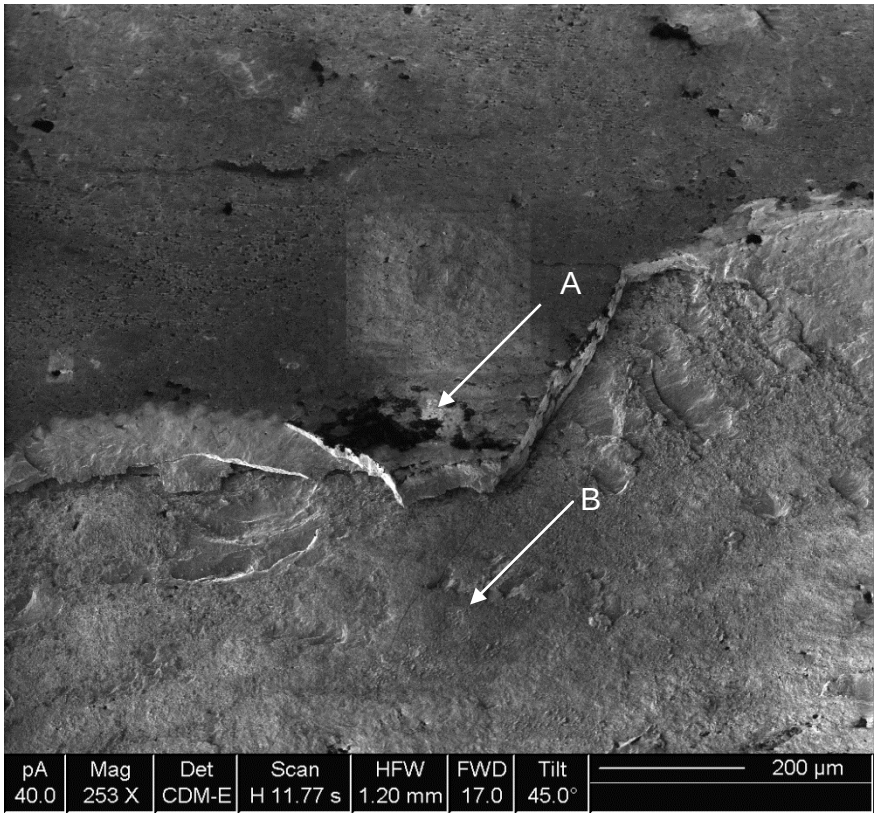

Figure 4-179 The locations of the points for SIMS analysis on T23 after 1000 hours exposure at 700°C with the highest steam flow (40 mm/s)

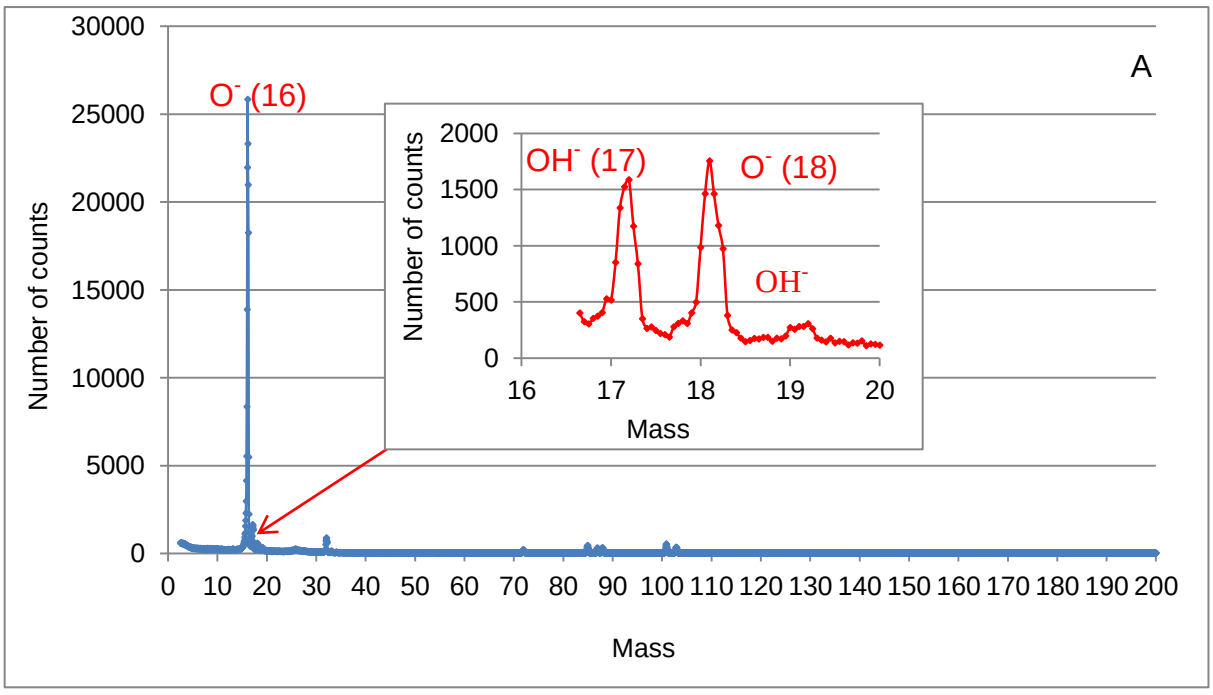

Figure 4-180 SIMS analysis of the outer scale formed on T23 after 1000 hours exposure at 700°C with the highest steam flow (40 mm/s) in Point A (Figure 4-179)

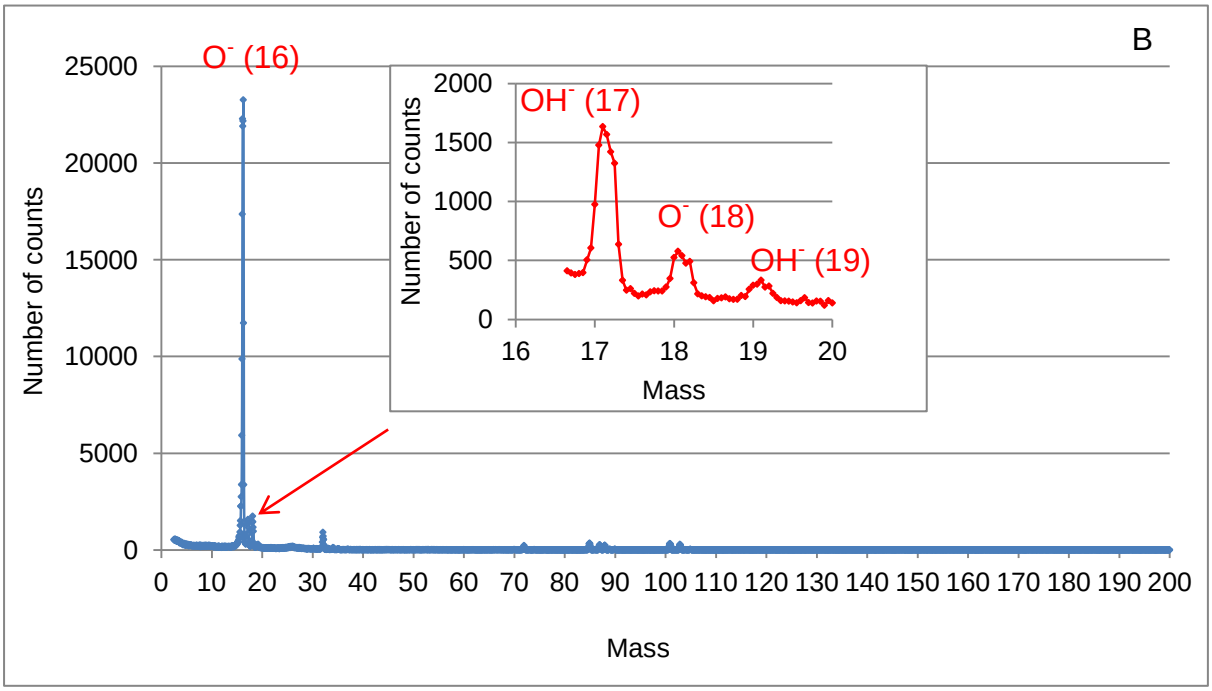

Figure 4-181 SIMS analysis of the inner scale formed on T23 after 1000 hours exposure at 700°C with the highest steam flow (40 mm/s) in Point B (Figure 4-179)

Analysis of the scales formed on T23 showed that the number of O^-(16), O^- (18) and OH^- (17) and OH^- (19) ions varied with distance from the surface. This suggests that oxygen was diffusing inwardly. T92 also developed a thick scale, therefore the SIMS analysis has been performed in a region where outer scale has exfoliated. For analysis three points has been selected A - outermost oxide layer, B – outer scale and C – inner scale.

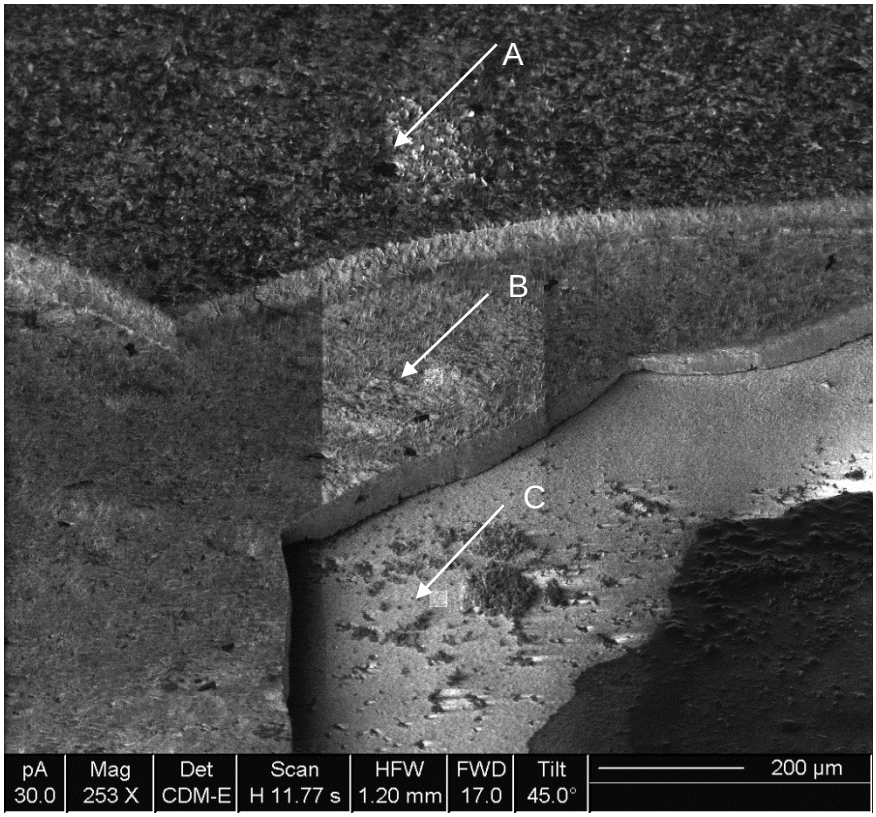

Figure 4-182 The locations of the points for SIMS analysis on T92 after 1000 hours exposure at 700°C with the highest steam flow (40 mm/s)

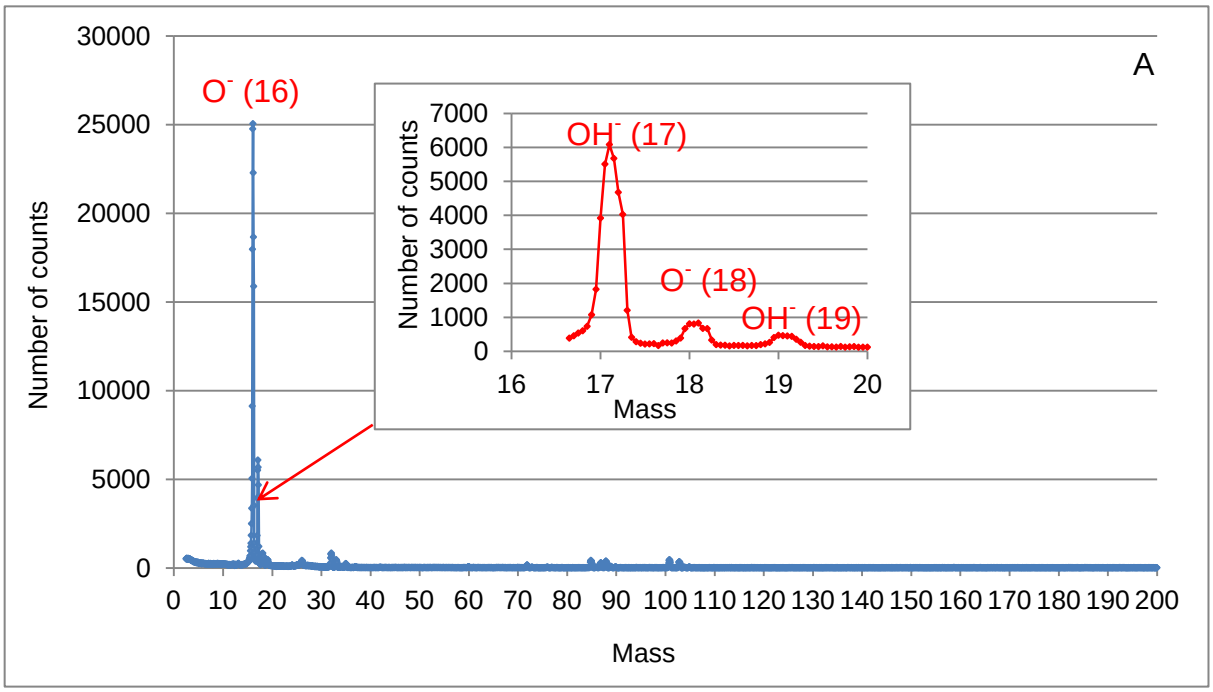

Figure 4-183 SIMS analysis of the outer scale formed on T92 after 1000 hours exposure at 700°C with the highest steam flow (40 mm/s) in Point A (Figure 4-182)

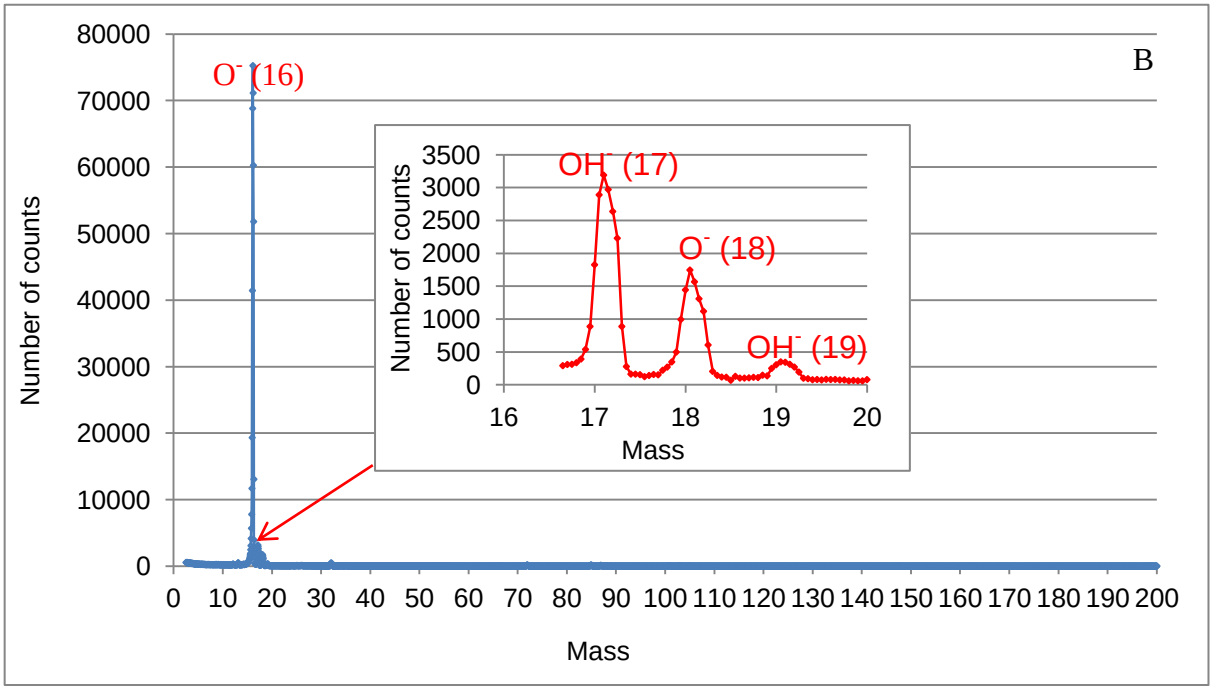

Figure 4-184 SIMS analysis of the Inner scale formed on T92 after 1000 hours exposure at 700°C with the highest steam flow (40 mm/s) in Point B (Figure 4-182)

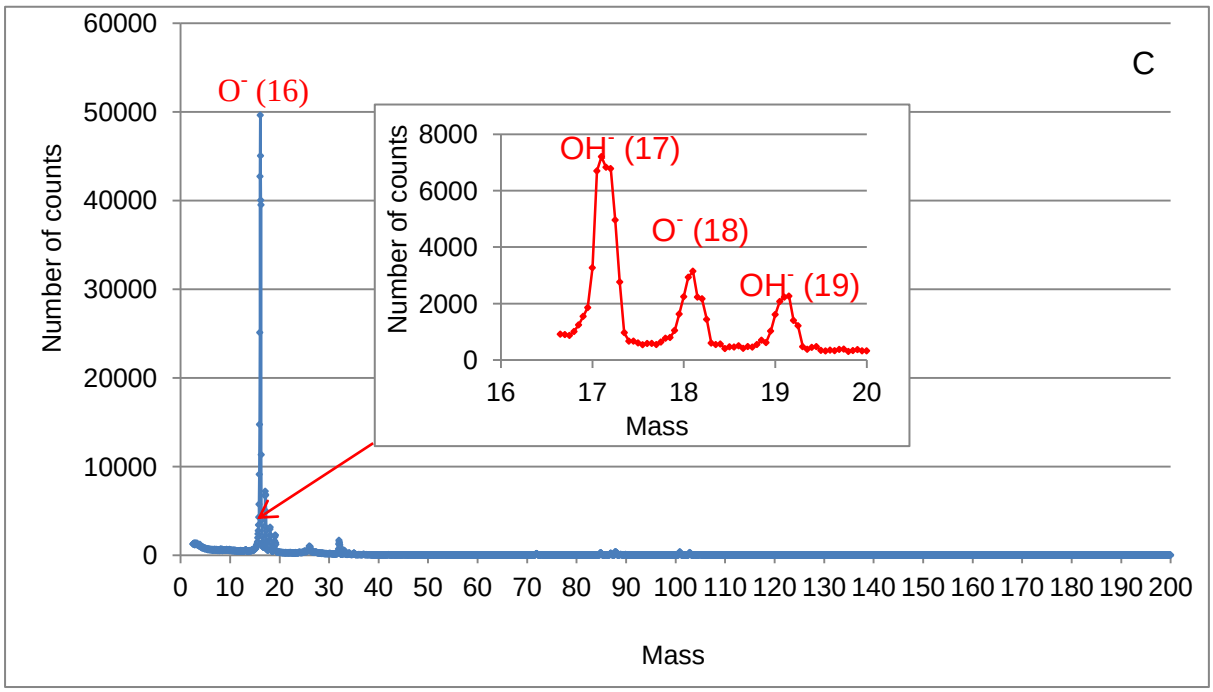

Figure 4-185 SIMS analysis of the innermost scale formed on T92 after 1000 hours exposure at 700°C with the highest steam flow (40 mm/s) in Point C (Figure 4-182)

Analysis of the data acquired showed that the number of counts for the oxygen ions changes with location of point for SIMS analysis. Clearly the counts for O^- (18) increase with distance from the surface, whereas there is less signal for O^- (16) ions. The signals for OH^- (17) and OH^- (19) ions also change with the distance from the surface, in the inner scale there is more OH^- (17) and OH^- (19) ions detected that in other points investigated, which is a clear evidence of the significance of inward migration of hydroxide ions on steam oxidation.

The scales formed on austenitic alloys Super 304H and HR3C (ground specimens) are much thinner than these found on ferritc steels. These austenitic steels exhibit the nodular scale growth; first there is a formation of relatively thin, protective scales, which break down after longer exposure and then nodules start to develop. Therefore, in order to understand the mechanisms responsible for such scale formation for both materials studied, two points have been selected for SIMS analysis; point A has been position on the semi-uniformed scale without nodule; point B has been located in the centre of nodule.

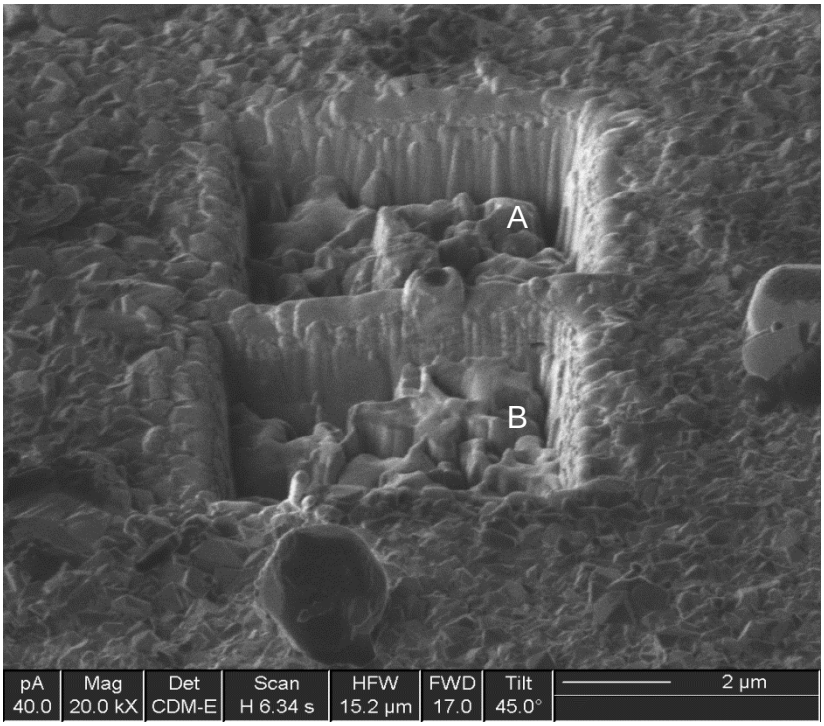

Figure 4-186 The locations of the points for SIMS analysis on Super 304H after 1000 hours exposure at 700°C with the highest steam flow (40 mm/s) (A – Nodule, B – Uniform scale)

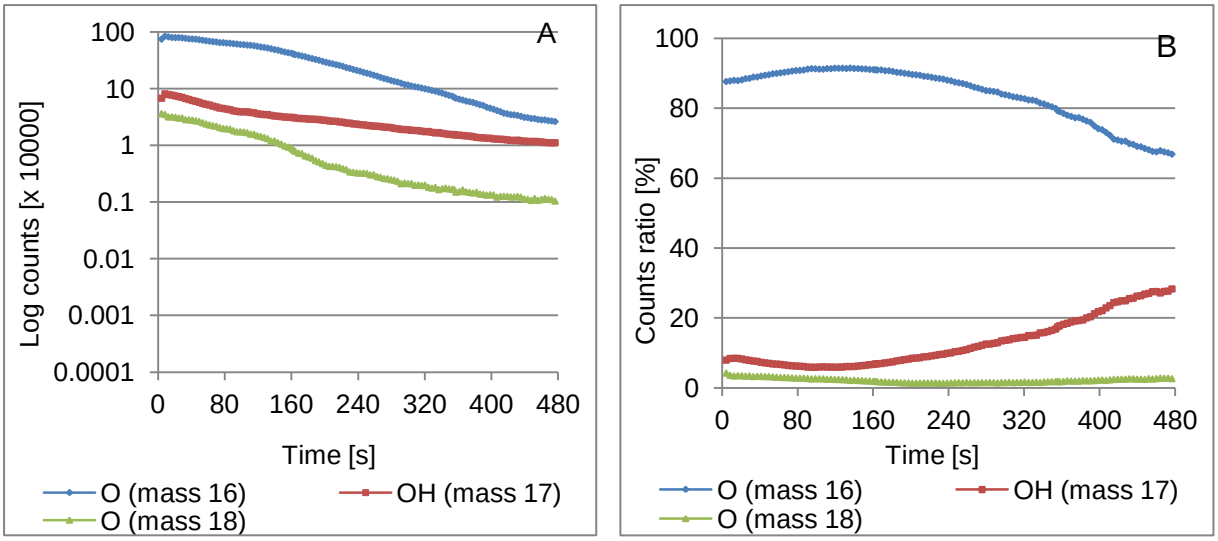

Figure 4-187 SIMS analysis of the nodule formed on Super 304H after 1000 hour exposure at 700°C (Figure 4-186 Point A); A – total counts for particular ion, B - ratio of counts

The results of the study showed that in the nodule formed the level of the oxygen 16 and 18 ions drops with distance from the oxide surface (Figure 4-187A). The highest level is next to the oxide surface and it starts to drop gradually with distance from the surface. The level of hydroxide ions also drops with distance from the oxide; however this drop is less significant. In the inner part of the nodule the signal for OH (17) ions is relatively stronger. Figure 4-187B indicates that the relative ratio of counts for the hydroxide ions increases with distance from the surface, whereas the signals for oxygen 16 continue to drop.

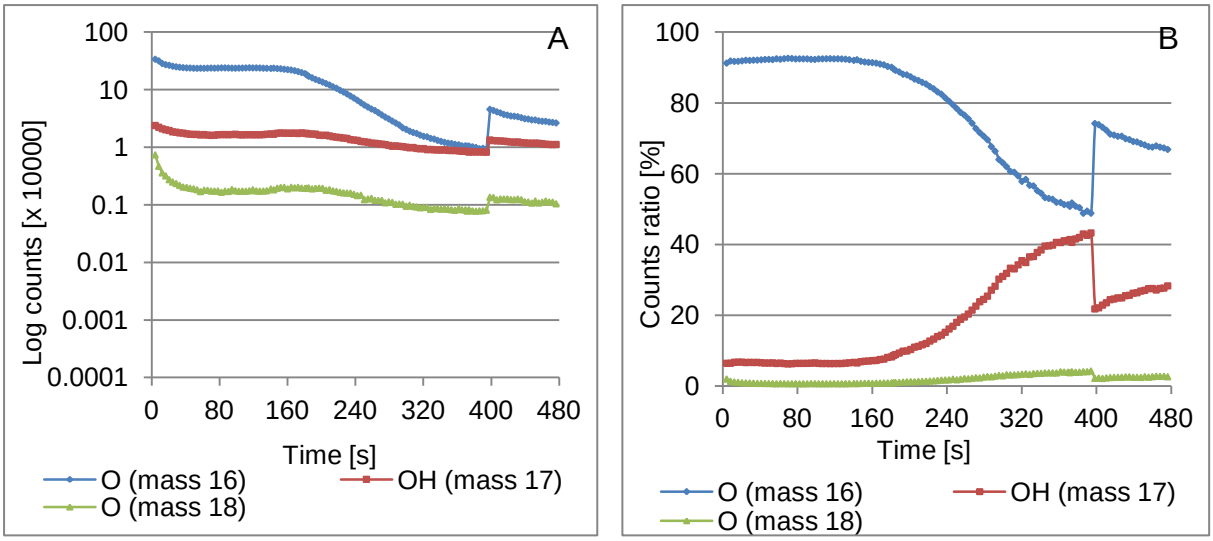

Figure 4-188 SIMS analysis of the uniform scale formed on Super 304H after 1000 hour exposure at 700°C (Figure 4-186B); A – total counts for particular ion, B - ratio of counts

Figure 4-188A shows that the within the uniform scale forming on the Super 304H (during exposure to steam at 700°C with a high steam flow rate) the signal counts for oxygen 16 and 18 and hydroxide ions drop slowly with distance from the oxide surface. Figure 4-188B indicates that the relative ration of counts for both oxygen and hydroxide ions does not fluctuates with distance up to half of the oxide scale, in inner part however the counts for O18 and OH17 ions increase whereas O16 signal decreases. Next to the material surface the relative counts for the O16 are still higher than for O18 and OH17.

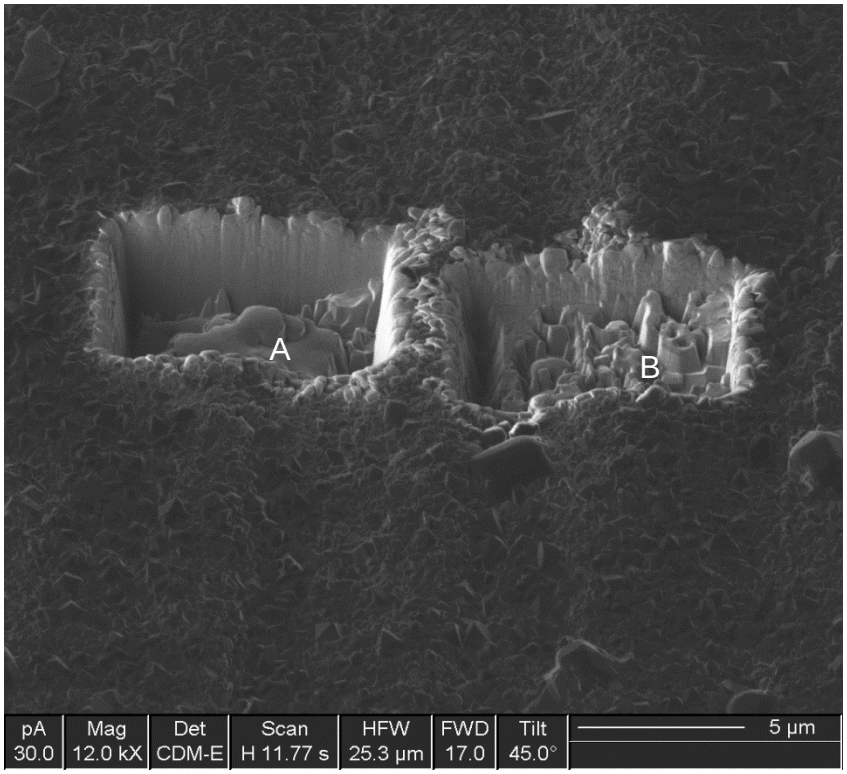

Figure 4-189 The locations of the points for SIMS analysis on HR3C after 1000 hours exposure at 700C with the highest steam flow (40 mm/s) (A – Nodule, B – Uniform scale)

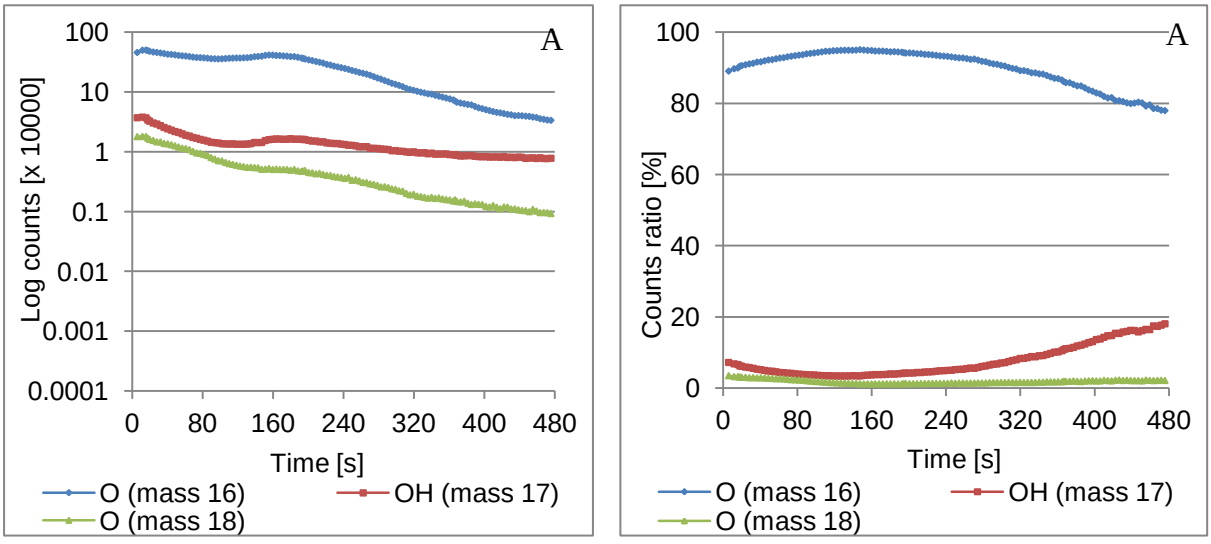

Figure 4-190 SIMS analysis of the nodule formed on HR3C after 1000 hour exposure at 700°C (A) (Figure 4-189)

Figure 4-190A indicates that in a nodule the level of oxygen 18 ions decreases with the distance from the oxide surface, whereas the signal for oxygen 16 decreases

initially (up to ~ 130 seconds) then growths (up to 170 seconds) and finally sharply drops. The signal for the hydroxide ions decreases slowly in the region close to the oxide surface then the counts increase and gradually slowly decrease with the distance from the oxide surface. Analysis of the relative ratio of counts for the ions studied showed that there is a slow increase in the oxygen 16 signal within outer part of the nodule which decreases within the inner part. This matches with the OH17 line, which shows an increase in the relative number of its counts close to the material surface.

The growth of the protective oxides forming on HR3C is more complex process, the results of the SIMS analysis (Figure 4-191A) shows that signal for the oxygen 16 and 18 ions decreases with distance from the surface whereas the counts for hydroxide ion do not change initially with time. Initially the level of oxygen 16 ions steeply drops and then increases to the level before the actual drop and continues to decrease gradually. Signal for oxygen 18 ion decreases with distance from the oxide surface however more slowly than for oxygen 16, but finally in the region close to the material surface there is a significant increase in number of counts. The level of hydroxide ions increases in two regions within the inner scale, with the highest level next to the material surface. Figure 4-191B shows significant drop in the relative number of counts for O16 ions with the distance from the surface for the whole test with the most significant drop in the interface between the outer and inner part of the scale. This drop corresponds to higher counts for O18 and OH17.

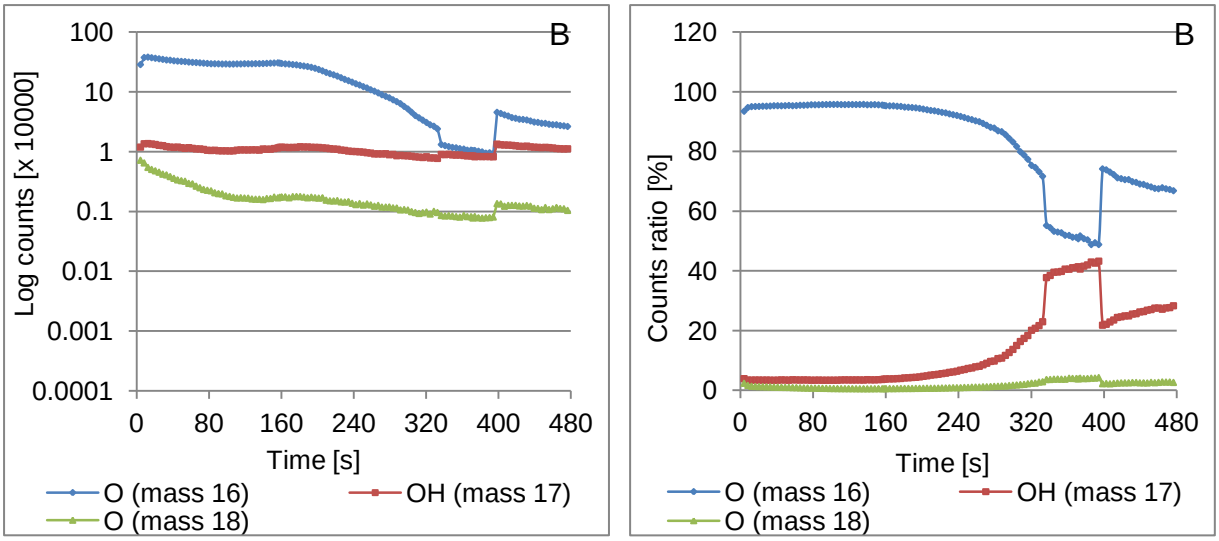

Figure 4-191 SIMS analysis of the uniform scale formed on HR3C after 1000 hour exposure at 700°C (A) (Figure 4-189)

4.2.4 Metal loss

The metal loss analysis, is limited to ferritic steels due to the standard error of the method which is combined error for the micrometer and the microscope with the image analysis software is +/- 5µm. The results acquired for the ground austenitic and nickel-based alloys are within the standard error of the method thus it was decided not to include them in this result chapter, the data are shown in appendix.....

The metal loss data is in agreement with the information obtained during the morphological studies; the median metal loss corresponds to the thicknesses of the inner scales developed. Figure 4-192 shows that the metal loss is significantly influenced by the alloy type above 650°C, at 600°C regardless of chromium content the two ferritic alloys lose around 50 – 60 µm. There is some change of the metal loss with the specimen geometry; however due to the standard error of the image analysis method (6 µm) there is an uncertainty if the discrepancies at low temperatures are result of geometry or method used. At higher temperatures, the differences in the metal loss increase between shapes analysed. Above 700°C and under faster steam conditions the bridge - shaped specimens have the largest metal loss. Higher temperature drives larger metal losses, above 600°C there are clear differences in performance of T23 and T92; the performance between T23 drops sharply with temperature, whereas T92 does not exhibit as significant changes. Figure 4-190 shows that the metal loss of T23 is clearly influence by temperature and that above 600°C the 50°C increase leads to around 2 – 3 times larger metal loss. T92 on the other hand does not show such a fast metal loss increases with temperature, which is in agreement with other data generated.

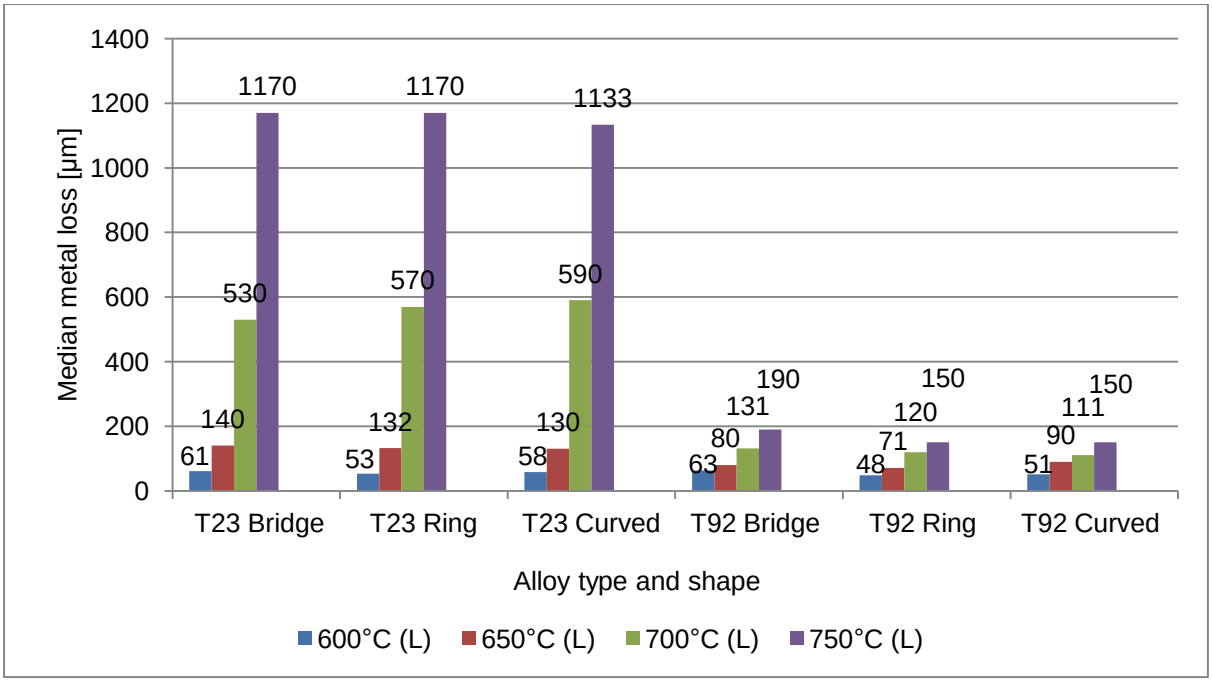

Figure 4-192 Median metal loss of the varies shapes specimens after 1000 hours exposures – temperature effect

The change of steam flow rates has an important impact on the performance of both steels exposed. The significance of the steam flow varies with temperature; at 600°C the increase of the flow rate has the lowest impact on the metal loss of both ferritic steels, however it does not change significantly with alloy type. This confirms that at low temperatures the chromium has less influence on the steam oxidation of ferritic steels regardless of flow rates. At 650°C the steam flow rates seem to have the most significant impact on the steam oxidation of the ferritics alloys. In comparison with results from 600°C exposure, the impact of the chromium level becomes more pronounce. For the high steam flow rates the metal losses of T23 increases almost 100%, in comparison to 700°C this difference is less significant. Analysis of the data acquired for T92 indicates that the steam flow rate effect is lower at both 650 and 700°C than for T23. Therefore, the conclusion that above 600°C regardless of the flow rate 9% the chromium concentration has clearly slowed down the oxidation.

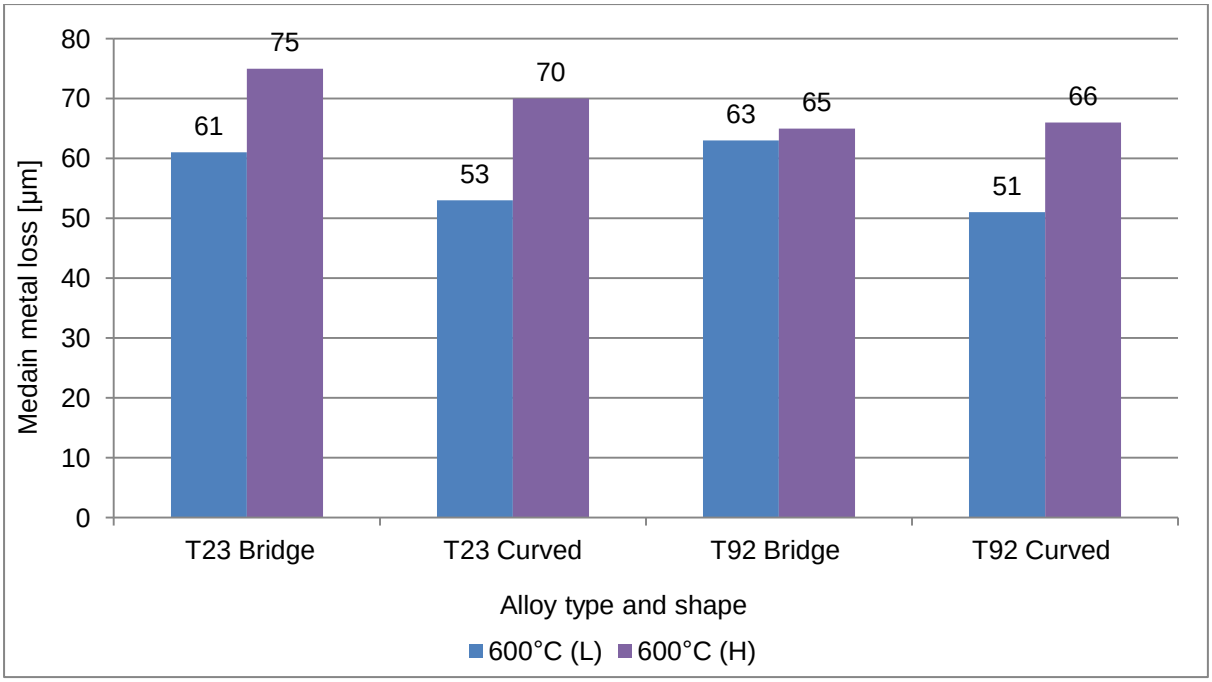

Figure 4-193 Median metal loss of the varies shapes specimens after 1000 hours exposures at 600°C – steam flow effect

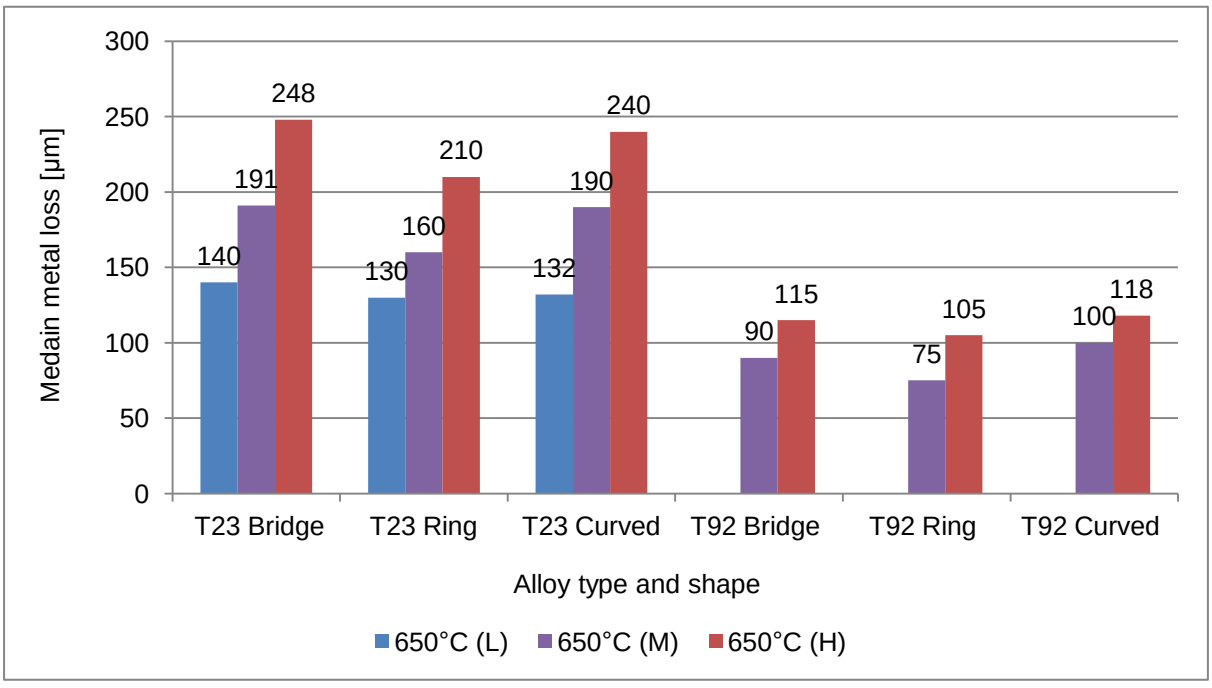

Figure 4-194 Median metal loss of the varies shapes specimens after 1000 hours exposures at 650°C – steam flow effect

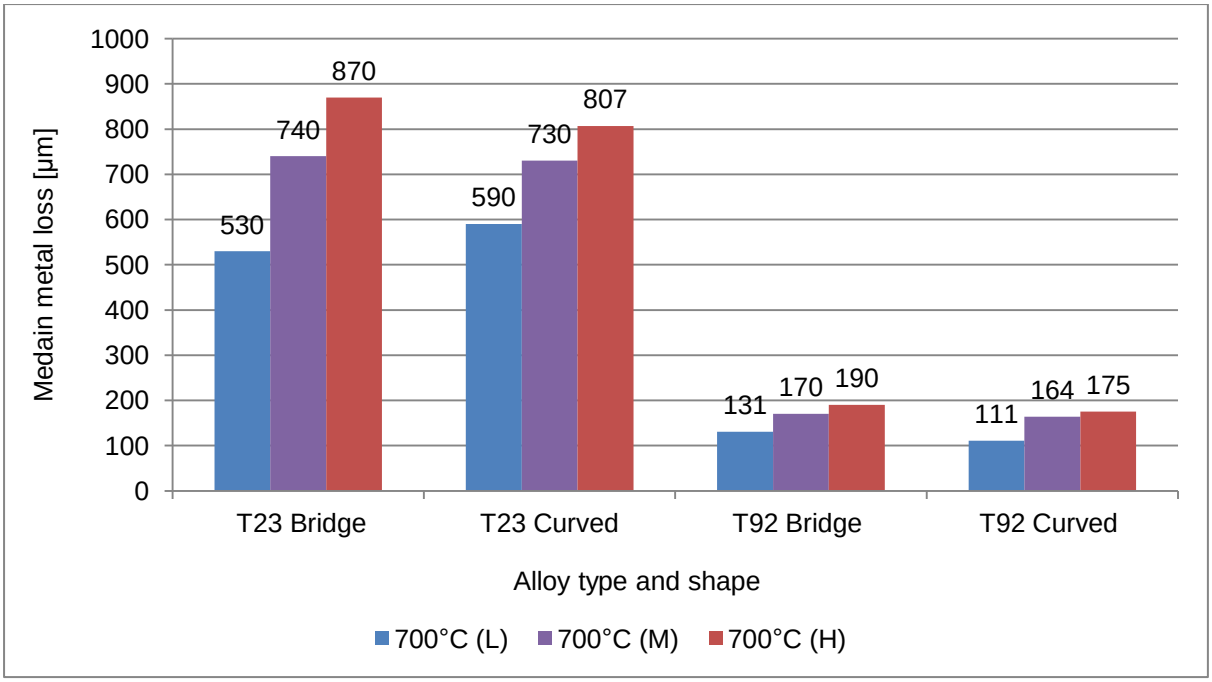

Figure 4-195 Median metal loss of the varies shapes specimens after 1000 hours exposures at 700°C – steam flow effect

4.3 Summary

Steam oxidation kinetics and morphological changes of the scales show that the behaviour and performance of materials vary with the alloy (chromium content, grain and crystal structures), exposure conditions (temperature, steam flow, orientation relative to steam flow) as well as time. The mass change and metal loss data correspond well with the morphological changes; alloys with the highest mass gain from the thickness scales and exhibit the largest metal loss.

Ferritic alloys show much faster oxidation than austenitic alloys and therefore are much less resistant intudied the temperature range s; the scales formed on them are triple-layered and double/triple-layered for T23 and T92 respectively. For T23 the structure of the scales change with the exposure conditions; below 700°C the scale is triple-layered (haematite, magnetite and (Fe,Cr) spinel) above 700°C and at higher steam flow rates the inner scales become micro-layered. In contrast the scale formed on T92 does not show any major changes with temperature, however there is a haematite formation at faster steam flow rates.

The austenitic steels tested showed much slower oxidation rates and fewer structural changes between the oxides formed. At low temperatures and steam flow rates, the materials are covert with discontinues chromium iron rich scales (the chromium content of these scales is dependent on alloy type) with local formation of the nodules. Above 700°C and at faster steam flow rates the number of nodules increases, however on the nodule-free surface a protective, adherent and continuous scales start to develop. The thickest scales were identified for ring - shaped specimens. Among austenitic steels tested 800H showed the best resistant. Its behaviour has similar to Inconel 740, which showed the slowest oxide formation among material changes, and the slowest oxidation kinetic. These two alloys have the best slowest mass change at 700°C. Tests performed show following ranking of the high temperature resistant alloy for the power plant applications: Inconel 740, 800H, HR3C, Super 304H, T347HFG, T92 and T23.

5 DISCUSSION

5.1 Introduction

The steam oxidation of materials used for the tubing and piping of superheater / reheater (SH/RH) is of growing interest as the quest for improvements in power plant efficiency leads to the use of progressively higher steam system conditions. Higher steam conditions (temperature, pressure) can significantly reduce the lifetime of such boiler components because of faster oxide growth. This also causes concern due to its effects on (a) limiting heat transfer and (b) oxide scale exfoliation, which can lead to flow blockages and/or steam turbine erosion. Mitigating of these problems involves understanding the evolution of the oxide scale structures, and their impact on performance of materials. Consequently, it is necessary to characterise and predict the materials' degradation to avoid expensive and unpredictable failures in service.

The study concerned seven types of materials with different structures and compositions: T23, T92, T347HFG, Super 304H, HR3C, 800H and Inconel 740. Each of the materials was exposed to 100% steam at 1 bar pressure in the tests conducted at 600-750°C for 1000 hours. In addition, the impact of the steam flow rates was investigated, with specimens being exposed to three different steam flow rates: low (4 mm/s), medium (16 mm/s) and high (40 mm/s). Moreover, the impact of specimen shapes was investigated using four specimen geometries: bridge, curve, ring and rectangular. The mass of each specimen was recorded after each 250 hour exposure period and the morphological changes investigated after 250, 500 and 1000 hours. This chapter discusses the influence of temperature, material composition, time, steam flow, specimen shape, orientation against steam flow and specimen surface finish on the steam oxidation. Additionally, the oxidation mechanisms for ferritic and austenitic steels are revised. In this chapter the steam oxidation models and heat transfer model for exchanger tube are developed and discussed.

5.2 Temperature and Time

The isothermal tests carried out have allowed the investigation and verification of the impact of temperature and time on the steam oxidation behaviour of seven different alloys: T23, T92, T347HFG, Super 304H, HR3C, 800H and Inconel 740. The result chapter clearly showed that steam oxidation and metal loss of the ferritic and some of the austenitic steels increased with temperature, whereas 800H and Inconel 740 have the best oxidation resistance at 700°C. For ferritic steels, the increasing temperatures lead to faster mass gain and metal loss as well as morphological changes of the scales formed. Moreover, the mass change oxidation kinetics of T23 and T92 changes with temperature; at low temperatures it closely follows a parabolic rate dependence, however with more severe conditions (higher temperatures) the mass change starts to deviate from the parabolic rate law. At 750°C T23 closely follows the linear rate dependence.

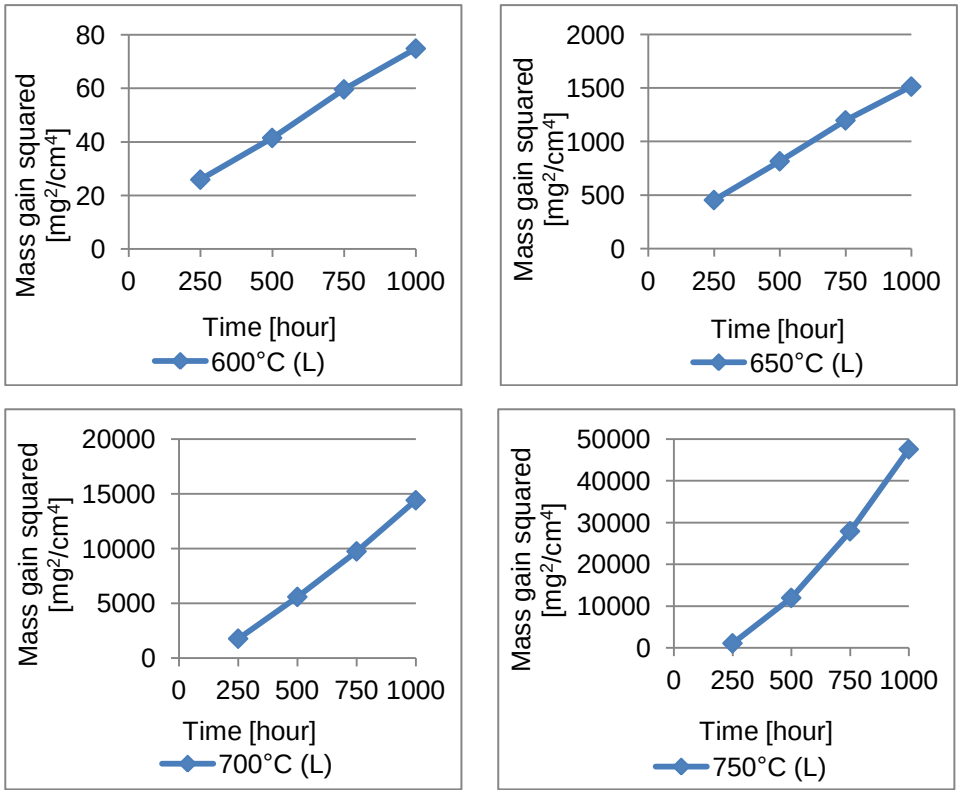

Figure 5-1 Oxidation kinetics for T23 in temperature between 600-750°C (L) (bridge samples)

For T92 there is small deviation from the parabolic rate law at all temperatures. This due to the scales' spallation and the fact that just part of the exfoliated oxides has been caught inside the crucible.

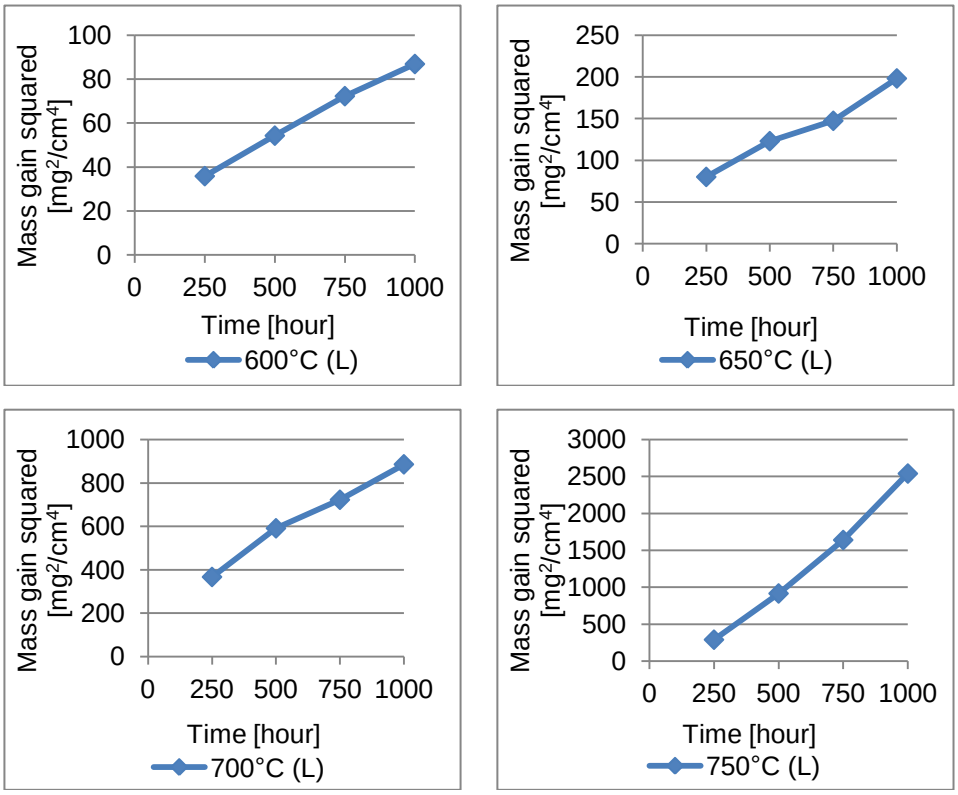

Figure 5-2 Oxidation Kinetics for T92 in temperature between 600-750°C (L) (bridge samples)

For an initial analysis of the mass change data the oxidation of both alloys was assumed to be parabolic (n=2); and so parabolic rate constants (k_p) were calculated for each specimen geometry, using following equation where x is the mass change [mg/cm^2], kp is the parabolic rate value [mg^2/cm^4/s] and C is the integration constant:

$$x^2 = k_p t + C \qquad \textbf{(5-1)}$$

Table 5-1 - Table 5-3 show the values of parabolic rate (k_p) and integration constant (C) obtained from T23 and T92 for bridge, curve and ring specimens at low steam flow rates:

Table 5-1 Values of the parabolic rate constant for T23 and T92 in temperature range tested (bridge samples)

Temperature/Alloy	T23		T92	
	$k_p\ [mg^2/cm^2s]$	C	$k_p\ [mg^2/cm^2s]$	C
600°C (L)	2.970E-05	2.247E-12	2.860E-05	4.831E-12
650°C (L)	6.400E-04	1.927E-11	2.540E-05	9.784E-13
700°C (L)	8.840E-03	3.701E-10	4.500E-04	-8.164E-08
750°C (L)	2.560E-02	1.395E-09	1.220E-03	6.888E-11

Table 5-2 Values of the parabolic rate constant for T23 and T92 in temperature range tested (ring samples)

Temperature/Alloy	T23		T92	
	$k_p\ [mg^2/cm^2s]$	C	$k_p\ [mg^2/cm^2s]$	C
600°C (L)	2.290E-05	2.311E-12	1.39E-05	-3.657E-05
650°C (L)	4.390E-04	8.031E-12	5.97E-05	3.375E-12
700°C (L)	5.160E-03	8.940E-11	3.02E-04	-2.813E-07
750°C (L)	2.180E-02	8.600E-10	1.13E-03	5.755E-11

Table 5-3 Values of the parabolic rate constant for T23 and T92 in temperature range tested (curve samples)

Temperature/Alloy	T23		T92	
	$k_p\ [mg^2/cm^2s]$	C	$k_p\ [mg^2/cm^2s]$	C
600°C (L)	3.380E-05	7.107E-13	2.860E-05	7.072E-13
650°C (L)	3.990E-04	2.218E-11	1.610E-04	-1.514E-07
700°C (L)	6.700E-03	2.249E-10	3.720E-04	-7.189E-08
750°C (L)	2.780E-02	1.278E-09	1.210E-03	6.690E-11

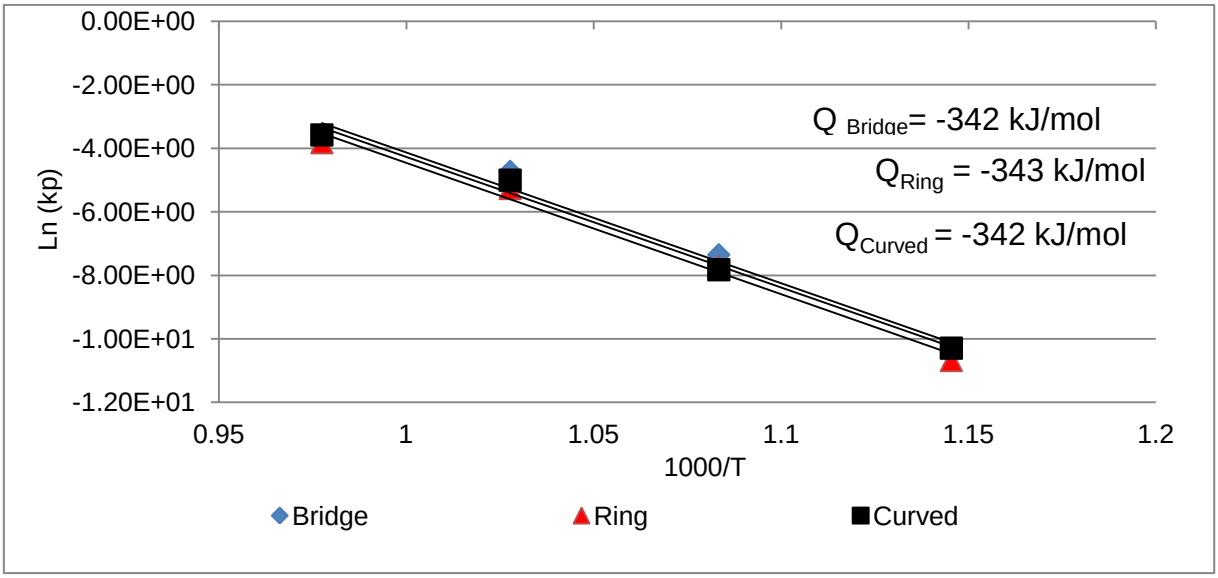

Figure 5-3 Arrhenius plot for T23 in the temperature between 600 - 750°C (L)

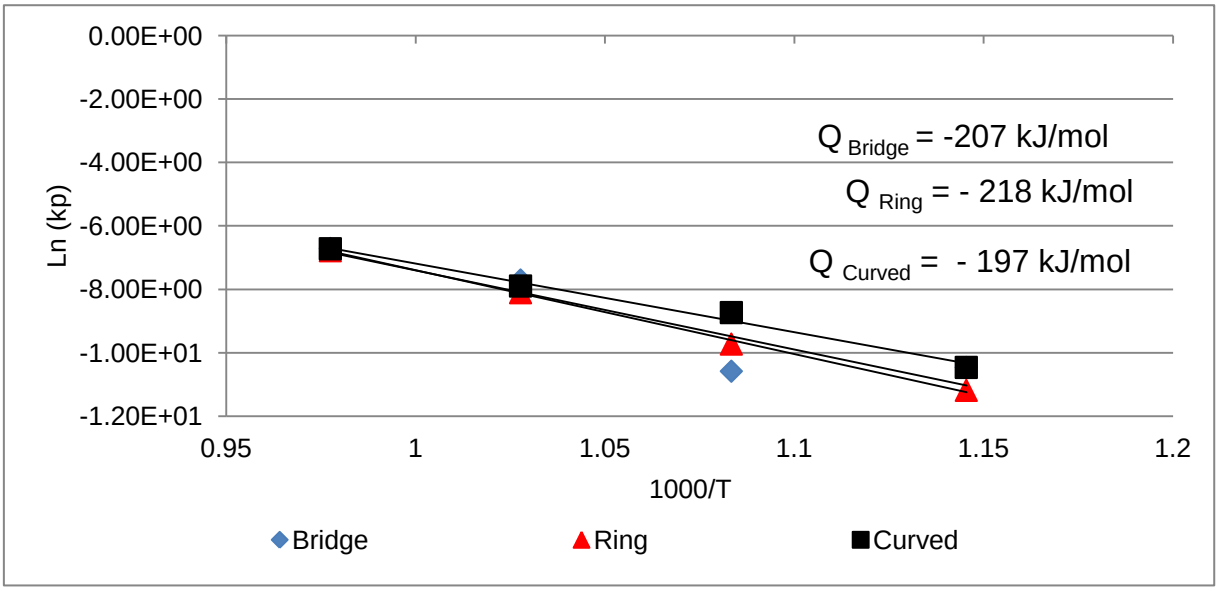

Figure 5-4 Arrhenius plot for T92 in the temperature between 600 - 750°C (L)

The temperature dependence of ferritic steels is described by the Arrhenius equation and is plotted in Figure 5-3 and Figure 5-4. Analysis of these data by fitting lines to the points representing the parabolic rate constants at particular temperatures allows the calculation of values of the activation energy required for the oxidation process to proceed. These parabolic rate constants and activation energies of steam oxidation match data found literature [15, 23, 24]. (see chapter 2.5) It is important to remember that the activation energies

obtained from such mass change data generated describe the overall, average steam oxidation process and therefore should be interpreted as an apparent activation energy, which combines both outward and inwards migration of ions [22] and other effects. In Appendix A1, the kinetics data corresponding to metal loss and oxide scale thickness change are presented. Their analysis indicates that the activation energies acquired from metal loss and oxide scale thickness change differ from those obtained from mass change. This is believed to be a result of the fact that metal loss and thickness data are obtained just after 250, 500 and 1000 hours and secondly because they are acquired for different specimens, which might cause some errors.

Table 5-4 Activation energies for steam oxidation of T23 and T92 in temperature between 600-650°C using metal loss and oxide scale thickness data obtained

Activation energy [kJ/mol]		
Alloy type	Metal loss	Oxide scale thickness
T23Bridge	-285	-280
T23 Curve	-349	-332
T92 Bridge	-113	-
T92 Curve	-110	-

The mass change of ferritic steels is fast in the initial period of oxidation due the clean, oxide free surface at the beginning of oxidation, and continues through the formation of the first oxides and the establishment of equilibrium at both alloy/scale and scale/oxide interfaces. After the formation of the first oxides, the oxidation process starts to slow down gradually. The first stage of oxidation is controlled by surface reactions. It involves adsorption of the oxidising species on the surface and short-cut diffusion of the metal ions. As a result of these two processes the first oxides develop. It is believed to follow the linear rate law and according to Ennis and Quadakkers [53] its duration varies with alloy type (chromium content). After the development of the first oxides, steam oxidation is controlled by the diffusion of oxidising species and metal ions through the scales [24, 96]. Diffusion process is temperature dependent; at

higher temperatures the atomic movements are faster and more frequent [62] and the concentration of the vacancies increases and therefore the diffusion process accelerates. It drives larger mass gain, thicker scales formation and more extensive metal loss, which corresponds well with data obtained for both ferritics alloys. The microscopic observations of the scales formed showed that there is a clear change in the scale thicknesses with temperature and time. In the temperature range tested the T92 forms double-layered scales, which consist of inner (Fe, Cr) spinel and outer magnetite (Fe_3O_4). In addition in the regions facing the steam flow patches of haematite have been identified. Fe_2O_3 was only found after longer exposure to low temperatures. The thermodynamic consideration suggests that haematite should form as a result of the fact that the partial pressure in equilibrium required for the Fe_2O_3 to nucleate (Table 5-6) is lower than the actual oxygen partial pressure (Table 5-5). Such a situation suggests that no equilibrium is established on the gas oxide interface, and therefore oxidation is believed to be controlled by the gas/solid reactions at the scale/gas interface [67]. The second explanation for the lack of haematite layer is the fact that the scales are spalling. This would suggest that the scale is growing by inward and outward diffusion.

Table 5-5 Oxygen partial pressure of the test environment calculated with equation (2-65) (see chapter 2.5.2)

Temperature [°C]	Oxygen partial pressure pO_2 [bar]
600	1.670E-08
650	5.450E-08
700	1.570E-07
750	4.110E-07

Table 5-6 Oxygen partial pressures in equilibrium for the particluar oxide formation

Oxide type	Oxygen partial pressure in equilibrium [bar]			
Temperature [°C]	600	650	700	750
Fe_2O_3	6.970E-16	2.880E-14	8.150E-13	1.660E-11
Fe_3O_4	5.080E-25	5.370E-23	3.520E-21	1.530E-19
Cr_2O_3	2.280E-36	6.030E-34	8.960E-32	8.160E-30
$FeCr_2O_4$	2.030E-29	6.680E-27	8.860E-26	3.160E-24

Ennis and Quadakkers [18] reported that 9% of chromium steels in the temperature range 600-650°C do not form Fe_2O_3 up to long exposures. Zurek et al. [67] also stated that no haematite is developed during steam oxidation in the temperature range 550-650°C. In general, the scales developed on T92 are brittle and tend to spall off during cooling (even at low temperatures). Exfoliation occurs above the inner/outer interface, and this is a second explanation for the lack of haematite on the surface. An analysis of the scales formed on T92 showed that there is a growing concentration of voids with temperature, which coalescence with gaps. The voids and gaps develop both in the inner and outer layers, as well as on the interfaces between the inner and outer layers [18]. The formation of voids and the coalescence of voids and gaps is believed to be a result of the restriction of the Fe diffusion due to formation of the (Fe, Cr) spinel, which significantly slows down the iron transport [98] .The test results at temperatures investigated showed clear spallation of the scales which occurs within the outer scales as well as at the interface between inner and outer scales. This spallation confirms that the oxides' growth is controlled by the iron diffusion. Such an explanation was also suggested by Ennis and Quadakkers [18]. Generally, the exfoliation of the scales on T92 is reported in literature [99, 100] to involve a separation of the oxides along the interface between inner and outer layers. Wright and Dooley [92] showed that the spalled flakes are mostly magnetite with some additions of haematite. Moreover, there is another phenomenon, which was reported by Wright and Dooley [92] and also identified

in this study: delamination of the magnetite. Scale lifting, as discussed, requires the magnetite layer to be put in compressive stress during cooling, which is a result of the different coefficients of thermal expansion (CTE) between the outer and inner layers [92]. Analysis of the CTE for different layers of oxide shows that there is very small difference in the CTE between magnetite and spinel; and so the development of haematite within the outer layer is required. The mixed Fe_3O_4 and Fe_2O_3 layer will have a significantly lower CTE than spinel and will result in compressive strain upon cooling and therefore delamination of the magnetite/haematite layer.

Table 5-7 Coefficients of thermal expansion [10^{-6}/°C] [92]

Temperature [°C]	Haematite (Fe_2O_3)	Magnetite (Fe_3O_4)	Spinel ($(Fe,Cr)_3O_4$)
600	13.00E6	16.00E6	18.00E6
650	14.00E6	-	17.00E6

The oxidation of T23 is more temperature dependent; there are a changes in the type of scales and oxidation rates with temperature. In the temperature range 600 - 650°C, with low steam flow rates the scales formed do not change with temperature. This suggests that there is the same rate controlling process involved (cationic ion diffusion) and that faster oxidation rates are a result of faster diffusion of cations with an increase in temperature. The scales developed are triple layered with inner (Fe, Cr) spinel, outer magnetite and outermost haematite. The formation of haematite is believed to be a result of the reduction of the transported iron from the alloy by the formation of the semi-protective inner spinel layer and the gradual increase in void development. Thus in the outer regions Fe_3O_4 oxidises to Fe_2O_3.

At 700°C there is less haematite on the surface than at lower temperatures, which is believed to be a result of:

- Changes in counter diffusion of Fe ions and oxidising species (oxygen, oxy-hydroxyl)

- The reduction of Fe_2O_3 to Fe_3O_4 resulting from a gap healing within the magnetite layer below the haematite.

Faster steam oxidation of T23 at 700°C and 750°C corresponds to a change in the type of scales developed. At these temperature exposures the inner scales consist of micro-layers of different oxides, which were identified by Wright and Dooley [24, 92] as a sequence of repeating layers of magnetite and mixed magnetite and iron/chromium spinel. Its formation is not clearly understood in laboratory studies. In power plants, the development of micro-layered inner scales has been suggested to be a result of the heat flux [96], which has not been stimulated in the tests performed. The formation of such micro-layers in the laboratory is believed to be the result of the decomposition of wustite (FeO), which forms at higher temperatures. Wustite decomposes to magnetite and this explains the composition of the micro-layered inner layer formed on T23.

The oxidation rates of austenitic and nickel-based alloys are significantly slower, and do not follow one single rate for all of the exposures. At low temperatures the linear dependence prevails whereas at higher temperatures it changes to parabolic. Wright and Dooley [24] suggest that oxidation of the 300-series steels exposed to steam exhibits a parabolic rate. In general, the oxidation of austenitic and nickel-based alloys is slow and the mass change is much lower than the ferritics. This is believed to be a result of the ability to form a protective chromia layer. The low mass change could be explained by spallation of the thin oxide layers formed on the specimen surface. There is also possibility of the volatilisation of the thin scales formed. However, volatilisation of chromia is reported to have less impact on steam oxidation at lower temperatures [24]; it becomes more significant above 700°C [23]. Young [101] believes that in laboratory studies the volatilisation of chromia in various water-containing environments up to 800°C is relatively slow and could be neglected. Holcomb [78] reported that volatilisation of chromia increases the oxidation rate and the rate dependence changes to linear. In general, the oxidation of austenitic steels is reported in the literature as being much slower than ferritics,

which was also confirmed in this study. However the scales on the austenitic steels are reported to be magnetite with significantly high void levels and haematite as the outermost layer. Such structures have not been observed on the ground specimens, however has formed on the polished and as-received specimens (the impact of the specimen surface finish is described in chapter 4.2.2.3).

Oxidation of T347HFG clearly changes with temperature, however due to extensive spallation of the oxides formed the oxidation rate dependence of this alloy could not been clearly identified. The results of the test showed that at lower temperature the alloy oxidise much slower and thin protective oxides layers are forming. At higher temperatures (above 700°C the mass change increases which is consistent with morphology; scales become more continuous and protective. At this stage oxidation is controlled by two mechanisms: diffusion of ions through the scales and grain boundary diffusion initially. In the regions where the protective scales have broken down nodules start to develop. Those nodules are double-layered; magnetite outer layer with Ni and Cr additions, and inner (Fe, Cr, Ni) spinel (see chapter 4.2.2.2). Such a composition suggests that nodule growth is controlled by the outward diffusion of metal ions and inward diffusion of the oxidising species. Jianmin et al. [88, 89] proposed that the nodular growth of such scales involves the same processes as those identified during the formation of the double-layered scale on ferritic steels. The inner layer of a nodule grows by penetration of Cr-rich Fe-Cr spinel precipitates along grain boundaries to surround the whole grain. The chromium within these boundaries is consumed by outward ionic diffusion and develops internal oxides. The chromium-depleted grains oxide to magnetite. The combination of these two processes the explains existence of the mixed magnetite and (Fe, Cr) spinel inner layer. The outer layer grows by oxidation of the inner layer due to counter diffusion of oxygen and iron ions. The number and size of nodules increase with temperature, which corresponds well with the oxidation rates. After longer exposures nodules are expected to spread along the surface and form double-layered scales (as is reported by Wright and

Dooley [24] and confirmed by Hansson and Montgomery [49, 87]). An analysis of the scales formed on T347HFG at high temperatures (700 and 750°C) showed growth of a protective oxide layer; such growth is believed to be a result of internal oxidation of Fe and Cr, which is in accordance Hansson and Montgomery [49], and Hansson et al. [93]. Super 304H also showed a clear temperature and time dependence. The oxidation rate for this steels could not been correctly assessed due to very low mass change which is believed to be a result of the scale spallation. The morphology of the scales forming clearly changing with conditions; at lower temperatures is less protective, the oxides do not cover whole surface. At higher temperatures the scales developed are believed to be more protective. The scales formed at 750°C are more protective, and the formation of nodules is suppressed because of the adherent scales, which do not break down. In contrast at 700°C the scales are discontinuous and nodules start to form in the regions where the protective oxides exfoliate. These nodules are double-layered, with a protective spinel as the main constituent of the inner layer and an outer layer of magnetite. The outer oxide exfoliates. This could be a result of the suppression of iron diffusion through the spinel which drives the formation of voids that in turn leads to scale exfoliation.

However, the oxidation rate of HR3C is dependent on the exposure condition; time seems to have less impact than for 18 Cr steels. The scales are non-adherent and discontinuous up to 700°C (L). At 750°C (L) the alloy develops protective oxides, whose formation slows down the oxidation. Oxidation of HR3C in the temperature range 600-700°C (L) is slow, the mass change data show small mass gain which could be result of the scale spallation at the condition tested. The slow oxidation in temperature range 600-700°C (L) and lack of the continuous oxide layer may also suggest that at theses temperatures the oxidation is controlled by the surface reactions. At 750°C (L) oxidation is much faster that at lower temperatures which could be explained by the change of the controlling mechanism or lack of scale exfoliation. At high temperature

the oxidation of HR3C is believed to be driven by counter-diffusion of metal and oxidising ions through the scale formed.

800H is a reference alloy that was used to fill in the gap between austenitic steels and nickel-based alloys. This material showed good oxidation resistance at all temperatures; however, its oxidation behaviour still changed with temperature. It has shown the smallest mass change at 700°C (L), which is explained by the formation of the most protective oxide layer that slows down the oxidation process (however the protective layers tends to spall of during specimens cooling). At 700°C (L) there is a clear change of concentration of the elements (Cr, Fe, Ni, O) at the material surface and closely underneath its surface. The concentration of oxygen is high at the surface, which suggests the formation of protective scales. At 750°C (L) steam oxidation leads to the formation of thicker scales. Moreover, nodules develop in the regions where the protective layers break down. The nodules are single-layered with a mixture of Ni, Cr and iron oxides. Their growth is controlled by the same mechanism as explained for the formation of the inner part of the nodules developed for T347HFG. However there is re-growth of the protective layer on the nodules, which slows down further nodular development. At 750°C (L) oxidation leads to the formation of thicker scales; however there is local breakdown of the scales and the formation of nodules. The nodules formed are single-layered with a mixture of Ni, Cr and Fe oxides as reported at 700°C (L). An analysis of the oxidation of 800H shows that clearly it changes with temperature however due to scale exfoliation the identification of the oxidation rate would be misleading. However, there is a indication that at higher temperatures the oxidation rate differs from this at lower temperature. This possible change could be explained by the change of the mechanism involved during oxidation from the surface reactions to ionic diffusion. The changes of the oxidation rate from linear to parabolic dependence could also be associated with the fact that at low temperature no full equilibrium is established and the critical mole fraction of chromium (N_{Crcrit}) for the formation of an external, protective oxide layer is not reached.

Inconel 740 is the most steam oxidation resistant among the materials investigated, it shows the slowest mass change and morphological changes. Oxidation of Inconel 740 varies with temperature and time. At 600 and 650°C (L) the mass change of the specimens is slow which corresponds well with the scale morphology. At 700 and 750°C (L) Inconel 740 shows faster mass change and formation of protective oxides which tend to exfoliate less than at oxides developed on specimens exposed at lower temperatures. Due low mass change of the specimens and possible exfoliation of the oxides scales forming the oxidation rate for Inconel 740 has not been derived from data available in this study. In general, there are only a limited number of publications concerning steam oxidation of nickel-based alloys. Pear et al. [94] suggested that oxidation of nickel-based alloys followed a linear rate law. This suggestion was opposed by Wright and Dooley [24], who reviewed data available in literature and proposed that at high temperatures steam oxidation of nickel-based alloys shows a parabolic rate dependence. The surprising finding is that at 700°C (L) Inconel 740 showed the slowest mass change and formation of protective oxides on the surface, which seems to be adherent to the surface. Wright and Dooley [24, 92] reported that alloys with chromium content above 22% show very good oxidation behaviour at 700°C, which is consistent with the collected data.

5.3 Material composition and structure

Table 5-8 Nominal composition of the materials tested

Alloy	C	Ni	Cr	Mo	W	Co	Al	Ti	Nb	Mn	Fe	Si	Cu	N
T23	0.06	-	2.25	1	1.5	-	-	-	0.04	0.45	bal	0.2	-	-
T92	0.13	0.4	9	1	1.87	-	-	-	0.09	0.6	bal	0.16	1	0.07
T347HFG	0.1	10	18	-	-	-	-	-	0.8	1.6	bal	0.6	-	-
Super 304H	0.1	9	18	-	-	-	-	-	0.4	0.8	bal	0.2	3	0.1
800H	0.08	32.5	21	0.4	-	-	0.4	0.5	-	0.8	46	0.5	0.4	-
HR3C	0.01	20	25	-	-	-	-	-	0.6	2	bal	0.75	-	0.35
Inonel 740	0.03	bal	25	0.5	-	20	0.9	1.8	2	0.3	0.7	0.5	-	-

In the literature, alloy composition is reported to have a significant impact on the performance of materials during high temperature oxidation [15, 23, 24]. There are a number of different elements which are used to improve oxidation resistance, among them chromium, silicon, manganese, molybdenum and tungsten which are believed to be the most importan. [23]. The materials are designed to promote the development of protective oxide scales; including two of the most desirable oxides are: alumina, chromia and silica [24]. For the purposes of this PhD, the stainless steels and Inconel 740 are analysed and the oxidation resistances of these materials are reported to be ideally the result of chromia layer formation. However, in this study, the protection of the oxide scales is associated with the formation of various types of the chromium and iron spinels. The alloy's ability to develop various protective chromium oxides is dependent on the chromium content [67]. An analysis of the impact of chromium on the oxidation of the alloys tested clearly showed that with higher levels, the oxidation rates slow down and more protective oxide scales form [66]. However, up to 600°C there is no difference in steam oxidation of 2.25Cr and 9Cr steels, which is also reported in the literature. Sanchez et al. [66] have indicated that the impact of chromium is much lower up to 570°C and therefore for components operating at temperatures below 570°C steels with low Cr levels

can be used. Viswanthan et al. [15] reported that steam oxidation of 2.25 – 9Cr is independent of chromium content up to 600°C. This was also confirmed by Watanabe et al. [102]. Moreover, the literature suggests that there is no significant difference in the oxidation of more advanced ferritic steels (9-12Cr) at low temperatures (below 600°C). The low impact of Cr levels (2.25 or 9%) can be explained by the slower diffusion of iron ions at < 600°C as the diffusion coefficient is temperature- dependent [57, 66]. A second explanation is that neither of these two steels has sufficient levels of chromium to suppress less-protective iron oxide scale growth [56]. Though it is well recognised that steels with higher chromium levels exhibit better oxidation resistance due to the formation of more protective oxides, there is still some uncertainty about the chromium threshold needed to achieve this transition with values ranging from ~10-12 weight % Cr [24]. Shibili and Starr [56] proposed that in the temperature range 600-650°C the minimum level required for external chromia formation is 10-11%, whereas Sanchez et al. [66] believe the threshold should be higher (11-12%).

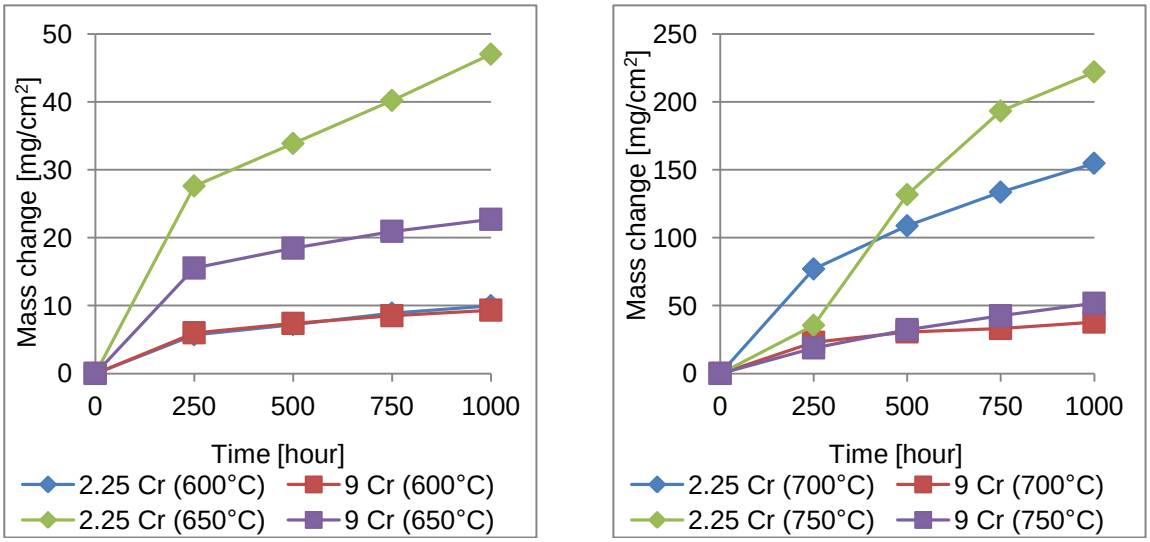

Figure 5-5 Change of the mass change with chromium content for ferritic steels in temperature between 600-750°C (L) (bridge specimens)

Above 600°C the oxidation of ferritics becomes more chromium-dependent. There are clear differences in the performance of 2.25 and 9Cr steel that is associated with the ability of 9Cr steel to form a more protective spinel, which

suppresses the outward diffusion of iron and therefore reduces the oxidation rate. The material composition of ferritic steels does not allow the identification of the impact of the other alloying elements due to large differences in the chromium content. However, in the literature silicon is also reported to have a significant impact on the oxidation of ferritic steels [15, 23] Silicon is believed to improve material resistance above 650°C. It has a greater impact on oxidation of 9-12Cr steels than difference in chromium [64]. The positive impact of silicon results from a segregation process that occurs beneath an external chromium-rich scale, where Si accelerates the outward diffusion of Cr due to reduction of the contact area between the external scale and alloy surface [23, 24, 85]. Although there is a clear positive impact of silicon on oxidation resistance, it also leads to embrittlement of the scales formed and it can deteriorate creep strength at elevated temperatures. An analysis of the impact of silicon on oxidation of low chromium steels showed that silicon content in the range 0-3% has an irregular impact on the steel performance at 500-600°C. A typical level of silicon in low chromium steel ~0.3% is proven to be beneficial above 500°C.

Chromium and silicon have the most significant and clear impact on steam oxidation resistance. However, there are other elements including manganese, molybdenum and tungsten. Manganese has been reported to promote the formation of protective scales and to suppress the loss of chromium via volatilisation [15, 23]. The combination of manganese and chromium is believed to diffuse into the scales and promote the formation of Cr-Mn spinel, which reduces the outward transport of iron and impedes the eventual development of chromium-rich scales [24]. Molybdenum and tungsten do not have a single, clear impact; the impact of these two elements is reported to be dependent on conditions and alloy type [15, 23, 24]. Kutsumi et al. [103] reported that Molybdenum has a greater impact on slowing down oxidation than tungsten. An analysis of the impact of W concentration on oxidation of 2.25 and 9 Cr showed that higher levels of tungsten for 9Cr produce higher levels of the steam oxidation change, whereas for 2.25Cr no impact has been reported [23].

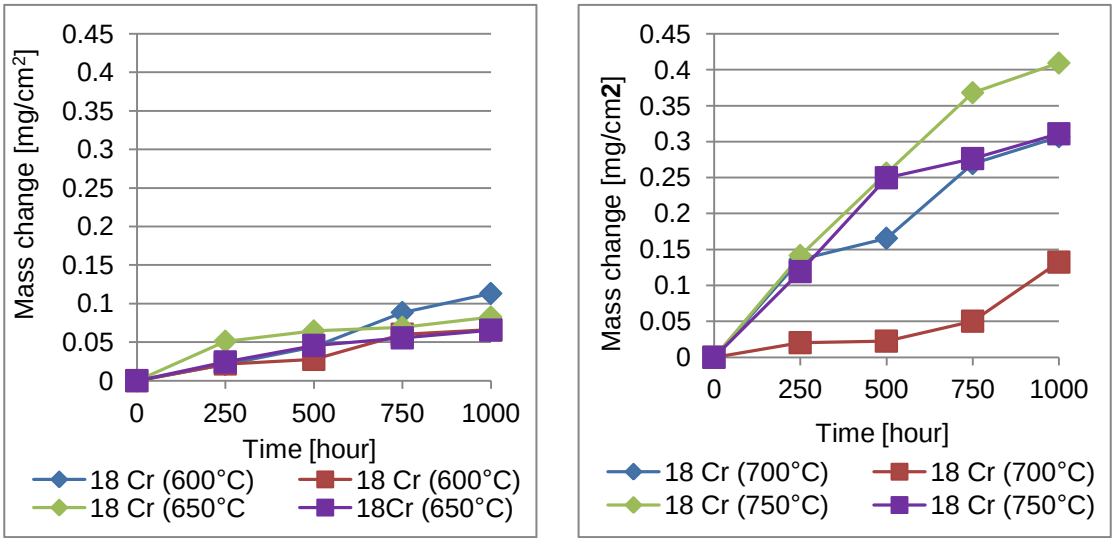

Figure 5-6 Change of the mass change with chromium content for austenitic steels (T347HFG, Super 304) in temperature between 600-750°C (L) (bridge specimens)

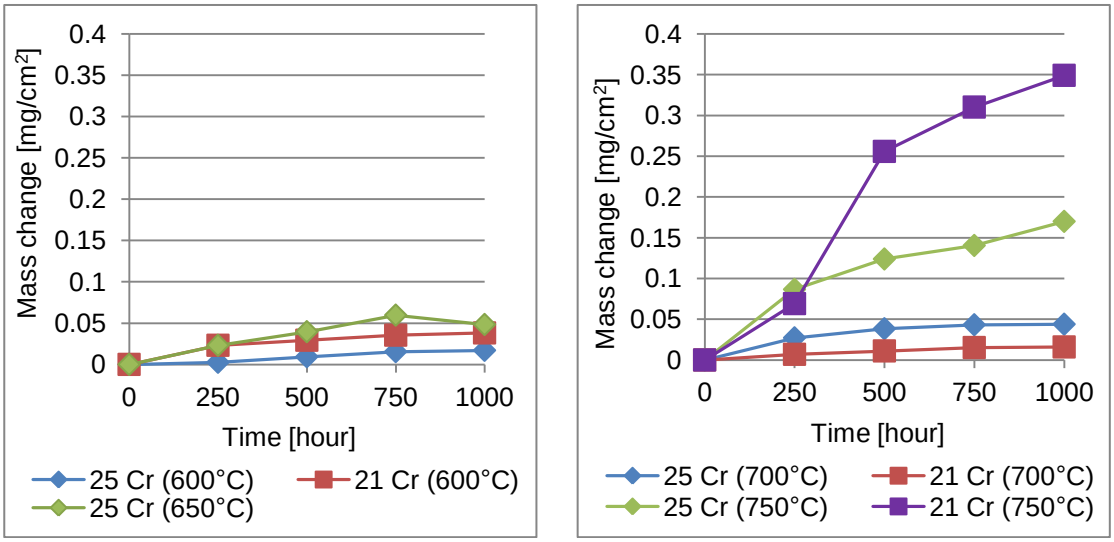

Figure 5-7 Change of the mass change with chromium content for austenitic steels (HR3C, 800H) in temperature between 600-750°C (L) (bridge specimens)

Alloys with chromium levels 18% and above showed an improved oxidation resistance (the mass change is much slower than for ferritic steels), which varies with temperature (see chapters 4.1.2 and 4.2.2.2)). An interesting finding was made regarding T347HFG and Super 304H. For the same

chromium level, these two materials showed different mass change and this is believed to be a result of the impact of the different alloying addictions.

Table 5-9 Composition of the T347HFG and Super 304H acquired with SEM-EDX analysis

Alloy	Ni	Cr	Mo	W	Co	Al	Ti	Nb	Mn	Fe	Si	Cu	N
T347HFG	10	18	-	-	-	-	-	0.8	1.6	bal	0.6	-	-
Super 304H	9	18	-	-	-	-	-	0.4	0.8	bal	0.2	3	0.1

A comparison of the compositions of both materials (Table 5-9) indicated that Super 304H has a lower concentration of Manganese and Silicon which suggests that T347HFG should have a slower mass change due to the positive impacts of Mn and Si on chromia formation, however results showed that Super 304H oxides slower at the conditions tested. The largest difference in composition between the two materials is copper. The literature showed that Cu can be incorporated in the growth of Cr-rich scales and can therefore improve the alloy oxidation [23]. The ideal concentration of Cu within the alloy is reported to be 2.5-3.5%. Such levels are expected to have the best combination of high-temperature strength and oxidation resistance [24]. This explains why Super 304H shows in the test conducted slower mass change and formation of more protective scales than T347HFG. The difference in mass change between these two alloys could also be the result of different specimen thicknesses. The thickness of the specimen may influence the oxidation process. In literature, the impact of the specimens thickness on oxidation of ferritic steels is explained due to the breakaway of the scales formed [104, 105] Since there is a limited data on scale morphology of the austenitic steelsin this study this mechanism could not be clearly confirmed. In spite of that it is believed to be one of the possible explanation of the changes in oxidation behaviour of the material with change of the specimen thickness. An analysis of the changes in material performance with thickness for nickel-based alloys showed that thin specimens oxidise faster. This is explained by Zurek et al. [106] through the different plastic deformation of thick and thin metallic substrates. Moreover, the effect of stress

on diffusion with the oxides is believed to be more closely related to stress-dependent defect concentration than diffusivity.

The differences in steam oxidation resistance between ferritic and austenitic steels as well as nickel-based alloys are partially the result of the crystallographic structure of each material. Ferritic steels have a body centred cubic (BCC) crystal structure, which is less packed than face centred cubic (FCC); therefore diffusion in a BCC structures is much faster. Moreover, in materials with a BCC structure the differences in mobility of atoms within the grains' centres and at the grains' boundaries are smaller; therefore in a BCC structure preferential grain boundary diffusion would occur to a lesser degree than in an FCC crystal structure [107]. Austenitic steels and nickel-based alloys have a FCC structure, in which diffusion in the grain is significantly slower than in BCC. Khanna [57] reported that the diffusion in FCC is 100 times slower than in BCC crystal structure. This suggests that for such alloys grain boundary diffusion is a more preferable phenomenon than diffusion in grains [49] and requires lower activation energy [93].

In the study conducted, the difference in oxidation of various grained structure materials was not investigated; however for purpose of this discussion the findings and conclusions of other researchers are presented. The grain structure of austenitic alloys is recognised as an important factor influencing the steam oxidation [23, 24, 92]. If we consider the grain structure, there are two main types of austenitic alloys [87]: coarse-grained, (where the alloy initially form a continuous and protective Cr-rich scale) and fine-grained (which promote the formation of chromia) [108]. The oxides formed on coarse-grained alloys typically consist of a thin single-layered Cr-rich scale near an emergent alloy grain boundary and Fe-enriched oxides developed over the grains' bodies. Such scales are reported to thicken with time. The diffusion of iron slows down with time and the line of voids on the interface between the inner and outer layers increases, which impedes further diffusion of iron. As a result, magnetite formed oxidises to haematite. In comparison, fine-grained alloys develop much thinner scales. Additionally, the spinel composition differs; in fine-grained

austenitic steels the innermost part is Cr-rich. After longer exposures, spinel formed shuts down the iron diffusion that supports the formation of an outer magnetite layer and leads to oxidation of magnetite to haematite. The significant difference between coarse and fine-grained alloys is the exfoliation of haematite upon cooling, which has not been identified for coarse-grained austenitic steels. Hannsson et al. [87] believe that the grain size and structure strongly influence the behaviour of 18% Cr austenitic steels; the fine-grained alloys oxides at much slower rate than coarse-grained alloys.

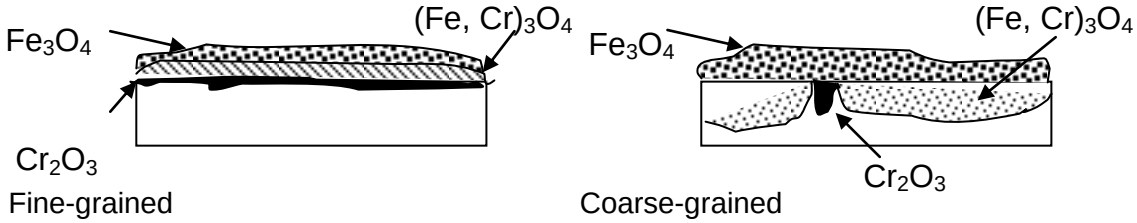

Figure 5-8 Scale morphology formed on Fine and Coarse-grained austenitic steels [15]

Figure 5-8 illustrates the scales formed on fine-grained steels, which are believed to be more protective than on coarse-grained steels due to the fully developed chromia layer.

5.4 Steam flow and orientation relative to steam flow

An analysis of the steam oxidation mass change at high steam conditions (Figure 5-9) showed a clear increase in oxidation damage with steam flow rate. Moreover, the specimens seem to indicate a deviation from a parabolic rate after a shorter time than in the case when they are exposed to slower steam flow rates. From the data available it can be concluded that steam flow is an important factor and has to be studied in detail to understand the processes leading to acceleration of oxidation rate.

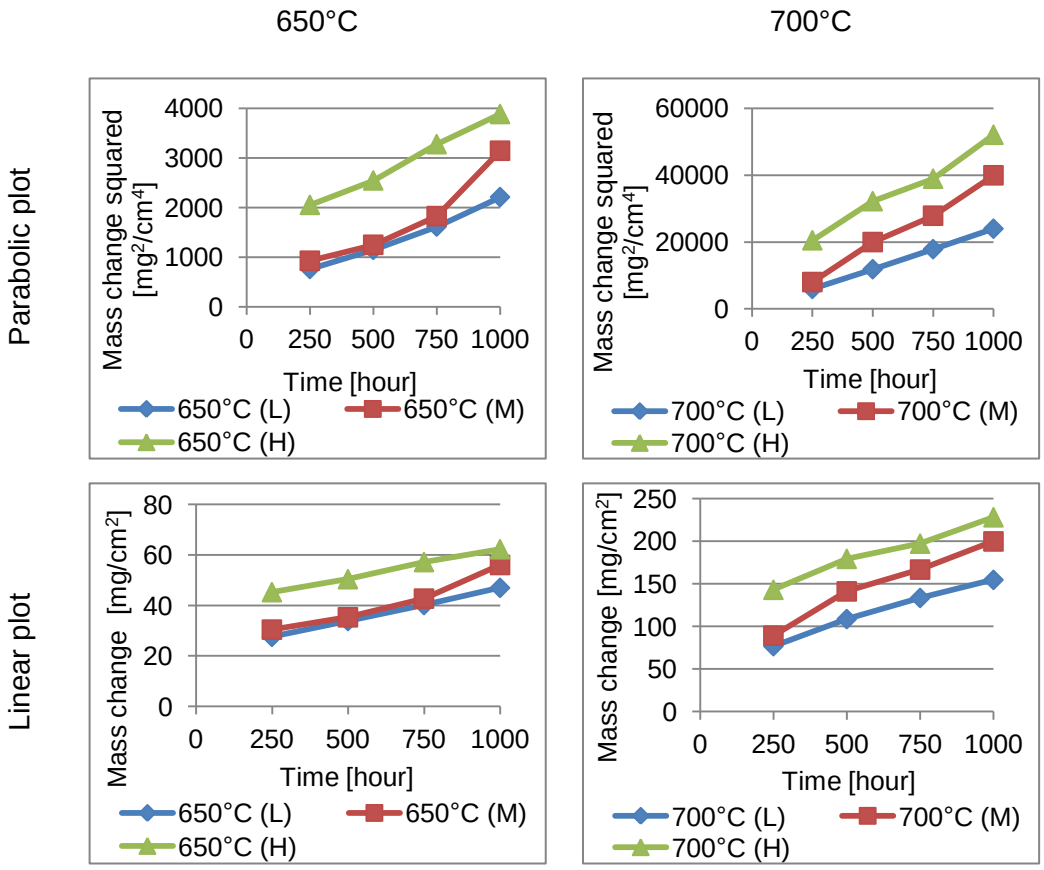

Figure 5-9 Oxidation kinetics for T23 At 650 and 700°C with change of the steam flow rates (L- low, M - Medium, H - high) (bridge - shaped)

Figure 5-10 compares the parabolic and linear plot for T92. It shows that regardless of the assumed rate law oxidation clearly increases with steam flow rate. At 650 and 700°C there is clear data showing the oxidation rate dependence of T92.

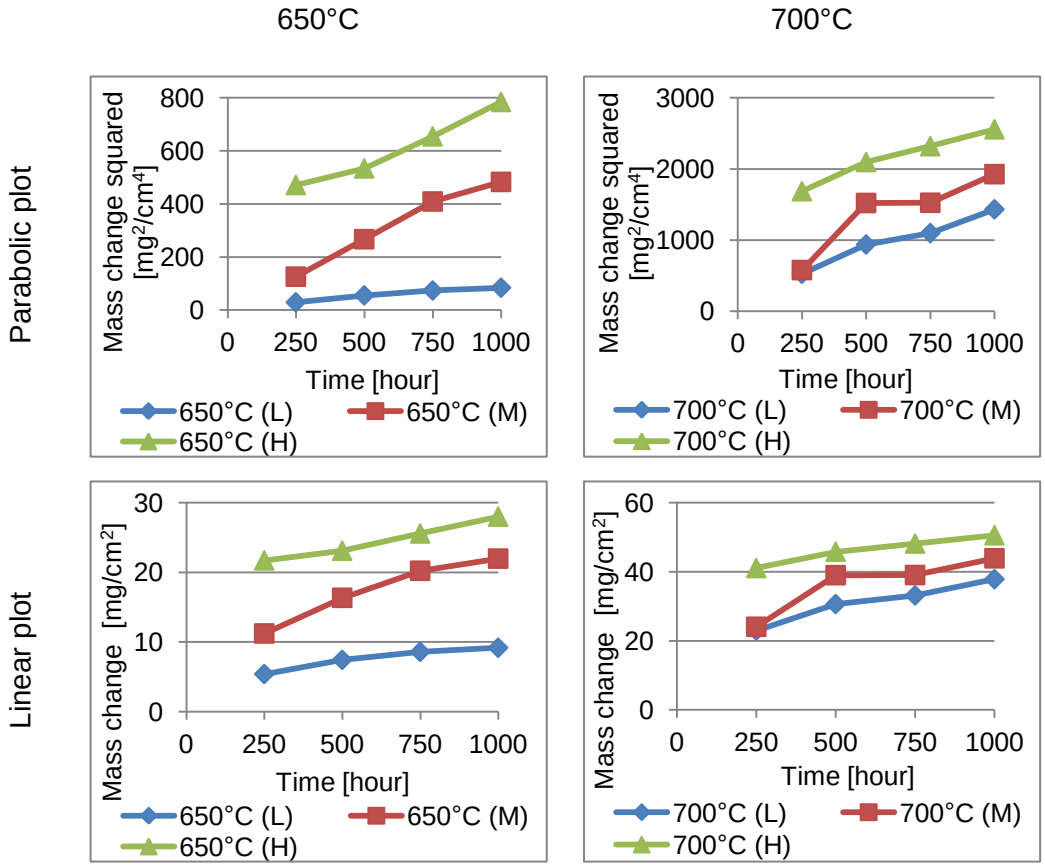

Figure 5-10 Oxidation kinetics for T23 At 650 and 700°C with change of the steam flow rates (L- low, M - Medium, H - high) (bridge - shaped)

Assuming that steam oxidation of both ferritic alloys studied follows the parabolic rate law, equation (5-1) has been used to calculate the parabolic rate constants and integration constants for T23 and T92 under the conditions considered. The data generated have been grouped in Table 5-10 and Table 5-11 for bridge and curve - shaped specimens respectively.

Table 5-10 Values of the parabolic rate constant forT23 and T92 in conditions investigated (bridge samples)

Temperature steam flow rate	T23		T92	
	k_p $[mg^2/cm^2s]$	C	k_p $[mg^2/cm^2s]$	C
600°C (L)	2.970E-05	2.250E-12	2.860E-05	4.830E-12
600°C (H)	6.500E-04	5.810E-11	9.060E-05	1.720E-11
650°C (L)	6.400E-04	1.930E-11	2.540E-05	9.780E-13
650°C (M)	1.160E-03	1.810E-10	1.430E-04	4.180E-12
650°C (H)	1.083E-03	7.690E-10	2.140E-04	5.920E-08
700°C (L)	8.840E-03	3.700E-10	4.500E-04	8.160E-08
700°C (M)	1.730E-02	2.940E-09	6.270E-04	8.900E-11
700°C (H)	1.640E-02	2.590E-09	5.770E-04	1.720E-11

Table 5-11 Values of the parabolic rate constant for T23 and T92 in conditions investigated (curve samples)

Temperature steam flow rate	T23		T92	
	k_p $[mg^2/cm^2s]$	C	k_p $[mg^2/cm^2s]$	C
600°C (L)	2.290E-05	2.311E-12	1.390E-05	3.657E-11
600°C (H)	9.533E-05	1.851E-11	7.905E-05	1.593E-11
650°C (L)	4.390E-04	8.031E-12	5.970E-05	3.375E-12
650°C (M)	6.730E-04	4.904E-12	8.274E-05	6.234E-12
650°C (H)	1.084E-03	2.253E-10	3.529E-04	4.693E-11
700°C (L)	5.160E-03	8.940E-11	3.020E-04	2.813E-11
700°C (M)	1.196E-02	1.301E-09	3.881E-04	3.554E-11
700°C (H)	1.434E-02	2.072E-09	7.855E-04	8.505E-11

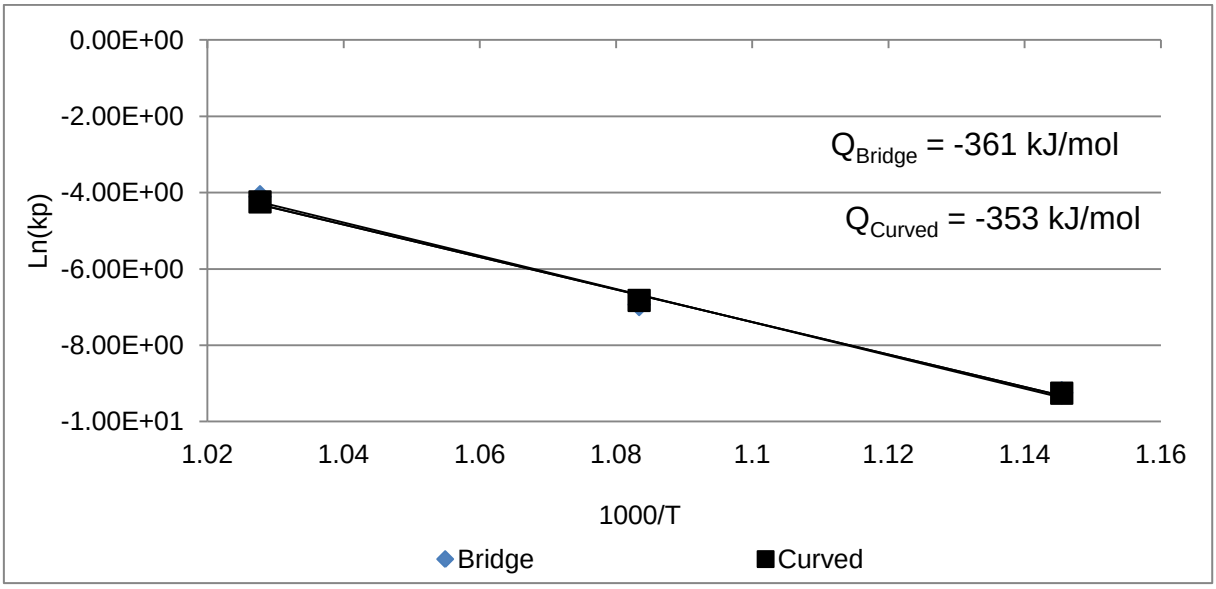

Figure 5-11 Arrhenius plot for T23 in the temperature between 600 - 700°C with high steam flow rate

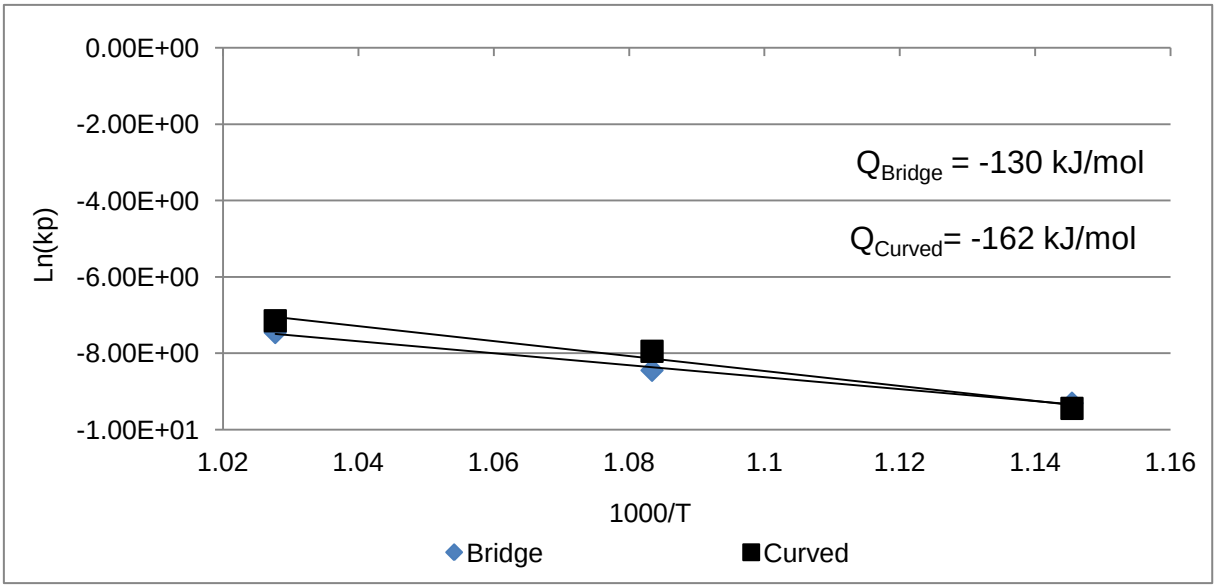

Figure 5-12 Arrhenius plot for T92 in the temperature between 600 - 700°C with high steam flow rate

The enhanced steam flow rates clearly increase the oxidation of ferritic steels; the materials exposed to higher flows show thicker scales. In addition to this there is a change in the type of scales produced: for T23 a micro-layered inner layer develops whereas for T92 haematite forms in the outermost layer. Those

changes are believed to due to the higher concentration of the oxidising (oxygen and hydroxides) or reducing (hydrogen) species available in the process (oxygen and hydroxides). The formation of haematite for T92 under higher steam conditions is explained by the increase of oxidising species supplied to the alloy surface and the formation of thicker oxides on the gas/oxide interface. An alternative explanation is faster steam flow, which sweeps away the hydrogen formed on the gas/oxide surface, allowing the formation of haematite on the surface. This is in accordance with Zurek et al., [109] who showed that the presence of H_2 on the surface suppresses the formation of Fe_2O_3.

The formation of a micro-layered inner scale on T23 is triggered by faster steam flow rate as a result of which more oxidising and reducing species forms including hydrogen. According to Cory et al. [110] around 30% of the total hydrogen formed during steam dissociation diffuses into the material. In this studies the results of the SIMS analysis (see chapter 4.2.3) showed that there is a diffusion of the oxy-hydroxides into the spinel which is probably a main source of the hydrogen in the spinel. Hydrogen within the spinel is believed to reduce the diffusion of chromium from the material to the spinel and therefore decreases its protectiveness [111]. The chromium-depleted inner scales are believed to be pure magnetite. The hydrogen accumulated within the inner scales could possibly reduce magnetite to wustite according to reaction $Fe_3O_4 + 2H_2^+ + e^- = 3FeO + H_2O$ [112]; this formation is believed to be the first step in the development of the micro-layered inner layer.

Steam oxidation is different from oxidation in dry gases; oxidation in water vapour is reported to be faster than in dry gas mixtures [23]. One of the reasons for this is volatilisation of the protective chromium oxide scales. This phenomenon is reported for the more advanced materials, which are able to form chromia or chromium-rich mixed oxides (spinels) [23, 24]. Volatilisation of such oxides leads to chromium depletion (and therefore to breakdown of the protective scales) and an increase of the oxidation rate due to nucleation of the iron oxides [24, 49, 101]. According to the literature, volatilisation is less

pronounced at low temperature; however above 700°C it is believed to influence the steam oxidation of austenitic and high chromium ferritic steels more significantly [113]. Literature showed that there is a relationship between the evaporation rates and the gas flow rates – an increased gas flow rate results in faster evaporation of chromium oxy-hydroxide [76, 114]:

$$P^{o}_{CrO_{2(OH)_2\,(Outgoing)}} = P^{o}_{CrO_{2(OH)_2(Incoming)}} + \frac{4k_e LRT}{dvM_{CrO_2(OH)_2}} \quad \textbf{(5-2)}$$

where $P^{O}_{CrO2(OH)2}$ is the partial of $CrO_2(OH)_2$ [in ppb], k_e is the evaporation rate [in mg/cm^2], L is the flow direction length [m], T is the temperature [K], $M_{CrO2(OH)2}$ is the molecular mass of $CrO_2(OH)_2$ [g/mol], d is the tube diameter [m], v is the steam velocity [m/s] and R is the gas constant [J/mol/K].

Volatilisation is a surface-controlled process and as such is dependent on the gas flow. Asteman et al. [113] explained that the volatile species diffuses from the surface through the low velocity boundary layer, which separates the main gas flow and surface, and is then transported away by the flowing gas. An increased gas flow reduces the boundary layer thickness, which results in a faster evaporation rate. Halvarsson et al. [114] confirm that vaporisation is dependent on the transport processes in gas. They explain the impact of vaporisation on steam oxidation as follows: as the rate of chromium oxy-hydroxide evaporation reaches a critical level the supply of Cr to the oxides is insufficient for maintaining the protectiveness and the scales break down. The chromium supply within the alloy varies; it is more rapid at the grains boundaries than at the grains' centres. The formation of nodules at the surface is a result of the fact that the chromium level at the grains centres drops below the critical value. This leads to a loss of protectiveness and scale breakdown. The breakdown of the protective scales triggers the outward iron and inward oxygen diffusion, which leads to the formation of nodules on the surface [114].

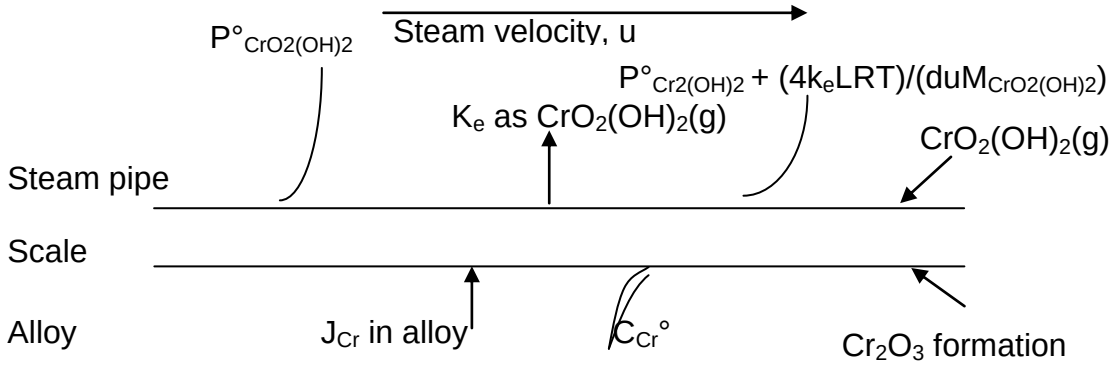

Figure 5-13 The combination of gas evaporation of $CrO_2(OH)_2$, gas saturation of $CrO_2(OH)_2$, and Cr depletion in the alloy is illustrated [77]

An analysis of the specimens' cross-sections and surfaces indicated that the scales formed on the part of the specimens facing direct steam flow are thicker than on the parts exposed to indirect flow. For the ferritic steels (T23 and T92) direct steam flow drives formation of the thicker scales and the oxidation of the outer magnetite to haematite. Initially two explanations were proposed:

1. Less oxygen is supplied to the parts of the specimens exposed to indirect steam flow;
2. As a result of oxidation of the part of the specimen facing direct steam flow steam is consumed and hydrogen is produced. This can possibly cause the second part of the specimen to be exposed to gas with a lower oxygen partial pressure than the front side.

However, these initial explanations were opposed firstly due to the fact that the oxygen partial pressure required for the three iron oxides to form is lower than the oxygen pressure in the environment tested; secondly, there is enough steam supplied to the system to ensure that the whole surface of the specimen is exposed to the same environment. After a more detailed analysis of the process the following explanation of the phenomenon was proposed: the difference in thickness of the scales is believed to be a result of hydrogen effect. Hydrogen being swept away from the surface facing the steam flow increases the oxidation rate that leads to the formation of thicker scales and influences the formation of haematite on the surface of the magnetite. Zurek et al., [109]

proposed that a higher concentration of hydrogen suppresses the formation of haematite so lower concentrations should encourage haematite formation. The haematite on the surface facing direct steam flow could also be explained by the higher levels of void within this sample region as well as higher stress levels (mainly associated with higher levels of the growth stress due to the different geometries). The voids within the oxides form a diffusion barrier for the iron ions and consequently magnetite oxidises to haematite. The gaps and voids are identified within the magnetite layer. Oxygen partial pressure within the gaps is expected to be lower than for haematite formation according to the reaction $2Fe_3O_4 + 1/2O_2 = 3Fe_2O_3$. Additionally, Ehlers et al. [20] reported that the oxygen flux is too low to cause the rapid growth of scales, beneath the voids region. Such a situation suggests that there is another process involved in scale growth, which is most likely associated with the presence of steam. This is in agreement with Rahmel and Tobolski [115]. Moreover, Ehlers et al. [20] have proposed that the main mechanism involved, is the formation of $Fe(OH)_2$ within the gaps. Assuming that there is a higher concentration of $Fe(OH)_2$ in the inner oxide layer than in the outer layer a gradient in $pFe(OH)_2$ is produced and this drives the outward transport of the hydroxide through the void to the oxide surface. Iron- hydroxide is not stable at high oxygen pressures and therefore deposits as a solid oxide, which is suggested to be haematite (in the outer scale); however there is also a possibility that within the inner scale $Fe(OH)_2$ could deposit as magnetite [20].

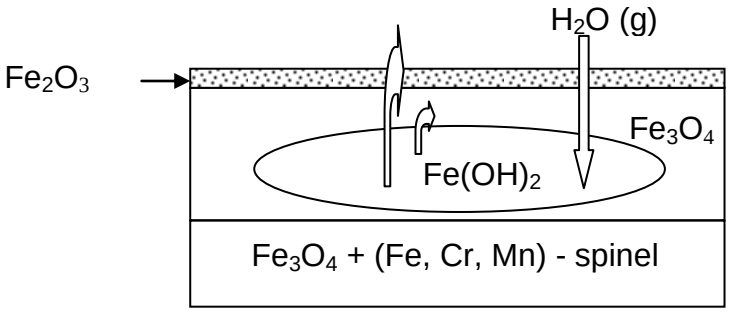

Figure 5-14 Schematic illustration of the process involving the iron-oxy-hydroxide [20]

Rahmel and Tobolski [115] proposed that there is a H_2O/H_2 bridge formation, which triggers the diffusion of oxygen and this could be another possibly explanation of the oxidation of magnetite to haematite.

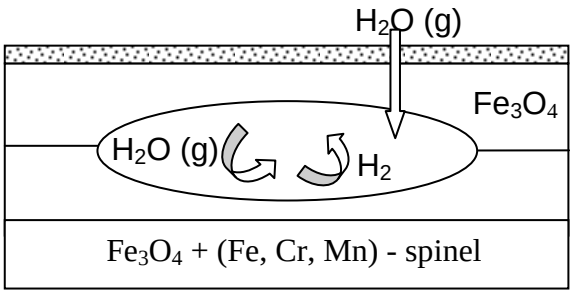

Figure 5-15 Schematic illustration of the process involving H_2O/H_2 bridges [115]

The impact of steam flow rate is also pronounced for austenitic steels. In the tests conducted, an interesting trend has been identified: steam flow rate has a more significant impact than temperature. This could be due to a higher concentration of the oxidising species and therefore a change in a equilibrium at the material surface/oxygen interface. The established equilibrium allows first oxides to form and also allows further oxidation to occur due to oxygen and metal counter-diffusion.

Austenitic steels show much better oxidation behaviour than ferritics. An analysis of the oxidation rate for Super 304H showed an increase of the rates with higher steam velocity; however, some mass loss is also identified and this is most likely due to scale spallation, or less likely due to volatilisation of chromia (see chapter). Volatilisation of chromia is not believed to occur at lower temperatures (<700°C); however there is a possibility that higher steam flow rates trigger the process because of a higher oxygen partial pressure at the specimens' surface. Oxidation of HR3C also accelerates with steam flow rates; however, the impact of steam velocity varies significantly with temperature. The interplay between steam flow and temperature is more pronounced for HR3C than for other austenitic steels due to its higher chromium level (25Cr), which is believed to improve the protectiveness of the oxide.

Increased steam flow rates promote the formation of nodules on surface of the T347HFG and Super 304H (18Cr), and their size grows with increase steam velocity; become more evenly distributed and cover a larger areas of the specimens' surface. The size of the nodules increases with a change in steam velocity as a result of faster diffusion of the metal and oxygen within the nodule. The faster growth and wider distribution of nodules drives the formation of thicker (yet not continuous) continues oxide layer on the surface. The oxides in the case of both austenitic steels are mixed iron and chromium oxides with some manganese and nickel additions.

In spite of the acceleration of the oxidation process as for lower alloyed materials with the enhanced steam flow rates, the surface investigation of HR3C did not show a significant change with faster steam velocities. There were still a small number of nodules which form with the same size as for low steam flow conditions. This is probably a result of the higher alloy chromium content allowing the re- growth of protective chromium-rich-mixed oxides even after the spallation of the initial oxide. After longer exposures, more nodules are expected to form on the surface and will spread evenly along the surface of HR3C as was identified for 18Cr austenitc steels.

To summarise, the tests showed reveal that steam flow rate is an important factor influencing steam oxidation. Steam flow rate has an impact not only on the oxidation kinetics but also on the formation of haematite in the case of ferritics (T23 and T92). It also changes the behaviour of the austenitic steels. Faster steam velocities accelerate the oxidation rates and drive nodular growth of the scales, which is most pronounced for 18Cr austenitic steels. The nodules are bigger and spread evenly along the surface, forming continuous scales in regions exposed to direct steam flow.

5.5 Specimen shape

The specimens for the steam oxidation tests were machined in three different geometries: bridge, curve and rectangular shape. An analysis of the data acquired showed that in the temperature range 650-700°C (L) the impact of the specimen geometry is most pronounced for ferritic steels, whereas for austenitic steels the effect of specimen shape increases above 650°C (L) and with the steam flow rates (M, H). During the exposures, the bridge - shaped specimens showed the largest mass change, which is in agreement with the oxide thickness and metal loss data. At 600°C (L) oxidation is slower due to slow diffusion; therefore thickness of the oxides which formed on the specimen's surface was the same regardless of specimen geometry. At 750°C (L) diffusion is much faster and the surface geometry does not have such a pronounced impact on the oxides formed as in the middle temperature range (650-750°C (L)). The second, significant impact of specimen shape is that less haematite is formed on the curve - shaped specimens. This could be the result of more severe oxide scale exfoliation as well as smaller steam/specimen contact surface. A smaller steam/specimen contact surface areas are believed to have an impact on the amount of hydrogen/steam/OH^- adsorbed by the oxide scales, due to the fact that adsorption is affected by both the area of the adsorbent and the pressure of the adsorbate. The higher levels of oxy-hydroxide dissolved in the oxide change the properties of the scales and are believed to influence ionic diffusion [62, 116]. Moreover, as was stated previously the hydrogen OH^- and steam could trigger oxidation due to iron-oxy-hydroxides and H_2O/H_2 bridge formation, which is consistent with the fact that in bridge - shaped specimens higher voidage levels were found than in curve- and ring - shaped samples.

As was discussed, in the material composition and structure section (see chapter 5.3) oxidation is believed to be influenced by the alloy grain structure, which for curve and bridge - shaped specimens is deformed as a result of the machining process. The most significant deformation of the structure and therefore the fastest oxidation is expected for the bridge - shaped specimens.

This is consistent with data obtained. The faster diffusion in the bridge - shaped specimens is expected to be the result of alloy grain-boundary diffusion, which is reported in the literature to be dependent on the inclination of the grain boundaries. This effect is most pronounced above 600°C and limited above 700°C [117]. The effect of high temperatures on grain boundary diffusion was reported by Suzuki and Mishin [118]. The overall stresses on specimens with more complicated geometries would therefore be expected to be greater, and so a loss of adherence and therefore haematite formation [26, 119]. The effect of specimen geometry for austenitic steels is most likely to be a result of the deformed grain structure for the bridge- and curve - shaped samples, which showed the largest mass gain and the nodular oxide growth due to the breakdown of more protective oxides. The ring specimens clearly showed growth of protective, adherent scales; thereby their significantly slowing down oxidation. The formation of such scales on the ring specimens results from the grain structures, which have not been changed during the machining processes.

5.6 Specimen surface finish

The final two tests have clearly revealed that a change in the surface finish of the austenitic steels resulted in the formation of different kinds of oxide scales (see chapter 4.2.2.3).

The ground specimens showed the best oxidation resistance. An investigation of the surface showed that grinding had significantly reduced the oxidation rate and enables fast formation of the protective oxides. This could be the result of the number of grinding marks, developed on the material's surface during grinding, which promote fast formation of external and protective chromium oxides [24, 87]. Faster formation of protective oxide scales and suppression of the development of non-protective scales are the result of enhanced chromium diffusion to the alloy surface via a path created by the deformation caused by machining. Such an acceleration of the diffusion process could be the result of relatively faster diffusion within the grain centre. An analysis of the gains close to the material surface showed that more than 10%

of the grain is damaged (opened). This significantly increases diffusion within the grain, which in austenitic steels is around 100 times slower than grain boundary diffusion [58] Although, this promotes fast formation of protective scales it also has a negative impact: the rapid use of chromium in the initial stage could lead to faster oxidation of the alloy after longer exposures due to Cr depletion [23, 24].

Polished specimens oxidised faster than the ground ones); this leads to thicker scale, which could be identified even after short exposures. An investigation of the surface of the polished specimen indicated that at the beginning of the exposures the surfaces are scratch-free, with low roughness. The relatively flat surface of the specimen, with no crevices, triggers the formation of the less protective chromium, iron oxides. This is believed to be the result of the relatively low roughness, which drives faster spallation of the initial, protective oxides due to their lower adherence to the material's surface.

Oxidation of pickled (as-received specimens) drives the formation of the thickest oxide scales, which start to develop after short exposures. The oxides nucleated on the surface are identified as mixed iron and chromium oxides. During exposures, no thin scales of protective chromia were identified; therefore, it can be concluded that as-received specimens do not form protective oxides due to relatively fast oxidation. The surfaces of the as-received specimens had the highest roughness among the specimens investigated; however no deep crevices were identified. Such a surface does not promote the fast formation of protective chromium oxides; instead less protective iron, chromium oxides develop.

To summarise, surface finish clearly influences the oxidation of austenitic alloys, and this is believed to be the result of sub-surface alloy deformation. The oxidation rates increase for different surface finishes as follows: ground, polished and pickled surface.

5.7 Steam oxidation mechanism

The literature review suggests that steam oxidation is a process controlled mainly by inward diffusion of oxidising species forming during steam dissociation (O^{2-}, OH^-, molecular water) and outward diffusion of the metal ions (in scale) and atoms (in alloy) [84]. Among the inwardly diffusing ions, the oxygen ions are believed to have the largest impact on steam oxidation [24]. However the results of the research conducted suggest that the hydroxide ions also significantly influence the oxidation process, in particular the formation of the inner scale. The molecular size of oxy-hydroxyl ions is similar to that of oxygen; however, their diffusion into the inner part of oxide scales seems to be faster. An SIMS analysis of the scales formed on ferritic and austenitic alloys indicated a significant increase in the signal for hydroxide ions, with distance from the oxide surface. This is believed to be a result of the inward diffusion of oxidising ions into the inner part of the scale where those ions start to be incorporated into the spinel and therefore promote faster outward diffusion of metal species [87]. This was also suggested by Wright and Dooley [24].

An analysis of the results (See chapter 4.2) for ferritic steels showed that scale growth on both T23 and T92 is controlled by the inward diffusion of oxidising species into the scale and outward migration of metal ions. An interesting finding is the increasing level of hydroxide ions with distance from the oxide surface. This is believed to be a result of the number of defects within the inner scale into which the hydroxide ions could diffuse to and affect the steam oxidation process.

The findings for austenitic steels suggest that nodules and uniform scale formation are controlled by different processes. Analyses revealed that double-layered nodules grow by inward diffusion of oxygen. Moreover, there is an inward diffusion of hydroxide ions, which contributes the most to the formation of the inner oxide. This is in agreement with Wright and Dooley [24] and EPRI [23] who proposed that oxidation involves the inward transport of OH^- with oxidation at the metal/oxide interface.

The growth of uniform, protective scales on austenitic alloys is believed to be controlled by two processes: the outermost part of the scale shows a constant level of oxygen and hydroxide ions. The oxide scale below it presumably grows by outward diffusion of the metal ions. Finally, the inner layer grows by inward diffusion of oxygen ions. The level of hydroxide ions is constant within the outer part of the scale whereas, in the inner layer, the number of OH^- ions increases. This could suggest that its inward diffusion contributes significantly to the formation of the inner oxide.

To summarise, an initial analysis of the results of the study conducted with SIMS has confirmed that inward diffusion of oxygen ions and outward metal ion diffusion are the controlling mechanisms of steam oxidation. In addition it has also shown that inward diffusion of hydroxide ions has a significant impact on the steam oxidation process. The diffusion of hydroxide ions contributes to the growth of the inner oxide layer. For a better understanding of this subject, more tests in O^{18} doped steam should be conducted. In such tests, the specimens could be exposed to different temperatures and various steam flows rates. This could explain whether the high level of hydroxide ions are a consequence of the fast steam flow rate and changes with it, or whether this is a more independent process. Additionally, tests in steam generated from using hydrogen isotope H^2 could be performed in order to explain the impact of the hydrogen ions on oxide formation in steam.

5.8 Scale spallation

The results shows that scale spallation occured during the exposures. It clearly varies with the alloy type and exposure conditions. For ferritic steels the exfoliation is more pronunced than for austenitic due to thicker scale formation and different oxides formed durring the process. The scale exfoliation varies within the ferritic steels itself. T23 steels shows less spalation then T92, for T23 only the outermost scale seems to spall which is mostlikelly result of the differnec in CTE between autermost haematite and magnetite. For T92 the scale spallation occurs on the interface between inner and outer scale which is

mostprobalby associated with the development of voids at the interface. In case if the exposure to faster steam flow rates it can be noted that there is an increase in the scale spallation for both alloys, which could be explain with the fact that the haematite forms on both alloys which can influece the exfoliation due to the larger differences in CTE between oxide layers.

Although, the crucible mass change show that the scale from austenitic steels exfoliates there is a concern if the oxides collected inside crucible are only the one exfoliated from the austenitic or the ferritic steels.

5.9 Steam oxidation modelling

This section describes an approach to the modelling of steam oxidation. Due to insufficient data for ground austenitic steels, which have shown slow oxidation the steam oxidation modelling was limited to ferritic steels. As was presented in the literature survey the steam oxidation of ferritic steels follows a parabolic rate dependence; this means that oxidation is controlled by the diffusion of metal or/and oxygen ions through the oxide lattice. However, it was also found during this survey that in reality oxidation cannot described be so easily, since there are 'factors which cause a deviation from the clear parabolic dependencies.

Modelling was divided into two separate stages, for which two different statistical methods and input equations were applied. For the first models a multi-regression method was employed. This allowed the identification of a single equation describing the behaviour of the materials exposed in steam. However, this approach has a significant limitation because in order to use the regression method the integration constant has had to be neglected and therefore the following equation has been used:

$$x^n = k_p t \tag{5-3}$$

where x is mass change [mg/cm^2], kp is parabolic rate constant [mg^2/cm^{4}s], t is time [s]. In order to include the temperature dependence of the parabolic rate values the Arrhenius equation was used and k_p (Table 5-1 - Table 5-3): has been substituted in equation (5-3)

$$x^n = k_o exp^{\left(\frac{-Q}{RT}\right)} t \tag{5-4}$$

where k_o is standard rate constant [mg^2/cm^{4}s], Q is activation energy [J/mol], R is gas constant [J/K mol], T is absolute temperature [K], t is time [s]. Finally, the input equation is derived in the form presented below:

$$nln(x) = a\ln(k_o) + b\left(-\frac{Q}{RT}\right) + c\ln(t) + d \tag{5-5}$$

equation (5-5) and the experimental data acquired were used to deriver the output equation that describes the behaviour of both T23 and T92 during steam oxidation in temperatures range 600-750°C:

$$nln(x) = -0.027\ln(k_o) - 0.019\left(-\frac{Q}{RT}\right) + 0.92\ln(t) - 7.12 \quad \textbf{(5-6)}$$

The comparison of mass change results with data obtained with use of equation (5-6) is presented in Figure 5-16

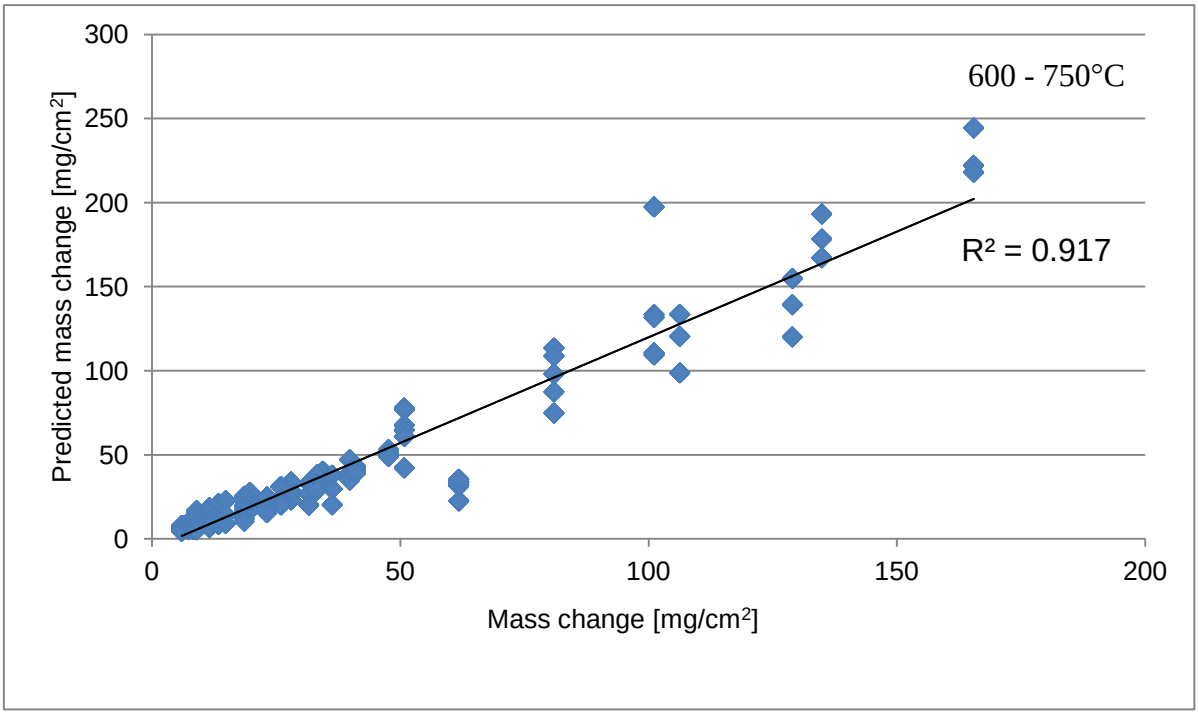

Figure 5-16 Comparison of the predicted mass change for ferritic steels with equation (5-6) and the data obtained during steam oxidation tests in the temperature between 600 -750°C

Figure 5-16 shows a good correlation between the data obtained with the initial model and actual test results. However, an analysis of the results obtained indicated that, at higher temperatures, there are some significant differences between the modelled and test results. Therefore, it was decided to generate two separate models for T23 and T92 oxidation. T23 is much less resistant at high temperature due to a lower chromium level (2.25Cr). Moreover, an analysis of its oxidation behaviour showed that there is a change of the oxidation

mechanism that drives the formation of micro-layered an inner scales. Such inner layer has not been a found on T92. To model steam oxidation of T23 the same procedure was applied as highlighted before, and the following output equation was acquired:

$$nln(x) = \ln(k_o) + 0.00094\left(-\frac{Q}{RT}\right) + 1.08\ln(t) - 9.52 \quad \textbf{(5-7)}$$

The results obtained with the model are presented in Figure 5-17. An analysis showed that there is better correlation between the modelled mass change and the actual mass gain in the first part of the graph which corresponds to lower exposure temperatures. This is most probably the result of one, single oxidation-controlling mechanism at low temperatures.

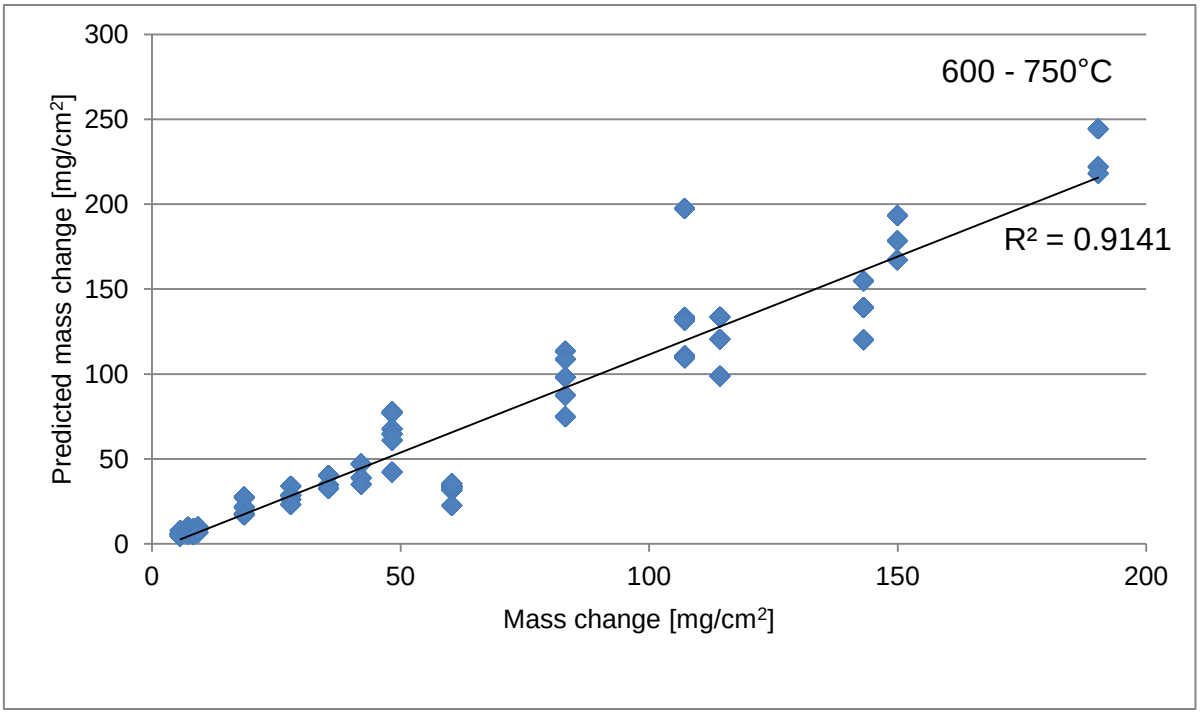

Figure 5-17 Comparison of the predicted mass change for T23 with equation (5-7) and the data obtained during steam oxidation tests in the temperature between 600 – 750°C (L)

In the temperature range 650-700°C the impact of the specimen's geometry is clearly visible. The discrepancy in mass change data at the highest temperatures (700-750°C) is believed to be also a result of the formation of

micro-layered inner scales. The formation of micro-layered inner scales most probably involves an additional process; thus there is a deviation in correlation between the predicted and obtained mass change data. Steam oxidation modelling at 650°C gave equation (5-8) and 700°C equation (5-9). These equations showed that the correlations between the calculated and actual mass change varies with specimen shape; this confirms that in the temperature range 650-750°C geometry is an important factor.

$$nln(x) = \ln(k_o) + \left(-\frac{Q}{RT}\right) + 0.85\ln(t) - 6.12 \quad \textbf{(5-8)}$$

$$nln(x) = \ln(k_o) + \left(-\frac{Q}{RT}\right) + 0.73\ln(t) - 4.28 \quad \textbf{(5-9)}$$

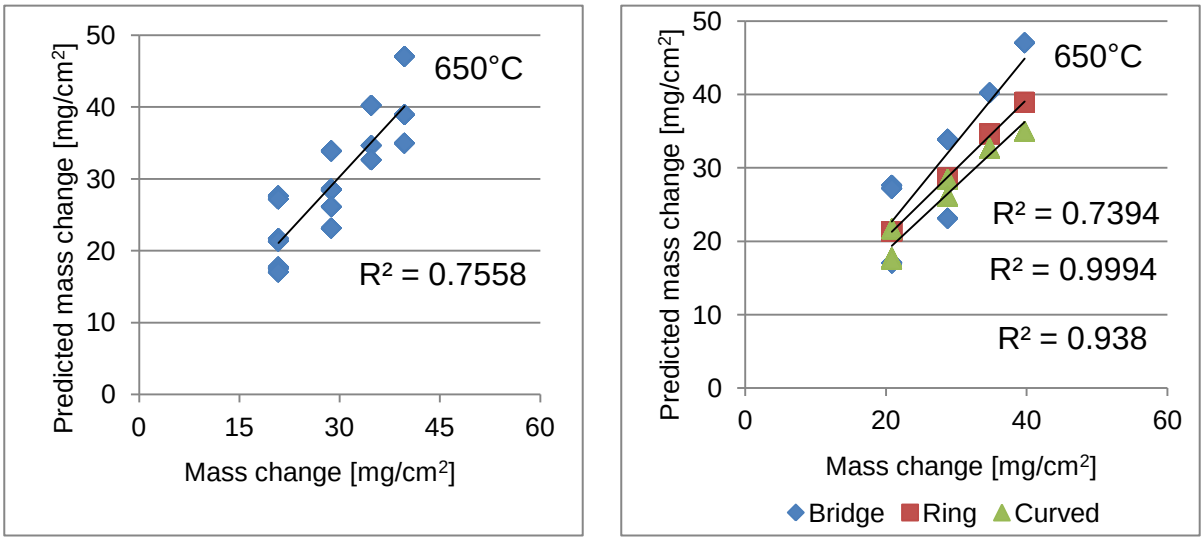

Figure 5-18 Comparison of the predicted mass change for T23 with equation (5-8) and the data obtained during steam oxidation tests at 650°C (L)

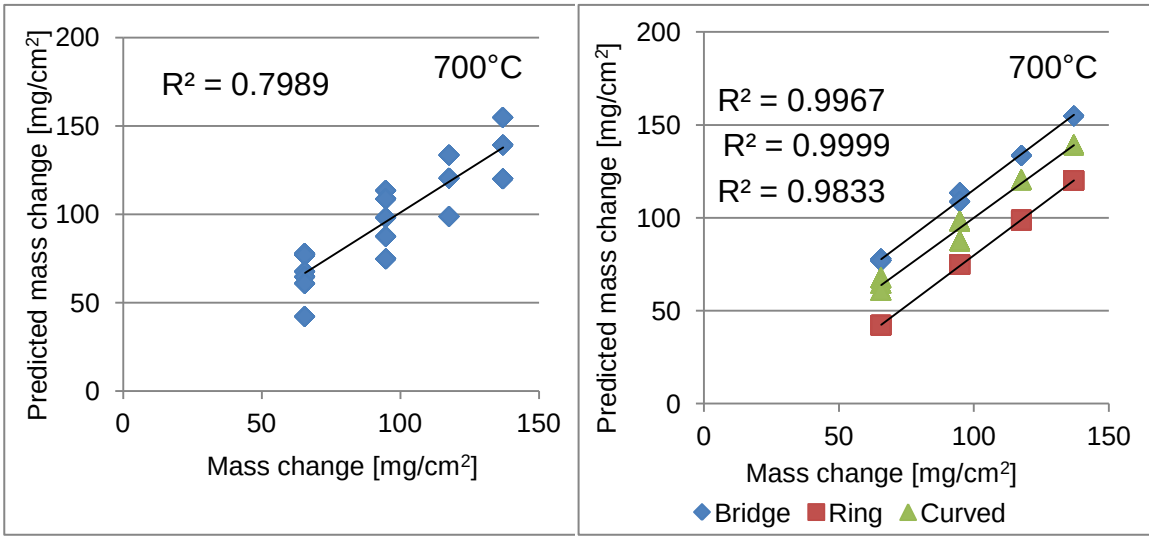

Figure 5-19 Comparison of the predicted mass change for T23 with equation (5-9) and the data obtained during steam oxidation tests At 700°C (L)

Steam oxidation of T92 was modelled using:

$$nln(x) = \ln(k_o) + 0.071\left(-\frac{Q}{RT}\right) + 0.77\ln(t) - 6.72 \quad \textbf{(5-10)}$$

The data obtained during the modelling of T92 show less correlations than that for the model describing the steam oxidation of both ferritic steels. This is believed to be the result of more severe spallation of the scales formed on T92. Following this conclusion a decision was made to build a model based on metal loss data, which is not influenced by scale spallation; and therefore the models developed should be more accurate. Additionally, metal loss is an important factor in that reduces the lifetime of heat exchanger tubing; therefore the accurate prediction of metal loss with time is crucial information for the power plant industry.

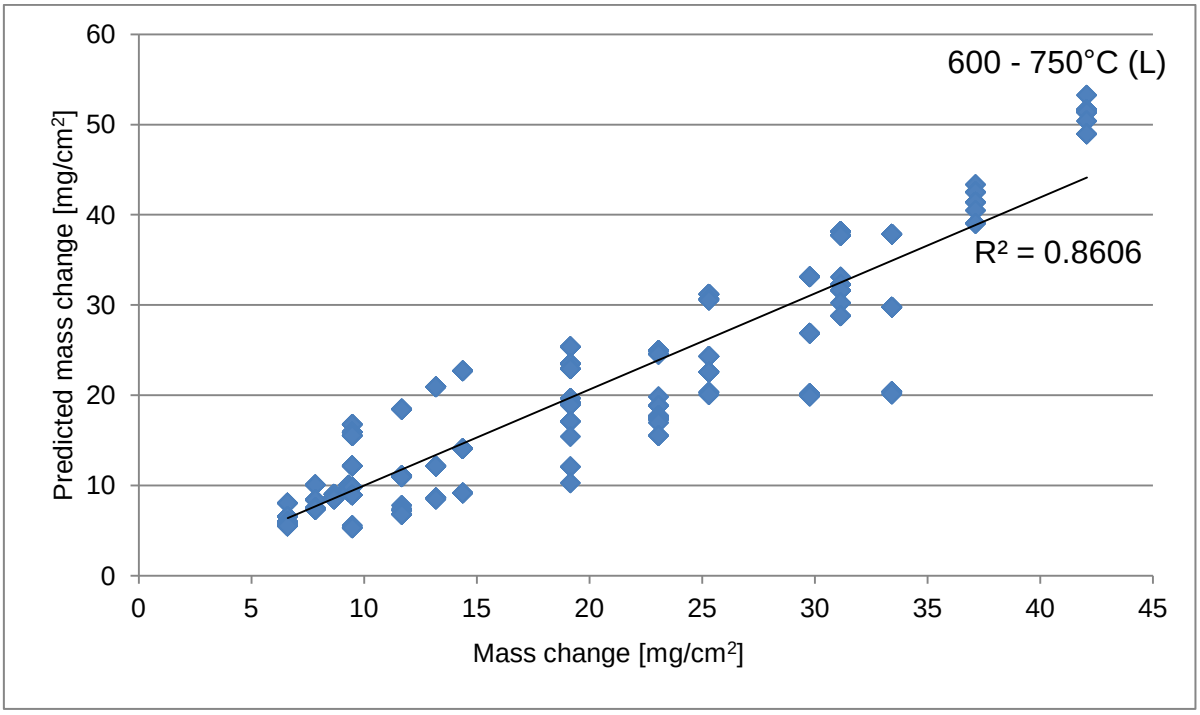

Figure 5-20 Comparison of the predicted mass change for T92 with equation (5-10) and the data obtained during steam oxidation tests in the temperature between 600 – 750°C (L)

The metal loss of the specimen is a direct consequence of the oxidation, and therefore assumed to be driven by the same mechanism. To model metal loss, the following input equation was employed:

$$n'ln(x) = \ln(k_o') + \left(-\frac{Q'}{RT}\right) + \ln(t) \qquad \textbf{(5-11)}$$

where x is metal loss [µm], k_o' is the standard rate constant [µm^2/s], Q' is activation energy [J/mol], R is gas constant [J/K mol], T is absolute temperature [K], t is time [s]. Following the result of the mass change modelling it was decided to model T23 and T92 separately; moreover, models were also derived for each specimen shape. An analysis of the modelled data showed that if metal loss is modelled separately for a particular specimen shape the correlation between the calculated metal loss and that obtained from the tests is better.

$$n'ln(x) = \ln(k_o') - 0.40\left(-\frac{Q'}{RT}\right) + 0.79\ln(t) + 11.54 \quad \textbf{(5-12)}$$

$$n'ln(x) = \ln(k_o') - 0.27\left(-\frac{Q'}{RT}\right) + 0.24\ln(t) + 4.77 \quad \textbf{(5-13)}$$

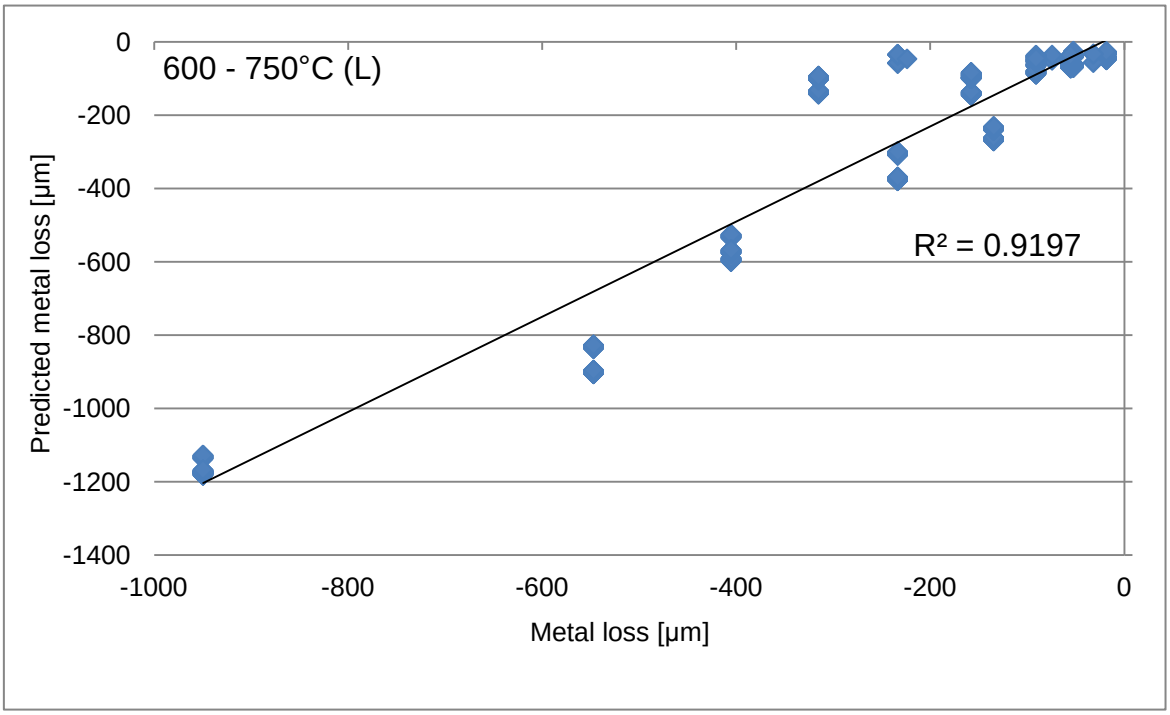

Figure 5-21 Comparison of the predicted metal loss for T23 with equation (5-12) and the data obtained during steam oxidation tests in the temperature between 600 – 750°C (L)

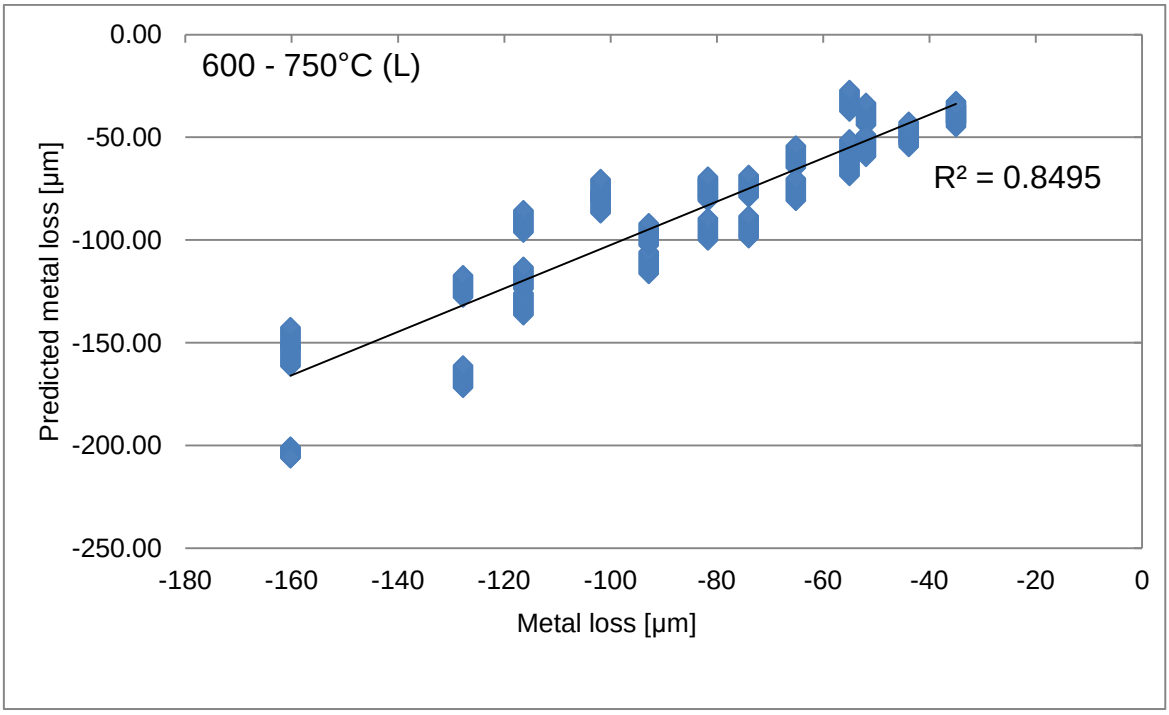

Figure 5-22 Comparison of the predicted metal loss for T92 with equation (5-13) and the data obtained during steam oxidation tests in the temperature between 600 – 750°C (L)

An analysis of Figure 5-22 showed that the correlation between the T92 data modelled with equation (5-13) and the test result is not as was expected. Therefore additional models were built for each particular geometry. Such an approach makes it possible to achieve greater model accuracy and confirms the impact of geometry on steam oxidation.

$$n'ln(x) = \ln(k_o') + 0.294\left(-\frac{Q'}{RT}\right) + 0.33\ln(t) + 3.96 \qquad \textbf{(5-14)}$$

$$n'ln(x) = \ln(k_o') - 0.368\left(-\frac{Q'}{RT}\right) + 0.8\ln(t) + 10.04 \qquad \textbf{(5-15)}$$

$$n'ln(x) = \ln(k_o') - 0.222\left(-\frac{Q'}{RT}\right) + 0.28\ln(t) + 3.52 \qquad \textbf{(5-16)}$$

equations (5-14) - (5-16) show the three models derived for bridge, ring and curve - shaped specimens respectively. Data obtained using these three equations show very good correlation with test results. This suggests that in

order to model steam oxidation more accurately and predict the performance of the material under certain conditions the specimen shape is an important factor to be considered.

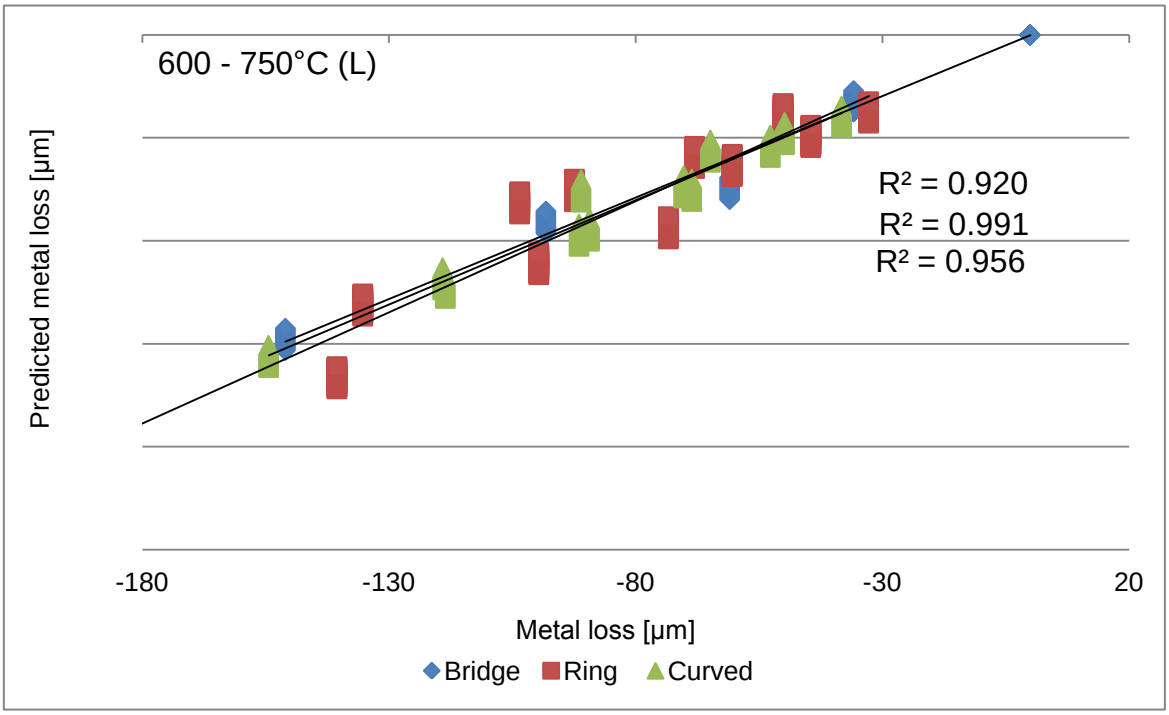

Figure 5-23 Comparison of the predicted metal loss for bridge, ring and curve-shaped specimens of T92 with equations (5-14) - (5-16) and the data obtained during steam oxidation tests in the temperature between 600 – 750°C (L)

The models built with the multi-regression method enable the identification of the corrosion product with relatively good accuracy and for this purpose the second modelling approach was employed. Due to the comparison required between the test results and the data available in the literature the curve-shape specimens were selected. In the literature, the oxidation is claimed to be parabolic; however the integration constant (C) in equation (5-1) is neglected often in order to build less complicated models. Therefore, in the following section a model derived for the full parabolic rate equation is presented and discussed. The data acquired during the tests performed made it possible to establish a direct relationship between temperature and oxidation rate, and this was achieved using the Arrhenius equation. The information acquired with it

was incorporated into equation (5-1) and the following models were created. The models were built in two steps; firstly, the data were used in the Arrhenius equation in order to identify the equations describing the relation between the parabolic rate constant and temperature. Secondly, equations identified in Step 1 were applied to equation (5-1) to establish the models as follows:

$$x^2 = \left(exp\left(-40.074\left(\frac{1000}{T}\right) + 36.934\right)\right)(3600t) + 7.17E - 10 \quad \textbf{(5-17)}$$

$$x^2 = \left(exp\left(-25.007\left(\frac{1000}{T}\right) + 18.554\right)\right)(3600t) + 5.65E - 11 \quad \textbf{(5-18)}$$

where x is mass change [mg/cm^2], T is absolute temperature [K], t is time [hour], C is integration constant. Equations (5-17) and (5.18) describe the steam oxidation of T23 and T92. These two models are characterised with greater accuracy than that acquired with the multi-regression method as presented in Figure 5-24 and Figure 5-25

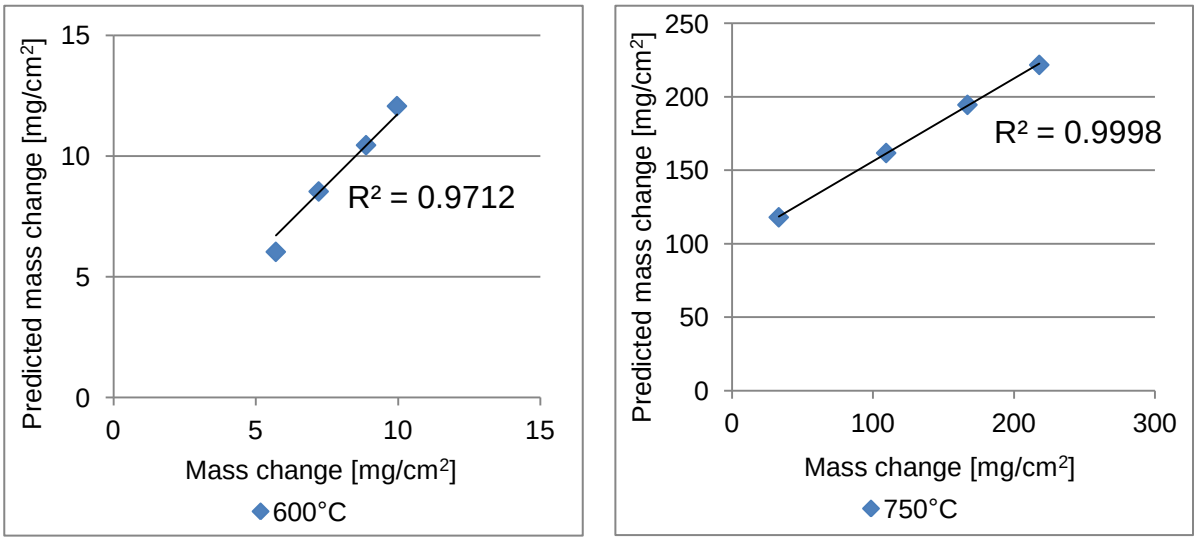

Figure 5-24 Comparison of predicted mass change data for T23 with equation (5-17) and the data obtained during steam oxidation tests at 600 and 750°C (L)

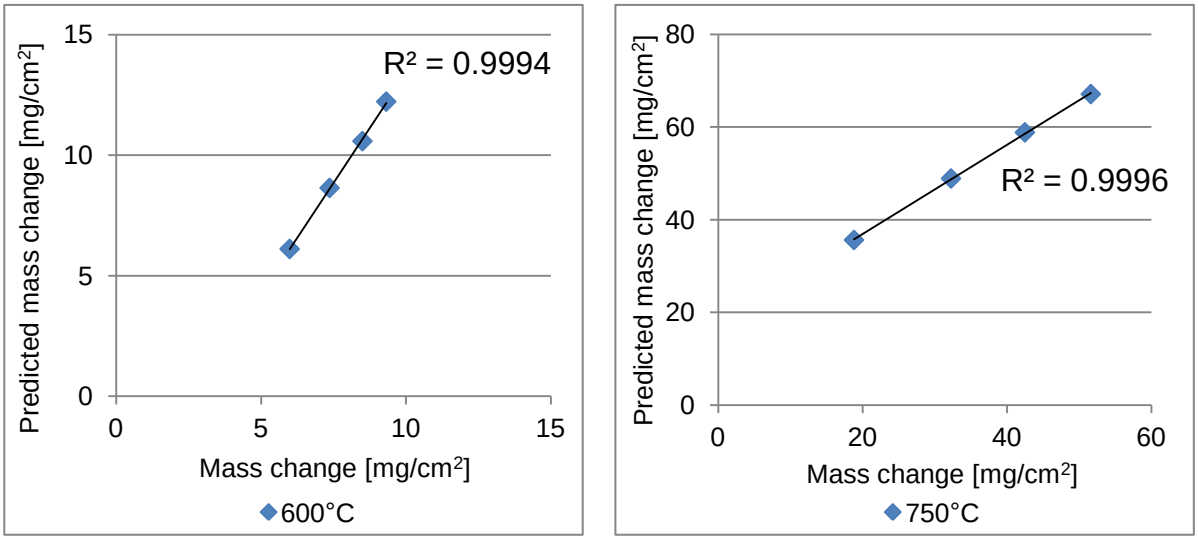

Figure 5-25 Comparison of predicted mass change data for T92 with equation (5-18) and the data obtained during steam oxidation tests at 600 and 750°C (L)

The same concept of modelling mass change was employed to build models the metal loss of a selected material under certain conditions of interest and the thickness of the scales formed. The equations proposed make it possible to predict the metal loss of T23 (equation (5-19)) and T92 (equation (5-20)), and the oxide thickness of T23 (equation (5-21)). The accuracy of the models changes with exposure conditions; however it is clear that the use of equations (5-19) - (5-21) allows the prediction of material performance in steam with acceptable accuracy.

$$x^2 = \left(exp\left(-41.976\left(\frac{1000}{T}\right) + 40.56\right)\right)(3600t) + 3.48E - 09 \quad \textbf{(5-19)}$$

$$x^2 = \left(exp\left(-13.628\left(\frac{1000}{T}\right) + 8.72\right)\right)(3600t) + 4.75E - 05 \quad \textbf{(5-20)}$$

where, x is metal loss [μm], T is absolute temperature [K], t is time [h]

$$x^2 = \left(exp\left(-38.032\left(\frac{1000}{T}\right) + 38.002\right)\right)(3600t) + 3.55E - 10 \quad \textbf{(5-21)}$$

where, x is oxide thickness [μm], T is absolute temperature [K], t is time [hour]. An analysis of the equation shows that at the beginning of the exposures, the

surfaces of the specimens are not oxide-free. Most probably there are very thin layers on the surface, and this is confirmed by the fact that the integration constants C are not zero. However there is also a possibly that there is initially a different oxidation mechanism before it settles down.

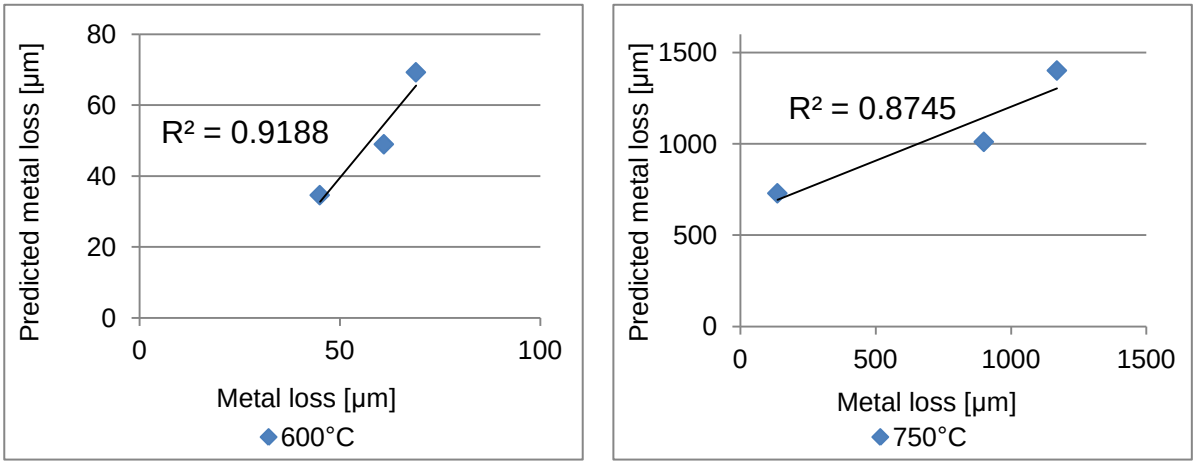

Figure 5-26 Comparison of predicted metal loss data for T23 with equation (5-19) and the data obtained during steam oxidation tests at 600 and 750°C (L)

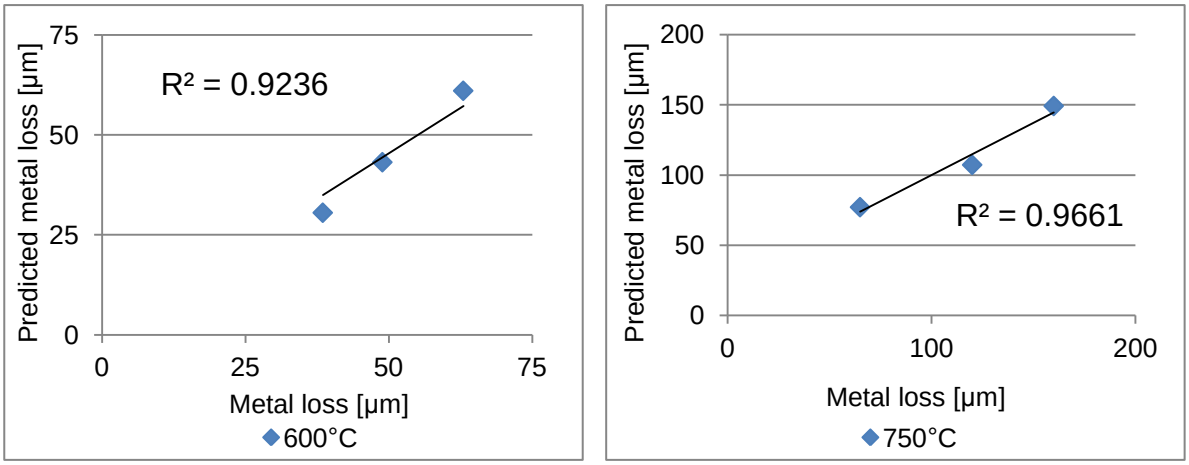

Figure 5-27 Comparison of predicted metal loss for T92 with equation (5-20) and the data obtained during steam oxidation tests at 600 and 750°C (L)

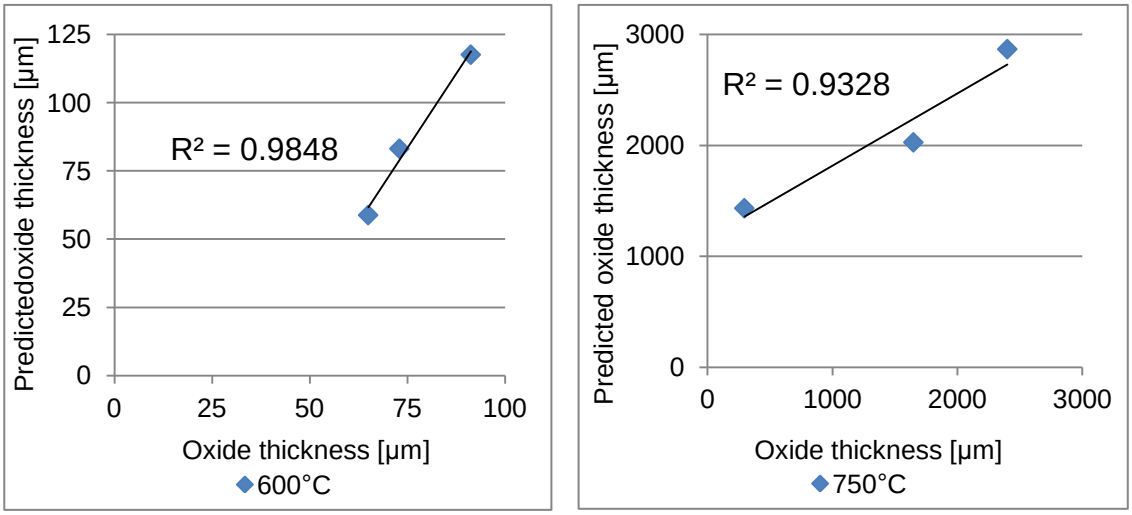

Figure 5-28 Comparison of predicted oxide thickness for T23 with equation (5.21) and the data obtained during steam oxidation tests at 600 and 750°C

The models presented are the first stage of modelling, which is often referred to as optimisation of results. With the derived equations, the models are able to predict the behaviour of T23 and T92. However, this is possible with good accuracy inside the results obtained. Based on this conclusion it was decided to generate models with an additional emphasis on the mechanistic understanding of steam oxidation. Such models incorporate not only the oxidation kinetics, as in the case of result optimisation, but also information regarding the morphology of oxide formed and a more detailed analysis of the processes controlling steam oxidation along with the associated oxidation rates and the identification of the prevailing controlling mechanism at each stage of the exposure. The first stage of the modelling procedure was to investigate in detail the oxidation kinetics of T23 in the temperature range between 600° and 750°C, the main conclusion being that there is a significant acceleration of the process above 650°C. An analysis of the specimens' cross-section showed that at 700° and 750°C the inner layers became micro-layered, which suggests that there is an additional controlling process involved; therefore the use of the same activation energy for the full temperature range studied would be a source of error. This resulted in the decision to divide the tests into two groups: low temperature up to 700°C and high temperature above 700°C. To predict the

dependence between temperature and oxidation rate within these two temperatures ranges the information from tests conducted at 675°C and 725°C were used. These tests were performed by different researchers at Cranfield University over the past years; however the methodology used for the steam oxidation testing has not changed. Therefore, the use of this data is not believed to generate errors for kinetic and Arrhenius calculations. The activation energies for the process and the rate constants were calculated within these two ranges. Here it is crucial to recall that steam oxidation is divided into three stages: firstly when oxidation is controlled by the surface reaction (including the nucleation of the first oxides and initial oxide thickening). Secondly, when cationic diffusion is the rate-determining process and oxidation is assumed to be initially parabolic; Thirdly after a longer exposures, when it becomes linear again due to exfoliation of the scales developed. The models presented before assumed that the oxidation rate is parabolic during the whole exposure, whereas in fact there is a switch between parabolic and linear rate dependencies. The precise time of such a change is hard to define and varies with the exposure conditions. The transition point between the rate dependencies was identified based on the results obtained by plotting a line through the points representing the mass change of T23 and assuming that oxidation follows linear and parabolic dependencies respectively.

Figure 5-29 shows the time of transition between parabolic and linear rate dependence at different exposure temperatures The transition points were calculated using the following equations

$$x^2 = k_p t + \mathrm{C''} \quad \textbf{(5-22)}$$

$$x = k_l t + C''' \quad \textbf{(5-23)}$$

where k_p, k_l are parabolic and linear rate constants, t is time [s] and C'' and C''' are parabolic and linear integration constants. The point of intersection of the plotted lines is assumed to be the transition point between the oxidation periods showing parabolic and linear law dependencies.

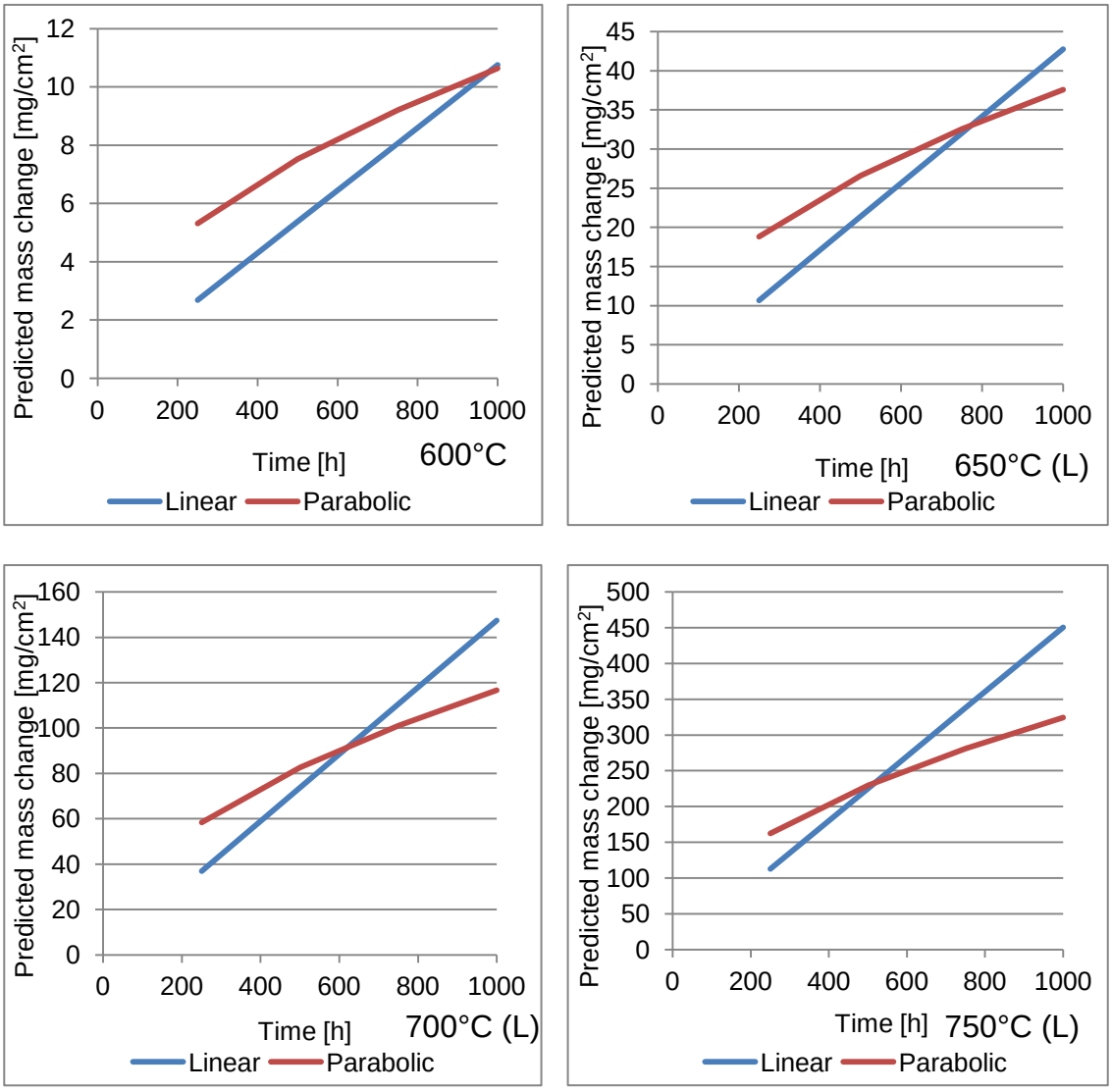

Figure 5-29 Identification of the transition point between linear and parabolic rate dependencies

Using the data presented the following relationship between the oxidation rates has been deduced: at 600°C (L) the oxidation rate is parabolic up to 965 hours, at 650°C (L) there is a switch between the rates after 750 hours, at 700°C (L) the linear rate dependence prevails after 620 hours and finally at 750°C (L) it prevails after 510 hours. In the literature it is reported that at higher temperatures there is a change between the parabolic and linear rate dependencies after longer exposures. However, such trends have not been identified for T23 during the exposure time. Considering the change of rate

dependence with time two separate models for steam oxidation have been created: one, for low temperatures (t < 650°C (L)) another one for high temperatures (t > 650°C (L)).

$$x = \left(\left(exp\left(-32.4\left(\frac{1000}{T}\right) + 26.946\right)\right)(3600t_1) + 3.01E - 10\right)^{\frac{1}{2}} + \\ + \left(\left(exp\left(-20.611\left(\frac{1000}{T}\right) + 10.975\right)\right)(3600t - t_1) + 3.26E - 11\right)^{1} \quad \textbf{(5-24)}$$

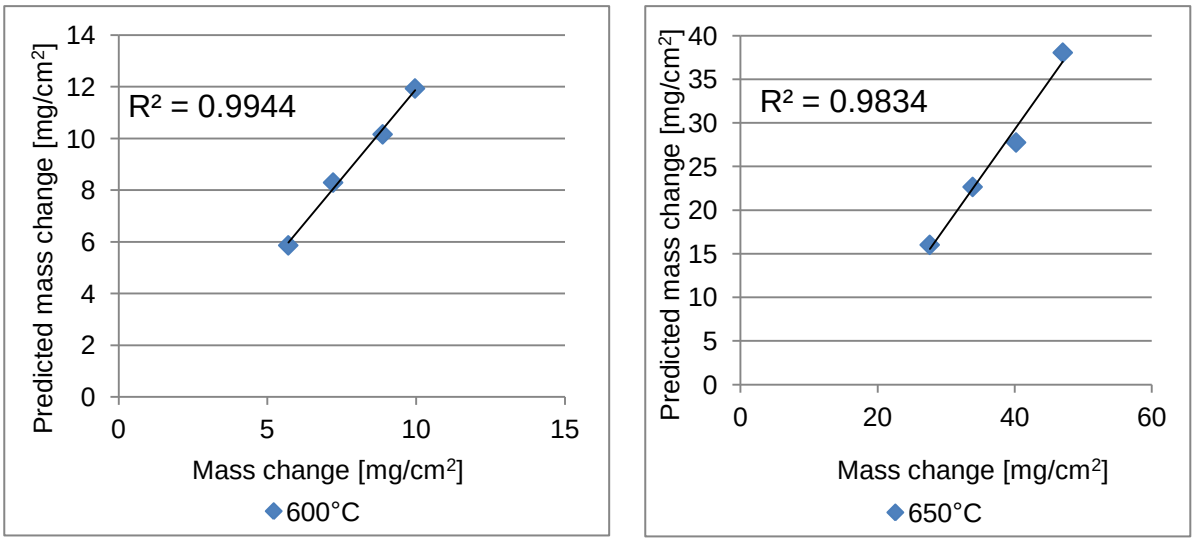

Figure 5-30 Comparison of predicted mass change data for T23 with equation (5-24) and the data obtained during steam oxidation tests at 600 and 650°C (L)

At higher temperatures, the oxidation rate increases, moreover the scale morphology varies from that identified below 650°C (L). As the oxidation rates change and the periods when the linear rate law is believed to prevail are longer. Moreover, there is a change in the activation energy at the higher temperatures and therefore the model is modified to predict steam oxidation at higher temperatures with greater accuracy.

$$x = \left(\left(exp\left(-20.492\left(\frac{1000}{T}\right) + 16.218\right)\right)(3600t_1) + 2.26E - 09\right)^{\frac{1}{2}} + \\ + \left(\left(exp\left(-28.732\left(\frac{1000}{T}\right) + 19.257\right)\right)(3600t - t_1) + 1.06E - 11\right)^{1} \quad \textbf{(5-25)}$$

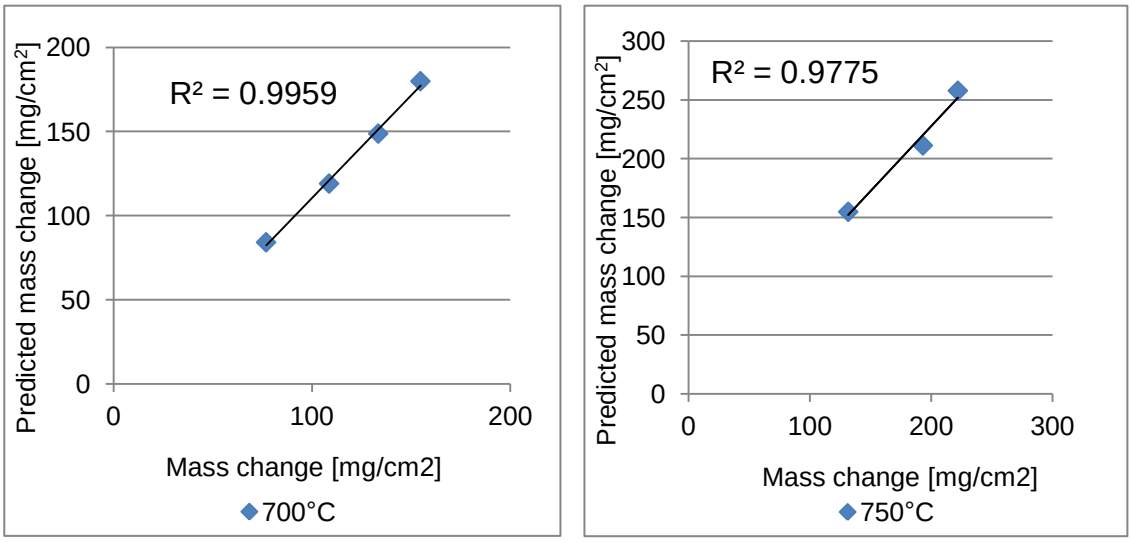

Figure 5-31 Comparison of predicted mass change data for T23 with equation (5-25) and the data obtained during steam oxidation tests at 600 and 650°C (L)

Models built with consideration of the fact that the oxidation rate changes with time of exposure have shown better accuracy than models assuming that oxide growth just follows a parabolic rate law. Such an improvement is more significant at lower temperatures, which is important for the application of the model by the industrial sponsors. The modelling shows a good results; however, there is a need to improve the identification of the precise time when oxide growth according to either a linear or parabolic rate prevails. More precisely, prediction of the transition point between linear and parabolic oxidation would reduce the error of the model generated. The precision of the model could be improved if information regarding the transient oxidation process is available and the oxidation rate dependence for that initial period of the initial period of that process was known. The application of such

data is believed to influence the accuracy of the model at the beginning of the process when the first oxides form.

The methodology used for mass change has been used to model the metal loss of T23 in the temperatures tested. Following that approach, the following equation used for the whole temperature range has been derived :

$$x = \left(\left(exp\left(-34.217\left(\frac{1000}{T}\right)+32.609\right)\right)(3600t_1)+5.86E-10\right)^{\frac{1}{2}} + \\ +\left(\left(exp\left(-19.703\left(\frac{1000}{T}\right)+11.038\right)\right)(3600t-t_1)+9.14E-12\right)^{1} \quad \textbf{(5-26)}$$

The transition times between the parabolic and linear laws are 930, 750, 600 and 510 hours for 600, 650, 700 and 750°C (L) respectively. By using these parameters in equation (5-26) as the period in which oxidation follows a parabolic rate law (t_1); the metal loss for T23 at certain temperature of interest has been calculated.

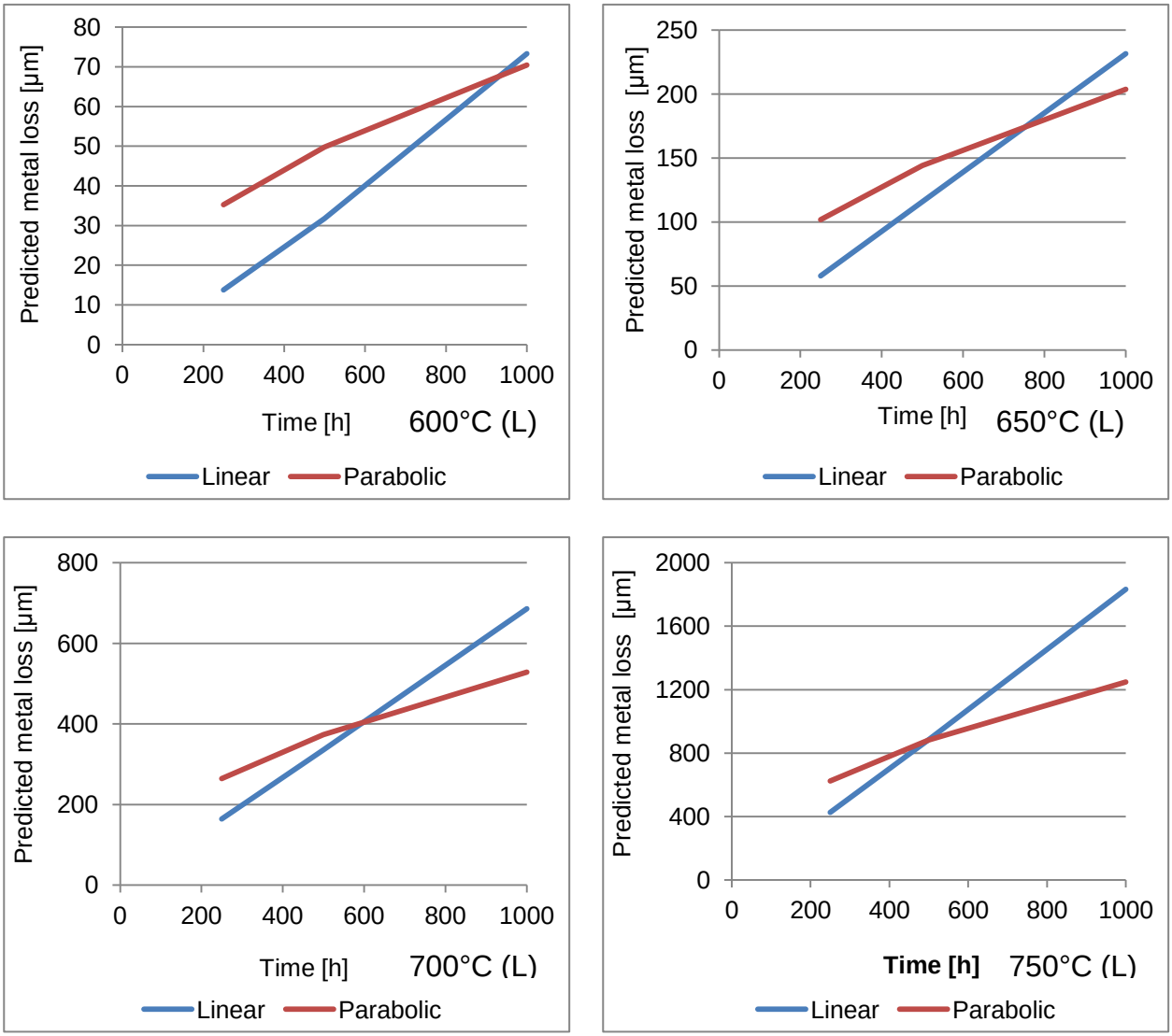

Figure 5-32 Identification of the transition point between linear and parabolic rate dependencies for T23

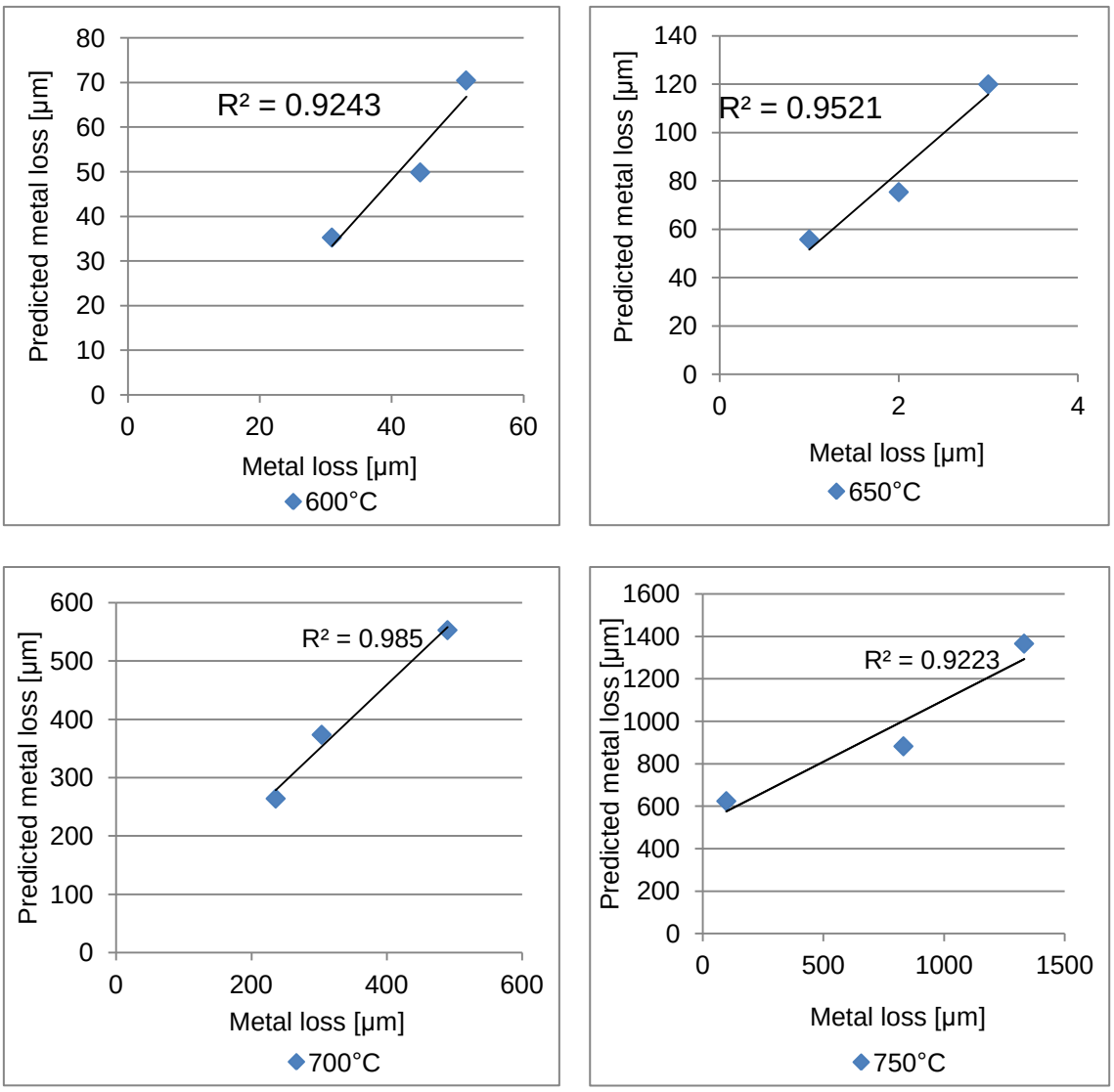

Figure 5-33 Comparison of predicted mass change data for T23 with equation (5-26) and the data obtained during steam oxidation tests at the temperature between 600-750°C (L)

The results of metal loss modelling using the method discussed are less accurate than those obtained for mass change; there is a larger discrepancy between the metal loss calculated with the equation generated equation (5-26) and the actual data acquired during the tests. The errors could be explained due to the fact that less data was available for modelling; this generates firstly differences in the activation energy calculations (the initial step of the modelling). There is a single equation derived from the Arrhenius relationship

which is used in the whole temperature range. In the second phase of modelling, the prediction of the actual transformation point between parabolic and linear rate law dependencies is influenced by a lack of the information about metal loss after 750 hours exposure, which possibly generates errors in prediction of those times. A comparison of the results of metal loss modelling between the approaches created clearly shows that use of the equation (5-26) allows the metal loss of T23 to be predicted with better accuracy than with the methods proposed before; this makes it more applicable to industry. To summarise, this section described the approaches used for modelling of the steam oxidation of T23. This material was selected due to its lack of scale spallation, which allows a better understanding of the process and therefore a more accurate prediction of the material's performance at selected temperatures.

The method designed and applied for the modelling of steam oxidation of T23 has also been used for the prediction of steam oxidation behaviour of T92. Using the same modelling approach for T92 as for T23 showed less accuracy than the models generated before; for T92 (when parabolic rate dependence was assumed to prevail). This is possibly a result of the spallation of the scales; therefore in both steps used for the modelling the results obtained have errors which cause the calculated mass change to deviate from the results obtained during the steam oxidation tests.

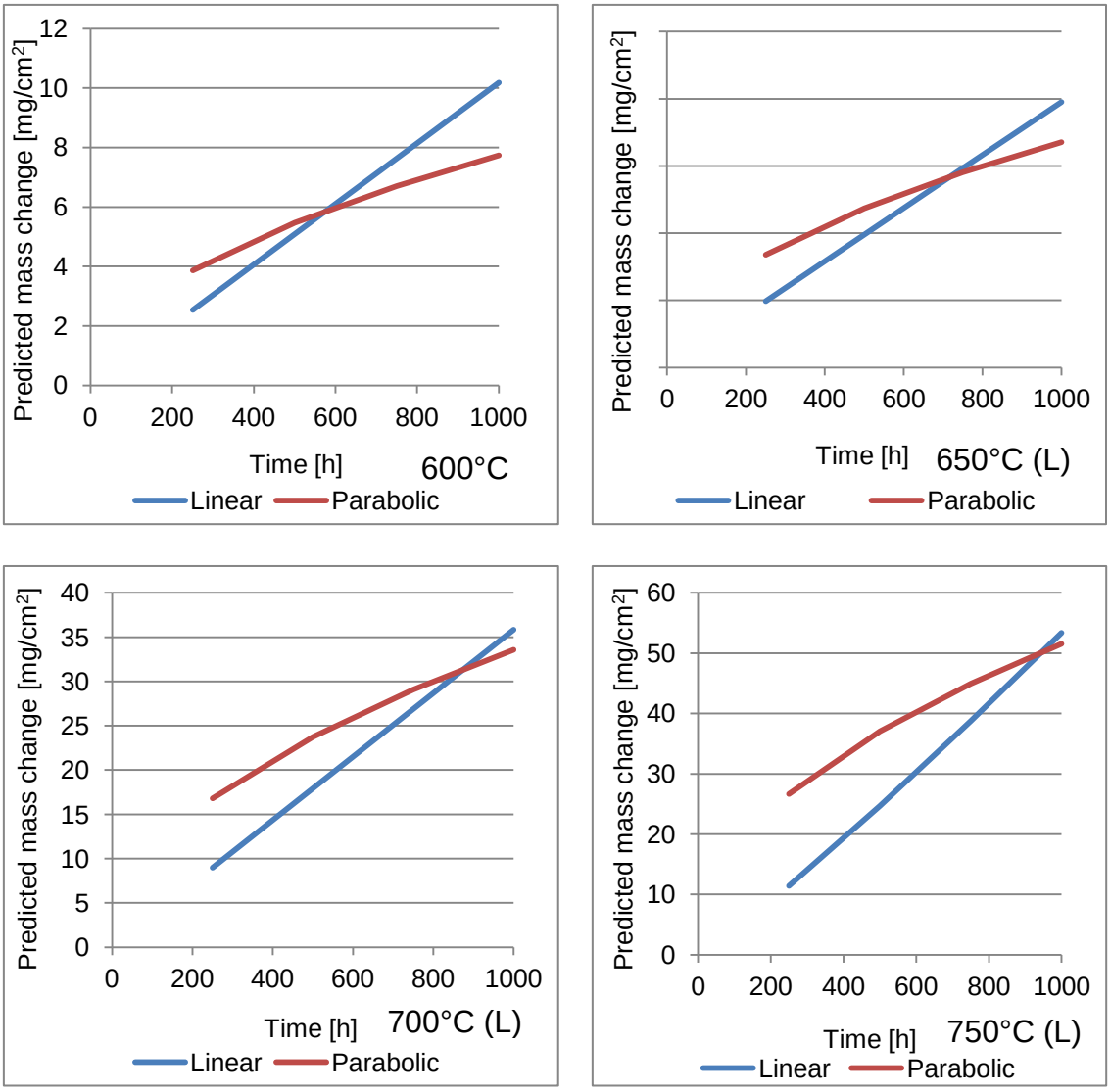

Figure 5-34 Identification of the transition point between linear and parabolic rate dependencies for T92

An analysis of the transformation point between the rate dependencies showed that the periods when the parabolic rate dependence prevails increase with temperature, which is in accordance with observations made during the tests performed. Figure 5-35 compares the actual test results with the results obtained using the generated equation for the whole temperature range.

$$x = \left(\left(exp\left(-24.93\left(\frac{1000}{T}\right) + 17.552\right)\right)(3600t_1) + 5.86E - 10\right)^{\frac{1}{2}} + \left(\left(exp\left(-10.94\left(\frac{1000}{T}\right) - 0.5265\right)\right)(3600t - t_1) + 9.14E - 12\right)^{1} \quad \textbf{(5-27)}$$

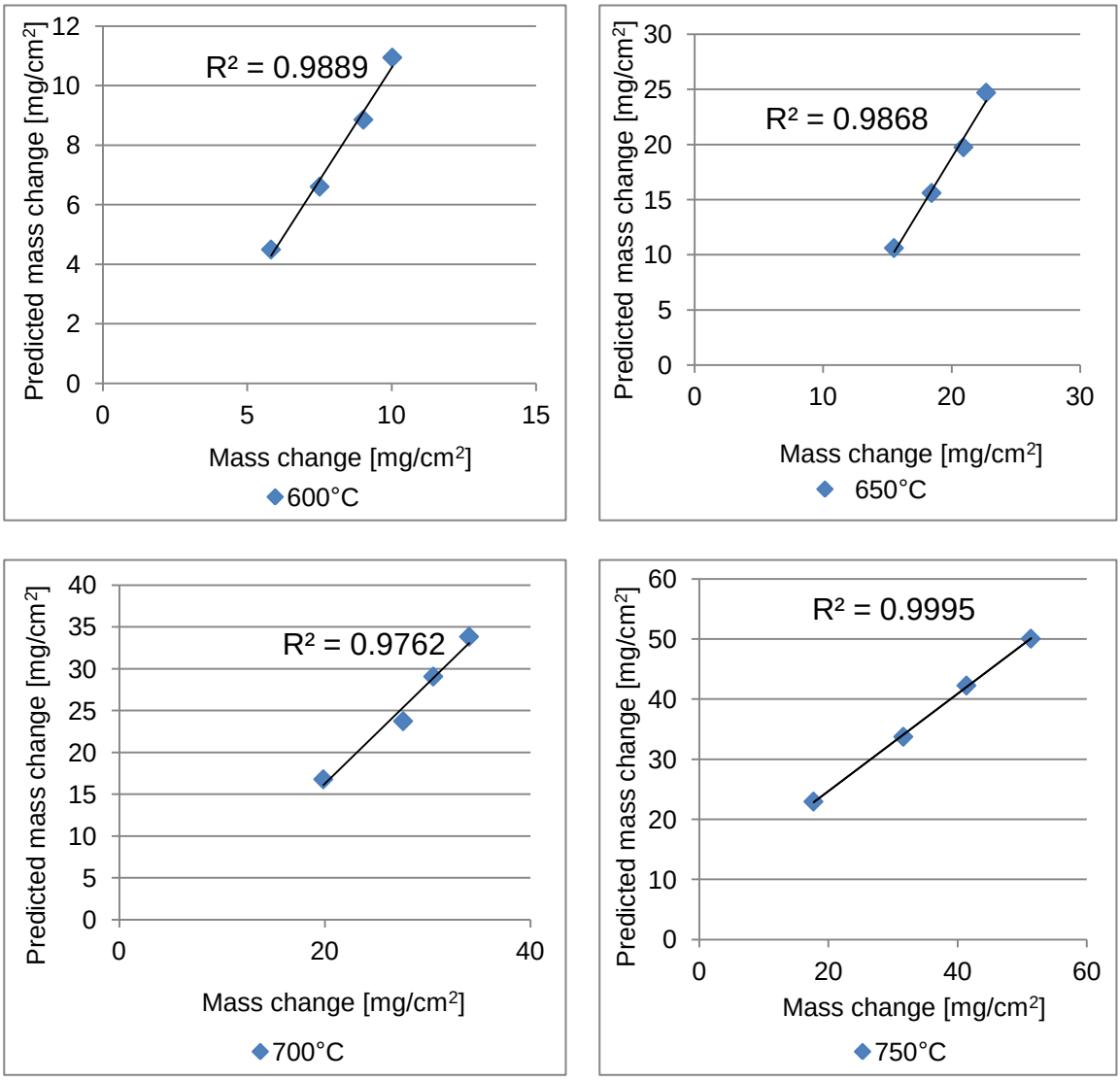

Figure 5-35 Comparison of predicted mass change data for T92 with equation (5-27) and the data obtained during steam oxidation tests at the temperature range 600-750°C (L)

Since the scales formed on T92 exfoliate heavily, a model has been derived for metal loss data. The method used for T92 metal loss modelling as was used

previously for T23. An analysis of the transformation point between the rates dependencies shows that there is a correspondence with data identified for mass change: a parabolic rate dependence prevails up to 530, 620, 700 and 800 hours for 600, 650, 700 and 750°C (L) respectively (Figure 5-36).

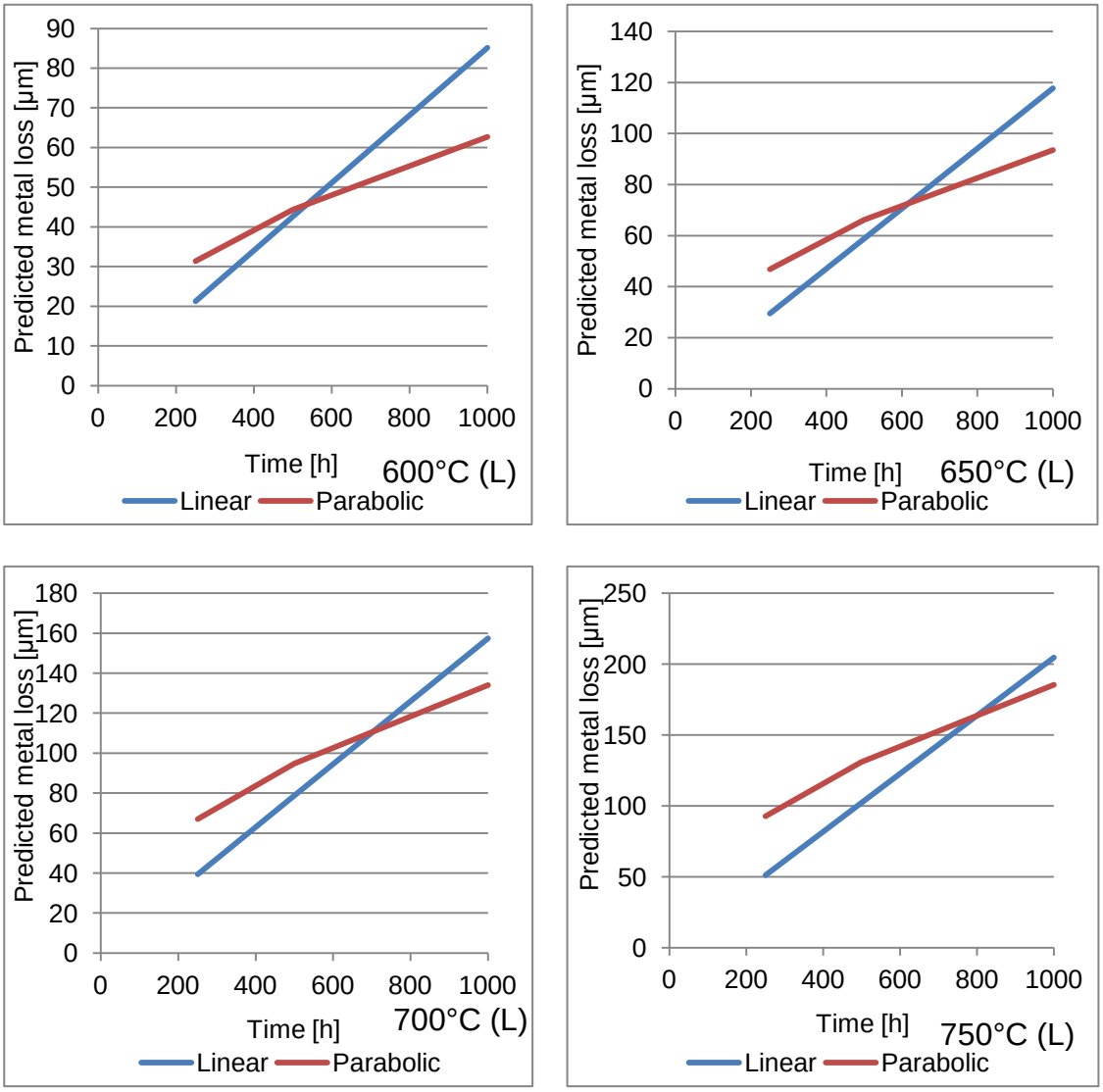

Figure 5-36 Identification of the transition point between linear and parabolic rate dependencies For T92

From equation (5-28) it is possible to predict the metal loss of T92 at the temperatures tested with higher accuracy than that obtained from the model that assumes that oxidation strictly follows a parabolic dependence.

$$x = \left(\left(exp\left(-12.91\left(\frac{1000}{T}\right) + 7.9685\right)\right)(3600t_1) + 5.86E - 10\right)^{\frac{1}{2}} + \left(\left(exp\left(-5.2214\left(\frac{1000}{T}\right) - 4.6711\right)\right)(3600t - t_1) + 9.14E - 12\right)^{1} \quad \textbf{(5-28)}$$

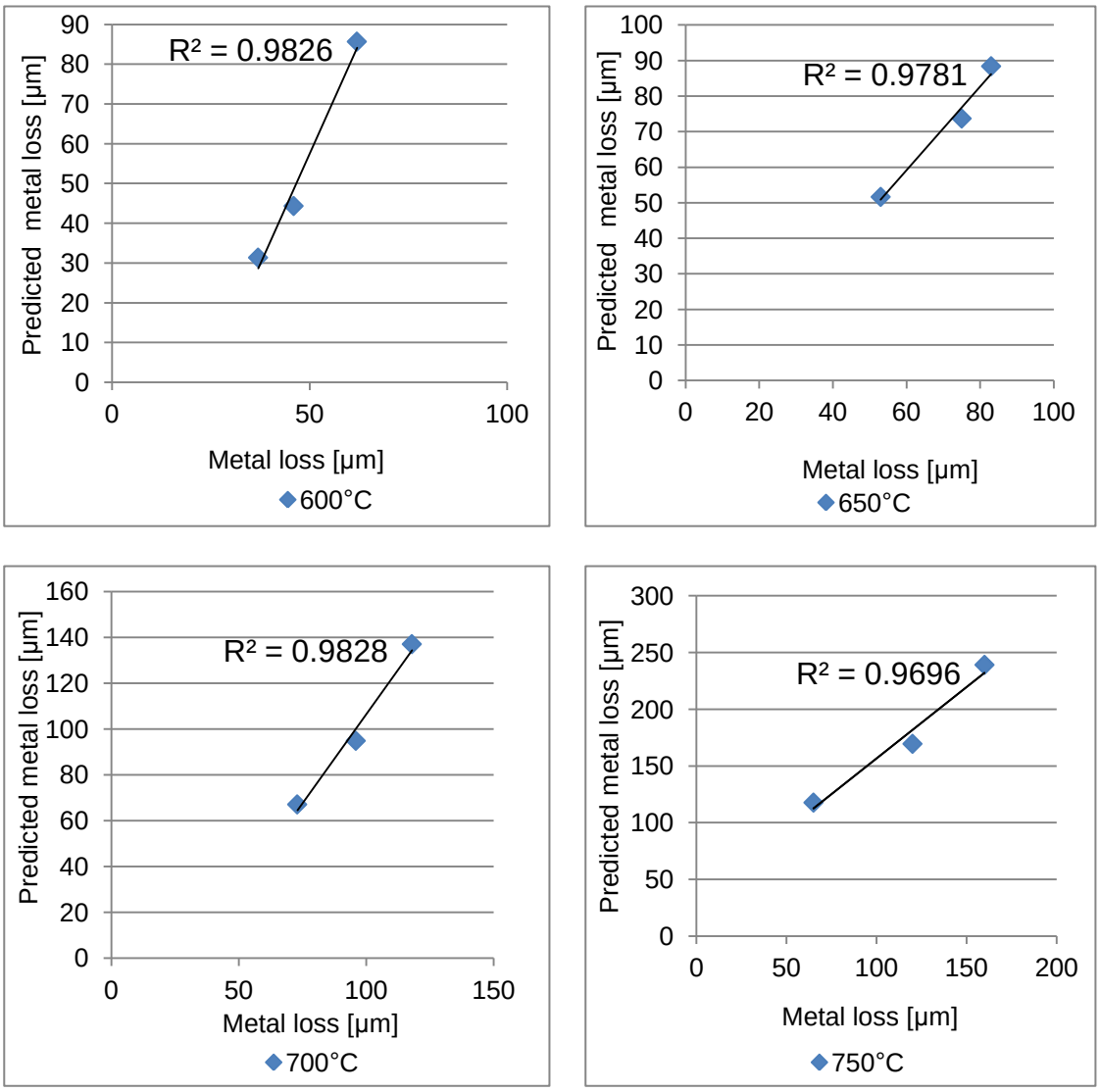

Figure 5-37 Comparison of predicted metal loss for T92 with equation (5-26) and the data obtained during steam oxidation tests at the temperature range 600-750°C

The differences between the results of the mass change and metal loss modelling for T92 are assumed to be a result of the fact that metal loss is not

influenced by scales spallation. The mass change readings could give errors within each step of the modelling and therefore lead to more significant discrepancies between the modelled and measured mass change data. In comparison the metal loss data show a clear trend in time, which is not influenced by oxide scale spallation; therefore such an approach to the steam performance modelling of T92 is believed to be more applicable to industry and is believed to generate more accurate results, which could possibly be used to assess the operational lifetime of superheater tubing.

5.10 Heat transfer and its influence on the accuracy of the steam oxidation models

Heat transfer is a crucial factor influencing the lifetime of the tube used for SH/RH tubing as well as the efficiency of the power generation. In this particular project the heat transfer modelling aims to assess the real exposure temperature of the metal surface of the heat exchanger tubes. It is well known that the metal surface temperature differs from the temperature of the liquid flowing through it. In order to calculate the metal surface temperature a heat transfer model was designed. Heat transfer along the outer surface of the tube, (between the combustion gas and tube) is considered to be forced convection. Inside the tube a heat transfer is assumed to be forced convection with full turbulent flow. Across the tube wall, heat is transferred via conduction across the wall layers. Figure 5-38 describes the process and illustrates the heat transfer.

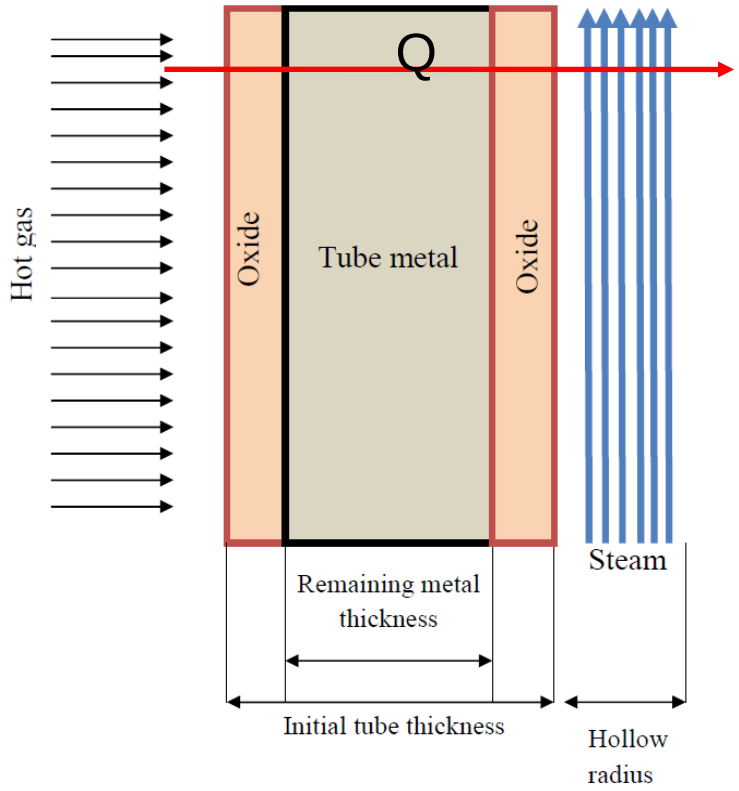

Figure 5-38 Heat transfer across the heat exchanger tube

For the heat transfer modelling the following assumptions were made:

- Gas temperature is 1000°C, composition of gas at 15% excess air is presented in Table 5-13;
- The tube is T23 ferritic steel with inner and outer diameters of 0.0438 and 0.0508 [m] respectively;
- The main oxide growing on the tube's surface from both sides is magnetite;
- The oxidation rate and metal loss are calculated using equations (5-38) and (5-39) respectively;
- The spallation rate is neglected due to insufficient data beaing available;
- 100% steam is flowing inside the tube; and
- Steam temperature is 560°C.

Table 5-12 Parameters for the heat transfer modelling [120]

Parameters	Steam	Hot gas
Density [kg/m^3]	0.2697	0.227
Steam flow [kg/h]	3,600	-
Gas velocity [m/s]	-	12
Dynamic viscosity [kg/m/s]	3.24E-05	4.86E-05
Specific heat coefficient [J/kg/C]	2957	1100
Thermal conductivity [W/m/C]	9.04E-02	8.20E-02

Table 5-13 Composition of the hot gas [120]

Elements	Composition [mole %]
Nitrogen	71.08
Oxygen	2.46
Carbon dioxide	8.29
Water	18.17

Considering the conditions within the tube as corresponding to fully developed turbulent flow the correlation for fully developed turbulent flow was used and expressed as Nusselt number [42]:

$$Nu = 0.023(Re)^{0.8}(\mathrm{Pr})^{0.4} \quad \textbf{(5-29)}$$

where Re and Pr are Reynolds and Prandtl numbers respectively. Reynolds and Prandtl numbers are defined using the following equations:

$$Re = \frac{4\dot{m}}{\pi d\mu} \quad \textbf{(5-30)}$$

$$\mathrm{Pr} = \frac{\mu C_p}{k} \quad \textbf{(5-31)}$$

where m is mass flow of the steam [kg/h], d is inner diameter of the tube [m], μ is the dynamic viscosity [kg/m/s], k [W/m/C] and Cp [J/kg/C] are thermal conductivity and specific heat coefficients respectively. Using the data obtained the convection coefficient of steam for fully developed turbulent flow in the tube was calculated [42]:

$$h_s = 0.023\ \frac{k}{d}(Re)^{0.8}(Pr)^{0.4} \quad \textbf{(5-32)}$$

where k is thermal conductivity [W/m/C], d is the inner diameter of the tube [m].

Heat transfer outside the tube is also considered as being forced convection as a result of the cross flow of the hot gas over the bare tubes. The correlation for the fully developed turbulent flow of the hot gas is defined as:

$$Nu = 0.23(Re)^{0.8}(\mathrm{Pr})^{0.33} \quad \textbf{(5-33)}$$

Reynolds and Prandtl numbers are defined using the following equations:

$$Re = \frac{w\rho L}{\mu} \quad \textbf{(5-34)}$$

$$\mathrm{Pr} = \frac{\mu C_p}{k_g} \quad \textbf{(5-35)}$$

where L is a characteristic linear dimension [m], w is gas velocity [m/s], μ is dynamic viscosity [kg/m/s], kg [W/m/C] and Cp [J/kg/C] are thermal conductivity and specific heat coefficients respectively. Using the calculated data the convection coefficient of the hot gas for fully developed turbulent flow was used [120]:

$$h_g = \frac{Nu}{k_g D} \quad \textbf{(5-36)}$$

where Nu is nusselt number, k_g is thermal conductivity [W/m/C], and D is outer diameter [m].

Heat transfer across the tube wall is described as conduction. The conduction coefficient of the wall will vary with exposure time. At the beginning of oxidation, the conduction coefficient only based on the pipe's conductivity; however, with time, oxides grow on both sides of the tube and therefore the overall conduction coefficient changes with the relation between oxide and metal thicknesses. Additionally, the heat transfer model takes metal loss into consideration. The conduction coefficient [W/m^2/C] for the multi-layered cylindrical wall in the case of the considered example was derived as follows:

$$conduction\ coefficent = \sum \frac{1}{2\lambda_i} \ln\left(\frac{d_{i+1}}{d_i}\right) \quad \textbf{(5-37)}$$

where λ_i is thermal conductivity for a particular layer [W/m/C] (Table 5-14) and d_i is a diameter i-layer [m].

Table 5-14 Tube wall properties

Material	Thermal conductivity [W/m/C]
2.25 Cr ferritic steel	34.606
Magnetite [Fe_3O_4]	0.592

Using the acquired data and assuming that the total heat transfer $\sum Q_i = 0$ the following equation was derived:

$$Q = \frac{\pi L(T_2 - T_1)}{\frac{1}{h_g D} + \left(\left(\frac{1}{2\lambda_{OX}} \ln\left(\frac{D + D_{ox}}{D}\right)\right) + \left(\frac{1}{2\lambda_{\text{met}}} ln\left(\frac{D}{d}\right)\right) + \left(\frac{1}{2\lambda_{\text{ox}}} ln\left(\frac{d}{d - d_{ox}}\right)\right)\right) + \frac{1}{h_s d}} \quad \textbf{(5-38)}$$

where D, d are the outer and inner diameters of the tube respectively [m], which change with exposure time due to metal loss, D_{ox} and d_{ox} are the outer and inner diameters of grown oxide respectively, λ_{met}, λ_{ox} are thermal conductivities of the metal and oxide respectively and h_g, h_s are the convection coefficients of the gas and steam respectively. Figure 5-39 shows how the metal surface temperature of the inner part of the heat exchanger tube changes with exposure time for 560°C steam. The outer surface of the metal is exposed to a hot gas (1000°C).

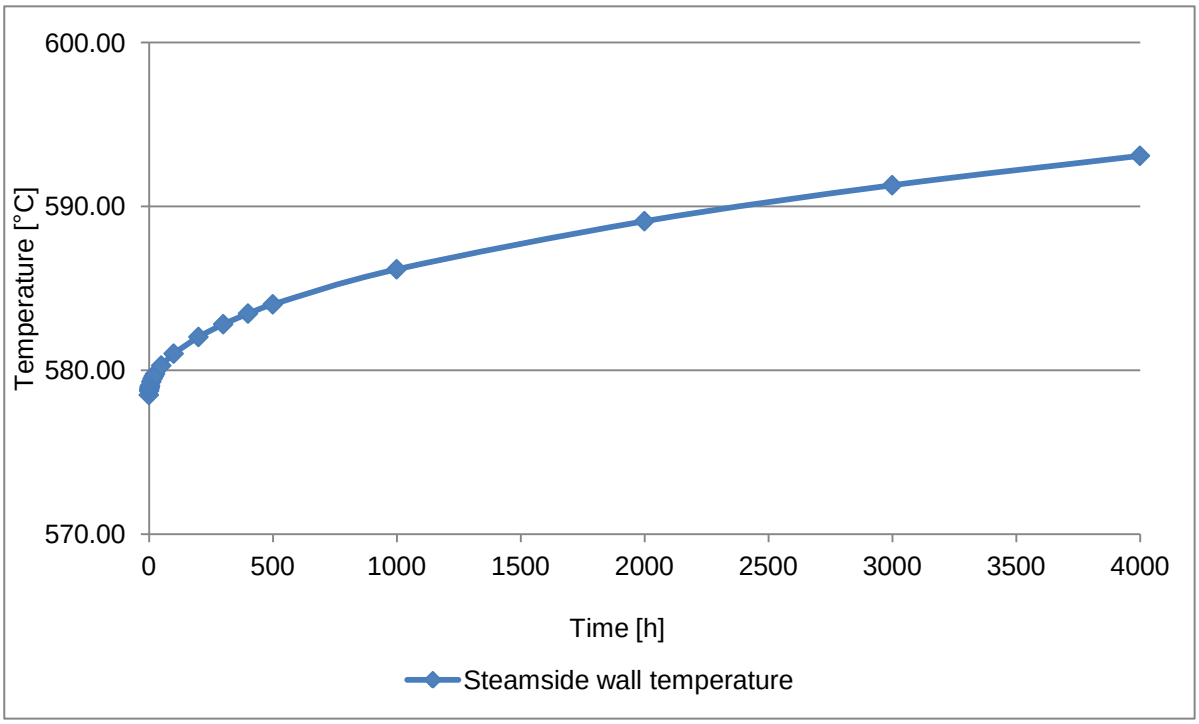

Figure 5-39 Change of the metal surface temperature with time for heat transfel model without radiation

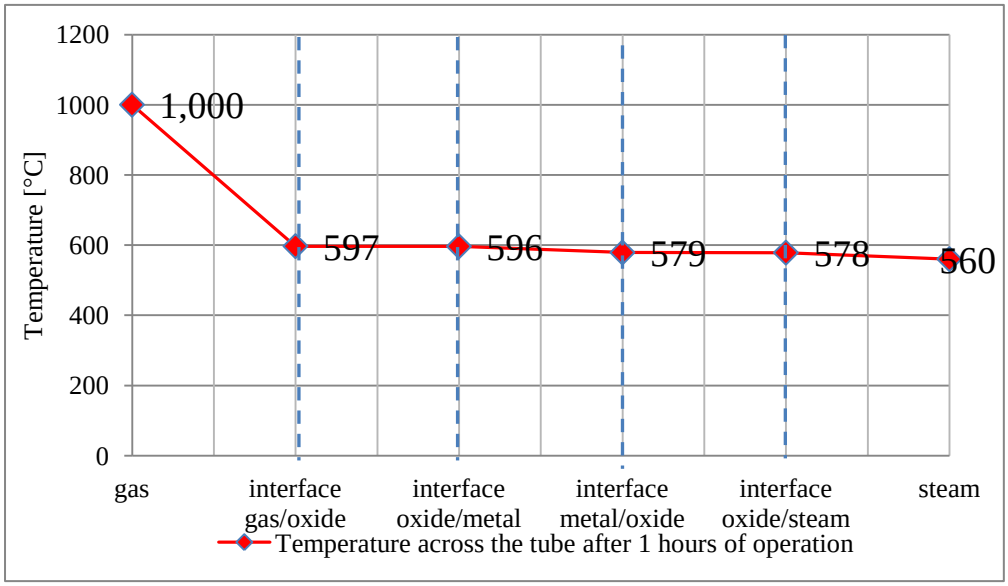

Figure 5-40 Change in temperature across the tube after 1 hour of operation

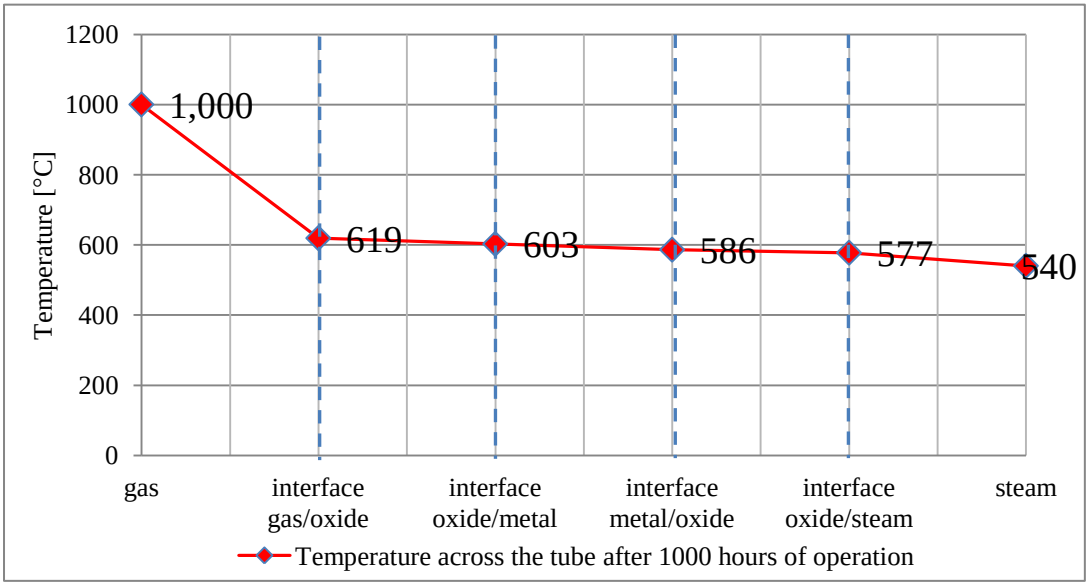

Figure 5-41 Change in temperature across the tube after 1000 hours of operation

Figure 5-40 and Figure 5-41 present the variation in temperature across the tube after two different exposure times of. It is clear that the temperatures of the different surfaces change with time, and this is associated with the oxide growth and the metal loss of the tube. The growth of the oxides and the metal loss change heat transfer across the tube, this could have severe consequences for power plant operations such as local overheating of the tube that could possibly

result in the tube cracks and boiler failures. Table 5-15 presents the calculated temperature variations across the heat exchanger tube with time.

Table 5-15 Change in the temperatures across the wall with time for heat transfer model without radiation

Exposure time [h]	T_{Oxide} [°C] gas side	T_{wall} [°C] gas side	T_{wall} [°C] steam side	T_{steam} [°C] steam side
0	596.12	596.12	578.50	578.50
1	596.95	596.33	578.75	578.46
2	597.30	596.43	578.86	578.45
3	597.57	596.50	578.94	578.44
4	597.79	596.56	579.01	578.43
5	597.99	596.61	579.07	578.42
6	598.75	596.81	579.31	578.38
7	599.34	596.96	579.49	578.36
8	599.83	597.09	579.64	578.34
9	600.27	597.21	579.78	578.32
10	601.95	597.64	580.29	578.24
100	604.32	598.26	581.02	578.14
200	608.62	599.12	582.04	578.00
300	610.14	599.79	582.82	577.89
400	610.23	600.34	583.46	577.81
500	610.06	600.83	584.03	577.73
1000	619.00	602.62	586.17	577.41
2000	630.46	605.11	589.10	577.00
3000	636.50	607.00	591.30	576.71
4000	639.24	608.54	593.09	576.47

The heat transfer modelling showed that the actual temperature of the heat exchanger tube surface from the steam side is much higher than the temperature of the steam flowing inside the tube. The temperature across the heat exchanger drops from the outer surface to the inner surface; the largest

drop is across the oxide, which is a result of its thermal conductivity. The model presented, shows one-dimensional heat transfer for a heat exchanger tube exposed to hot gas.

The heat transfer modelling of superheater/reheater tubing often neglects gas side radiation, which generates errors in the model (5-10% dependent on the location of the tube) [55] It is possible to neglect radiation for the modelling of heat transfer for those sections of the Heat recovery area (HRA) which are not exposed; to the source of heat. In such a situation, the impact of the radiation heat transfer is less significant and therefore may be neglected. In order to study the impact of radiation on the heat transfer across the SH/RH tubing the model analysing the combined effect of convection and radiation heat transfer outside the tube has been created. equation (5-39) combines both convection and radiation heat transfer from the hot gas, whereas the rest of the heat transfer model has not been changed:

$$Q = \frac{\pi L(T_2 - T_1)}{\frac{1}{(h_g + h_r)D} + \left(\left(\frac{1}{2\lambda_{OX}}\ln\left(\frac{D + D_{ox}}{D}\right)\right) + \left(\frac{1}{2\lambda_{\mathrm{met}}} ln\left(\frac{D}{d}\right)\right) + \left(\frac{1}{2\lambda_{\mathrm{ox}}} ln\left(\frac{d - d_{ox}}{d_{ox}}\right)\right)\right) + \frac{1}{h_s d}} \quad \textbf{(5-39)}$$

where h_r is a radiation coefficient. To calculate the radiation coefficient, the method proposed by Hottel and Sarofim has been used:

$$h_r = \sigma \frac{1 + \varepsilon_w}{\varepsilon_g} \frac{{T_g}^4 - {T_w}^4}{T_g - T_w} \quad \textbf{(5-40)}$$

where σ is the Stefan Boltzmann constant [W/m^2/K^4], ε_w, ε_g are the wall and gas emissivity respectively, T_w, T_g are the wall and gas temperatures respectively [K]. Figure 5-42 shows how the temperature of the inner wall of the tube changes with time. A comparison of the data presented in Figure 5-39 and Figure 5-42 shows that there are differences between these wall temperatures when the heat transfer model includes radiation heat transfer. The change in the metal surface temperature from the steam side due to radiation varies with time and is more significant at the beginning of the exposure. An analysis of

temperatures obtained with those two models showed between 5-10% difference in the heat transfer across the tube, this is associated with more heat transfer from the gas into the tube and then across it.

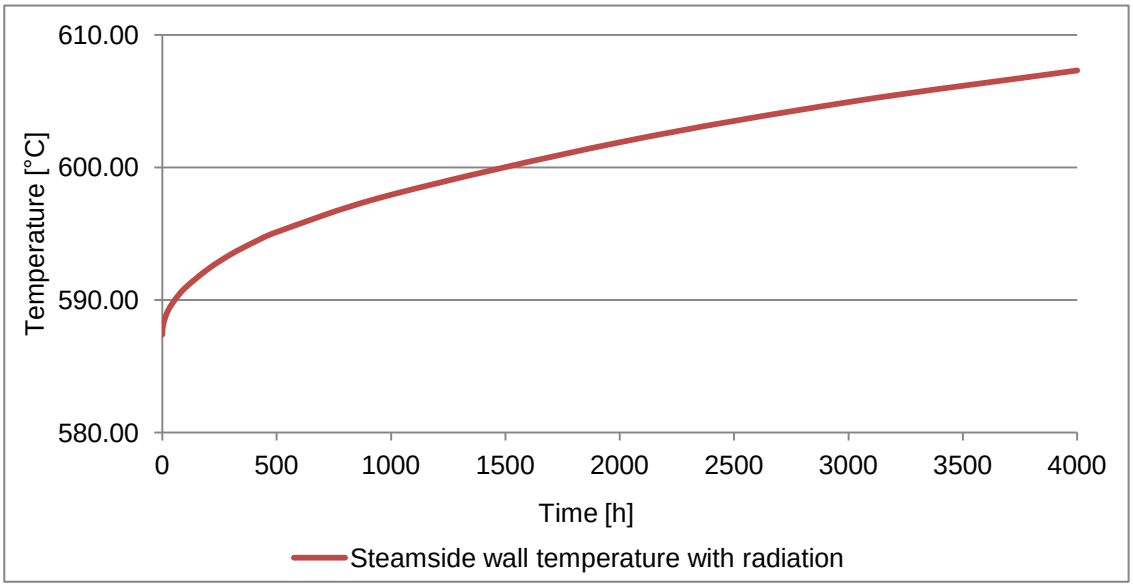

Figure 5-42 Change of the metal surface temperature with time for heat transfer model with radiation

Figure 5-43 and Figure 5-44 show the temperature variation through the system obtained with the heat transfer model including radiation after 1 and 1000 hours of operation. An analysis of these data indicates that there is a significant increase in the temperature at each particular surface when radiation is included in the model.

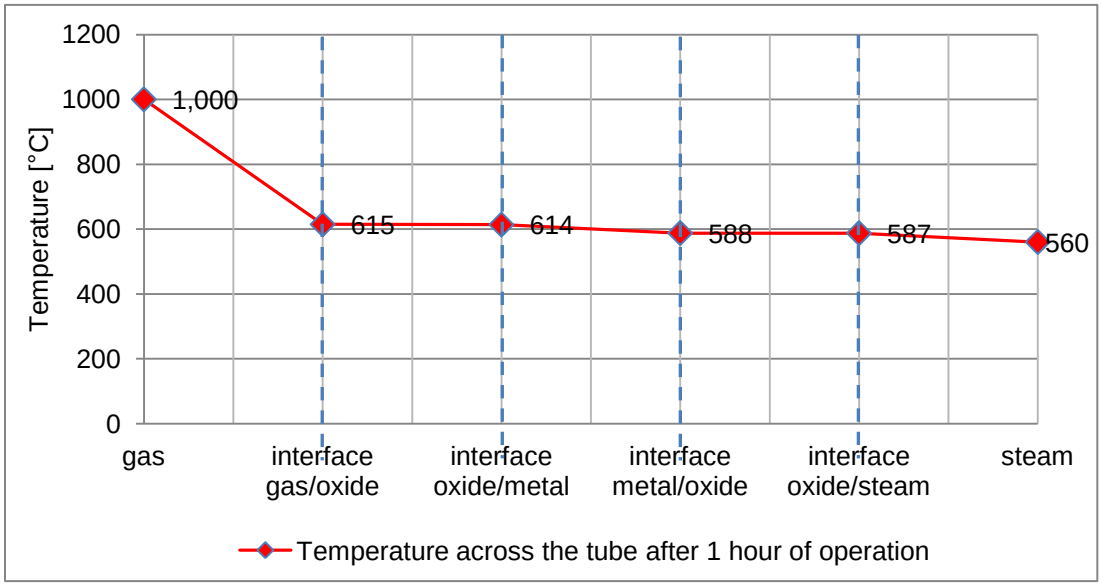

Figure 5-43 Change in temperature across the tube after 1 hour of operation including radiation

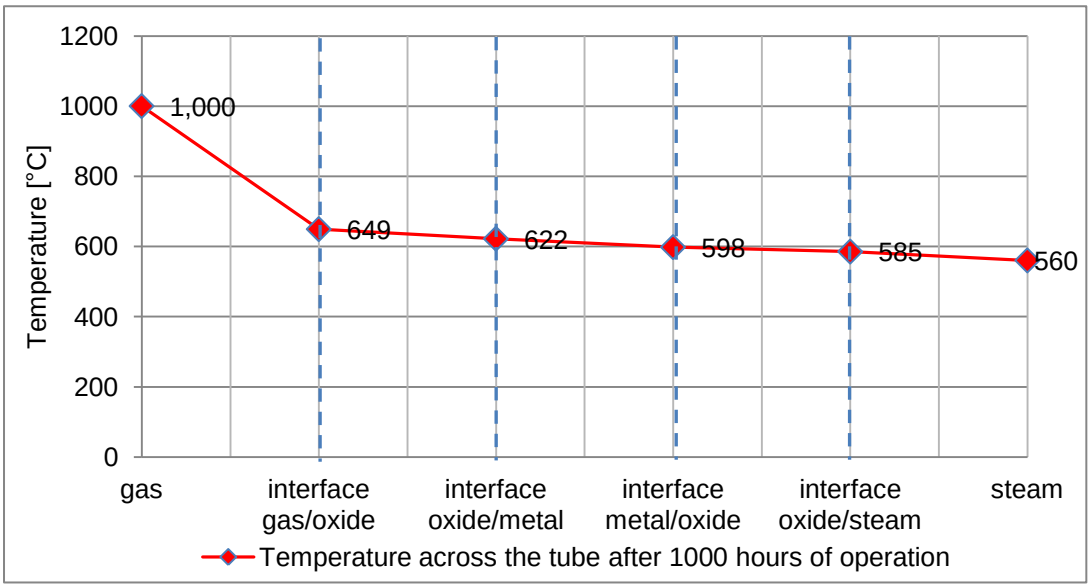

Figure 5-44 Change in temperature across the tube after 1000 hour of operation including radiation

Table 5-16 presents the temperature change across the heat exchanger tube with time up to 4000 hours.

Table 5-16 Change in the temperatures across the wall with time for heat transfer model with radiation

Exposure time [h]	T_{Oxide} [°C] gas side	T_{wall} [°C] gas side	T_{wall} [°C] steam side	T_{steam} [°C] steam side
0	613.46	613.46	587.38	587.38
1	614.71	613.72	587.73	587.30
2	615.20	613.88	587.90	587.29
3	615.58	613.98	588.02	587.27
4	615.90	614.06	588.12	587.25
5	616.18	614.13	588.20	587.23
6	617.32	614.37	588.52	587.16
7	618.16	614.59	588.78	587.12
8	618.87	614.76	589.00	587.08
9	619.49	614.91	589.18	587.04
10	621.98	615.44	589.89	586.87
100	625.43	616.26	590.91	586.67
200	630.23	617.39	592.33	586.40
300	633.80	618.32	593.44	586.22
400	636.75	619.05	594.34	586.06
500	639.28	619.67	595.11	585.90
1000	649.23	621.79	597.93	585.23
2000	662.54	624.95	601.89	584.45
3000	672.18	627.47	604.92	583.96
4000	679.87	629.41	607.31	583.52

In summary, the presented heat transfer models have shown the significance of oxidation on the temperature change across the heat exchanger tube as function of time. It was demonstrated that with the oxide growth and the metal loss of the tube the heat transfer across the tube drops and thus the energy efficiency decreases; Considering tube temperature increase this could possibly lead to expensive and problematic failures of the boiler's tubing. The

models presented do not include spallation of the scales formed, which is in agreement with the results of the tests performed on T23. However for the heat transfer modelling of the more advanced materials oxide scale exfoliation has to be considered, due to its implication on the overall heat transfer across the tube. The data obtained with the designed models confirmed that the temperature of the material from the steam side is significantly higher than the actual steam temperature. Therefore, to predict steam oxidation in real power plant conditions, heat transfer has to be incorporated into the model.

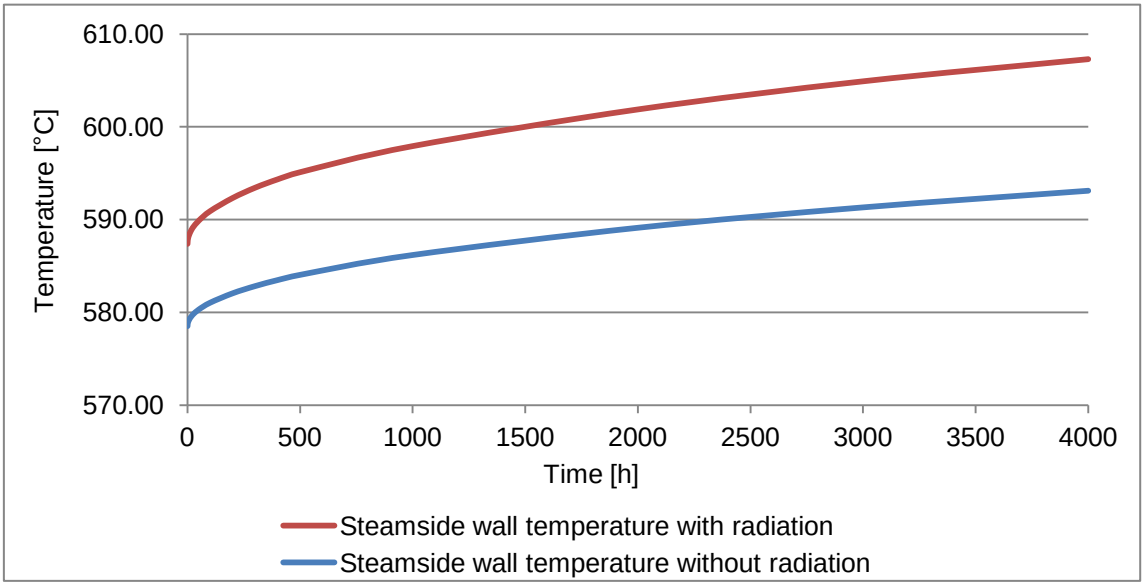

Figure 5-45 Comparison of the change of the steam side metal surface temperature with time for heat transfer model with and without radiant heat transfer

Figure 5-45 shows how the metal temperature from the steam side when radiation heat transfer is included in the heat transfer modelling. The heat transfer model without radiation shows that the temperature at the metal/oxide interface increase more slowly than in case of the model that includes combustion gas side radiation heat transfer.

6 CONCLUSIONS

6.1 Introduction

Isothermal oxidation tests in 100% steam at atmospheric pressure have been carried out at four temperatures 600, 650, 700, 750°C and three steam flow rates 4, 16, 40 mm/s, for up to 1000 hours exposure. The effects of time, temperature, alloy type and composition, steam flow rate, orientation relatively to steam flow, specimen geometry and surface finish have been investigated. Additionally, the mechanisms of steam oxidation have been studied in order to improve understanding of the species controlling the steam oxidation processes. Based on the results of tests conducted a series of conclusions have been derived. For better transparency, this conclusions chapter has been broken into seven sections presenting conclusions for each alloy investigated separately. In addition, the main conclusions are summarised in a general conclusions section.

6.2 General conclusions

- Steam oxidation of heat exchanger alloys is clearly temperature dependent, but its significance varies with alloy type and chromium content:
    - For ferritic steels the impact of chromium content is less significant up to 650°C, the oxidation of T23 (2.25Cr) and T92 (9Cr) does not differ up to 650°C with low steam flow rate, above 650°C the steam oxidation of T23 accelerates;
    - Oxidation of austenitic steels varies with temperature; up to 700°C the oxidation rate is slow, it increases above 700°C and during exposures to faster steam flow rate; and
    - 800H and Inconel 740 show very slow oxidation in the whole temperature range studied.
- Steam oxidation varies with alloy content:
    - Chromium is believed to have the largest impact on slowing down the steam oxidation;

    - For ferritic steels the chromium impact does not show up to 650°C exposure;
    - Austenitic steels with 18 % chromium content show relatively slow oxidation due to formation of the protective oxides; and
- Steam oxidation of austenitic steels varies significantly with specimen surface finish:
    - Ground specimens show the slowest oxidation, due to fast formation of the continues layer of the protective oxides; formation of the protective oxides is enhanced due to relatively deep dislocation-zone in which chromium diffusion is much faster therefore the protective oxides forming faster than for polished or as-received specimens;
    - Polished specimens show faster oxidation than ground specimen which is believed to be a result of the slower diffusion of chromium and lower adherence of the oxides forming to the specimen surface;
    - Pickled specimens (as received) show the fastest oxidation and formation of less protective iron oxides;
- Steam oxidation accelerates with increase in steam flow rate, which could be a result of:
    - Higher partial pressure of oxygen;
    - Faster adsorption process at the beginning of the oxidation process due to fact that adsorption is dependent on the pressure of adsorbate;
    - Faster gas flow rate sweeps away hydrogen from the material surface;
    - Faster diffusion hydroxides to inner layer, where it decomposes the protective spinel and triggers faster outward diffusion of metal; and
    - Volatilisation of the chromium-rich scales as volatile chromium oxy-hydroxides.

- Geometry does have an impact on steam oxidation of ferritic and austenitic steels; however it is less significant than impact of temperature or steam flow rates;
- Steam oxidation is driven by inner diffusion of oxygen, hydrogen and hydroxides ions and outward diffusion of atoms from the metal and ions form the oxide scales;
- Based on the tests conducted the following ranking of the high temperature resistant materials has been proposed for steam oxidation (best to worst): Inconel 740, 800H, HR3C, Super 304H, T347HFG, T92, T23:
    - Ferritic T23 and T92 should not be used above 600 and 650°C respectively;
    - Austenitic steels show good resistance at all temperature tested, however their application are limited due to their lower creep resistance;
    - Inconel 740 are the best candidates for the USC power plant applications.

6.3 Conclusions for T23

- Steam oxidation of T23 ferritic steel clearly increases with temperature;
- Steam oxidation rate dependence varies with exposure conditions:
    - Up to 650°C the oxidation shows parabolic/sub-parabolic rate dependence but above 650°C the rate dependence changes to sub-linear/linear;
- Steam oxidation of T23 differs with steam flow rate; for slow steam flow the oxidation follows a sub-parabolic rate law, whereas at higher gas velocities it has a more linear rate dependence;
- Type of the scales formed on T23 change with exposure conditions:
    - Up to 700°C with low steam flow rate the scales are triple-layered with haematite, magnetite and low chromium (Fe, Cr) spinel as outermost, outer and inner layers respectively;

- Above 700°C the inner layer of the scales formed becomes micro-layered with repeating, parallel layers of magnetite and (Fe, Cr) spinel; this could be developed as a result of due to wustite and chromium oxide formation, with the FeO decomposing during cooling to Fe_3O_4 and iron after longer exposures;

- Oxide types change also with steam flow rate; the inner layer became micro-layered (as also found at high temperatures). The formation of such scales are explained as a result of accumulation of hydrogen within spinel.
- Steam oxidation of T23 is influenced by specimen geometry, however its impact is less pronounced than temperature and steam flow. The specimen shape influences the process due to more extensive spallation of the scales forming on geometries that are more complex;
- More voids forming within the scale facing the direct steam flow, which is believed to be result of faster inward diffusion of hydroxides, which are transported into the voids and influence formation of volatile iron oxides.

6.4 Conclusions for T92

- Steam oxidation of T92 varies with temperatures, the oxidation rate dependence of T92 varies with temperature:
    - Up to 700°C with low steam flow rates shows a parabolic rate dependence, but this switches to sub-parabolic above 700°C;
- Faster steam flow rates drive a change in oxidation rate dependence; in case of high steam flow the oxidation of T92 follows more closely sub-linear/linear, whereas for specimens exposed to medium steam flow rate dependence is believed to be sub-parabolic;
- Scale morphology changes with tests conditions. Specimens exposed to slow steam flow rates are double/triple layered with magnetite, (Cr, Fe) spinel and additional mixed, chromium-rich oxide next to the alloy surface. Specimens exposed to faster steam flow rate do develop an additional haematite layer on the surface of magnetite, however there is no chromium-rich oxides identified next to the alloys surface;

- Specimens exposed to faster steam flow rates show extensive spallation due to large difference in the coefficients of thermal expansion (CTE) between inner ((Fe, Cr) spinel) and outer (haematite + magnetite) layers. It could be also result of the cracks and void within the scale or at the interface between inner/outer layers which could lead to scale exfoliation.

6.5 Conclusions for T347HFG

- T347HFG show good oxidation resistance at all temperature and conditions tested, steam oxidation varies with temperature, however due to extensive spallation there were not enough data to tell the oxidation rates;
- Faster steam, flow increase the oxidation rate;
- Scale morphology of the ground specimens changed with exposure conditions:
    - The oxide scale became more protective, more adherent and continuous with higher temperatures and faster steam flow rates;
    - After longer exposure nodules start to grow, these nodules become larger and spread more evenly along the material surface;
    - Nodule grow faster with steam flow rate, they become larger and are more evenly distributes at the surface;
- Scale morphology of polished and pickled (as-received) specimens changes with exposure temperatures:
    - With change of the temperature there is more nodule forming on the polished specimen;
    - The thickness of the oxides formed on pickled specimens increases with exposure temperature, moreover the oxides became less protective.

6.6 Conclusions for Super 304H

- Steam oxidation of Super 304H varies with temperature;
- In general, the steam oxidation accelerates with steam flow rate, which is result of either higher surface concentration of oxidising species (oxygen, hydroxides) or faster volatilisation of the protective oxides or reduction in reducing species (hydrogen);
- Oxide scale developed on ground specimens changes with exposures conditions:
    - At higher temperature double-layered nodules form as most probably the result of result of faster oxidation there can be a local breakdown of the scales and formation of double-layered nodules; and
    - On specimens exposed to faster steam flow rate the breakdown of the scale is more extensive and therefore more nodules form, which are spread evenly along the surface. The breakdown of the protective scales could be explained as a result of protective scale volatilisation, insufficient level of chromium within the material to continue the growth of the adherent, continues and protective oxides or not enough flux of chromium to the material surface.
- Scale morphology of polished and as-received (pickled) specimens varies with exposure temperatures:
    - Polish specimens show spalation of the protective oxides at higher temperature;
    - Pickled (as received) specimens develop thicker oxides on the surface with change of the exposure temperature, which could be explained due to faster diffusion of oxygen and metal ions.

6.7 Conclusions for HR3C

- Oxidation rate is slow at all temperatures studied which is explained due to high content of chromium which enables fast formation of the protective chromium oxides on the specimen surface;
- HR3C exposed to faster steam flows does not indicate so significant changes in oxidation as identified for other austenitic steels. This could be the result of very protective scales forming on the surfaces, which effectively suppress nodule formation;
- The scale morphologies formed on ground specimens do not change significantly with temperature and steam conditions, the scales are protective and do not tend to exfoliate even after 1000 hours exposures.

6.8 Conclusions for 800H

- 800H shows very good oxidation resistance. In the temperature range tested this alloy show very slow mass change therefore the oxidation rate dependence of this alloy cannot be identified;
- 800H does not show significant morphological changes at the temperatures investigated. It forms relatively thin, protective scales of mixed nickel, iron chromium oxides:
    - There is no nodule growth, even at 750°C the surface is nodule free. This could be explained as a result of the high chromium content of this alloy which enables formation of protective oxides, which effectively suppress nodular growth of the scale;
- Scale morphology of 800H does not change with steam flow rate.

6.9 Conclusions for Inconel 740

- Inconel 740 is the most steam oxidation resistant of the materials tested;
- It shows a slow change in steam oxidation rate with exposure temperate in range 600 - 750°C; moreover the steam flow rate has a limited effect on the steam oxidation of this alloy. There is not significant increase in mass change with exposure to faster steam flow rate;
- Oxide morphology changes with exposure conditions:

- There is no nodular growth identified with exception at 750°C when one nodule has developed after 1000 hours exposure, the high concentration of nickel and chromium enables formation of the protective oxides which are believed to suppress less protective oxide growth;
- Steam flow rate does not have a clear impact on the oxidation of Inconel 740, there have not been a significant change in either oxidation kinetics or morphology with change from slow to faster steam flow rate conditions.

7 RECOMMENDATION

Based on the conclusions of the research carried out, a number of recommendations are proposed:

- Continue research with different steam flow rates, preferably similar to power plant exposures;
- Tests should be performed for longer exposure times (2000-10000 hours), especially in case of austenitic and nickel-based alloys; however, in the first 500 hours exposure the specimens should be analysed in shorter cycles (preferably 25-50 hours);
- Tests should be also conducted at higher pressures (>10 bar);
- Investigation of the ionic diffusion should be continue with FIB-SIMS in order to understand in more detail the impact and role of different ions on steam oxidation:
    - More tests should be performed in steam generated from oxygen 18 doped water, such tests have to be conducted at different temperatures and different steam flow rates;
    - Tests in steam generated from heavy water should be considered, this could allow identification of an impact of hydrogen on steam oxidation.
- Standardisation of the specimen geometry, which could allow easier comparison of results between different research organisations;
- Standardisation of test procedures, which would include guidance for specimen surface preparation, surface cleaning, steam generation method (if internal or external), testing procedures; steam flow and post-exposure specimen preparations.

REFERENCES

1. Rossa, S. "Sustainable development handbook". Lilbum : The Fairmont Press, 2008.

2. Boyle G, Everett B, Ramage J. "Energy Systems and Sustainability". Oxford : Oxford University Press, 2003. 0 19 926179 2 .

3. US Energy Information Administration. US Energy Information Administration.International Energy Outlook 2010. [Online] US Energy Information Administration, 2010. [Cited: 10 03 2011.] http://www.eia.doe.gov/oiaf/ieo/world.html.

4. Sangster, A. Energy for a Warming World; "A Plan to Hasten the Demise of Fossil Fuels". 2010 : Springer, London. 978-1-84882-833-9.

5. Breeze, P. Power Generation Technologies. London : Elsevier, 2005.

6. Babcock & Wilcox. "Developments in Pulverized Coal-Fired Boiler Technology" . 1996.

7. Nag, P. "Power Plant Engineering". New Delphi : Tata McGraw-Hill, 2008.

8. Dorf, R. "Coal Energy Systems". San Diego : Elsevier Academic Press, 2005. 0 12 497451 1.

9. Lindsley, D. "Power-plant control and instrumentation The control of boilers and HRSG systems". London : The Institution of Electrical Engineers, 2005. 0 85296 765 9.

10. Muller, I., Muller, W. "Fundamentals of thermodynamics and applications: with historical annotations and many citations from Avogadro to Zermelo". Berlin : Springer, 2009.

11. Wright, I., Maziasz, P., Ellis, F., Gibbons, T., Woodford, D. "Materials Issues for turbines for operation in ultra-supercritical steam" Clearwater : s.n., 2004. 29th International Technical Conference on Coal Utilization and fuel systems.

12. Massoud, M. "Engineering thermofluids: thermodynamic, fluid mechanics and heat tranfer". Berlin : Springer, 2005.

13. Burmeister & Wain Energy A/S. "Experiences with Coal fired USC Boilers". Burmeister & Wain Energy A/S. [Online] 2003. [Cited: 10 03 2011.] http://www.bwe.dk/pdf/art-pge2003.pdf.

14. Buggea, J., Kjæra S., Blum, R. "High-efficiency coal-fired power plants development". Energy. 2006.

15. Viswanathan R., Sarver, J., Tanzosh, J. "Boiler Materials for Ultra-Supercritical Coal Power Plants - Steamside Oxidation". 2005, Journal of Materials Engineering and Performance, pp. 255-263.

16. Viswanathan, R., Purgert, R., Rao, U. "Materials technology for advance coal power plants". s.l. : EPRI, 2002.

17. Viswanathan, R.,. Bakker, W. "Materials for Boilers in Ultra Supercritical Power Plants". Miami Beach : ASME, 2000. 2000 International Joint Power Conference. pp. 2-22.

18. Ennis, P., Quadakkers, W. "Implications of steam oxidation for service life of the high-strenght martensitic steel components in high-temperature plant". 2007a, International Journal of Pressure Vessels and Piping.

19. Wright, I., Pint, B. "An assessment of the high-temperature oxidation behaviour of Fe-Cr steels in water vapour and steam". Denver : s.n., 2002. NACE CORROSION/2002.

20. Ehlers, J., Young, D., Smaardijk, E., Tyagi, A., Penkalla, H., Singheise,r L., Quadakkers, W. 2006 "Enhanced oxidation of the 9% Cr steel P91 in water vapour containing environments"., Corrosion Science, pp. 3428-3454.

21. Maziasz, P., Wright, I., Shingeldecker, J., Gibbons, T., Romanosky, R. "Defining the Materials Issues and Research for Ultra-Supercritical Steam

Turbines". 2005. 4th International Conference on Advance Materials Technology for fossil Power Plants . pp. 602-620.

22 Laverde, D., Gomez-Acebo, T., Castro, F. "Contnuous and cyclic oxidation of T91 ferritic steel under steam". 2004, Corrosion Science, pp. 613-631.

23. Electric Power Research Institute. "Program on Technology Innovation: Oxide Growth and Exfoliation on Alloys Exposed to Steam". Palo Alto : EPRI, 2007.

24. Wright, I., Dooley, R. "A review of the oxidation behaviour of structureal alloys in steam". International Materials Reviews. 2010, Vol. 55.

25. Lee, N., Kim, S., Cheo, B., Yoon, K., Kwon, D. "Failure analysis of a boiler tube in USC coal power plant" 2009, Engineering failure analysis, pp. 2031 - 2035.

26. Nishimura, N., Komai, N., Hirayama, Y., Masuyama, F. "Japanese experience with steam oxidation of advanced heat-resistant steel tubes in power boilers". 2005, Materials at high temperatures, pp. 3-10.

27. N Komai, F Masuyama, M Igarashi. "10-year experience with T23 (2.25Cr-1.6W) and T122 (12Cr-0.4Mo-2W) in a Power Boiler". 2005, Journal of Pressure Vessel Technology, pp. 190-197.

28. Fry, T., Osgerby, S., Wright, I. "Oxidation of Alloys in Steam Environments - A Review". Teddington : National Physical Laboratory , 2002.

29. Sarver, J., Tanzosh, J. "Steam oxidation testing of candidate Ultrasupercritical boiler materials. Clearwater : s.n., 2003. 28th International Technical Conference on Coal Utilization and Fuel Systems .

30. Saunders, S., Monteiro, M., Rizzo, F. "The oxidation behaviour of metals and alloys at high temperatures in atmospheres containing water vapour: A review". 2008, Progress in Materials Science , pp. 775-837.

31. World Energy Conference. World Energy Resources. Guildford : IPC Science and Technology press, 1978. 0 902852 90 6.

32. Spliethoff, H. "Power Generation". Berlin : Springer, 2010.

33. Flynn, D. "Thermal Power Plant, Simulation and Control". London : The Institution of Electrical Engineers, 2003. 0 85296 419 6.

34. Winkle, P. "Power Generation Retrofitting, Optimizing Power Plant Performance". London : Professional Engineering Publishing, 2002. 1 86058 392.

35. Strauß, K. "Kraftwerkstechnik: Zur Nutzung fossiler, nuklearer und regenerativer". Berlin : Springer, 2006.

36. Kitto, J., Stultz, S. "Steam in generation and use". Barberton : The Babcock & Wilcox Company, 2005.

37. Yuchun, C., Xinli, W., Jinxin, W., Baodong, W., Yan, L. "Development of Ultra-supercritical Power Plant in China".

38. Goidich, S., Wu, S., Fan, Z. Bose, A. Design Aspects of the Ultra-Supercritical CFB Boiler. Foster Wheeler. [Online] 2005. [Cited: 21 3 2011.] http://www.fwc.com/publications/tech_papers/files/TP_CFB_05_02.pdf.

39. Janna, W. "Engineering heat transfer" . Boca Raton : CRS Press, 2009.

40. Kreith, F, Bohn, M. "Principles of Heat Trasfer". Pacific Grove : Brooks/Cole, 2001. 0 534 37596 0.

41. Y, Cengel. "Heat Transfer Practical Approach". New York : McGraw-Hill Companies Inc., 2003. 0 07 245893 3.

42. Incropera, F., DeWitt, D. "Introduction to heat transfer". New York : John Wiley, 1996.

43. Rolle, K. "Thermodynamics and Heat transfer". Columbus : Merrill Publishing Company, 1989. 0 675 21016 X.

44. Purbolaksono, J., Khinami, A., Rashid, A., Ali, A., Nordin, N. "Prediction of oxide scale growth in superheater and reheater tubes". Corrosion Science. 2009.

45. Pronobis, M., Wojnar, W. "The rate of corrosive wera in superheaters of boilers for supercritical parameters of steam". Engineering Failure Analysis. 2011, Vol. 19.

46. Callister, W. "Materials science and engineering : an introduction". Sydney : Wiley, 2006.

47. Ashby, M., Schercliff, H., Cebon, D. "Materials Engineering, Science, Processing and Design". Oxford : Butterwirth-Heinemann, 2007. 07506-8391-0.

48. Lemaitre, J., Desmorat, R. "Engineering Damage Mechanics Ductile, Creep, Fatigue and Brittle Failures". Berlin : Springer, 2005. 3 540 21503 4.

49. Hansson, A., Montgomery, M. "Steam Oxidation of TP 347H FG in Power Plants". 2006, Materials Science Forum, pp. 181-188.

50. Betten, J. "Creep Mechanics". Berlin : Springer, 2008. 978 3 540 85050 2.

51. Ashby, M. "Materials Selection in Mechanical Design". Oxford : Butterworth-Heinemann, 2005. 0 7506 6168 2.

52. Holcomb, C., Cramer, S.,. Covino, B., Ziomek-Moroz. M. "Ultra Supercritical Steamside oxidation". 2005. 4th International Conference on Advance Materials Technology for Fossil Power Plant. pp. 451-462.

53. Ennis, P., Quadakkers, W. "Mechanisms of steam oxidation in high strenght martensitic steels". 2007b, International Journal of Pressure Vessels and Piping, pp. 75-81.

54. Song, Ki., Cho, Tong., Yoon, Jae., Lee, Chan., Shin, Kee., Lee, Seon., Urm, Kee., Lee, Jong., Kim, In. "Steam Oxidation and Surface Hardness of Power Plant Valve Materials Under the Ultra Supercritical Steam Conditions". 2008, Metals and Materials International, pp. 721-727.

55. Essuman, E., Meier, G., Zurek, J., Hansel, M., Quadakkers, W. "The effect of water vapour on selective oxidation of Fe - Cr alloys". 2008, Oxidation of Metal , pp. 143 - 162.

56. Shibili, A., Starr, F. "Some aspects of plant and reserch experience in the use of new high strength martensitic steel P91". Pressure Vessels and Piping. 2007, Vol. 84, pp. 114-122.

57. Khanna, A. "Introduction to high temperature oxidation and corrosion". s.l. : ASM International , 2002.

58. Young, D. "High Temperature Oxidation and Corrosion of Metals". Amsterdam : Elsevier, 2008.

59. Kofstad, Per. "High-temperature oxidation of metals" . s.l. : Wiley, 1966.

60. Birks, N., Meier, G., Pettit, F. "Introduction to the high-temperature oxidation of metals". London : Cambridge University Press, 2006.

61. Machlin, E. "An Introduction to Aspects of Thermodynamics and Kinetics Relevant to Materials Science". s.l. : Elsevier Science Ltd, 2007.

62. Glicksman, M. "Diffusion in solids Field theory, solid-state principles and applications". Torronto : John Wiley & Sons, Inc., 2000.

63. Gaskell, D. "Introduction to the thermodynamics of materials". London : Taylor & Francis, 2008.

64. Huntz, A., Bague, V., Beauple, G., Haut, C., Severac, C., Lecour, P., Longaygue,. X, Ropital, F. "Effect of Silicon on the oxidation of 9% Cr steels". 2003, Applied Surface Science, pp. 255 - 275 .

65. Ennis, P., Quadakkers, W. "High chromium martensitic steels-Microstructure, properties and potential for further development". 2001, VGB PowerTech, pp. 87 - 90 .

66. Sanchez, L., Hierro, M., Perez, F. "Effect of Chromium Content on the Oxidation Behaviour of Ferritic Steels for Applications in steam atmospheres at high temperatures". 2009, Oxidation of Metal , pp. 173 - 186 .

67. Zurek, J., Wessel, E., Niewolak, L., Schmitz, F., Kern, T., Singheiser, L., Quadakkers, W. "Anomalous temperature dependence of oxidation kinetics during steam oxidation of ferritic steels in the temperature range 550 - 650 C" 2004, Corrosion Science , pp. 2301-2317.

68. Moore, J. "Chemical Metallurgy". London : Butterworth & Co Ltd, 1981.

69. University of Cambridge. DoITPoMS Teaching and Learning Packages. University of Cambridge. [Online] 2009. [Cited: 15 09 2009.] http://www.doitpoms.ac.uk/tlplib/ellingham_diagrams/ellingham.php.

70. Inglezakis, V., Poulopoulos, S. "Adsorption, Ion Exchange and Catalysis Design of operations and Environmental Applications". Amsterdam : Elsevier, 2006.

71. Hosford, W. "Material Science an intermediate text". New York : Cambridge University Press, 2007. 978 0 521 86705 4.

72. Osgerby, S., Fry, T. "Simulating Steam Oxidation of high temperature plant under laboratory conditions: Practice and interpretation of data". s.l. : Ma, 2004, Materials Research , pp. 141 - 145 .

73. Fukuda, Y. "Development of Advance Ultra Supercritical Fossil Power Plants in Japan: Materials and High Temperature Corrosion Properties". Materials Science Forum. 2011, Vol. 696.

74. Saunders, S., McCartney, L. "Current Understanding of steam oxidation - Power plant and laboratory experience". Materials Science Forum. 2006.

75. Perez, F., Castaneda, S. "Study of oxyhydroxides formation on P91 ferritic steel and slurry coated by Al in contact with Ar+80%H2O at 650 °C by TG-Mass spectrometry". Surface & Coatings Technology. 2007, Vol. 201.

76. Asteman, H., Svensson, J., Johansson, L. "Evidence for Chromium Evaporation Influencing the Oxidation of 304L: The Effect of Temperature and flow rate". Oxidation of Metals. 2002, Vol. 57.

77. Holcomb, G. "Steam Oxidation and Chromia Evaporation in Ultrasupercritical Steam Boilers and Turbines". Journal of the Electrochemical Society. 2009, Vol. 156.

78. Holcomb, G. "Calculation of Reactive-evaporation Rates of Chromia". Oxidation of metals. 2008, Vol. 69.

79. Osgerby, S., Quadakkers, J. "The influence of the laboratory test procedures on the scale growth kinetics and microstructurure during steam oxidation testing". Materials at high temperatures. 2005.

80. Ennis, P., Quadakkers, W. "Mechanisms of steam oxidation in high strenght martensitic steels". 2007b, International Journal of Pressure Vessels and Piping, pp. 75-81.

81. Khanna, A., Rodrigues, P., Gnanamoorthy, J. "Oxidation kinetics, breakaway oxidation and inversion phenomenon in 9Cr-1Mo steels". Oxidation of metals . 1986, Vol. 26, pp. 171 - 200.

82. Lepingle, V., Louis, G., Petelot, D., Lefevre, B., Vandenberghe, B. "Steam corrosion resistance of new 12% Cr ferritic boiler steels". Materials Science Forum. 2004.

83. Cory, N., Herrington, T. "Kinetics of oxidation of ferrous alloys by superheated steam". Oxidation of metals. 1987, Vol. 28.

84. Nakagawa, K., Matsunaga, Y. and Yanagisawa, T. "Corrosion behaviour of ferritic steels on air sides of boiler tube ins steam/air dual environmen"t. Materials at high temperatures. 2003, Vol. 20.

85. Tomlinson, L., Cory, N. "Hydrogen emission during the steam oxidation of ferritic steels, kinetics and mechanism". Corrosion Science. 1989.

86. Matsuo, H., Nishiyama, Y., Yamadera, Y. "Steam oxidation property of Fine-grain steels". Hilton Head Island : ASM International , 2005. 0-87170-818-3.

87. Hansson, A., Montgomery, M., Somers, M. "Development of the inner oxide zone upon oxidation of an austenitic stainless steel". Materials at high temperatures. 2009.

88. Jianmin, J., Montgomery, M., Larsen, O., Jensen, "A. Invastigation on stema oxidation behaviour of TP347HFG Part 1: Exposure at 256bar". Materials and Corrosion. 2005a.

89. Jianmin, J., Montgomery, M., Larsen, O., Jensen, A. "Invastigation on steam oxidation of TP347HFG Part 2: Exposure at 91 bar". Materials and Corrosion. 2005b.

90. Sumida, T., Ikuno, T., Otsuka, N., Saburi, T. "High-temperature oxidation behavior of SUS321H and SUS347H boiler tubes in long-term exposure to superheated steam". Journal of Japanese Institue of Materials. 1995.

91. Montgomery, M., Larsen, O., Jensen, S., Biede, O. "Field invastigation of steamside oxidation for TP347H". Material Science Forum. 2004.

92. Wright, I., Dooley, B. "Morphologies of oxide growth and exfoliation in superheater and reheater tubing of steam boilers". Material at high temperatures. 2011, Vol. 28.

93. Hansson, A., Pantleon, K., Grumsen, F., Somers, M. "Microstructure Evolution during steam oxidation aof Nb stablilized austenitic stainless steel". Oxidation of Metals. 2009.

94. Pearl, W. Brush, E., Gaul, G., Leistikow, S. "General corosion of Inconel Alloy 625 in stimulated superheat reactor environment". Nuclear Application. 1967.

95. Stringer, J. "High temperature corrosion problems in steam boilers". 1983, The Electrochemical society , p. .

96. Quadakkers, W., Ennis, P., Zurek, J., Michalik, M. "Steam oxidation of ferritic steels - laboratory test kinetics data". 2005, Materials at High Temperatures, pp. 27-33.

97. Hierro, L., Rohr, V., Ennis, P., Schutze, M., Quadakkers, W. "Steam oxidation and its potential effects on creep strenght of power station materials". 2005, Materials and Corrosion, pp. 890 - 896.

98. Murata, Y., Minai, H., Nagai, K., Shiraki, A., Morinaga, M. "(Fe,Cr)304 spinel layer as the key solving tha accelerated oxidation of high Cr Iron alloy in high-temperature steam". ISIJ International. 2008, Vol. 48.

99. Wright, I., Tortorelli, P., Schutze, P. "Oxide growth and exfoliation on alloys exposed to steam". s.l. : EPRI, 2007. 1013666.

100. Dooley, R., Paterson, S. "Oxide growth and exfoliation in steam: plant experience". s.l. : National Physical Laboratory, 2003.

101. Young, D. "Effects of Water Vapour on the Oxidation of Chromia Formers". Materials Science Forum. 2008, Vols. 595-598.

102. Watanabe, Y., Kondo, T., Inui, K. Kishinami, T., Kimura, H., Sato, M. Sydney : s.n., 2000. Proceedings of the 9th International Conference on Pressure Vessel Technology . pp. 545 - 552.

103. Kutsumi, H., Muneki, S., Itagaki, T., Abe, F. "Steam oxidation behavior of precipitation strengthened carbon free martensitic alloys". Journal of the Japan Institute of Metals . 2002, Vol. 66, 10.

104. Huczkowski, P., Ertl, S., Piron-Abellan, J., Christiansen, N., Höfler, T., Shemet, V., Singheiser, L., Quadakkers, W.J. "Effect of component thickness on lifetime and oxidation rate of chromia forming ferritic steels in low and high pO2 environments". Materials at high temperatures. 2005, Vol. 22, 3-4.

105. Huczkowski, P., Christiansen, N., Shemet, V., Piron-Abellan, J., Singheiser, L., Quadakkers, W. "Oxidation limited life times of chromia forming ferritic steels". Materials and Corrosion. 2004, Vol. 55, 11.

106. Zurek, J., Meier G., Essuman, E., Hansel, M., Singheiser, L., Quadakkers W. "Effect of specimen thickness on the growth rate of chromia scales on Ni-base alloys in high- and low pO2 gases". Journal of Alloys and Compounds. 2009, Vol. 465, 1-2.

107. Haynes, C., Smoluchowski, R. "Grain boundary diffusion in a body-centered cubic lattice". Acta metallurgica. 1955, Vol. 3.

108. Trindade, V., Krupp, U., Hanjari, B., Yang, S., Christ, H. "Effect of alloy grain size on the high-temperature oxidation behavior of the austenitic steel TP 347". Materials Research. 2005, Vol. 8, 4.

109. Zurek, J., Michalik, M., Schmitz, F., Kern, T., Singheiser, L., Quadakkers, W. "The effect of water-vapor content and gas flow rate on the oxidation mechnisms of 10%Cr ferritic steels in Ar-H2O mixtures". Oxidation of Metals. 5/6, 2005, Vol. 63.

110. Cory, N., Herrington, T., Tomlinson, L., "Hydrogen emission during the steam oxidation of ferritic steels: experimental technique". Corrosion Science. 1988, Vol. 28.

111. Nakai, M., Nagai, K., Murata, Y., Morinaga, M. "Improvement in steam oxidation resistance of Fe -10%Cr-0.08C steel by suppressing hydrogen dissolution". 2006, pp. 3869 - 3885.

112. Guo, X., Sasaki, Y., Kashiwaya, Y., Ishii, K. "Microreaction mechanism in reduction of magnetite to wustite". Metallurgical and Materials transction B. 2004, Vol. 35B.

113. Asteman, H., Svensson, E., Norell, M., Johansson, L. "Influence of Water Vapour and Flow Rate on the High - Temperature Oxidation of 304L; Effect of

Chromium Oxide Hydroxide Evaporation". 2000, Oxidation of Metals, pp. 11 - 26.

114. Halvarsson, M., Tang, J., Asteman, H., Svensson, J., Johansson, L. "Microstructural invastigation of the breakdown of the protective oxides scale on a 304 steel in the presence of the oxygen and water vapour a 600°C". Corrosion Science. 2006, Vol. 48.

115. Rahmel, A., Toborski, J. 1965, Corrosion Science, pp. 333 - 340.

116. Danielewski, M., Wierzba, B. "Diffusion processes determining the oxidation rate of multicomponent alloys". Corrosion Science. p 1161-1168, 2008, Vol. 50, 4, pp. 1161 - 1168.

117. Mendelev, M., Zhang, H., Srolovitz, D. "Grain boundary self-diffusion in Ni: Effect of boundary inclination". Journal of Materials Research. 2005, Vol. 20, 5.

118. Suzuki, A., Mishin, Y. "Atomic mechanisms of grain boundary diffusion: Low versus high temperatures". Journal of materials science. , 2005, Vol. 40.

119. Wright, I., Schutze, M., Paterson, S., Tortorelli,. P, Dooley, R. "Progress in prediction and control of scale exfoliation on superheater and reheater alloys" San Diego : EPRI International Conference on Boiler Tube and HRSG Tube and Inspections , 2004.

120. Ganapathy, V,. "Industrial Boilers and Heat Recovery Steam Generators: Design, Applications and Calculations". New York : Marcel Dekker, 2003. 0824708148.

APPENDICES

Appendix A

A.1 OXIDATION KINETICS

A.1.1 Metal loss

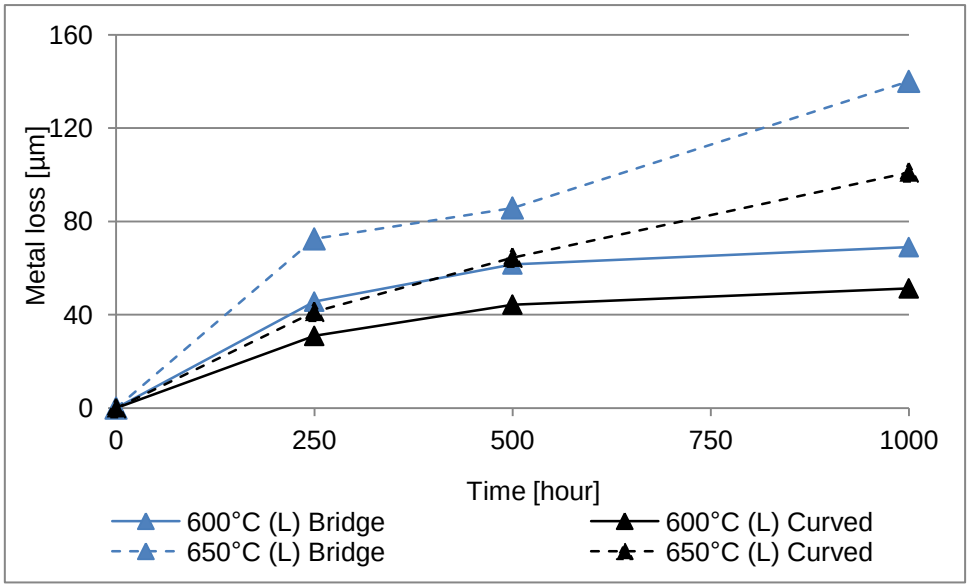

Figure A-1 Oxidation kinetics of T23 steel in the temperature between 600 - 650°C (L)

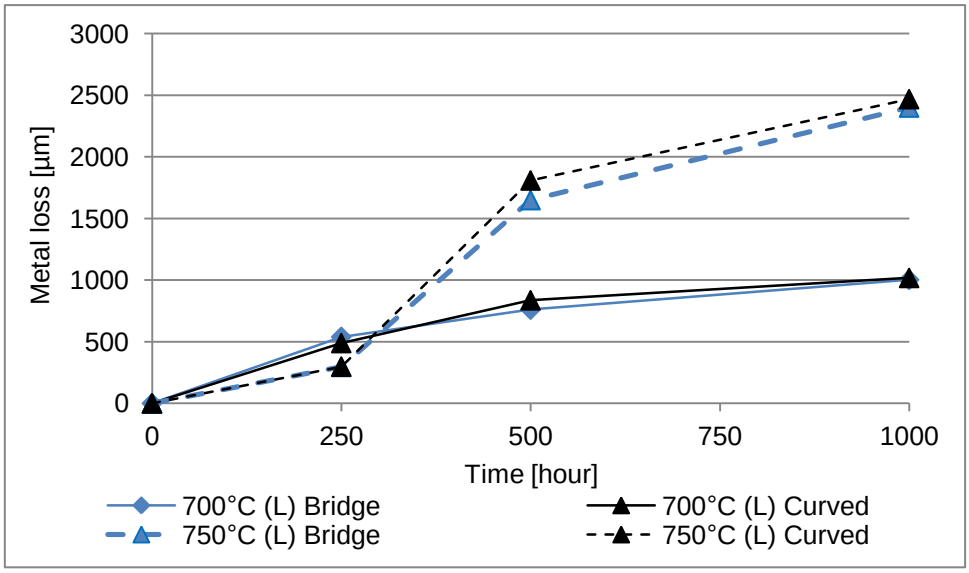

Figure A-2 Oxidation kinetics of T23 steel in the temperature between 700 - 750°C (L)

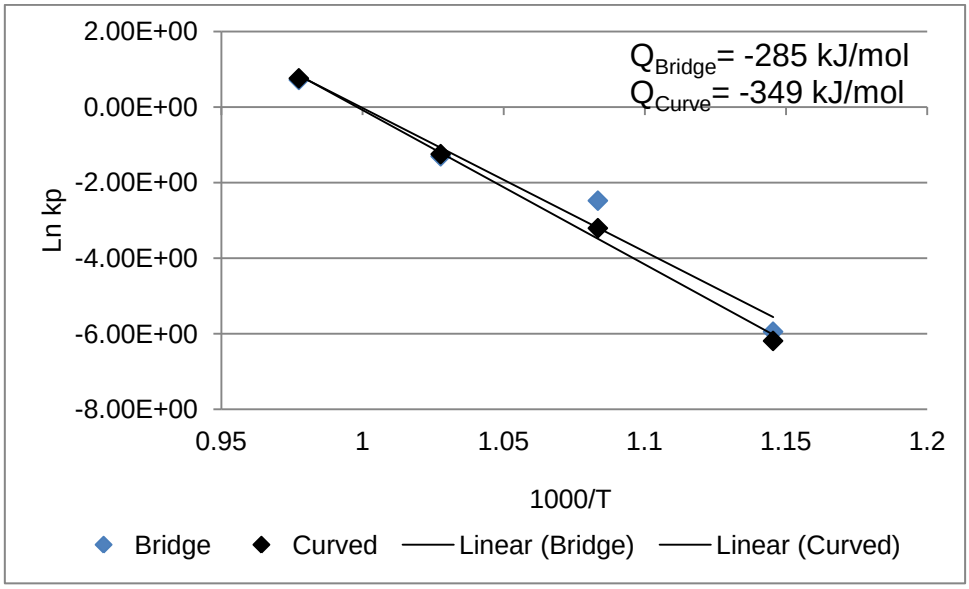

Figure A-3 Arrhenius plot for T23 steel exposed to steam in temperature between 600 – 750°C (L)

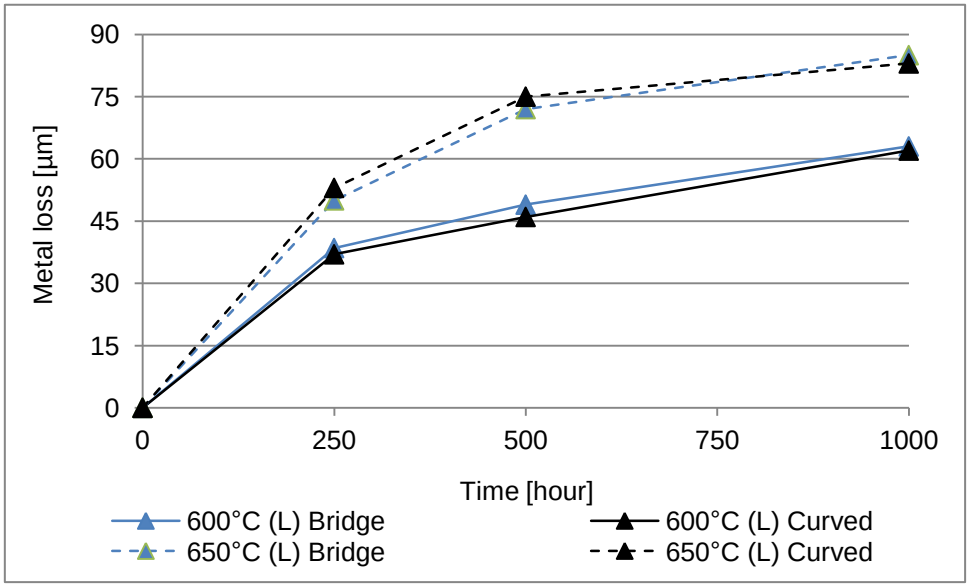

Figure A-4 Oxidation kinetics of T92 steel in the temperature between 600 - 650°C (L)

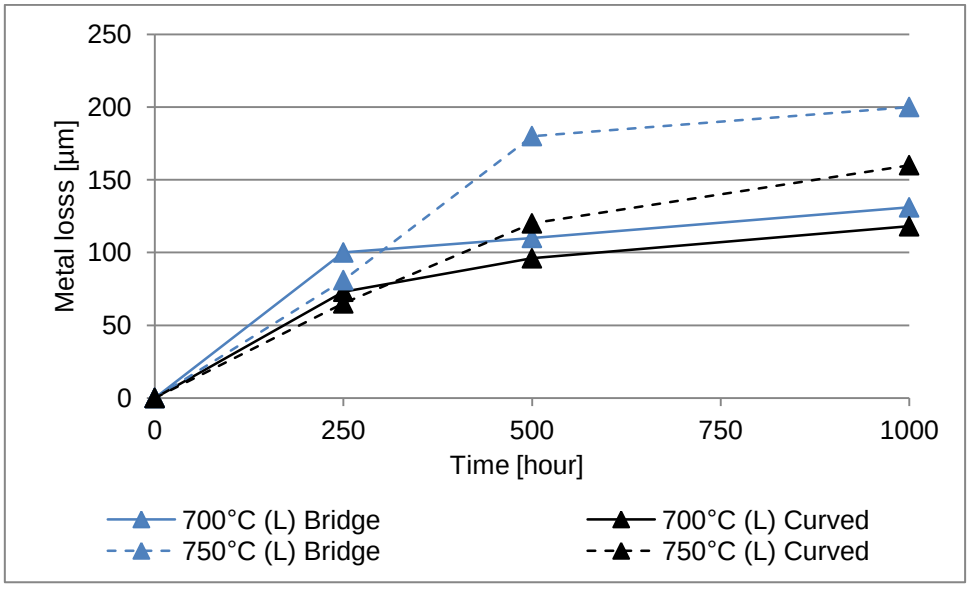

Figure A-5 Oxidation kinetics of T92 steel in the temperature between 700 - 750°C (L)

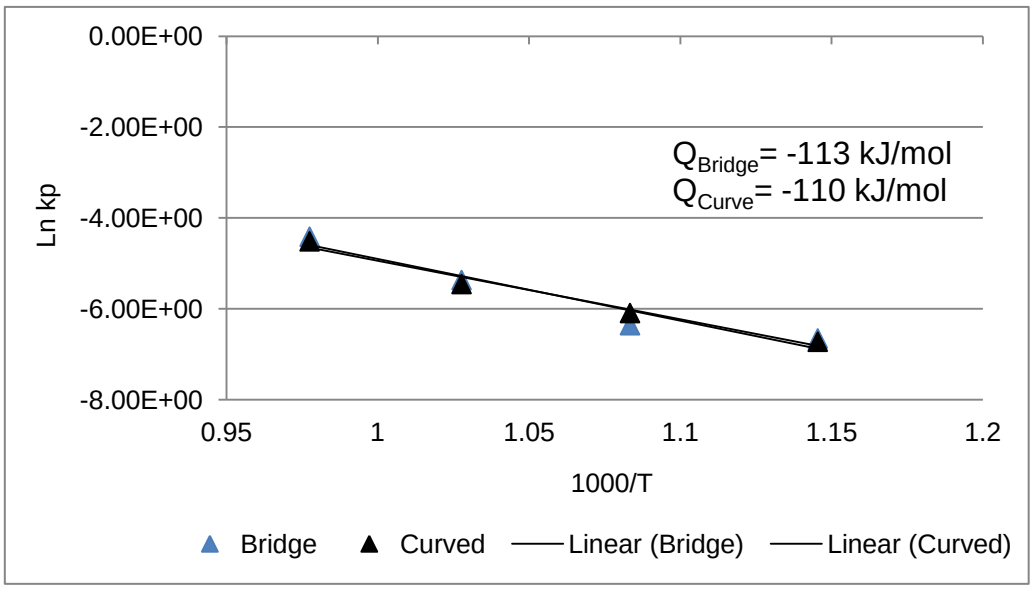

Figure A-6 Arrhenius plot for T23 steel exposed to steam in temperature between 600 – 750°C (L)

A.1.2 Thickness change

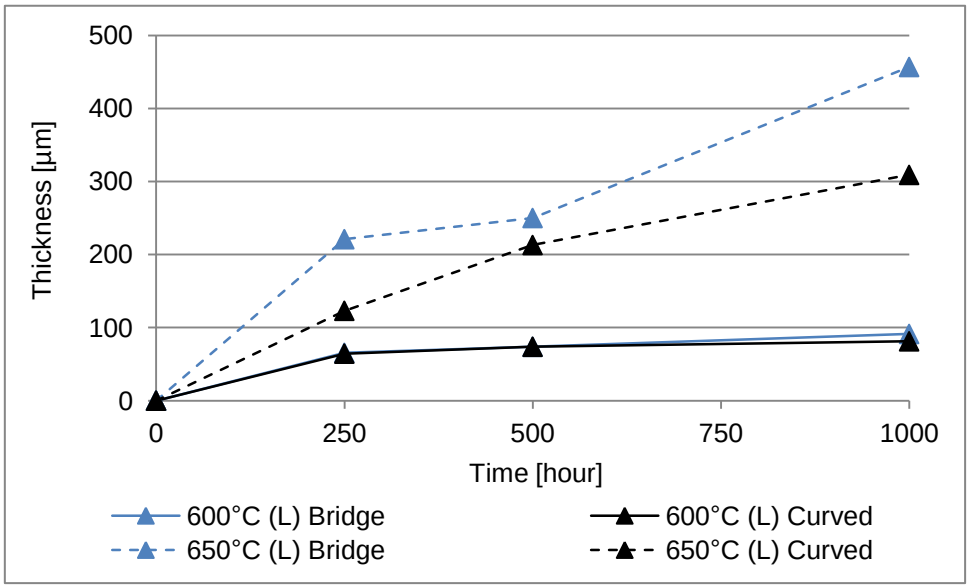

Figure A-7 Oxidation kinetics of T23steel in the temperature between 600 - 650°C (L)

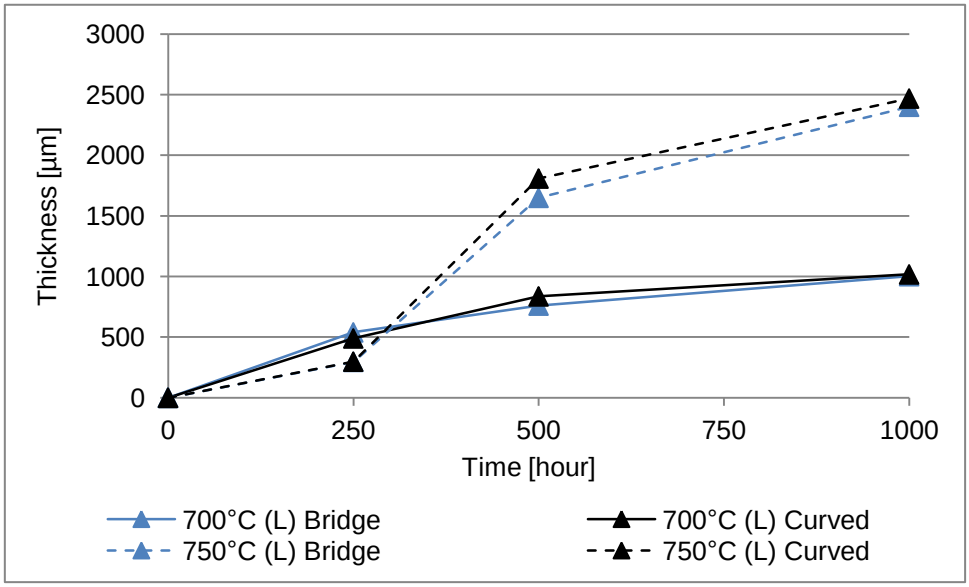

Figure A-8 Oxidation kinetics of T23 steel in the temperature between 700 - 750°C (L)

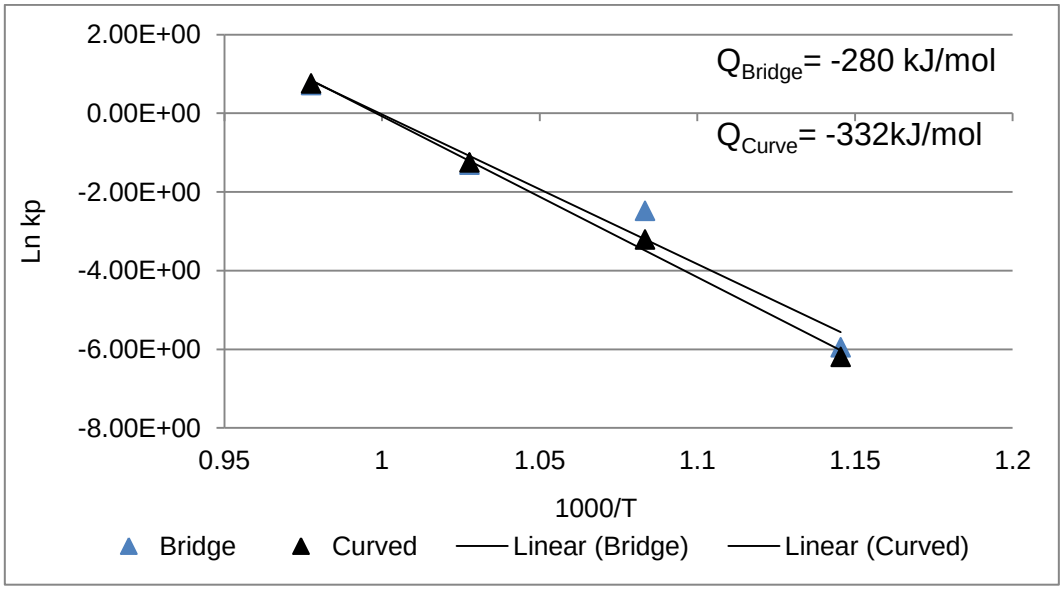

Figure A-9 Arrhenius plot for T23 steel exposed to steam in temperature between 600 – 750°C (L)

A.2 APPENDIX SCALES MORPHOLOGY

A.2.1 Oxides scales morphology formed on T23

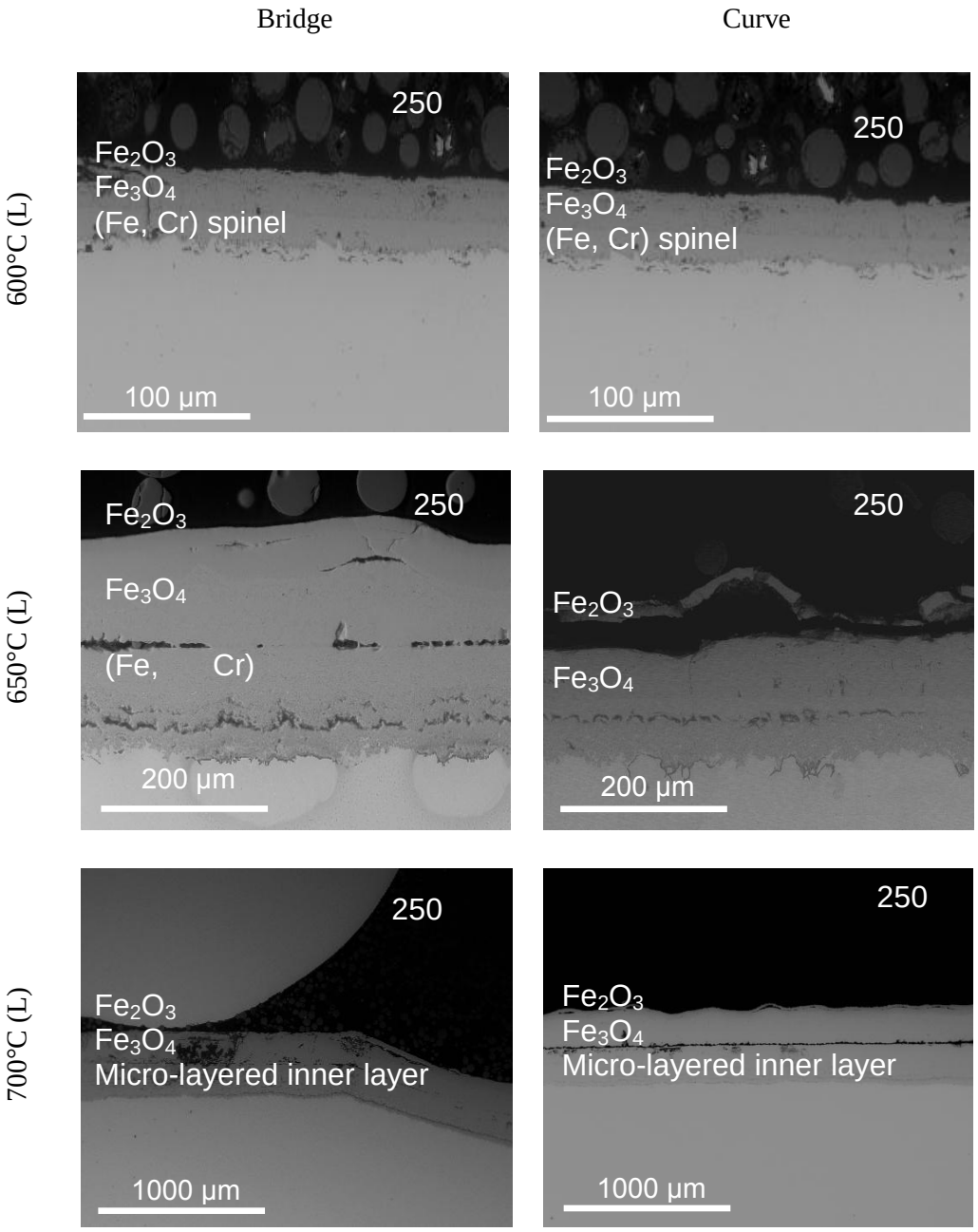

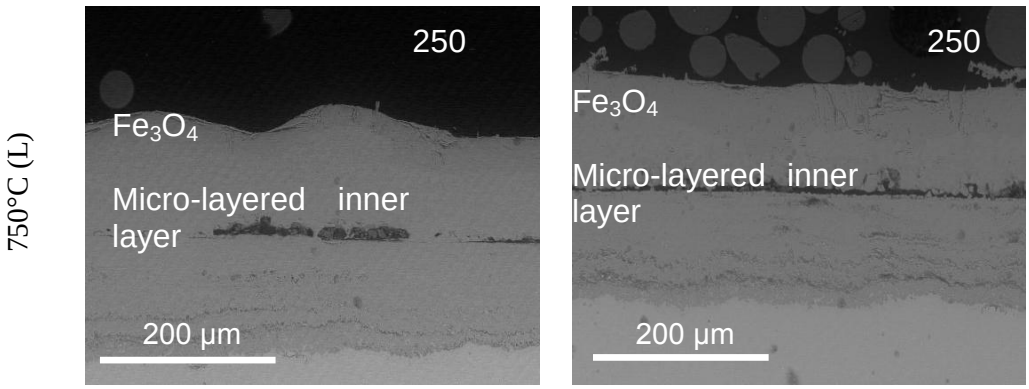

Figure A-10 BSE SEM pictures of the scales developed on T23 exposed to steam in temperature between 600 – 750°C (L) after 250 hour exposure

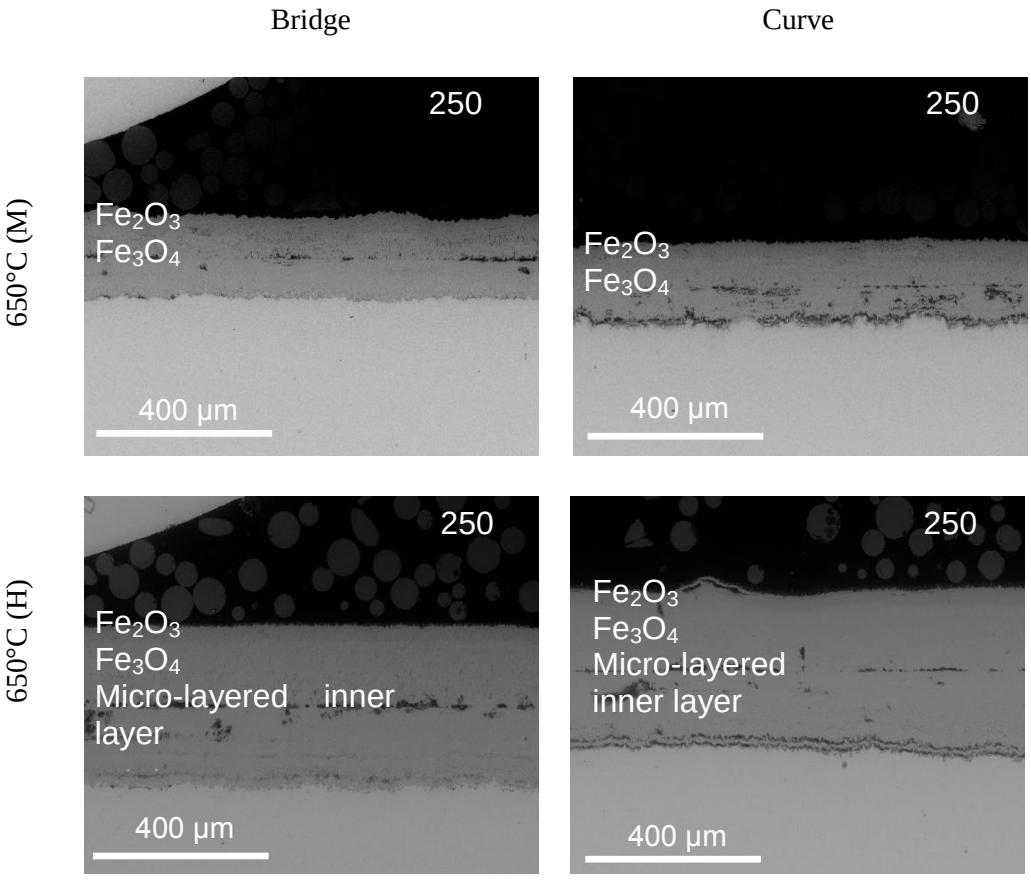

Figure A-11 BSE SeM pictures of the scales developed on T23 exposed to steam at 650°C with Medium (M) and Fast (F) steam flow rates after 250 hour exposure

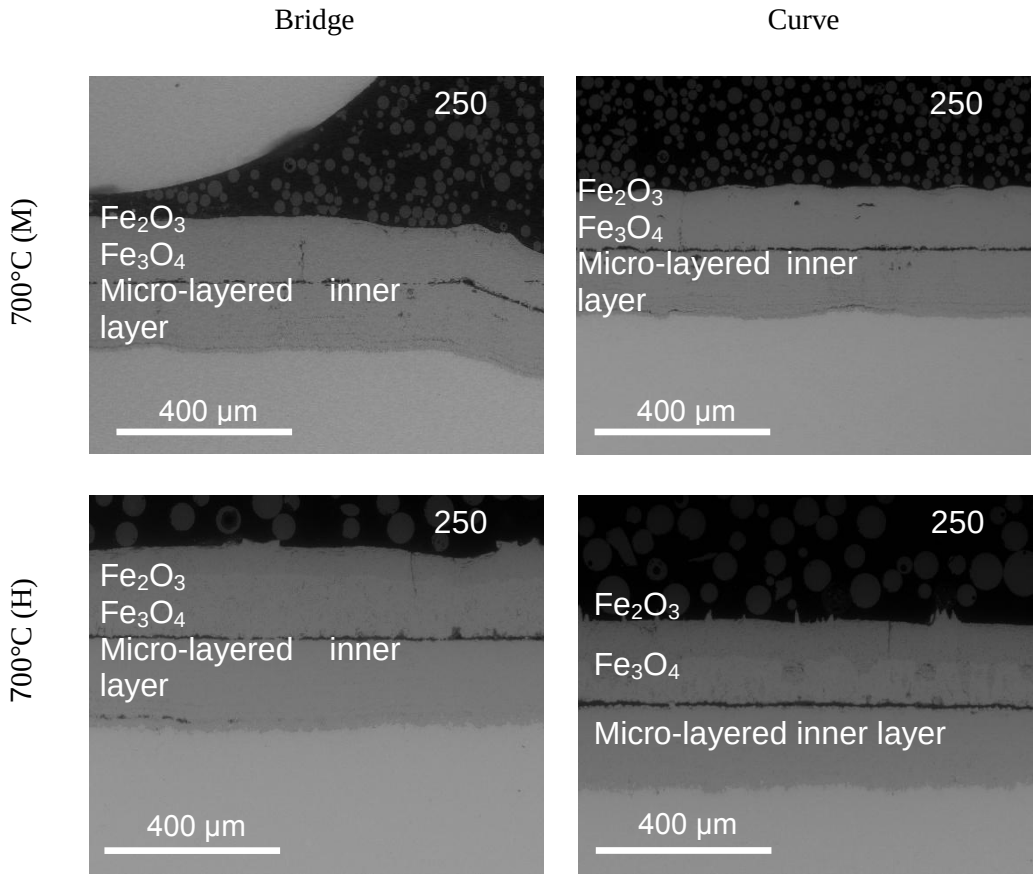

Figure A-12 BSE SEM pictures of the scales developed on T23 exposed to steam at 700°C with Medium (M) and Fast (F) steam flow rates after 250 hour exposure

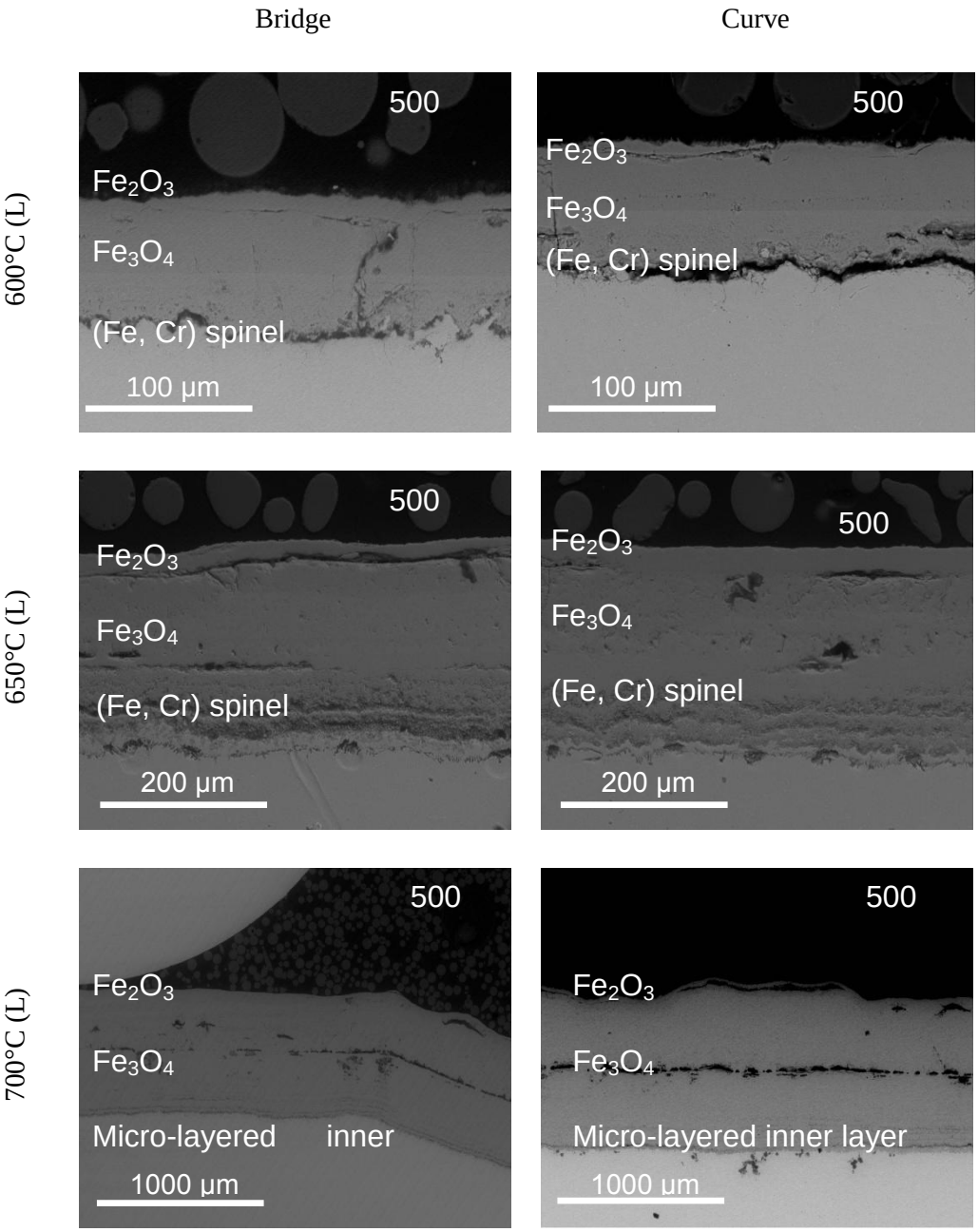
Bridge
Curve
600°C (L)
650°C (L)
700°C (L)
500
Fe2O3
Fe3O4
(Fe, Cr) spinel
100 μm
200 μm
Micro-layered inner layer
1000 μm

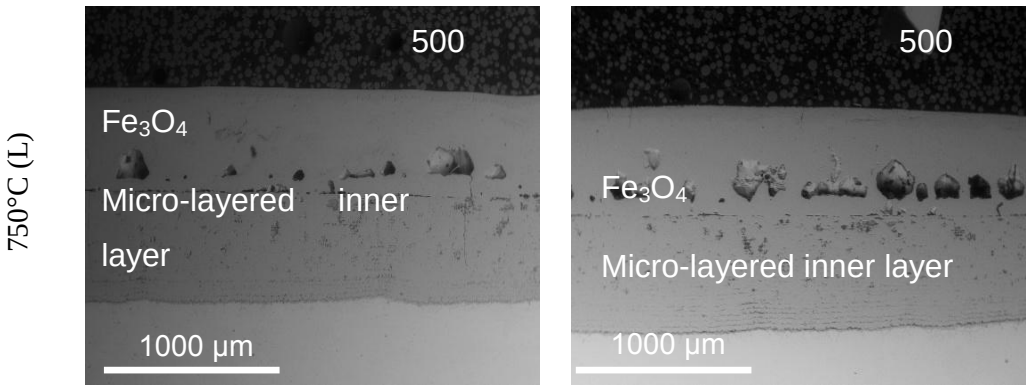

Figure A-13 BSE SEM pictures of the scales developed on T23 exposed to steam in temperature between 600 – 750°C (L) after 500 hour exposure

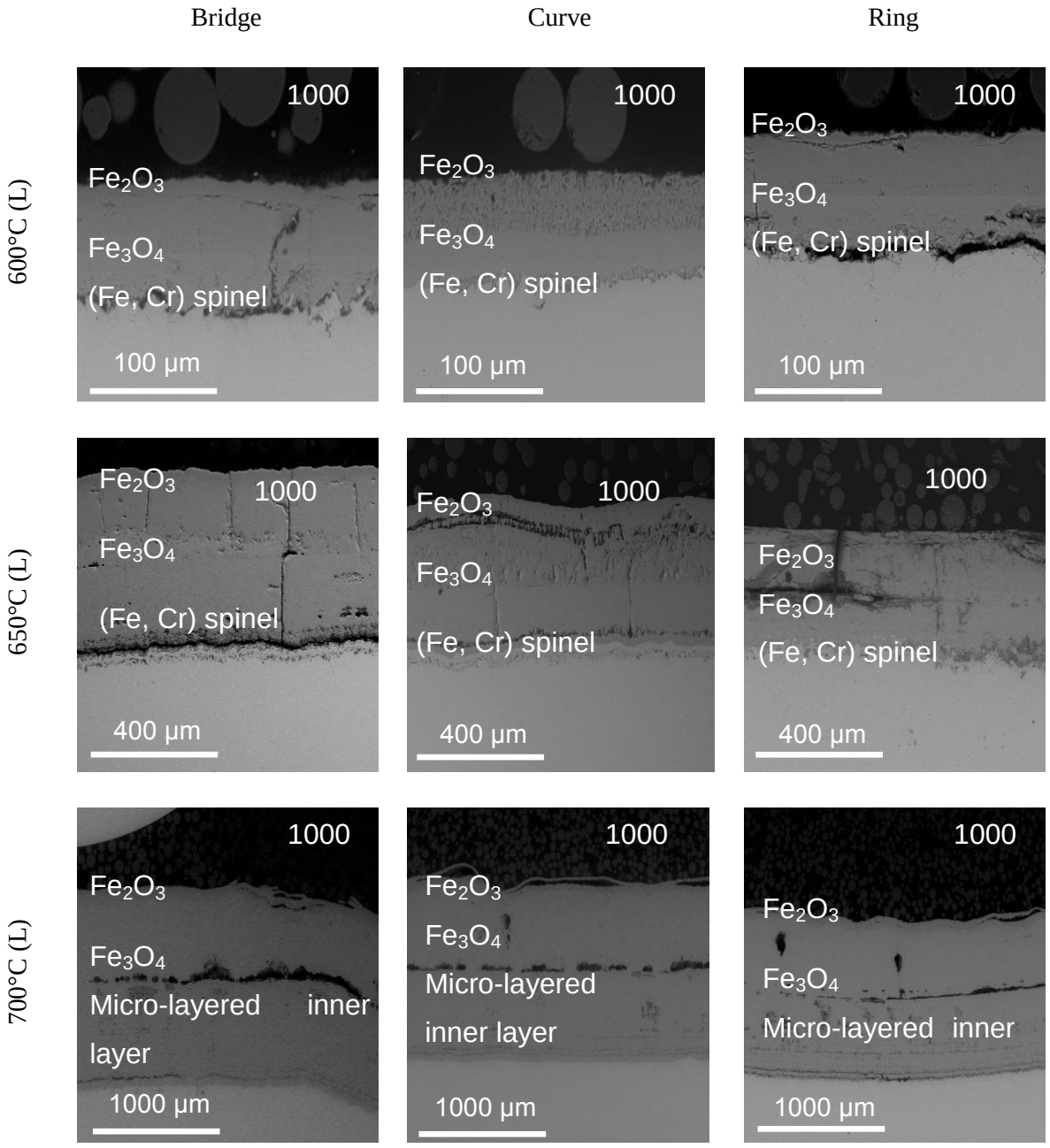
Bridge
Curve
Ring
600°C (L)
650°C (L)
700°C (L)
1000
Fe2O3
Fe3O4
(Fe, Cr) spinel
100 μm
400 μm
Micro-layered inner layer
1000 μm

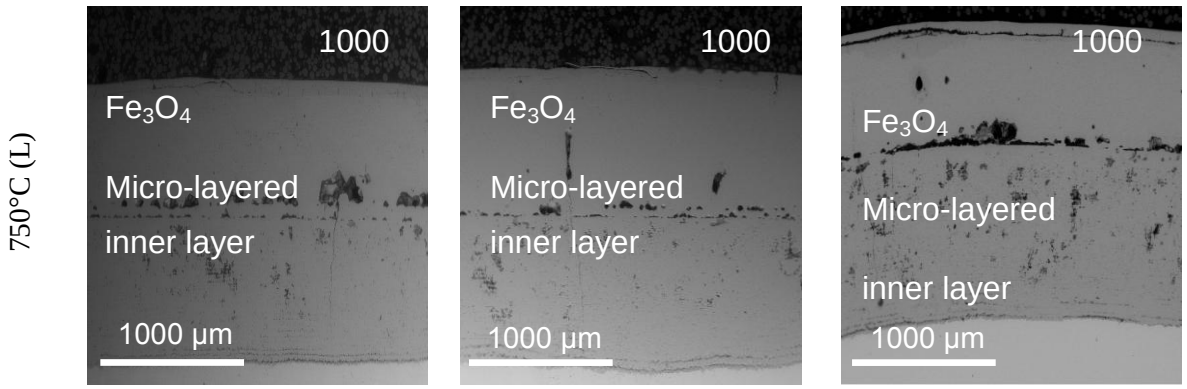

Figure A-14 BSE SEM pictures of the scales developed on T23 exposed to steam in temperature between 600 – 750°C (L) after 1000 hour exposure

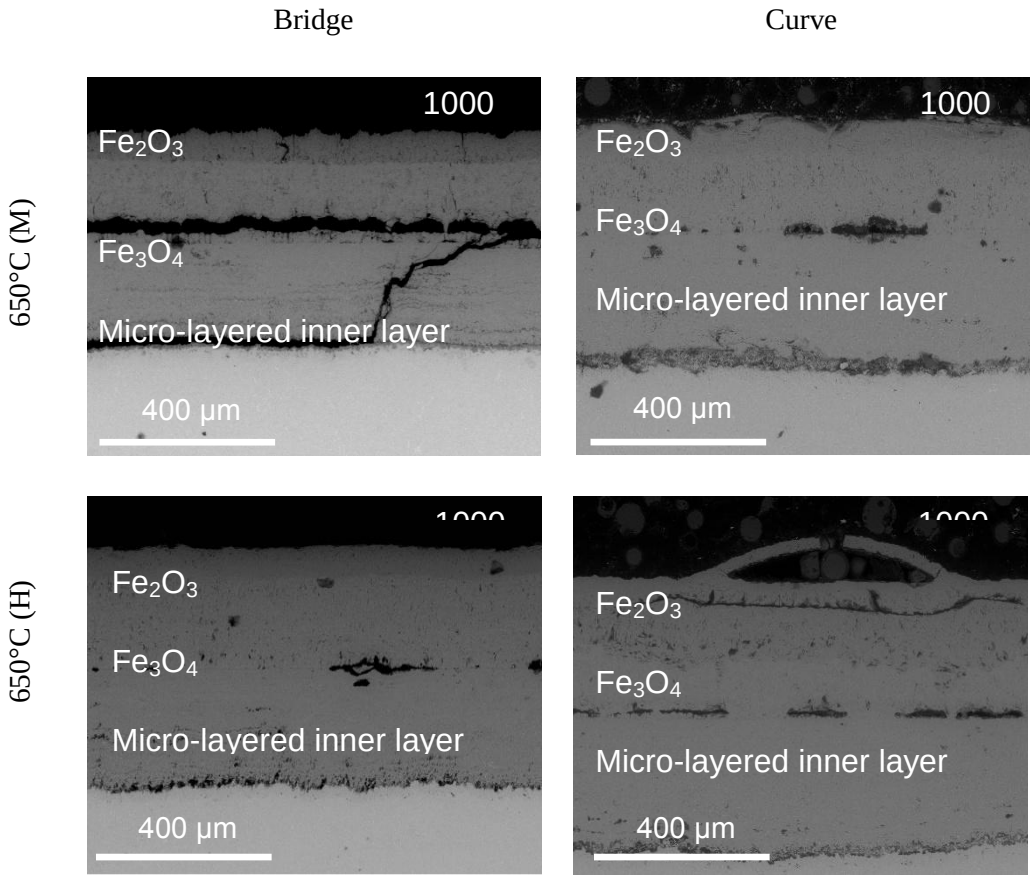

Figure A-15 SEM pictures of the scales developed on T23 exposed to steam at 650°C with Medium (M) and Fast (F) steam flow rates after 1000 hour exposure

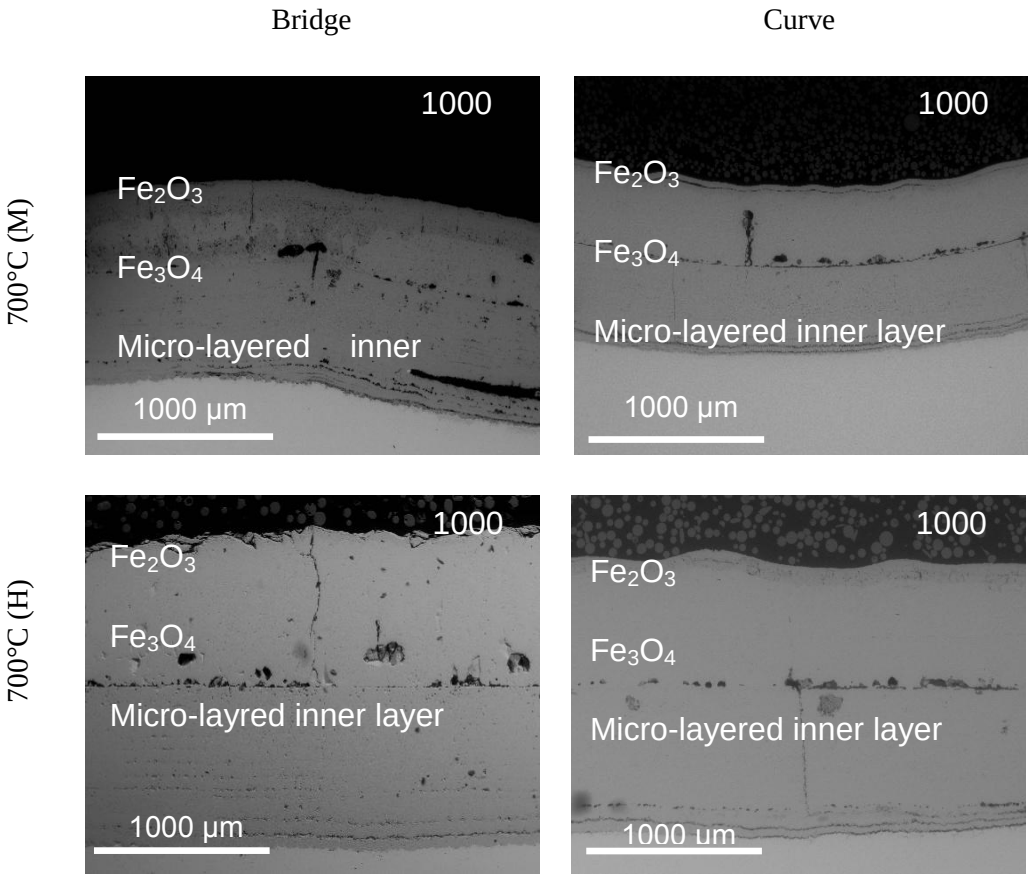

Figure A-16 BSE SEM pictures of the scales developed on T23 exposed to steam at 700°C with Medium (M) and Fast (F) steam flow rates after 1000 hour exposure

A.2.2 Oxides scales morphology formed on T92

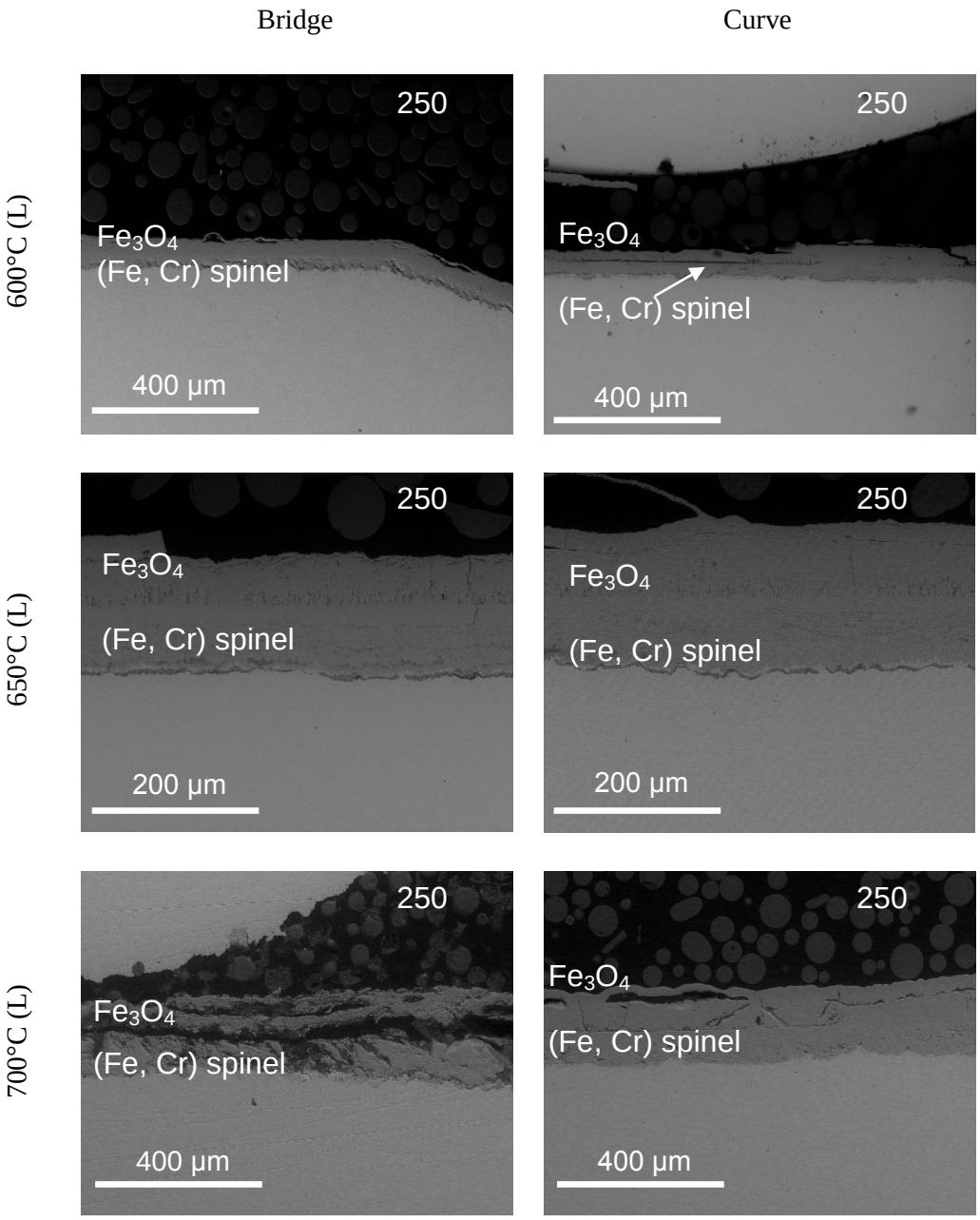

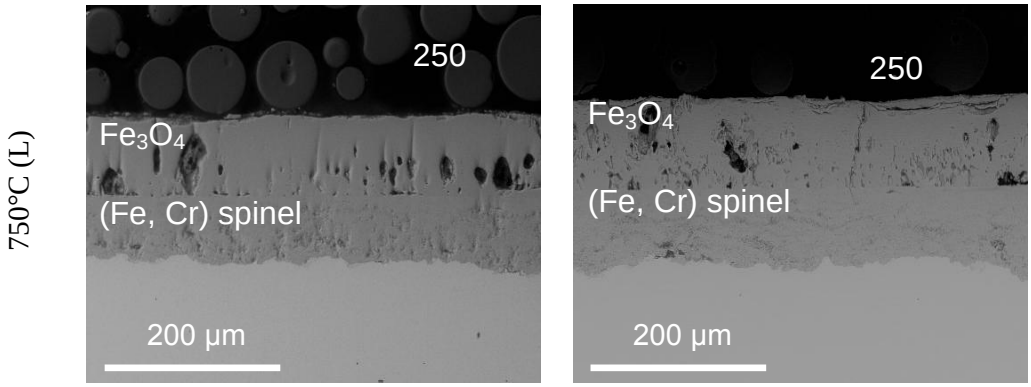

Figure A-17 BSE SEM pictures of the scales developed on T92 exposed to steam in temperature between 600 – 750°C (L) after 250 hour exposure

Bridge Curve

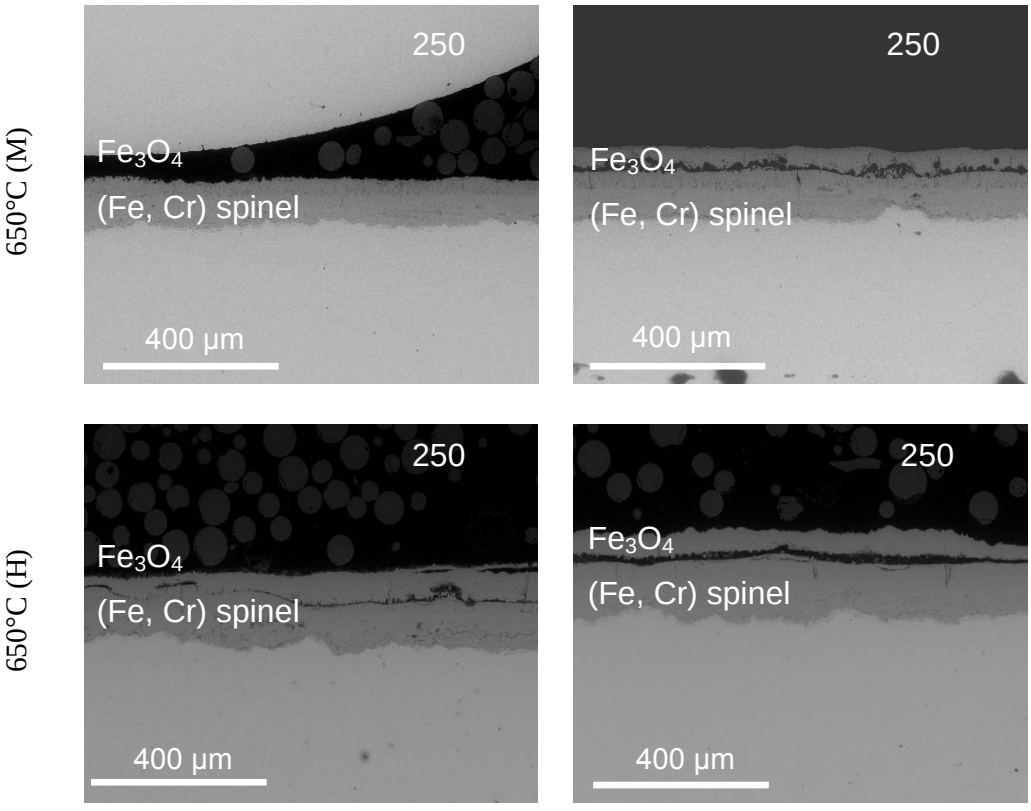

Figure A-18 BSE SEM pictures of the scales developed on T92 exposed to steam at 650°C with Medium (M) and Fast (F) steam flow rates after 250 hour exposure

Bridge Curve

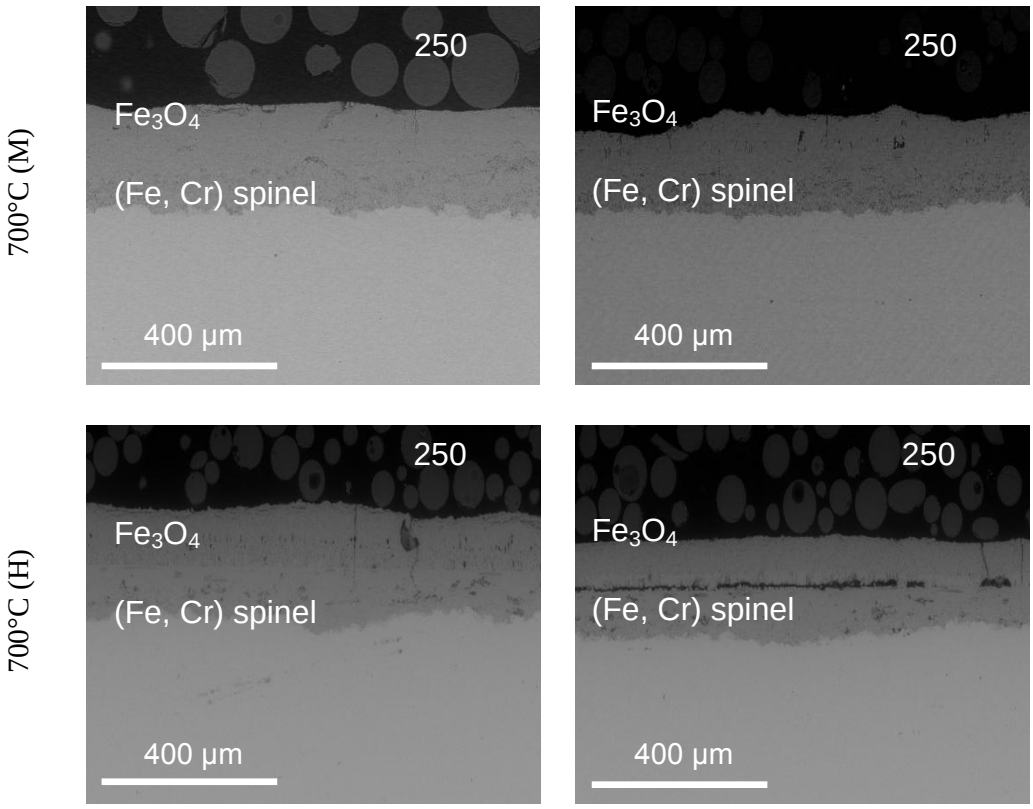

Figure A-19 BSE SEM pictures of the scales developed on T92 exposed to steam at 700°C with Medium (M) and Fast (F) steam flow rates after 250 hour exposure

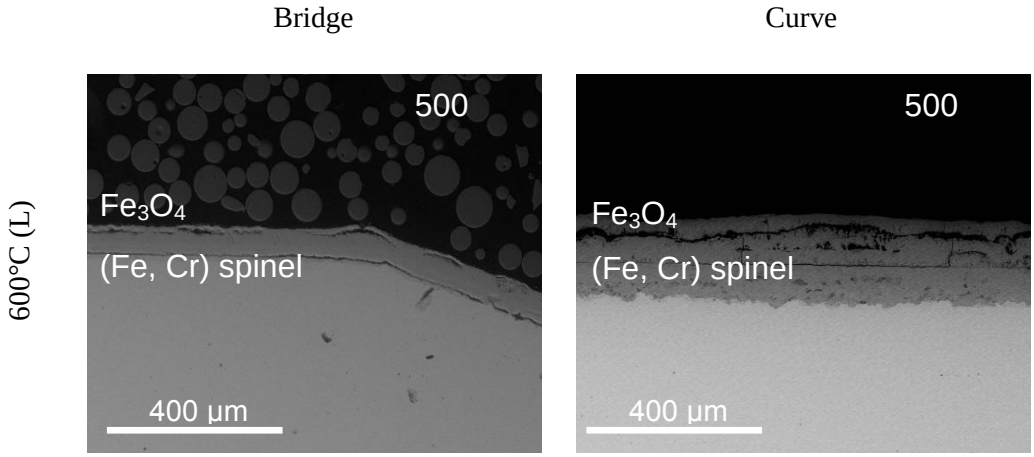

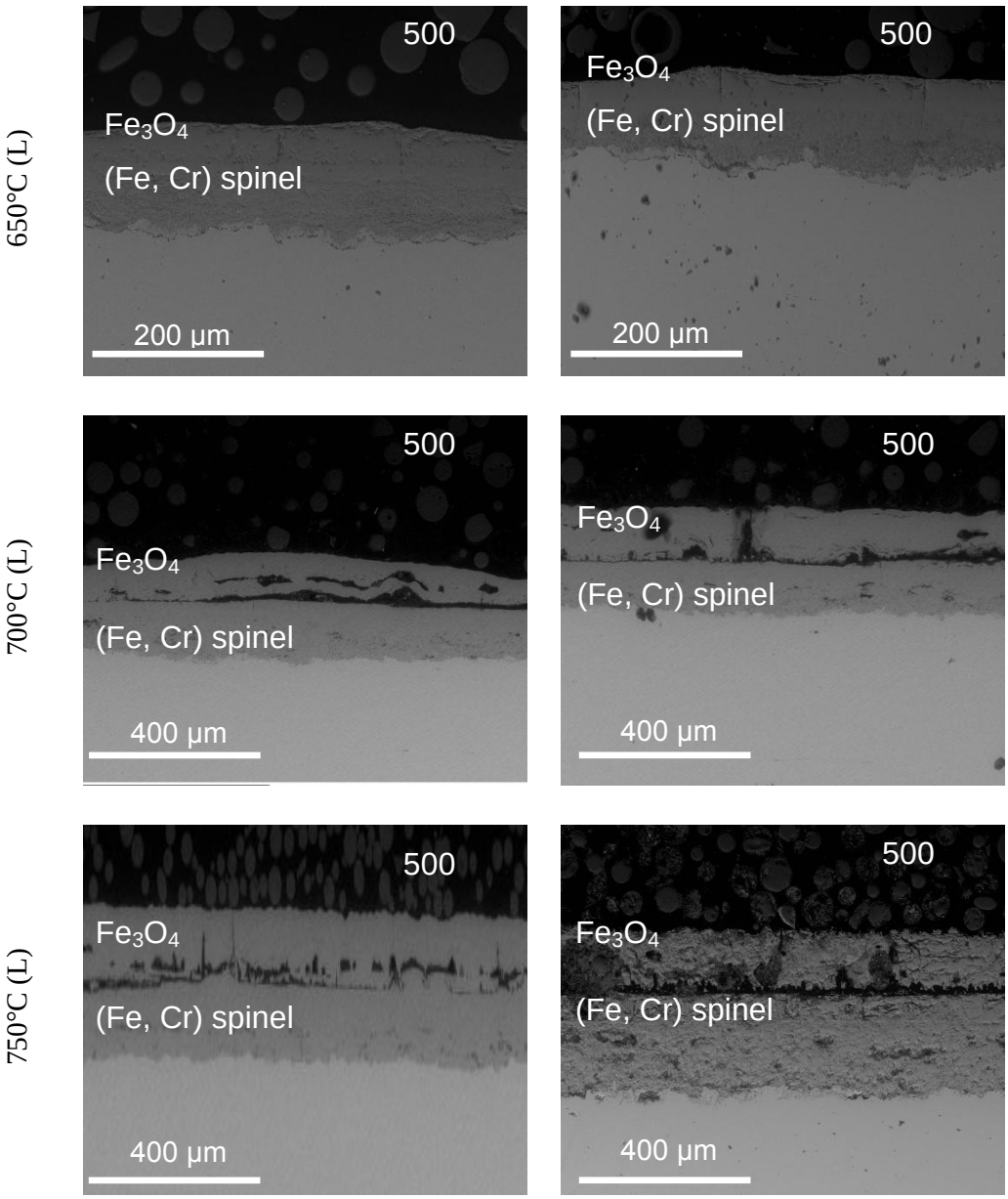

Figure A-20 BSE SEM pictures of the scale developed on T92 exposed to steam in temperature between 600 – 750°C (L) after 500 hour exposure

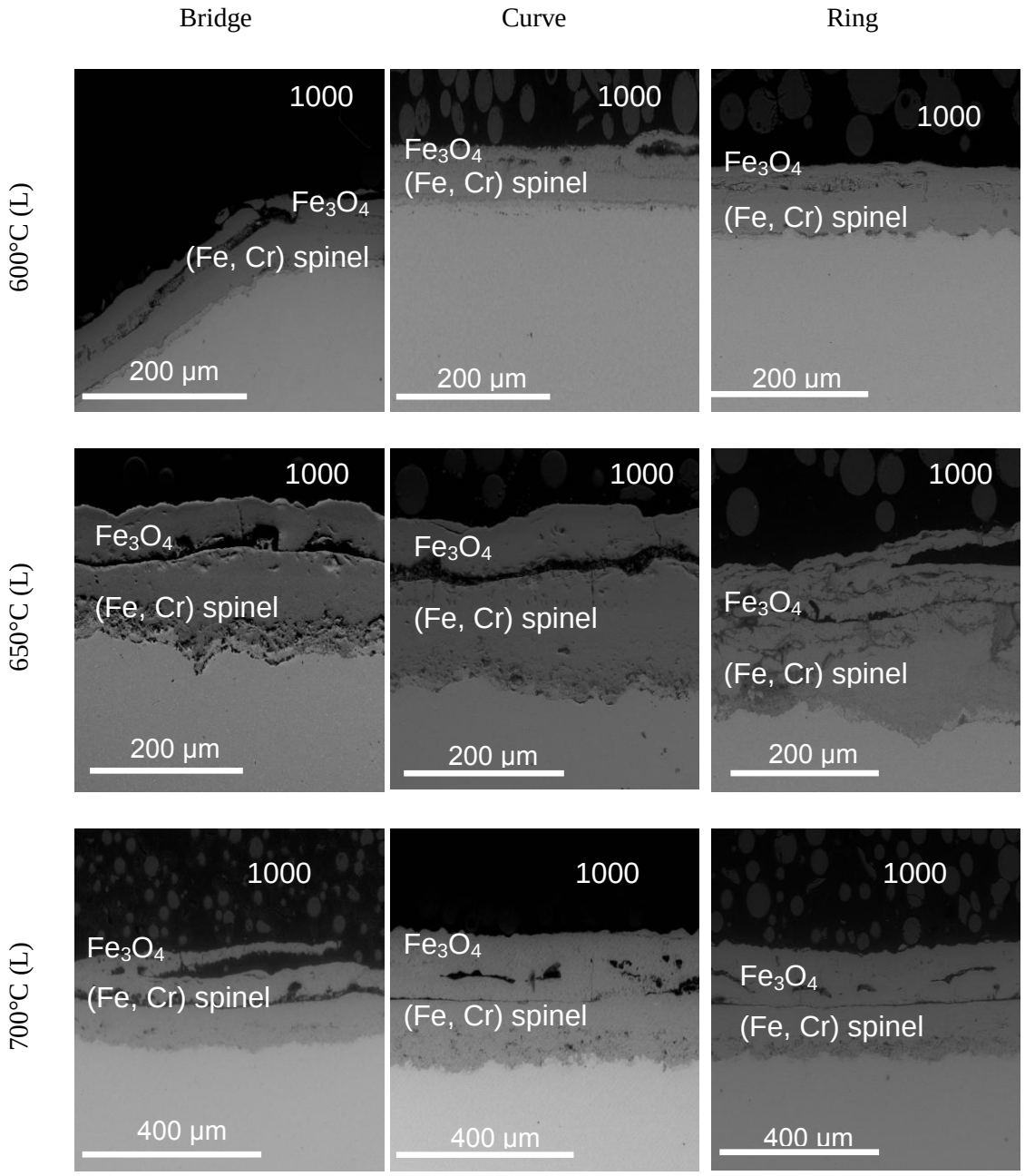
Bridge
Curve
Ring
600°C (L)
650°C (L)
700°C (L)
1000
Fe3O4
(Fe, Cr) spinel
200 μm
400 μm

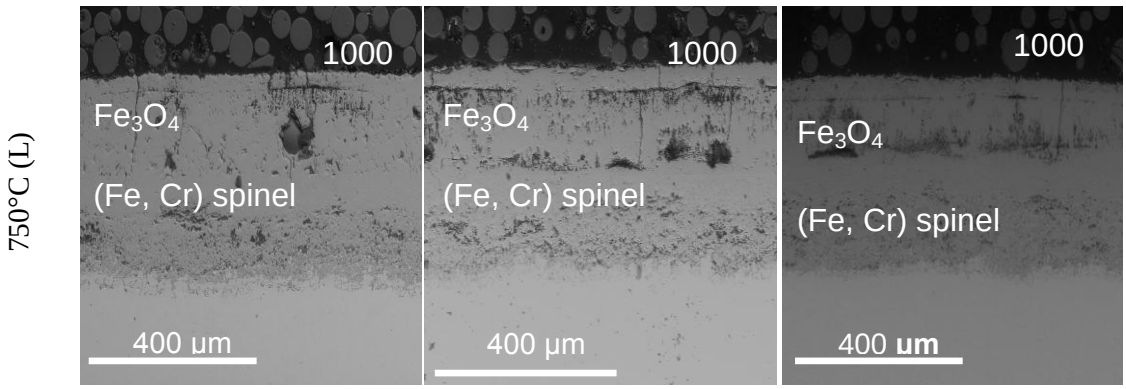

Figure A-21 BSE SEM pictures of the scale developed on T92 exposed to steam in temperature between 600 – 750°C (L) after 1000 hour exposure

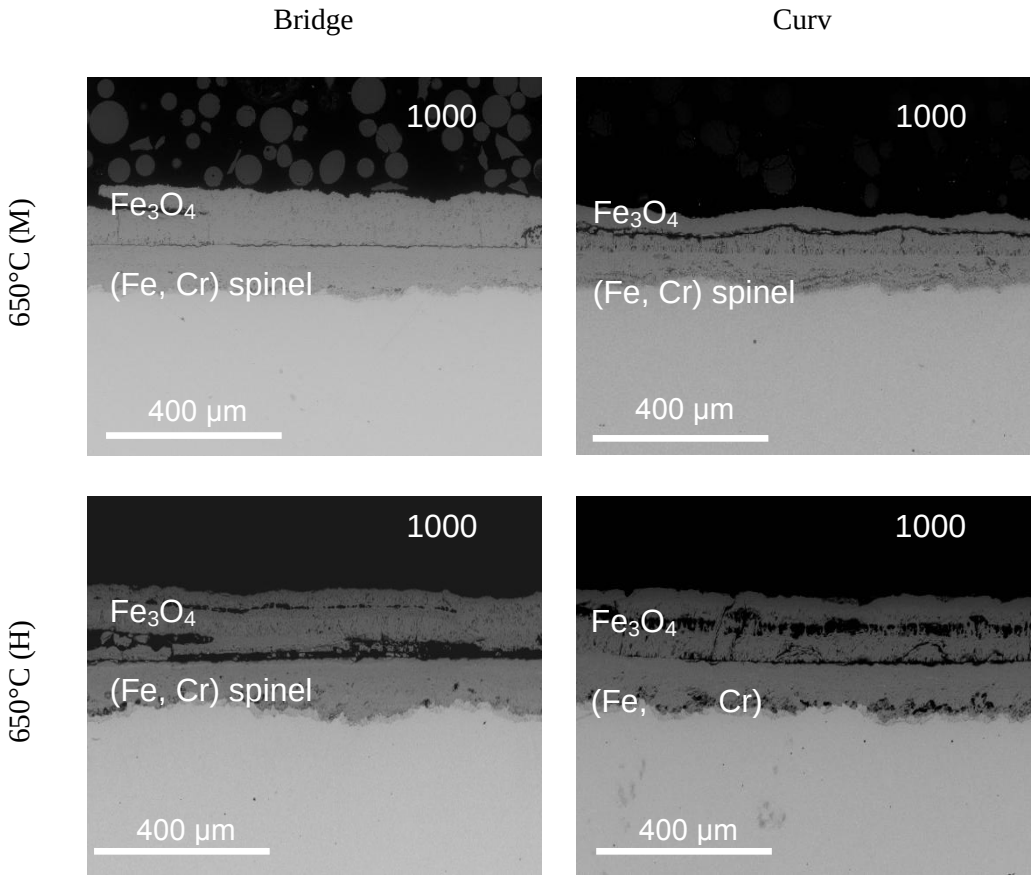

Figure A-22 BSE SEM pictures of the scales developed on T92 exposed to steam at 650°C with Medium (M) and Fast (F) steam flow rates after 1000 hour exposure

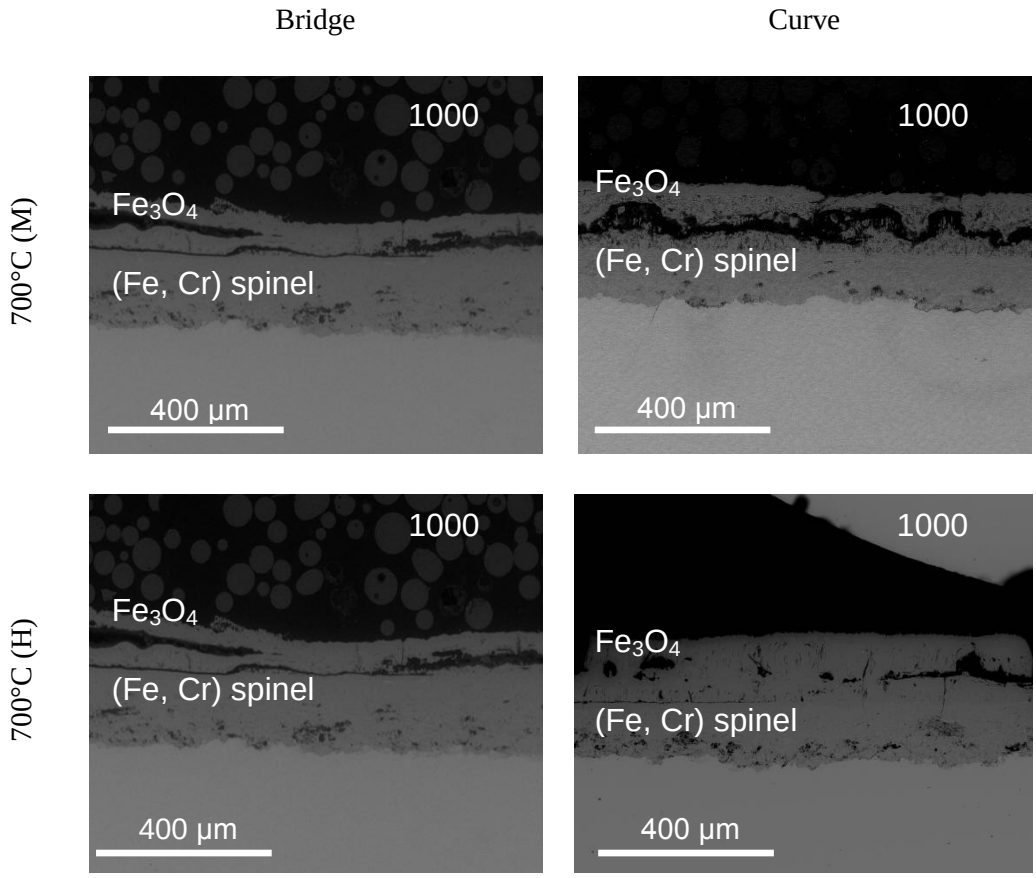

Figure A-23 BSE SEM pictures of the scales developed on T92 exposed to steam at 700°C with Medium (M) and Fast (F) steam flow rates after 1000 hour exposure

A.2.3 Oxides scales morphology formed on T347HFG

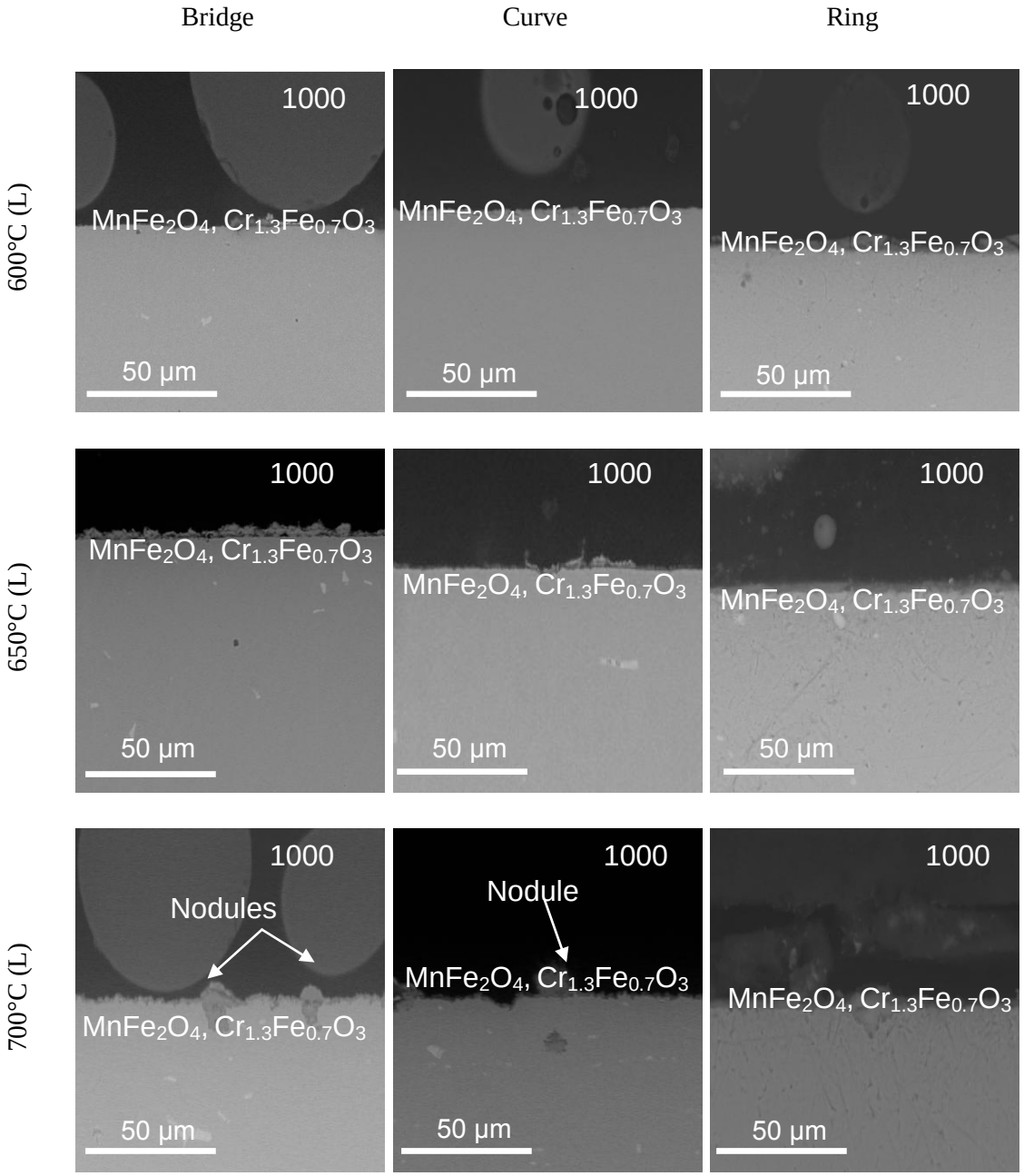

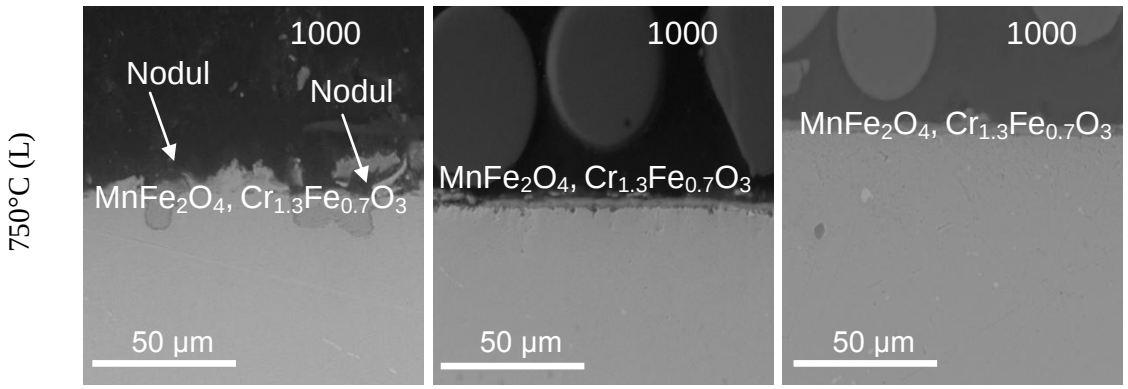

Figure A-24 BSE SEM pictures of the scale developed on T347HFGexposed to steam in temperature between 600 – 750°C (L) after 1000 hour exposure

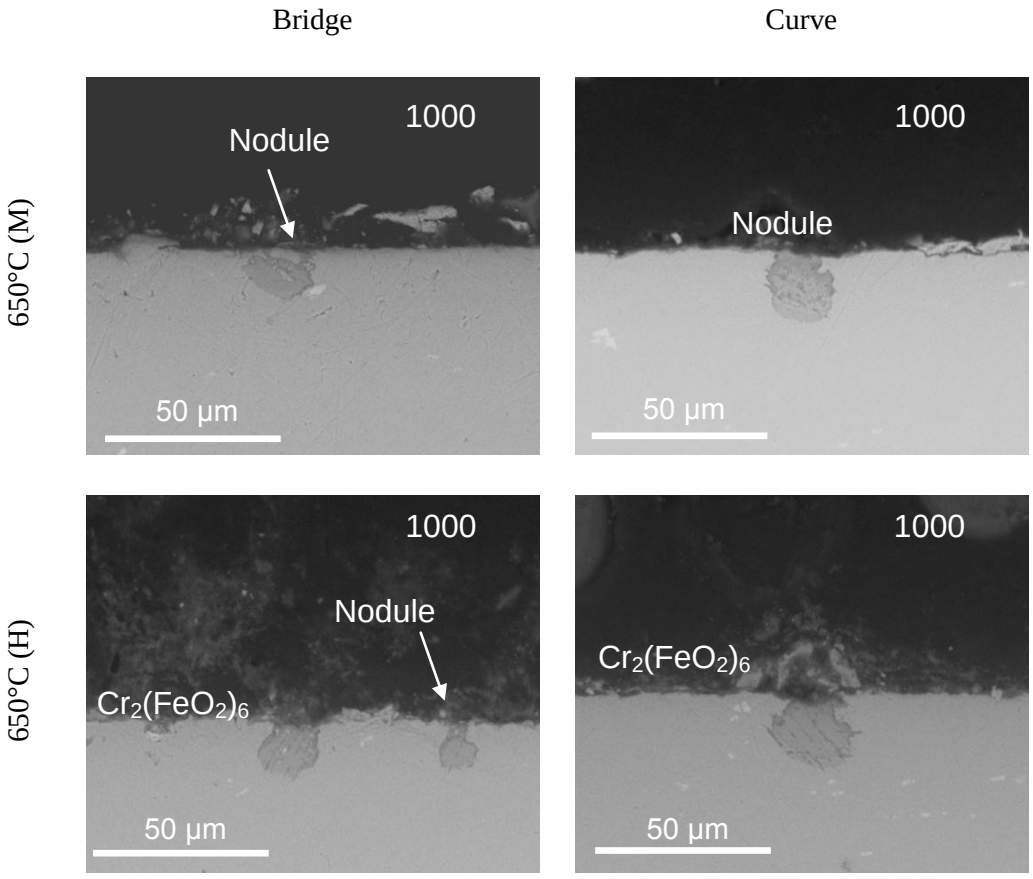

Figure A-25 BSE SEM pictures of the scales developed on T347 HFG exposed to steam at 650°C with Medium (M) and Fast (F) steam flow rates after 1000 hour exposure

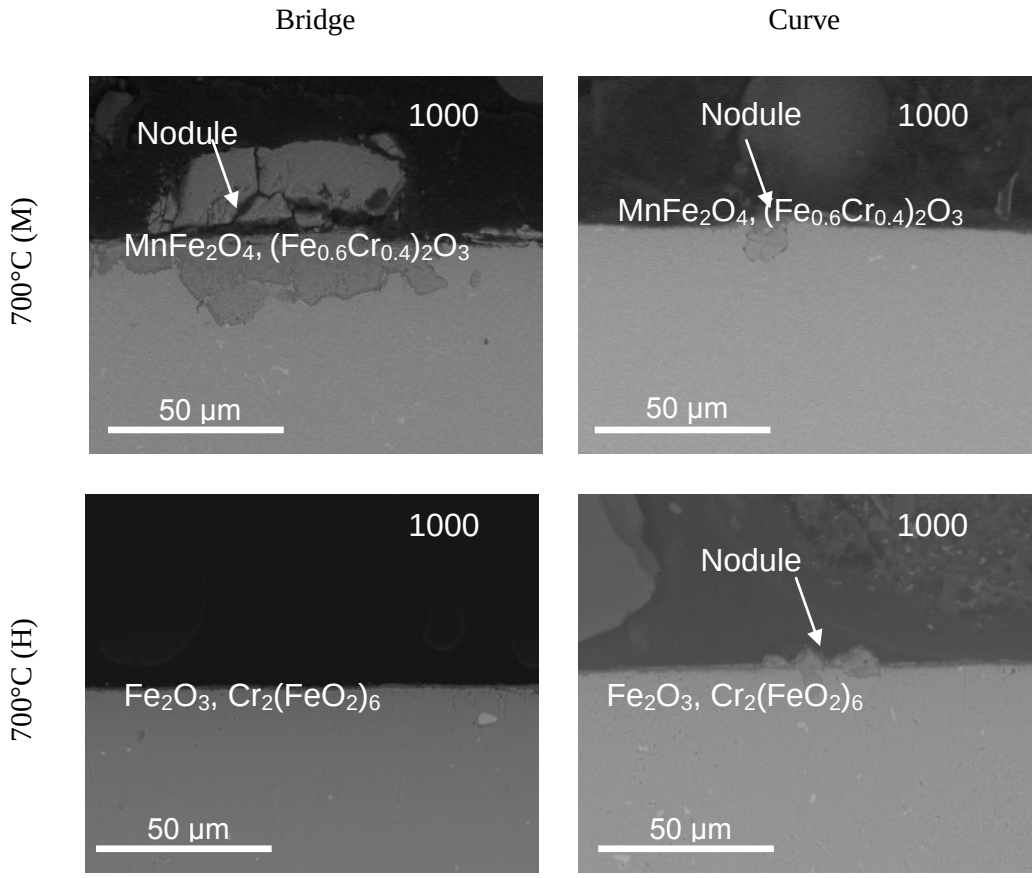

Figure A-26 BSE SEM pictures of the scales developed on T347 HFG exposed to steam at 700°C with Medium (M) and Fast (F) steam flow rates after 1000 hour exposure

A.2.4 Oxides scales morphology formed on Super 304H

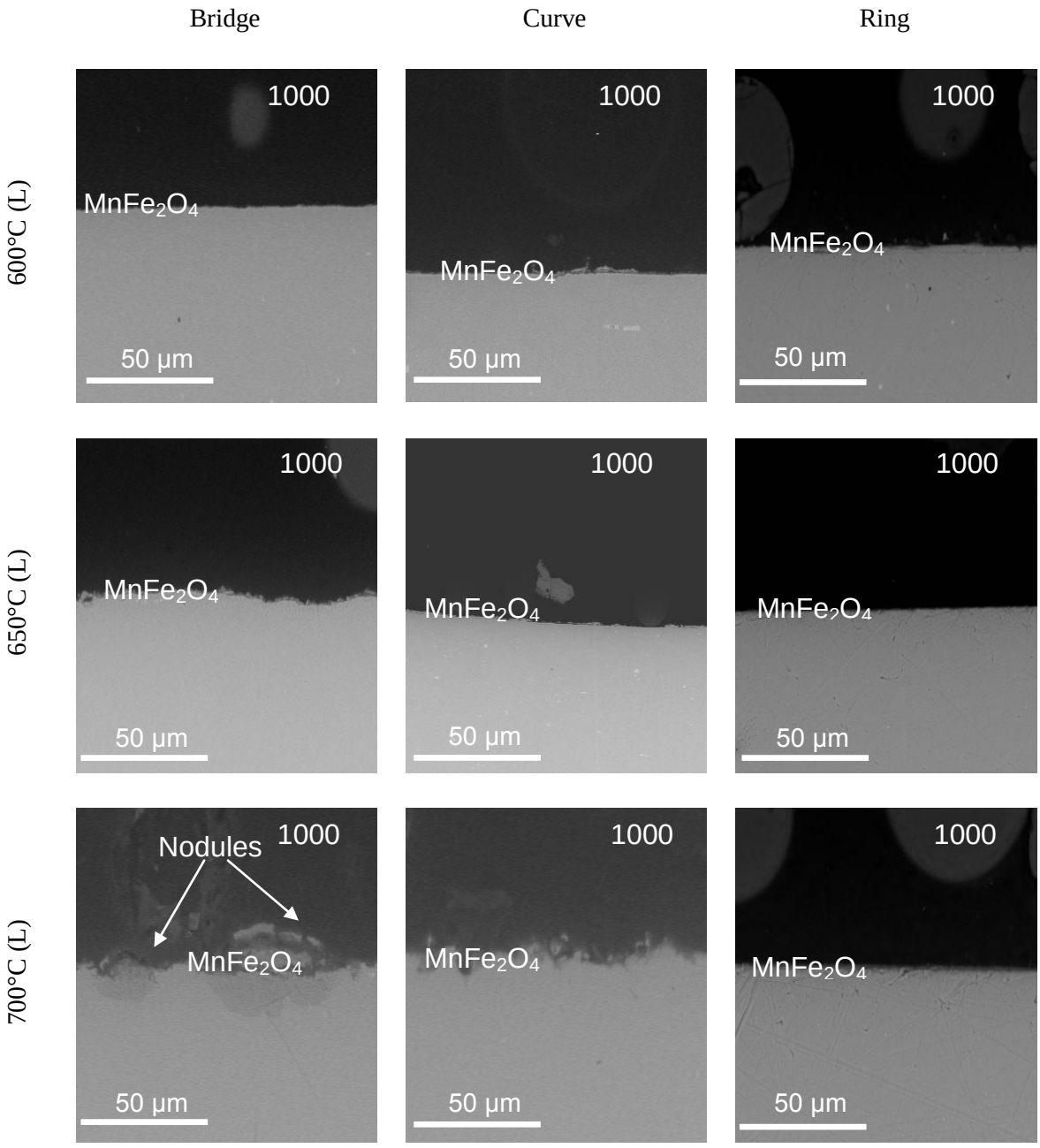

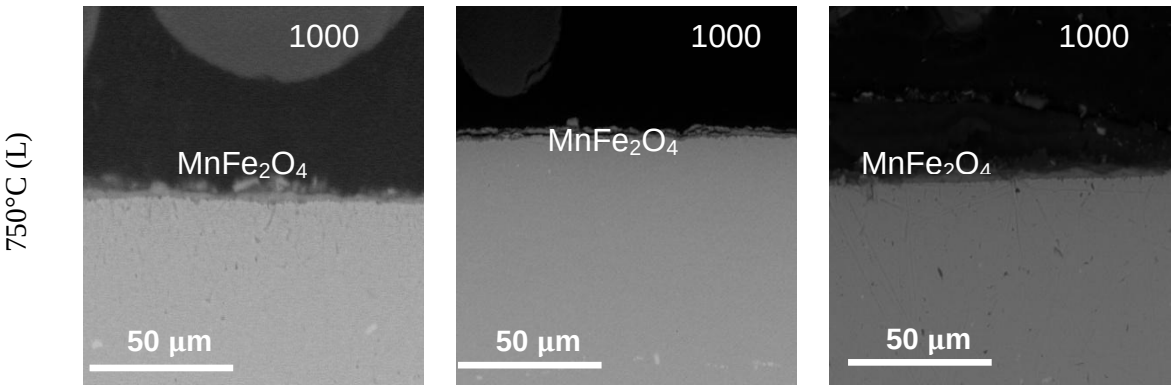

Figure A-27 BSE SEM pictures of the scale developed on Super 304H exposed to steam in temperature between 600 – 750°C (L) and under faster steam conditions after 1000 hour exposure

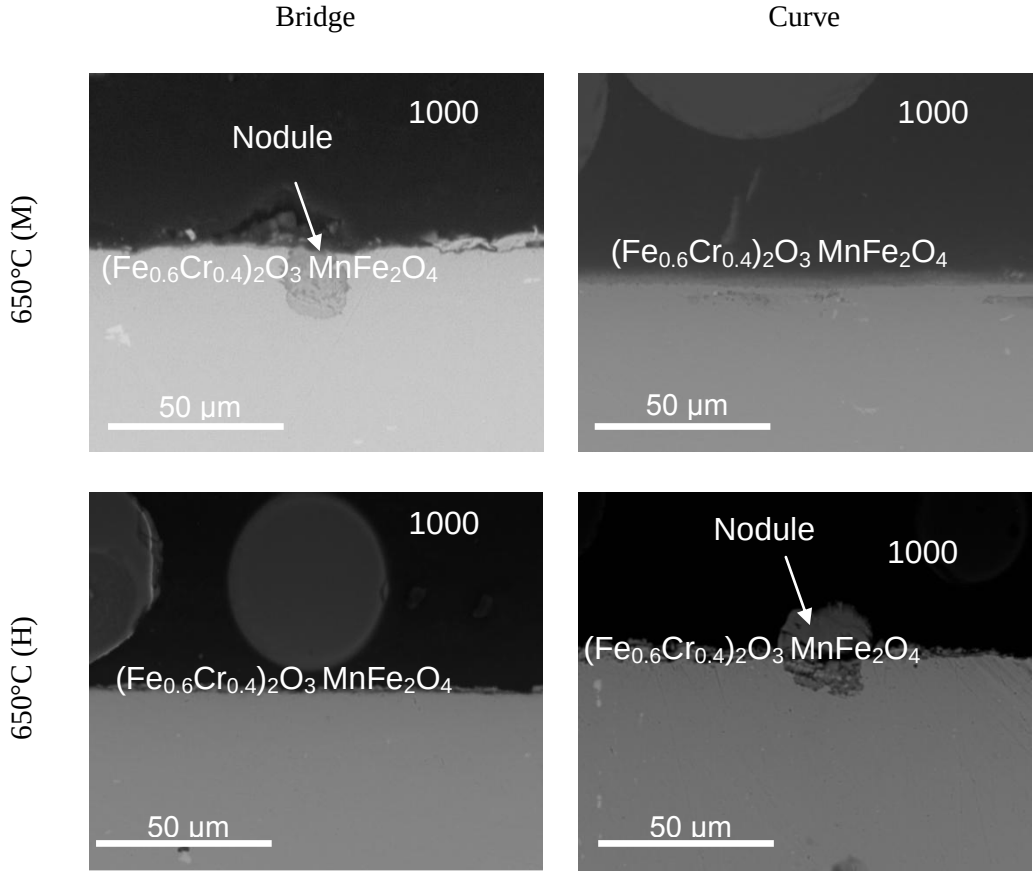

Figure A-28 BSE SEM pictures of the scales developed on Super 304H exposed to steam at 700°C with Medium (M) and Fast (F) steam flow rates after 1000 hour exposure

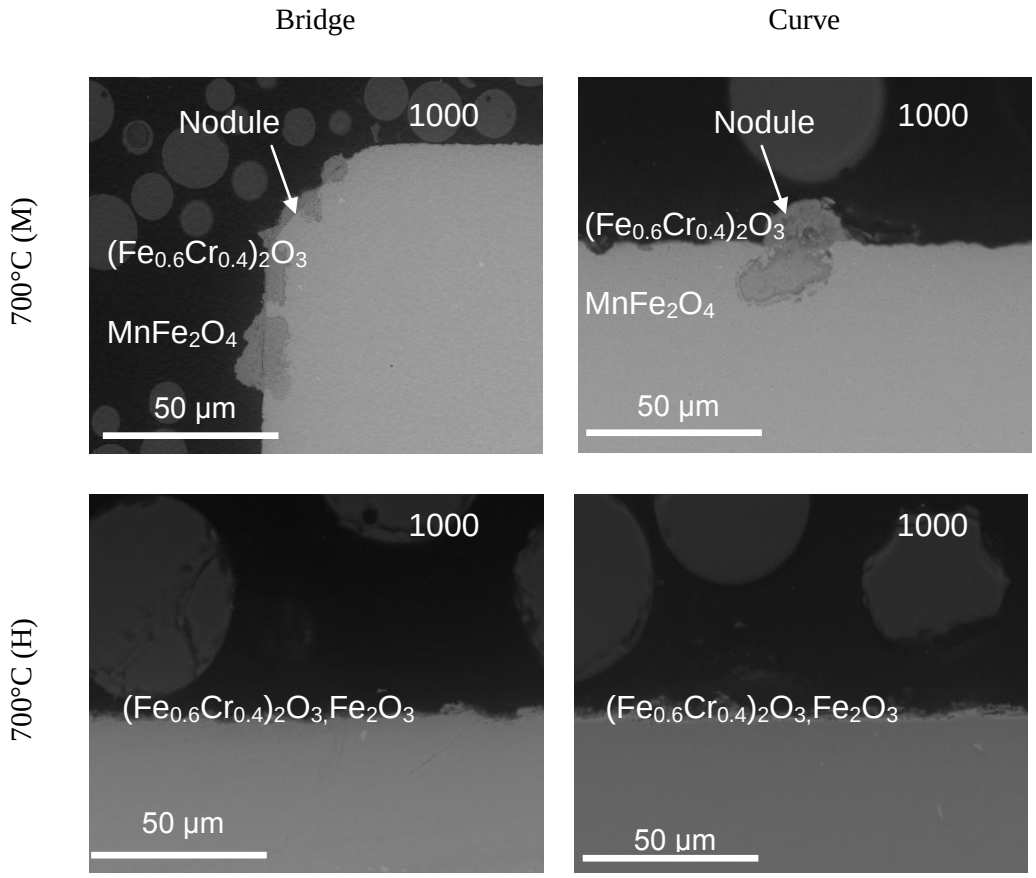

Figure A-29 BSE SEM pictures of the scales developed on Super 304H exposed to steam at 650°C with Medium (M) and Fast (F) steam flow rates after 1000 hour exposure

A.2.5 Oxides scales morphology formed on HR3C

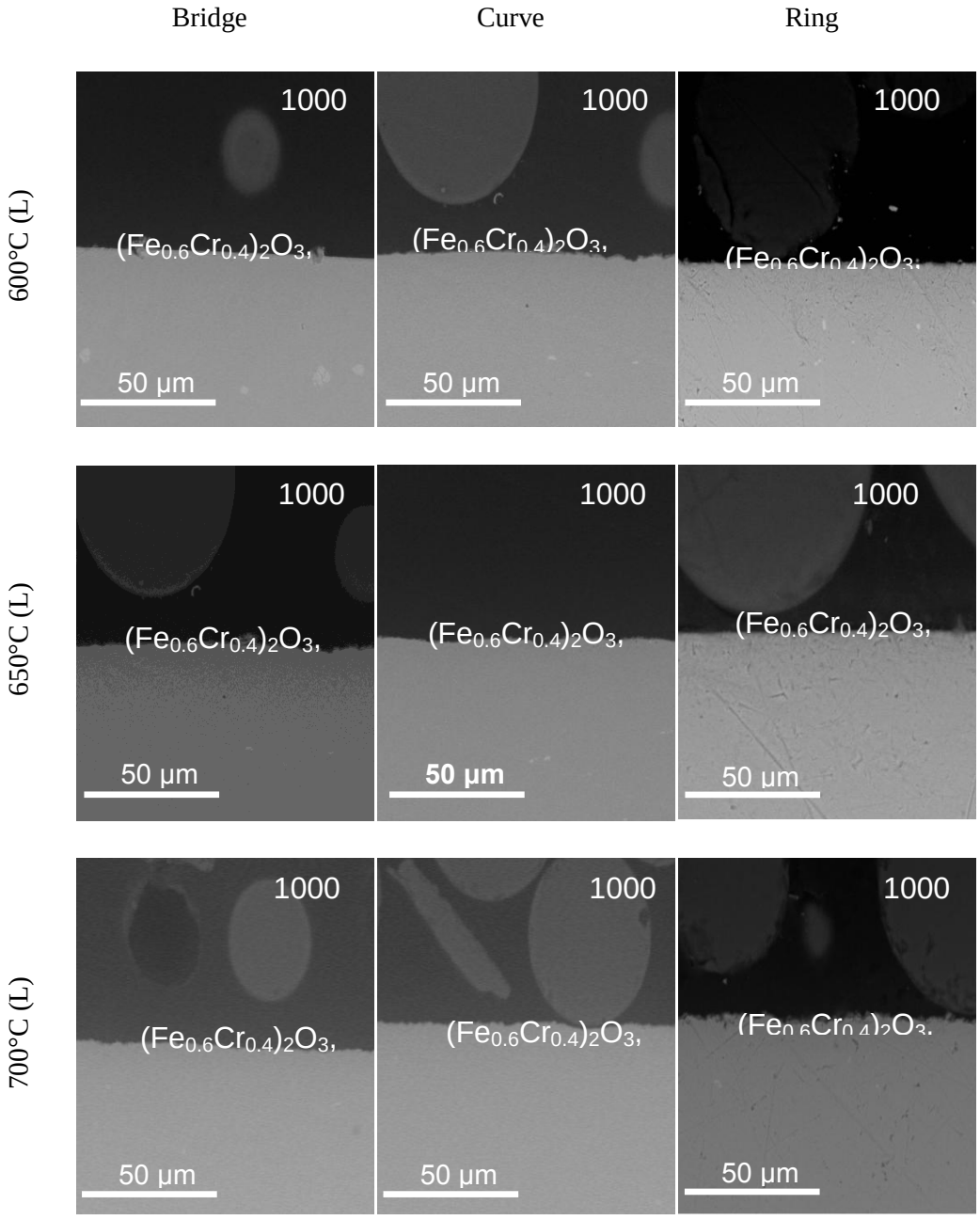

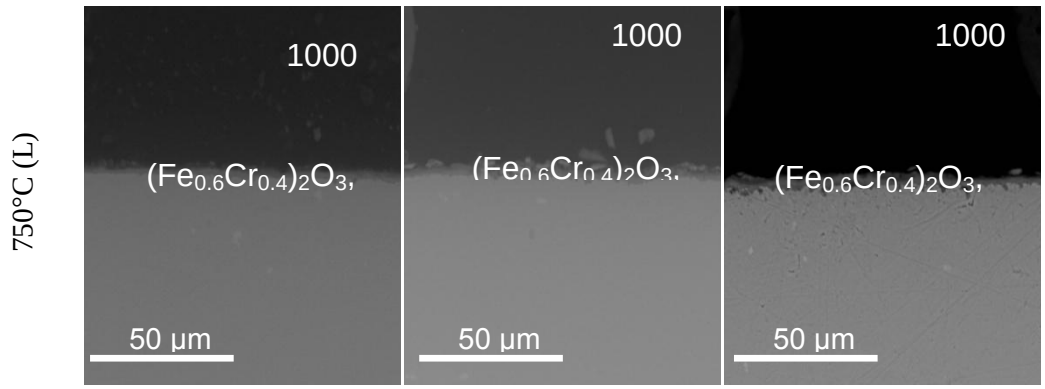

Figure A-30 BSE SEM pictures of the scale developed on HR3C exposed to steam in temperature between 600 – 750°C (L) after 1000 hour exposure

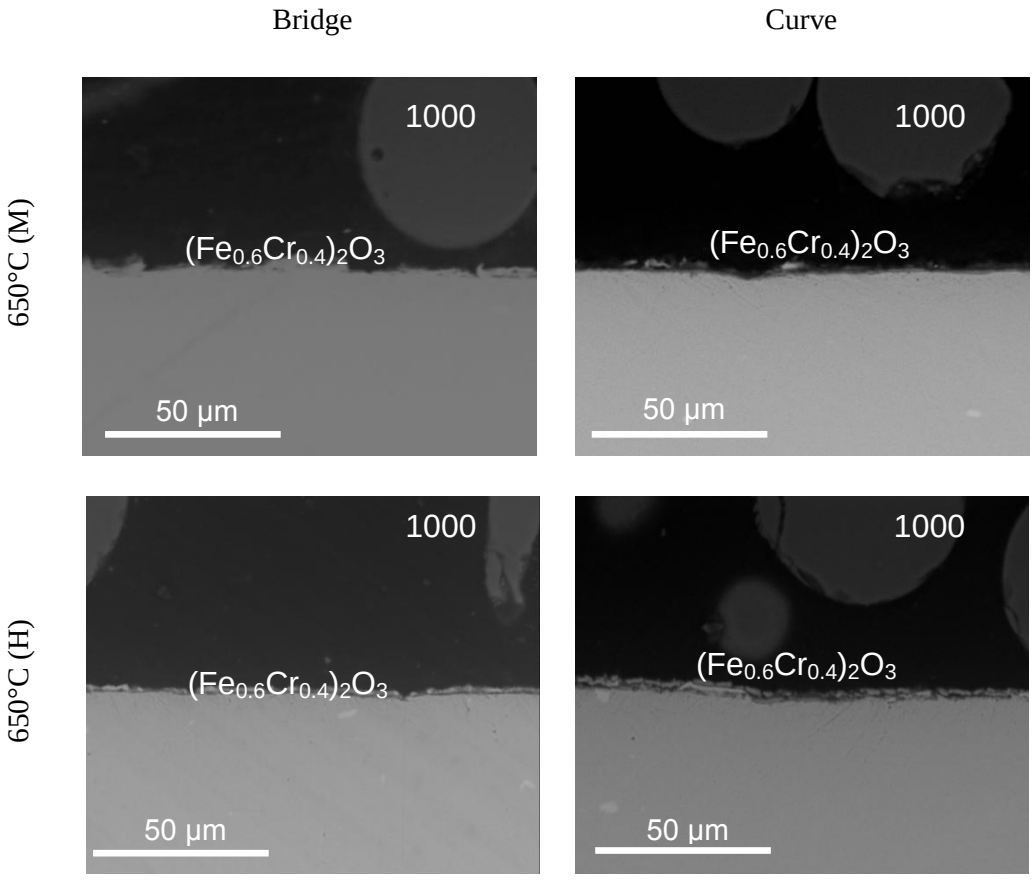

Figure A-31 BSE SEM pictures of the scales developed on Super HR3C exposed to steam at 650°C with Medium (M) and Fast (F) steam flow rates after 1000 hour exposure

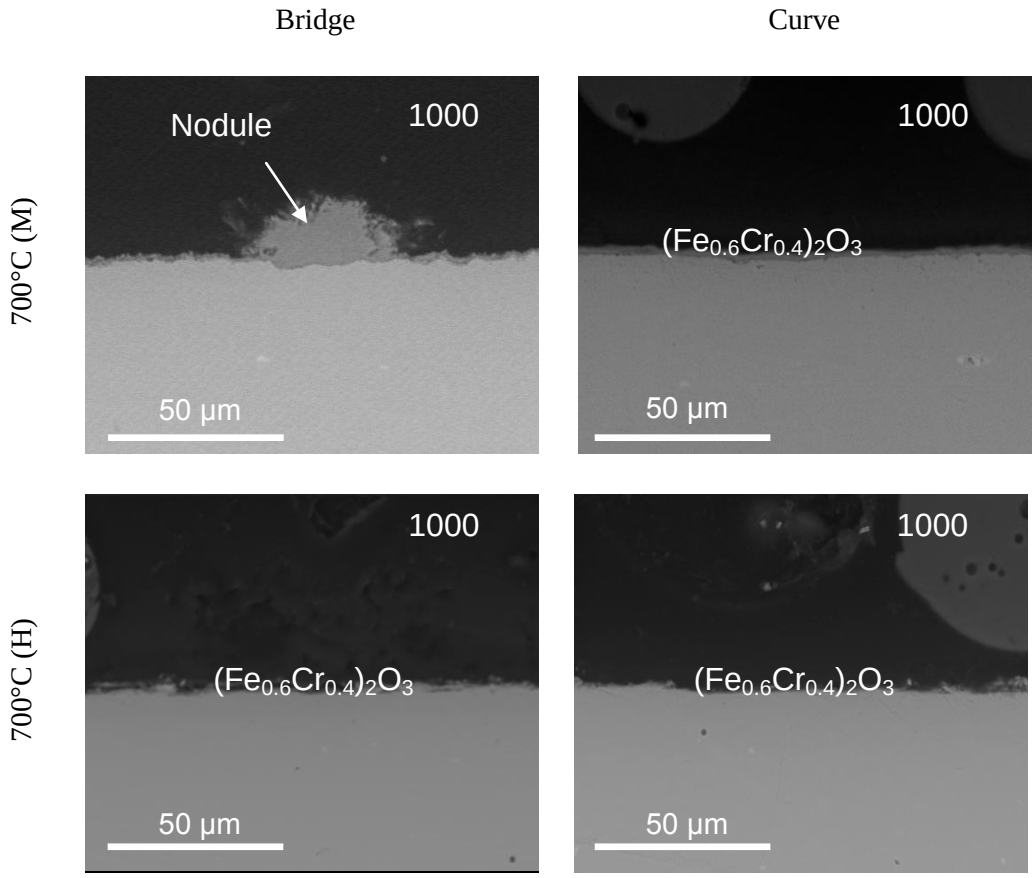

Figure A-32 BSE SEM pictures of the scales developed on Super HR3C exposed to steam at 700°C with Medium (M) and Fast (F) steam flow rates after 1000 hour exposure

A.2.6 Oxides scales morphology formed on 800H and Inconel 740

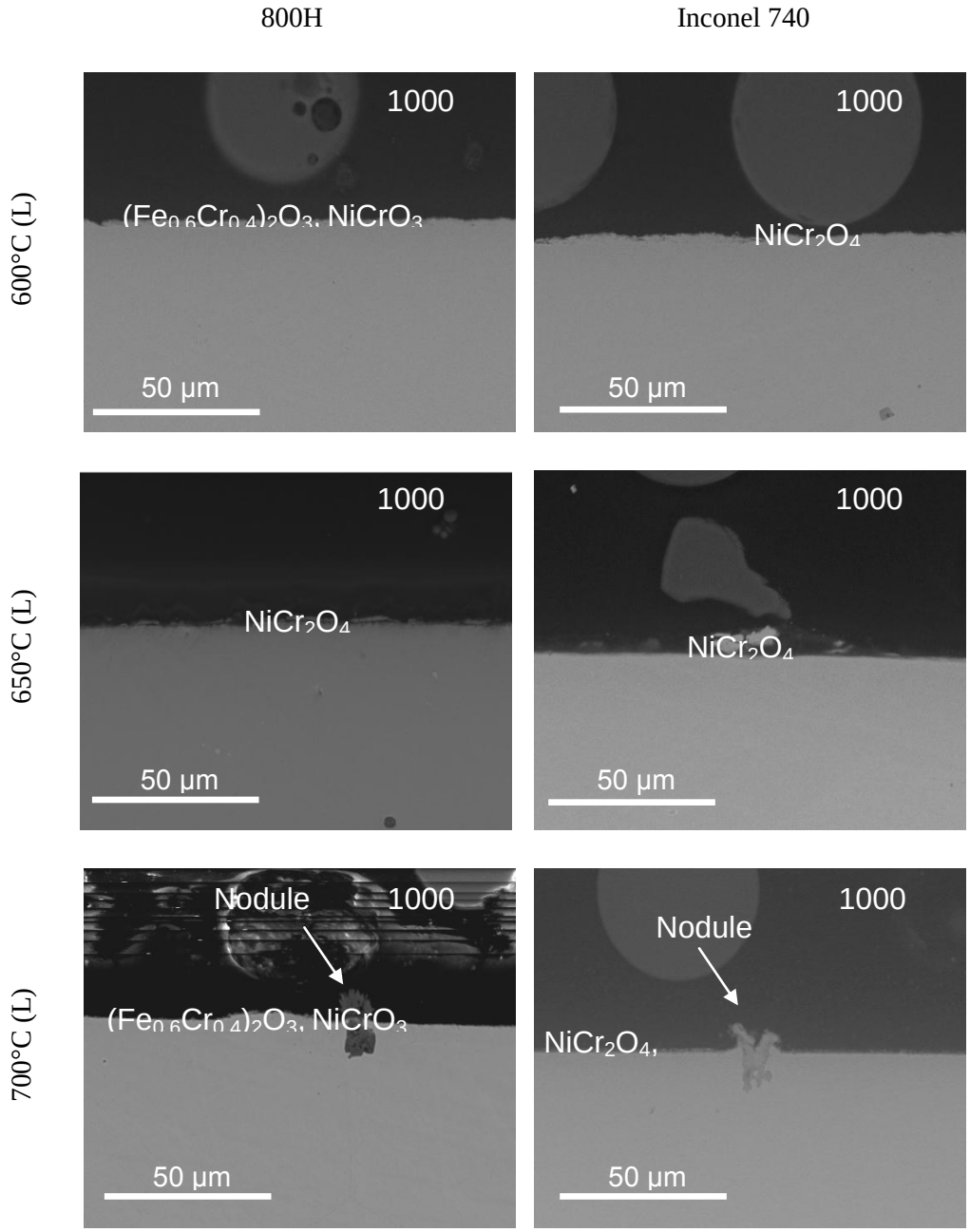

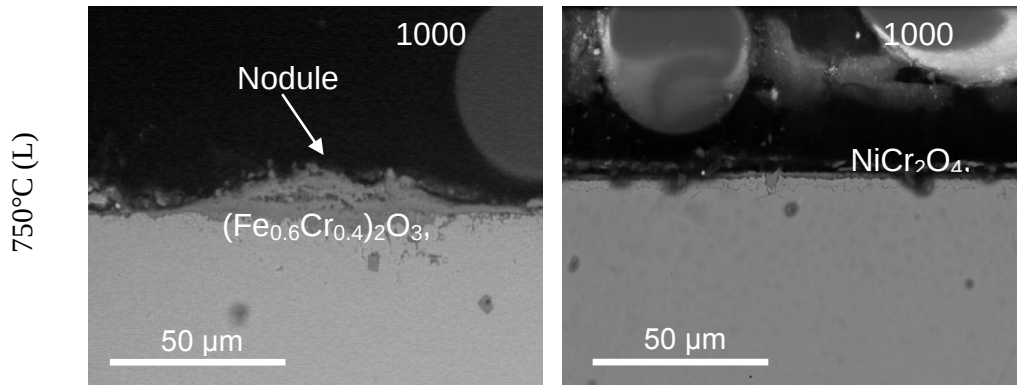

Figure A-33 BSE SEM pictures of the scale developed on 800H and Inconel 740 exposed to steam in temperature between 600 – 750°C (L) after 1000 hour exposure

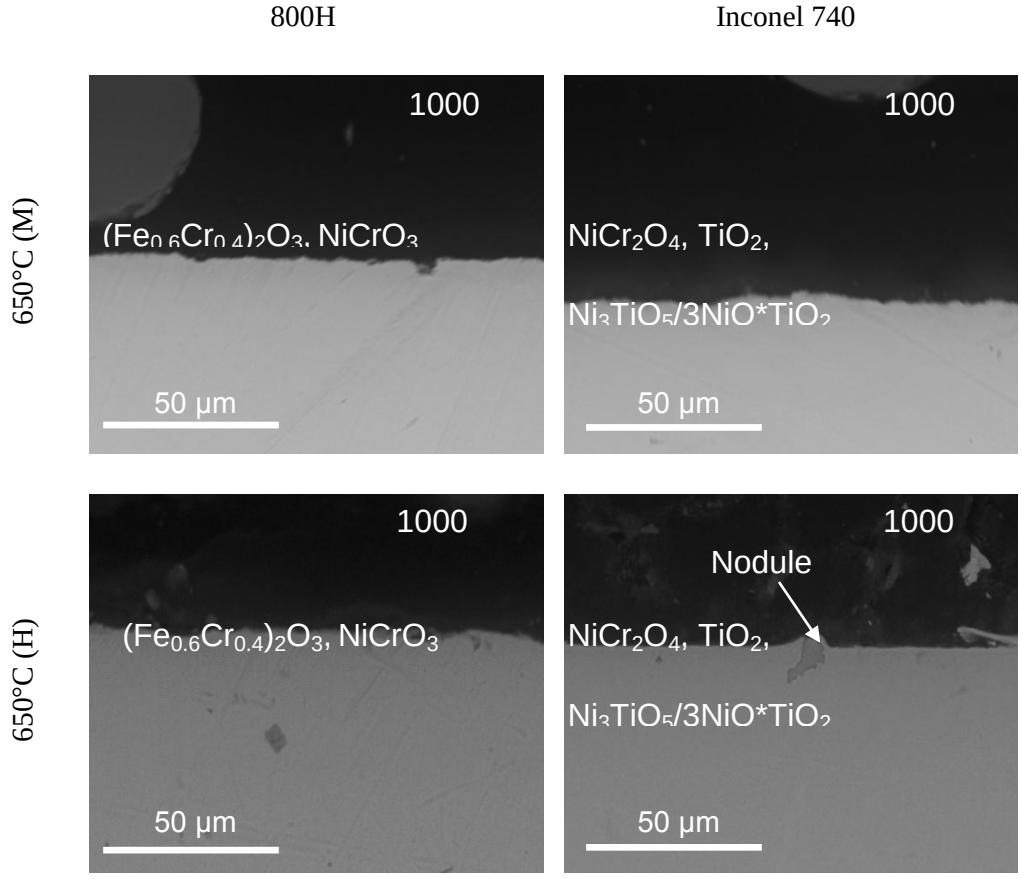

Figure A-34 BSE SEM pictures of the scales developed on 800H and Inconel 740 exposed to steam at 650°C with Medium (M) and Fast (F) steam flow rates after 1000 hour exposure

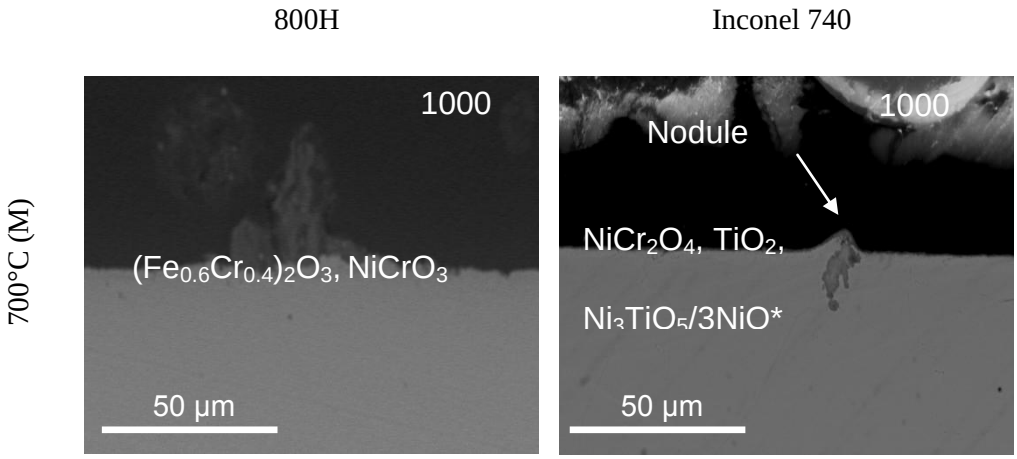

Figure A-35 BSE SEM pictures of the scales developed on 800H and Inconel 740 exposed to steam at 650°C with Medium (M) and Fast (F) steam flow rates after 1000 hour exposure

A.3 APPENDIX A3 – METAL LOSS

A.3.1 Metal loss data for T23 (Steam flow rate: 4 mm/s (L))

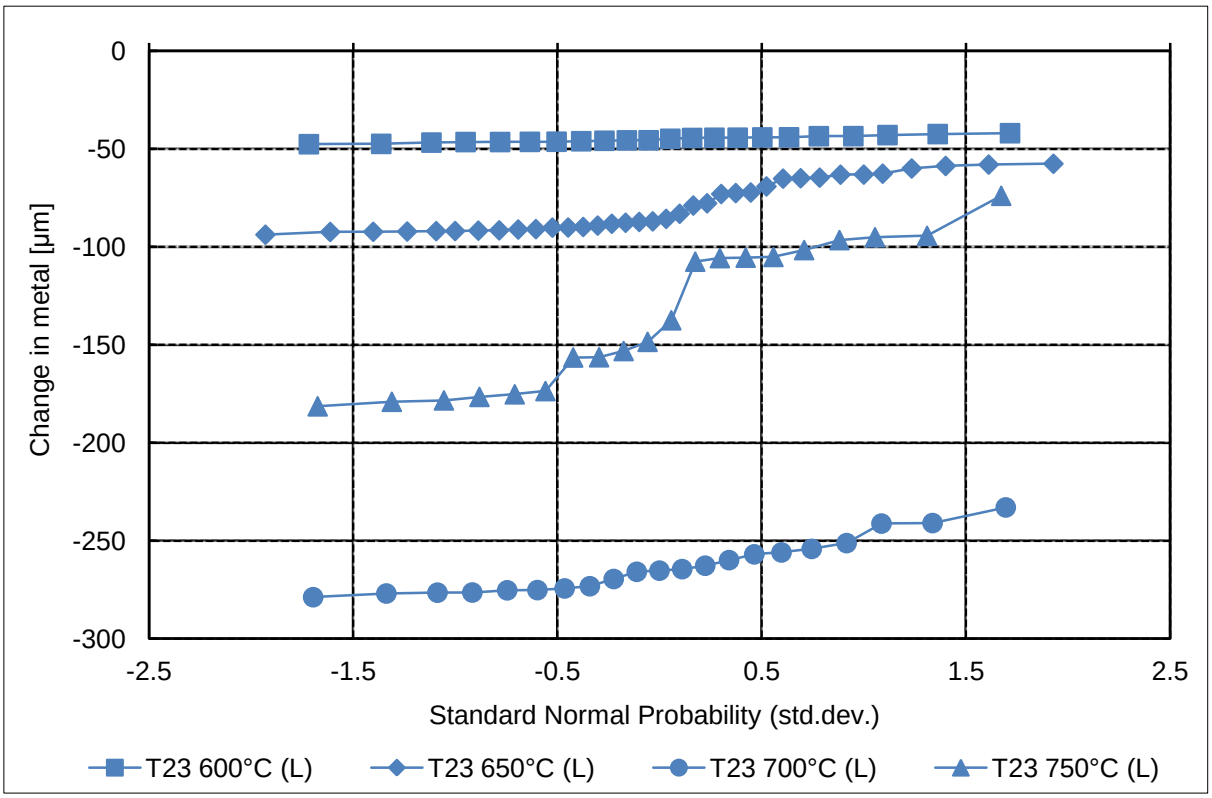

Figure A-36 Change in metal of T23 bridge – shaped specimen after 250 hours exposure in temperature between 600 – 750°C (L)

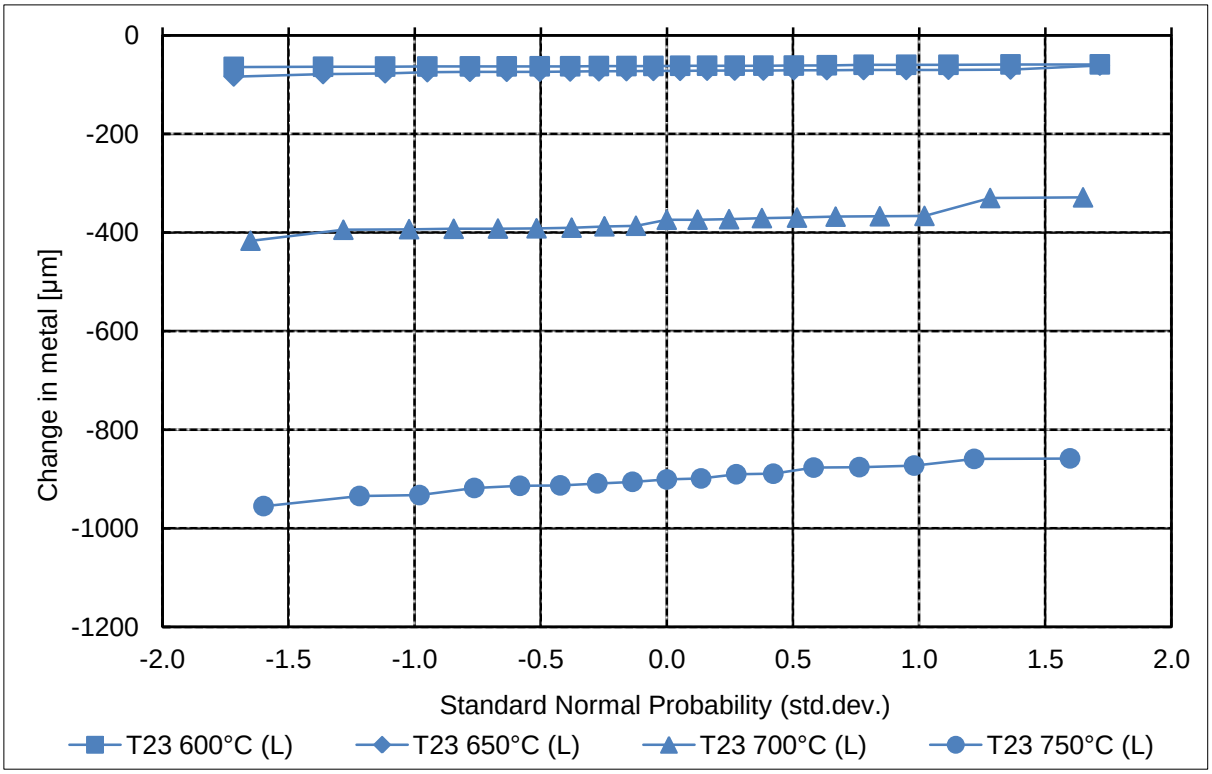

Figure A-37 Change in metal of T23 bridge – shaped specimen after 500 hours exposure in temperature between 600 – 750°C (L)

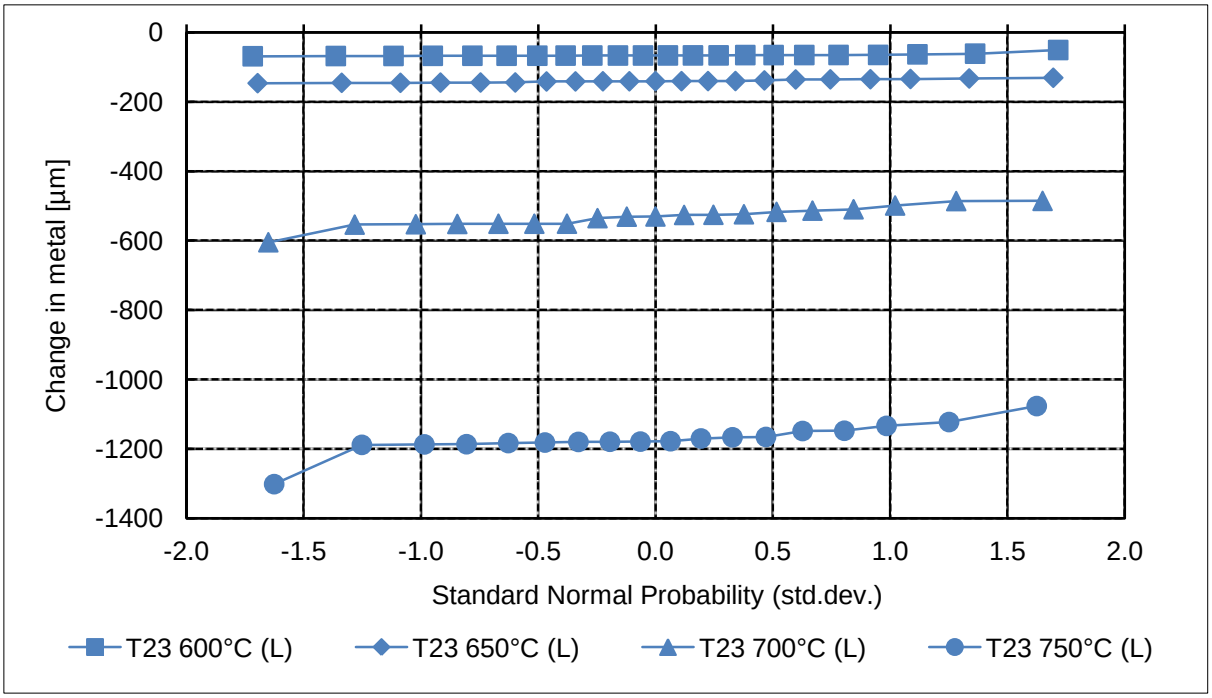

Figure A-38 Change in metal of T23 bridge – shaped specimen after 1000 hour exposure in temperature between 600 – 750°C (L)

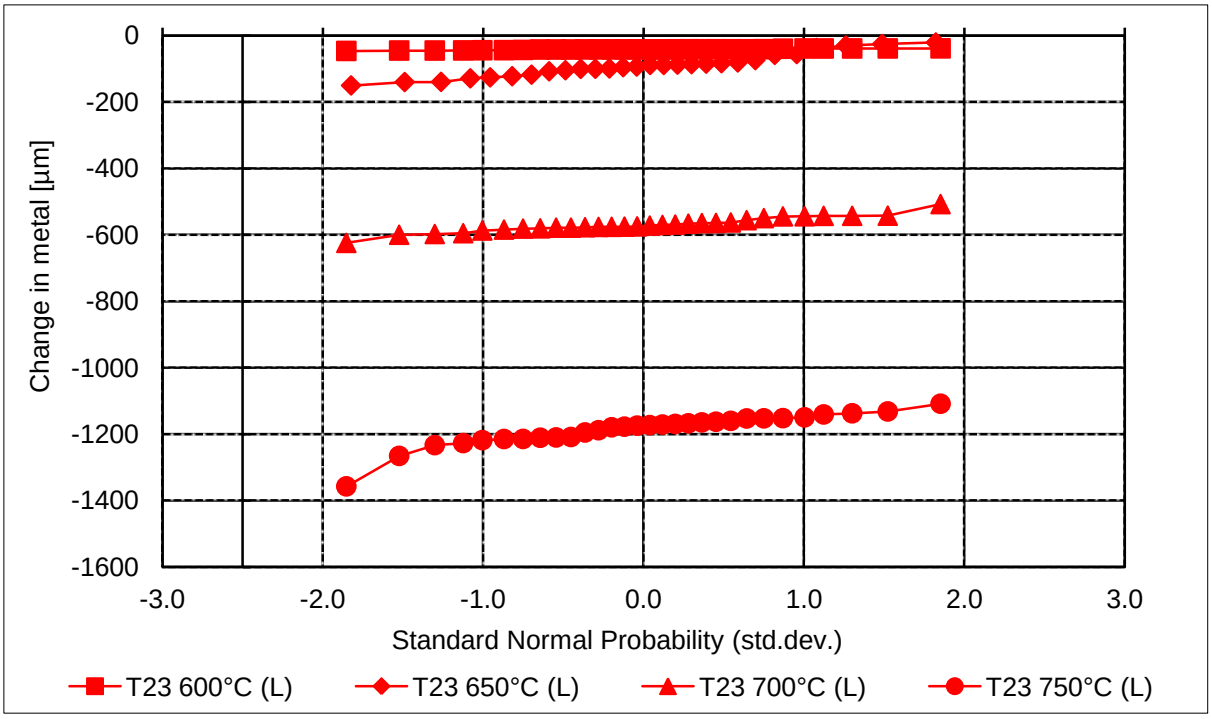

Figure A-39 Change in metal of T23 ring – shaped specimen after 1000 hour exposure in temperature between 600 – 750°C (L)

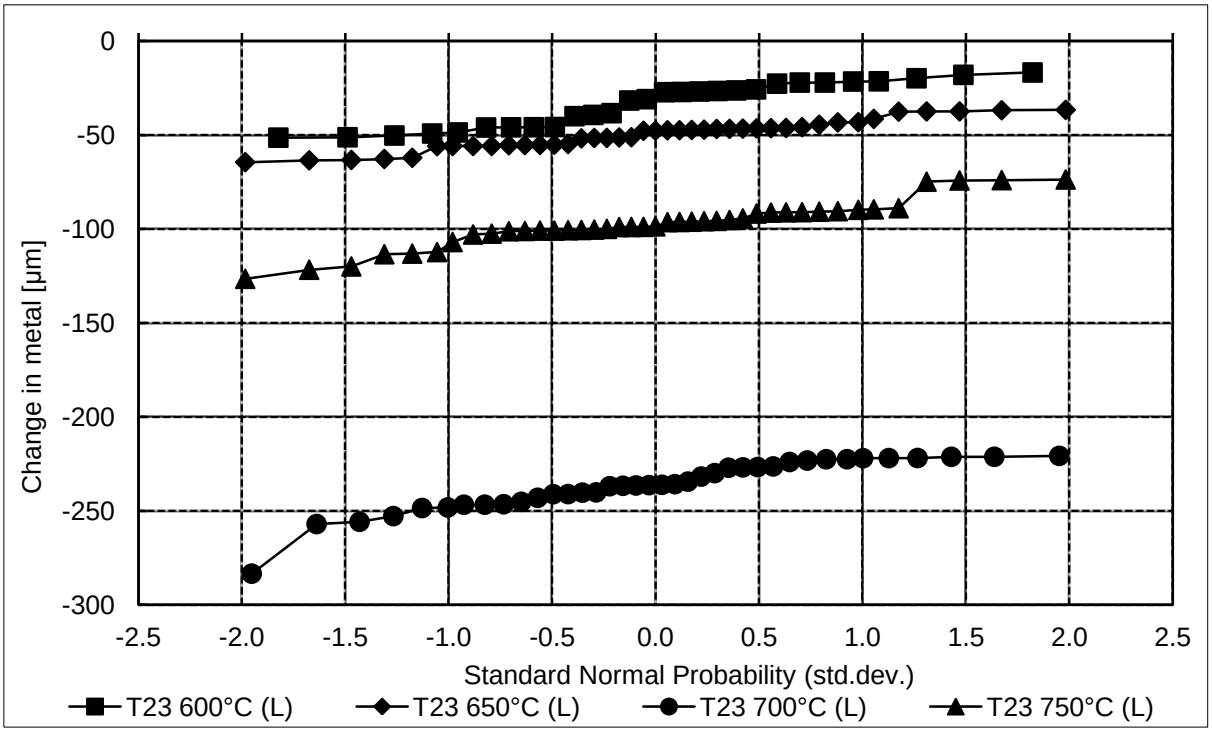

Figure A-40 Change in metal of T23 curve – shaped specimen after 250 hours exposure in temperature between 600 – 750°C (L)

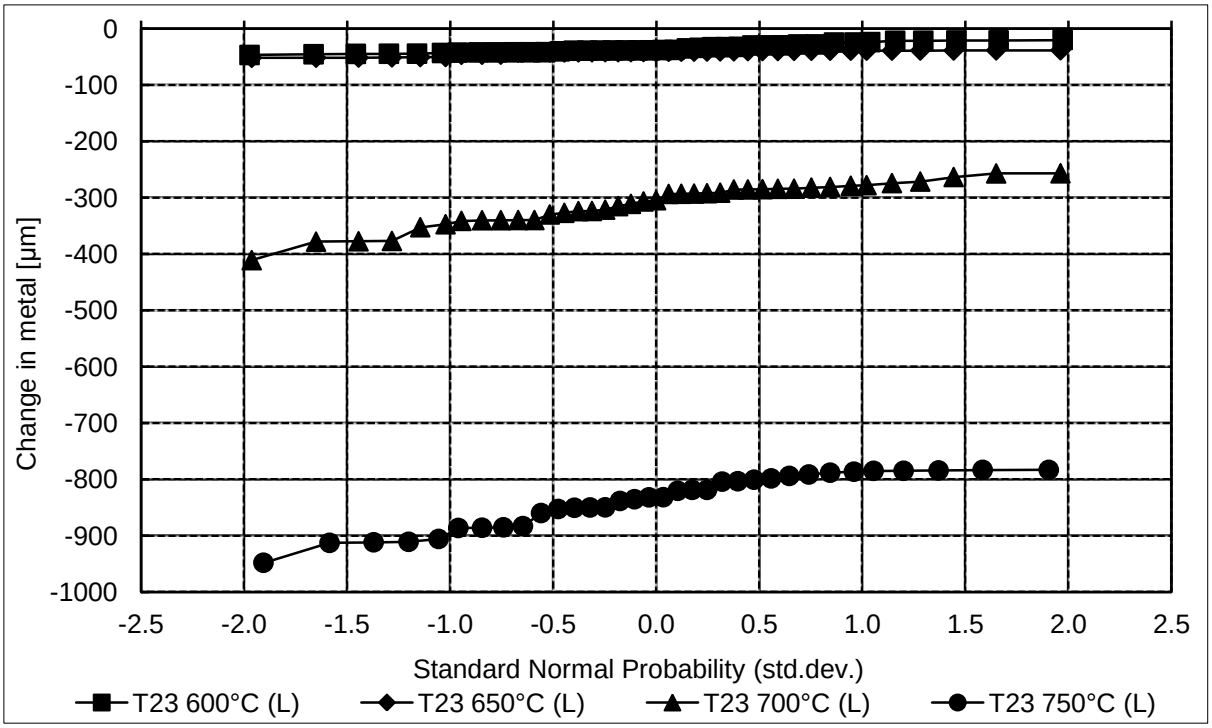

Figure A-41 Change in metal of T23 curve – shaped specimen after 500 hours exposure in temperature between 600 – 750°C (L)

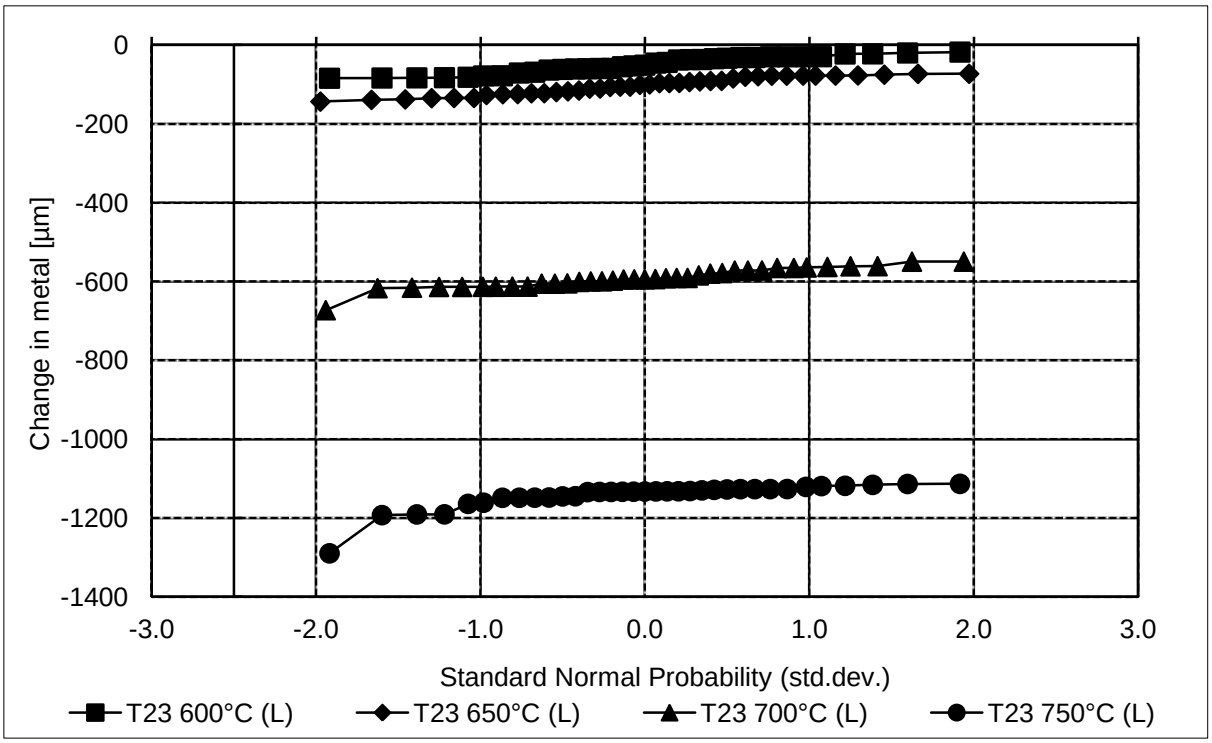

Figure A-42 Change in metal of T23 curve – shaped specimen after 1000 hour exposure in temperature between 600 – 750°C (L)

A.3.2 Metal loss data for T23 (Steam flow rate: 16 mm/s (M))

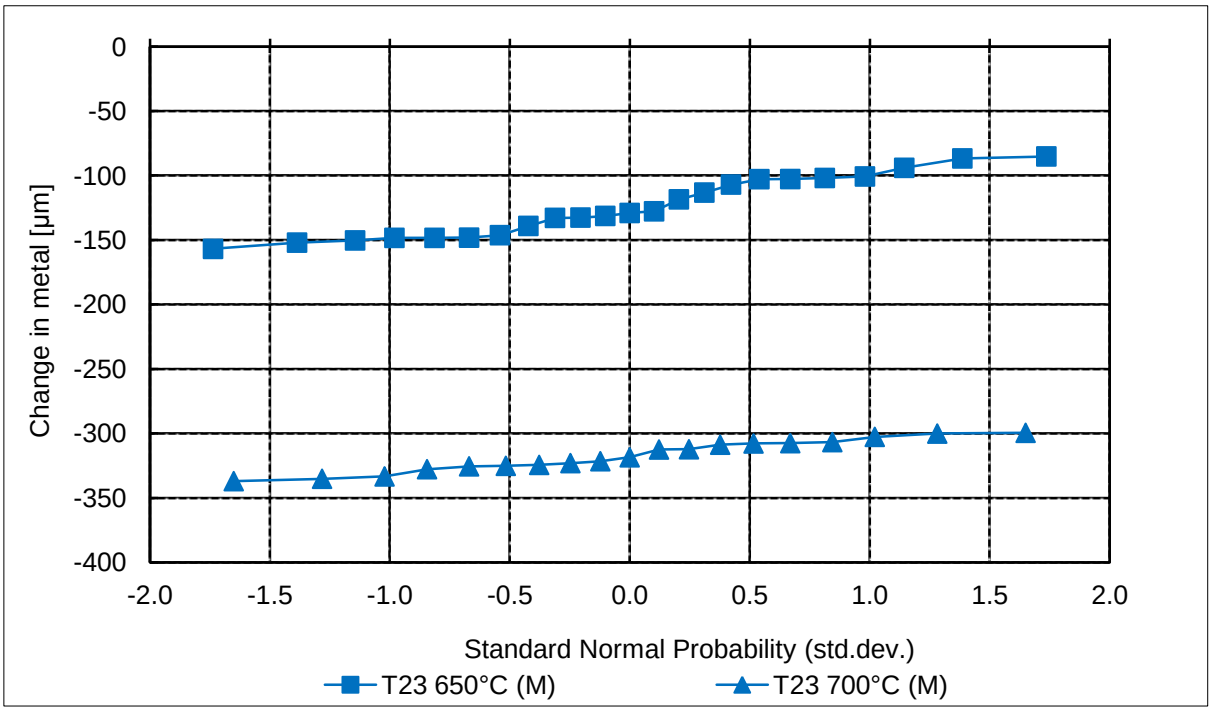

Figure A-43 Change in metal of T23 bridge – shaped specimen after 250 hour exposure To Medium steam flow (M)

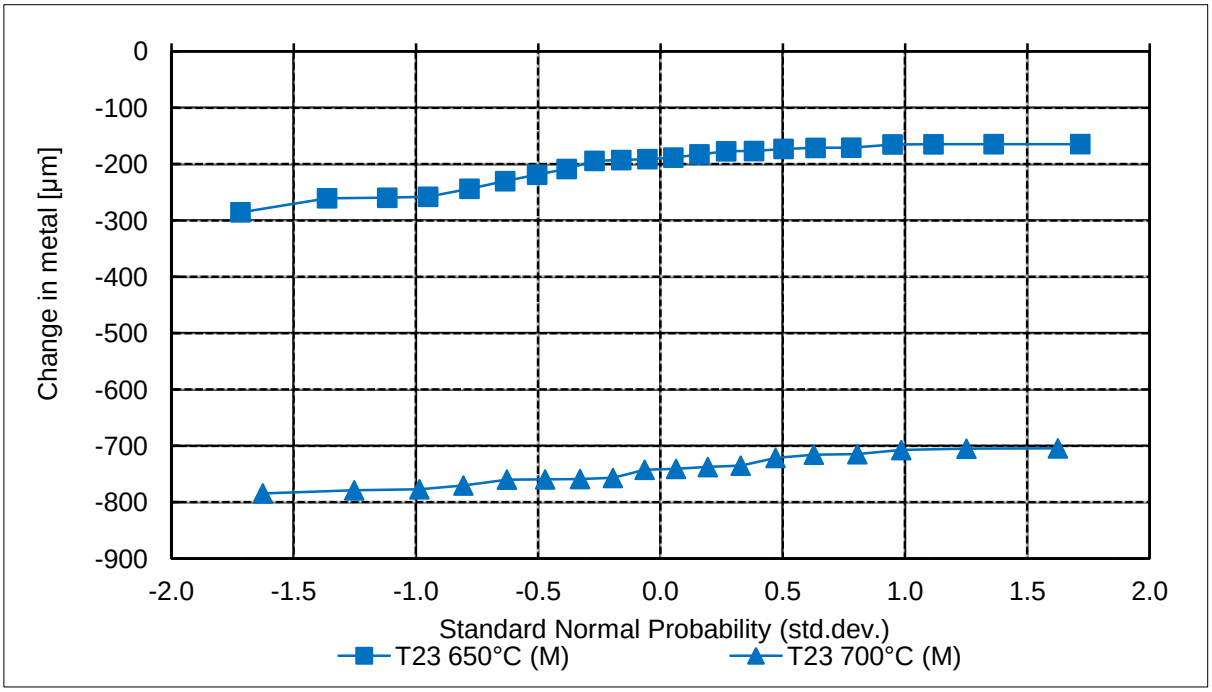

Figure A-44 Change in metal of T23 bridge – shaped specimen after 1000 hour exposure to medium steam flow (M)

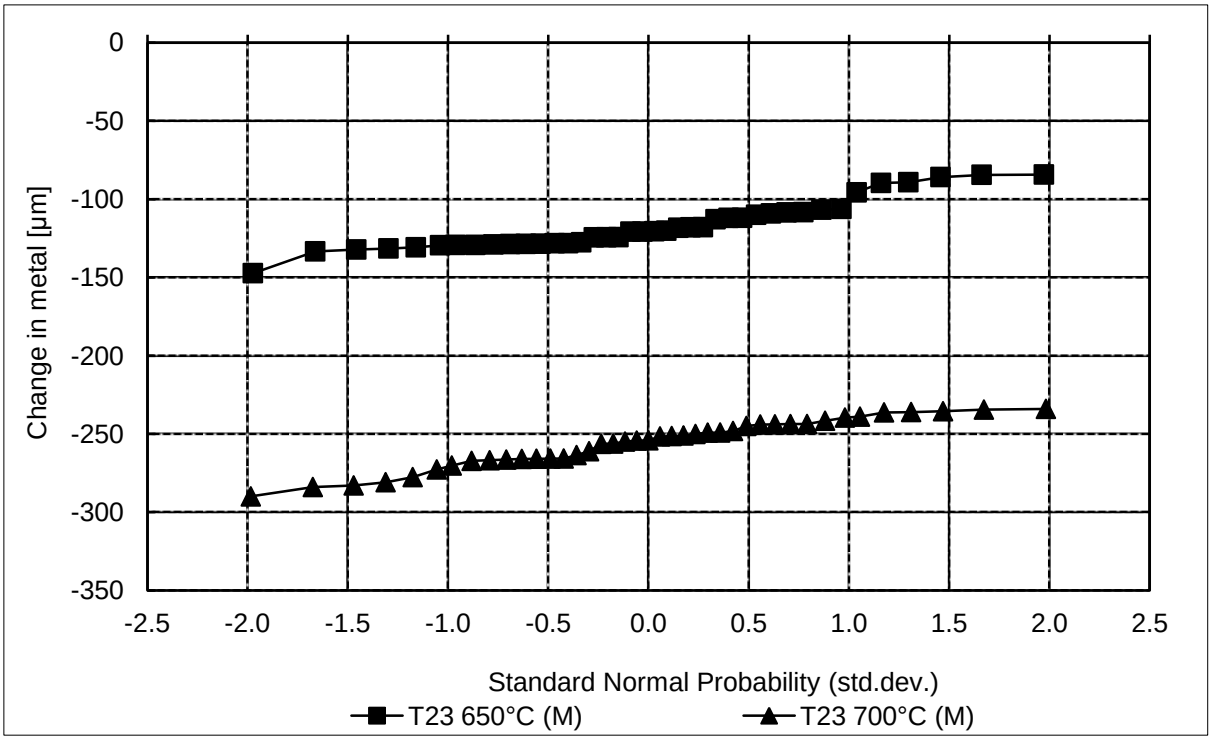

Figure A-45 Change in metal of T23 curve – shaped specimen after 250 hour exposure to medium steam flow (M)

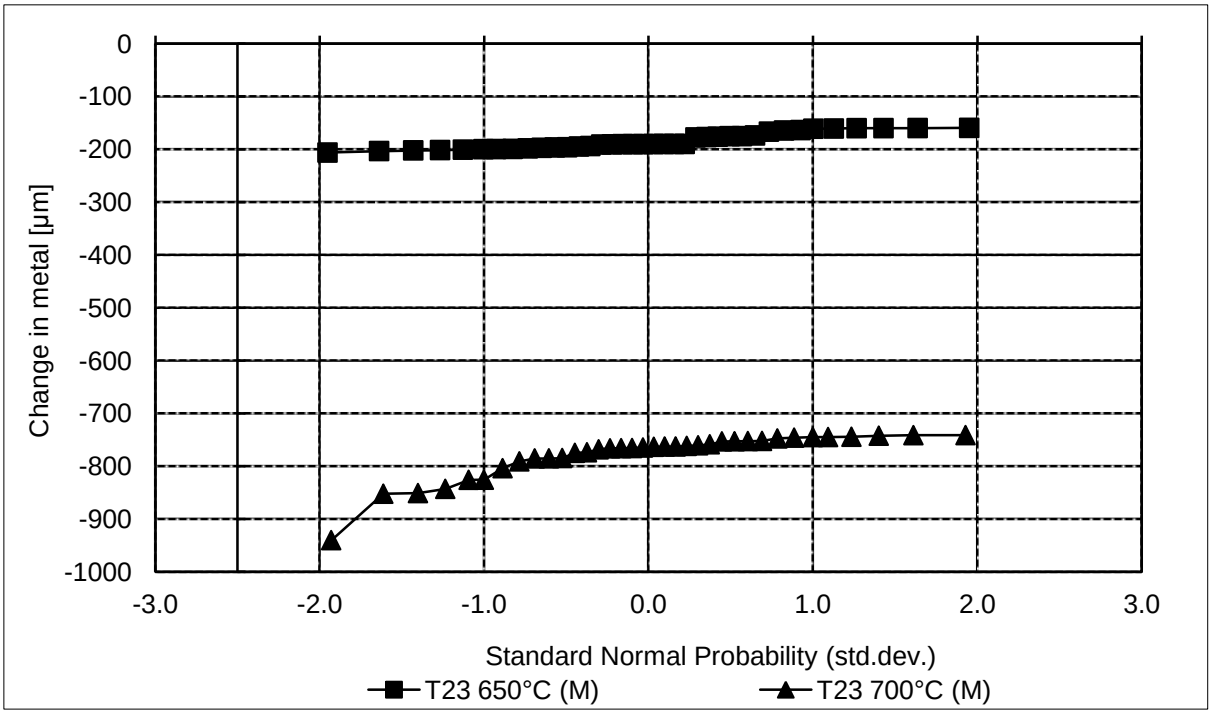

Figure A-46 Change in metal of T23 curve – shaped specimen after 1000 hour exposure to medium steam flow (M)

A.3.3 Metal loss data for T23 (Steam flow rate: 40 mm/s (H))

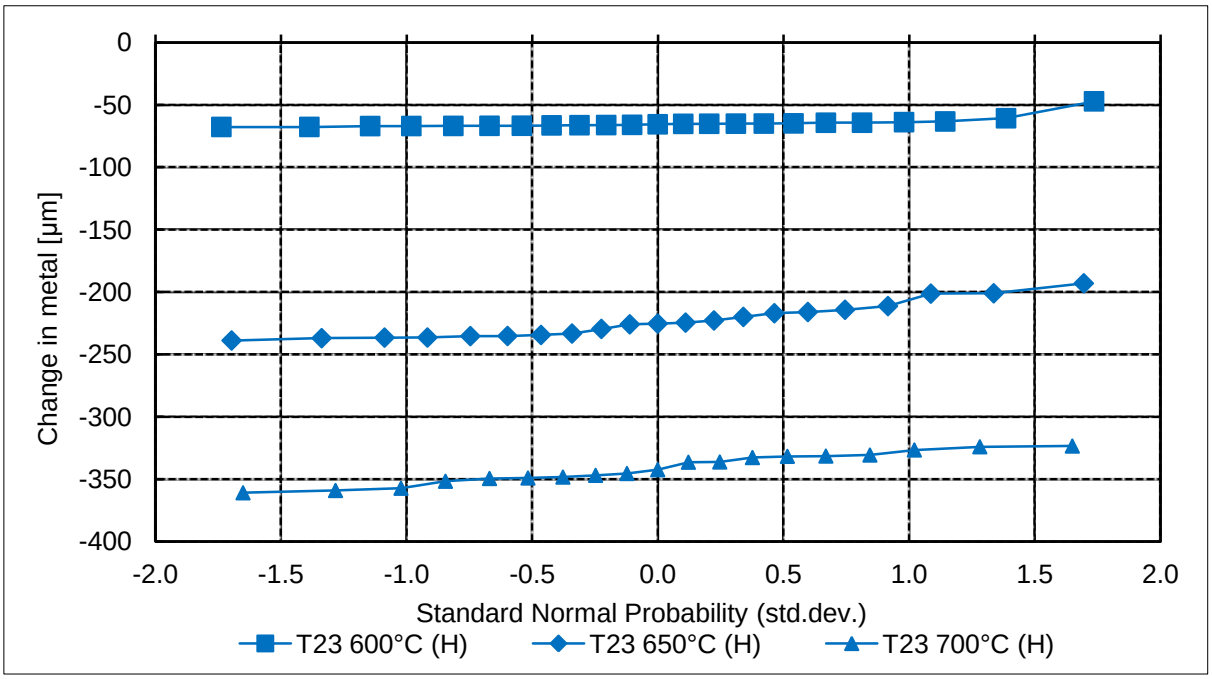

Figure A-47 Change in metal of T23 bridge – shaped specimen after 250 hour exposure to high steam flow (H)

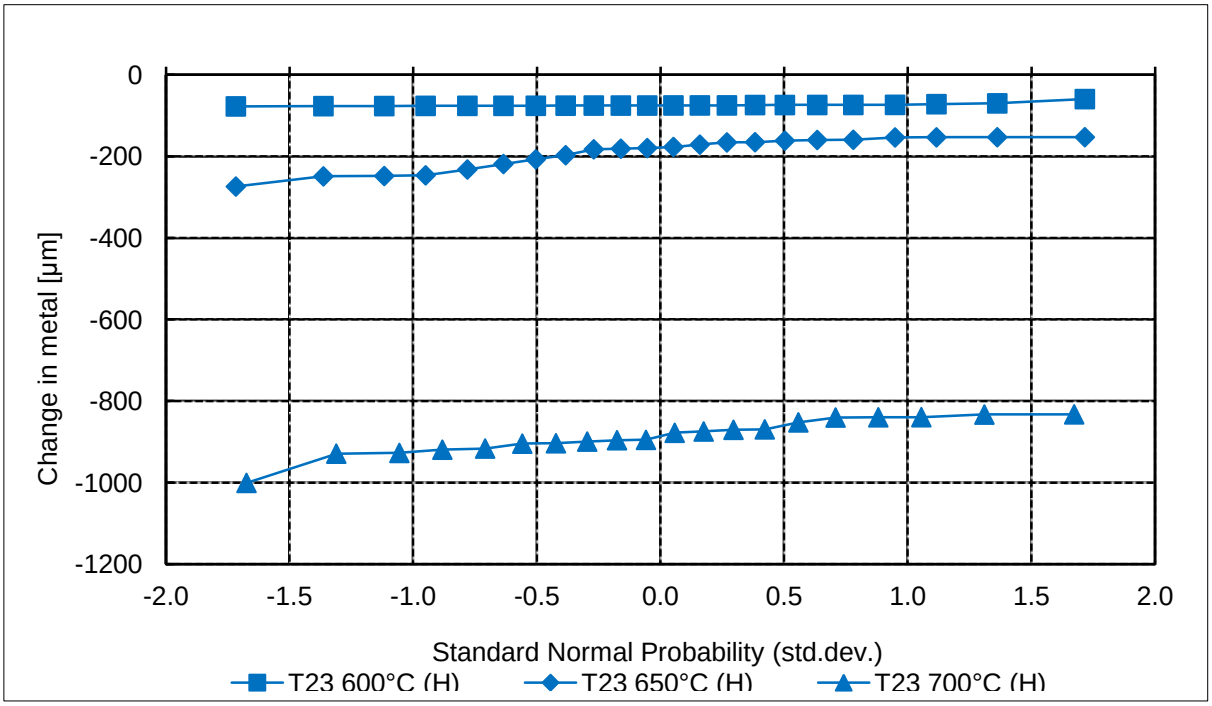

Figure A-48 Change in metal of T23 bridge – shaped specimen after 1000 hour exposure to high steam flow (H)

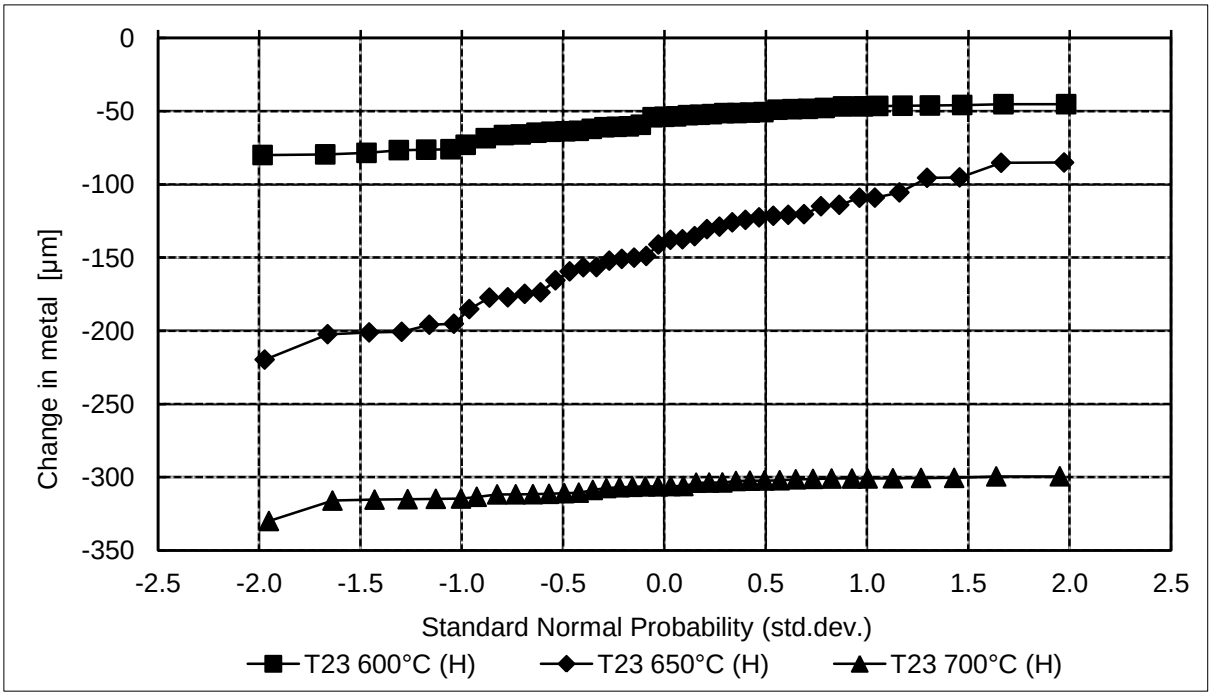

Figure A-49 Change in metal of T23 curve – shaped specimen after 250 hour exposure to high steam flow (H)

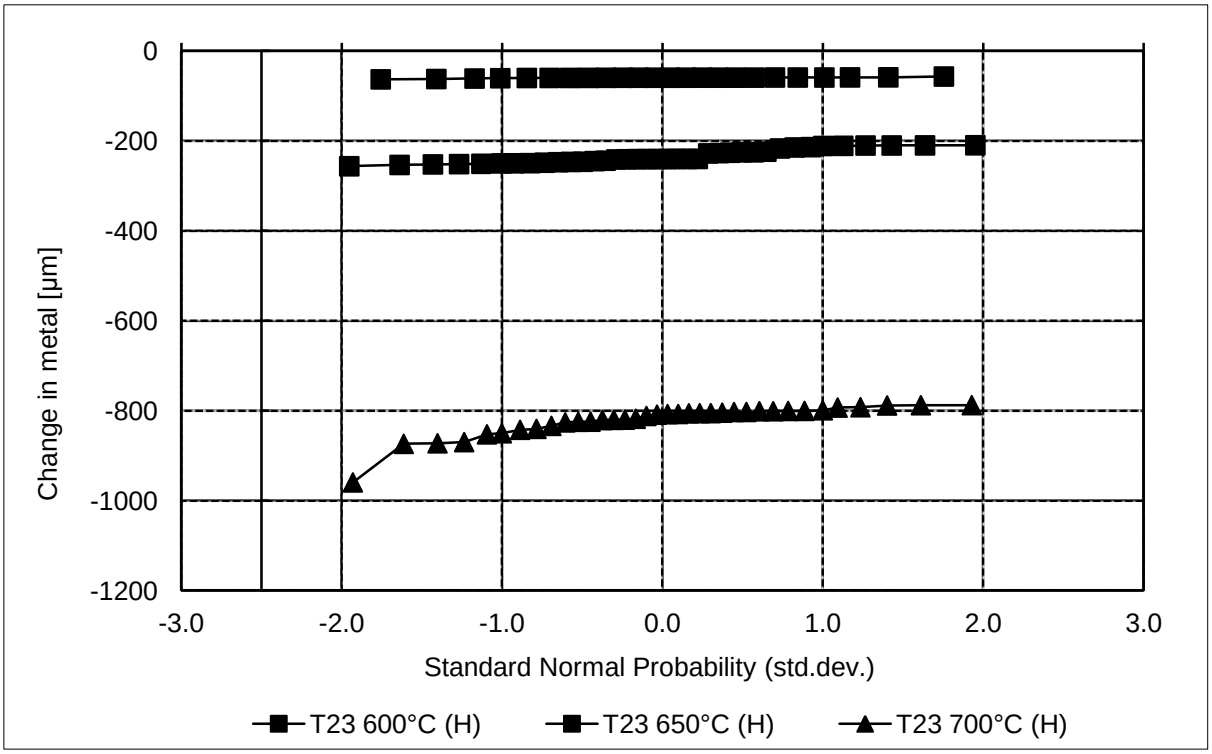

Figure A-50 Change in metal of T23 curve – shaped specimen after 1000 hour exposure to high steam flow (H)

A.3.4 Metal loss data for T92 (Steam flow rate: 4 mm/s (L))

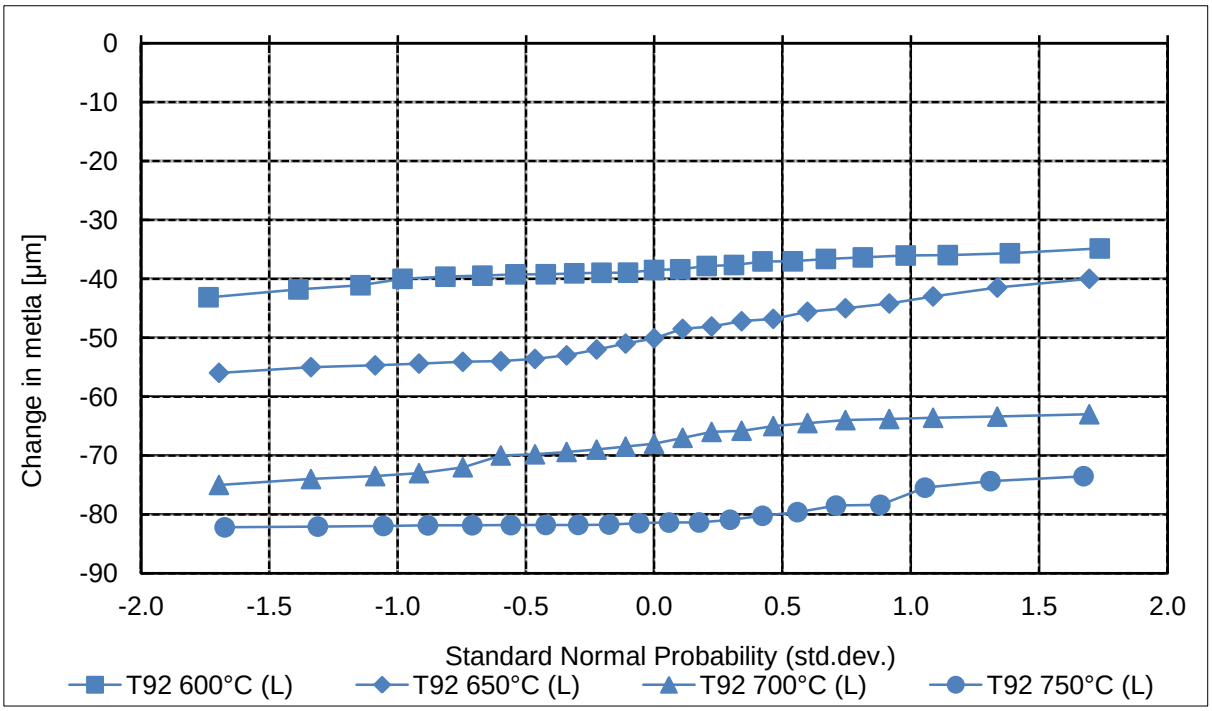

Figure A-51 Change in metal of T92 bridge – shaped specimen after 250 hour exposure in temperature between 600 – 750°C (L)

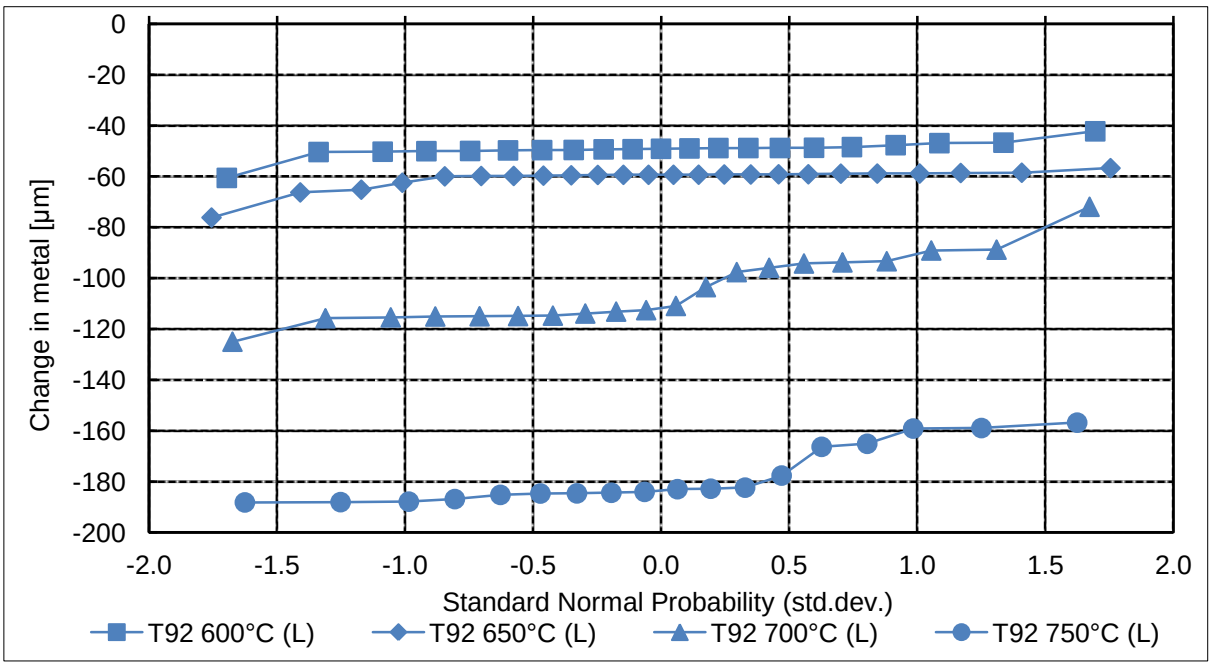

Figure A-52 Change in metal of T92 bridge – shaped specimen after 500 hour exposure in temperature between 600 – 750°C (L)

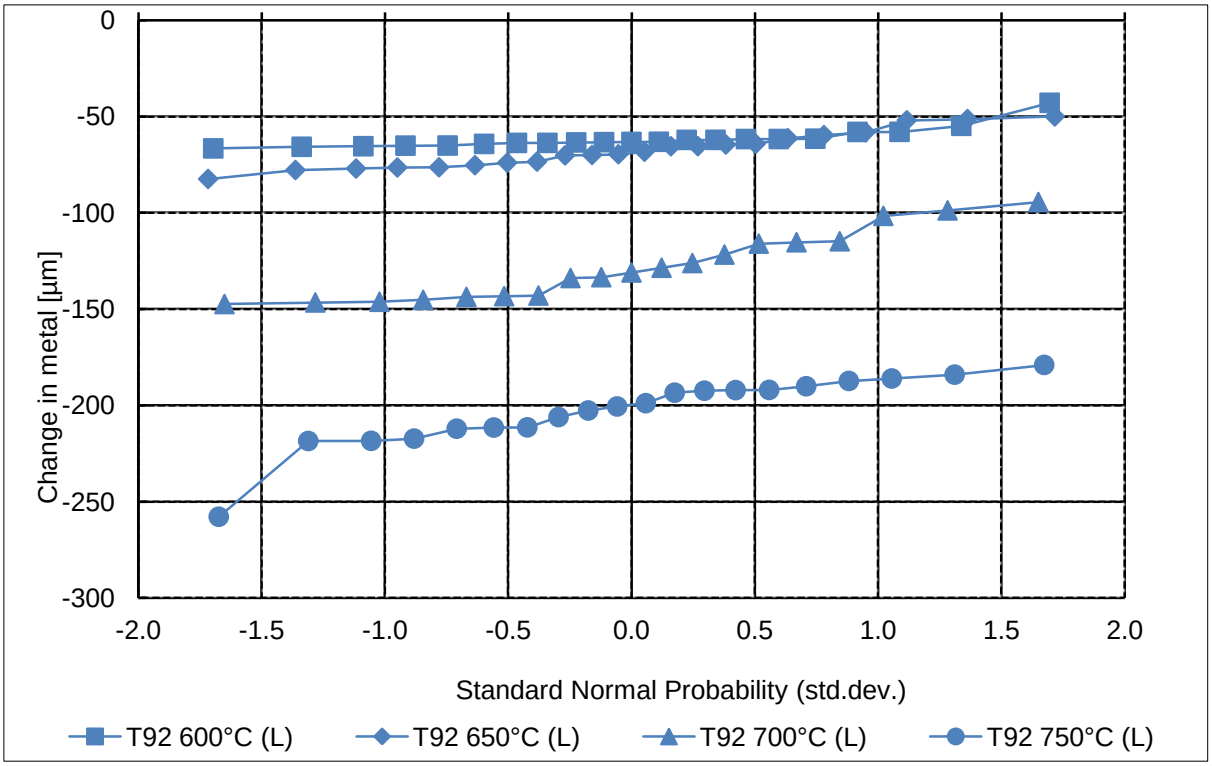

Figure A-53 Change in metal of T92 bridge – shaped specimen after 1000 hour exposure in temperature between 600 – 750°C (L)

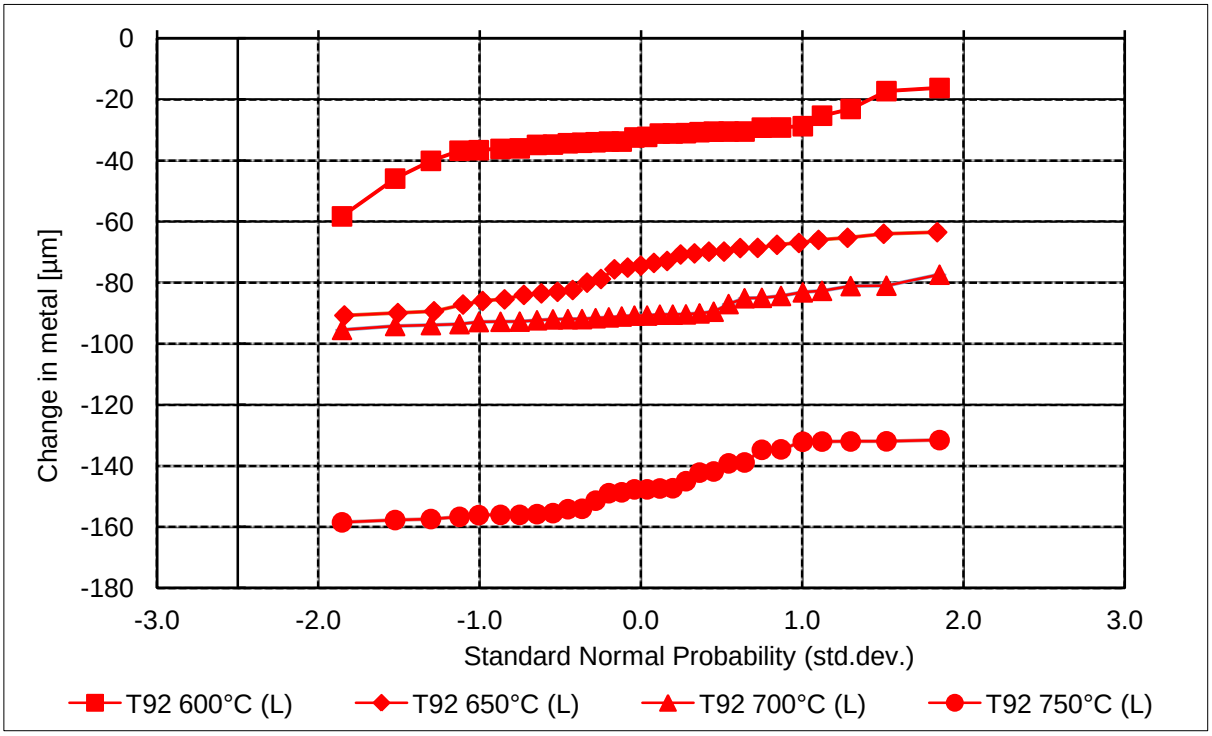

Figure A-54 Change in metal for T92 ring – shaped specimen after 1000 hour exposure in temperature between 600 – 750°C (L)

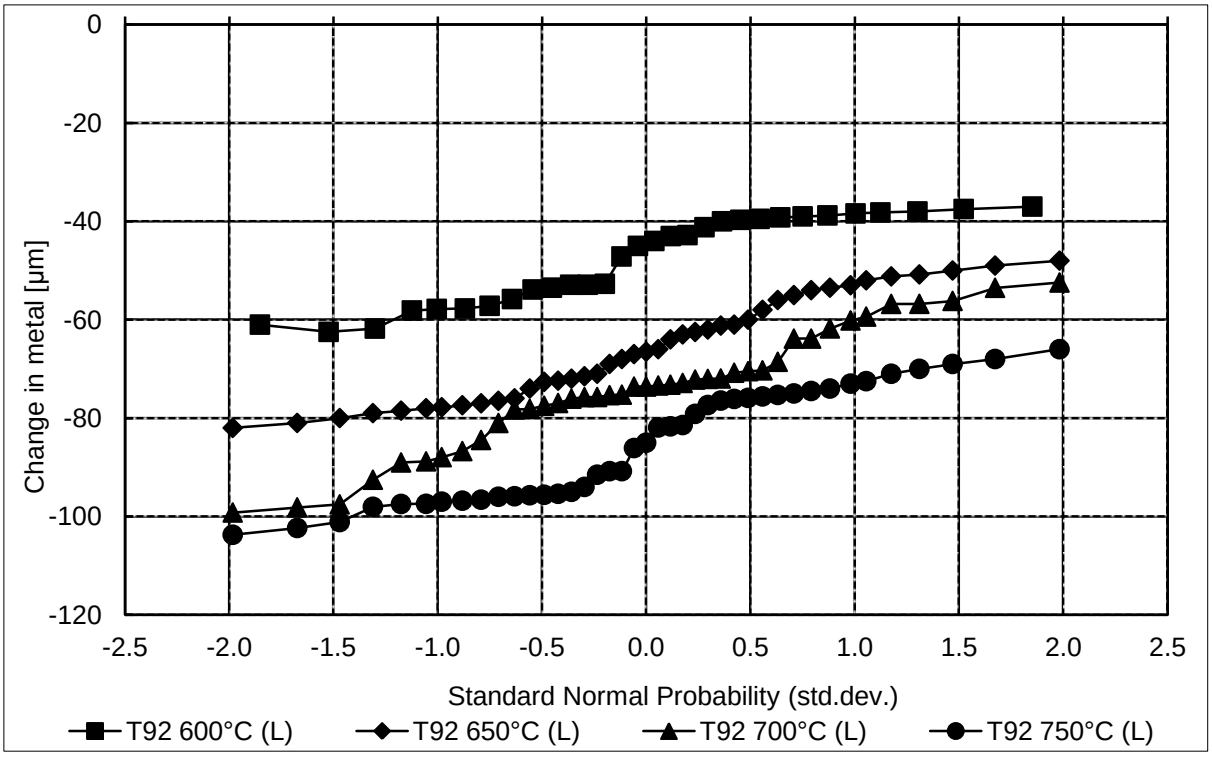

Figure A-55 Change in metal of T92 curve – shaped specimen after 250 hour exposure in temperature between 600 – 750°C (L)

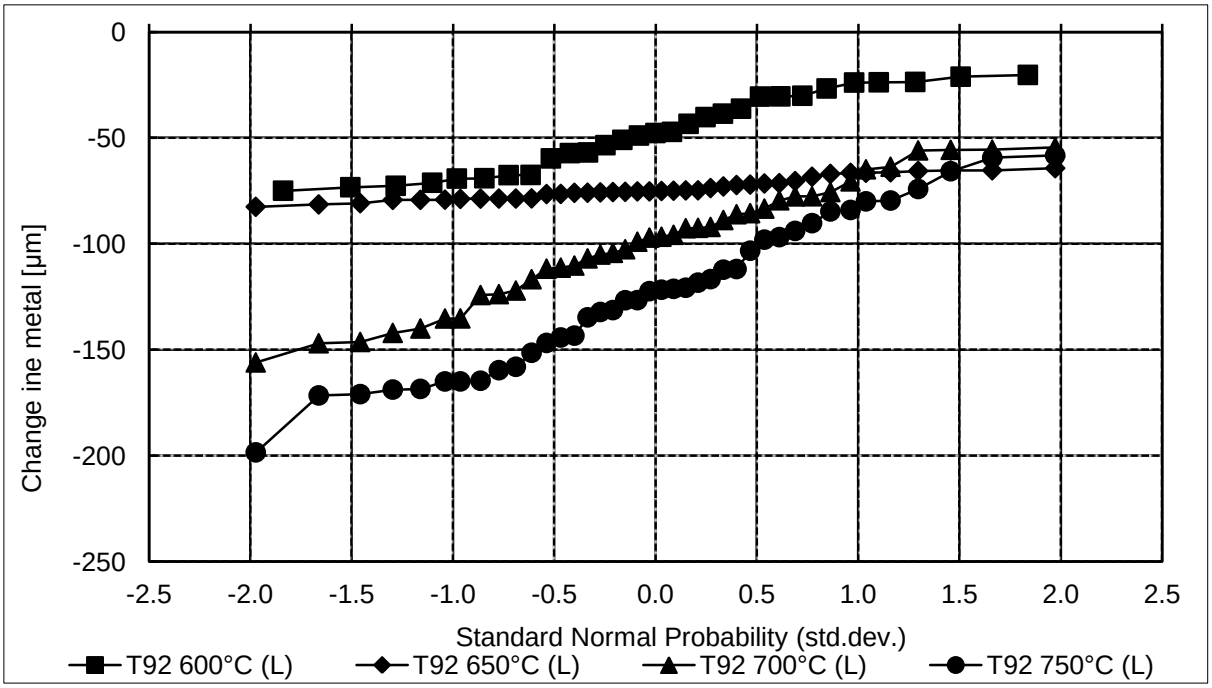

Figure A-56 Change in metal T92 curve – shaped specimen after 500 hour exposure in temperature between 600 – 750°C (L)

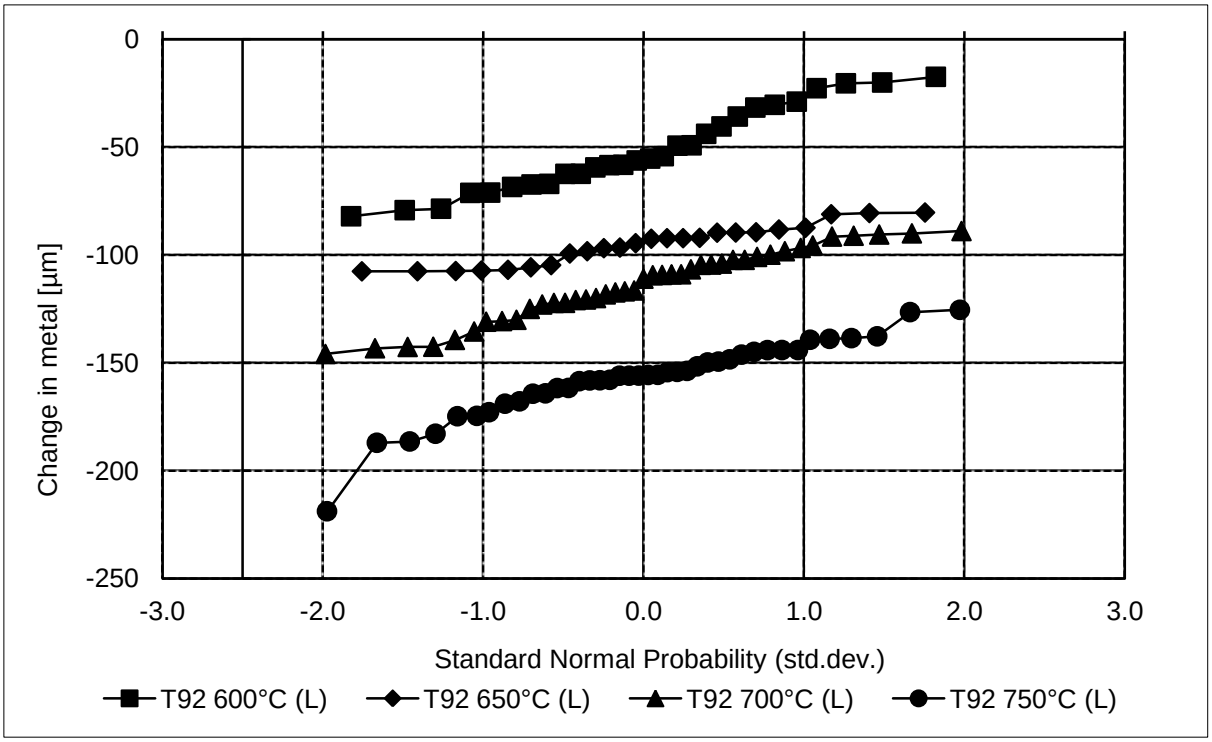

Figure A-57 Change in metal of T92 curve – shaped specimen after 1000 hour exposure in temperature between 600 – 750°C (L)

A.3.5 Metal loss data for T92 (Steam flow rate: 16 mm/s (M))

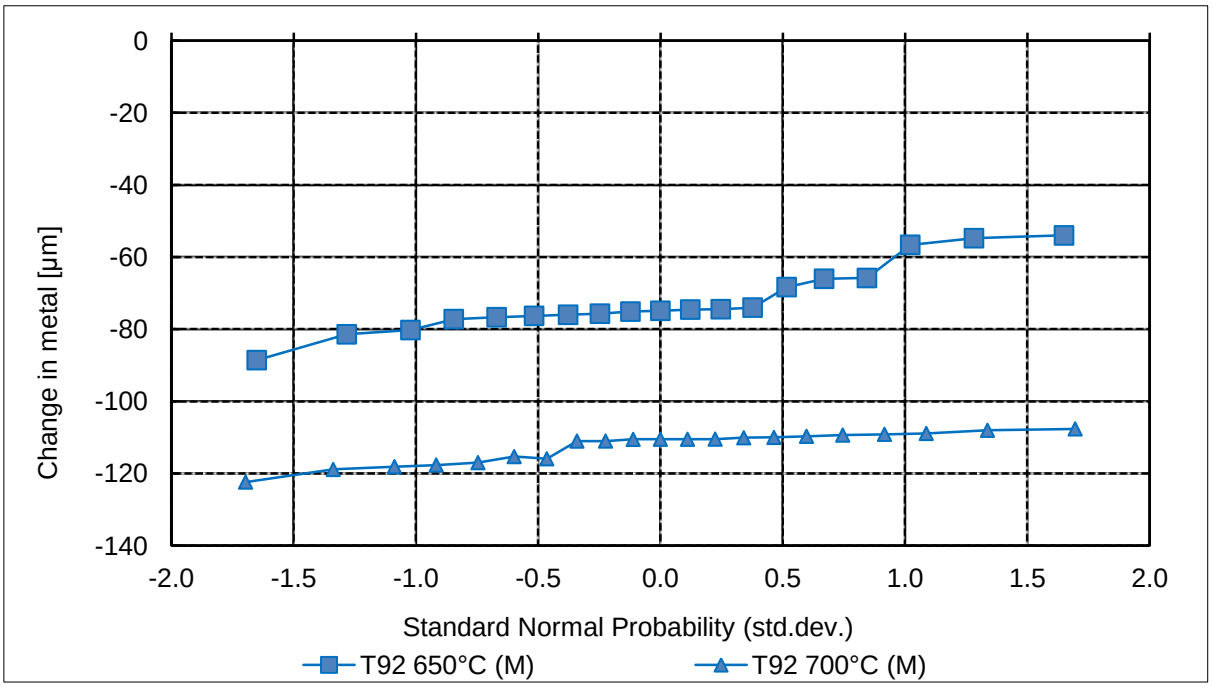

Figure A-58 Change in metal of T92 bridge – shaped specimen after 250 hour exposure to medium steam flow (M)

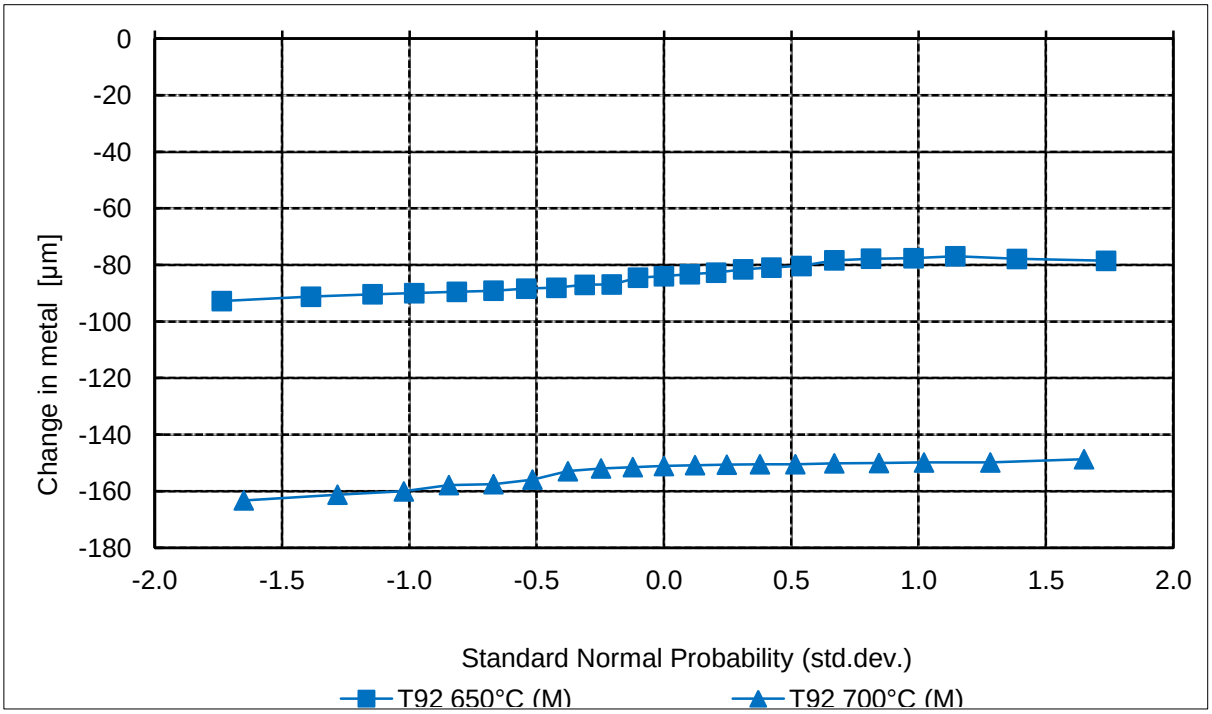

Figure A-59 Change in metal of T92 bridge – shaped specimen after 1000 hour exposure to medium steam flow (M)

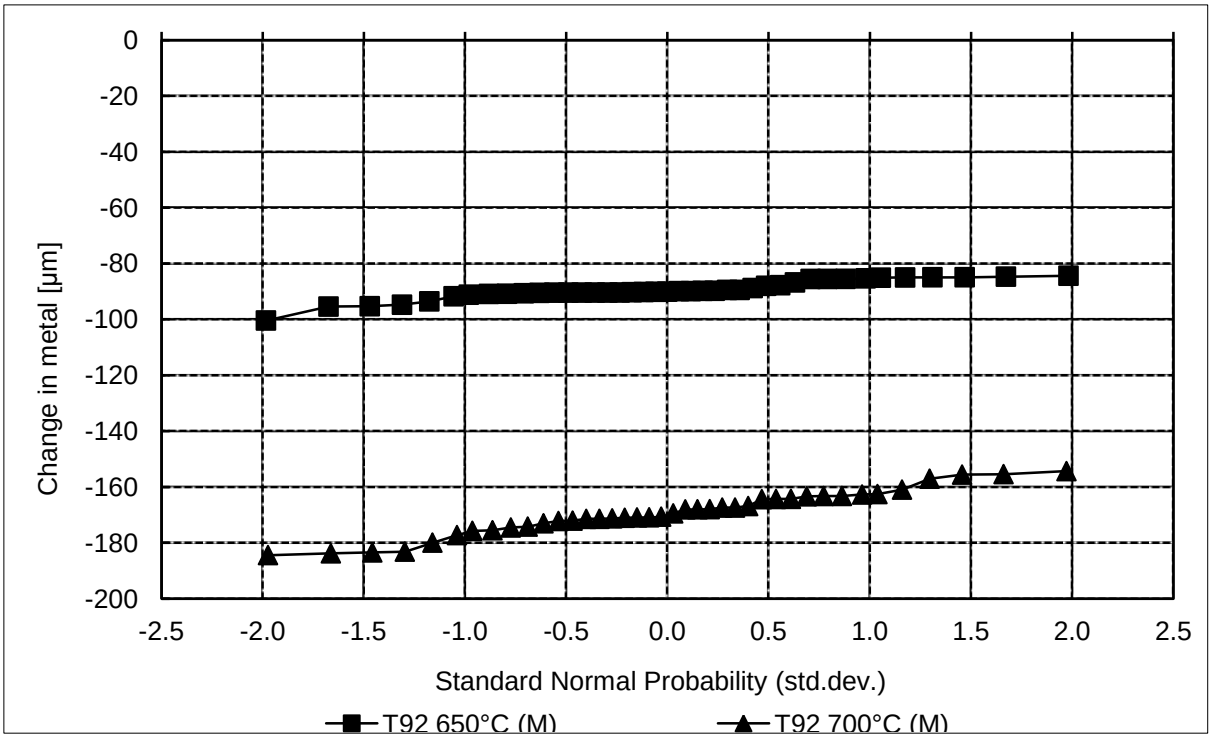

Figure A-60 Metal loss of T92 curve – shaped specimen after 250 hour exposure to medium steam flow (M)

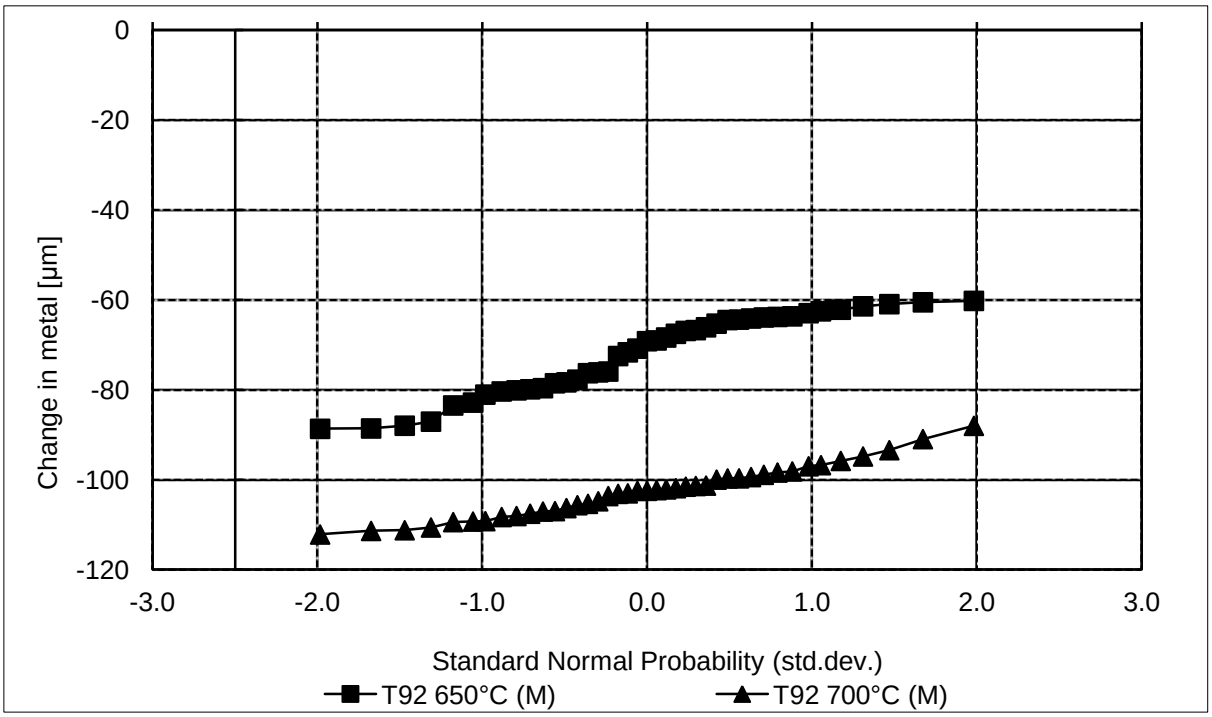

Figure A-61 Change in metal of T92 curve – shaped specimen after 1000 hour exposure to medium steam flow (M)

A.3.6 Metal loss data for T92 (Steam flow rate: 40 mm/s (H))

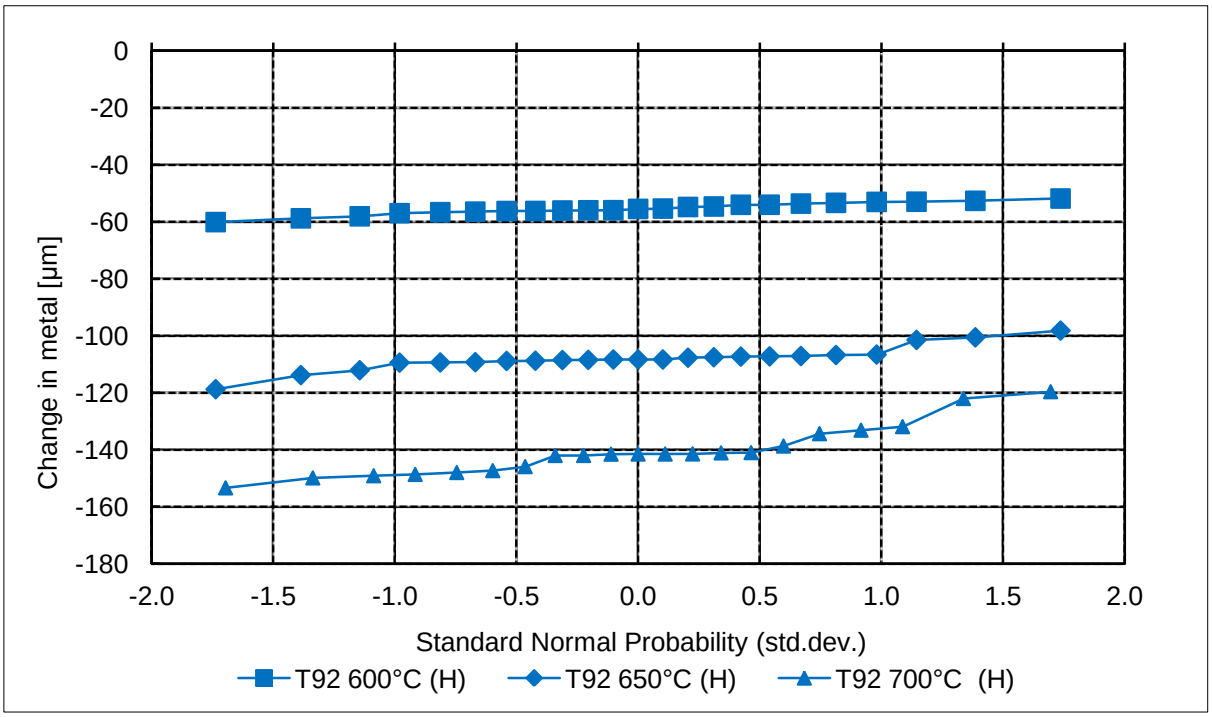

Figure A-62 Change in metal of T92 bridge – shaped specimen after 250 hour exposure to high steam flow (H)

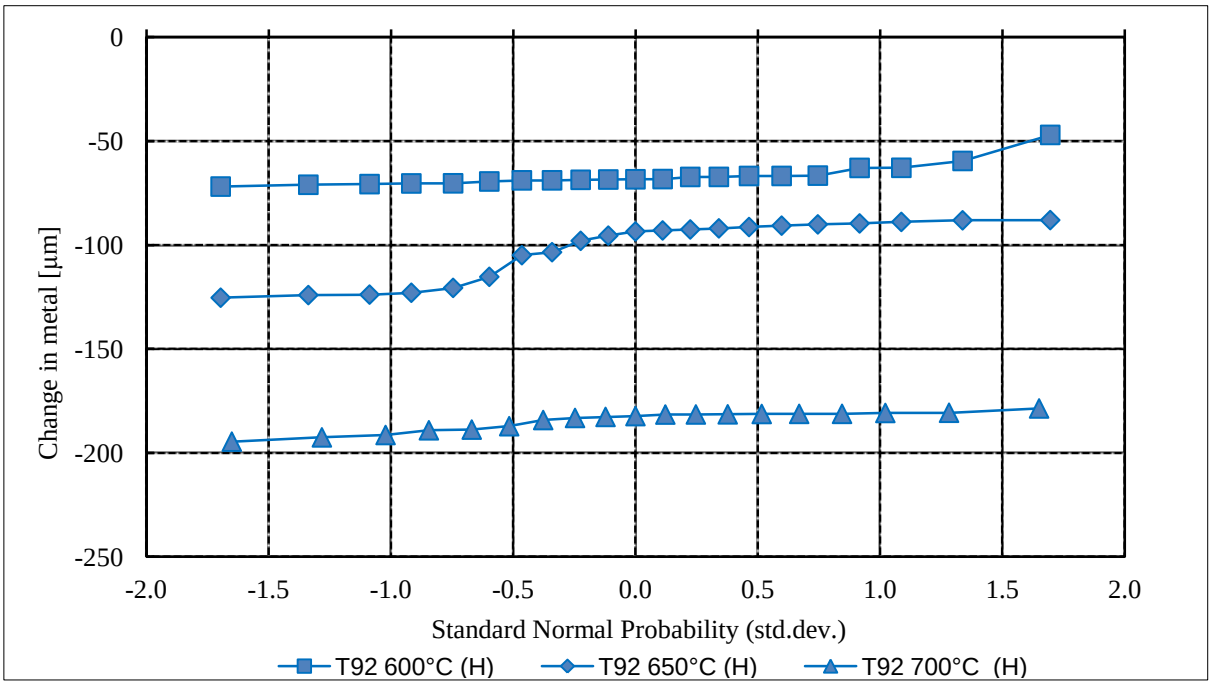

Figure A-63 Change in metal of T92 bridge – shaped specimen after 1000 hour exposure To high steam flow (H)

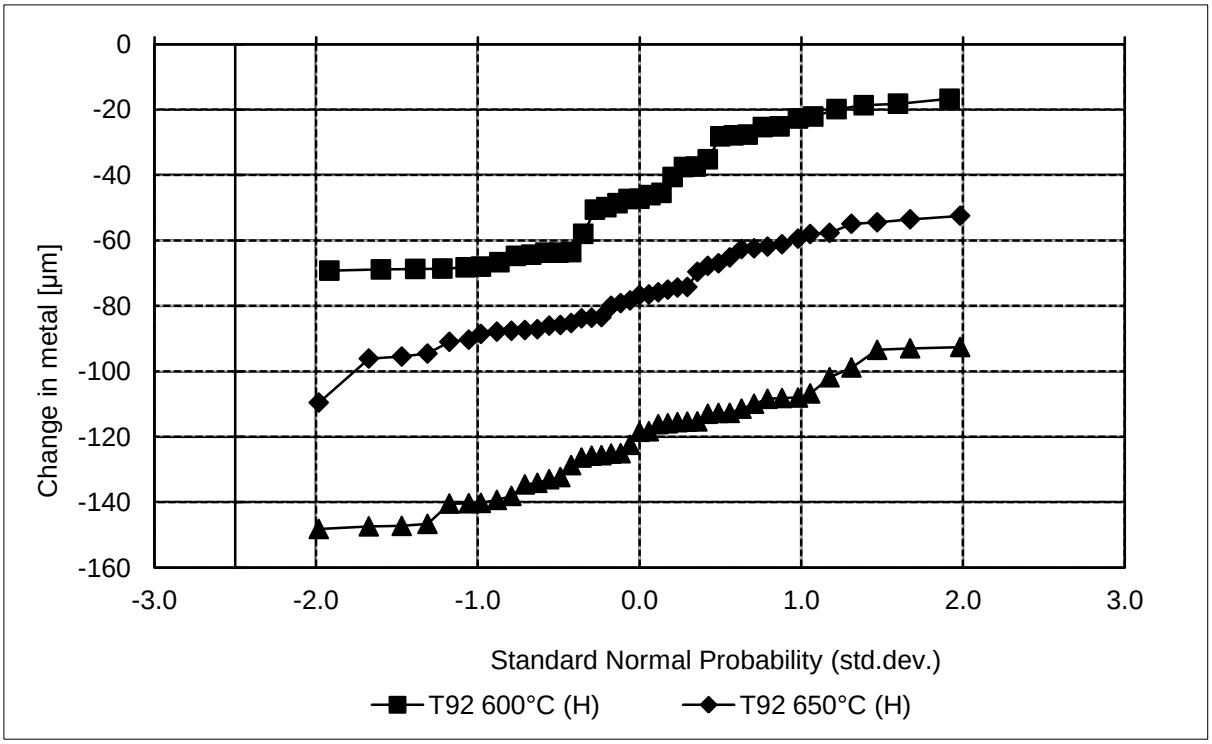

Figure A-64 Change in metal of T92 curve – shaped specimen after 250 hour exposure to high steam flow (H)

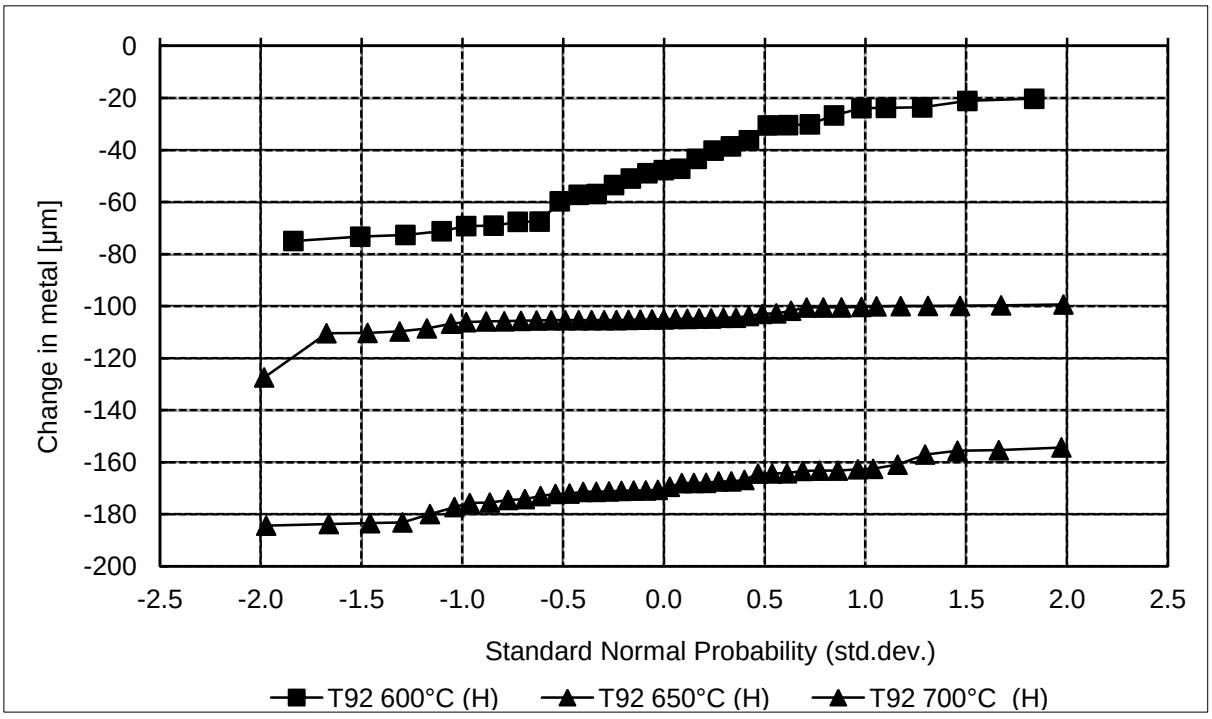

Figure A-65 Change in metal of T92 curve – shaped specimen after 1000 hour exposure to high steam flow (H)

Appendix B

B.1 MODELLING (Mass change)

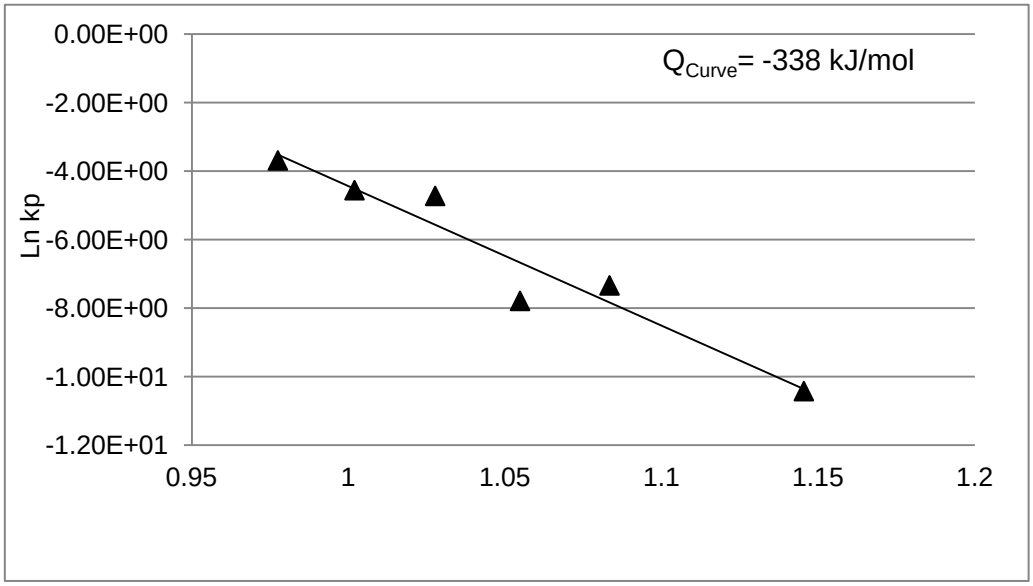

Figure B-1 Arrhenius plot for T23 steel exposed to steam in temperature between 600 – 750°C (L) (parabolic)

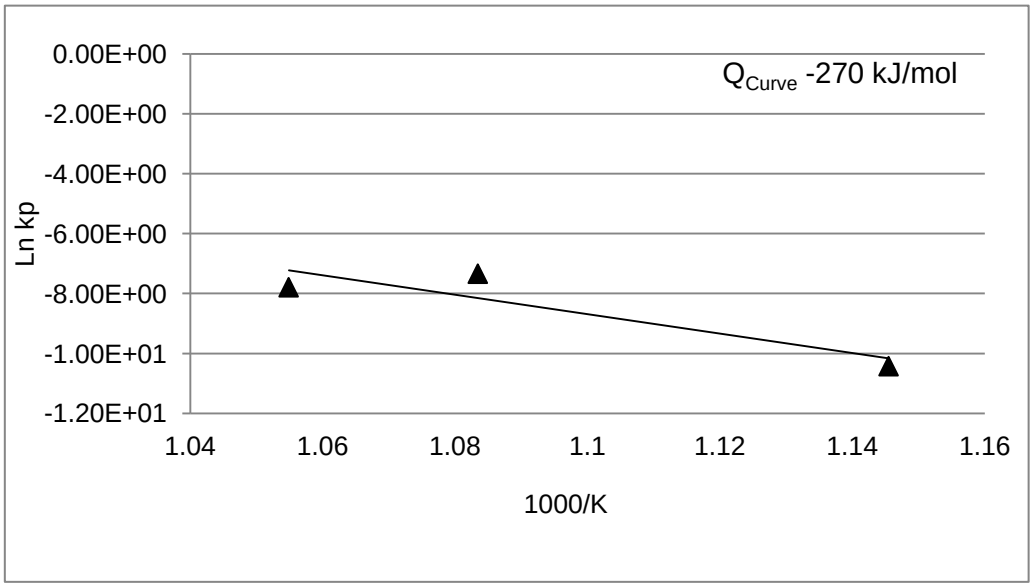

Figure B-2 Arrhenius plot for T23 steel exposed to steam in temperature between 600 – 675°C (L) (parabolic)

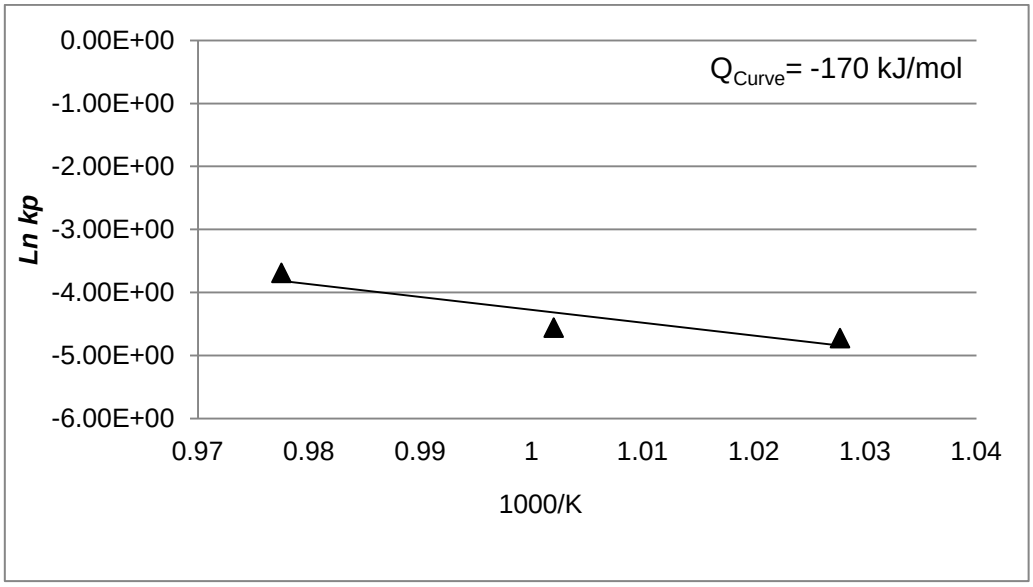

Figure B-3 Arrhenius plot for T23 steel exposed to steam in temperature between 700 – 750°C (L) (parabolic)

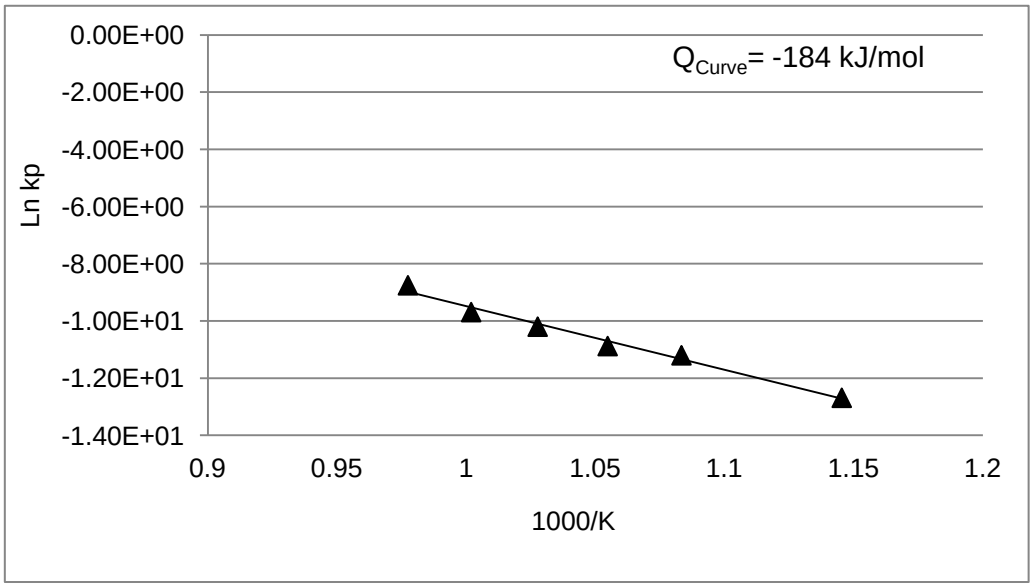

Figure B-4 Arrhenius plot for T23 steel exposed to steam in temperature between 600 – 750°C (L) (linear)

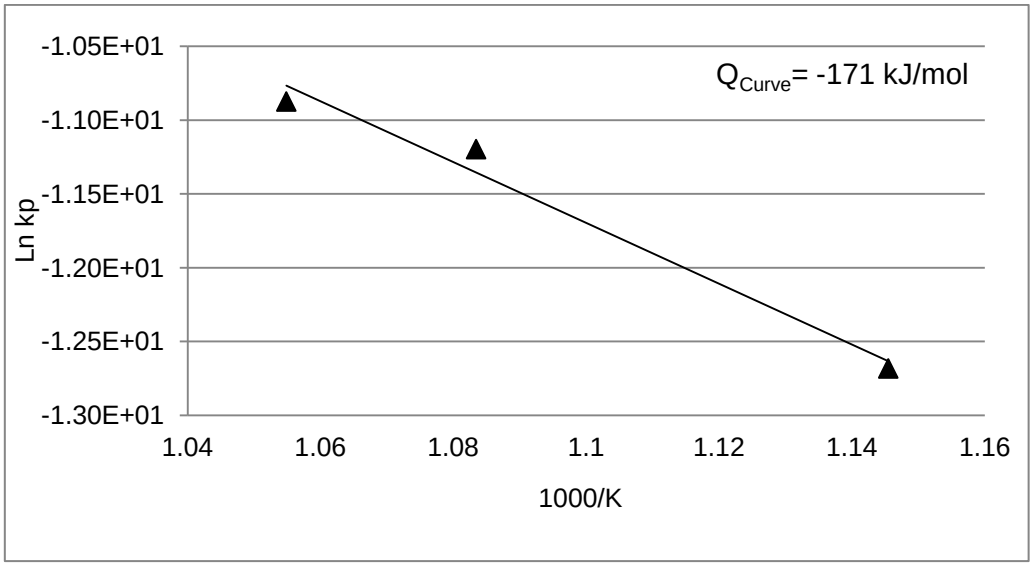

Figure B-5 Arrhenius plot for T23 steel exposed to steam in temperature between 600 – 650°C (L) (linear)

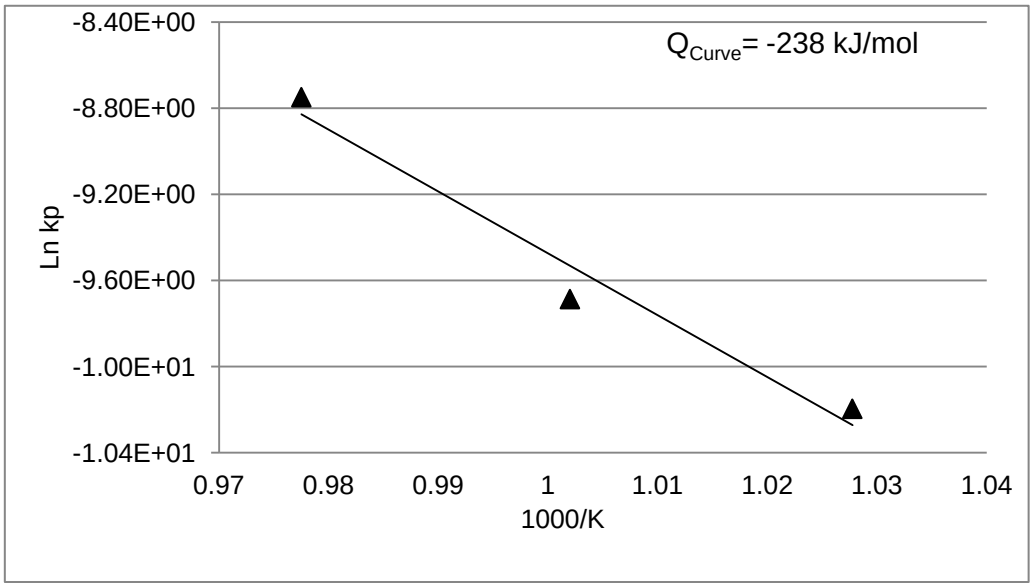

Figure B-6 Arrhenius plot for T23 steel exposed to steam in temperature between 700 – 750°C (L) (linear)

Appendix C

C.1 List of publication

1. Co-author of Conference paper entitled: “Oxidation of heat exchanger alloys in steam at 550 – 750°C”, 1st International Conference on Materials for Energy, 04-08.07.2010, Karlsruhe, Germany, (Presented by Dr T. Dudziak)
2. Co-author of Conference paper entitled: “Characterisation of oxide scales developed on the high temperature resistant alloys in pure steam environment”; 8th International Conference on Microscopy of Oxidation, 11-13 April 2011, University of Liverpool, United Kingdom, (Poster presented by M. Lukaszewicz)
3. Co-author of Conference paper entitled: “Steam oxidation of superheater/reheater alloys: impact of steam flow rates and specimen geometries”; EuroCorr 2011**,** 4-8 September 2011, Stockholm International Fairs, Sweden, (Presented by M. Lukaszewicz)
4. Co-author of Conference poster entitled: “Steam oxidation of superheater / reheater alloys: impact of steam flow rates and specimen geometries”, Gordon Research Conference (GRC) on High Temperature Corrosion (2011), 24-29 July 2011, Colby-Sawyer College, New London, USA, (Presented by Dr N. Simms)
5. Co-author of Article entitled: “Performance of T23 and T347HFG steels in steam oxidation”; being prepared for Oxidation of Metals
6. Co-author of Article entitled: “Analysis of the high temperature steam oxidation of superheater materials used in coal-fired boilers ”; being prepared for Corrosion Science
7. Co-author of Article entitled “Steam oxidation of T347HFG, Super 304H and HR3C; Analysis of the significance of the steam flow rate and the specimen surface finish”, (being prepared for Corrosion Science)

8. Co-author of Conference paper entitled: “Influence of the steam flow rates and specimens orientation on steam oxidation of ferritic and austenitic steels at 650°C and 700°C” 8th International Symposium on High-Temperature Corrosion and Protection of Materials (HTCPM8), 20 - 25 May 2012, LES EMBIEZ, France (accepted for poster presentation)
9. Co-author of Article entitled: “Steam oxidation behaviour of the selected alloys in 100 % steam for 500 hours at 675 and 725°C”, (being prepared by Dr T. Dudziak)
10. Co-author of Article entitled: “Steam oxidation of heat exchanger alloys at 700 – 800°C”, (being prepared by Dr T. Dudziak)